How to build a better battery through nanotechnology *p. 1044*

Making gene therapy affordable *p. 1059*

Colitis risk determined by genes and microbes *p. 1116*

Science

$15
27 MAY 2016
sciencemag.org

AAAS

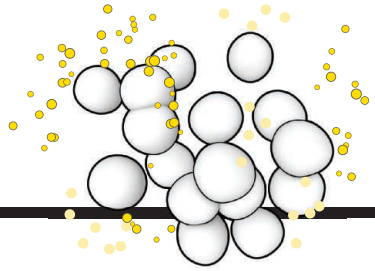


THE BIRTH OF CLOUDS

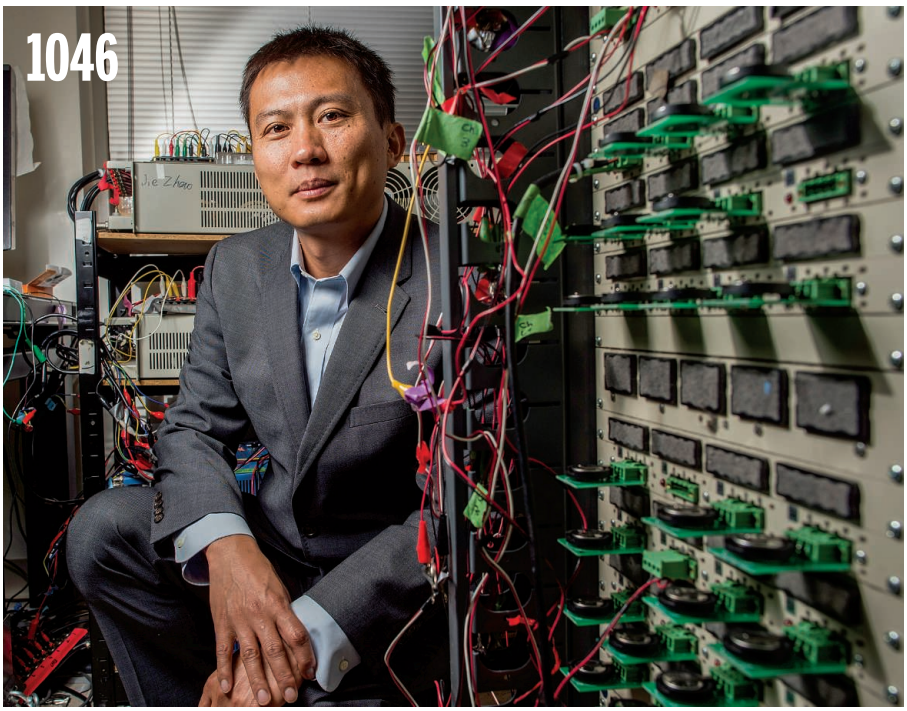
How new particles form in the free troposphere *p. 1109*

CONTENTS

27 MAY 2016 • VOLUME 352 • ISSUE 6289



1055 & 1105
Microbes seeking metals



NEWS

IN BRIEF

1036 News at a glance

IN DEPTH

1039 NEAR MISS AT FUKUSHIMA IS A WARNING FOR U.S.
Panel says spent reactor fuel in a storage pool could have boiled dry and caught on fire *By R. Stone*

1040 SHOOTING FOR A STAR
Internet billionaire explains his plan to send very small spaceships a very long way *By Z. Merali*

1042 GOVERNMENT 'NUDGES' PROVE THEIR WORTH
U.S. trials show low-cost interventions can influence choices by people needing help from state services *By J. Bohannon*

1043 INDIA NEARS PUTTING GM MUSTARD ON THE TABLE
Activists hope to derail approval, citing regulators' reluctance to release safety data *By P. Pulla*

1044 BRAZILIAN CRISIS THREATENS SCIENCE AND ENVIRONMENT
Proposed constitutional amendment could gut environmental protections *By L. Wade*

FEATURE

1046 THE BATTERY BUILDER
Yi Cui is pioneering efforts to use nanotechnology to revolutionize battery design, and just perhaps save the world *By R. F. Service*

INSIGHTS

PERSPECTIVES

1050 HOW TO BREAK DOWN CRYSTALLINE CELLULOSE
Biochemical and genomic data elucidate how a fungal enzyme attacks polysaccharides *By A. T. Martínez*
▸ REPORT P. 1098

1052 THE CANCER PREDISPOSITION REVOLUTION
How was the inherited basis of cancer foreshadowed? *By D. Malkin* et al.

1053 ORGANIC PHOTOCATALYSTS FOR CLEANER POLYMER SYNTHESIS
Metal-free catalysts enable synthesis of polymers for biomedical and electronics applications *By S. Shanmugam and C. Boyer*
▸ REPORT P. 1082

1055 A METAL SHUTTLE KEEPS PATHOGENS WELL FED
The metal-binding compound staphylopine captures nutrient metal ions for pathogens *By E. M. Nolan*
▸ REPORT P. 1105

1056 MATCHING MARKETS IN THE DIGITAL AGE
Digital markets make it easier to match companies and customers *By E. M. Azevedo and E. G. Weyl*
▸ PODCAST

1058 UNWINDING INDUCIBLE GENE EXPRESSION
Relieving DNA torsional stress may follow chromatin remodeling to facilitate transcription *By S. D. Pope and R. Medzhitov*
▸ RESEARCH ARTICLE P. 1074

1059 PAYING FOR FUTURE SUCCESS IN GENE THERAPY
We must consider potential value, pricing, and sustainability of emerging gene therapies *By S. H. Orkin and P. Reilly*

BOOKS *ET AL.*

1062 SERENDIPITY
By J. A. Estes, reviewed by E. Forbes et al.

1063 YOU MAY ALSO LIKE
By T. Vanderbilt, reviewed by S. Iyengar

LETTERS

1065 PUBLIC PARTICIPATION IN CHINA'S PROJECT PLANS
By G. Qi et al.

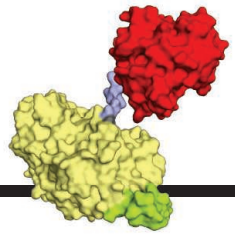
1065 INFECTION AND THE FIRST EUKARYOTES
By S. B. Gould

1065 RESPONSE
By S. G. Ball et al.

1066 ERRATA

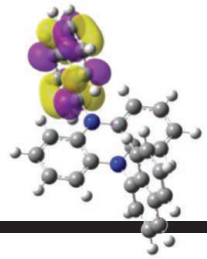
Downloaded from http://science.sciencemag.org/ on May 26, 2016

Published by AAAS



1050 & 1098

Fueling cellulose degradation



1053 & 1082

Metal-free polymerization

RESEARCH

IN BRIEF

1071 From *Science* and other journals

RESEARCH ARTICLE

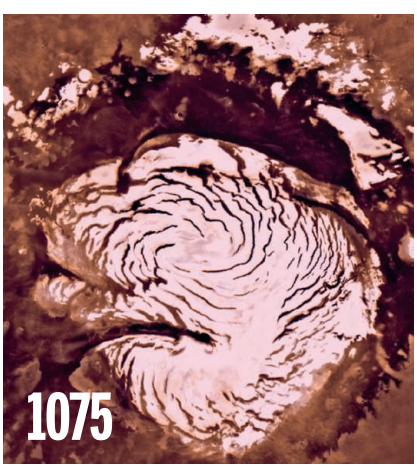
1074 INFLAMMATION
Topoisomerase 1 inhibition suppresses inflammatory genes and protects from death by inflammation *A. Rialdi* et al.
RESEARCH ARTICLE SUMMARY; FOR FULL TEXT: dx.doi.org/10.1126/science.aad7993
▸ PERSPECTIVE P. 1058

REPORTS

1075 MARTIAN CLIMATE
An ice age recorded in the polar deposits of Mars *I. B. Smith* et al.

1078 ORGANIC CHEMISTRY
Enantioselective synthesis of an ophiobolin sesterterpene via a programmed radical cascade *Z. G. Brill* et al.

1082 POLYMER CHEMISTRY
Organocatalyzed atom transfer radical polymerization driven by visible light *J. C. Theriot* et al.
▸ PERSPECTIVE P. 1053



1087 QUANTUM PHYSICS
A Schrödinger cat living in two boxes *C. Wang* et al.

QUANTUM SIMULATION
1091 Experimental reconstruction of the Berry curvature in a Floquet Bloch band *N. Fläschner* et al.

1094 Bloch state tomography using Wilson lines *T. Li* et al.

1098 BIOCHEMISTRY
Extracellular electron transfer systems fuel cellulose oxidative degradation *D. Kracher* et al.
▸ PERSPECTIVE P. 1050

1102 PLANT SCIENCE
Nuclear-localized cyclic nucleotide–gated channels mediate symbiotic calcium oscillations *M. Charpentier* et al.

1105 METAL ACQUISITION
Biosynthesis of a broad-spectrum nicotianamine-like metallophore in *Staphylococcus aureus* *G. Ghssein* et al.
▸ PERSPECTIVE P. 1055

1109 ATMOSPHERIC PARTICLES
New particle formation in the free troposphere: A question of chemistry and timing *F. Bianchi* et al.

1113 GENETIC MAPPING
CRISPR-directed mitotic recombination enables genetic mapping without crosses *M. J. Sadhu* et al.

1116 MUCOSAL IMMUNOLOGY
Gene-microbiota interactions contribute to the pathogenesis of inflammatory bowel disease *H. Chu* et al.

1121 CELL CYCLE
Cyclin-dependent kinase 1–dependent activation of APC/C ubiquitin ligase *K. Fujimitsu* et al.

1124 CELL DIVISION
A force-generating machinery maintains the spindle at the cell center during mitosis *C. Garzon-Coral* et al.

DEPARTMENTS

1035 EDITORIAL
Implicit bias
By Marcia McNutt
▸ AAAS NEWS AND NOTES P. 1067

1138 WORKING LIFE
Three strikes and research is out
By Michael J. Orsini



ON THE COVER



Clouds surrounding the Sphinx Observatory, which is part of the high-altitude research station Jungfraujoch (3580 meters above sea level) in the middle of the Swiss Alps, a stone's throw from the Eiger north face. This location is ideal for hunting the tiny particles upon which cloud droplets grow, as well as for studying how these particles are formed at high altitude. See page 1109. *Photo: Jonathan Reid*

Science Staff 1032
AAAS News & Notes 1067
New Products 1128
Science Careers 1129

SCIENCE (ISSN 0036-8075) is published weekly on Friday, except the last week in December, by the American Association for the Advancement of Science, 1200 New York Avenue, NW, Washington, DC 20005. Periodicals mail postage (publication No. 484460) paid at Washington, DC, and additional mailing offices.

Copyright © 2016 by the American Association for the Advancement of Science. The title SCIENCE is a registered trademark of the AAAS.

Domestic individual membership and subscription (51 issues): $165 ($74 allocated to subscription). Domestic institutional subscription (51 issues): $1522; Foreign postage extra: Mexico, Caribbean (surface mail) $55; other countries (air assist delivery) $89. First class, airmail, student, and emeritus rates on request. Canadian rates with GST available upon request, GST #1254 88122. Publications Mail Agreement Number 1069624. **Printed in the U.S.A.**
Change of address: Allow 4 weeks, giving old and new addresses and 8-digit account number. **Postmaster:** Send change of address to AAAS, P.O. Box 96178, Washington, DC 20090–6178. **Single-copy sales:** $15.00 current issue, $20.00 back issue prepaid includes surface postage; bulk rates on request.

Authorization to photocopy material for internal or personal use under circumstances not falling within the fair use provisions of the Copyright Act is granted by AAAS to libraries and other users registered with the Copyright Clearance Center (CCC) Transactional Reporting Service, provided that $35.00 per article is paid directly to CCC, 222 Rosewood Drive, Danvers, MA 01923. The identification code for *Science* is 0036-8075. *Science* is indexed in the *Reader's Guide to Periodical Literature* and in several specialized indexes.

Published by AAAS

Downloaded from http://science.sciencemag.org/ on May 26, 2016

Science
AAAS
1200 New York Avenue, NW, Washington, DC 20005
Bateman House, 82-88 Hills Road, Cambridge, UK CB2 1LQ

Editor-in-Chief Marcia McNutt
Executive Editor Monica M. Bradford **News Editor** Tim Appenzeller
Managing Editor, Research Journals Katrina L. Kelner
Deputy Editors Lisa D. Chong, Andrew M. Sugden(UK), Valda J. Vinson, Jake S. Yeston

Research and Insights

DEPUTY EDITOR, EMERITUS Barbara R. Jasny **SR. EDITORS** Caroline Ash(UK), Gilbert J. Chin, Julia Fahrenkamp-Uppenbrink(UK), Pamela J. Hines, Stella M. Hurtley(UK), Paula A. Kiberstis, Marc S. Lavine(Canada), Kristen L. Mueller, Ian S. Osborne(UK), Beverly A. Purnell, L. Bryan Ray, Guy Riddihough, H. Jesse Smith, Jelena Stajic, Peter Stern(UK), Phillip D. Szuromi, Sacha Vignieri, Brad Wible, Nicholas S. Wigginton, Laura M. Zahn **ASSOCIATE EDITORS** Brent Grocholski, Keith T. Smith **ASSOCIATE BOOK REVIEW EDITOR** Valerie B. Thompson **LETTERS EDITOR** Jennifer Sills **CHIEF CONTENT PRODUCTION EDITOR** Cara Tate **SR. CONTENT PRODUCTION EDITORS** Harry Jach, Lauren Kmec **CONTENT PRODUCTION EDITORS** Jeffrey E. Cook, Chris Filiatreau, Cynthia Howe, Barbara P. Ordway, Catherine Wolner **SR. EDITORIAL COORDINATORS** Carolyn Kyle, Beverly Shields **EDITORIAL COORDINATORS** Aneera Dobbins, Joi S. Granger, Lisa Johnson, Anita Wynn **PUBLICATIONS ASSISTANTS** Jeffrey Hearn, Dona Mathieu, Le-Toya Mayne Flood, Shannon McMahon, Scott Miller, Caitlyn Phillips, Jerry Richardson, Alice Whaley(UK), Brian White **EXECUTIVE ASSISTANT** Anna Bashkirova **ADMINISTRATIVE SUPPORT** Janet Clements(UK), Lizanne Newton(UK), Maryrose Madrid

News

NEWS MANAGING EDITOR John Travis **INTERNATIONAL EDITOR** Richard Stone **DEPUTY NEWS EDITORS** Robert Coontz, Elizabeth Culotta, David Grimm, David Malakoff, Leslie Roberts **CONTRIBUING EDITOR** Martin Enserink(Europe) **SR. CORRESPONDENTS** Daniel Clery(UK), Jeffrey Mervis, Elizabeth Pennisi **NEWS WRITERS** Adrian Cho, Jon Cohen, Jennifer Couzin-Frankel, Carolyn Gramling, Eric Hand, Jocelyn Kaiser, Catherine Matacic, Kelly Servick, Robert F. Service, Erik Stokstad(Cambridge, UK), Emily Underwood **INTERNS** Patrick Monahan **CONTRIBUTING CORRESPONDENTS** John Bohannon, Warren Cornwall, Ann Gibbons, Mara Hvistendahl, Sam Kean, Eli Kintisch, Kai Kupferschmidt(Berlin), Andrew Lawler, Christina Larson(Beijing), Mitch Leslie, Charles C. Mann, Eliot Marshall, Virginia Morell, Dennis Normile(Shanghai), Heather Pringle, Tania Rabesandratana(London), Gretchen Vogel(Berlin), Lizzie Wade(Mexico City) **CAREERS** Donisha Adams, Rachel Bernstein(Editor) **COPY EDITORS** Julia Cole, Dorie Chevlen, Jennifer Levin (Chief) **ADMINISTRATIVE SUPPORT** Jessica Adams

Executive Publisher Rush D. Holt
Interim Publisher Bill Moran **Chief Digital Media Officer** Rob Covey

BUSINESS OPERATIONS AND PORTFOLIO MANAGEMENT DIRECTOR Sarah Whalen **PRODUCT DEVELOPMENT DIRECTOR** Will Schweitzer **PRODUCT DEVELOPMENT ASSOCIATE** Hal Moore **BUSINESS SYSTEMS AND FINANCIAL ANALYSIS DIRECTOR** Randy Yi **MANAGER OF FULFILLMENT SYSTEMS** Neal Hawkins **SYSTEMS ANALYST** Nicole Mehmedovich **ASSISTANT DIRECTOR, BUSINESS OPERATIONS** Eric Knott **MANAGER, BUSINESS OPERATIONS** Jessica Tierney **SENIOR BUSINESS ANALYST** Cory Lipman **BUSINESS ANALYSTS** David Garrison, Meron Kebede, Sandy Kim **FINANCIAL ANALYST** Drew Sher **DIRECTOR, COPYRIGHTS LICENSING SPECIAL PROJECTS** Emilie David **PERMISSIONS ASSOCIATE** Elizabeth Sandler **RIGHTS, CONTRACTS, AND LICENSING ASSOCIATE** Lili Kiser

MARKETING DIRECTOR Elise Swinehart **ASSOCIATE MARKETING DIRECTOR** Christina Schlecht **MARKETING MANAGER** Elizabeth Sattler **MARKETING ASSOCIATE** Steven Goodman **CREATIVE DIRECTOR** Scott Rodgerson **SENIOR ART ASSOCIATES** Seil Lee, Paula Fry **ART ASSOCIATE** Kim Huynh **PROGRAM DIRECTOR, AAAS MEMBER CENTRAL** Peggy Mihelich **FULFILLMENT SYSTEMS AND OPERATIONS** membership@aaas.org **MANAGER, MEMBER SERVICES** Pat Butler **SPECIALISTS** Terrance Morrison, Latasha Russell **MANAGER, DATA ENTRY** Mickie Napoleoni **DATA ENTRY SPECIALISTS** Brenden Aquilino, Fiona Giblin

PUBLISHER RELATIONS MANAGER Catherine Holland **PUBLISHER RELATIONS, EASTERN REGION** Keith Layson **PUBLISHER RELATIONS, WESTERN REGION** Ryan Rexroth **SALES RESEARCH COORDINATOR** Aiesha Marshall **MANAGER, SITE LICENSE OPERATIONS** Iquo Edim **SENIOR OPERATIONS ANALYST** Lana Guz **FULFILLMENT ANALYST** Judy Lillibridge **ASSOCIATE DIRECTOR, MARKETING** Christina Schlecht **MARKETING ASSOCIATE** Isa Sesay-Bah

WEB TECHNOLOGIES PORTFOLIO MANAGER Trista Smith **TECHNICAL MANAGER** Chris Coleman **PROJECT MANAGER** Nick Fletcher **DEVELOPERS** Ryan Jensen, Jimmy Marks, Brandon Morrison

DIGITAL MEDIA DIRECTOR OF ANALYTICS Enrique Gonzales **DIGITAL REPORTING ANALYST** Eric Hossinger **SR. WEB PRODUCER** Sarah Crespi **WEB PRODUCER** Alison Crawford **VIDEO PRODUCER** Nguyen Nguyen **SOCIAL MEDIA PRODUCER** Brice Russ

DIRECTOR OF OPERATIONS PRINT AND ONLINE Lizabeth Harman **DIGITAL/PRINT STRATEGY MANAGER** Jason Hillman **QUALITY TECHNICAL MANAGER** Marcus Spiegler **PROJECT ACCOUNT MANAGER** Tara Kelly **DIGITAL PRODUCTION MANAGER** Lisa Stanford **ASSISTANT MANAGER DIGITAL/PRINT** Rebecca Doshi **SENIOR CONTENT SPECIALISTS** Steve Forrester, Antoinette Hodal, Lori Murphy, Anthony Rosen **CONTENT SPECIALISTS** Jacob Hedrick, Kimberley Oster

DESIGN DIRECTOR Beth Rakouskas **DESIGN EDITOR** Marcy Atarod **SENIOR DESIGNERS** Garvin Grullón, Chrystal Smith **GRAPHICS MANAGING EDITOR** Alberto Cuadra **SENIOR SCIENTIFIC ILLUSTRATORS** Chris Bickel, Katharine Sutliff **SCIENTIFIC ILLUSTRATOR** Valerie Altounian **INTERACTIVE GRAPHICS EDITOR** Jia You **SENIOR ART ASSOCIATES** Holly Bishop, Nathalie Cary **PHOTOGRAPHY MANAGING EDITOR** William Douthitt **PHOTO EDITOR** Christy Steele

DIRECTOR, GLOBAL COLLABORATION, CUSTOM PUBLICATIONS, ADVERTISING Bill Moran **EDITOR, CUSTOM PUBLISHING** Sean Sanders: 202-326-6430 **ADVERTISING MARKETING MANAGER** Justin Sawyers: 202-326-7061 science_advertising@aaas.org **ADVERTISING SUPPORT MANAGER** Karen Foote: 202-326-6740 **ADVERTISING PRODUCTION OPERATIONS MANAGER** Deborah Tompkins **SR. PRODUCTION SPECIALIST/GRAPHIC DESIGNER** Amy Hardcastle **SR. TRAFFIC ASSOCIATE** Christine Hall **SALES COORDINATOR** Shirley Young **ASSOCIATE DIRECTOR, COLLABORATION, CUSTOM PUBLICATIONS/CHINA/TAIWAN/KOREA/SINGAPORE** Ruolei Wu: +86-186 0082 9345, rwu@aaas.org **COLLABORATION/CUSTOM PUBLICATIONS/JAPAN** Adarsh Sandhu + 81532-81-5142 asandhu@aaas.org **EAST COAST/E. CANADA** Laurie Faraday: 508-747-9395, FAX 617-507-8189 **WEST COAST/W. CANADA** Lynne Stickrod: 415-931-9782, FAX 415-520-6940 **MIDWEST** Jeffrey Dembksi: 847-498-4520 x3005, Steven Loerch: 847-498-4520 x3006 **UK EUROPE/ASIA** Roger Goncalves: TEL/FAX +41 43 243 1358 **JAPAN** Katsuyoshi Fukamizu(Tokyo): +81-3-3219-5777 kfukamizu@aaas.org **CHINA/TAIWAN** Ruolei Wu: +86-186 0082 9345, rwu@aaas.org

WORLDWIDE ASSOCIATE DIRECTOR OF SCIENCE CAREERS Tracy Holmes: +44 (0) 1223 326525, FAX +44 (0) 1223 326532 tholmes@science-int.co.uk **CLASSIFIED** advertise@sciencecareers.org **U.S. SALES** Tina Burks: 202-326-6577, Nancy Toema: 202-326-6578 **EUROPE/ROW SALES** Sarah Lelarge **SALES ASSISTANT** Kelly Grace **JAPAN** Hiroyuki Mashiki(Kyoto): +81-75-823-1109 hmashiki@aaas.org **CHINA/TAIWAN** Ruolei Wu: +86-186 0082 9345 rwu@aaas.org **MARKETING MANAGER** Allison Pritchard **MARKETING ASSOCIATE** Aimee Aponte

AAAS BOARD OF DIRECTORS, CHAIR Geraldine L. Richmond **PRESIDENT** Barbara A. Schaal **PRESIDENT-ELECT** Susan Hockfield **TREASURER** David Evans Shaw **CHIEF EXECUTIVE OFFICER** Rush D. Holt **BOARD** Cynthia M. Beall, May R. Berenbaum, Carlos J. Bustamante, Stephen P.A. Fodor, Claire M. Fraser, Michael S. Gazzaniga, Laura H. Greene, Elizabeth Loftus, Mercedes Pascual

SUBSCRIPTION SERVICES For change of address, missing issues, new orders and renewals, and payment questions: 866-434-AAAS (2227) or 202-326-6417, FAX 202-842-1065. Mailing addresses: AAAS, P.O. Box 96178, Washington, DC 20090-6178 or AAAS Member Services, 1200 New York Avenue, NW, Washington, DC 20005

INSTITUTIONAL SITE LICENSES 202-326-6730 **REPRINTS:** Author Inquiries 800-635-7181 **COMMERCIAL INQUIRIES** 803-359-4578 **PERMISSIONS** 202-326-6765, permissions@aaas.org **AAAS Member Services** 202-326-6417 or http://membercentral.aaas.org/discounts

Science serves as a forum for discussion of important issues related to the advancement of science by publishing material on which a consensus has been reached as well as including the presentation of minority of conflicting points of view. Accordingly, all articles published in *Science*—including editorials, news and comment, and book reviews—are signed and reflect the individual views of the authors and not official points of view adopted by AAAS or the institutions with which the authors are affiliated.

INFORMATION FOR AUTHORS See pages 624 and 625 of the 5 February 2016 issue or access www.sciencemag.org/authors/science-information-authors

SENIOR EDITORIAL BOARD
Gary King, *Harvard University,* **Susan M. Rosenberg,** *Baylor College of Medicine,*
Ali Shilatifard, *Northwestern University Feinberg School of Medicine*

BOARD OF REVIEWING EDITORS (Statistics board members indicated with **(S)**

Adriano Aguzzi, *U. Hospital Zürich*
Takuzo Aida, *U. of Tokyo*
Leslie Aiello, *Wenner-Gren Foundation*
Judith Allen, *U. of Edinburgh*
Sonia Altizer, *U. of Georgia*
Sebastian Amigorena, *Institut Curie*
Kathryn Anderson, *Memorial Sloan-Kettering Cancer Center*
Meinrat O. Andreae, *Max-Planck Inst. Mainz*
Paola Arlotta, *Harvard U.*
Johan Auwerx, *EPFL*
David Awschalom, *U. of Chicago*
Clare Baker, *University of Cambridge*
Nenad Ban, *ETH Zurich*
Jordi Bascompte, *University of Zurich*
Franz Bauer, *Instituto de Astrofisica*
Ray H. Baughman, *U. of Texas, Dallas*
David Baum, *U. of Wisconsin*
Carlo Beenakker, *Leiden U.*
Kamran Behnia, *ESPCI-ParisTech*
Yasmine Belkaid, *NIAID, NIH*
Philip Benfey, *Duke U.*
May Berenbaum, *U. of Illinois*
Gabriele Bergers, *U. of California, San Francisco*
Bradley Bernstein, *Massachusettes General Hospital*
Peer Bork, *EMBL*
Bernard Bourdon, *Ecole Normale Supérieure de Lyon*
Chris Bowler, *École Normale Supérieure*
Ian Boyd, *U. of St. Andrews*
Emily Brodsky, *U. of California, Santa Cruz*
Ron Brookmeyer, *U. of California Los Angeles* **(S)**
Christian Büchel, *U. Hamburg-Eppendorf*
Joseph A. Burns, *Cornell U.*
Carter Tribley Butts, *U. of California, Irvine*
Gyorgy Buzsaki, *New York U. School of Medicine*
Blanche Capel, *Duke U.*
Mats Carlsson, *U. of Oslo*
Ib Chorkendorff, *U. of Denmark*
David Clapham, *Children's Hospital Boston*
Joel Cohen, *Rockefeller U., Columbia U.*
James J. Collins, *MIT*
Robert Cook-Deegan, *Duke U.*
Lisa Coussens, *Oregon Health & Science U.*
Alan Cowman, *Walter & Eliza Hall Inst.*
Robert H. Crabtree, *Yale U.*
Roberta Croce, *Vrije Universiteit*
Janet Currie, *Princeton U.*
Jeff L. Dangl, *U. of North Carolina*
Tom Daniel, *U. of Washington*
Frans de Waal, *Emory U.*
Stanislas Dehaene, *Collège de France*
Robert Desimone, *MIT*
Claude Desplan, *New York U.*
Dennis Discher, *U. of Pennsylvania*
Gerald W. Dorn II, *Washington U. School of Medicine*
Jennifer A. Doudna, *U. of California, Berkeley*
Bruce Dunn, *U. of California, Los Angeles*
William Dunphy, *Caltech*
Christopher Dye, *WHO*
Todd Ehlers, *U. of Tuebingen*
David Ehrhardt, *Carnegie Inst. of Washington*
Tim Elston, *U. of North Carolina at Chapel Hill*
Gerhard Ertl, *Fritz-Haber-Institut, Berlin*
Barry Everitt, *U. of Cambridge*
Ernst Fehr, *U. of Zurich*
Anne C. Ferguson-Smith, *U. of Cambridge*
Michael Feuer, *The George Washington U.*
Toren Finkel, *NHLBI, NIH*
Kate Fitzgerald, *U. of Massachusetts*
Peter Fratzl, *Max-Planck Inst.*
Elaine Fuchs, *Rockefeller U.*
Daniel Geschwind, *UCLA*
Karl-Heinz Glassmeier, *TU Braunschweig*
Ramon Gonzalez, *Rice U.*
Julia R. Greer, *Caltech*
Elizabeth Grove, *U. of Chicago*
Nicolas Gruber, *ETH Zurich*
Kip Guy, *St. Jude's Children's Research Hospital*
Taekjip Ha, *U. of Illinois at Urbana-Champaign*
Wolf-Dietrich Hardt, *ETH Zurich*
Christian Haass, *Ludwig Maximilians U.*
Sharon Hammes-Schiffer, *U. of Illinois at Urbana–Champaign*
Michael Hasselmo, *Boston U.*
Martin Heimann, *Max-Planck Inst. Jena*
Yka Helariutta, *U. of Cambridge*
James A. Hendler, *Rensselaer Polytechnic Inst.*
Janet G. Hering, *Swiss Fed. Inst. of Aquatic Science & Technology*
Kai-Uwe Hinrichs, *U. of Bremen*
David Hodell, *U. of Cambridge*
Lora Hooper, *UT Southwestern Medical Ctr. at Dallas*
Tamas Horvath, *Yale University*
Raymond Huey, *U. of Washington*
Fred Hughson, *Princeton U.*
Auke Ijspeert, *EPFL Lausanne*
Stephen Jackson, *USGS and U. of Arizona*
Steven Jacobsen, *U. of California, Los Angeles*
Kai Johnsson, *EPFL Lausanne*
Peter Jonas, *Inst. of Science & Technology (IST) Austria*
Matt Kaeberlein, *U. of Washington*
William Kaelin Jr., *Dana-Farber Cancer Inst.*
Daniel Kahne, *Harvard U.*
Daniel Kammen, *U. of California, Berkeley*
Abby Kavner, *U. of California, Los Angeles*
Masashi Kawasaki, *U. of Tokyo*
V. Narry Kim, *Seoul National U.*
Joel Kingsolver, *U. of North Carolina at Chapel Hill*
Robert Kingston, *Harvard Medical School*
Etienne Koechlin, *Ecole Normale Supérieure*
Alexander Kolodkin, *Johns Hopkins U.*
Thomas Langer, *U. of Cologne*
Mitchell A. Lazar, *U. of Pennsylvania*
David Lazer, *Harvard U.*
Thomas Lecuit, *IBDM*
Virginia Lee, *U. of Pennsylvania*
Stanley Lemon, *U. of North Carolina at Chapel Hill*
Ottoline Leyser, *Cambridge U.*
Wendell Lim, *U.C. San Francisco*
Marcia C. Linn, *U. of California, Berkeley*
Jianguo Liu, *Michigan State U.*
Luis Liz-Marzan, *CIC biomaGUNE*
Jonathan Losos, *Harvard U.*
Ke Lu, *Chinese Acad. of Sciences*
Christian Lüscher, *U. of Geneva*
Laura Machesky, *CRUK Beatson Inst. for Cancer Research*
Anne Magurran, *U. of St. Andrews*
Oscar Marin, *CSIC & U. Miguel Hernández*
Charles Marshall, *U. of California, Berkeley*
C. Robertson McClung, *Dartmouth College*
Graham Medley, *U. of Warwick*
Tom Misteli, *NCI*
Yasushi Miyashita, *U. of Tokyo*
Mary Ann Moran, *U. of Georgia*
Richard Morris, *U. of Edinburgh*
Alison Motsinger-Reif, *NC State U.* **(S)**
Thomas Murray, *The Hastings Center*
Daniel Neumark, *U. of California, Berkeley*
Kitty Nijmeijer, *U. of Twente*
Helga Nowotny, *European Research Advisory Board*
Ben Olken, *MIT*
Joe Orenstein, *U. of California Berkeley & Lawrence Berkeley National Lab*
Harry Orr, *U. of Minnesota*
Pilar Ossorio, *U. of Wisconsin*
Andrew Oswald, *U. of Warwick*
Margaret Palmer, *U. of Maryland*
Steve Palumbi, *Stanford U.*
Jane Parker, *Max-Planck Inst. of Plant Breeding Research*
Giovanni Parmigiani, *Dana-Farber Cancer Inst.* **(S)**
John H. J. Petrini, *Memorial Sloan-Kettering Cancer Center*
Samuel Pfaff, *Salk Institute for Biological Studies*
Joshua Plotkin, *U. of Pennsylvania*
Albert Polman, *FOM Institute AMOLF*
Philippe Poulin, *CNRS*
Jonathan Pritchard, *Stanford U.*
David Randall, *Colorado State U.*
Felix Rey, *Institut Pasteur*
Trevor Robbins, *U. of Cambridge*
Jim Roberts, *Fred Hutchinson Cancer Research Ctr.*
Barbara A. Romanowicz, *U. of California,Berkeley*
Amy Rosenzweig, *Northwestern University*
Mike Ryan, *U. of Texas, Austin*
Mitinori Saitou, *Kyoto U.*
Shimon Sakaguchi, *Kyoto U.*
Miquel Salmeron, *Lawrence Berkeley National Lab*
Jürgen Sandkühler, *Medical U. of Vienna*
Alexander Schier, *Harvard U.*
Vladimir Shalaev, *Purdue U.*
Robert Siliciano, *Johns Hopkins School of Medicine*
Denis Simon, *Arizona State U.*
Uri Simonsohn, *U. of Pennsylvania*
Alison Smith, *John Innes Centre*
Richard Smith, *U. of North Carolina* **(S)**
John Speakman, *U. of Aberdeen*
Allan C. Spradling, *Carnegie Institution of Washington*
Jonathan Sprent, *Garvan Inst. of Medical Research*
Eric Steig, *U. of Washington*
Paula Stephan, *Georgia State U. and National Bureau of Economic Research*
Molly Stevens, *Imperial College London*
V. S. Subrahmanian, *U. of Maryland*
Ira Tabas, *Columbia U.*
Sarah Teichmann, *Cambridge U.*
John Thomas, *North Carolina State U.*
Shubha Tole, *Tata Institute of Fundamental Research*
Christopher Tyler-Smith, *The Wellcome Trust Sanger Inst.*
Herbert Virgin, *Washington U.*
Bert Vogelstein, *Johns Hopkins U.*
Cynthia Volkert, *U. of Göttingen*
David Wallach, *Weizmann Inst. of Science*
Ian Walmsley, *U. of Oxford*
Jane-Ling Wang, *U. of California, Davis* **(S)**
David A. Wardle, *Swedish U. of Agric. Sciences*
David Waxman, *Fudan U.*
Jonathan Weissman, *U. of California, San Francisco*
Chris Wikle, *U. of Missouri* **(S)**
Ian A. Wilson, *The Scripps Res. Inst.* **(S)**
Timothy D. Wilson, *U. of Virginia*
Rosemary Wyse, *Johns Hopkins U.*
Jan Zaanen, *Leiden U.*
Kenneth Zaret, *U. of Pennsylvania School of Medicine*
Jonathan Zehr, *U. of California, Santa Cruz*
Len Zon, *Children's Hospital Boston*
Maria Zuber, *MIT*

BOOK REVIEW BOARD
David Bloom, *Harvard U.,* **Samuel Bowring,** *MIT,* **Angela Creager,** *Princeton U.,*
Richard Shweder, *U. of Chicago,* **Ed Wasserman,** *DuPont*

Published by AAAS

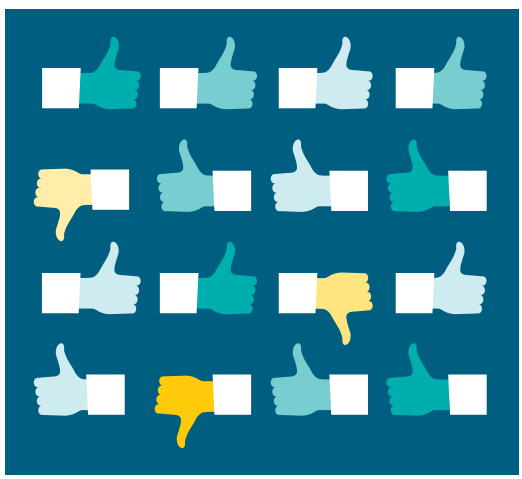
EDITORIAL

Implicit bias



Marcia McNutt
Editor-in-Chief
Science *Journals*

We all have it. Implicit bias was the shorthand that allowed our distant ancestors to make split-second decisions (friend or foe?) based on incomplete information. It provided a razor-thin reaction-time advantage that could mean life or death. But today, we no longer need to assume that people who do not look or sound like us pose an immediate threat. Instead, successful organizations and people welcome those who do not necessarily look, think, and act like they do. They must overcome that implicit bias wired into the human DNA if they are to reap the benefits of diversity. To explore the extent of implicit bias in peer review, and what can be done to counter it, the American Association for the Advancement of Science (AAAS, the publisher of *Science*) recently convened a day-long forum of editors, publishers, funders, and experts on implicit bias in Washington, DC (see p. 1067).



"...successful organizations and people welcome those who do not...act like they do."

From the journal perspective, there was some good news from a panel representing major journals. Scientific publishers such as the American Chemical Society (ACS) and the American Geophysical Union (AGU) find that female authors are published either at a rate proportional to that at which they submit to those journals, or at proportionally higher rates, as compared with their male colleagues. One expert on bias in peer review suggested that editors and program managers who make final decisions in single-blind review systems compensate for implicit bias to ensure an equitable outcome.

However, when panelists examined international representation in the journals, they noted that publication rates are not proportional to the rates at which papers are submitted from various nations. Even for the journal *Social Psychological and Personality Science* (*SPPS*), which conducts double-blind peer review (removing information regarding country of origin, institution, and authors before review), data show that blinding is no assurance that geographic discrepancies will disappear. There are several possible explanations for the continued persistence of geographic disparities in acceptance rates, other than geographic variations in quality. For example, reviewers might infer the country of origin from other clues in the paper (such as field sites, special facilities, or use of English), even without names, institutions, and addresses.

Moreover, all journal representatives participating in the panel (ACS, AGU, *Nature, The New England Journal of Medicine,* and *SPPS*) agreed that the reviewer pool is dominantly male and from the Western Hemisphere as compared to the author base. An interesting dichotomy arose among the journals regarding editorial staff. Journals staffed by professional full-time editors (*Nature* and *Science*) reported excellent gender balance, if not a tendency toward more female than male editors. The opposite situation exists for journals staffed by volunteer editors, likely driven by the greater demands on women's discretionary time.

One possible direction, suggested by the forum, to reduce implicit bias is for journals to broaden, diversify, and internationalize their pool of editors and reviewers. Even journals already conducting double-blind reviews could benefit from such actions. This would allow a more equitable distribution of the reviewing process across a discipline's scientific community. To meet the demand, journals will need to devise new means of identifying a more diverse pool of experienced reviewers, or train a new cohort in the journal's expectations for review quality and reviewer ethics. Reviewers who repeatedly provide useful advice could eventually serve on editorial boards.

Implicit bias is, by definition, subconscious, making it an easy issue for any individual to overlook or not even realize, and thus difficult to address. Some processes, such as double-blind review, attempt to overcome such prejudice, but blinding in all dimensions is a challenge. Building a peer evaluation system that is truly as diverse as the publication enterprise we desire would be a big step toward eliminating unfair bias that harms the scientific enterprise.

– Marcia McNutt

10.1126/science.aag1695

IMAGES: (INSET) G GRULLÓN/*SCIENCE*; (TOP RIGHT) STACEY PENTLAND PHOTOGRAPHY

Downloaded from http://science.sciencemag.org/ on May 26, 2016

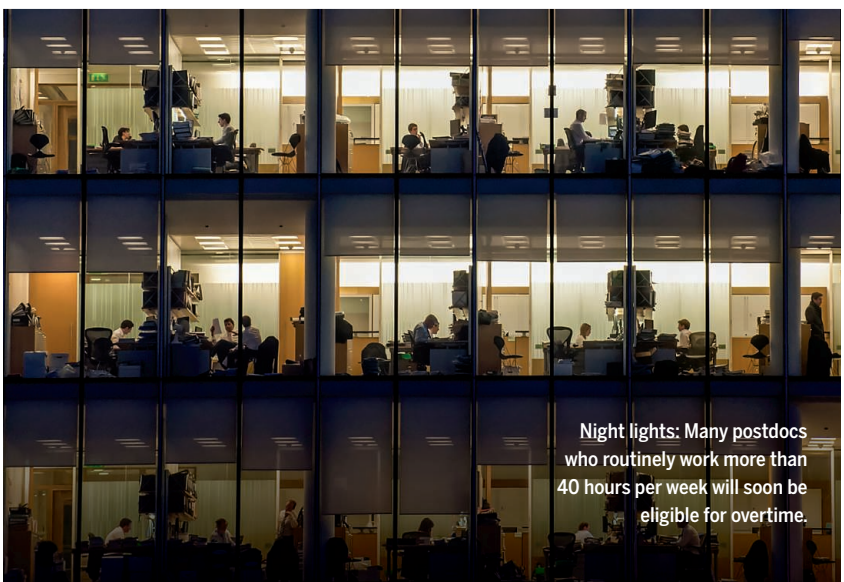
Published by AAAS

"The [National Football League] attempted to use its 'unrestricted gift' as leverage to steer funding away from one of its critics."

Conclusion of a congressional committee study, released 23 May, on whether NFL used a $30 million donation to influence concussion research overseen by the U.S. National Institutes of Health. NFL denied the charge.

IN BRIEF

Overtime rule may bump postdoc pay



Night lights: Many postdocs who routinely work more than 40 hours per week will soon be eligible for overtime.

Joy and worry are rippling through the U.S. research community in reaction to a new labor law that will require that postdoctoral researchers be paid at least $47,476—thousands of dollars more than many earn now—or else get overtime pay. Although welcomed by many, the change could have major impacts on the budgets of labs and universities, which only have until 1 December to comply. The overtime pay rule, released on 18 May, will double the salary threshold that delineates employees eligible for overtime when they work more than 40 hours per week—which most of the roughly 80,000 U.S. postdocs do. Employers can either log their hours and pay them overtime, or—as U.S. officials suggest—increase their salaries. The National Institutes of Health expects to raise stipends for its postdoctoral fellowships. But most biomedical postdocs are paid from research grants, and investigators will now have to find the extra money in their budgets. The effect of the new rule on fields outside biomedicine may vary by discipline, institution, and geographic area. For example, most physical science postdocs working at Department of Energy labs already receive at least $59,000 a year, but in chemistry and agricultural research median salaries are close to $40,000. http://bit.ly/overtimepostdocs

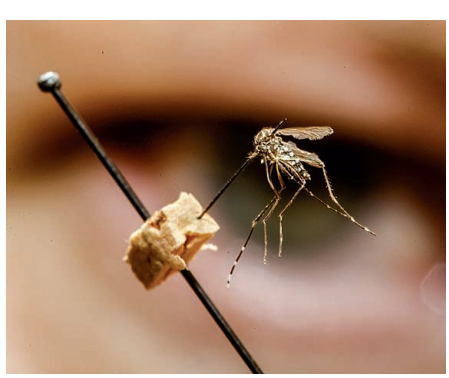
AROUND THE WORLD

Retrial of HIV vaccine approach

JOHANNESBURG, SOUTH AFRICA | An HIV vaccine strategy that showed modest efficacy 7 years ago will receive a second chance to prove its worth. South Africa plans to launch the $130 million study in November, and it will recruit 5400 men and women at risk of HIV infection. The U.S. National Institute of Allergy and Infectious Diseases, which is footing half the bill, will oversee the trial. Participants will each receive two vaccines: One contains the HIV surface protein, gp120, delivered by a canarypox virus; the second booster shot contains gp120 mixed with an immune stimulant called an adjuvant. A study in Thailand in 2009 reported that this one-two punch reduced the risk of infection by 31.2%. Results are expected in 2020.

Yellow fever not emergency—yet

GENEVA, SWITZERLAND | After weeks of growing alarm about ongoing urban outbreaks of yellow fever in Angola and the Democratic Republic of the Congo (*Science*, 8 April, p. 128), an emergency committee convened by the World Health Organization (WHO) lowered the pitch a little last week. Yellow fever is caused by a virus spread by *Aedes aegypti*, the same mosquito that spreads Zika; when the virus gets into the mosquito population of a major city, it can cause devastating outbreaks. This happened in December of last year in Luanda, where 2267 suspected cases of yellow fever have been reported,



The *Aedes aegypti* mosquito transmits yellow fever.

PHOTOS: (LEFT TO RIGHT) KULICKI/ISTOCKPHOTO.COM; JUNGE. HEIKO/ZUMA PRESS/NEWSCOM

Downloaded from http://science.sciencemag.org/ on May 26, 2016

Published by AAAS

with at least 293 deaths. WHO called the outbreak "a serious public health event," but because the international spread of the disease has slowed and vaccine supplies are recovering, the committee stopped short of declaring it a "public health emergency of international concern" (PHEIC). That label would have given any recommendations from WHO greater power. (The organization has declared a PHEIC four times: for H1N1 influenza, the resurgence of polio, the Ebola outbreak in West Africa, and, most recently, the Zika virus.) **http://bit.ly/WHOyellowfever**

Brazilian Zika in Cape Verde

PRAIA | Cape Verde lies just off Africa, but the Zika virus causing an outbreak there is the same strain that is spreading in Brazil, on the other side of the Atlantic. The outbreak, which has sickened more than 7500 people since October 2015, had puzzled researchers who wondered whether the virus had spread to the islands from Brazil or from the African continent, where Zika is endemic—or whether both variants of the virus might be circulating on the island. Researchers at the Pasteur Institute in Dakar have finally settled the question, the World Health Organization reported on 20 May: The virus's genome sequences point to Brazil as the source of the outbreak. So far, Cape Verde has identified three cases of microcephaly in babies born since the outbreak began. One of the babies was born in Boston after the mother had traveled to Cape Verde. Unlike other regions afflicted with Zika, the country has not reported any cases of serious complications, such as Guillain-Barré syndrome, in adults.

France tightens trial rules

PARIS | The French government is taking measures to lower the health risks to volunteers in clinical trials in the wake of the final report about a study that killed one person and landed five others in the hospital in January (*Science*, 12 February, p. 642). In the fatal trial, the Rennes, France–based contract research company Biotrial tested a drug that acts on the body's endocannabinoid system for possible treatment of a wide range of conditions, including anxiety, mood disorders, and Parkinson's disease. The 127-page report released this week by France's General Inspectorate of Social Affairs doesn't pinpoint why the potential drug caused brain damage in the previously healthy control subjects, but calls on the government to "mobilize the international scientific community" to find out what went wrong. At a 23 May press conference, French health minister Marisol Touraine announced several measures aimed at improving safety and strengthening the response when a trial goes awry. She also said that Biotrial must provide a plan of action within a month explaining how it will avoid repeating its mistakes, or risk losing its operating license. **http://bit.ly/trialrules**



Populations of cephalopods like these giant Australian cuttlefish (*Sepia apama*) are on the rise.

PHOTO: S. PORTELLI

World octopus, squid populations are booming

Humans' impacts on the oceans bring some good news this week—if you're a fan of the squishy and tentacled. A new study using data from both fisheries and scientific surveys confirms that populations of cephalopods—the class that includes octopuses, squids, and cuttlefish—have boomed worldwide since 1953. That includes both species that live closer to the shore and those that swim out in the open ocean, the researchers write this week in *Current Biology*. Although the exact reason for the surge is unclear, cephalopods' short life spans and rapid breeding make them well adapted to changing environmental conditions, causing some researchers to refer to them as "the weeds of the sea." But with continued fishing and the unpredictable effects of climate change, their future is anything but certain. **http://bit.ly/cephalopodboom**

Push for Alpha Centauri

WASHINGTON, D.C. | The recently announced Breakthrough Starshot project—to send a privately funded fleet of tiny spacecraft on a journey to Alpha Centauri, our nearest star system—may have started a star-rush (*Science*, 15 April, p. 276). Now, a senior U.S. lawmaker who helps write NASA's budget is calling on the agency to begin developing its own interstellar probes with the aim of launching a mission to Alpha Centauri in 2069 (the centenary of the Apollo 11 moon landing). Representative John Culberson (R–TX), chair of the House of Representatives appropriations subpanel that oversees NASA, included the call in a committee report released 23 May, encouraging NASA "to study and develop propulsion concepts that could enable an interstellar scientific probe with the capability of achieving a cruise velocity of 0.1c [10% of the speed of light]." The report accompanies a bill setting NASA's budget for the 2017 fiscal year, which begins 1 October. **http://bit.ly/CentauriNASA**

U.S. Zika funding battle

WASHINGTON, D.C. | President Barack Obama insists that the United States needs more money to battle the Zika epidemic than either the Senate or the House of Representatives agreed to spend last week. "Bottom line is, Congress needs to get me a bill … that has sufficient funds to do the job," he said 20 May after a Zika briefing from the Department of Health and Human

Downloaded from http://science.sciencemag.org/ on May 26, 2016

Published by AAAS

Services, the Centers for Disease Control and Prevention, and the U.S. National Institutes of Health. The White House had requested $1.885 billion in an emergency appropriations proposal on 22 February. But last week, the Senate agreed to spend $1.11 billion in emergency funds that would carry through 2017; that proposal cut out about $350 million targeted to help hard-hit Puerto Rico. The House, meanwhile, passed a bill last week that offers $622 million for Zika support, but stipulates that the money must be spent by 30 September, and that $352 million come from existing funding for the United States's Ebola response. The next move is a conference between the House and the Senate to reconcile their differences. Obama also said he'll veto a final bill that provides only $622 million.
http://bit.ly/USZikafunding



Is your dog a fanatical fetcher? Darwin's Dogs aims to find the genes responsible.

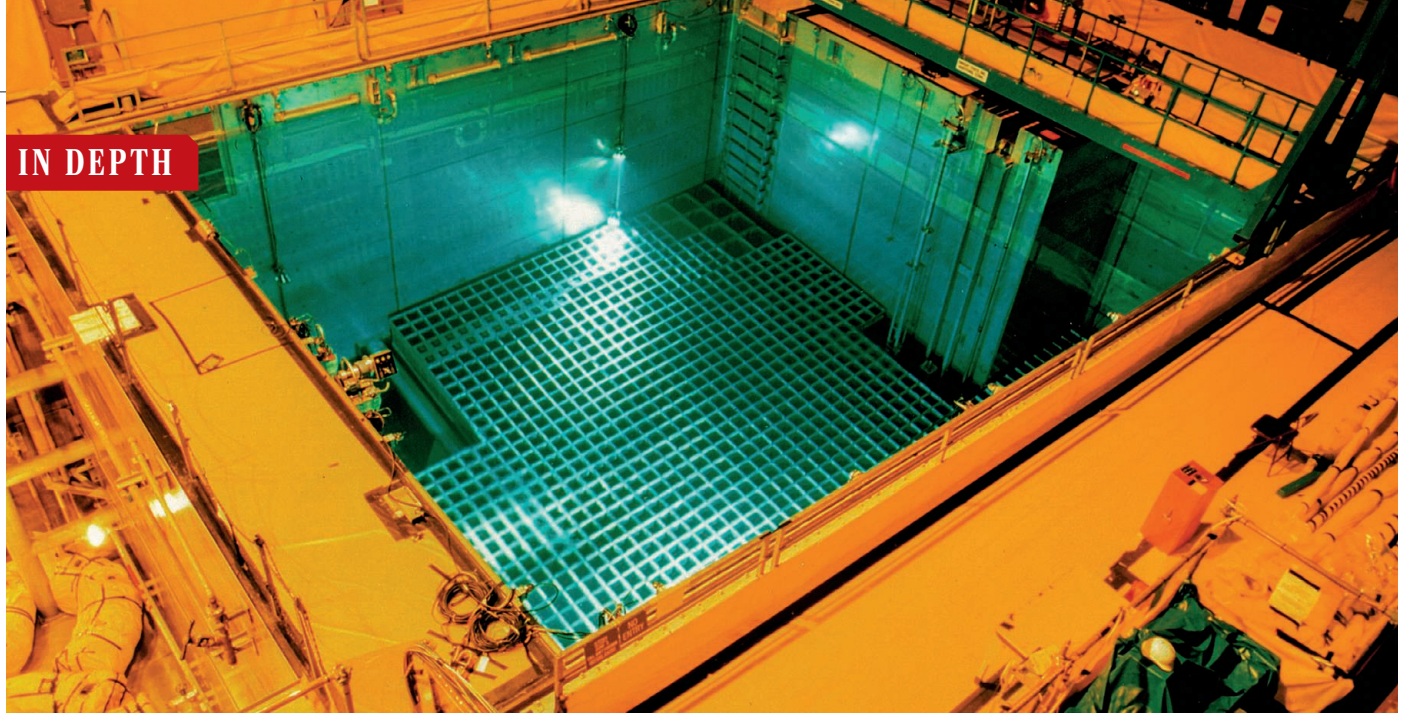
PHOTO: TO_CSA/ISTOCKPHOTO.COM

Dogs 'come' when called for citizen science project

Last October, bioinformatician Elinor Karlsson and animal behaviorist Jesse McClure put out a call looking for dogs to participate in a study on the genetic basis of behavior. They were hoping to collect perhaps a thousand participants over a couple years—but they dramatically underestimated the enthusiasm of dog owners. More than 6000 have already enrolled in the Darwin's Dogs project (**http://darwinsdogs.org/**), sending in saliva samples and answering extensive surveys about their pets. The questions focus on heritable, easy to identify behaviors, such as whether the dog crosses its paws, buries toys or bones, licks its empty bowl, whines a lot, or is an escape artist. So far, with more than 570,000 answers, some trends have already emerged, Karlsson reported this month at the Biology of Genomes meeting in Cold Spring Harbor, New York—for example, more than half of the pets never escape their yards or crates, whereas 2% are canine Houdinis. The researchers, both at the University of Massachusetts Medical School in Worcester, have also sequenced the genomes of 21 of the mutts: Three look to be at least 20% one breed, but the rest possibly come from mixes of dozens of different breeds. And although dog owners don't seem to need much encouragement, Karlsson says, the team also plans to eventually add some fun apps for them to play with, such as a customized exercise plan to match the dog's personality. And more dogs are always welcome, she says.

Downloaded from http://science.sciencemag.org/ on May 26, 2016

Published by AAAS



New report warns of the risk of calamitous fires at spent fuel pools, such as this one at the San Onofre Nuclear Generating Station near San Clemente, California.

PHOTO: NRC

NUCLEAR SAFETY

Near miss at Fukushima is a warning for U.S.

Panel says spent reactor fuel in a storage pool could have boiled dry and caught on fire

By **Richard Stone**

Japan's chief cabinet secretary called it "the devil's scenario." Two weeks after the 11 March 2011 earthquake and tsunami devastated the Fukushima Daiichi Nuclear Power Plant, causing three nuclear reactors to melt down and release radioactive plumes, officials were bracing for even worse. They feared that spent fuel stored in pools in the reactor halls would catch fire and send radioactive smoke across a much wider swath of eastern Japan, including Tokyo.

Thanks to a lucky break detailed in a report released last week by the U.S. National Academies of Sciences, Engineering, and Medicine, Japan dodged that bullet. But the report warns that spent fuel accumulating at U.S. nuclear plants is also vulnerable. The near calamity "should serve as a wake-up call for the industry," says Joseph Shepherd, a mechanical engineer at the California Institute of Technology in Pasadena who chaired the academies committee that produced the report.

A major spent fuel fire at a U.S. nuclear plant "could dwarf the horrific consequences of the Fukushima accident," says Edwin Lyman, a physicist at the Union of Concerned Scientists, a nonprofit in Washington, D.C., who was not on the panel. Unpublished modeling from one panel member presents chilling scenarios for a hypothetical spent fuel fire at the Peach Bottom nuclear power plant in Pennsylvania. "We're talking about trillion-dollar consequences," says Frank von Hippel, a nuclear security expert at Princeton University, who led the modeling.

After spent fuel is removed from a reactor core, the radioactive fission products continue to decay, generating heat. All nuclear power plants store the fuel in deep pools for at least 4 years while it cools. To keep it safe, the academies panel recommends that the U.S. Nuclear Regulatory Commission (NRC) and plant operators beef up systems for monitoring the pools and topping up water in case a facility is damaged. The panel also says plants should be ready to tighten security after a disaster. "Disruptions create opportunities for malevolent acts," Shepherd says.

At Fukushima, the earthquake and tsunami cut power to pumps that circulated coolant through the reactors and cooled the water in the spent fuel pools. The pump failures led to the meltdowns; in the pools, located in all six of Fukushima's reactor halls, they allowed water temperatures to rise dangerously. Of preeminent concern were the pools in reactor units 1 through 4: Explosions had heavily damaged three of those buildings in the days after the tsunami.

The "devil's scenario" nearly played out in Unit 4, where the reactor was shut down for maintenance. The entire reactor core—all 548 fuel assemblies—was resting in the Unit 4 pool along with another 783 assemblies, shedding vast amounts of heat. When an explosion blew off Unit 4's roof on 15 March, operators assumed the cause was hydrogen—and they feared it had come from fuel in the pool that had been exposed to air.

Confirmation was impossible because the power loss on 11 March had disabled the pool's water level indicators. (Analysts now concur that the hydrogen had come not from exposed spent fuel, but from the melted reactor core in the adjacent Unit 3.) Concerns abated after a helicopter overflight on 16 March captured video of sunlight glinting off water in the pool. But the crisis was actually worsening: The water was evaporating away because of the hot fuel. As the level fell perilously close to the top of the fuel assemblies, something "fortuitous" happened, Shepherd says. As part of routine maintenance, workers had flooded Unit 4's reactor well, where the core normally sits. Separating the well and the spent fuel pool is a gate through which fuel assemblies are transfered. The gate leaked, allowing water from the well to partly refill the pool.

Without that leakage, the panel's modeling predicts that the tops of the fuel assemblies would have been exposed by early April 2011, and the odds of the assemblies' zirconium cladding catching fire would have skyrocketed. Only good fortune and makeshift measures to pump water into all the spent fuel pools averted that disaster, the academies panel notes.

Downloaded from http://science.sciencemag.org/ on May 26, 2016

Published by AAAS

A similar scenario could play out at a U.S. nuclear plant if a pool lost water via evaporation or leakage. At most plants, spent fuel is densely packed in pools, heightening the fire risk. NRC has estimated that a major fire at the Peach Bottom nuclear plant's pool would displace 3.46 million people from 31,000 square kilometers of contaminated land, an area larger than New Jersey. But Von Hippel and others think that NRC has grossly underestimated the scale and societal costs of such a fire.

NRC used a program called MACCS2 for modeling the dispersal and deposition of radioactivity from a Peach Bottom fire. Princeton's Michael Schoeppner and Von Hippel instead used HYSPLIT, a program able to craft more sophisticated scenarios based on historical weather data for the whole region.

In their simulations, the Princeton duo focused on Cs-137, a radioisotope with a 30-year half-life that has made large tracts around Chernobyl and Fukushima uninhabitable. They assumed a release of 1600 petabecquerels, which is the average amount of Cs-137 that NRC estimates would be released from a fire at a densely packed pool, and approximately 100 times the Cs-137 spewed at Fukushima. They simulated such a release on the first day of each month in 2015.

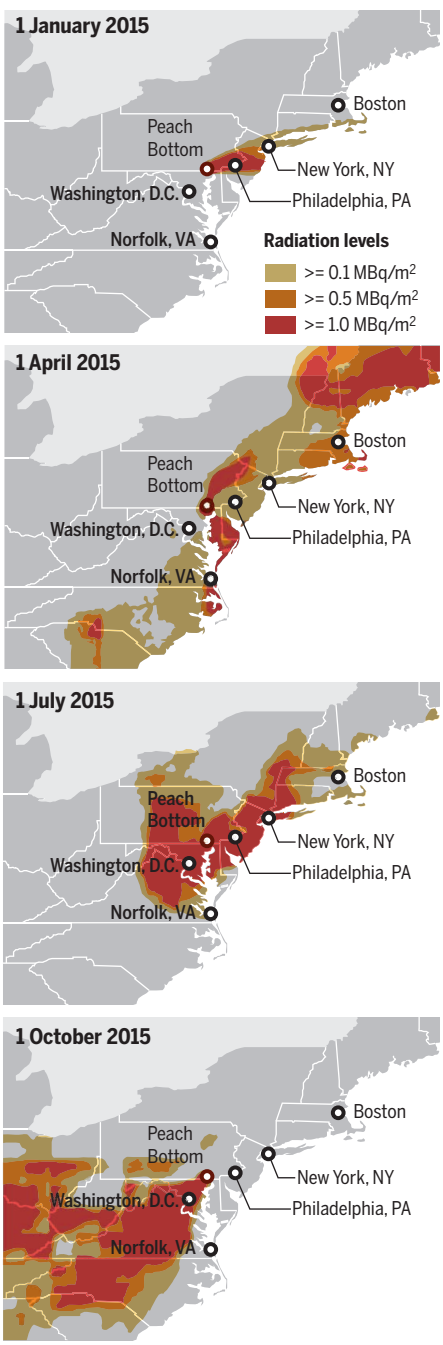
The contamination from such a fire on U.S. soil "would be an unprecedented peacetime catastrophe," the Princeton researchers conclude in a paper to be submitted to the journal *Science & Global Security*. For a fire on 1 January 2015, with the winds blowing due east, the radioactive plume would sweep over Philadelphia, Pennsylvania, and nearby cities (see maps, left). For a fire on 1 July 2015, shifting winds would deposit Cs-137 over much of the mid-Atlantic. Averaged over 12 monthly calculations, the area of heavy contamination—exceeding 1 megabecquerel per square meter, the level that would trigger a relocation—is 101,000 square kilometers. That's more than three times NRC's estimate and would force the relocation of 18.1 million people on average, about five times NRC's estimates.

NRC's first look at the academies report "did not identify any safety or security issues that would require immediate action," says spokesperson Scott Burnell in Washington, D.C. The agency has long mulled whether to compel the nuclear industry to move most of the cooled spent fuel in densely packed pools to concrete containers called dry casks, which would reduce the consequences and likelihood of a spent fuel fire. As recently as 2013, NRC concluded that the projected benefits do not justify the roughly $4 billion cost of a wholesale transfer. But the benefits of expedited transfer to dry casks are fivefold greater than NRC has calculated, the academies found. "NRC's policies have underplayed the risk of a spent fuel fire," Lyman says.

The academies panel recommends that NRC "assess the risks and potential benefits of expedited transfer." Burnell says that NRC's technical staff "will take an in-depth look" at the issue and report to NRC commissioners later this year. ■

Nightmare scenarios

Models of a hypothetical spent fuel fire at a Pennsylvania nuclear plant. Depending on weather, the Cs-137 plume displaces up to 41 million people (1 July) and contaminates up to 274,000 square kilometers (1 October).



GRAPHIC: A. CUADRA/*SCIENCE*

Q&A

Shooting for a star

Internet billionaire explains his plan to send very small spaceships a very long way

By **Zeeya Merali**

Last month, Russian internet billionaire Yuri Milner announced plans to send thousands of tiny spacecraft to visit Alpha Centauri, the closest star system at 4.4 light-years from Earth. Dubbed Breakthrough Starshot, the mission aims to take close-up images and collect data from any potentially habitable planets there. In order to cover the vast distance—41 trillion kilometers—in a reasonable time, the proposed spacecraft will each weigh less than a gram. Once in space, they will unfurl lightweight sails to catch laser beams shot from Earth, accelerating to one-fifth the speed of light under light pressure. Launch could be 30 years off, and the trip to Alpha Centauri would take a further 2 decades.

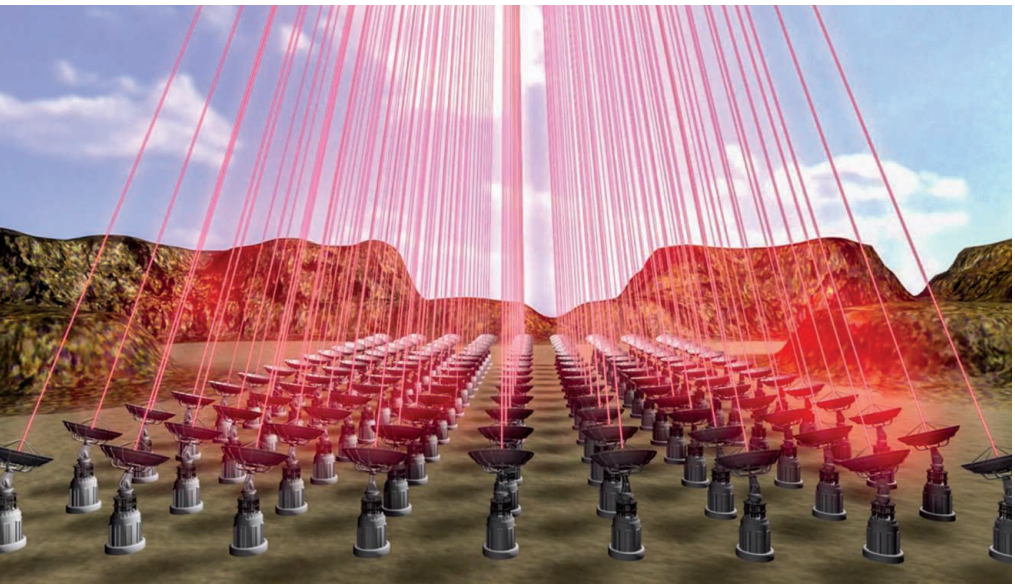
Milner, who also supports the multimillion-dollar Breakthrough Prizes and Breakthrough Listen, a search for signs of extraterrestrial intelligence, has committed $100 million to this venture. But Breakthrough Starshot has polarized opinion: Some are enthused by its ambition, whereas others say it is costly and unnecessary, isn't feasible, or is downright dangerous. Milner spoke with *Science* by phone about the challenges facing the project and how he answers his critics. His responses have been edited for clarity and brevity.

Q: How did your interest in space travel and in this mission to Alpha Centauri come about?
A: I was named Yuri after Yuri Gagarin because I was born the same year the Russian cosmonaut was launched on the first manned space flight. So I've carried this message about space travel in my name my whole life!

Breakthrough Starshot came from a small working group we put together to devise a practical space project to a neighboring star system that could achieve results within the lifetime of a generation. They considered various propulsion mechanisms for interstellar travel—including fusion engines and matter-antimatter propulsion—and concluded that the sail configuration is the most feasible in a reasonable time frame.

Downloaded from http://science.sciencemag.org/ on May 26, 2016

Published by AAAS



Breakthrough Starshot will require lasers many times more powerful than any existing today.

The idea of using spacecraft with solar-powered sails is actually very old, but until recently it was purely theoretical. Over the past 20 years there has been significant progress in microelectronics, nanomaterials, and laser technology that means we can now have a sensible conversation about making a gram-scale starship and accelerating it to 20% of the speed of light.



Starstruck: Yuri Milner

Q: You've contributed $100 million dollars, but the final project could cost $10 billion. Where will this extra money come from?
A: We've been open from day one that this is not something you can build in a garage and no one person can finance this machine. If this is going to happen, I envisage this as something that will need international collaboration on a financial scale comparable to CERN [the particle physics laboratory near Geneva, Switzerland].

The seed money covers the first 5 to 10 years' research and development phase, and within that time we should know if the challenges the project faces can be overcome or if they are insurmountable. The second phase will be to build a prototype and I think that can be financed by private investors, too. The final machine will need international backing.

Q: Might the money be better spent on a new planet-hunting telescope?
A: We're actually in negotiations to spend some of the money to increase the capability of some ground-based telescopes to take a direct image of possible planets around Alpha Centauri. That would use existing infrastructure and we hope to announce it soon. This is important because we don't even know with any degree of certainty if there are potentially habitable planets in the Alpha Centauri system to target with Breakthrough Starshot.

But there is no substitute for a flyby and taking close-up images. This would be the equivalent of the New Horizons mission to Pluto. To get an equal quality image with a ground or near-Earth telescope, you would need a telescope on the scale of a few hundred kilometers and that's not a small endeavor.

Q: Even if the project's giant lasers can be built, what about the damage they could potentially cause to the environment or their misuse as a weapon?
A: Laser technology is following its own Moore's law trajectory, so in a couple of decades' time we think laser power will have increased sufficiently and such lasers will not be prohibitively expensive. But from the outset we identified that there must be some form of global consensus on its use. It may be that we have the technological capability but the project stalls because there is no agreement about the governance of such a machine.

Q: Won't laser beams fired through the atmosphere lose power through dispersion? Wouldn't a space-based array be better?
A: That would increase the cost 100 times and push the mission back a few hundred years. So for a space-based system, let's just stop talking now. It's not going to happen in our lifetime. A space-based laser also poses more serious policy issues because it could be pointed at Earth and is more difficult to control.

The power from Earth-based lasers will not be dramatically different. The basic principle would be to utilize the adaptive optics already used by ground-based telescopes to deal with the challenges of the distortion of light passing through the atmosphere.

Q: Critics have warned that the powerful laser beam could set the tiny craft spinning out of control or destroy the fragile sails. Have you considered such scenarios?
A: Our experts have been looking into this and now think that a spinning craft may actually be more stable than a nonspinning one. But we don't know whether the sails will melt when the laser hits them or what the craft will meet in interstellar space. We've identified more than 20 technological challenges to the successful completion of this project. More work is needed and that's what the research phase is for.

Q: Can you miniaturize the sensors, imaging, and signaling equipment to fit on such a small craft?
A: We have carried out pretty detailed calculations that show we can shrink down the imaging equipment and sensors, even today. And surprisingly, to send a signal over trillions of miles you only need a small laser on board, powered by a watt-scale battery, and that can be made gram-scale. The sail would then be used as a dish to help transmit the signal, while the laser array on Earth would act as a receiver. So miniaturization of nanocraft is probably the least of the problems—the sails and the lasers are bigger obstacles.

Q: You have identified many ways this project might fail. Are you worried that your investment might ultimately go to waste?
A: Honestly, we are a very lucky generation because we are the first that could pull this off and, if we do, it will be incredible. But if not, we have promised to keep all the results of our research open to the public. One day our civilization will make use of it. It is human nature to explore the world around us and I don't think that curiosity will ever go away. ■

Zeeya Merali is a writer in London.

PHOTOS: BREAKTHROUGH INITIATIVES

Downloaded from http://science.sciencemag.org/ on May 26, 2016

Published by AAAS

SOCIAL SCIENCES

Government 'nudges' prove their worth

U.S. trials show low-cost interventions can influence choices by people needing help from state services

By **John Bohannon**

Over the past 5 years, on behalf of state governments, nearly 100,000 Americans were gently manipulated by a team of social scientists. In 15 randomized, controlled trials, people in need of social services either encountered the standard application process or received a psychological nudge, in which the information was presented slightly differently—a postcard reminded them of deadlines, for example, or one choice was made easier than another. In 11 of the trials, the nudge modestly increased a person's response rate or influenced them to make financially smarter choices.

The results, presented this week at the annual meeting of the Association for Psychological Science in Chicago, Illinois, add to the growing evidence that nudges developed by psychologists can make a real difference in the success of government programs. "These interventions have positive effects," says Sim Sitkin, director of the Behavioral Science & Policy Center at Duke University in Durham, North Carolina, who was not involved with the nudge trials. "They should be applied now."

The idea of influencing people's choices by making subtle changes to the available information or context of their decisions has been around for generations. After all, what are the advertising and marketing industries if not nudges paid for by businesses? But rigorous academic research on public-interest nudges is relatively new, says Caitlin Anzelone, a behavioral scientist based at the New York City offices of the Manpower Demonstration Research Corporation (MDRC), a social policy research organization created by the U.S. government in 1974.

MDRC launched the social service nudge trials in 2010 with funding from the U.S. Department of Health and Human Services. "To some extent we're reinventing the wheel for a new purpose," says Anzelone, who oversaw the effort. But rather than influencing people to buy a product, MDRC's aim is to nudge them into choices that lead to positive outcomes for their health, family, and finances.

MDRC's trials took place in seven U.S. states and focused on everything from tax credits and welfare for needy families to child support programs. For example, Texas has a program to help alleviate the financial disasters that can develop when a parent is incarcerated. Without income, prisoners often face mounting debt as child support bills rack up, with knock-on effects that can drag the entire family deeper into poverty. The state allows child support payments to be lowered during a prison term, but the incarcerated parent has to actually apply for the modification—and most fail to take advantage of this option.

To see whether the complexity of the application process is the bottleneck, one of MDRC's trials randomly assigned 2000 Texas inmates with children either to a control group or to be nudged. The latter received postcards reminding them about the program, as well as an application form that came pre-filled with personal information. Those who received the reminders and the simplified application were 11% more likely to take advantage of the child support modification option.

Most of the other MDRC nudges also worked, boosting the odds that the person would make a choice that seemed to be in their interest. The other interventions generally had smaller effects, however, shifting the frequency of a decision by 2% to 3%.

"Given the simplicity and the relatively low costs of the interventions, these [results] are impressive," says Dilip Soman, a behavioral scientist at the University of Toronto in Canada. In the case of the Texas inmate program, for example, MDRC estimates that the intervention costs an extra $1.73 per person per month, and at that price even a small effect is worthwhile. According to Sitkin, "we tend to too readily dismiss small effect sizes." However, "multiple small interventions can accumulate," he says, adding up to a large impact.

To some, government nudges suggest mind control. In 2010, when the U.K. government launched its Behavioural Insights Team—dubbed the Nudge Unit by many—conservative bloggers railed against it as a tool for a "nanny state" that trampled on people's free will. But other governments have followed the U.K. example, Soman notes. The White House now has its own nudge unit—the Social and Behavioral Sciences Team (SBST)—and the Canadian government has similar groups conducting research at the provincial level. "[Governments] are warming up to the idea of using behavioral insights in program delivery and design," he says.

What's next for the science of nudges? Behavioral scientist Crystal Hall of the University of Washington, Seattle, a member of the White House's SBST, suggests it's time "for researchers and practitioners to think more about moving beyond client-focused interventions." Rather than just aiming at citizens, nudges could be tailored to the front-line social services staff who interact with them, she says. For example, the state could remind officials at child care centers to notify parents of deadlines they must meet to keep their kids enrolled.

"There is still a lot left to understand in terms of the nuance of nudges," Sitkin says, but he hopes that won't slow down their application by policymakers. Several states, having seen MDRC's results, have already made their nudge permanent. "If we find an intervention with a positive effect, why not use it? And in the meantime, we can continue studying it," Sitkin says. ■

Successful nudges

In 11 of 15 trials, subtle changes to messaging from state agencies—emails, postcards, etc.—had significant effects on people's decisions. Below are three examples.

Texas: Incarcerated parents

Nudge: Reference peers

Message: "Other parents have had courts lower their child support by $200 to $500 per month."

Result: +11% in applications

California: Families in need of welfare

Nudge: Emphasize losses

Message: "By not attending your appointment, you may: LOSE up to $2508 a year in cash benefits."

Result: +3.6% in attendance

Ohio: Parents overdue on child support payments

Nudge: Reminders

Message: "Your child support payment is due in 3 days. Pay on time to avoid penalties."

Result: +2.9% in payments

Downloaded from http://science.sciencemag.org/ on May 26, 2016

Published by AAAS



Yields from India's conventional mustard varieties lag; GM strains promise a boost.

PHOTO: ABHIJIT KAR GUPTA/FLICKR CC BY 2.0

TRANSGENIC CROPS

India nears putting GM mustard on the table

Activists hope to derail approval, citing regulators' reluctance to release safety data

By **Priyanka Pulla**, *in Bangalore, India*

Six years after it backed down from approving cultivation of a transgenic food crop, India's government is trying again. But it is encountering stiff headwinds as it mulls whether to approve what would be India's first such crop, a genetically modified (GM) mustard. Environmentalists argue that the mustard, grown for its edible leaves and for cooking oil, could harm local varieties and that the toxicity tests being carried out to evaluate GM mustard's safety as a food are inadequate. Heightening suspicion, regulators have repeatedly spurned calls to release biosafety data.

India for years has planted GM cotton, but transgenic food crops have been off the table. In 2010, activists won a moratorium on approval of commercial planting of GM brinjal, a kind of eggplant, on the grounds that it hadn't been tested adequately. But India's environment minister, Prakash Javadekar, is determined to open the door to GM technologies, saying they can help ensure food security and that rejecting them is like "saying 'no' to science." The government is again allowing field trials of a variety of GM crops, frozen since the brinjal controversy, and a decision on GM mustard is expected this summer.

Even though India is one of the world's largest mustard (*Brassica juncea*) producers by area, growing it on more than 6 million hectares, it lags in yields. One reason is that traditional plant breeding techniques haven't been able to create popular and high-yielding Indian mustard hybrids, says Deepak Pental, a plant geneticist at the University of Delhi. Mustard flowers have male and female sexual parts, enabling the plant to pollinate itself and preventing crosses.

To create hybrid mustards, breeders must impede pollen development in one parent. Pental and other Indian researchers have used cytoplasmic male sterility (CMS) systems, in which a wild mustard variety carrying a gene that stops pollen development is crossed with a cultivated mustard to transfer the gene, creating a female parent. Next, the female parent is crossed with another cultivated mustard variety. Because the second plant carries a gene that counteracts the CMS gene, the resulting hybrid is fertile. But the approach is prone to glitches. For example, the female parent of Pental's CMS hybrid tends to revert to producing pollen in colder conditions, which cuts the yield of hybrid seeds. "CMS systems are stuck," Pental says.

Seeking a better approach, about 20 years ago Pental began tinkering with a method pioneered in Canada in GM canola, a mustard relative that can also self-pollinate. The method relies on genes from a soil microbe that accomplish roughly the same thing as the CMS system, but more reliably. One gene codes for barnase, an enzyme that kills cells needed for pollen development. The second gene counteracts it. Pental inserted the barnase gene into an Indian strain of *B. juncea* to create a female parent and the other gene into an east European mustard. The resulting hybrid produces more than 25% more seed than mustards planted widely in India. A third introduced gene confers resistance to an herbicide to streamline seed production.

Critics such as the Coalition for a GM-free India argue that GM mustard could spread genes into landraces—traditional varieties that farmers have cultivated for centuries. Landraces in India, a center of diversity for *B. juncea*, are a valuable source of genetic material for breeding programs, says coalition member Kavitha Kuruganti here. "If GMOs [genetically modified organisms] contaminate these varieties," she asks, "where will you get future gene stocks from?"

Such fears are overblown, plant researchers say. The risk of genetic contamination from GM crops is no higher than the risk of contamination from new non-GM crops, they say. In both cases, the risk is low because these genes are unlikely to persist unless they benefit landraces. And most mustard landraces are already safeguarded in national germplasm banks, according to Kailash C. Bansal, a plant biotechnologist at Delhi's National Agricultural Education Project. "To me, the danger to biodiversity from transgenic mustard is not a big concern," he says.

The Indian government has held talks with GM mustard opponents, but its secrecy with toxicity data has done little to allay concerns. Last month, India's Central Information Commission, an agency tasked with ensuring government transparency, directed the regulator, the Genetic Engineering Approval Committee (GEAC), to release the data from toxicity tests. GEAC still hasn't done so. "GEAC should be transparent," says Rakesh Tuli, a plant geneticist at Punjab University in Chandigarh and a former GEAC member. "I don't know why we believe safety data is a holy cow and cannot be made public."

GEAC member Ranjini Warrier in Delhi told *Science* that the committee is still reviewing the data and could not comment on when they would be made public. Javadekar has promised to build a consensus with environmentalists before any decision, hoping to avoid another impasse. ■

Priyanka Pulla is a writer in Bangalore.

Downloaded from http://science.sciencemag.org/ on May 26, 2016

Published by AAAS



An amendment proposed in Brazil may soon make it impossible to challenge the construction of hydroelectric dams, like this one on the Madeira River.

LATIN AMERICA

Brazilian crisis threatens science and environment

Proposed constitutional amendment could gut environmental protections

By **Lizzie Wade**

In the midst of Brazil's political turmoil, pro-development forces are moving ahead on a constitutional amendment that could speed approval for dams, highways, mines, and other megaprojects. The measure has alarmed scientists, environmentalists, and indigenous rights advocates, who fear it would gut the country's environmental licensing process. It is just one of a series of actions that has the scientific community on edge after Dilma Rousseff was removed as president on 12 May. Rousseff faces an impeachment trial for illegally borrowing money from state banks to cover budget deficits.

The new interim government, led by former Vice President Michel Temer, has set out to trim government spending and boost business. Days after taking power, it merged the science ministry into the communications ministry, leaving researchers fearing for what's left of their already diminished budgets (*Science*, 28 August 2015, p. 909). Meanwhile, powerful political players are attempting to remove roadblocks to development. "We are very worried about these actions that represent the demoting of science and innovation in the country," says Luiz Davidovich, president of the Brazilian Academy of Sciences in Rio de Janeiro.

Currently, Brazil has a three-step licensing process for infrastructure and development projects. During each phase, a project can be challenged or halted by lawsuits, and delays can last for years. The amendment, known as PEC 65, would eliminate all but the first step: the submission of a preliminary environmental impact statement. After that requirement is met—and regardless of how serious the impact seems to be—a project could not be delayed or canceled for environmental reasons, barring the introduction of substantially new facts.

"If this legislation is approved, it will probably be catastrophic for the environment and the people who depend on it," says Hani Rocha El Bizri, an ecologist at the Federal Rural University of the Amazon in Belém, Brazil. Representatives of several government agencies agree. In practice, PEC 65 "proposes the end of licensing," says Thomaz Miazaki de Toledo, the director for environmental licensing at the Brazilian Institute of Environment and Renewable Natural Resources in Brasília, an arm of the Ministry of the Environment. If the amendment passes, he says, "mitigation and compensation, now required and supervised by the licensing authority, would be voluntary."

That is particularly worrying to the National Indian Foundation (FUNAI), the government agency charged with protecting indigenous peoples. Without a chance to review and challenge preliminary environment impact statements, the agency cannot ensure that mitigation strategies are in place to protect indigenous tribes, says FUNAI spokesperson Mônica Machado Carneiro in Brasília—for instance, to compensate them if a dam would diminish their access to water and fish stocks. "We believe [PEC 65] is a clear setback to the fundamental right to the environment," Carneiro says.

Supporters counter that vital infrastructure projects should not face the possibility of long and unpredictable delays. "Works fundamental to meet the needs of Brazilian society are paralyzed for a long time," wrote Senator Acir Gurgacz in a statement justifying the amendment. He has complained to the Brazilian press about a 10-year legal battle to do maintenance on a highway that connects Porto Velho to Manaus, running through the Amazon rainforest. (The senator's father owns a bus company that carries passengers along that route.) The amendment was also supported in the Senate by Senator Blairo Maggi, a soybean magnate who was recently named Temer's minister of agriculture.

PEC 65 was first proposed in 2012 but languished until 27 April, when the Senate's Committee on Constitution, Justice, and Citizenship quietly voted to approve it. Critics say it is no accident that PEC 65 re-emerged during the height of Brazil's political crisis. "Of course some people will pick up on [the chaos] as an opportunity to approve things that should require longer discussions and push forward changes like this one," says Jonathan Bausch Macedo, an ecologist at the Mamiraúa Institute for Sustainable Development in Tefé, Brazil.

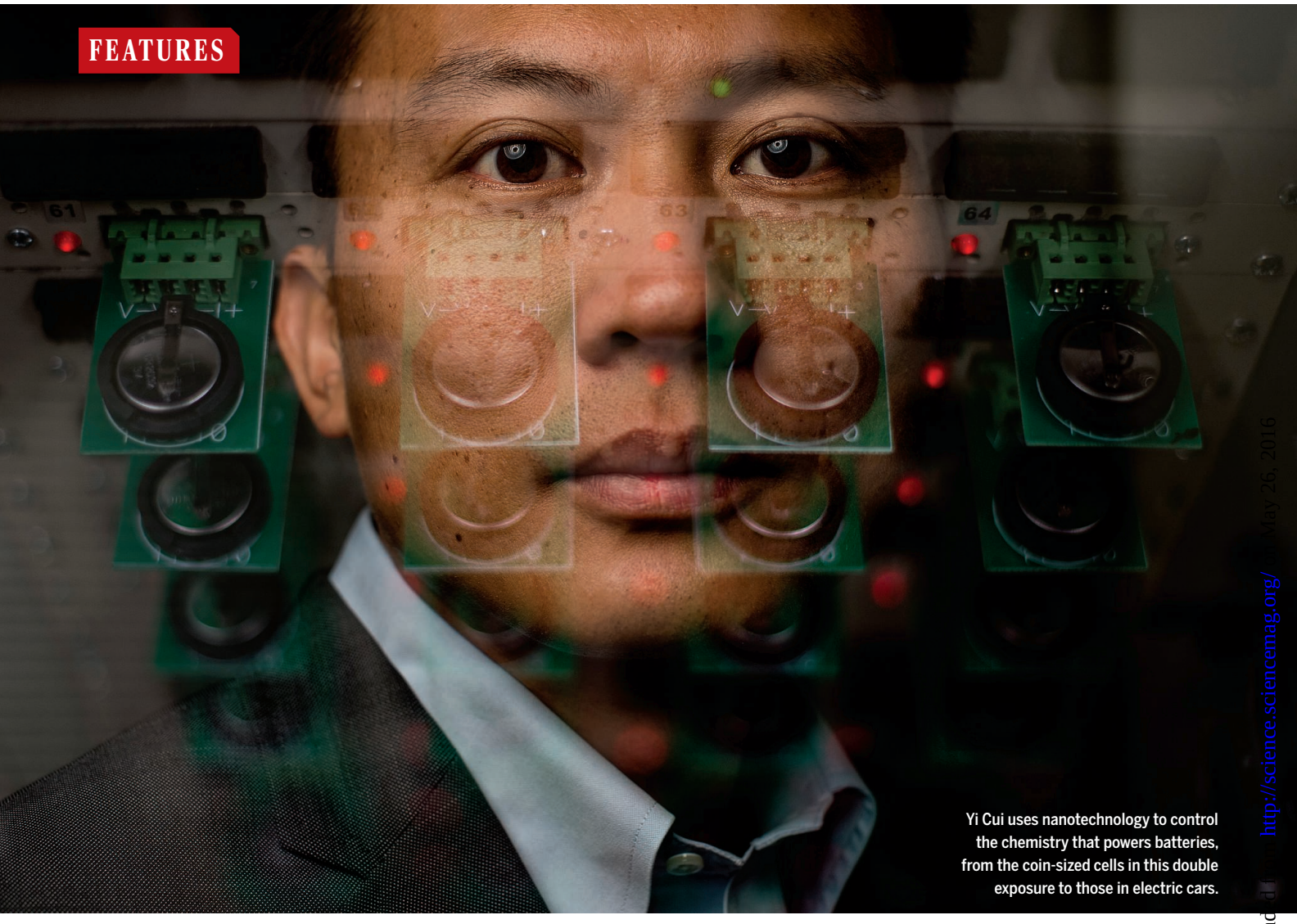
The amendment will go to the full Congress for a vote any day. If approved, it would go back to the Senate and, finally, to the president. "Amendments to the constitution should be considered very carefully, with lots of discussion," Davidovich says. "We should be careful about doing them in moments of crisis." ■

PHOTO: PULSAR IMAGES/ALAMY STOCK PHOTO

Downloaded from http://science.sciencemag.org/ on May 26, 2016

Published by AAAS

FEATURES



Yi Cui uses nanotechnology to control the chemistry that powers batteries, from the coin-sized cells in this double exposure to those in electric cars.

Downloaded from http://science.sciencemag.org/ May 26, 2016

THE BATTERY BUILDER

Yi Cui is pioneering efforts to use nanotechnology to revolutionize battery design, and just perhaps save the world

By **Robert F. Service**, *in Palo Alto, California; Photography by* **Noah Berger**

On a drizzly, gray morning in April, Yi Cui weaves his scarlet red Tesla in and out of Silicon Valley traffic. Cui, a materials scientist at Stanford University here, is headed to visit Amprius, a battery company he founded 6 years ago. It's no coincidence that he is driving a battery-powered car, and that he has leased rather than bought it. In a few years, he says, he plans to upgrade to a new model, with a crucial improvement: "Hopefully our batteries will be in it."

Cui and Amprius are trying to take lithium-ion batteries—today's best commercial technology—to the next level. They have plenty of company. Massive corporations such as Panasonic, Samsung, LG Chem, Apple, and Tesla are vying to make batteries smaller, lighter, and more powerful. But among these power players, Cui remains a pioneering force.

Unlike others who focus on tweaking the chemical composition of a battery's electrodes or its charge-conducting electrolyte, Cui is marrying battery chemistry with nanotechnology. He is building intri-

Published by AAAS

cately structured battery electrodes that can soak up and release charge-carrying ions in greater quantities, and faster, than standard electrodes can, without producing troublesome side reactions. "He's taking the innovation of nanotechnology and using it to control chemistry," says Wei Luo, a materials scientist and battery expert at the University of Maryland, College Park.

In a series of lab demonstrations, Cui has shown how his architectural approach to electrodes can domesticate a host of battery chemistries that have long tantalized researchers but remained problematic. Among them: lithium-ion batteries with electrodes of silicon instead of the standard graphite, batteries with an electrode made of bare lithium metal, and batteries relying on lithium-sulfur chemistry, which are potentially more powerful than any lithium-ion battery. The nanoscale architectures he is exploring include silicon nanowires that expand and contract as they absorb and shed lithium ions, and tiny egglike structures with carbon shells protecting lithium-rich silicon yolks.

Amprius already supplies phone batteries with silicon electrodes that store 10% more energy than the best conventional lithium-ion batteries on the market. Another prototype beats standard batteries by 40%, and even better ones are in the works. So far, the company does not make batteries for electric vehicles (EVs), but if the technologies Cui is exploring live up to their promise, the company could one day supply car batteries able to store up to 10 times more energy than today's top performers. That could give modest-priced EVs the same range as gas-powered models—a revolutionary advance that could help nations power their vehicle fleets with electricity provided by solar and wind power, dramatically reducing carbon emissions.

Cui says that when he started in research, "I wanted to change the world, and also get rich, but mainly change the world." His quest goes beyond batteries. His lab is exploring nanotech innovations that are spawning startup companies aiming to provide cheaper, more effective air and water purification systems. But so far Cui has made his clearest mark on batteries. Luo calls his approach "untraditional and surprising." Jun Liu, a materials scientist at the Pacific Northwest National Laboratory in Richland, Washington, put it more directly: Cui's nanotech contributions to battery technology are "tremendous."

MAKING LEAPS in battery technology is surprisingly hard to do. Even as Silicon Valley's primary innovation, the computer chip, has made exponential performance gains for decades, batteries have lagged. Today's best lithium-ion cells hold about 700 watt-hours per liter. That's about five times the energy density of nickel-cadmium batteries from the mid-1980s—not bad, but not breathtaking. In the past decade, the energy density of the best commercial batteries has doubled.

Battery users want more. The market for lithium-ion batteries alone is expected to top $30 billion a year by 2020, according to a pair of recent reports by market research firms Transparency Market Research and Taiyou Research. The rise in production of EVs by car companies that include Tesla, General Motors, and Nissan accounts for some of that surge.

> ***"I wanted to change the world, and also get rich, but mainly change the world."***
> **Yi Cui**, Stanford University

But today's EVs leave much to be desired. For a Tesla Model S, depending on the exact model, the 70- to 90-kilowatt-hour batteries alone weigh 600 kilograms and account for about $30,000 of the car's price, which can exceed $100,000. Yet they can take the car only about 400 kilometers on a single charge, substantially less than the range of many conventional cars. Nissan's Leaf is far cheaper, with a sticker price of about $29,000. But with a smaller battery pack, its range is only about one-third that of the Tesla.

Improving batteries could make a major impact. Doubling a battery's energy density would enable car companies to keep the driving range the same while halving the size and cost of the battery—or keep the battery size constant and double the car's range. "The age of electric vehicles is coming," Cui says. But in order for EVs to take over, "we have to do better."

He recognized the need early in his career. After finishing his undergraduate degree in his native China in 1998, Cui moved first to Harvard University and then to the University of California (UC), Berkeley, to complete a Ph.D. and postdoc in labs that were pioneering the synthesis of nanosized materials. Those were the early days of nanotechnology, when researchers were struggling to get a firm handle on how to create just the materials they wanted, and the world of applications was only beginning to take shape.

While at UC Berkeley, Cui spent time with colleagues next door at the Lawrence Berkeley National Laboratory (LBNL). At the time, LBNL's director was Steven Chu, who pushed the lab to invent renewable energy technologies that had the potential to combat climate change, among them better batteries for storing clean energy. (Chu later went on to serve as President Barack Obama's secretary of energy from 2009 to 2013.)

"At the beginning, I wasn't thinking about energy. I had never worked on batteries," Cui says. But Chu and others impressed on him that nanotechnology could give batteries an edge. As Chu says now, it offers "a new knob to turn, and an important one," enabling researchers to control not only the chemical composition of materials on the smallest scales, but also the arrangement of atoms within them—and thus how chemical reactions involving them proceed.

After moving to Stanford, Cui quickly gravitated to the nexus between nanotechnology and the electrochemistry that makes batteries work—and accounts for their limitations. Take lithium-ion rechargeable batteries. In principle, these batteries are simple: They consist of two electrodes divided by a membrane "separator" and a liquid electrolyte that allows ions to glide back and forth between the electrodes. When a battery is charging, lithium ions are released from the positive electrode, or cathode, which consists of a lithium alloy, commonly lithium cobalt oxide or lithium iron phosphate. They are drawn toward the negatively charged electrode, called the anode, which is usually made of graphite. There they snuggle in between the graphite's sheets of carbon atoms. Voltage from an external power source drives the whole ionic mass migration, storing power.

When a device—say, a power tool or a car—is turned on and demands energy, the battery discharges: Lithium atoms in the graphite give up electrons, which travel through the external circuit to the cathode. Meanwhile, the lithium ions slip out of the graphite and zip through the electrolyte and the separator to the cathode, where they meet up with electrons that have made the journey through the circuit (see diagram, p. 1048).

Graphite is today's go-to anode material because it is highly conductive and thus readily passes collected electrons to the metal wires in a circuit. But graphite is only so-so at gathering lithium ions during charging. It takes six carbon atoms in graphite to hold on to a single lithium ion. That weak grip limits how much lithium the electrode can hold and thus how much

Downloaded from http://science.sciencemag.org/ on May 26, 2016

Published by AAAS

power the battery can store.

Silicon has the potential to do far better. Each silicon atom can bind to four lithium ions. In principle, that means a silicon-based anode can store 10 times as much energy as one made from graphite. Electrochemists have struggled in vain for decades to tap that enormous capacity.

It's easy enough to make anodes from chunks of silicon; the problem is that the anodes don't last. As the battery is charged and lithium ions rush in to bind to silicon atoms, the anode material swells as much as 300%. Then, when the lithium ions rush out during the battery's discharge cycle, the anode rapidly shrinks again. After only a few cycles of such torture, silicon electrodes fracture and eventually split into tiny, isolated grains. The anode—and the battery—crumbles and dies.

CUI THOUGHT he could solve the problem. His experience at Harvard and UC Berkeley had taught him that nanomaterials often behave differently from materials in bulk. For starters, they have a much higher percentage of their atoms at their surface relative to the number in their interior. And because surface atoms have fewer atomic neighbors locking them in place, they can move more easily in response to stresses and strains. Other types of atomic movement explain why thin sheets of aluminum foil or paper can bend without breaking more easily than chunks of aluminum metal or wood can.

In 2008, Cui thought that fashioning a silicon anode from nanosized silicon wires might alleviate the stress and strain that pulverize bulk silicon anodes. The strategy worked. In a paper in *Nature Nanotechnology*, Cui and colleagues showed that when lithium ions moved into and out of the silicon nanowires, the nanowires suffered little damage. Even after 10 repeated cycles of charging and discharging, the anode retained 75% of its theoretical energy storage capacity.

Unfortunately, silicon nanowires are much more difficult and expensive to fashion than bulk silicon. Cui and colleagues started devising ways to make cheaper silicon anodes. First, they found a way to craft lithium-ion battery anodes from spherical silicon nanoparticles. Though potentially cheaper, these faced a second problem: The shrinking and swelling of the nanoparticles as the lithium atoms moved in and out opened cracks in the glue that bound the nanoparticles together. The liquid electrolyte seeped between the particles, driving a chemical reaction that coated them in a nonconductive layer, known as a solid-electrolyte interphase (SEI), which eventually grew thick enough to disrupt the anode's charge-collecting abilities. "It's like scar tissue," says Yuzhang Li, a graduate student in Cui's lab.

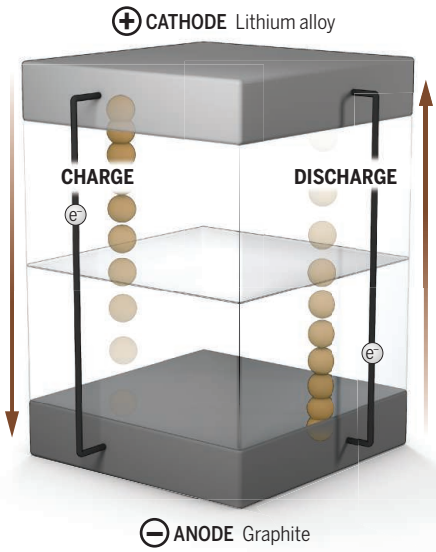
A few years later, Cui and his colleagues hit on another nanotech solution. They created egglike nanoparticles, surrounding each of their tiny silicon nanoparticles—the yolk—with a highly conductive carbon shell through which lithium ions could readily pass. The shell gave silicon atoms in the yolk ample room to swell and shrink, while protecting them from the electrolyte—and the reactions that form an SEI layer. In a 2012 paper in *Nano Letters*, Cui's team reported that after 1000 cycles of charging and discharging, their yolk-shell anode retained 74% of its capacity.

They did even better 2 years later. They assembled bunches of their yolk-shell nanoparticles into micrometer-scale collections resembling miniature pomegranates. Bunching the silicon spheres boosted the anode's lithium storage capacity and reduced unwanted side reactions with the electrolyte. In a February 2014 issue of *Nature Nanotechnology*, the group reported that batteries based on the new material retained 97% of their original capacity after 1000 charge and discharge cycles.

Earlier this year, Cui and colleagues reported a solution that outdoes even their complex pomegranate assemblies. They

Tiny tweaks tackle major battery problems

When a lithium-ion battery discharges current to an external circuit, lithium ions (tan) give up electrons and move from the anode through a separator to the cathode. There, they meet up with the electrons that traveled through the circuit. When the battery is charged, the flow of electrons and lithium ions is reversed.



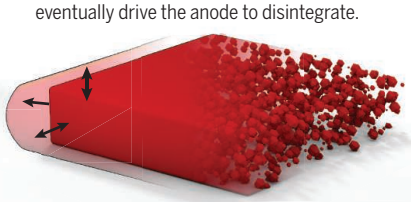
Silicon's promise

In a conventional graphite anode, it takes six carbon atoms to hold one lithium ion. In a silicon anode, each silicon atom can hold four—a huge advantage.



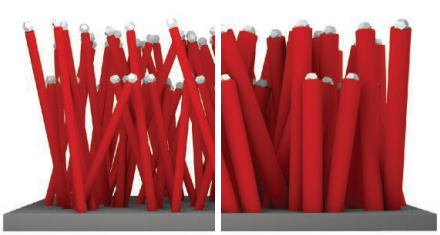
Silicon's problem

Unfortunately, silicon anodes swell and shrink as batteries charge and discharge; the changes in size eventually drive the anode to disintegrate.



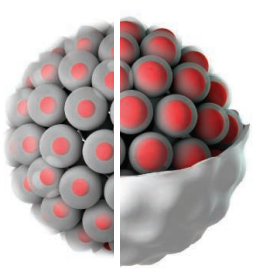
Nano to the rescue

Cui and colleagues have applied several nanotechnology-inspired solutions to keep silicon anodes from breaking down and to prevent battery-killing side reactions.





In one early fix, anodes forged from silicon nanowires swell and shrink without fracturing.





In another, clusters of egglike capsules shield silicon nanoparticles from unwanted reactions.

GRAPHIC: V. ALTOUNIAN/*SCIENCE*

Downloaded from http://science.sciencemag.org/ on May 26, 2016

Published by AAAS

simply hammered large silicon particles down to the micrometer scale and then wrapped them in thin carbon sheets made from graphene. The hammered particles wound up larger than the silicon spheres in the pomegranates—so big that they fractured after a few charging cycles. But the graphene wrapping prevented the electrolyte compounds from reaching the silicon. It was also flexible enough to maintain contact with the fractured particles and thus carry their charges to the metal wires. What's more, the team reported in *Nature Energy*, the larger silicon particles packed more mass—and thus more power—into a given volume, and they were far cheaper and easier to make than the pomegranates. "He has really taken this work in the right direction," Jun Liu says.

POWERED BY SUCH IDEAS, Amprius has raised more than $100 million to commercialize lithium-ion batteries with silicon anodes. The company is already manufacturing cellphone batteries in China and has sold more than 1 million of them, says Song Han, the company's chief technology officer. The batteries, based on simple silicon nanoparticles that are cheap to make, are only 10% better than today's lithium-ion cells. But at Amprius's headquarters, Han showed off nanowire-silicon prototypes that are 40% better. And those, he says, still represent only the beginning of how good silicon anodes will eventually become.

Now, Cui is looking beyond silicon. One focus is to make anodes out of pure lithium metal, which has long been viewed as the ultimate anode material, as it has the potential to store even more energy than silicon and is much lighter.

But there have been major problems here, too. For starters, an SEI layer normally forms around the lithium metal electrode. That's actually good news in this case: Lithium ions can penetrate the layer, so the SEI acts as a protective film around the lithium anode. But as the battery cycles, the metal swells and shrinks just as silicon particles do, and the pulsing can break the SEI layer. Lithium ions can then pile up in the crack, causing a metal spike, known as a dendrite, to sprout from the electrode. "Those dendrites can pierce the battery separator and short-circuit the battery and cause it to catch fire," says Yayuan Liu, another graduate student in Cui's group.

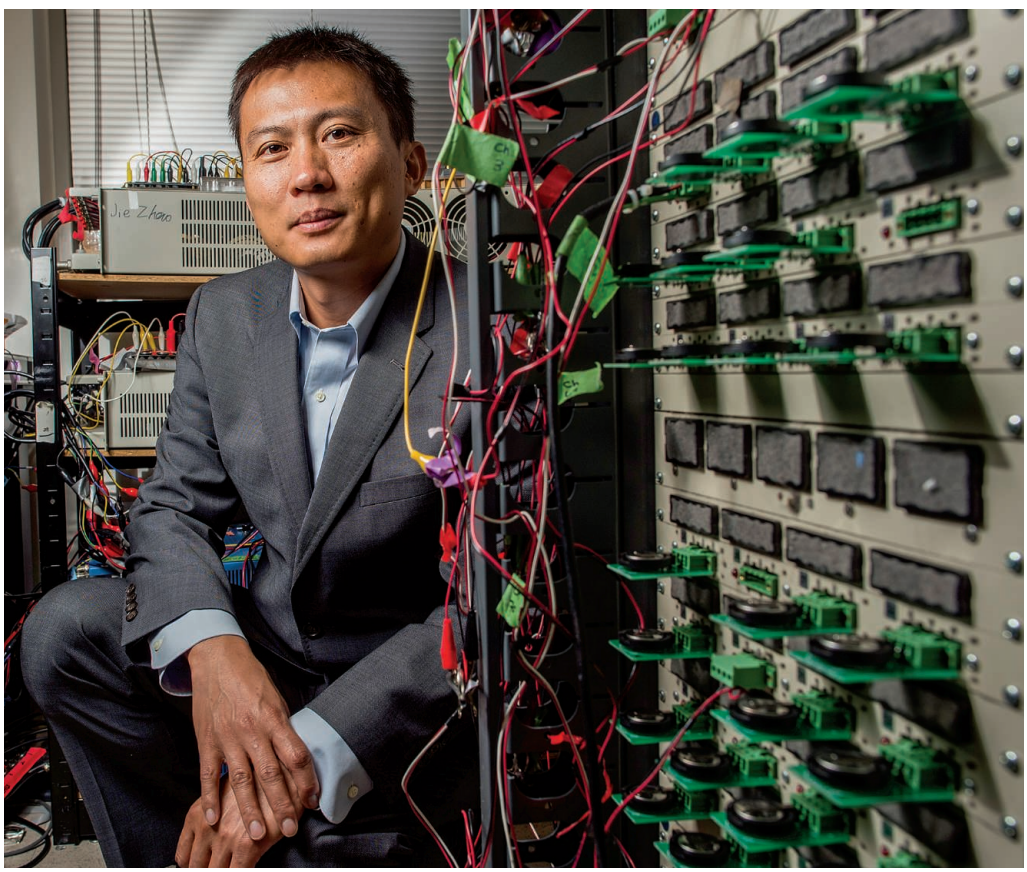
Conventional approaches haven't solved the problem. But nanotechnology might. In one approach to preventing dendrite formation, Cui's team stabilizes the SEI layer by coating the anode with a layer of interconnected nanocarbon spheres. In another, they've created a new type of yolk-shell particle, made of gold nanoparticles inside much larger carbon shells. When the nanocapsules are fashioned into an anode, the gold attracts lithium ions; the shells give the lithium room to shrink and swell without cracking the SEI layer, so dendrites don't form.

Improving anodes is only half the battle in making better batteries. Cui's team has taken a similar nanoinspired approach to improving cathode materials as well, in particular sulfur. Like silicon on the anode side, sulfur has long been seen as a tantalizing option for the cathode. Each sulfur atom can hold a pair of lithiums, making it possible in principle to boost energy storage severalfold over conventional cathodes. Perhaps equally important, sulfur is dirt cheap. But it, too, has problems. Sulfur is a relatively modest electrical conductor, and it reacts with common electrolytes to form chemicals that can kill the batteries after a few cycles of charging and discharging. Sulfur cathodes also tend to hoard charges instead of giving them up during discharge.

Seeking a nanosolution, Cui's team encased sulfur particles inside highly conductive titanium dioxide shells, boosting battery capacity fivefold over conventional designs and preventing sulfur byproducts from poisoning the cell. The researchers have also made sulfur-based versions of their pomegranates, and they have trapped sulfur inside long, thin nanofibers. These and other innovations have not only boosted battery capacity, but also raised a measure known as the coulombic efficiency—how well the battery releases its charges—from 86% to 99%. "Now, we have high capacity on both sides of the electrode," Cui says.

Down the road, Cui says, he intends to put both of his key innovations together. By coupling silicon anodes with sulfur cathodes, he hopes to make cheap, high-capacity batteries that could change the way the world powers its devices. "We think if we can make it work, it will make a big impact," Cui says.

It just might help him change the world, and get rich on the side. ■



With his battery company up and running, Cui plans to launch startups that apply nanotech to air and water purification.

PHOTO: NOAH BERGER

Downloaded from http://science.sciencemag.org/ on May 26, 2016

Published by AAAS



Cellulose breakdown. Insights into how fungal enzymes break down crystalline cellulose fibers may be useful for industrial processes. The false-color SEM image shows cellulose fibers in a paper towel. Each fiber is about 10 to 15 μm wide.

CHEMISTRY

How to break down crystalline cellulose

Biochemical and genomic data elucidate how a fungal enzyme attacks polysaccharides

By **Angel T. Martínez**

Biomass-degrading microorganisms use lytic polysaccharide monooxygenase (LPMO) enzymes to help digest cellulose, chitin, and starch. By cleaving otherwise inaccessible crystalline cellulose chains, these enzymes provide access to hydrolytic enzymes. LPMOs are of interest to biotechnology because efficient depolymerization of cellulose is a major bottleneck for the production of biologically based chemicals and fuels. On page 1098 of this issue, Kracher *et al.* (*1*) compare LPMO-reducing substrates in fungi from different taxonomic groups and lifestyles, based on both biochemical and genomic evidence. The results provide insights into reductive activation of LPMO that are important for developing more efficient industrial enzymes for lignocellulose biorefineries.

Early studies (*2*) on microbial cellulose degradation proposed a two-component system, in which a first, unidentified component (C_1) helps to overcome the polysaccharide crystallinity and a second component (C_x) corresponds to the glycoside hydrolases (cellulases) that were discovered at the time. Sixty years passed between these studies and the description of the missing enzyme in cellulose degradation: fungal and bacterial copper-containing LPMOs that act on crystalline polysaccharides (*3*–*5*). Addition of ascorbic acid enabled demonstration of the monooxygenase activity of these enzymes and the associated breakdown of cellulose and chitin chains (*5*). However, to understand the reaction mechanism and better use it industrially, scientists had to identify the natural LPMO reductant(s).

Since then, Phillips *et al.* have shown that another redox enzyme, cellobiose dehydrogenase (CDH), acts as a source of electrons for LPMOs (see the figure) (*6*). CDH is an oxidoreductase that oxidizes cellobiose at its flavin domain and reduces LPMOs at its heme domain after intramolecular electron transfer (*7*). CDH is likely to have a physiological role in activating fungal LPMOs, given that its electron-transfer rate is orders of magnitude faster than that of other reductants. Furthermore, Kracher *et al.* show that the two enzymes are more often found together in the genomes of white-rot, soft-rot, and plant pathogenic fungi than in the genomes of fungi with no or a limited number of cellulose-hydrolyzing enzymes.

Centro de Investigaciones Biológicas, CSIC, Madrid, Spain.
Email: atmartinez@cib.csic.es

Downloaded from http://science.sciencemag.org/ on May 26, 2016

PHOTO: DR. DENNIS KUNKEL MICROSCOPY, INC./VISUALS UNLIMITED, INC.

Published by AAAS

Other LPMO reductants in species lacking CDH are substituted phenols from lignin degradation or present as plant extractives. However, extractives, such as gallic acid, would be scarce in decayed lignocellulose. Moreover, even if phenols and quinones are among lignin-degradation products, a continuous supply is required to fully support LPMOs. Such supply would be considerably easier if these compounds were recycled by a chemical or enzymatic mechanism.

Chemical recycling has been reported in a reaction including LPMO oxidation of low–molecular mass phenols, and lignin reduction of the phenoxy radicals formed (*8*). However, Kracher *et al*. show that only phenols with very low redox potential (such as hydroquinones) can be oxidized by the enzyme; the radicals formed in these reactions are not expected to be strong lignin oxidizers. In contrast, enzymatic redox cycling of quinones is fully operative in the presence of glucose dehydrogenase (GDH). Both GDH and CDH are members of the glucose-methanol-choline (GMC) oxidoreductase superfamily, which also includes other quinone-reducing enzymes. As Kracher *et al*. show, the enzymatic mechanism for LPMO activation involving GDH is very efficient.

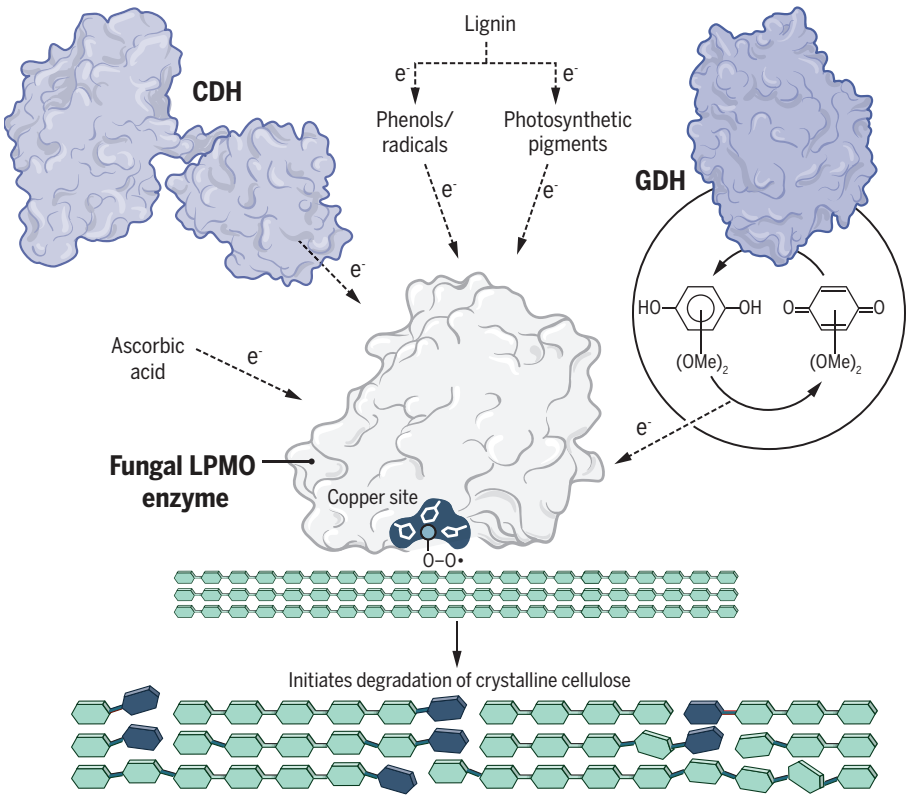
Photosynthetic pigments, once activated by light, can also transfer electrons to LPMOs and be reduced back by lignin preparations (*9*). The environmental relevance of light-driven cellulose degradation by LPMOs remains unclear, but the reaction is of applied interest because it proceeds 100 times faster than with standard reductants.

However, several questions about LPMO remain. First, although polysaccharide oxygenation takes place directly at the copper site, no agreement exists about the Cu(II) reduction site and mechanism. Several studies suggest a long-range electron transfer pathway (*10*), but others have suggested direct reducing-substrate oxidation at the same copper site (*7*). Moreover, although a Cu(II)-superoxide radical complex is formed after O_2 activation by Cu(I) (*10*), it is not clear whether this is the main catalytic species or whether a more reactive Cu(II)-oxyl radical is formed in a later step, as suggested by some molecular dynamics studies.

Second, the diversity of LPMOs remains little explored. The number of identified LPMOs in genomes has increased exponentially since 2010, with 328 genes in the family of cellulose-cleaving fungal LPMOs, 1840 genes of chitin- and cellulose-cleaving bacterial LPMOs, 66 genes of chitin-cleaving fungal LPMOs, and 14 genes of starch-cleaving fungal LPMOs. This diversity shows that LPMOs are very ancient enzymes and offers a lot of potential for biotechnology. Biochemical studies must explore expected differences in catalytic and kinetic properties between these LPMO families.

Finally, biotechnology applications of these oxidoreductases are in their infancy. The enzyme industrial sector was strongly involved in the discovery and characterization of both LPMOs that act on cellulose (*3, 4*) and starch (*11*). Since 2012, several commercial cellulase preparations have included LPMOs (*12*), resulting in improved hydrolyzability and reduced cellulose crystallinity (*13*). These cocktails now need to be formulated for every raw material, process, and application, considering both the benefit from lowering the cellulase dosage and the concomitant formation of nonfermentable oxidized sugars.

On the basis of evidence provided by Kracher *et al*., we can conclude that lignocellulose-degrading fungi developed different lifestyle-related mechanisms for electron supply to LPMO. These mechanisms operate continuously and involve oxidation of simple sugars (in the cases of CDH and GDH) or lignin (in the cases of phenols and pigments). In this way, cellulose and other polysaccharides are efficiently depolymerized to monosaccharides by the combined action of LPMOs and glycoside hydrolases. Kracher *et al*. also show that GMC oxidoreductases contribute directly (CDH) or through quinone redox cycling (GMC dehydrogenases) to activating LPMO for cellulose depolymerization. These findings reveal unexpected connections between polysaccharide and lignin biodegradation in plant materials. ■



Fuel for cellulose degradation. LPMOs are key enzymes in crystalline cellulose degradation. LPMO activity was first detected with ascorbic acid as an electron source. Since then, several natural electron sources have been identified, including enzymes (such as CDH), simple phenols, and even light-activated photosynthetic pigments. The electrons reduce a catalytic copper ion, enabling LPMO to activate O_2 by forming a reactive Cu(I)-superoxide. The latter initiates degradation by breaking down cellulose chains and lowering crystallinity. Kracher *et al*. compare the above electron sources for the enzyme and show that quinone redox cycling by GMC oxidoreductase (such as GDH) is a particularly efficient LPMO activation mechanism.

REFERENCES

1. D. Kracher *et al*., *Science* **352**, 1098 (2016).
2. E. T. Reese *et al*., *J. Bacteriol.* **59**, 485 (1950).
3. P. V. Harris *et al*., *Biochemistry* **49**, 3305 (2010).
4. R. J. Quinlan *et al*., *Proc. Natl. Acad. Sci. U.S.A.* **108**, 15079 (2011).
5. G. Vaaje-Kolstad *et al*., *Science* **330**, 219 (2010).
6. C. M. Phillips *et al*., *ACS Chem. Biol.* **6**, 1399 (2011).
7. T.-C. Tan *et al*., *Nat. Commun.* **6**, 7542 (2015).
8. B. Westereng *et al*., *Sci. Rep.* **5**, 18561 (2015).
9. D. Cannella *et al*., *Nat. Commun.* **7**, 11134 (2016).
10. W. T. Beeson *et al*., *Annu. Rev. Biochem.* **84**, 923 (2015).
11. L. Lo Leggio *et al*., *Nat. Commun.* **6**, 5961 (2015).
12. P. V. Harris *et al*., *Curr. Opin. Chem. Biol.* **19**, 162 (2014).
13. X. Ju *et al*., *Appl. Microbiol. Biotechnol.* **98**, 4409 (2013).

10.1126/science.aaf8920

ILLUSTRATION: K. SUTLIFF/*SCIENCE*

Downloaded from http://science.sciencemag.org/ on May 26, 2016

Published by AAAS

CANCER

The cancer predisposition revolution

How was the inherited basis of cancer foreshadowed?

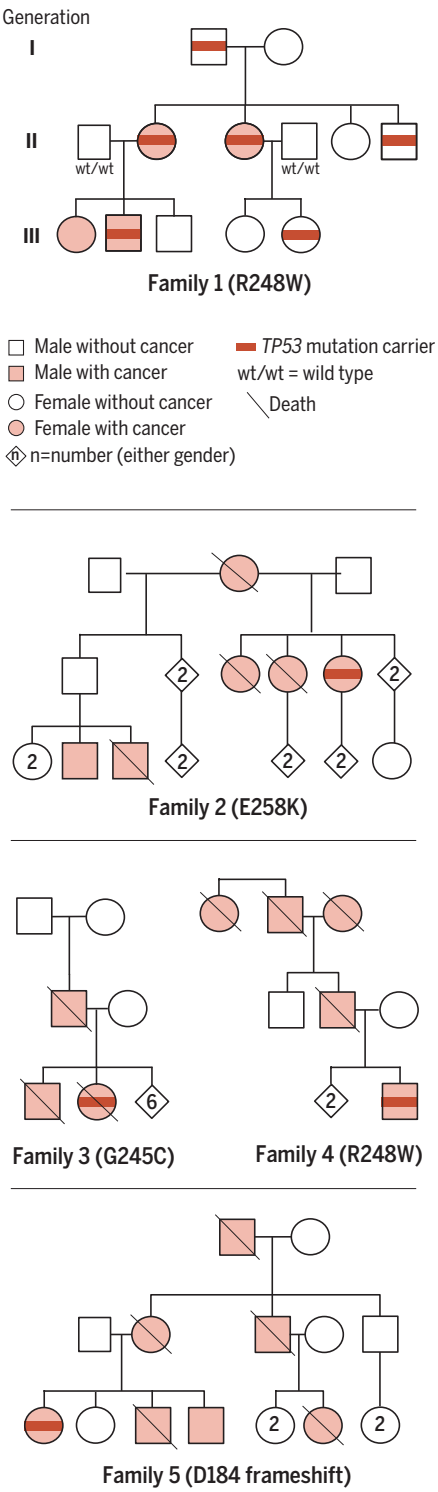
By David Malkin,[1] Judy E. Garber,[2] Louise C. Strong,[3] Stephen H. Friend[4]

Studies of rare cancer predisposition syndromes often lead to the identification of genes critical to carcinogenesis. In 1969, Li and Fraumeni described a constellation of various cancers in the family members of four unrelated children who were diagnosed with soft tissue sarcomas (*1*). They posited that the cancers best fit an autosomal dominant pattern of inheritance, attributable to a genetic defect. At that time, cancer was not generally thought of as a genetic disease. Their hypothesis set the stage for establishing germline mutations in the tumor suppressor gene *TP53* as the underlying genetic event in Li-Fraumeni syndrome (LFS) families (*2*) (see the figure). It also foreshadowed dozens of discoveries, still ongoing, that associate mutations in tumor suppressor genes, activated oncogenes, mitochondrial genes, and DNA repair genes with cancer predisposition phenotypes in which multiple different neoplasms occur across generations.

What makes the prescience of Li and Fraumeni remarkable is how little was known at the time. Their observation preceded both Knudson's "two-hit" theory of carcinogenesis and the technical ability to look for heritable mutations in genes, and it was not until 1986 that the first cancer susceptibility gene, *Rb1*, was shown to be responsible for retinoblastoma, a rare heritable cancer (*3*). In 1979, two groups discovered the p53 oncoprotein (*4*–*6*). The field then exploded with seminal papers that paved the way for the ultimate discovery of the link between p53 and LFS: the "classic" clinical features of LFS were defined (*7*); inactivating somatic *TP53* mutations were discovered in a wide spectrum of cancers (*8*); and a *Trp53* transgenic mouse was created that facilitated further research (*9*).

Remarkably, well into the 21st century, not only do new genes continue to be discovered to account for long-known cancer syndromes [e.g., *protection of telomeres 1* (*POT1*); *partner and localizer of BRCA2* (*PALB2*)], but new syndromes also continue to be defined. These include biallelic mismatch repair deficiency, in which early-onset cancers occur as a result of a perfect storm of inherited biallelic microsatellite gene mutations followed by somatic inactivation of a DNA polymerase (*10*), and DICER1 syndrome, in which an array of childhood and adult-onset tumors are caused by inactivation of a gene that is essential for microRNA processing (*11*). Thus, systematic clinical cancer epidemiology, as established by Li, Fraumeni, and Miller in the 1960s, continues to influence the discovery of cancer syndromes and cancer susceptibility genes and inform our understanding of the fundamental biology of human cancer.

Although different *TP53* mutations confer different degrees of penetrance, the overall lifetime risk of cancer is at least 75% in males and approaches 100% in females; the risk of developing multiple cancers is higher than in the general population by a factor of 85 (*12*). Despite progress in understanding the central role played by wild-type p53 in maintaining genome stability, and that of mutant p53 in cellular transformation, it is still nearly impossible to prevent or delay cancer in LFS, to predict age of onset, likelihood, or type(s) of cancers that will develop, to reduce the incidence of subsequent malignancies, or to optimally treat the cancers once they occur. Radiation-free clinical surveillance protocols may empower families to detect cancers early, offering hope for improved survival (*13*). However, the availability of whole-body magnetic resonance imaging (MRI) is limited in some jurisdictions because definitive evidence of efficacy is not yet available—a challenging problem in a rare syndrome. Whole-body MRI is being studied in many other cancer syndromes as well, particularly when cancer risk in childhood is a feature. Intensive screening efforts without risk reduction are fraught with additional challenges, including the establishment of detection precision, demonstration of definitive improvement in outcomes such as prolonged survival, and the complex psychological risk-benefit considerations of frequent examina-



The first families. Pedigrees of the first Li-Fraumeni syndrome families in whom germline *TP53* mutations were detected (*1*). The amino acid substitutions are shown for each family: C, Cys; D, Asp; E, Glu; G, Gly; K, Lys; R, Arg; W, Trp.

GRAPHIC: N. CARY/*SCIENCE*

[1]Division of Hematology/Oncology, Hospital for Sick Children and Department of Pediatrics, University of Toronto, Toronto, Ontario M5G 1X8, Canada. [2]Division of Population Sciences, Dana-Farber Cancer Institute, Harvard Medical School, Boston, MA 02215, USA. [3]Department of Genetics, University of Texas M. D. Anderson Cancer Center, Houston, TX 77030, USA. [4]Sage Bionetworks, Seattle, WA 98109, USA. Email: david.malkin@sickkids.ca

Downloaded from http://science.sciencemag.org/ on May 26, 2016

Published by AAAS

tions and potential false positives.

However, with the advent of affordable and rapid next-generation sequencing platforms, LFS germline and tumor genomes are being mapped with great precision. These efforts should reveal clues as to the genetic and epigenetic events that modify the effect of a *TP53* mutation on cancer phenotype. This information could lead to the development of more precise patient-specific algorithms to predict tumor type, which should lead to better surveillance strategies, perhaps including circulating tumor DNA and other biomarkers. Targeting the p53 signaling pathway with drugs offers opportunities to reprogram p53-dependent events, reengage wild-type p53 function, and reverse early p53-induced cellular transforming events. Animal models of p53 dysfunction to explore chemopreventive or therapeutic avenues are also critical to this line of discovery. Expanded access to comprehensive genetic data will permit more accurate mutation-specific penetrance estimates and more complete evaluation to correlate molecular alterations with pathogenicity.

Advances in LFS research have benefited from impressive international collaborative networks. Scientists studying the basic principles of p53 biology recognize the immense value of the LFS phenotype in understanding this fundamental cancer gene. At the same time, better syndrome recognition by physicians and expanded germline genetic testing have led to the identification of thousands of LFS families. The "glue" that keeps clinicians, clinician-investigators, and basic scientists working toward a common goal is the LFS families themselves. Through the international Li-Fraumeni Exploration (LiFE) Research Consortium or as individuals, patients contribute samples to research studies, share personal stories, and challenge the research community to address questions that are relevant to their lives. As the p53-LFS marriage enters its second quarter century, its history and evolution will continue to inspire and motivate all who work in the dynamic field of hereditary cancer. ■

REFERENCES AND NOTES

1. F. P. Li, J. F. Fraumeni Jr., *Ann. Intern. Med.* **71**, 747 (1969).
2. D. Malkin *et al.*, *Science* **250**, 1233 (1990).
3. S. H. Friend *et al.*, *Nature* **323**, 643 (1986).
4. D. I. Linzer, A. J. Levine, *Cell* **17**, 43 (1979).
5. D. P. Lane, L. V. Crawford, *Nature* **278**, 261 (1979).
6. M. Mowat *et al.*, *Nature* **314**, 633 (1985).
7. F. P. Li *et al.*, *Cancer Res.* **48**, 5358 (1988).
8. S. J. Baker *et al.*, *Science* **244**, 217 (1989).
9. A. Lavigueur *et al.*, *Mol. Cell. Biol.* **9**, 3982 (1989).
10. A. Shlien *et al.*, *Nat. Genet.* **47**, 257 (2015).
11. D. A. Hill *et al.*, *Science* **325**, 965 (2009).
12. M. Hisada *et al.*, *J. Natl. Cancer Inst.* **90**, 606 (1998).
13. A. Villani *et al.*, *Lancet Oncol.* **12**, 559 (2011).

ACKNOWLEDGMENTS

Dedicated in memory of Frederick P. Li—physician, scientist, scholar, colleague, mentor, and great friend.

10.1126/science.aag0832

POLYMER SYNTHESIS

Organic photocatalysts for cleaner polymer synthesis

Metal-free catalysts enable synthesis of polymers for biomedical and electronics applications

By **Sivaprakash Shanmugam** *and* **Cyrille Boyer**

The material properties of synthetic polymers can be tuned by changing their chain length and branching and the way in which monomer units repeat. For example, high-density polyethylene, which has little chain branching, is a stiff polymer used for food containers and drain pipes, whereas low-density polyethylene, which has more chain branching, is flexible and used to make grocery bags and bottles for chemicals. Polymers are usually made through thermal polymerization, but recent efforts focusing on green chemistry have led to a push toward using solar energy to drive chemical reactions. On page 1082 of this issue, Theriot *et al.* (*1*) report on metal-free visible-light photocatalysts that produce well-defined polymers free of metal contamination through radical polymerization.

"...this technique may become viable for synthesis of materials for industrial and biomedical applications."

Free-radical polymerization, in which a thermally decomposing radical initiates the addition of one monomer unit to another, is commonly used in industry. However, this approach cannot control chain length because of the rapid termination of growing chains. To ensure perpetual growth of polymer chains with homogeneous chain lengths, atom-transfer radical polymerization (ATRP) is commonly used (*2*–*4*). Unlike free-radical polymerization, ATRP generates chains with excellent chain-end functionality, which enables reactivation for further monomer addition or even postpolymerization modification. Moreover, atom-transfer radical polymerization provides the means to generate polymers with predetermined molecular weight, narrow molecular weight distribution, and copolymer composition (*5*). By controlling these properties, a new range of high-value applications have emerged in diagnosis, nanomedicine, and nanotechnology (*6*).

Nevertheless, ATRP has required transition-metal catalysts, predominantly copper halides, which become part of the polymer. The Cu^{I} state activates polymerization, whereas Cu^{II} deactivates it, but unavoidable chain termination can lead to accumulation of Cu^{II}. Thus, relatively high Cu concentrations—10,000 parts per million (ppm)—are required to maintain the equilibrium between Cu^{I} and Cu^{II}. Alternative solutions, specifically ARGET (activators regenerated by electron transfer) atom-transfer radical polymerization, have been proposed to reduce the amount of Cu (from 10,000 to 10 ppm) through the use of organic reducing agents, such as ascorbic acid and glucose, that maintain the Cu^{I} and Cu^{II} equilibrium (*2*). Alternatively, the use of ion-exchange resin and absorbent, such as alumina, silica, or talcum, can further reduce the concentration of catalyst in the final polymer product (*5*).

Although Cu contamination can be minimized by these approaches, complete removal of this transition metal is necessary for applications involving microelectronics and biomaterials, which has spurred the development of metal-free catalyst systems. The recent work of the groups of Hawker and Matyjaszewski introduced control over atom-transfer radical polymerization through electrochemistry (*7*) and photochemistry [for selected examples and a review, see (*8*–*10*)]. Remarkable spatial, temporal, and sequence control has enabled fine tuning of the properties of the generated materials.

Realizing the potential of photochemical polymerization, Miyake and Theriot (*11*) initially explored the use of perylene as a photocatalyst for activation of photo-atom-transfer radical polymerization under visible light

Centre for Advanced Macromolecular Design (CAMD) and Australian Centre for NanoMedicine (ACN), School of Chemical Engineering, UNSW Australia, Sydney, NSW 2052, Australia. Email: cboyer@unsw.edu.au

Downloaded from http://science.sciencemag.org/ on May 26, 2016

Published by AAAS

and sunlight. Although metal-free atom-transfer radical polymerization was possible by using perylene to reduce alkyl bromide initiators, this approach provided poor control over polymerization because deactivation was inefficient. Nevertheless, this initial work laid the foundations for the establishment of organocatalyzed atom-transfer radical polymerization, which Theriot *et al.* used in a computationally directed discovery approach that narrowed down candidates to a class of photocatalysts with a 5,10-diphenyl-5,10-dihydrophenazine backbone (see the figure). Two major focuses of the study were the identification of photocatalysts (PCs) that, when excited, could reduce an alkyl bromide initiator through electron transfer, and the formation of stable radical cations ($PC^{+\cdot}$) that efficiently deactivated the propagating radical to yield controlled radical polymerization.

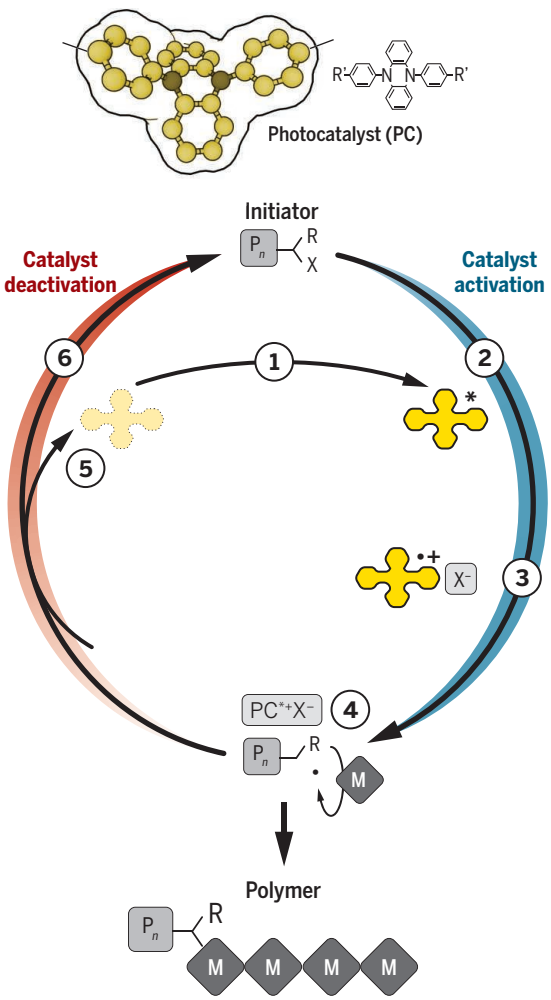
The substituent groups on the dihydrophenazine backbone were decorated with electron-donating, neutral, and electron-withdrawing groups, which resulted in PCs with strongly reducing excited states that readily reduced alkyl bromides. Upon light activation, the alkyl bromide initiators were activated by the PCs through single-electron transfer that resulted in the generation of radicals and oxidized PC^{+}. The propagating radical then moved on to add monomers with the probability of encountering the oxidized photocatalyst, which can result in back electron transfer to regenerate the PC and reversibly terminate the polymerization. The use of organocatalyzed atom-transfer radical polymerization resulted in polymerization of different methacrylates with a precise control of chain length.

Although the elimination of metallic contaminants opens up new avenues for atom-transfer radical polymerization, the organic route has several shortcomings that need to be addressed to increase viability and versatility. First, successful polymerization with organocatalyzed atom-transfer radical polymerization is limited to conjugated monomers such as methacrylates and acrylates. Unconjugated monomers such as vinyl acetate and electron-rich monomers such as styrene were not successfully polymerized. In addition, this approach requires a minimum catalyst loading of at least 200 ppm with respect to monomer ratio. Further development is required in this field in terms of expanding monomer compatibility, reducing or recycling the photocatalyst, and moving toward biocompatible solvents such as water.

One of the greatest challenges faced by atom-transfer radical polymerization is premature termination by oxygen. Trace amounts of oxygen can be tolerated after rigorous purging with nitrogen, but bypassing oxygen removal would greatly simplify synthesis. Such a leap has been made with radical polymerization techniques such as PET-RAFT (photoinduced electron/energy transfer reversible addition-fragmentation chain transfer), thus creating an opportunity for the development of oxygen tolerance for organocatalyzed atom-transfer radical polymerization (*12*).

Nevertheless, upon overcoming current drawbacks of organocatalyzed atom-transfer radical polymerization, this technique may become viable for synthesis of materials for industrial and biomedical applications. For example, by solving the issues of high catalyst loading and recyclability of the catalyst, organocatalyzed atom-transfer radical polymerization could be adapted to a flow system to scale up polymer production in industry. A further step would be to carry out simultaneous orthogonal reactions in a single pot, which has been a recent topic of focus for organic transformations under visible light. In addition, adapting organocatalyzed atom-transfer radical polymerization for initiation under lower-energy wavelengths, such as the near-infrared, can open up avenues for surface modification where penetration depth of visible light becomes an issue (*13*). Greater monomer versatility would allow metal-free synthesis of biomedically relevant polymers that respond to environmental triggers such as pH, light, and pressure. Perhaps the most important biomedical contribution of organocatalyzed atom-transfer radical polymerization will come from reducing toxicity of traditional ATRP through elimination of transition-metal contamination, especially protein-polymer and nucleic acid–polymer conjugates currently being developed as platforms for drug and gene delivery in the treatment of cancer and various other illnesses (*6*, *14*). ■

Light-driven polymerization. The scheme shows how light activates the photocatalyst (PC), which then reduces an alkyl bromide (RX) initiator. Upon forming a radical, additional monomer M adds to the polymer chain P_n with *n* subunits. Deactivation ensures that the process can be tightly controlled.



1 Light activates the photocatalyst into an excited state

2 Neutral initiator bearing a polymer chain P_n interacts with excited photocatalyst

3 Excited photocatalyst transfers an electron to the halide X, creating a radical polymer

4 Radical polymer initiator reacts with monomer M

5 Photocatalyst returns to ground state

6 Radical catalyst eventually deactivates, but can be reactivated by PC*

REFERENCES

1. J. C. Theriot *et al.*, *Science* **352**, 1082 (2016).
2. L. Frazer, *Environ. Health Perspect.* **115**, A258 (2007).
3. J.-S. Wang, K. Matyjaszewski, *J. Am. Chem. Soc.* **117**, 5614 (1995).
4. N. J. Treat *et al.*, *ACS Macro Lett.* **3**, 580 (2014).
5. N. V. Tsarevsky, K. Matyjaszewski, *Chem. Rev.* **107**, 2270 (2007).
6. C. Boyer *et al.*, *Chem. Rev.* **116**, 1803 (2016).
7. A. J. D. Magenau *et al.*, *Science* **332**, 81 (2011).
8. N. J. Treat *et al.*, *J. Am. Chem. Soc.* **136**, 16096 (2014).
9. T. G. Ribelli *et al.*, *J. Am. Chem. Soc.* **136**, 13303 (2014).
10. A. J. Teator, D. N. Lastovickova, C. W. Bielawski, *Chem. Rev.* **116**, 1969 (2016).
11. G. M. Miyake, J. C. Theriot, *Macromolecules* **47**, 8255 (2014).
12. J. Xu *et al.*, *J. Am. Chem. Soc.* **136**, 5508 (2014).
13. S. Shanmugam, J. Xu, C. Boyer, *Angew. Chem. Inter. Ed.* **55**, 1036 (2016).
14. D. J. Siegwart, J. K. Oh, K. Matyjaszewski, *Prog. Polym. Sci.* **37**, 18 (2012).

10.1126/science.aaf7465

GRAPHIC: V. ALTOUNIAN/SCIENCE

Downloaded from http://science.sciencemag.org/ on May 26, 2016

Published by AAAS

A metal shuttle keeps pathogens well fed

The metal-binding compound staphylopine captures nutrient metal ions for pathogens

By **Elizabeth M. Nolan**

Staphylococcus aureus is a Gram-positive bacterium that is a leading cause of life-threatening infections in humans. Knowledge of how this pathogen colonizes the human host and causes disease is crucial for the development of strategies to prevent and treat *S. aureus* infections (see the image, next page). On page 1105 of this issue, Ghssein *et al.* report the discovery, isolation, and functional evaluation of staphylopine (see the figure), a compound biosynthesized by *S. aureus* that captures metal ions from the pathogen's surroundings and thereby enables it to grow (*1*).

Transition metal ions are essential nutrients for all organisms. Metals provide structural integrity to proteins, enable processes such as electron transfer and catalysis, and act as signaling agents. More than 30% of all proteins contain a transition metal cofactor (*2*). To thrive, all organisms must acquire metals from their diet or the environment. They must also, however, maintain appropriate levels of metals to avoid toxic overload. Sophisticated mechanisms for metal acquisition, transport, and storage contribute to the regulation of metal ion levels in each cell and the whole organism (*3*).

In microbial infections, pathogens must obtain nutrient metals from the host to colonize and cause disease (*4*). Many studies using animal models of infection have shown that the ability of a pathogen to acquire nutrient metals confers virulence. In response to microbial infection, mammalian hosts launch a metal-withholding response to restrict metal availability and starve the pathogen (*4*). This tug-of-war for nutrient metals is a central and conserved component of the pathogenesis of infectious disease.

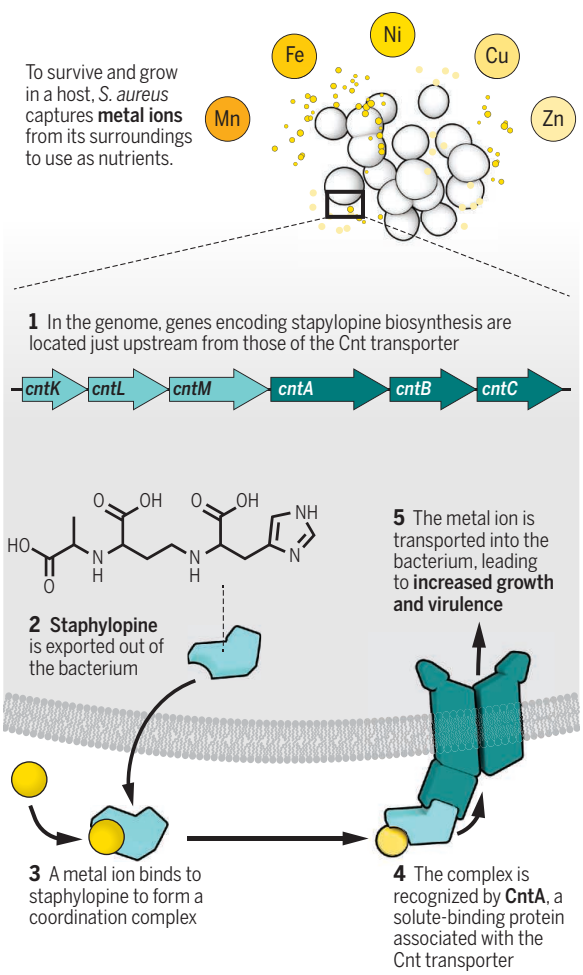
Ghssein *et al.* now provide further insight into how *S. aureus* acquires metal ions from its host. About 10 years ago, computational analyses of *S. aureus* genomes identified four putative adenosine triphosphate (ATP)–binding cassette (ABC) peptide transport systems (*5*). Experimental work showed that only one of these ABC transporters delivered polypeptides into *S. aureus*, leading to the hypothesis that the others transport different nutrients. Indeed, bioinformatic analyses suggested that the ABC transporter Opp1 delivers transition metals (*5*). Later studies showed that Opp1 transports nickel and cobalt when *S. aureus* is cultured under metal-deplete conditions (*6*). This ABC transporter, renamed Cnt (cobalt and nickel transporter), contributes to staphylococcal virulence in animal models of infection (*6*).

It remained unclear, however, how Cnt recognizes and transports metals. ABC transporters consist of a solute-binding protein, a transmembrane permease, and a cytoplasmic ATP hydrolase (*3*). For metal uptake by Gram-positive bacteria, the solute-binding protein must recognize and bind the metal ion in the extracellular space and deliver it to the permease. The molecular recognition event may require the metal ion to be bound to a metabolite, such as an amino acid or a more complex molecule. Recent biochemical studies have shown that the Cnt solute-binding protein (CntA) binds a Ni(II) coordination complex and suggested the existence of an as yet unidentified metal-chelating metabolite (*7*). Further analysis of the *S. aureus* genome revealed three biosynthetic genes (*cntK*, *cntL*, and *cntM*) upstream of the genes encoding the Cnt transporter, suggesting enzymatic machinery for the production of a metal-binding metabolite (*7*). One of the genes is homologous to plant nicotianamine synthase, which catalyzes the biosynthesis of nicotianamine, a metal chelator (*8*).

Building on these observations, Ghssein *et al.* elucidate the chemical structure and biosynthetic pathway of the nickel-binding staphylococcal metabolite, staphylopine (see the figure) (*1*). Enzymatic activity assays show that the proteins encoded by *cntK*, *cntL*, and *cntM* are necessary and sufficient for the biosynthesis of staphylopine. Reminiscent of nicotianamine, functional studies reveal that staphylopine binds and mediates the transport of nickel, iron, cobalt, copper, and zinc ions. Staphylopine thus seems to be a versatile metal carrier (metallophore) that contributes to staphylococcal virulence.

The authors also find that staphylopine production is not limited to *S. aureus*. Homologous biosynthetic genes are encoded by other microbial pathogens, including *Pseudomonas aeruginosa* and *Yersinia pestis*. Gi *et al.* recently concluded that *P. aerugi-*

Metal capture. The human pathogen *S. aureus* biosynthesizes staphylopine, a small molecule that is exported and binds first-row transition metals in the extracellular space. Cellular uptake of metal-bound staphylopine provides *S. aureus* with essential metal nutrients, enhancing growth and virulence.



GRAPHIC: V. ALTOUNIAN/*SCIENCE*

Department of Chemistry, Massachusetts Institute of Technology, Cambridge, MA 02139, USA. Email: lnolan@mit.edu

Downloaded from http://science.sciencemag.org/ on May 26, 2016

Published by AAAS

nosa deploys a metallophore of unknown molecular identity in airway mucus secretions to colonize the lungs of cystic fibrosis patients (*9*). Ghssein *et al.*'s findings suggest that this metallophore is staphylopine.

Staphylopine is likely to play a central role in the competition between host and microbe for nutrient metals. Future chemical and biological investigations should aim to decipher the interactions between CntA and metal-bound staphylopine. The interplay between staphylopine and host factors that contribute to the metal-withholding response also warrants exploration. Given that *S. aureus* contributes to polymicrobial infections, it will also be important to determine whether staphylopine affects microbe-microbe interactions and the compositions of polymicrobial communities. ■



A strategy for growth. *Staphylococcus aureus* is commonly found in the nose, in the respiratory tract, and on the skin; this false-color SEM image shows the bacteria (0.5 to 1.0 μm in diameter) on finger ridges. Ghssein *et al.* show that the bacteria use staphylopine to capture metals from their environment and support their growth.

REFERENCES

1. G. Ghssein *et al.*, *Science* **352**, 1105 (2016).
2. K. J. Waldron *et al.*, *Nature* **460**, 823 (2009).
3. Z. Ma *et al.*, *Chem. Rev.* **109**, 4644 (2009).
4. M. I. Hood *et al.*, *Nat. Rev. Microbiol.* **10**, 525 (2012).
5. A. Hiron *et al.*, *J. Bacteriol.* **189**, 5119 (2007).
6. L. Remy *et al.*, *Mol. Microbiol.* **87**, 730 (2013).
7. H. Lebrette *et al.*, *Metallomics* **7**, 613 (2015).
8. K. Higuchi *et al.*, *Plant Physiol.* **119**, 471 (1999).
9. M. Gi *et al.*, *Sci. Rep.* **5**, 14644 (2015).

10.1126/science.aaf8755

ECONOMICS

Matching markets in the digital age

Digital markets make it easier to match companies and customers

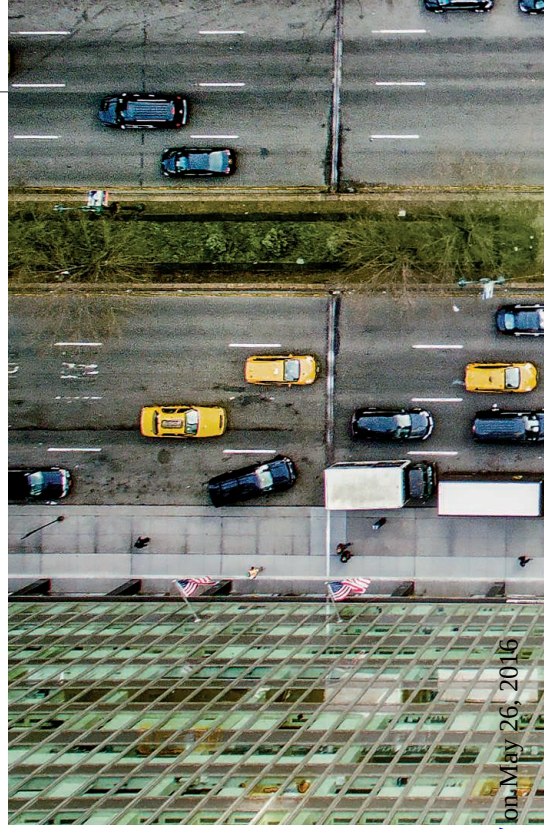
By **Eduardo M. Azevedo**[1] *and* **E. Glen Weyl**[2,3]

Recent advances in information technology are enabling new markets and revolutionizing many existing markets. For example, taxicabs used to find passengers through chance drive-bys or slow central dispatching (see the photo). Location tracking, computer navigation, and dynamic pricing now enable ride-sharing services such as Uber to offer low and consistent delay times of only a few minutes. In a recent study, Cramer and Krueger (*1*) show that ride-sharing has dramatically increased the usage of drivers and their cars, cutting costs for riders. The results highlight the opportunities provided by digital markets. Further efficiency gains may come from academia-industry collaborations, which could also help to ensure that the markets develop in ways that further the public interest.

Taxi services are an example of what economists call "matching markets." In such markets, participants care about who they transact with, rather than just about whether a transaction takes place. In the case of taxis, getting a ride from a driver who is miles away is much less convenient for both rider and driver than being matched with a nearby taxi. Similarly, a consumer looking for a new car may find advertising on this topic useful, whereas an automobile manufacturer will find it valuable to reach just these consumers. Other consumers will find such an advertisement to be an annoying distraction. Other examples include dating, travel lodging, personal entertainment, and payments.

Traditionally, these markets have been decentralized and used little technology. Finding a good match has been difficult and time-consuming. Information technology has improved matching efficiency by dramatically increasing the ability to process the data relevant to making a good match. Cramer and Krueger provide clear empirical evidence of this effect. UberX drivers, who use their own vehicles to drive Uber customers, spend roughly 40% more time and miles with a passenger in their cars than do standard cabs. Other studies have shown that standard cabs are clustered in the wrong parts of cities and that dynamic pricing, which charges higher prices when demand peaks, helps to ensure the consistent availability of cars (*2*–*5*). Thus, ride-sharing provides transportation services at a much lower cost than standard cabs by using fewer drivers and cars. It also ensures that consumers who value rides the most get them, even in times of peak demand.

Today's ride-sharing technology has made personal transport more efficient, in the same way that the industrial revolution's power loom made the textile industry more efficient. Many other services have seen remarkable improvements. Advertisements used to be broadcast uniformly across a whole population, many of whom found them useless or worse. On the Internet, tracking technology has made advertisements more relevant to consumers and more useful to firms (*6*). Elsewhere, people learn in real time about potential romantic matches in their physical vicinity. Listeners discover music through personalized recommendations. In recent years, economists have researched the functioning and design aspects of these markets (*7*).

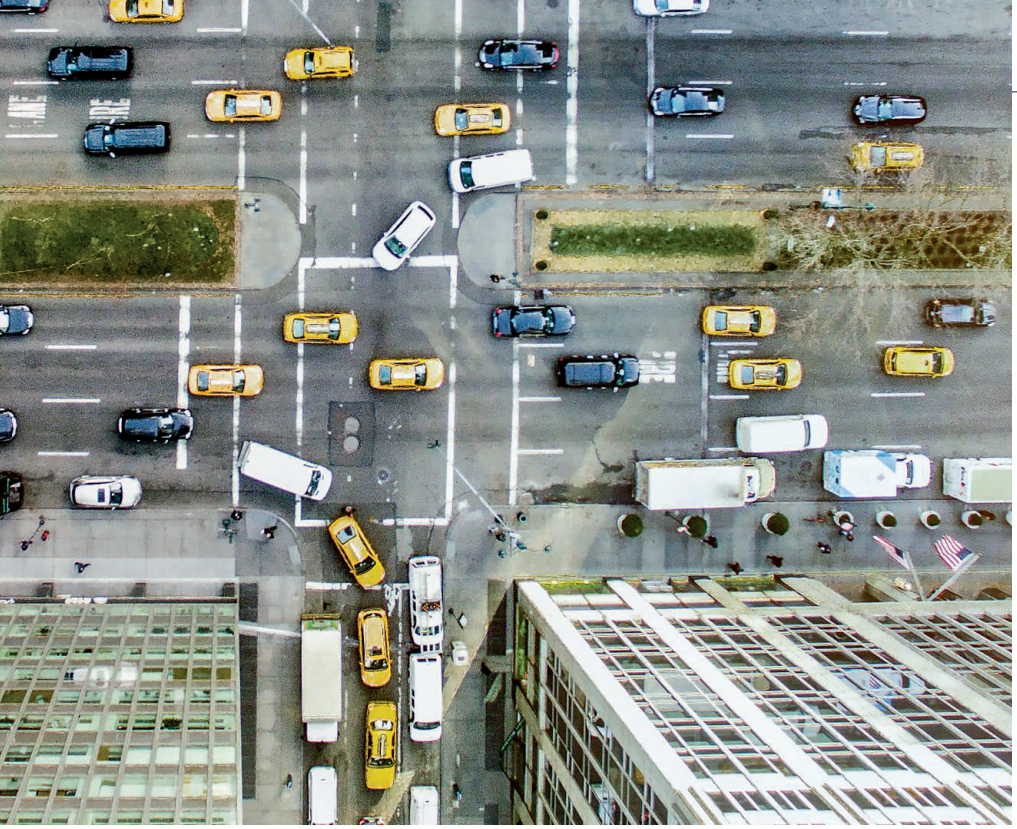


PHOTOS: (LEFT TO RIGHT) STANLEY FLEGLER/VISUALS UNLIMITED, INC.; ALIJA/ISTOCKPHOTO

[1]*Wharton School, University of Pennsylvania, Philadelphia, PA 19104, USA.* [2]*Microsoft Research New England, Cambridge, MA 02142, USA.* [3]*University of Chicago, Chicago, IL 60637, USA. Email: eazevedo@wharton.upenn.edu; glenweyl@microsoft.com*

Downloaded from http://science.sciencemag.org/ on May 26, 2016

Published by AAAS



Picking up business. Traditional taxis—such as those on Park Avenue, New York, shown here—tend to find customers through chance drive-bys. By using location tracking, dynamic pricing, and ride-sharing, companies such as Uber achieve much higher usage of drivers and their cars (*1*).

However, advances in enabling these digital marketplaces have emerged mostly from the private sector. Academic involvement has been limited, possibly because these advances require the integration of a range of skills. Cramer and Krueger highlight many factors critical to the value that UberX creates: Computerized optimization of routing allows multiple riders on different routes to share a car through the UberPool system; a simple user interface supplies necessary information; and tight targeting of prices across time and space responds to supply and demand conditions. Given the highly specialized nature of most academic institutions—how often do professors in design schools collaborate with economists?—it is not surprising that such collaboration failed to emerge in academia.

Nevertheless, academic research can augment the performance of these markets for three reasons. First, start-up companies implemented many features while growing rapidly, and the resulting systems are therefore not always optimal. Research can help to fine-tune these features. For example, Chen *et al.* (*8*) argue that Uber's pricing algorithm, by reacting to instantaneous supply and demand, causes short-lived price spikes. Drivers moving across the city to respond to these spikes often find that prices have fallen by the time they arrive. Hall *et al.* (*3*) suggest that this may lead to persistent fluctuations in prices following an initial shock. Economists have been familiar with these phenomena since 19th-century agricultural markets (*9*, *10*). It took the introduction of commodities futures to stabilize markets by allowing consumers and producers to anticipate future prices. Economists who have studied these markets for years may develop more stable algorithms for clearing markets dynamically. More generally, market design researchers may engineer rules to make markets work more efficiently (*11*).

Second, academic research is important because it produces innovations that are freely available through publications, whereas innovations developed in industry may take years to spread. An example of this spread occurred in the 1990s, when the U.S. government started auctioning radio spectrum rights. It used an auction format developed by academic game theorists in which different goods being sold are bid up in parallel to one another. Many other countries have since adopted this format.

Finally, because matching markets exhibit economies of scale, they tend to be dominated by a few powerful platforms. These platforms may enhance efficiency, but their primary interest is in profit. It is not in the industry's interests to highlight the inconvenient failures of these two standards to align. By contrast, academic research often focuses on how matching platforms should be regulated to ensure that they use their market power in the public interest (*12*).

For example, Nobel Laureate Jean Tirole has analyzed when credit card companies' practice of requiring merchants to accept both debit and credit cards if they accept one may align or conflict with social welfare (*13*). In particular, Rochet and Tirole have shown that this "honor all cards" rule is often useful to help establish the right balance of payments between credit and debit cards, when only credit cards are subject to competition given that debit cards are tied to a bank account; however, this rule may also in some cases limit the ability of merchants to steer consumers toward the most cost-effective payment method, reducing the efficiency of transactions (*14*). Similar controversies have arisen regarding the pricing and labor practices of Uber, which have been the subject of legal battles around the world over the past year.

Digital markets offer an exciting chance to make the economy work better. If economists wish to contribute to these gains, they will have to engage in new and challenging collaborations. The increasing presence of economists in the technology industry (one of us works at and the other is visiting a corporate research lab designed precisely to facilitate this sort of collaboration) is a natural locus for this interaction. However, academic institutions should also actively foster this collaboration to harness opportunities for research on unique data and employment of their graduates. ■

REFERENCES AND NOTES

1. J. Cramer, A. B. Krueger, *Disruptive change in the taxi business: The case of Uber*, NBER working paper 22083; www.nber.org/papers/w22083 (2015).
2. N. Buchholz, *Spatial equilibrium, search frictions and efficient regulation in the taxi industry*, working paper (2015).
3. J. Hall, C. Kendrick, C. Nosko, The effects of Uber's surge pricing: A case study, working paper (2015).
4. K. M. Chen, M. Sheldon, Dynamic pricing in a labor market: Surge pricing and flexible work on the Uber platform, working paper (2015).
5. G. P. Cachon, K. M. Daniels, R. Lobel, *The role of surge pricing on a service platform with self-scheduling capacity*; available at http://ssrn.com/abstract=2698192 (2015).
6. M. Gentzkow, *Am. Econ. Rev.* **104**, 5 (2014).
7. L. Einav, C. Farronato, J. Levin, *Ann. Rev. Econ.* **8** (2016).
8. L. Chen, A. Mislove, C. Wilson, Proc. of the 2015 ACM Conf. on Internet Measurement 495 (2015).
9. N. Kaldor, *Rev. of Econ. Studies* **1**, 122 (1934).
10. S. Rosen, K. M. Murphy, J. A. Scheinkman, *J. Pol. Econ.* **102**, 468 (1994).
11. A. E. Roth, *Nobel Lecture* (2012); www.nobelprize.org/nobel_prizes/economic-sciences/laureates/2012/roth-lecture.html.
12. E. G. Weyl, A. White, *Comp. Policy Intl.* **10**, 28 (2014).
13. J. Tirole, *Nobel Lecture* (2014); www.nobelprize.org/nobel_prizes/economic-sciences/laureates/2014/tirole-lecture.html.
14. J.-C. Rochet, J. Tirole, *Intl. J. Indust. Org.* **26**, 1333 (2008).

ACKNOWLEDGMENTS

We thank M. Carneiro, M. Frederickson, A. Holland, P.-P. Jiang, and S. Keynes for helpful comments on this article.

10.1126/science.aaf7781

Published by AAAS

Downloaded from http://science.sciencemag.org/ on May 26, 2016

GENE EXPRESSION

Unwinding inducible gene expression

Relieving DNA torsional stress may follow chromatin remodeling to facilitate transcription

By **Scott D. Pope** *and* **Ruslan Medzhitov**

The inflammatory response is coordinated by hundreds of genes that promote host defense against infection and injury. Inducible expression of these genes is mediated by distinct mechanisms, including transcriptional elongation, histone modifications, and nucleosome remodeling. On page 1074 of this issue, Rialdi *et al.* (*1*) report that a subset of the genes activated by viral infections depends on topoisomerase 1 (Top1) for induced expression. Pharmacological targeting of specific gene subsets has many clinical applications in inflammatory diseases. Because Top1 inhibition primarily affects genes dependent on nucleosome remodeling, many of which are key drivers of inflammation, it holds promise for gene-specific manipulation of the inflammatory response.

Eukaryotic DNA is packaged into nucleosomes in which DNA is wrapped around octamers of histone proteins. Through biochemical modifications (acetylation, methylation, ubiquitination, and phosphorylation), histones can coordinate the recruitment, stabilization, or exclusion of transcription regulatory complexes and demarcate functional regions of the genome such as promoters, enhancers, and gene coding sequences (*2*). This nucleosomal organization can be compacted even further to control the activity of specific genes. Genomic regions with more "open" or "loose" chromatin are associated with gene transcription, whereas more "closed" chromatin is associated with gene repression. The level of compaction is largely controlled by nucleosome remodeling complexes (*3*).

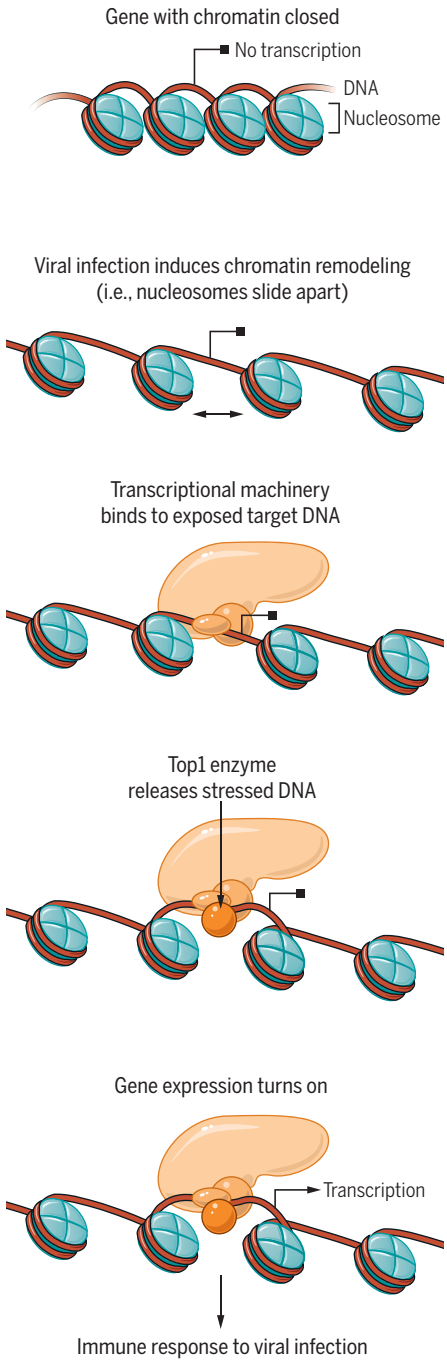
> ***"...selectivity may enable... Top1 inhibitors to treat acute hyperactive inflammation..."***

The induced expression of so-called primary response genes involves transcription factors that are activated by extracellular signals. The induced expression of secondary response genes requires primary response gene products. For genes that require chromatin remodeling for induced expression, remodeling complexes evict or slide the nucleosomes to expose binding sites for the transcription machinery (*4*).

Topoisomerase enzymes disentangle supercoiled DNA caused by the unwinding and rewinding of DNA during chromatin remodeling, transcription, DNA replication, and DNA recombination. Top1 is a member of the topoisomerase IB family and is an essential protein found in all eukaryotic cells. It relieves torsional stress by introducing a single-strand nick and allowing the DNA to rotate around the intact strand. Top1 functions by forming a transient, reversible bond between the 3′-phosphoryl end of the DNA and a tyrosine at the Top1 active site, thus causing a single-strand break in the DNA. After the bond is reversed, the DNA ligates, re-forming the double helix (*5*).

By using chemical inhibitors, as well as by reducing the amount of Top1 messenger RNA (mRNA) with small interfering RNAs, Rialdi *et al.* discovered that Top1 is required for inducing the expression of a subset of genes in cultured human lung epithelial cells in response to virus infection (see the figure). Top1 inhibition reduced the recruitment of RNA polymerase II, TATA-binding protein (which positions RNA polymerase for initiating transcription), and Top1 itself to the promoters of these genes, but did not affect housekeeping genes. Furthermore, the authors mapped the genome-wide distribution of inhibited Top1 during viral infection by using chemical-chromatin immunoprecipitation (chem-ChIP), followed by massively parallel DNA sequencing. After infection of epithelial cells, Top1 that was bound to an inhibitory compound was found at promoters, but not throughout the gene coding sequence, of the subset of virally induced genes whose expression is reduced by the compound. By contrast, for genes whose induced expression was not affected by the compound, Top1 (bound to the compound) was distributed throughout the promoter and gene coding sequence.

Rialdi *et al.* further observed that Top1 inhibitors increased survival in mouse models of infection, including infection



Inflammatory response, with a twist. Viral infection can elicit the expression of genes located within closed chromatin. Chromatin remodeling, which slides nucleosomes apart to expose such genes, reveals binding sites for factors to induce transcription. Top1 may alter the winding of DNA to facilitate this mechanism. Compounds that inhibit Top1 reduce the inflammatory response to viral infection.

ILLUSTRATION: K. SUTLIFF/*SCIENCE*

Department of Immunobiology and Howard Hughes Medical Institute, Yale University School of Medicine, New Haven, CT 06510, USA. Email: ruslan.medzhitov@yale.edu

Downloaded from http://science.sciencemag.org/ on May 26, 2016

Published by AAAS

with Ebola virus and *Staphyloccocus aureus*, where excessive inflammation is a major driver of pathology. These infections are associated with sepsis, a life-threatening condition caused by inflammatory tissue damage and organ failure (*6*). Top1 inhibition improved animal survival in these conditions, implicating Top1-dependent genes in the pathogenesis of sepsis.

Most genes in epithelial cells affected by Top1 inhibition require the nucleosome remodeling complex switch-sucrose nonfermentable (SWI-SNF) for their induced expression (*7, 8*). Furthermore, upon infection, the authors found a defect in histone H3 removal from the promoters of those genes for which induced expression was blocked by Top1 inhibition. This suggests that nucleosome remodeling, at least for some genes, is dependent on Top1. This could be because the sliding or removal of nucleosomes must exert torsional stress on the DNA, which would require the action of a topoisomerase for stress release.

A number of inhibitors of chromatin-interacting or -modifying proteins have shown promise as therapeutics. JQ1 (*9*) and I-BET (*10*) are compounds that block the interaction between histone modifications that activate gene expression and components of the transcriptional machinery. Histone deacetylase inhibitors prevent the removal of an activating histone modification (acetylation) and are used to counteract epigenetic changes in cancer (*11*). Top1 inhibitors stabilize the Top1-DNA bond that can lead to DNA damage, and are currently used to treat lung and ovarian cancer (*12*). Rialdi *et al.* show that Top1 inhibition attenuates the expression of genes that require chromatin remodeling and that by blocking just this subset of genes, survival is increased during pathological inflammation. This selectivity may enable the use of Top1 inhibitors to treat acute hyperactive inflammation such as sepsis. ■

REFERENCES

1. A. Rialdi *et al.*, *Science* **352**, aad7993 (2016).
2. E. I. Campos, D. Reinberg, *Annu. Rev. Genet.* **43**, 559 (2009).
3. C. R. Clapier, B. R. Cairns, *Annu. Rev. Biochem.* **78**, 273 (2009).
4. S. T. Smale, A. Tarakhovsky, G. Natoli, *Annu. Rev. Immunol.* **32**, 489 (2014).
5. S. H. Chen, N. L. Chan, T. S. Hsieh, *Annu. Rev. Biochem.* **82**, 139 (2013).
6. D. J. Stearns-Kurosawa *et al.*, *Annu. Rev. Pathol.* **6**, 19 (2011).
7. V. R. Ramirez-Carrozzi *et al.*, *Cell* **138**, 114 (2009).
8. V. R. Ramirez-Carrozzi *et al.*, *Genes Dev.* **20**, 282 (2006).
9. P. Filippakopoulos *et al.*, *Nature* **468**, 1067 (2010).
10. E. Nicodeme *et al.*, *Nature* **468**, 1119 (2010).
11. J. E. Bolden, M. J. Peart, R. W. Johnstone, *Nat. Rev. Drug Discov.* **5**, 769 (2006).
12. Y. Pommier, *Nat. Rev. Cancer* **6**, 789 (2006).

10.1126/science.aag0365

MEDICINE

Paying for future success in gene therapy

We must consider potential value, pricing, and sustainability of emerging gene therapies

By **Stuart H. Orkin**[1] *and* **Philip Reilly**[2]

Imagine a young man with hemophilia A who no longer has to self-administer factor VIII replacement; an individual with sickle cell disease who is free of chronic pain and intermittent crises; a girl functionally blind since the age of 5 who can now see; or a baby rescued from a fatal, inherited neurodegenerative disease.

POLICY

For decades, gene therapy has tantalized us with such futuristic scenarios. However, these goals are now coming into focus, and it is the time to consider some of the consequences of success.

DEVELOPMENT OF GENE THERAPY. Forty-four years have elapsed since an article appeared in *Science* on the possible therapeutic benefits of gene therapy (*1*). The early history was marked by poor trial design and a need for greater attention to basic aspects of viral gene transfer and disease biology (*2*). After some tragic setbacks and years of research to redesign existing vectors and identify safer ones, several trials have recently delivered promising results in regard to both safety and efficacy in several immunodeficiency disorders (*3*, *4*), hemophilia B (*5*), a form of congenital blindness (*6*, *7*), beta-thalassemia (*8*), and metachromatic leukodystrophy (*9*). We presume that gene therapy for at least one disorder currently in clinical trials will be established as safe and efficacious and that will lead to U.S. Food and Drug Administration (FDA) approval in the next 3 years.

> ***"New models for payment of approved gene therapies are needed..."***

Improving prospects have been met with accelerating financial investment by pharmaceutical and biotechnology firms. Many companies committed to gene therapy (including Audentes Therapeutics, Bluebird Bio, Dimension Therapeutics, Juno Therapeutics, REGENXBIO, Spark Therapeutics, uniQure, and Voyager Therapeutics) and to gene editing using either zinc-finger nucleases (Sangamo Biosciences) or CRISPR/Cas9 (Editas, Intellia, and CRISPR Therapeutics) have raised substantial capital, and most are, or will soon be, publicly traded. Moreover, large pharmaceutical companies have partnered with many of these entities and/or are also developing internal capabilities. Similar commercial interest in modified cells for cancer immunotherapy has emerged. At this writing, despite a dramatic recent downturn in the biotech sector, the market value (based on NASDAQ quotes on 11 March 2016) of just five (Bluebird Bio, Editas, Spark Therapeutics, uniQure, and Voyager Therapeutics) of the relatively new, publicly traded gene therapy companies (none of which have product revenues) exceeds $4 billion.

CHALLENGES POSED BY SUCCESS. As opposed to the majority of conditions that are the focus of much of the pharmaceutical and biotechnology industries, gene therapies often center on rare disorders affecting a very small fraction of the population—and, often disproportionately, children. Furthermore, unlike a traditional medical therapy that must be administered repeatedly, gene therapy is more similar to a surgical procedure, where the intent is to intervene once with a cure lasting a lifetime. Thus far, we have little human data to determine the duration of benefit in gene therapy. However, emerging data in trials involving the treatment of dogs and humans with rare monogenic eye disorders, and in one for patients with beta-thalassemia, suggest that therapeutic benefit lasting for years or perhaps decades may be achievable (*6*, *8*). As several gene therapies approach FDA approval, the critical matter of how such new therapies are to be valued will take front and center and will determine the economic sustainability of the entire field. Patients and families will regard therapies for their

[1]*Dana Farber Cancer Institute and Boston Children's Hospital, Howard Hughes Medical Institute, Harvard Medical School, Boston, MA 02115, USA.* [2]*Third Rock Ventures, Boston, MA 02116, USA. Email: stuart_orkin@dfci.harvard.edu; philip@thirdrockventures.com*

Downloaded from http://science.sciencemag.org/ on May 26, 2016

Published by AAAS

own disorders as priceless. For a one-time therapy that is the product of a lengthy and expensive preclinical and clinical effort, what is the appropriate price to charge the patient and, ultimately, society? How should that price be determined? Who will pay? Historical precedents, such as assisted reproduction and organ transplantation, instruct that transformative medical interventions are accepted by patients (and society) and eventually penetrate the marketplace, almost regardless of the cost.

ASSIGNING A VALUE TO GENE THERAPY. In considering the potential value of gene therapy, it is useful to reflect on the cost of current management of human genetic disorders (see the table). Although each disorder affects fewer than 100,000 individuals in the United States, in aggregate they represent an enormous cost to the health care system. For instance, treatment of the >70,000 patients with sickle cell disease (SCD) in the United States exceeds $1 billion per year. These estimates do not take into account lost opportunities from days out of work and the drain on families. Emerging immunotherapies will raise costs of treatment for certain cancers to unprecedented levels. FDA-approved immunotherapy combinations may approach $1 million per patient. The sole gene therapy treatment approved to date (in Europe), Glybera, aimed at rare patients with lipoprotein lipase deficiency, is priced at >$1 million per patient, despite doubts as to its efficacy (*14*).

Society has long supported expensive clinical interventions, if successful. Organ transplants (heart, liver, lung) cost on the order of $0.5 to $1.2 million in the first year (*15*). Some genetic disorders that involve multiple surgeries to correct cranial abnormalities require care that easily exceeds $1 million. Bone marrow transplantation (BMT) is used to treat hematopoietic malignancies, and sometimes used to treat SCD or beta-thalassemia and some genetic storage disorders. The full costs of BMT often exceed $0.5 million (*15*). We believe that $0.5 to $1.0 million for a highly efficacious gene therapy for a severe disorder would be in line with the accepted costs of established therapies. Current management programs for some monogenic disorders exceed $200,000 annually, and maintenance therapy for severely ill children can exceed that amount.

Unfortunately, clinical advances in gene therapy are unfolding in the midst of a complicated and bitter debate about the ethics of drug pricing in other sectors. For example, as the number of prescriptions written annually has steadily increased, so has the listed retail price for a year's treatment of the anticancer drug Gleevec in the United States—from about $26,000 in 2004 to over $120,000 in 2016 (*16*). In drug development, great scientific success creates short-term monopolies limited by patent life, legislative protections, and other forces.

Costs per patient of managing selected disorders

These approximate estimates are drawn from references (*10*–*13*). CFTR, cystic fibrosis transmembrane conductance regulator.

DISEASE ENTITY	MANAGEMENT PLAN	~COST/YEAR ($)	~COST/LIFETIME ($)
Cystic fibrosis	General support	25,000	750,000
	Drug to enhance CFTR function (Kalydeco)	300,000	5,000,000
Gaucher disease	Regular enzyme replacement	200,000	5,000,000
Hemophilia A	Prophylactic or periodic factor administration	300,000	5,000,000–10,000,000
Sickle cell disease	General medical support and hydroxyurea as standard of care	25,000	1,000,000

PRICING GENE THERAPY. There is a paucity of data to support decisions about pricing of new gene therapies. Estimates of the "savings" of one-time gene therapy versus chronic administration (such as factor replacement for hemophilia) appear straightforward. However, comparing the costs and benefits of one-time surgery for deep brain stimulation for persons with advanced cases of Parkinson's disease to those of stereotactically delivered gene therapy for the same condition (for which a trial is under way) is more complicated. Of course, for many genetic disorders, effective treatment is entirely lacking, and few benchmarks exist. Aside from evaluating current costs and options, we suggest some additional parameters that should be used to determine "reasonable" cost for gene therapies.

The modality of the specific gene therapy. Procedures to treat hemoglobin disorders, immunodeficiency, and neurodegenerative diseases entail acquisition of patient hematopoietic stem cells, ex vivo treatment with a lentiviral vector containing the therapeutic gene, preconditioning of the patient to destroy the endogenous hematopoietic system, and readministration of the modified cells. The supportive care is similar to that of typical BMT. Where gene therapy does not involve such labor- and resource-intensive procedures, the overall cost should be proportionately less.

Development costs. We estimate conservatively a time of 8 years and direct costs of several hundred million dollars (not to mention the need to amortize the costs of failed trials) to develop and secure approval for a new gene therapy. These costs will be roughly the same for efforts to treat ultrarare genetic disorders as for disorders that are more common. It is not too early to think about new models for supporting the development of drugs for extremely small populations of children with severe genetic disorders. Would society find it acceptable (or ethical) for biotech companies to recapture costs of developing a new drug for ultrarare disorders by increasing their profit margin on a drug that treats a less rare disorder?

Drug production costs. The manufacture and quality control of viral vectors is expensive, especially if the drug must be given systemically. Cost will vary greatly depending on the target organ. As defective cells in the eye reside in a localized region, current trials that involve direct subretinal delivery of a virus containing the therapeutic gene may be much less expensive than delivery of agents to multiple muscle groups in a patient with muscular dystrophy. In gene therapy for blindness, the major expenses are the amortization of the huge costs entailed in securing FDA approval and the ongoing costs involved in producing and delivering the product. Between the extremes of ex vivo transduction of stem cells and vector injection into the subretinal space are situations in which therapy is performed in vivo—for example, by infusion of virus in hemophilia B due to factor IX deficiency. As the field of gene therapy matures, the costs of drug production may decline. We know of no published analysis of this issue, but there may already be enough data to enable case studies about the impact of production costs on plans for pricing.

The treatable population. Simply put, the fewer the treatable patients, the higher the price will have to be for the therapy to pay a reasonable return to its investors. For example, although prospects for treating children with Tay-Sachs disease with gene therapy hold promise, only about 10 to 20 such children are born each year in the United States. Under the current U.S. system of drug development, it would be nearly impossible to recapture the investment costs to

Downloaded from http://science.sciencemag.org/ on May 26, 2016

Published by AAAS

gain approval for such a therapy, even at a charge of several million dollars per treatment. To encourage the development of gene therapy for ultrarare disorders, novel regulatory pathways should be considered. For example, should the federal government fund a new initiative or institute within the U.S. National Institutes of Health that is dedicated to drug development for severe ultrarare disorders (for example, those with an annual birth incidence or population prevalence of <1 in 250,000). We chose this number because some companies interested in rare genetic diseases will pursue such disorders, at least under current, unconstrained, pricing models. Working closely with the FDA, such a federally funded effort could conceivably drive many more therapies forward under a not-for-profit model.

Quality of the outcome. This is almost certainly the critical variable. A pivotal parameter for reimbursement should be the efficacy and duration of the therapeutic intervention. The range of success will vary widely both with the state of the disease at intervention and the long-term outcome as measured against historical knowledge. If gene therapy halts a progressive, fatal disorder (such as X-linked adrenoleukodystrophy) and leaves a child with a compromised, but meaningful, life, we think most would view the outcome as a major, albeit imperfect, clinical advance. If the intervention is demonstrably better than current therapy (which, if diagnosed early, is BMT with its attendant risks, but, if diagnosed late, is largely supportive), the therapy will almost certainly replace current treatments. Tying costs to efficacy will generate discussions about annuity payments, such as a large initial up-front payment with lower periodic payments made annually so long as the therapy remains efficacious. However, the health insurance industry does not customarily carry large contingent obligations on its books. The idea of an outcome-based annuity schedule will surely generate discussion as to whether future obligations stay with the patient, if he or she changes insurers.

The United States stands virtually alone in letting a free market determine drug prices. In England, the National Institute of Health and Care Excellence (NICE) decides whether a new drug offers sufficient benefit (e.g., over existing therapies) to be added to the national pharmacopoeia (*17*). It may be inevitable that such an approach will take hold in the United States, but that is unlikely to occur soon. But, even in case of life-threatening genetic disorders, meaningful therapeutic benefit can be a high bar. NICE recently advised against paying for Orkambi, a drug marketed by Vertex to treat cystic fibrosis, despite the fact that the EMA has approved it (*18*). In some important markets, even when the efficacy of a new therapy is clear, governments greatly influence pricing. For example, in Japan, regulatory authorities recently imposed a 30% price cut on the new drugs for treating (effectively curing) hepatitis C (*19*). But, hepatitis C affects hundreds of thousands of patients in the United States, Europe, and Japan. We think that pricing battles engulfing antiviral drugs are not likely to apply to life-saving therapy provided to a few hundred children a year with rare genetic diseases.

GOING FORWARD. Health care economists have developed sophisticated models to value new therapies. These models use many variables, including lifetime costs of current care, impact of the disease on the family and society, possible improvements offered by new therapies (such as whether a person would be able to work), and increase in life expectancy. They frequently calculate the gain that the therapy provides in terms of quality-adjusted life years (*20*). We applaud such efforts, but until we learn much more about the duration of the therapeutic effect of gene therapy, such analysis is premature. But, by any yardstick, successful, efficacious one-time (or a few times) gene therapy should be valued highly.

"...by any yardstick,... efficacious one-time (or a few times) gene therapy should be valued highly."

Over the past two decades, the biotech industry has invested >$10 billion in gene therapy and related technologies without generating a single dollar of product revenue. New models for payment of approved gene therapies are needed to ensure that patients have access to the best available options, to encourage payers (largely insurers, including cash-strapped, state Medicaid programs in the Unted States) to embrace transformative solutions for longer-term economic benefit in lieu of short-term gain, and to sustain (and expand) the efforts of biotechnology and pharmaceutical companies. Careful analysis of lump-sum or annuitized payment, also based on the "quality" of outcome, is warranted. The number of new regulatory approvals will steadily rise over the next decade, and the cost and pricing questions concerning the provision of new therapies for rare genetic disorders will not soon abate.

To catalyze discussion in the United States, we suggest possible, albeit partial, solutions. First, very expensive gene therapies with large up-front payments should require that the burden of retreatment be borne by the drugmaker or its successors. This would, in effect, help to cap drug costs and would require negotiated contracts between drugmakers and payers. Second, some reasonable portion of the economic benefits that under the Orphan Drug Act flow to companies that develop therapies for "orphan" disorders might be redirected to reducing the price of the drug, perhaps by greatly reducing the pricing of copays. This would require legislative action that would probably take several years to accomplish but is certainly possible. Third, the U.S. National Academy of Medicine (or a similar body) should commission a study to explore new methods to streamline the regulatory process for developing genetic and perhaps other therapies for ultrarare disorders. This might lead to a shorter and less expensive path to clinical trials and more reliance on postmarketing evaluation of risks and benefits. Success might encourage more companies to undertake clinical development for ultrarare disorders. We recognize that there are many other approaches that thoughtful study might uncover, but we need to begin to ensure that economic challenges are given the attention they deserve. ■

REFERENCES AND NOTES

1. T. Friedmann, R. Roblin, *Science* **175**, 949 (1972).
2. S. H. Orkin, A. G. Motulsky, *Orkin-Motulsky Report: Report and Recommendations of the Panel to Assess the NIH Investment in Research on Gene Therapy* (NIH, Bethesda, MD, 1995); http://bit.ly/InvestGeneTher.
3. S. Hacein-Bey-Abina *et al*., *N. Engl. J. Med.* **371**, 1407 (2014).
4. A. Aiuti *et al*., *Science* **341**, 1233151 (2013).
5. A. C. Nathwani *et al*., *N. Engl. J. Med.* **371**, 1994 (2014).
6. J. W. Bainbridge *et al*., *N. Engl. J. Med.* **372**, 1887 (2015).
7. F. Simonelli *et al*., *Mol. Ther.* **18**, 643 (2010).
8. M. Cavazzana-Calvo *et al*., *Nature* **467**, 318 (2010).
9. A. Biffi *et al*., *Science* **341**, 1233158 (2013).
10. J. Kaiser, *Science* **335**, 645 (2012).
11. T. A. Burrow, R. J. Hopkin, N. D. Leslie, B. T. Tinkle, G. A. Grabowski, *Curr. Opin. Pediatr.* **19**, 628 (2007).
12. B. M. Feldman *et al*., *Haemophilia* **18**, 680 (2012).
13. T. L. Kauf, T. D. Coates, L. Huazhi, N. Mody-Patel, A. G. Hartzema, *Am. J. Hematol.* **84**, 323 (2009).
14. L. M. Bryant *et al*., *Hum. Gene Ther. Clin. Dev.* **24**, 55 (2013).
15. National Foundation for Transplants, FAQ (2016); https://bit-ly/TransplantCosts.
16. C. Y. Johnson, *Washington Post*, 9 March 2016; http://wapo.st/1NrJ15K.
17. The National Institute for Health and Care Excellence; https://NICE.org.uk/.
18. P. Bonanas, Ed., "NICE rebuffs Vertex's Orkambi," in *BioCentury Extra*, 22 March 2016.
19. E. Schoonveld, Re-pricing rules in Japan slash prices for "huge sales" drugs (2016); https://bit.ly/27x5BAL.
20. F. Sloan, C.-R. Hsieh, *Health Economics* (MIT Press, Cambridge, MA, 2012).

ACKNOWLEDGMENTS

Boston Children's Hospital has nonexclusive license agreements with Sangamo Biosciences, BlueBird Bio, and CRISPR Therapeutics based on a patent issued to S.H.O. pertaining to *BCL11A* as a gene therapy target. P.R. is a cofounder, consultant to, and holds stock in the gene therapy companies Bluebird Bio and Voyager Therapeutics.

10.1126/science.aaf4770

Downloaded from http://science.sciencemag.org/ on May 26, 2016

Published by AAAS



In the absence of sea otters, burgeoning sea urchin populations threaten to decimate kelp forests and the diverse underwater ecosystems they support.

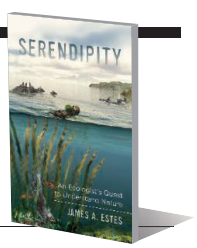
AUTOBIOGRAPHY

Navigating the cascades of circumstance

An ecologist reflects on the unexpected twists and turns that shaped his scientific career

By **Elizabeth Forbes, Ana Miller ter Kuile, Devyn Orr, Georgia Titcomb**

Serendipity
An Ecologist's Quest to Understand Nature
James A. Estes
University of California Press, 2016. 291 pp.



In the current job market, a mere 12 to 13% of Ph.D. students in the STEM fields (science, technology, engineering, and mathematics) will attain a tenure-track position in academia (*1*). Those of us tenacious enough to pursue a Ph.D. enter the running with the odds stacked against us.

In such a climate, it can become easy to lose sight of what initially motivated us to pursue a career in science. We, and many other ecologists, are driven by awe and curiosity to understand nature's patterns. And as individuals just embarking on our careers, it's exhilarating and terrifying to realize that some of the most exciting discoveries in science occur by chance. In his new book, *Serendipity*, eminent ecologist James A. Estes emphasizes these realities in an elegant narrative of his 45-year career studying sea otters and kelp forests.

Serendipity opens with Estes's account of his start in coastal marine ecology after chance events prevented him from serving in the Vietnam War. With his newly wide-open future, he combined service and science, beginning his research career in the western Aleutian archipelago as an employee of the Atomic Energy Commission. What started as a 2-year study of the effects of underground atomic weapons testing on sea otter populations evolved into a career focused on the dramatic effect of otters on the entire coastal ecosystem.

Estes's first major discovery, that a crucial relationship exists between sea otters, urchins, and kelp, is one of the most well-known examples of a trophic cascade. Sea otters prey on kelp-grazing urchins, thereby maintaining a kelp-dominated system. Without otters, urchins overgraze the kelp forests, creating barren expanses devoid of kelp and the rich communities that they support.

Estes's refreshing narrative deftly weaves rigorous science with personal reflection to create an absorbing and introspective read that is equal parts memoir, ecological textbook, and motivational guidebook for young ecologists. Throughout, he graciously acknowledges the external influences on his work by giving credit to fellow ecologists who were critical in understanding the otter-urchin-kelp cascade. In addition, he shares the many serendipitous moments that have driven his career. These include a pivotal conversation with renowned community ecologist Robert Paine that convinced Estes to consider sea otters as drivers of the kelp forest ecosystem; an unexpected sea otter population crash that prompted him to expand his research to the open ocean; and a last-minute decision to work at a new field site, resulting in a surprising explanation for the otter declines he witnessed. Moments such as these guided Estes as he expanded scientific understanding of coastal kelp forest dynamics and their far-ranging connections to pelagic and terrestrial ecosystems. His story transforms readers into fearless ecologists, fueled by curiosity and eager to decipher the patterns that do not quite add up, which are often at the brink of important discoveries.

While providing ample advice to young ecologists, *Serendipity* is refreshing and frank, capturing emotions that every scientist experiences: uncertainty, excitement, and curiosity. For those searching for the secrets to a fulfilling career, Estes's straightforward style opens a window into the life of a highly successful scientist. Other readers, who are well into their careers, will find that the same narrative serves as a revitalizing reminder of the self-doubt and exhilaration that go hand-in-hand with scientific discovery. *Serendipity* belongs on every field ecologist's bookshelf. Its lessons go far beyond the science of the otter-urchin-kelp cascade, instructing us to embrace the unpredictable twists and turns in our scientific careers.

Advice is infused throughout Estes's stories, but two recommendations resonated with us long after the last page had been turned. First, take advantage of serendipity; when seized upon and combined with hard work, chance encounters create career opportunities that you "will never anticipate in the beginning." Second, Estes advises us to pour our hearts into the quest for scientific knowledge, as he concludes, "I can't imagine anything more challenging, more humbling, and more important to the future welfare of our planet than the quest to understand nature."

The reviewers are graduate students in the Department of Ecology, Evolution, and Marine Biology, University of California, Santa Barbara, Santa Barbara, CA 93106, USA. Email: forbeselizabeth.s@gmail.com

REFERENCES
1. R. C. Larson, N. Ghaffarzadegan, Y. Xue, *Syst. Res. Behav. Sci.* **31**, 745 (2014).

10.1126/science.aaf7138

PHOTO: © IMAGEBROKER/ALAMY STOCK PHOTO

Downloaded from http://science.sciencemag.org/ on May 26, 2016

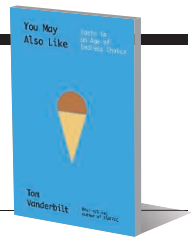
Published by AAAS

PSYCHOLOGY

Like. Share. Retweet.

A treatise on taste explores how our preferences form and evolve over time

By **Sheena Iyengar**



You May Also Like
Taste in an Age of Endless Choice
Tom Vanderbilt
Knopf, 2016. 315 pp.

Parents are privileged to witness a strange alchemy. It manifests through innumerable signs, and you can be sure it will come: Once-beloved stuffed animals are suddenly rendered anathema; cartoons that formerly commanded hours of attention are dismissed as kid's stuff; and the music you can hear from behind the door is no longer a tween band's album but sounds surprisingly moodier, darker, and sometimes—although we hesitate to admit it—more adult. We observe these changes in taste and shrug our shoulders, offering, by way of explanation, that it's all just a matter of "growing up."

But we grown-ups are not static creatures either, although our shifts in taste may be less immediately obvious. We prune our wardrobes each spring of drab patterns and colors (products of lapsed judgment). Even as we convince ourselves that we're true cineastes, we'll sit down with the latest blockbusters (guilty pleasures). And certain drinks and foods, perhaps shunned for years, one day don't seem so bad (we're open-minded, after all). Many of us are nonplussed when personal inconsistencies of taste are brought to our attention. Do we never stop, in a certain sense, growing up?

Tom Vanderbilt's *You May Also Like: Taste in an Age of Endless Choice* sets out to understand this mysterious phenomenon of how our preferences change and come to be. Jockeying between the various definitions of taste (what one likes; what our society sanctions as good or bad standards of judgment; the sensory experience itself), the book moves on a whirlwind tour of taste across its many domains, from food and music to color and even cats. Given the breadth of the topic, each chapter is wisely broken down with a series of subquestions that harken back to the main theme: How do we identify our tastes? What determines the tastes we already have? What causes our tastes to change?

Writing in a style that is at once journalistic and anecdotal, Vanderbilt takes us to the headquarters of Pandora, Netflix, McCormick, and a host of other organizations and scientists who make it their business to understand (and, in some cases, predict) the nature of human taste. We learn the pitfalls and limitations of attempts to quantify taste with one- to five-star ratings and the familiar thumbs up or down; how categories play a vital role in our ability to like something; and why, for professional tasters (of beer, pretzels, and foods of all kinds), a facility for identifying and naming flavors is so much more important than any natural talent for detecting them. Ultimately, the book isn't interested in mounting an argument but in assembling a constellation of insights that resonate with one another, each serving to reveal another joint or detail of the bigger picture.

Vanderbilt occasionally runs the risk of overwhelming his reader with a barrage of facts and tidbits about the intricacies of our taste, but by persistently anchoring findings and principles to everyday experiences, he manages to keep the inquiry from going far off course. The book is at its best when it highlights the processes behind such rites of passage as coming to appreciate the initially repellent bitterness of coffee or offers compelling explanations (and excuses) for our odd and embarrassing behaviors, like mistaking a fire extinguisher for part of a modern art exhibit (as Vanderbilt notes, museums prime us such that "we suddenly see the building fixture in a new light").

For all the fun of its examples, at the heart of the book is a fundamental anxiety about the self. As Vanderbilt writes, "what could be more authentic to us than the things we like?" It's for precisely this reason that the surprising degree to which we are "strangers to our tastes" so unsettles: Not only are our preferences inconsistent, all of us—even trained judges—are imperfect enforcers of predetermined codes and standards, susceptible to biases of memory and context. What the science of taste reveals again and again is how manipulable and prone to error our judgments are.

Yet the importance of taste remains, in the end, less about any outcome than the adventure of its formation. Or as Vanderbilt phrases it, "Liking is learning and learning is liking." *You May Also Like* thus offers passionate encouragement to continue "growing out" one's tastes and embracing new experiences. In a world saturated by endless listicles, top 10s, and "all-time" rankings, it's enormously refreshing to read a book less concerned with what we like and more focused instead on how and why we come to like it.



"Where economists tend to think that a choice 'reveals' a preference, psychologists often suspect a choice *creates* the preference," writes Tom Vanderbilt in *You May Also Like*.

PHOTO: ANDRESR/ISTOCKPHOTO.COM

The reviewer is the author of The Art of Choosing *(Twelve, New York, 2010). Email: ss957@gsb.columbia.edu*

10.1126/science.aaf7350

Downloaded from http://science.sciencemag.org/ on May 26, 2016

Published by AAAS

LETTERS

Edited by **Jennifer Sills**

Public participation in China's project plans

THE SUCCESS OF China's government-funded megaprojects, including the South-to-North Water Diversion (SNWD) project (*1*, *2*) and the Three Gorges Dam project (*3*), is in question. A change in the Chinese government's top-down decision-making process for such projects would help.

Although Chinese laws and regulations require public participation in the decision process (*4*), it remains limited in practice. State agencies and their leaders should play a much greater role in which projects are selected for implementation. The SNWD project began well before its feasibility report was approved by the state in 2008. Individuals and groups who are positively or negatively affected by a proposed mega-project should also play an important role in project selection. Public participation in the appraisal of government-funded projects would improve the effectiveness of the decision-making process, reduce conflict between the government and the general public, and facilitate project implementation.

A number of proposals for government-funded megaprojects are expected in the near future, with the goal of boosting the economy. Public hearings and surveys have been put in place to register public comments on these projects. However, controversial projects such as Pengze Nuclear Power Station in Jiangxi Province (*5*) show that conducting the process objectively and engaging all stakeholders must still be improved. The development of such projects has substantial social, environmental, and economic impacts. Therefore, facilitating and implementing public participation would be of great practical value. To be effective, a policy to promote greater public involvement must ensure that project information is transparent and that the public's voice is heard.

Guoyou Qi,[1] Yanhong Jia,[2] Saixing Zeng,[3]* Jonathan J. Shi[4]

[1]School of Business, East China University of Science and Technology, Shanghai 200237, China. [2]School of Geographic Sciences, East China Normal University, Shanghai 200241, China. [3]Antai College of Economics and Management, Shanghai Jiao Tong University, Shanghai 200030, China. [4]College of Engineering, Louisiana State University, Baton Rouge, LA 70803, USA.
*Corresponding author. Email: zengsaixing@sjtu.edu.cn

REFERENCES

1. J. Liu, W. Yang, *Science* **337**, 649 (2012).
2. J. Barnett, S. Rogers, M. Webber, B. Finlayson, M. Wang, *Nature* **527**, 295 (2015).
3. R. Stone, *Science* **321**, 628 (2008).
4. The National People's Congress of the People's Republic of China, Environmental impact assessment law of People's Republic of China (2002); http://www.npc.gov.cn/nc/zt/qt/2013zhhbsjx/2013-07/11/content_1800745.htm [in Chinese].
5. A. King, M. V. Ramana, *Asian Perspect.* **39**, 607 (2015).

10.1126/science.aaf8338



Three Gorges Dam on the Yangtze River.

PHOTO: R.V. BULCK/ISTOCKPHOTO.COM

Infection and the first eukaryotes

IN THEIR PERSPECTIVE "Pathogen to powerhouse" (12 February, p. 659), S. G. Ball *et al.* argue that the endosymbiotic events that led to the evolution of eukaryotes involved infection of an already complex host. They write that "the first challenges for an endosymbiont are to avoid being digested...." There are, however, issues associated with such a concept.

In the case of plastid endosymbiosis, Ball *et al.* advocate involvement of chlamydial pathogens (the MAT hypothesis), but independent analyses have rejected this idea (*1*). In the case of mitochondrial endosymbiosis, Ball *et al.* suggest that a relative of the *Rickettsia* pathogen infected an archaeon, with one caveat being that all *Rickettsia* are obligate intracellular pathogens that depend on eukaryotic cells and their mitochondria for survival. Furthermore, Ball *et al.* assume that the interplay of the endosymbiotic partners was not symbiotic. Yet, such symbioses are common, *Paulinella chromatophora* and all secondary endosymbioses being two examples.

For mitochondrial endosymbiosis, the authors envision an archaeal host that could endocytose (i.e., incorporate large particles including bacteria). Lokiarchaea currently represent the closest relatives of such a host. However, pangenome data (*2*) show that Lokiarchaea lack critical endocytosis components, including those that mediate membrane curvature toward the cytosol and dynamins responsible for membrane scission; the latter are likely of mitochondrial origin (*3*). Endocytosis is selective and requires vesicle formation, an acidified lysosome, and a multivesicular body, which also matures through vesicles that mitochondria secrete (*4*). It is thus misleading to say "It is likely that endocytosis in Archaea originally evolved...," particularly in the absence of endocytosing prokaryotes.

Ball *et al.* also suggest that autophagy evolved earlier than mitochondria to remove incidentally captured prokaryotes. Yet, the initiation of the phagophore depends on mitochondria-associated endoplasmic reticulum membranes (*5*). The endomembrane system appears to depend a lot on mitochondria, not vice versa. Most important, advocating a complex host that was infected by a *Rickettsia* relative fails to explain the universal presence of mitochondria in eukaryotes and offers no rationale for why mitochondria came about in the first place.

Sven B. Gould

Institute for Molecular Evolution, Heinrich Heine University Düsseldorf, 40225, Düsseldorf, Germany.
Email: gould@hhu.de

REFERENCES

1. D. Domman *et al.*, *Nat. Commun.* **6**, 6421 (2015).
2. A. Spang *et al.*, *Nature* **521**, 173 (2015).
3. R. Purkanti, M. Thattai, *Proc. Natl. Acad. Sci. U.S.A.* **112**, 2800 (2015).
4. V. Soubannier *et al.*, *Curr. Biol.* **22**, 135 (2012).
5. L. C. Gomes, I. Dikic, *Mol. Cell* **54**, 224 (2014).

10.1126/science.aaf6478

Response

WE DISAGREE WITH Gould that the phylogenetic analyses of Domman *et al.* (*1*) reject our hypothesis that plastid endosymbiosis relied on an interaction between cyanobacteria, a chlamydial pathogen, and a single-celled eukaryote (the MAT hypothesis). The phylogenetic trees shown by Domman *et al.* are very similar to ours

Downloaded from http://science.sciencemag.org/ on May 26, 2016

Published by AAAS

and emphasize uncertainties that we have accounted for through straightforward interpretation of carbohydrate biochemistry (*2*).

With regard to the metabolic capacities of the mitochondrion ancestor, we [and others (*3*)] do not trust that the anaerobic capacity in many extant mitochondria was encoded on the genome of the organelle donor (*4*, *5*). Rather, we believe that it originated through horizontal gene transfers.

Mitochondrion origin necessitated entry of an alpha-proteobacterium into another prokaryote that would ultimately become the eukaryote host cell. This process required the ability to invade the host cell and likely also to escape its antibacterial defenses. Thus, we argue that the mitochondrial forerunner was preadapted to intracellular life. Recent phylogenetic data continue to identify the deep-branching Rickettsiales bacteria as the most likely mitochondrial donor lineage (*6*).

Regarding the genetic capacity of the Lokiarchaeota, genome reconstruction from metagenome-derived sequences provides presence (not absence) data. To speculate on what is missing is unwise until a closed, high-quality genome sequence is available.

Regarding the origin of autophagy, recent work on yeast mutants that can no longer form endoplasmic reticulum–mitochondrion contact sites is instructive. These mutants are not defective in bulk autophagy: They can still form a phagophore (*7*). Thus, initiation of the phagophore does not depend on mitochondrion-associated endoplasmic reticulum membranes, but is part of host-controlled removal of mitochondria (*7*). In our view, the importance of mitochondrion–endoplasmic reticulum interplay (*8*) suggests that the endomembrane system was a prerequisite for mitochondrion origin, and not vice versa.

Finally, we suggest that switching from the ancestral state of nutrient endocytosis to full-fledged phagocytosis necessitated a substantial increase in cell size and motility. Because larger, motile cells need more energy, this likely required oxidative phosphorylation and hence the presence of mitochondria (*9*). We surmise that preying on prokaryotes was a major ecological advantage of early eukaryotes. This implies that membrane trafficking was the earlier innovation, followed by presence of the mitochondrion, leading to the remarkable diversification of this lineage (*10*).

Steven G. Ball,[1] Debashish Bhattacharya,[2]* Andreas P. M. Weber[3]

[1]Université de Lille CNRS, UMR 8576-UGSF-Unité de Glycobiologie Structurale et Fonctionnelle, F 59000 Lille, France. [2]Department of Ecology, Evolution and Natural Resources, Rutgers University, New Brunswick, NJ 08901, USA. [3]Institute for Plant Biochemistry, Cluster of Excellence on Plant Sciences, Heinrich-Heine-University, D-40225 Düsseldorf, Germany.

*Corresponding author. Email: debash.bhattacharya@gmail.com

REFERENCES

1. D. Domman *et al.*, *Nat. Commun.* **6**, 6421 (2015).
2. S. G. Ball *et al.*, *Front. Cell Infect. Microbiol.* **6**, e00043 (2016).
3. V. Hampl *et al.*, *Mob. Genet. Elements* **1**, 71 (2011).
4. Z. Wang, M. Wu, *PLOS One* **9**, e110685 (2014).
5. T. Gabaldón, M. A. Huynen, *Science* **301**, 609 (2003).
6. Z. Wang, M. Wu, *Sci. Rep.* **5**, 7949 (2015).
7. S. Böckler, B. Westermann, *Dev. Cell.* **28**, 450 (2014).
8. T. Tatsuta *et al.*, *Trends Cell Biol.* **24**, 44 (2014).
9. N. Lane, *Cold Spring Harb. Perspect. Biol.* **6**, a015982 (2014).
10. A. A. Pittis, T. Gabaldon, *Nature* **531**, 101 (2016).

10.1126/science.aaf6733

ERRATA

Erratum for the Research Article "Gating of hippocampal activity, plasticity, and memory by entorhinal cortex long-range inhibition" by J. Basu *et al.*, *Science* **351**, aaf2878 (2016). Published online 29 January 2016; 10.1126/science.aaf2878

Downloaded from http://science.sciencemag.org/ on May 26, 2016



From left: Geraldine Richmond, Suzanne C. Iacono, Shirley Malcom, Simine Vazire, and Brooks Hanson

PHOTO: AAAS/EPNAC.COM

Journals and funders confront implicit bias in peer review

Experts brainstorm ways to allow a more diverse community of science and technology innovators

By **Ginger Pinholster**

Deeply rooted assumptions creep into decision-making in unrecognized ways—even among the most well-intentioned peer-reviewers, journal editors, and science funders—and that can prevent the best science from being sponsored or published, experts said at a recent AAAS forum on implicit bias.

To demonstrate such ingrained assumptions, social psychologist Brian Nosek put forum participants to the test. First, he asked them to shout out whether different words were "male" or female," and he clocked their answers. Beginning with gender-specific pronouns such as "he" and "she," the Implicit Association test seemed easy at first. It was not much more difficult when the categories were "career or male" and "family or female." When the categories became "career or female" and "family or male," however, response times lagged. Conflicting answers and embarrassed laughter followed.

The order of word-pairings affected the test results only slightly, said Nosek, a professor at the University of Virginia and executive director of the Center for Open Science. Our brains' automatic, continuous efforts to make sense of the world, combined with life experiences, are the key drivers of implicit bias, he added: "We didn't evolve to be fair—we evolved to survive and thrive," he said, but "if we can be more humble about the biases that exist in us that are counter to our values, then we open up the possibility for external strategies to help us uphold our values while making decisions."

Unconscious assumptions about gender, ethnicity, disabilities, nationality, and institutions clearly limit the science and technology talent pool and undermine scientific innovation, said AAAS Board Chair Geraldine Richmond. As an early-career faculty member in the 1980s, Richmond—now presidential chair in science and professor of chemistry at the University of Oregon—recalled how a fear of gender bias prompted her to use initials, rather than her full name, on her first major journal article. She convened the 28 April forum at AAAS to identify next steps toward minimizing implicit bias in peer review.

The problem of implicit bias is not only about fairness, said speaker Jo Handelsman, associate director for science in the White House Office of Science and Technology Policy. Publishing opportunities and research grants are "gateways to success," she said, and certain science and engineering fields need more candidates from different backgrounds to pass through those gateways. At the same time, she added, "Diverse groups are more productive, more creative, and generate more innovation."

The AAAS forum featured presentations by journal editors, federal funders, and researchers. Editors cited a U.S.-centric bias as a major problem in peer review. Edward Campion, of the *New England Journal of Medicine* noted, for instance, that countries with fewer resources disproportionately suffer "diseases of poverty," yet those countries are poorly represented among reviewers, and therefore risk receiving less attention than they deserve. Similarly, at the American Chemical Society (ACS), a large portion of submissions in 2015 came from China and other countries in Asia, but those authors remain somewhat underrepresented in terms of published output, said Heather L. Tierney, managing editor, ACS Publications.

Journal data presented at the forum seemed to suggest that publishers may be somewhat further along in addressing gender bias, although speakers described a need for more female editors and peer-reviewers. Brooks Hanson, director of publications at the American Geophysical Union (AGU), said that, at his organization, papers with women listed as the first author now have a higher acceptance rate than those with men as first authors. However, he added, "Significantly more editors and reviewers are male compared to the distribution of AGU members and accepted first

Downloaded from http://science.sciencemag.org/

Published by AAAS



From left: Stephen Meacham, Shirley Malcom, and Molly Carnes

authors, and this may have important effects on career development." Recruiting more women to the ranks of elite journals can prove challenging, given the many career and family demands on women in science, said Simine Vazire, editor-in-chief of *Social Psychological and Personality Science*. Some 40% of the journal's associate editors are women, said Vazire, an associate professor at the University of California, Davis, but she added, "To get six men to agree to serve as editors, I invited seven. To get four women to agree, I invited twenty-one."

To help eliminate bias, Vazire recommended double-blind peer review, in which authors and peer-reviewers are unaware of each other's identity, or even triple-blind review, which also prevents editors from seeing authors' names. Sowmya Swaminathan, head of editorial policy at *Nature*, said that acceptance of double-blind review may vary across scientific fields as well as geographic regions. In a 2012 experiment, only about one-fifth of monthly submissions to a *Nature* journal undertook the double-blind option, Swaminathan said, although three-fourths of surveyed readers were "supportive" of the option. A double-blind option was introduced across all primary *Nature* research journals in 2015. The greatest use of the option was seen among submissions from China and the United States, and in climate science, Swaminathan reported.

Other speakers at the forum described funding-agency efforts to address concerns raised by a 2015 report of the U.S. Government Accountability Office (GAO), which called for better data and information-sharing related to female researchers. That report, *Women in STEM Research*, identified "no disparities in success rates between women and men" applying for research grants at three federal agencies, but insufficient data at three other agencies. Suzanne C. Iacono, head of the Office of Integrative Activities at the National Science Foundation (NSF), reported a "slight rise in awards to women" between 2001 and 2014, but she noted that only one-quarter of all proposals to the agency were submitted by women scientists. In 2014, 23% of all proposals were funded, she said, while the success rate for women was 24%, yet men submitted a little more than 31,000 proposals, compared with about 11,000 from women.

For African-American researchers, the situation is more troubling, Iacono reported: The success rate for African-American submitters is about 18%, but such applicants represent only about 2% of the NSF's total submissions. Sonny Ramaswamy, director of the National Institute of Food and Agriculture, and Richard Nakamura, director of the Center for Scientific Review at the National Institutes of Health (NIH), expressed similar concerns about grant applications from African-American scientists. At NIH, African-American researchers "receive awards at "55% to 60% the rate of white applicants," Nakamura said. "That's a huge disparity that we have not yet been able to seriously budge," despite special mentoring and networking programs, as well as an effort to boost the number of scientists from underrepresented minorities who evaluate proposals.

Studies of the peer-review process have shown that African-Americans and women "are held to higher standards to be judged competent," said Molly Carnes, a professor of medicine, psychiatry, and industrial & systems engineering at the University of Wisconsin-Madison. Training can help to reduce implicit bias, Nosek said, but the positive impacts of such interventions tend to be short-lived. Moreover, Carnes noted, making reviewers aware of the neurological roots of implicit bias can backfire, causing some to believe that there is no way to avoid it. Nosek recommended structuring external processes to help minimize bias, while also encouraging reviewers to accept and become more mindful of the problem. To recruit and retain more diverse panelists, NSF's Iacono said that giving reviewers the choice to remain at home or travel to NSF has increased the rate at which women participate in review panels. Carnes and colleagues are meanwhile studying how bias might affect NIH research project grants called RO1s. Interaction among reviewers, dubbed "Score Calibration Talk," may set up a potential for bias, Carnes said.

Shirley Malcom, director of Education and Human Resources programs at AAAS, noted that data on implicit bias remains incomplete, and it tends to focus more on gender than on ethnicity. Data on implicit biases that favor elite institutions over others are also in short supply, she said, also adding that "we look not at all at persons with disabilities."

In breakout groups, forum participants identified a need for more uniform data-collection and data-sharing as critical next steps toward minimizing implicit bias in peer review. Marcia McNutt, editor-in-chief of the *Science* family of journals, said that technologies such as PRE, the Peer Review Evaluation service (which is owned by AAAS, publisher of *Science*), might be able to help publishers, by providing bias training for reviewers. Eric Hall, PRE's product director, said that this is in the works. "PRE has in its roadmap a plan to help address bias in peer review, as part of online training modules for reviewers. We look forward to working with like-minded organizations to develop a curriculum that will be applicable to every discipline."

U.S. Representatives Eddie Bernice Johnson (D-Texas), Rosa DeLauro (D-Connecticut), Louise Slaughter (D-New York), and Jackie Speier (D-California) served as honorary co-chairs of the forum. Speier, who made an appearance at the event, commended AAAS for confronting the problem. "Bias in peer review rots the scientific enterprise from within," she said. "We all need the best, the most creative ideas to rise to the top." ■

SCREENERS NEEDED FOR JOURNALISM AWARDS

Scientists from the United States and abroad who will be in the Washington, D.C., area between late August and late September are needed to review the scientific accuracy of entries in the prestigious AAAS Kavli Science Journalism Awards competition. If you can volunteer, please contact Nkongho Beteck (nbeteck@aaas.org) for screening dates and categories.

PHOTO: AAAS/EPNAC.COM

Downloaded from http://science.sciencemag.org/ on May 26, 2016

Published by AAAS

Research shows gun owners support gun-violence prevention

With federal funding of firearm injury prevention stalled, a top scientist says policies to reduce gun violence not as polarizing as politicians may think

By **Kathleen O'Neil**

Efforts to reduce gun violence are often viewed as coming at the expense of gun owners' rights. As a result, congressional lawmakers have avoided the contentious issue for years, and have severely restricted government funding for firearm violence prevention research. That's unnecessary, a leading researcher said, since many policies that are effective at reducing gun violence also have the support of the majority of gun owners.

"Often there's no statistical difference between gun owners and non–gun owners," in support for policies designed to keep guns out of the hands of people who are more likely to commit crimes, said Daniel Webster, director of the Johns Hopkins Center for Gun Policy and Research.

One example of an effective policy that gun owners support, at least in surveys, is universal background checks, Webster said.

> ***"Often there's no statistical difference between gun owners and non–gun owners," in their support for policies to keep guns away from people more likely to commit crimes.***
>
> **Daniel Webster,** Researcher

"For policies like background checks, as an example, we found anywhere from 75% to 85% of gun owners supported those regulations," Webster said, also explaining that support is "very high" for handgun-purchaser licensing among gun owners who live in states with such laws.

Webster, who presented his research at the 14 to 15 April AAAS Forum on Science & Technology Policy, said that ignoring "this enormous agreement" between gun owners and others wanting to reduce gun-related deaths could prove politically disadvantageous to lawmakers seen as blocking those efforts.

There is one important difference between gun owners and others: Gun owners often don't trust that the government will carry out firearm policies fairly. "We have to find ways to do this that people trust," Webster said.

It was that lack of trust that led Jay Dickey, a former Congressman from Arkansas, to urge Congress to take away funding for research on firearm injury prevention at the Centers for Disease Control and Prevention (CDC) in 1996. Congress also passed the "Dickey Amendment," adding language prohibiting CDC—and in later years, other federal agencies—from using federal funds for activities that could be characterized as advocating or promoting gun control.

"At one time, I thought research was tantamount to gun control," Dickey said at the forum. Now, years after he became friends with the CDC researcher he once opposed, he has reversed his position.

Mark Rosenberg was director of the CDC's National Center for Injury Prevention and Control, which funded the controversial research. After a congressional hearing where Dickey grilled Rosenberg, the two met in Dickey's office, and they found common ground talking about their children. Over time, they came to understand each other's positions on this contentious issue, they said.

"[H]aving a friendship with Mark, I have now come back around to where I'm seeing that research is important and that we can do the research without endangering the Second Amendment or having gun control," Dickey said.

Rosenberg, addressing scientists and science policy-makers at the forum, suggested that gun-violence prevention policies be assessed, not only for how effective they are in reducing gun violence, but also with regard to their effect on responsible gun owners. "We can measure a reduction in gun deaths and gun injuries, but we need help in developing a scale to quantify the impact of a policy on the rights of law-abiding gun owners."

Rosenberg and Dickey said they now agree that there should be a dramatic increase in funding for gun-violence prevention research, and that federal agencies should still abide by the Dickey clause. Including that provision "will help reassure supporters of the Second Amendment that the CDC will use the money for important research and not for gun-control advocacy," Rosenberg said.

After the Dickey amendment was passed, many federal administrators were unwilling to let researchers test the parameters of the law and stopped almost all research involving guns. While some research continued, it had a chilling effect on the field. President Obama called for an end to the CDC freeze in 2013 following the mass shooting at Sandy Hook Elementary in Newtown, Connecticut, but Congress has not yet restored the funding. Science organizations, including AAAS, have also urged Congress to restore funding for gun-violence prevention research.

FORUM'S BROADER MESSAGE. In the forum's keynote address, John Holdren, director of the White House Office of Science and Technology Policy, said that researchers need to be more transparent and increase efforts to tell policy-makers and the public about their work and its value while they develop innovations to confront such global issues as climate change.

"There is simply an inadequate understanding of how important science, technology, and innovation are to our economy, to our quality of life, to our national security," said Holdren. "Until we lift up that level of public understanding, we won't have public support for the kinds of increases in investment by the federal government that will be warranted."

Kathryn D. Sullivan, administrator of the National Oceanic and Atmospheric Administration (NOAA), told attendees of the forum's William D. Carey lecture that the public expects science to make important contributions to health, safety, and prosperity while justifying research funding. Scientists are facing increased demand for transparency in the scientific process and in science-based decisions from interest groups, the media, citizens, and Congress, she said.

NOAA researchers have been the target of a recent congressional inquiry after they published findings in *Science* that a 15-year slowing in the rate of global warming early in the 21st century was likely due to incorrect temperature estimates, and that warming had continued at the same rate during that period.

The "apparent decline in society's confidence in science as an enterprise of special value to society and of scientists as respected and trustworthy people," is very concerning, Sullivan said.

Steve Case, founder of AOL, gave the Gilbert S. Omenn Grand Challenges Address. Case said that the next wave of innovators and entrepreneurs need to productively coordinate with policy-makers to further integrate the Internet throughout such important arenas as health, education, transportation, and energy.

The 2016 forum, which drew hundreds of participants, was the Association's 41st. ■

Downloaded from http://science.sciencemag.org/ on May 26, 2016

Published by AAAS

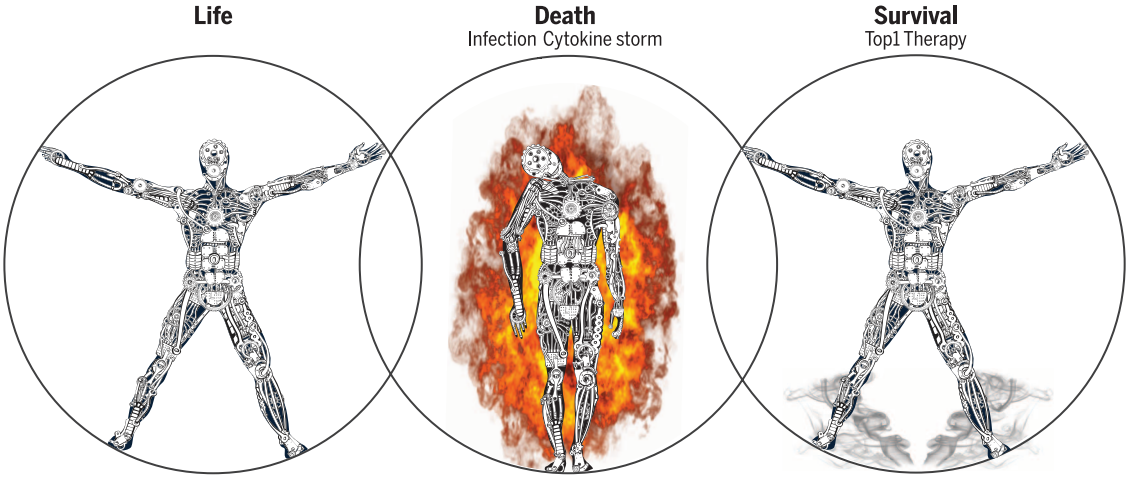
RESEARCH ARTICLE SUMMARY

INFLAMMATION

Topoisomerase 1 inhibition suppresses inflammatory genes and protects from death by inflammation

Alex Rialdi,* Laura Campisi,* Nan Zhao, Arvin Cesar Lagda, Colette Pietzsch, Jessica Sook Yuin Ho, Luis Martinez-Gil, Romain Fenouil, Xiaoting Chen, Megan Edwards, Giorgi Metreveli, Stefan Jordan, Zuleyma Peralta, Cesar Munoz-Fontela, Nicole Bouvier, Miriam Merad, Jian Jin, Matthew Weirauch, Sven Heinz, Chris Benner, Harm van Bakel, Christopher Basler, Adolfo García-Sastre, Alexander Bukreyev, Ivan Marazzi†

INTRODUCTION: Infection causes inflammation, which contributes to pathogen clearance and organismal survival. The balance between the intensity and resolution of an inflammatory response is key for the fitness of the organism. Sepsis, for example, is a life-threatening condition caused by an excessive host response to infection, which in turn leads to multi-organ failure and death. Worldwide, millions of people each year succumb to sepsis. With an overall mortality rate of 20 to 50%, sepsis is the 10th leading cause of death (more than HIV and breast cancer) in the United States, according to the Centers for Disease Control and Prevention. Estimates indicate that 250,000 to 500,000 people die from sepsis annually in the United States. Children and the elderly are especially vulnerable to sepsis; it is the most common cause of death in infants and children. Childhood pneumonia, often caused by virus-bacteria co-infection, leads to septic shock and lung destruction. This occurs after bacterial invasion even in the presence of an appropriate antibiotic therapy. Finding remedies to treat sepsis and diseases associated with detrimental acute inflammatory reactions is thus pivotal for humankind.



RATIONALE: We reasoned that if excessive inflammation in response to infection leads to lethal consequences, dampening inflammation could be advantageous for the host. At least two strategies could be used to suppress inflammatory responses associated with infection. One is indirect and targets the pathogen (antibiotics). The second one, which we used, directly acts on the host response itself. In such a strategy, the suppression of acute inflammation would bypass the fatal outcome associated with overt inflammation and would "buy time" to allow the host immune response to eliminate the pathogen. After microbial invasion, many steps could be targeted between the early phases of the cellular response (sensing of the pathogen and signal transduction) and the information flow from DNA to RNA to proteins that act as inflammatory mediators (i.e., cytokines). We decided to identify and chemically inhibit cellular factors that act at the DNA (chromatin) level and play a primary role in activating the expression of inflammatory genes.

RESULTS: We found that chemical inhibition of topoisomerase 1 (Top1), an enzyme that unwinds DNA, suppresses the expression of infection-induced genes with little to no effect on housekeeping gene expression and without cellular damage. In vitro, depletion or chemical inhibition of Top1 in epithelial cells and macrophages suppresses the host response against influenza and Ebola viruses as well as bacterial products. At the mechanistic level, as shown by chemical genetics and epigenetic approaches, Top1 inhibition primarily suppresses RNA polymerase II (RNAPII) activity at pathogen-associated molecular pattern (PAMP)–induced genes. These genes require SWI/SNF chromatin remodeling for activation and display unique genetic and epigenetic features, such as the presence of IRF3 binding sites, low basal levels of RNAPII, histone H3 Lys^{27} acetylation marks, DNA hypersensitivity, and CpG islands. This gene "signature" of specificity was also validated using public data sets. In vivo, Top1 inhibition therapy rescued 70 to 90% mortality caused by exacerbated inflammation in three mouse models: acute bacteria infection, liver failure, and virus-bacteria co-infection. Strikingly, one to three doses of inhibitors were sufficient for the protective effect in all models, without overt side effects.

ON OUR WEBSITE

Read the full article at http://dx.doi.org/10.1126/science.aad7993

CONCLUSION: The inflammatory immune response against microbes is essential in protecting us against infections. In some cases, such as highly pathogenic and pandemic infections, the organism turns against itself and responds too acutely, with an excessive inflammation that can have fatal consequences. Our results suggest that a therapy based on Top1 inhibition could save millions of people affected by sepsis, pandemics, and many congenital deficiencies associated with acute inflammatory episodes and "cytokine storms." ■

The list of author affiliations is available in the full article online.
*These authors contributed equally to this work.
†Corresponding author. Email: ivan.marazzi@mssm.edu
Cite this article as A. Rialdi *et al.*, *Science* **352**, aad7993 (2016). DOI: 10.1126/science.aad7993

Downloaded from http://science.sciencemag.org/ on May 26, 2016

CREDIT: RYGER/SHUTTERSTOCK

RESEARCH ARTICLE

INFLAMMATION

Topoisomerase 1 inhibition suppresses inflammatory genes and protects from death by inflammation

Alex Rialdi,[1,2]* Laura Campisi,[1,2]* Nan Zhao,[1,2] Arvin Cesar Lagda,[1,2] Colette Pietzsch,[3] Jessica Sook Yuin Ho,[4] Luis Martinez-Gil,[1,5] Romain Fenouil,[6] Xiaoting Chen,[7] Megan Edwards,[1] Giorgi Metreveli,[1,2] Stefan Jordan,[8] Zuleyma Peralta,[6] Cesar Munoz-Fontela,[9] Nicole Bouvier,[1] Miriam Merad,[8] Jian Jin,[10] Matthew Weirauch,[7] Sven Heinz,[11,12] Chris Benner,[12] Harm van Bakel,[6] Christopher Basler,[1] Adolfo García-Sastre,[1,2] Alexander Bukreyev,[3] Ivan Marazzi[1,2]†

The host innate immune response is the first line of defense against pathogens and is orchestrated by the concerted expression of genes induced by microbial stimuli. Deregulated expression of these genes is linked to the initiation and progression of diseases associated with exacerbated inflammation. We identified topoisomerase 1 (Top1) as a positive regulator of RNA polymerase II transcriptional activity at pathogen-induced genes. Depletion or chemical inhibition of Top1 suppresses the host response against influenza and Ebola viruses as well as bacterial products. Therapeutic pharmacological inhibition of Top1 protected mice from death in experimental models of lethal inflammation. Our results indicate that Top1 inhibition could be used as therapy against life-threatening infections characterized by an acutely exacerbated immune response.

The innate immune response is a key defense mechanism against infections. Activation of innate immune cells relies on the expression of a large family of pattern recognition receptors (PRRs), which detect distinct conserved microbial structures, called pathogen-associated molecular patterns (PAMPs) (*1*, *2*). The immunological response that follows PRR downstream signaling is then governed by the combinatorial expression of PAMP response genes (*3*).

Although the function of many of the PAMP response genes and their antiviral or inflammatory activity remains elusive, their expression is essential for the host defense against pathogens (*4*). Failure in regulating the induction and post-induction repression of these antimicrobial genes can alter the balance between pro- and anti-inflammatory states, often leading to detrimental effects for the host (*5*–*7*). Indeed, hyperactivation of antimicrobial genes has been suggested to be responsible for the high mortality rates during highly pathogenic infections (*8*, *9*). Another well-known example is the syndrome called "septic shock," where the uncontrolled expression of proinflammatory genes in response to bacterial PAMPs leads to severe collateral effects, such as local and systemic tissue injury, which can often be lethal to the host (*10*). In these contexts, pharmacological inhibition of factors that control the magnitude of the innate immune response could be useful for therapy.

Here, we show that the enzyme topoisomerase 1 (Top1) exerts an activating role on the transcriptional response against infection in cells and at the organismal level. This effect is achieved via Top1-assisted transcriptional activation of pro-inflammatory genes. We demonstrate that chemical inhibition, as well as reduced expression of Top1, limits the overexpression of inflammatory genes characteristic of infection with influenza and Ebola viruses and bacterial products. Notably, Top1 inhibition rescues mortality in mouse models of lethal inflammation caused by overexposure to bacterial and viral PAMPs. Our results suggest that Top1 inhibitors offer therapeutic efficacy for the treatment of diseases characterized by exacerbated innate immune responses.

[1]Department of Microbiology, Icahn School of Medicine at Mount Sinai, New York, NY 10029, USA. [2]Global Health and Emerging Pathogens Institute, Icahn School of Medicine at Mount Sinai, New York, NY 10029, USA. [3]Department of Pathology, Microbiology, and Immunology, University of Texas Medical Branch, Galveston, TX 77555, USA. [4]Laboratory of Methyltransferases in Development and Disease, Institute of Molecular and Cell Biology, Singapore. [5]Department of Biochemistry and Molecular Biology, Universitat de Valencia, Valencia, Spain. [6]Icahn Institute for Genomics and Multiscale Biology, Icahn School of Medicine at Mount Sinai, New York, NY 10029, USA. [7]Center for Autoimmune Genomics and Etiology (CAGE) and Divisions of Biomedical Informatics and Developmental Biology, Cincinnati Children's Hospital Medical Center, Cincinnati, OH 45229, USA. [8]Department of Oncological Sciences, Tisch Cancer Institute and Immunology Institute, Icahn School of Medicine at Mount Sinai, New York, NY 10029, USA. [9]Heinrich Pette Institute, Leibniz Institute for Experimental Virology, Hamburg, Germany. [10]Department of Structural and Chemical Biology, Department of Oncological Sciences, and Department of Pharmacology and Systems Therapeutics, Icahn School of Medicine at Mount Sinai, New York, NY 10029, USA. [11]Department of Cellular and Molecular Medicine, University of California, San Diego, 9500 Gilman Drive, La Jolla, CA 92093, USA. [12]Salk Institute for Biological Studies, 10010 North Torrey Pines Road, La Jolla, CA 92037, USA.
*These authors contributed equally to this work. †Corresponding author. Email: ivan.marazzi@mssm.edu

Topoisomerase 1 promotes PAMP-induced gene expression

Our goal was to identify novel regulatory mechanisms controlling the transcriptional response to pathogens by the innate immune system. We designed a reporter assay to compare the potency of the transcriptional response to viral PAMPs and its dependence on a chromatin environment (fig. S1A). We used both the influenza A virus strain PR8ΔNS1 and Sendai virus because they are known to be strong inducers of PAMP-mediated gene expression (fig. S1C) (*11*). We then selected nine chemical inhibitors (fig. S1B) with already known or inferred chromatin targets and gauged their activity at various concentrations (fig. S1C) (*12*–*20*).

Our analysis revealed that flavopiridol (FVD), thienotriazolodiazepine [(+)-JQ1], and camptothecin (CPT) effectively inhibit the interferon-β (IFN-β)–driven transcription from chromatinized templates (Fig. 1A and fig. S1C). These observations were further reinforced by the efficacy of the three compounds in suppressing the endogenous expression of two key PAMP-induced genes—those encoding IFN-β and IFIT1 (IFN-induced protein with tetratricopeptide repeats 1)—in the human lung epithelial cell line A549 at 4 hours and 12 hours after PR8ΔNS1 virus infection (Fig. 1B). Notably, our analysis was performed using all of the compounds at concentrations that do not induce cytotoxicity in treated cells (fig. S1D).

The cellular targets of FVD, (+)-JQ1, and CPT are P-TEFb (the inhibitor of positive transcription elongation factor b), BET proteins (bromodomain and extra-terminal motif), and Top1, respectively (*20*–*22*). P-TEFb, BET proteins, and Top1 are ubiquitously expressed and are thought to control basal transcriptional levels of many genes. However, recent studies showed that P-TEFb and BET protein inhibitors have a specific effect on genes induced by innate immune stimuli (*23*) and during oncogenic transformation (*24*), highlighting their usage in what is often referred to as epigenetic therapy (*25*). For this reason, our observation that FVD and (+)-JQ1 suppress PAMP-induced genes, as well as the validation that such an effect is phenocopied by small interfering RNA (siRNA)–mediated depletion of their cellular targets (fig. S2), was not surprising. In contrast, the impact of CPT treatment on PAMP-induced genes, although previously observed (*26*–*28*), was less expected in light of recent genome-wide analyses demonstrating that Top1 inhibition suppresses the expression of the majority of long genes (>100 kb) while inducing a fraction of smaller genes (*29*, *30*). The inhibitory effect at long genes is believed to be caused by Top1-mediated resolution of topological constraints occurring on long templates as a result of RNA polymerase II (RNAPII) activity (*29*, *31*). The

Downloaded from http://science.sciencemag.org/ on May 26, 2016

activating effect is instead thought to be dependent on gene-specific features such as topology, promoter sequence, or indirect effects (*30*–*33*). A concentration-dependent effect of the inhibitor CPT is also known, whereby high concentration and prolonged treatment lead to DNA damage (*34*).

To analyze the role of Top1 independently of its chemical inhibition, we examined the effect of transient Top1 depletion via siRNA. We infected control (siCtrl) and Top1-depleted (siTop1) A549 cells with influenza PR8ΔNS1 virus and assessed global differences in gene expression by microarray analysis (Fig. 1C, fig. S3, and table S1). Upon infection, Top1 depletion significantly decreased expression of 84 genes in infected cells relative to controls (siCtrl) (Fig. 1C). Remarkably, none of the down-regulated genes were long, but they were highly enriched for transcripts encoding inflammatory cytokines and interferon-stimulated genes (ISGs) (Fig. 1C, fig. S3, A and B, and table S2). The expression of housekeeping genes was unaffected independently of their level of expression (fig. S3C), indicating that Top1 depletion does not suppress gene expression "tout court" but predominantly affects genes induced in response to infection. Notably, our gene knockdown experiments rule out the possibility that the suppression of PAMP-induced genes that we observed is the consequence of CPT-mediated stabilization of covalent complexes or induced cell damage, which are known to be caused by high dosage and prolonged chemical inhibition

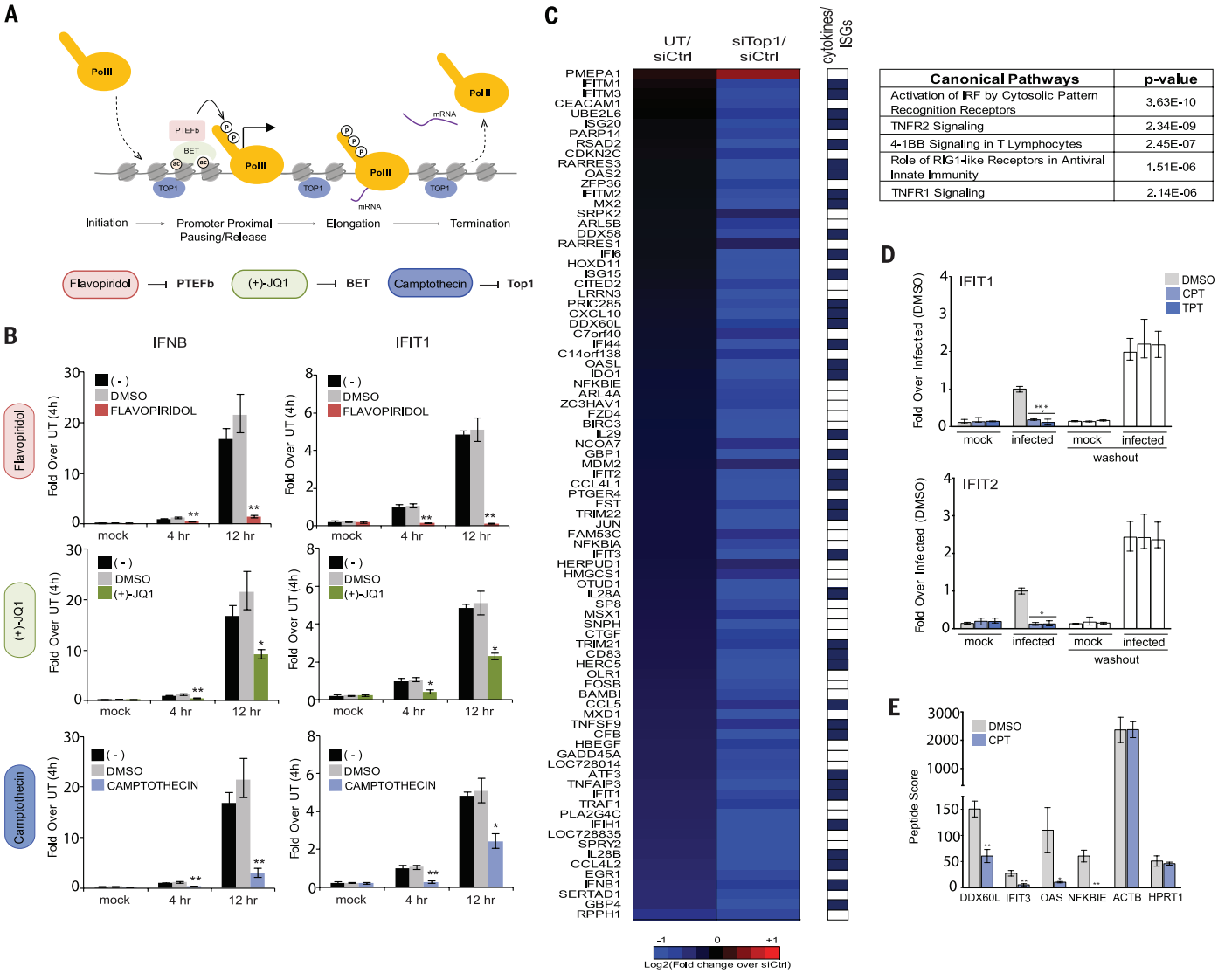


Fig. 1. Top1 inhibition suppresses PAMP-induced gene expression. (**A**) Schematic representation of factors controlling different phases of RNAPII-mediated transcription. Chemical inhibitors FVD (red), (+)-JQ1 (green), and CPT (blue) are color-coded according to their protein targets. (**B**) Quantitative PCR (qPCR) results showing the expression levels of representative viral PAMP-induced genes IFNB and IFIT1, in response to the influenza PR8ΔNS1 virus infection in A549 cells, either untreated (–) or treated with DMSO or 5 μM inhibitors. (**C**) Heat map showing relative change in gene expression levels in A549 cells not transfected (UT) or transfected with a Top1-specific siRNA (siTop1), as compared to non-targeting control siRNA-treated (siCtrl) cells during infection with influenza PR8ΔNS1 for genes differentially expressed between siTop1 and siCtrl at 4 hours after infection ($P < 0.01$; ANOVA with post hoc Tukey HSD test). Known interferon-stimulated genes (ISGs) and cytokine-coding genes are indicated in the adjacent heat map. A table summarizing the top five pathways affected by Top1 depletion during infection is also shown (top right). (**D**) Expression levels of IFIT1 and IFIT2 genes in response to influenza PR8ΔNS1 infection in A549 cells treated with 0.5 μM CPT, 100 nM TPT, or DMSO at 4 hours after infection (left bars) or 16 hours after washout (white, right bars). (**E**) Mass spectrometry data showing representative virus-induced and housekeeping protein levels in response to influenza PR8ΔNS1 infection in A549 cells treated with 0.5 μM CPT or DMSO at 6 hours after infection. $^{*}P < 0.05$, $^{**}P < 0.005$ (Student's *t* test with Holm-Bonferroni sequential correction). Data are means ± SD from three [(B) to (D)] and two (E) independent experiments.

Downloaded from http://science.sciencemag.org/ on May 26, 2016

of Top1 (fig. S1D) (29). To strengthen this point, we performed a washout experiment in the presence and absence of Top1 inhibition. As shown in Fig. 1D, the effect of Top1 inhibition on inflammatory genes was fully reversible upon drug washout, indicating the absence of any permanent change or damage in treated cells.

We then performed a global proteomic analysis in influenza virus–infected A549 cells in the presence and absence of CPT treatment. Mass spectrometry analysis indicates that the protein levels of PAMP-induced genes were compromised upon Top1 inhibition (Fig. 1E), as indicated by the representative proteins DDX60L [DEAD (Asp-Glu-Ala-Asp) box polypeptide 60-like], IFIT3, OAS (2′,5′-oligoadenylate synthetase), and NFBKIE. The production of housekeeping proteins was unaffected independently of their expression level [Fig. 1E; low expressed, HPRT (hypoxanthine-guanine phosphoribosyltransferase); high expressed, ACTB (β-actin)]. Overall, these results indicate that Top1 is required to up-regulate antiviral gene expression after recognition of viral PAMPs.

Top1 controls RNAPII activity at PAMP-induced gene loci

To confirm the specificity of Top1 activity in our system, we first investigated whether the inhibition of PAMP-induced genes could be reproduced using a different Top1 inhibitor. We therefore used topotecan (TPT), an FDA-approved Top1 inhibitor. Our results indicate that both CPT and TPT suppress virus-induced genes (Fig. 2A) but not viral entry or replication (fig. S4). This was further supported by the observed PAMP-induced gene suppression in response to infection with Sendai virus and polyinosinic-polycytidylic acid [poly(I:C)] treatment (fig. S5). We reproduced the inhibitory effect of CPT and TPT on PAMP-induced gene expression using a different cell line, the murine macrophage RAW 264.7 (fig. S6A). Top1 inhibition did not suppress the response to other stimuli such as estrogen signaling and heat shock, as indicated by analysis of prototypical target genes (fig. S7, A and B, respectively).

Furthermore, chemical inhibition and loss-of-function experiments in A549 cells indicated that class II topoisomerase enzymes (Top2) do not fully phenocopy Top1 activity during PAMP-responsive gene induction (fig. S8); along with previous observations (29, 35, 36), this finding suggests that inhibition of topoisomerases can elicit both cell type–specific and gene-specific effects. Notably, and in line with what others have recently shown (29), neither TPT- nor CPT-treated cells displayed DNA damage at the concentration we used (fig. S9).

We then characterized the genomic distribution of RNAPII and Top1 during infection in the presence and absence of Top1 inhibition. Our results show reduced promoter levels of RNAPII and Top1 at PAMP-induced genes in infected A549 cells (Fig. 2B) and macrophages (fig. S6B) when Top1 is inhibited. Notably, RNAPII and Top1 levels at housekeeping genes were not reduced as a result of Top1 inhibition (Fig. 2B and fig. S6B), consistent with their unaffected gene expression (Fig. 2A and fig. S6A). Reduced RNAPII targeting at PAMP-induced loci was confirmed by chromatin immunoprecipitation sequencing (ChIP-seq) (Fig. 2C) and by analysis of the RNAPII tracks at representative PAMP-induced genes and housekeeping genes (Fig. 2D).

To link cause (Top1 inhibition) and effect (RNAPII levels at promoters), we devised a strategy to map the genomic distribution of Top1 inhibitors via chem-ChIP, a method used to reveal the genomic localization of drugs (37). In brief, we first synthesized an analog of TPT (we did not succeed with CPT), which is amenable for coupling with a derivative of biotin. This compound was called TPT-alkyne (TPT-A; Fig. 2E). TPT-A synthesis and experimental strategy are shown in fig. S10, A and B; the validation that TPT-A is as effective as TPT is shown in fig. S10, C and D. We then performed chem-ChIP and analyzed the distribution of TPT-A on chromatin. At basal state, TPT-A was enriched at promoters and gene bodies of active genes such as ACTB and HPRT genes (Fig. 2F), as expected from results showing that Top1 travels with elongating RNAPII and that Top1 is distributed across the genome (31, 38).

During infection, TPT-A distribution peaks at promoters of inducible genes IFIT1 and IFIT2 (Fig. 2F) but not into gene bodies, which suggests that the presence of the inhibitor does not allow RNAPII and Top1 into productive transcriptional cycles. Indeed, TPT-A distribution is inversely correlated with RNAPII and Top1 density only at promoters of PAMP-induced genes (Fig. 2B). This indicates that TPT-A suppression of Top1 activity leads to a specific inhibition of RNAPII targeting at most PAMP-responsive loci (Fig. 2C). These results (i) corroborate the absence of an effect of Top1 inhibition at housekeepers, (ii) indicate that such genes can escape the transcriptional consequences of Top1 inhibition (likely via Top2; fig. S8D), and (iii) designate a RNAPII activator-like function for Top1 at PAMP-induced loci.

Top1 facilitates expression of genes that require nucleosome remodeling for activation

Previous work has characterized how classes of inducible genes respond temporally to induction of Toll-like receptor (TLR; a class of PRRs) according to genetic and epigenetic features (39–42). These studies provide a framework for addressing the specificity of Top1's effect during viral PAMP stimulation.

We first selected the Top1-affected genes whose expression was up-regulated by more than a factor of 2 upon infection (Fig. 3 and table S1). Similarly to (40), we then characterized this gene set according to dependence on IRF3 (interferon regulatory factor 3) and the SWI/SNF (switch/sucrose nonfermenter)–nucleosome remodeling complex for transcriptional activation. To do so, we performed RNA interference (RNAi)–mediated depletion of the two catalytic subunits of the SWI/SNF complex, SMARCA2 and SMARCA4, before and after infection with influenza virus or IFN treatment (Fig. 3A). This resulted in four distinct classes of Top1-affected genes (Fig. 3B).

We found that the vast majority (75%) of genes controlled by Top1 were dependent on SWI/SNF nucleosome remodeling. At basal state, these genes (relative to SWI/SNF-independent genes and housekeeping genes) were almost devoid of TATA-binding protein (TBP) and RNAPII, and displayed high levels of histone H3 at their promoters (Fig. 4A). These features indicate that nucleosome remodeling at these genes precedes recruitment of RNAPII and transcriptional initiation. Upon infection, Top1-affected genes are linked to transcriptional induction (as measured by histone H4 acetylation; fig. S11) and to broad expression levels, as measured by RNAPII recruitment (Fig. 4A) and expression data (Fig. 4A, inset). Inhibition of Top1 led to diminished RNAPII and TBP with a concomitant re-integration of H3 at promoters (Fig. 4A).

Genes that require remodeling for their activation are dependent on coactivators (42) and possess unique chromatin features at basal state, namely low levels of active histone marks, low levels of preloaded RNAPII, and low CpG island content (40). All these identifying features were recapitulated in Top1-affected genes by using genome-wide analyses and mathematical modeling of public data sets (Fig. 4, B to D, fig. S12, and table S3).

Top1 inhibition suppresses the response to bacterial stimuli and proinflammatory cytokines

To understand whether Top1 is required to activate the expression of proinflammatory genes induced by stimuli other than viruses, we characterized the effect of Top1 inhibition after exposure to bacterial PAMPs and exogenous cytokines. First, we treated both epithelial and macrophage cell lines with the bacterial PAMP lipopolysaccharide (LPS). Top1 inhibition suppressed the expression of antimicrobial genes, as indicated by the transcriptional analysis of representative proinflammatory cytokines (Fig. 5, A and B). Accordingly, Top1 inhibition resulted in reduced levels of Top1 and RNAPII at promoters of the affected genes (fig. S13, A and B).

The expression of antimicrobial genes upon PRR stimulation induces the secretion of proinflammatory signals, which trigger the maturation and activation of other innate immune cells expressing the corresponding receptors (43). To further extend our findings on cells activated via stimulation by inflammatory cytokines, we incubated both A549 and RAW cells with exogenous IFN-β and tumor necrosis factor–α (TNF-α). We then monitored gene expression changes, as well as promoter levels of RNAPII and Top1, in untreated and Top1-inhibited cells. As shown by the expression of multiple target genes (fig. S14, A and B) and respective chromatin occupancies (fig. S14, C and D), repression of Top1 activity inhibited IFN-β– and TNF-α–induced gene expression

Downloaded from http://science.sciencemag.org/ on May 26, 2016

in both cell types analyzed, paralleling our results using viral and bacterial stimuli.

Top1 protects against lethal inflammation in vivo

Together, our data suggested that Top1 inhibition could be an effective way to suppress the exacerbated response to pathogenic stimuli, prompting us to characterize the role of Top1 inhibition in vivo. We first analyzed whether in vivo preventive inhibition of Top1 activity rescued animals from lethal endotoxic shock. This was indeed the case, where 90% of animals pretreated with CPT were rescued (Fig. 5C). The protective effect of Top1 inhibition in vivo is caused not by cellular damage (Fig. 5, F to H) but by suppression of inflammatory cytokines (Fig. 5, D and E).

To test the potential of Top1 inhibition therapy in a model of bacterial disease, we infected mice with *Staphylococcus aureus*, which is one of the predominant pathogens causing nosocomial infections and sepsis in humans (*44*). Our results indicate that therapeutic treatment with CPT allowed 70% of the mice to survive the lethal challenge (Fig. 6A). Because the inflammatory response against influenza is believed to be responsible for the enhanced susceptibility to pneumonia after secondary infection with *S. aureus* in both mice and humans (*45*), we also tested whether CPT treatment could reverse the outcome of viral-bacterial co-infection. For this, mice inoculated with the influenza virus PR8 (H1N1 PR8 A/Puerto Rico/8/1934 strain) were treated with CPT at 12, 24, and 36 hours after infection. Three days after viral infection, mice received a challenge with *S. aureus*. As shown in Fig. 6B, CPT treatment rescued 94% of the animals from the lethal co-infection challenge without impairing the differentiation of virus-specific CD8 T cells into IFN-γ– and TNF-α–producing effector cells (fig. S15). Strikingly, a similar protective effect (90% rescue of mortality) was also present when therapeutically inhibiting Top1 in an endotoxin-induced mouse model of acute liver failure, where the pathology is caused by high levels of secreted cytokines such as TNF-α (Fig. 6C) (*46*). These data suggest that in experimental models of lethal inflammation, therapeutic Top1 inhibition provides meaningful protection at the organismal level.

Finally, because an elevated mortality rate associated with an exacerbated proinflammatory

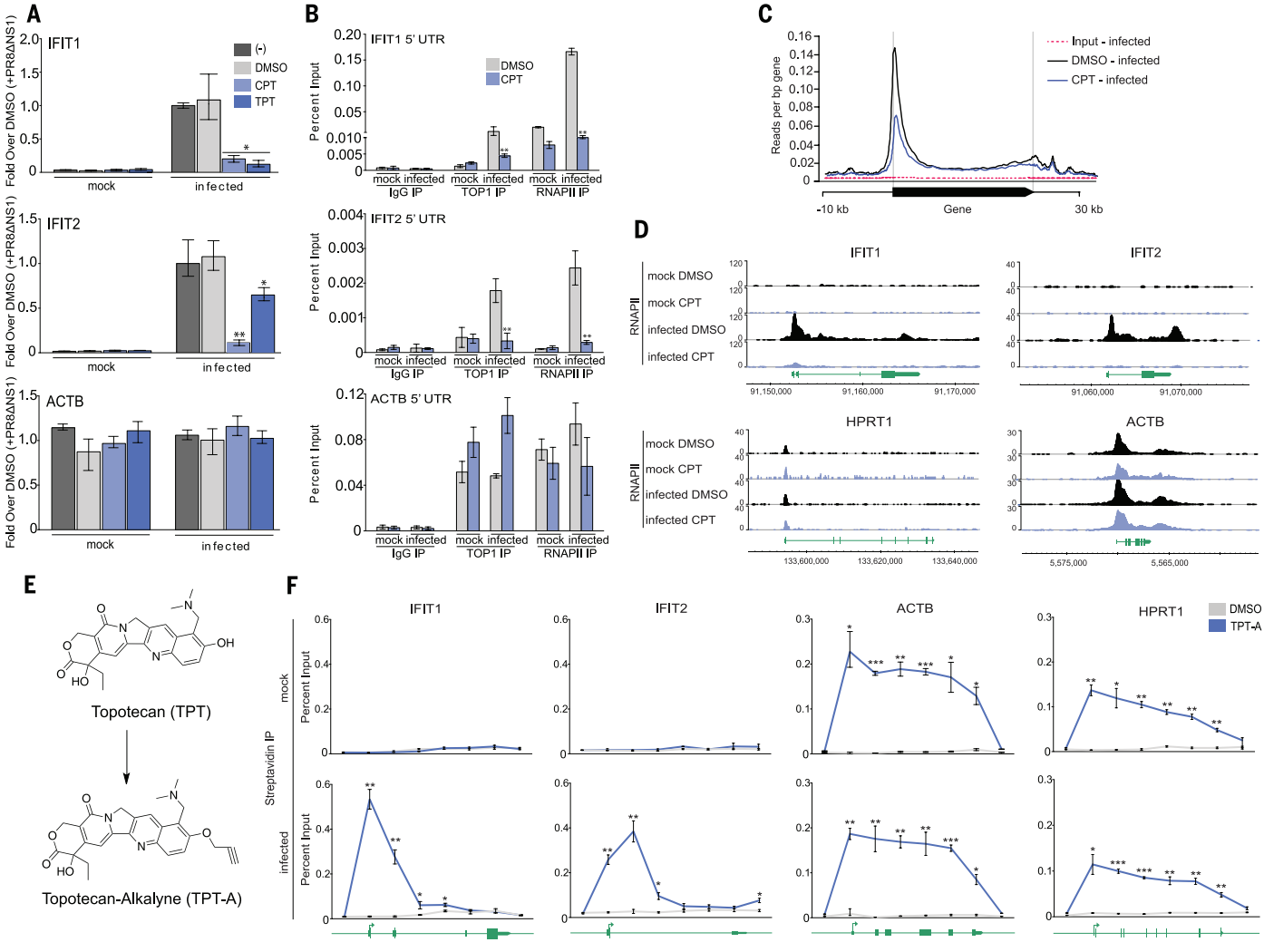
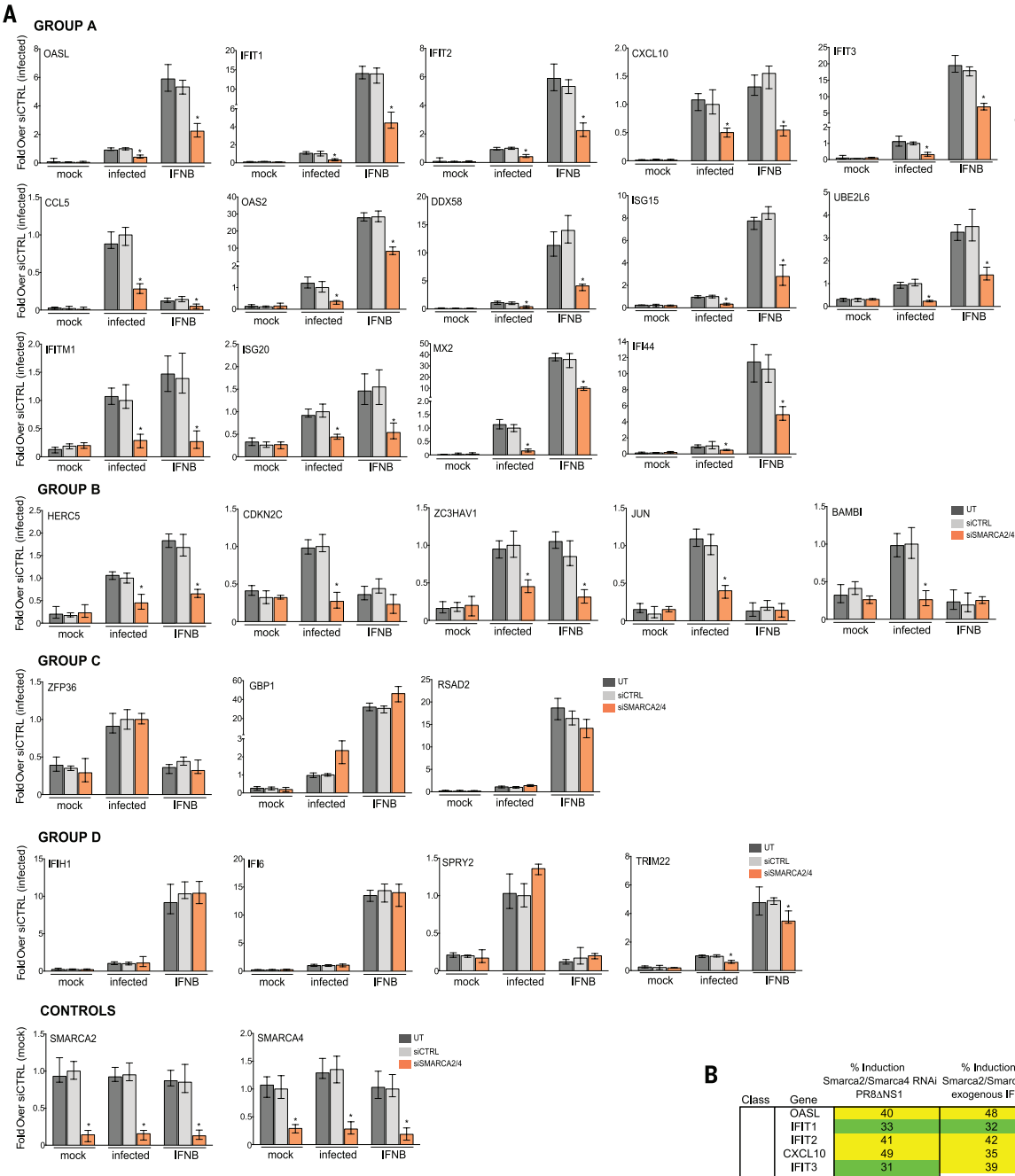


Fig. 2. Topotecan (TPT) and camptothecin (CPT) suppress RNAPII at PAMP-induced genes. (**A**) Gene expression in human A549 cells, left untreated (–) or treated with 0.5 μM CPT, 100 nM TPT, or DMSO, at 4 hours after mock treatment or PR8ΔNS1 virus infection. (**B**) ChIP-qPCR analysis of endogenous RNAPII and Top1 at the promoters of IFIT1, IFIT2, and ACTB in A549 cells treated with 0.5 μM CPT or DMSO, at 4 hours after mock treatment or infection with influenza PR8ΔNS1. (**C**) ChIP-seq metaplot of endogenous RNAPII in A549 cells treated with 0.5 μM CPT or DMSO 6 hours after mock treatment or PR8ΔNS1 virus infection. Plots represent RNAPII occupancy at genes showing a factor of 2 up-regulation in their expression after infection. (**D**) ChIP-seq tracks of representative antiviral genes IFIT1 and IFIT2, and housekeeping genes ACTB and HPRT1. (**E**) Schematic representation of the chemical synthesis of TPT-A from TPT. (**F**) Chem-ChIP qPCR analysis of TPT-A occupancy across IFIT1, IFIT2, ACTB, and HPRT1 genes in A549 cells treated with DMSO or 100 nM TPT-A, at 6 hours after mock treatment or PR8ΔNS1 infection. **P* < 0.05, ***P* < 0.005, ****P* < 0.0005 (Student's *t* test with Holm-Bonferroni sequential correction). Data are means ± SD from three (A) and two [(B) and (F)] independent experiments.

Downloaded from http://science.sciencemag.org/ on May 26, 2016



B

Class	Gene	% Induction Smarca2/Smarca4 RNAi PR8ΔNS1	% Induction Smarca2/Smarca4 RNAi exogenous IFN-β		% Induction
A	OASL	40	48	SWI/SNF-Dependent IRF3-Dependent	>50
	IFIT1	33	32		34-49
	IFIT2	41	42		0-33
	CXCL10	49	35		
	IFIT3	31	39		
	IFNB1	21	ND		
	CCL5	28	41		
	OAS2	37	29		
	DDX58	40	29		
	ISG15	33	33		
	UBE2L6	24	39		
	TRIM21	36	48		
	IFITM1	29	19		
	ISG20	45	35		
	MX2	16	28		
	IFI44	48	46		
B	HERC5	45	39	SWI/SNF-Dependent IRF3-Independent	
	CDKN2C	27	ND		
	ZC3HAV1	45	37		
	JUN	41	ND		
	BAMBI	27	ND		
C	RSAD2	139	87	SWI/SNF-Independent IRF3-Dependent	
	ZFP36	101	ND		
	GBP1	235	151		
D	IFIH1	110	101	SWI/SNF-Independent IRF3-Independent	
	IFI6	109	97		
	SPRY2	137	ND		
	TRIM22	58	71		

Fig. 3. Classification of SMARCA2/4-dependent PAMP-induced genes. (**A**) Expression of genes up-regulated by a factor of >2 after infection and suppressed by Top1 inhibition in A549 cells at 4 hours after mock treatment, infection with PR8ΔNS1 virus (infected), or stimulation with exogenous IFN-β (IFNB). Cells were dual-transfected with siRNAs targeting SMARCA2 and SMARCA4 (orange bars). SWI/SNF dependency was evaluated via transient knockdown of SMARCA2/4, and IRF3-dependent genes were compiled from the literature and cross-compared with a list of genes induced by IRF35D in STAT1$^{-/-}$ cells. (**B**) Table summarizing the results for genes in (A). Columns 2 and 3 show the effect of SMARCA2/4 knockdown on PR8ΔNS1 and exogenous interferon (IFN-β)–induced mRNA levels, respectively. Levels of mRNA are shown as a percentage of the mRNA level determined by qPCR in siCtrl-treated A549 cells (set at 100% for each gene). Column 4 classifies the genes: A and B (21/28 genes) are SWI/SNF-dependent (inducibility levels <50%), C and D (7/28) are SWI/SNF-independent (inducibility >50%). Color-coded legends for columns 2 and 3 are shown at the top right. *$P < 0.05$ (Student's t test with Holm-Bonferroni sequential correction). Data are means ± SD from three independent experiments.

Downloaded from http://science.sciencemag.org/ on May 26, 2016

response and clinical symptoms similar to septic shock is also observed in humans after infection with highly pathogenic viruses, we focused on *Zaire ebolavirus* (Ebola virus), which recently caused a large outbreak of illness with a high fatality rate in West Africa (*47*). We profiled the global gene expression response during Ebola (wild-type strain Zaire-Mayinga) infection in the human leukemic cell line THP-1 in the presence and absence of Top1 inhibition. Our analysis shows that Ebola virus–induced genes encoding interleukin-8 (IL-8), IL-1β, and TNF are suppressed by Top1 inhibition (Fig. 7 and table S4). Overall, these data highlight a protective role for Top1 inhibition during infections both in vitro and in vivo.

Discussion

Topoisomerase activities are required at all genes to resolve topological constraints that result from RNAPII activity. Recent work (*29*, *30*) has shown that short and reversible Top1 inhibition specifically suppresses the expression of long genes. This indicated a differential susceptibility of genes to Top1 inhibition and redundant Top1 activities at the promoters of housekeepers. Our results provide evidence that during infection, short and reversible inhibition of Top1, as well as Top1 depletion, specifically suppresses genes induced by microbial agents. Our study

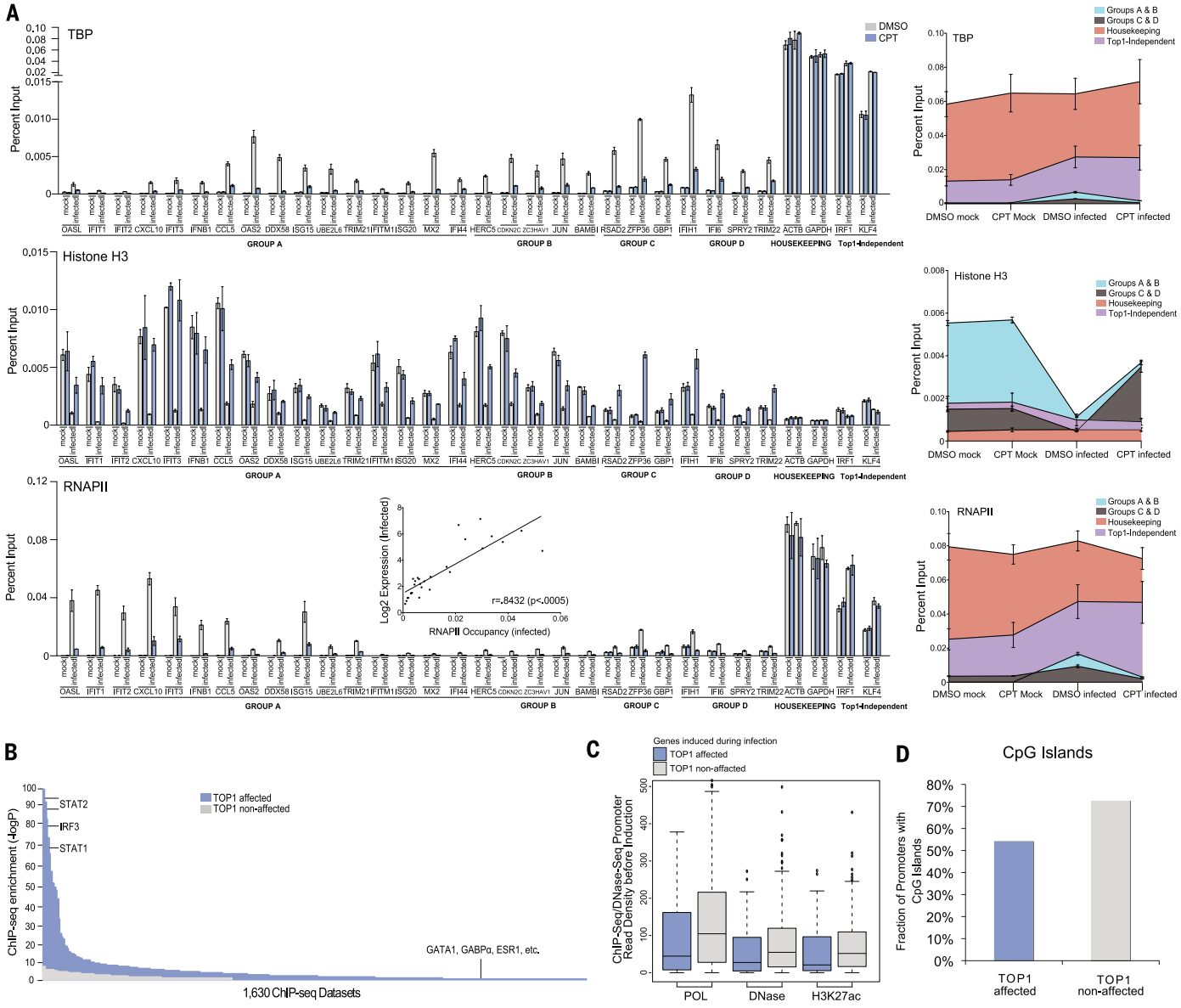


Fig. 4. Top1 inhibition suppresses PAMP-induced genes that require nucleosome remodeling for activation. (**A**) Left: ChIP-qPCR analysis of endogenous TBP, histone H3, and RNAPII at the promoters of classes A to D, housekeeping, and PAMP-induced Top1-independent genes (IRF1, KLF4) in A549 cells treated with 0.5 μM CPT or DMSO, at 6 hours after mock treatment or infection with influenza PR8ΔNS1. Right: Summation plots of each individual protein's occupancy (percent input). Inset: Correlation plot of gene expression (infected) versus RNAPII occupancy (infected) for genes shown in Fig. 3A. Data are means ± SD from two independent experiments. (**B**) Results of testing of 1630 ChIP-seq data sets for transcription factor (TF) enrichment at the promoters of Top1-affected genes during infection (see materials and methods). Negative log of the *P* value of each of these data sets (blue) and results of the same procedure are applied to genes unaffected by Top1 depletion (gray). The displayed data are the result of defining promoters as (−1000, +1) relative to the transcriptional start site. The top three TFs and examples of insignificant TFs are shown. (**C**) Basal state meta-analysis of RNAPII (POL) occupancy, DNase hypersensitivity, and H3K27ac occupancy at the promoters of genes designated as either Top1 affected (*N* = 84) or Top1 nonaffected (*N* = 296) after infection. Data sets used are from ENCODE (see materials and methods). (**D**) Basal state meta-analysis of CpG island occupancy at the promoters of genes designated as either Top1 affected or Top1 nonaffected after infection.

Downloaded from http://science.sciencemag.org/ on May 26, 2016

reveals a gene-specific activator-like role for Top1. Concordantly, such an effect was shown using in vitro transcriptional assays (*32*, *33*). The consequence of Top1 inhibition during infection is a suppression of RNAPII recruitment at PAMP-induced promoters. This effect is more prominent at genes with a bigger difference in the levels of RNAPII at basal and induced states, which explains why compromising Top1 function affects inducibility of PAMP-responsive genes. The specificity of Top1 inhibition is then geared toward genes that are not prone to immediate activation but require coactivator (IRF3) assisted nucleosome remodeling. Other gene-specific co-transcriptional events such as the dynamics of pause release and elongation, along with RNA stability or transport, are likely to contribute to PAMP gene suppression by Top1 inhibition.

At the mechanistic level, Top1 inhibitors may create a local chromatin environment that is non-permissive to transcription, or alternatively, could titrate out new recruitment of Top1. Both scenarios would lead to defects in RNAPII recycling and reinitiation and would cause the observed suppressive effect at pathogen-induced genes. Because Top1 facilitates the expression of inflammatory genes, Top1 depletion or chemical inhibition during infection reduces the immune response associated with microbial recognition. This effect was evident in vitro by chemical inhibition of Top1 causing suppression of both virus-induced and inflammatory signal–induced host gene expression, and in vivo by displaying protective effects in mouse models of lethal inflammation. The cellular response against microbes is essential in protecting us against infection, but its hyperactivation can have fatal consequences. Our results suggest that a Top1 inhibition therapy could be useful in many instances, such as in

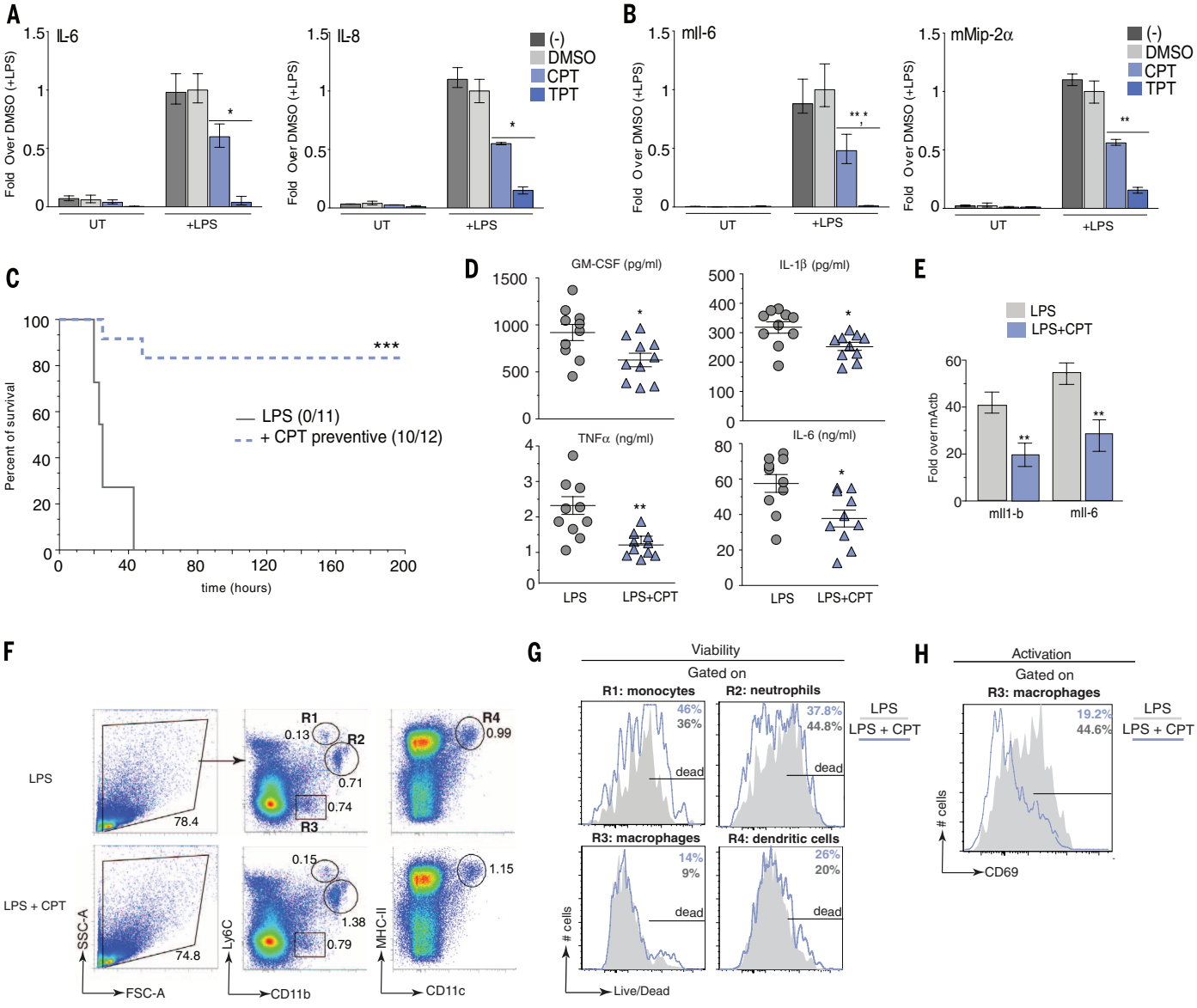


Fig. 5. Top1 regulates LPS-induced inflammation in vitro and in vivo. (**A** and **B**) Gene expression in A549 (A) or RAW 264.7 (B) cells, left untreated (−) or treated with 0.5 μM CPT, 100 nM TPT or DMSO, in the presence of LPS stimulation or not (UT). (**C** to **H**) C57BL/6J mice left untreated or treated with CPT in response to LPS-induced septic shock. (C) Survival curve. (D) Serum titers of indicated cytokines at 4 hours after LPS injection. [(E) to (H)] Ninety minutes after LPS injection spleens were harvested to perform transcriptional analysis of indicated inflammatory genes (E) and to determine cell viability and activation by flow cytometry [(F) to (H)]. (F) Gating strategy. (G) Histograms comparing the incorporation of a live/dead dye after gating on R1, R2, R3, and R4. (H) CD69 expression after gating on R3. *P < 0.05, **P < 0.005, ***P < 0.0005 (Student's t test with Holm-Bonferroni sequential correction) for [(A), (B), (D), (E)] or log rank test (C). Data are means ± SD from three independent experiments [(A) to (C)] with n = 11 (LPS) and n = 12 (LPS + CPT) individual mice, or two independent experiments [(D) to (H)] with n = 6 (LPS) and n = 7 CPT (LPS + CPT) individual mice.

Downloaded from http://science.sciencemag.org/ on May 26, 2016

pandemics and many congenital deficiencies, whereby an overt immune response is acutely induced.

Materials and methods

Cell lines and viruses

The following cell lines were originally obtained from the American Type Culture Collection (ATCC): A549 cells (adenocarcinomic human alveolar basal epithelial cells), 293T cells (human embryonic kidney cells), RAW 264.7 cells (mouse leukemic monocyte macrophage cell line), and HTBE cells (human primary bronchial/tracheal epithelial cells).

The 293T-FF cell line was generated by transfection with the plasmid pGL4.17-IFN-FF, encoding a cassette with the firefly luciferase gene under the control of the murine IFN-β promoter, as previously described (*48*), and was a gift from P. Palese.

Cells were maintained in culture at 37°C with 5% CO_2 in Dulbecco's minimal essential medium (DMEM, Gibco, Life Technologies) supplemented with 2 mM glutamine (Life Technologies), 10% fetal bovine serum (FBS; Hyclone), penicillin (100 U/ml; Life Technologies), and streptomycin (100 μg/ml; Gibco, Life Technologies).

The influenza virus PR8ΔNS1, which is the H1N1 PR8 A/Puerto Rico/8/1934 strain lacking the expression of the NS1 protein, was propagated in Madin-Darby canine kidney (MDCK) cells expressing the viral nonstructural protein 1 (NS1) (*49*). The influenza virus PR8 expressing green fluorescent protein (GFP) (PR8-GFP) and deficient for the viral protein hemagglutinin (HA) was propagated in MDCK-HA–expressing cells (*50*).

The influenza virus H3N2, which is the strain A/Philippines/2/82, was propagated in 10-day-old embryonated chicken eggs and was a gift from F. Kramer.

The Sendai virus (SeV), Cantell strain, was propagated in 10-day-old embryonated chicken eggs (*51*), and was a gift from P. Palese.

Viral infections using the strains described above were performed at a multiplicity of infection (MOI) of 3 and cells were analyzed at different time points as indicated in the figures.

Infections with the Ebola virus were performed in THP-1 cells, a human monocytic cell line that naturally expresses several PRRs. We used the wild-type Ebola Zaire-Mayinga strain and its VP-35 mutant, which fails to block the type I interferon response in the host (*52*). Cells were recovered 24 hours after Ebola infection.

IRF3 dependent genes were compiled from the literature and cross-compared with a list of genes induced by IRF3-5D in $STAT1^{-/-}$ cells (courtesy of S. Tripathi).

Cell viability assay

The Cell Titer Glo Cell Viability Assay (Promega) detects adenosine triphosphate (ATP) levels as a function of cell viability, and was used according to manufacturer's specifications. Briefly, cells were seeded into 96-well plates (5000 cells/well), and 18 hours later, 25 μl of fresh media containing the indicated compounds (serially diluted) were included. After 6 hours of incubation, 50 μl of CellTiterGlo was added and the luminescence was measured. Vehicle-treated cells were used to normalize (100%) the ATP activity.

The CytoTox 96 Non-Radioactive Cytotoxicity Assay (Promega), a colorimetric assay measuring the release of the cellular enzyme lactate dehydrogenase (LDH), was also used according to manufacturer's specifications.

Inhibitors and cell treatments

Cell culture: CPT (Sigma) was dissolved in a 4:1 mixture of chloroform and methanol at a concentration of 0.5 mM, heated at 55°C until fully dissolved and then added to cells in DMEM medium at a final concentration of 0.5 μM. TPT (Sigma) and TPT-A were dissolved in dimethyl

Downloaded from http://science.sciencemag.org/ on May 26, 2016

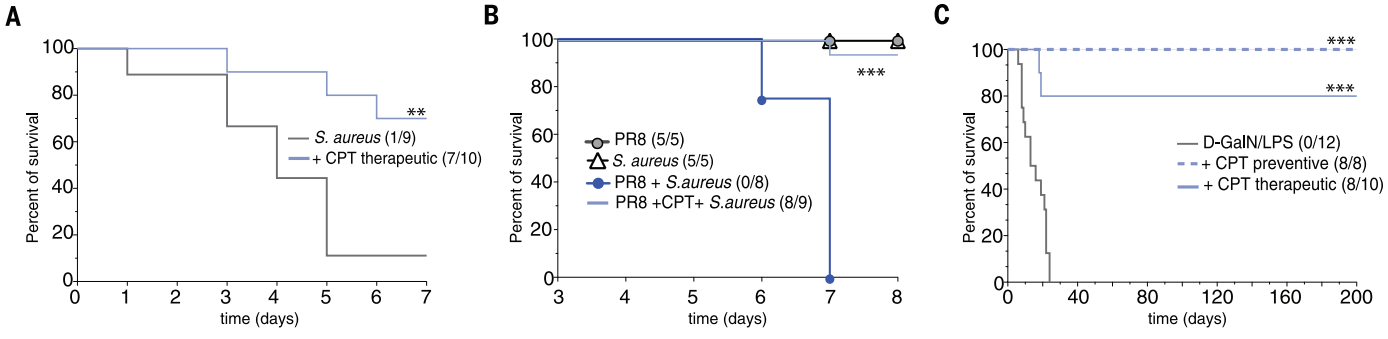


Fig. 6. Top1 inhibition blocks lethal inflammation in vivo. (**A** to **C**) Survival curves of C57BL/6J mice left untreated or treated with CPT in response to *S. aureus* infection (A), PR8–*S. aureus* co-infection (B), or D-GalN/LPS injection (C). Mice were treated with CPT 3, 24, and 48 hours after *S. aureus* infection (A); 12, 24, and 36 hours after PR8 infection (B); or 2 hours and 30 min after D-GalN/LPS injection (C). $^{**}P < 0.005$, $^{***}P < 0.0005$ (log rank test). Data are from three independent experiments (A) with $n = 8$ to 12 individual mice, and two independent experiments [(B) and (C)] with $n = 5$ to 9 individual mice.

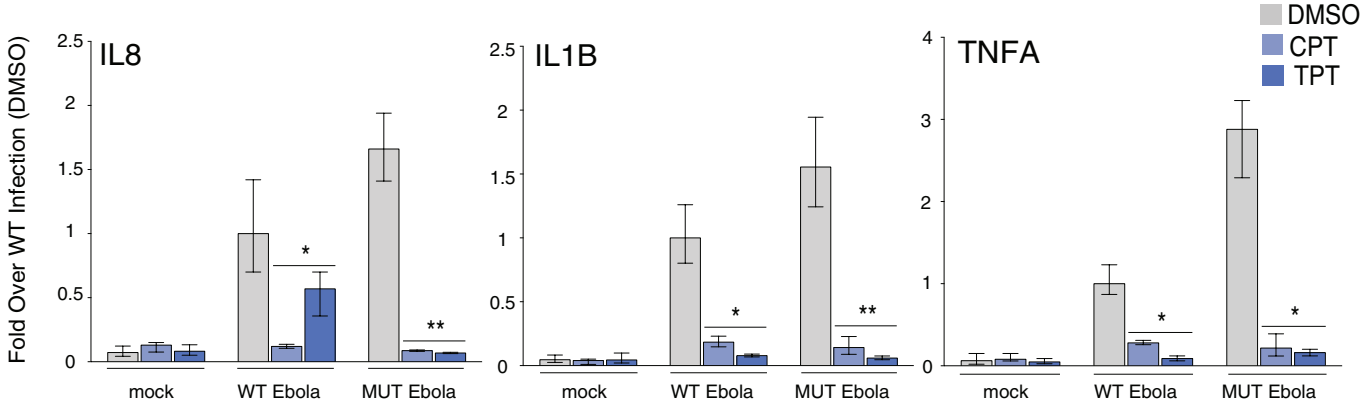


Fig. 7. Suppression of Ebola virus induced inflammation by Top1 inhibitors. THP-1 cells were mock-treated or infected with wild-type (WT) Ebola virus (Zaire-Mayinga strain) in the presence of 0.5 μM CPT, 100 nM TPT, or DMSO. Bar graphs show the relative expression of selected genes. Data are means ± SD from three independent experiments. $^{*}P < 0.05$, $^{**}P < 0.005$ (Student's *t* test with Holm-Bonferroni sequential correction).

sulfoxide (DMSO, Fisher) at the concentration of 100 μM and then added to cells in DMEM medium at a final concentration of 100 nM. FVD and (+/−)-JQ1 (both from Sigma) were dissolved in DMSO at a concentration of 0.5 mM and then added to cells in DMEM medium at a final concentration of 0.5 μM. Doxorubicin (Sigma) was dissolved in water at a concentration of 50 μM and then added to cells in DMEM medium at final concentrations of 0.5 and 5 μM.

All the compounds and the vehicle control DMSO were added to the cell cultures at 1 hour before and after stimulation or infection.

Lipopolysaccharide (LPS, Sigma, tlrl-3pelps) was added to cells in DMEM medium at a final concentration of 100 ng/ml for 2 hours. TNF-α (Sigma, human: T0157, mouse: T7539), IFN-β (PBL Assay Science, human: 11415-1, mouse: 12400-1), and poly(I:C) (Sigma, P1530) were added to cells in DMEM medium for 4 hours at final concentrations of 10 ng/ml, 100 U/ml, and 10 μg/ml, respectively.

For hormone treatment, A549 cells were grown in DMEM containing 5% charcoal-dextran–treated FBS (Sigma) for 2 days before addition of 17β-estradiol (10 nmol/liter; Sigma, E2758).

For heat shock, A549 cells were incubated at 42°C for 2 hours.

In vivo experiments: CPT was dissolved in a 4:1 mixture of chloroform and methanol, followed by heating at 55°C until fully dissolved. CPT was then brought up with water to the necessary volume corresponding to 200 μl per mouse and centrifuged for 5 min at 4000 rpm. The top aqueous fraction, containing the CPT, was recovered and dissolved at a final concentration of 30 mg/kg of mouse weight in 200 μl of water for each injection.

Immunofluorescence

A549 and RAW 264.7 cells were cultured on cover slips overnight and then treated with 0.5 and 10 μM CPT or 100 nM and 10 μM TPT 1 hour before and after infection with PR8ΔNS1 or H3N2 viruses. At 6 hours after infection, cells were fixed for 10 min at 4°C in 4% formaldehyde (EMS). Cover slips were washed in phosphate-buffered saline (PBS; Life Technologies) and cells were permeabilized for 10 min at room temperature in 0.5% NP-40 (Sigma). Cover slips were washed again in PBS and nonspecific binding was blocked by incubation for 30 min at room temperature with a solution containing 3% BSA (Sigma) in PBS. Cells were then probed for 2 hours with a rabbit anti-phospho-histone H2A.X antibody (Cell Signaling), followed by detection with Alexa Fluor 488-conjugated (green) goat anti-rabbit immunoglobulin G (IgG) (heavy and light chain, Life Technologies). DNA was counterstained with 4′,6-diamidino-2-phenylindole (DAPI, Thermo Scientific).

For visualization of the PR8-GFP virus, an EVOS FL (Thermo Scientific) microscope was used.

Quantitative polymerase chain reaction (qPCR)

For RNA extraction, cells were homogenized with QIAshredder columns; RNA was extracted using the RNeasy Mini Kit and then treated with the RNase-free DNase kit (all Qiagen). Proteins were also simultaneously recovered from cell lysates by acetone precipitation of the flow-through from RNeasy spin columns, according to manufacturer's instructions.

cDNA was in vitro transcribed using a High-Capacity cDNA RT Kit (Thermo Fisher Scientific) or a SuperScript III First-Strand Synthesis SuperMix (Life Technologies). qPCR was performed using the iTaq Universal SYBR Green One-Step Kit (Bio-Rad) according to manufacturer's instructions.

The statistical significance of all pairwise comparisons in qPCR assays' change in cycling threshold (ΔC_T) values was determined with a two-tailed Student's t test under the assumption of equal variances between groups. We did not find significant differences (false discovery rate, $q < 0.05$) between contrast groups in Levene's tests of equality of variances, or departures from normality as assessed by Shapiro-Wilk tests.

Primers

Primers were designed using the Primer3 online tool or by using already available primers from Harvard's PrimerBank database. Sequences of primers used for qPCR were as follows:

Human: β-actin forward, 5′-ACCTTCTACAATGAGCTGCG-3′; β-actin reverse, 5′-CCTGGATAGCAACGTACATGG-3′; GAPDH forward, 5′-GCAAATTCCATGGCACCGT-3′; GAPDH reverse, 5′-GCCCCACTTGATTTTGGAGG-3′; 18S forward, 5′-GTAACCCGTTGAACCCCATT-3′; 18S reverse, 5′-CCATCCAATCGGTAGTAGCG-3′; IFIT2 forward, 5′-AGGCTTTGCATGTCTTGG-3′; IFIT2 reverse, 5′GAGTCTTCATCTGCTTGTTGC-3′; IFIT1 forward, 5′-TTCGGAGAAAGGCATTAGA; IFIT1 reverse, 5′-TCCAGGGCTTCATTCATAT; IFNB1 forward, 5′-TCTGGCACAACAGGTAGTAGGC; IFNB1 reverse, 5′-GAGAAGCACAACAGGAGAGCAA; HPRT1 forward, 5′-GAAAAGGACCCCACGAAGTGT; HPRT1 reverse, 5′-AGTCAAGGGCATATCCTACAACA; BRD4 forward, 5′-GAGCTACCCACAGAAGAAACC; BRD4 reverse, 5′-GAGTCGATGCTTGAGTTGTGTT; IL-1β forward, 5′-ATGATGGCTTATTACAGTGGCAA; IL-1β reverse, 5′-GTCGGAGATTCGTAGCTGGA; IL-6 forward, 5′-ACTCACCTCTTCAGAACGAATTG; IL-6 reverse, 5′-CCATCTTTGGAAGGTTCAGGTTG; IL-8 forward, 5′-TTTTGCCAAGGAGTGCTAAAGA; IL-8 reverse, 5′-AACCCTCTGCACCCAGTTTTC; CDK9 forward, 5′-ATGGCAAAGCAGTACGACTCG; CDK9 reverse, 5′-GCAAGGCTGTAATGGGGAAC; CCNT1 forward, 5′-ACAACAAACGGTGGTATTTCACT; CCNT1 reverse, 5′-CCTGCTGGCGATAAGAAAGTT; CXCL10 forward, 5′-GTGGCATTCAAGGAGTACCTC-3′; CXCL10 reverse, 5′-TGATGGCCTTCGATTCTGGATT-3′; IFIT3 forward, 5′-AGAAAAGGTGACCTAGACAAAGC-3′; IFIT3 reverse, 5′-CCTTGTAGCAGCACCCAATCT-3′; ZFP36 forward, 5′-GAGAACAAATTCCGGGACCG-3′; ZFP36 reverse, 5′-GCGTGGAGTTGATCTGGGAG-3′; CCL5 forward, 5′-CCAGCAGTCGTCTTTGTCAC-3′; CCL5 reverse, 5′-CTCTGGGTTGGCACACACTT-3′; GBP1 forward, 5′-AACGACAGGGTCCAGTTGCTGAAAG; GBP1 reverse, 5′-TAGGGGTGACAGGAAGGCTCTGG; OASL forward, 5′-CTGATGCAGGAACTGTATAGCAC; OASL reverse, 5′-CACAGCGTCTAGCACCTCTT; IFIH1 forward, 5′-TCACAAGTTGATGGTCCTCAAGT; IFIH1 reverse, 5′-CTGATGAGTTATTCTCCATGCCC; IFI6 forward, 5′-GGTCTGCGATCCTGAATGGG; IFI6 reverse, 5′-TCACTATCGAGATACTTGTGGGT; OAS2 forward, 5′-ACGTGACATCCTCGATAAAACTG; OAS2 reverse, 5′-GAACCCATCAAGGGACTTCTG; SPRY2 forward, 5′-CCTACTGTCGTCCCAAGACCT; SPRY2 reverse, 5′-GGGGCTCGTGCAGAAGAAT; DDX58 forward, 5′-TGCGAATCAGATCCCAGTGTA; DDX58 reverse, 5′-TGCCTGTAACTCTATACCCATGT; RSAD2 forward, 5′-TTGGACATTCTCGCTATCTCCT; RSAD2 reverse, 5′-AGTGCTTTGATCTGTTCCGTC; TRIM22 forward, 5′-AATGTGCTGGATAACCTGGCA; TRIM22 reverse, 5′-TCTACTGACGATCCCCTCAAC; ISG15 forward, 5′-CGCAGATCACCCAGAAGATCG; ISG15 reverse, 5′-TTCGTCGCATTTGTCCACCA; UBE2L6 forward, 5′-TGGACGAGAACGGACAGATTT; UBE2L6 reverse, 5′-GGCTCCCTGATATTCGGTCTATT; TRIM21 forward, 5′ -TCAGAGCTAGATCGAAGGTGC; TRIM21 reverse, 5′-ACTCACTCCTTTCCAGGACAAT; IFITM1 forward, 5′-GGGCCTTCTGGATTCCGAG; IFITM1 reverse, 5′-CGTGGGGTTGGTCATCGTC; HERC5 forward, 5′-GGTGAGCTTTTTGCCTGGG; HERC5 reverse, 5′-TTCTCCGGCAGAAATCTGAGC; CDKN2C forward, 5′-GGGGACCTAGAGCAACTTACT; CDKN2C reverse, 5′-CAGCGCAGTCCTTCCAAAT; ISG20 forward, 5′-TCTACGACACGTCCACTGACA; ISG20 reverse, 5′-CTGTTCTGGATGCTCTTGTGC; ZC3HAV1 forward, 5′-TCACGAACTCTCTGGACTGAA-3′; ZC3HAV1 reverse, 5′-ACTTTTGCATATCTCGGGCATAA-3′; JUN forward, 5′-ATCAAGGCGGAGAGGAAGCG-3′; JUN reverse, 5′-TGAGCATGTTGGCCGTGGAC-3′; BAMBI forward, 5′-ATGCTCTCCCGTTTGCACTAC-3′; BAMBI reverse, 5′-AGGATCTTATCGTTGCTGAGGT-3′; MX2 forward, 5′-CAGAGGCAGCGGAATCGTAA-3′; MX2 reverse, 5′-TGAAGCTCTAGCTCGGTGTTC-3′; IFI44 forward, 5′-GGTGGGCACTAATACAACTGG; IFI44 reverse, 5′-CACACAGAATAAACGGCAGGTA; TNF-α forward, 5′-CCTCTCTCTAATCAGCCCTCTG; TNF-α reverse, 5′-GAGGACCTGGGAGTAGATGAG; GFP forward, 5′-AAGCTGACCCTGAAGTTCATCTGC; GFP reverse, 5′-CTTGTAGTTGCCGTCGTCCTTGAA; PR8 HA forward, 5′-AAAGAAAGCTCATGGCCCAACC; PR8 HA reverse, 5′-TCCTTCTCCGTCAGCCATAGCA; PR8 PB1 forward, 5′-TCATGAAGGGATTCAAGCCG; PR8 PB1 reverse, 5′-GGAAGCTCCATGCTGAAATTG; HSP70 forward, 5′-CATCGCCTATGGGCTGGAC; HSP70 reverse, 5′-GGAGAGAACCGACACATCGAA; HSP27 forward, 5′-ACGGTCAAGACCAAGGATGG; HSP27 reverse, 5′-AGCGTGTATTTCCGCGTGA; PGR1 forward, 5′-TCCACCCCGGTCGCTGTAGG; PGR1 reverse, 5′-TAGAGCGGGCGGCTGGAAGT; TFF1 forward, 5′-TTGGAGAAGGAAGCTGGATGG; TFF1 reverse, 5′-ACCACAATTCTGTCTTTCACGG; GREB1 forward, 5′-GTGGTAGCCGAGTGGACAAT; GREB1 reverse, 5′-ATTTGTTTCCAGCCCTCCTT; TOP1 forward, 5′-AAGGTCCAGTATTTGCCCCAC; TOP1 reverse, 5′-ATTCATGGTCGAGCATTTTTGC; TOP2A forward, 5′-ACCATTGCAGCCTGTAAATGA; TOP2A reverse, 5′-GGGCGGAGCAAAATATGTTCC; TOP2B forward, 5′-TTGGACAGCTTTTAACATCCAGT; TOP2B reverse, 5′-GCACCATAACCATTACGACCAC; SMARCA2 forward, 5′-AGGGGATTGTAGAAGACATCCA; SMARCA2 reverse, 5′-TTGGCTGTGTTGATCCATTGG; SMARCA4 forward, 5′-AATGCCAAGCAAGATGTCGAT; SMARCA4 reverse, 5′-GTTTGAGGACACCATTGACCATA.

Downloaded from http://science.sciencemag.org/ on May 26, 2016

Mouse: Actb forward, 5′-TTACGGATGTCAACGTCACAGTTC; *Actb* reverse, 5′-ACTATTGGCAACGAGCGGTTC; *Mip1a* forward, 5′-CGAGTACCAGTCCCTTTTCTGTTC; *Mip1a* reverse, 5′-AAGACTTGGTTGCAGAGTGTCATG; *Il-6* forward, 5′-TGAGATCTACTCGGCAAACCTAGTG; *Il-6* reverse, 5′-CTTCGTAGAGAACAACATAAGTCAGATACC; *Ifit1* forward, 5′-GCCTATCGCCAAGATTTAGATGA; *Ifit1* reverse, 5′-TTCTGGATTTAACCGGACAGC; *Ifit2* forward, 5′-AGAACCAAAACGAGAGAGAGTGAGG; *Ifit2* reverse, 5′-TCCAGACGGTAGTTCGCAATG; *Mip-2* forward, 5′-GTCCCTCAACGGAAGAACCAA; *Mip-2* reverse, 5′-ACTCTCAGACAGCGAGGCACAT; *Rantes* forward, 5′-TGCCCACGTCAAGGAGTATTTC; *Rantes* reverse, 5′-TCCTAGCTCATCTCCAAATAGTTGATG; *Il-1β* forward, 5′-GCAACTGTTCCTGAACTCAACT; *Il-1β* reverse, 5′-ATCTTTTGGGGTCCGTCAACT.

Sequences of primers used for ChIP followed by qPCR were as follows:

Human: ACTB 5′ forward, GAGGGGAGAGGGGGTAAAA; ACTB 5′ reverse, AGCCATAAAAGGCAACTTTCG; IFIT1 5′ forward, AGAGGAGCCTGGCTAAGCA; IFIT1 5′ reverse, GGTTGCTGTAAATTAGGCAGC; IFIT2 5′ forward, TGCACTGCAACCATGAGG; IFIT2 5′ reverse, TGACTCAACAGCACTACCGA; IL-6 5′ forward, CCCAATAAATATAGGACTGGAGATG; IL-6 5′ reverse, GAGTTCATAGCTGGGCTCCT; IL-8 5′ forward, TATAAAAAGCCACCGGAGCA; IL-8 5′ reverse, GCCAGCTTGGAAGTCATGTT; CXCL10 5′ forward, CAGCAGAGGAACCTCCAGTC; CXCL10 5′ reverse, TGATGTTCCTTACCTTGAATGC; IFIT3 5′ forward, CGGAACAGCAGAGACACAGA; IFIT3 5′ reverse, GGGAAAAACCCCTCAAACAT; ZFP36 5′ forward, ACTTCAGCGCTCCCACTCT; ZFP36 5′ reverse, AGTTGGAGAAGGGAGGCAAG; CCL5 5′ forward, CGAATTTCCGGAGGCTATTT; CCL5 5′ reverse, CGTGCTGTCTTGATCCTCTG; GBP1 5′ forward, ATGAGGAAATCCCAGCCCTA; GBP1 5′ reverse, TCCTTAGTTCACGAGCACTGG. OASL 5′ forward, AAATGCTCCTGCCTCAGAAA; OASL 5′ reverse, GGGACAGAGATGGCACTGAT; IFIH1 5′ forward, GAAGGAGGTTCAGCAGTTGG; IFIH1 5′ reverse, AGCACCTTGGAGAAGGGAGT; IFI6 5′ forward, TGATGCCCACACTTCATAGC; IFI6 5′ reverse, GGGAGGATCCACAAGTGATG; OAS2 5′ forward, TTTCAGTTTCCTGGCTCTGG; OAS2 5′ reverse, TGGATAAACCAACCCAGCTT; SPRY2 5′ forward, AAAGAGAATTCGGAGCCAGA; SPRY2 5′ reverse, ATCTGCCAGGAAAAGGGACT; DDX58 5′ forward, CCTTTCACCTCTTTCCCAGA; DDX58 5′ reverse, CTTTTCCAGACCGAATAGCTT; RSAD2 5′ forward, CCAATGACAGGTTGCTCAGA; RSAD2 5′ reverse, CAGCTGCTGCTTTCTCCTCT; TRIM22 5′ forward, CTGAGTGCCTTGCCAGTACA; TRIM22 5′ reverse, CAAATGAGTTTCCCCACAGG; ISG15 5′ forward, GCTGAGAGGCAGCGAACTC; ISG15 5′ reverse, CCCCACCTGTGACATCTGC; UBE2L6 5′ forward, CCGGGACTCACGGTCTTT; UBE2L6 5′ reverse, CGGAGCGAAGACTGGAAC; TRIM21 5′ forward, GCTCAAGGATGGAGACTGGA; TRIM21 5′ reverse, CCTCCCCTTTCCTCTCAGAC; IFITM1 5′ forward, AACTGAAACGACAGGGGAAA; IFITM1 5′ reverse, ACAGCCACCTCATGTTCCTC; HERC5 5′ forward, ACCAGGCGTTCTCTCCTCTC; HERC5 5′ reverse, CTGGGAAAGAGCCAGAGC; IFNB1 5′ forward, GGAATCCAAGCAAGTTGTAGC; IFNB1 5′ reverse, AACCTTTCGAAGCCTTTGCT; CDKN2C 5′ forward, GCCGAGCCTCCTTAAAACTC; CDKN2C 5′ reverse, ACAATTGCTGCTTCTGTTGC; ISG20 5′ forward, GGTAGCCCAGGAGATGGAG; ISG20 5′ reverse, CTCACGTCTGCCTCTCTGCT; ZC3HAV1 5′ forward, CGCATCTGCATTTAGACGAA; ZC3HAV1 5′ reverse, CTCAACAGGGCTCTCAGGAC; JUN 5′ forward, CCGTTGCTGGACTGGATTAT; JUN 5′ reverse, CCCCAAGATCCTGAAACAGA; BAMBI 5′ forward, CGTGCTGTGGAGACCCTACT; BAMBI 5′ reverse, CCAGGAGCCCAGAAAAGTT; MX2 5′ forward, CCACAGCTCTCCCAGGATT; MX2 5′ reverse, TGTGGCATATGAACCACTCC; IFI44 5′ forward, TGAGAGAAGTTGGCATGCTG; IFI44 5′ reverse, AGCTGAGGGTAGCTGCTCTGT; IRF1 5′ forward, AAGAGGGAAGAAGGCAGAGG; IRF1 5′ reverse, CTTAGTCGAGGCAAGACGTG; KLF4 5′ forward, TCTCTCTGGTCGGGAAACTG; KLF4 5′ reverse, GCGCCGAGTTTGTTGATTTA; GAPDH 5′ forward, ACAGTCAGCCGCATCTTCTT; GAPDH 5′ reverse, TTCTCTCCGCCCGTCTTC.

Mouse: Actb 5′ forward, GGGCTACAGTGGGTGAAAGG; *Actb* 5′ reverse, GGGCTACAGTGGGTGAAAGG; *Ifit1* 5′ forward, TGAAAAGAGCACACCCCCTA; *Ifit1* 5′ reverse, CTCCTCAGAAACCTGCCTTG; *Ifit2* 5′ forward, AGCCACACCCGACTAACG; *Ifit2* 5′ reverse, CTTGGTGCTTTGAGGGATCT; *Il-6* 5′ forward, AATGTGGGATTTTCCCATGA; *Il-6* 5′ reverse, GCGGTTTCTGGAATTGACTATC; *Mip2-a* 5′ forward, GGGCTTTTCCAGACATCGT; *Mip2-a* 5′ reverse, TGAAGTGTGGCTGGAGTCTG.

Sequences of primers used for chem-ChIP followed by qPCR were as follows:

Human: ACTB upstream forward, CTGCAGAAGGAGCTCTTGGA; ACTB upstream reverse, GACCCACCCAGCACATTTAG; ACTB-1 forward, GAGGGGAGAGGGGGTAAAA; ACTB-1 reverse, AGCCATAAAAGGCAACTTTCG; ACTB-2 forward, GTCATCTTCTCGCGGTTGG; ACTB-2 reverse, GGCATCCTCACCCTGAAGTA; ACTB-3 forward, CCTACACCCACAACACTGTCT; ACTB-3 reverse, TGACCTGAGTCTCCTTTGGAA; ACTB-4 reverse, CAGGTCCAGACGCAGGAT; ACTB-4 reverse, GCCATGTACGTTGCTATCCA; ACTB-5 forward, GTGCCAGGGCAGTGATCT; ACTB-5 reverse, CTGTGGCATCCACGAAACTA; ACTB-6 forward, CTAAGTCATAGTCCGCCTAGAAGC; ACTB-6 reverse CTGTCCACCTTCCAGCAGAT; ACTB downstream forward, CGCCCAGTCTCCAGTCAC; ACTB downstream reverse, GTTGGGGTAGGGGGTCCA; HPRT1 upstream forward, TAGTCGGGGTTCTCCACAAA; HPRT1 upstream reverse, CCTTCAGATTTTGGACTCAACA; HPRT1-1 forward, GAAAATTCCCACGGCTACCT; HPRT1-1 reverse, GGGAAAGCCGAGAGGTTC; HPRT1-2 forward, GACAGAGTCTTGCTCTGTTTCC; HPRT1-2 reverse, AAAATTAGCCGGGTGTGGT; HPRT1-3 forward, GCCTGGGCTAGACTTTTGAG; HPRT1-3 reverse, TGACAGGTGTCTGGTTCTGG; HPRT1-4 forward, CTGGACCTCCTGGAATTGAG; HPRT1-4 reverse, AAACACAGGTAGAACTATAAAAGCAAA; HPRT1-5 forward, GATGCTCACCTCTCCCACAC; HPRT1-5 reverse, CCCTGACTACCCATGTGTCC; HPRT1-6 forward, TGTCATTAGTGAAACTGGAAAAGC; HPRT1-6 reverse, CATGCAAAAAGCTCTACTAAGCA; HPRT1 downstream forward, CGTCTGGGGTCATACAGGTT; HPRT1 downstream reverse, CTGAGGGCAGGGATAGTTTG; IFIT1 upstream forward, CAAGACTGCTGCCAAATTCA; IFIT1 upstream reverse, CATGATCAGGCCATAAGCAA; IFIT1-1 forward, AGAGGAGCCTGGCTAAGCA; IFIT1-1 reverse, GGTTGCTGTAAATTAGGCAGC; IFIT1-2 forward, AACAGGTTTTCGCAATCAGG; IFIT1-2 reverse, CTTCCCAAGCAGATGTGGAT; IFIT1-3 forward, AACATTTTTCTCGCTATGTGGA; IFIT1-3 reverse, GACAGAAAGCAGATTAACAGTTGC; IFIT1-4 forward, TTTTCATGGCTGTCATCAGATT; IFIT1-4 reverse, TTCCACTCAGATTGGCAAGA; IFIT1-5 forward, ACTATTTGAGATCCCTTGACATTT; IFIT1-5 reverse, GATGTCAATACTACCCAAAGTGATCT; IFIT1-6 forward, GAAATATGAATGAAGCCCTGGA; IFIT1-6 reverse, GGCTGATATCTGGGTGCCTA; IFIT1 downstream forward, AGCTGCAGCCTGAGAGTTTG; IFIT1 downstream reverse, CCAGTCCCCATGATCTGAGT; IFIT2 upstream forward, GAGGACTTTAAATGATACCAACACA; IFIT2 upstream reverse, TTTCCCCCTTTTTATTGATGT; IFIT2-1 forward, TGCACTGCAACCATGAGG; IFIT2-1 5′ reverse, TGACTCAACAGCACTACCGA; IFIT2-2 forward, TCAGAGAAAGAAGGCAGCAGA; IFIT2-2 reverse, AAGACAGGGTCAGTGCACAA; IFIT2-3 forward, AACCCAAAATCAAGCAGTGAA; IFIT2-3 reverse, TGTGCATTTGCAGGATAGAGA; IFIT2-4 forward, TCCCAATCAAAATGGGAGTG; IFIT2-4 reverse, TGTGGCAGGATCACTTATGAA; IFIT2-5 forward, CCAATCTGATAAAAGCTCAGAAA; IFIT2-5 reverse, AGTTCTCCTTCATTTGCCTTT; IFIT2-6 forward, GCAGCCCTGGAATGCTTAC; IFIT2-6 reverse, CAGGCATAGTTTCCCCAGGT; IFIT2 downstream forward, TGAGTCATAGTTTGTGTTATTTCTGA; IFIT2 downstream reverse, GGATTCTGGAAAGGTAAAGAAAGA.

Transfection with siRNA

Transfection experiments were performed using the Lipofectamine RNAiMAX transfection reagents according to the manufacturer's instructions (Invitrogen). Cells were transfected with siRNA pools (all from Dharmacon) targeting the genes encoding human Top1, BRD4, CDK9, CCNT1, SMARCA2, SMARCA4, TOP2A, TOP2B, or with a control nontargeting pool, at a final concentration of 50 nM. Cells were used 48 hours after transfection, and the efficiency of gene knockdown was determined by qPCR or immunoblotting.

Microarray analysis

A549 cells were transfected with siRNA targeting the gene encoding Top1 or control nontargeting siRNA (siCtrl), then infected in triplicate with the PR8ΔNS1 virus (MOI = 3). Nontransfected cells were also infected, as a further control. RNA was isolated from infected and uninfected cells with a Qiagen RNeasy kit and 200 ng of RNA per sample was then used to prepare labeled RNA that was hybridized to Human HT-12 v4 Expression BeadChips (Illumina). Data were analyzed using the Genespring software (version 12.5).

To determine the effect of Top1 depletion on the magnitude of cell response during infection, raw signal values obtained from uninfected and infected cells in all siRNA treatments were quantile-normalized before being baseline-transformed to

Downloaded from http://science.sciencemag.org/ on May 26, 2016

the medians of signal values for the corresponding uninfected siRNA-treated samples. For identification of probe sets with statistically significant differences in magnitude of response ($P < 0.01$), we conducted an analysis of variance (ANOVA) followed by a post hoc [Tukey's honest significant difference (HSD)] test.

We selected genes differentially expressed after treatment with siTop1 using a threshold of a factor of ≥1.5 change ($P < 0.01$) in their expression relative to siCtrl-treated cells. When indicated, infection-induced genes were identified as the ones showing a factor of ≥1.5 change ($P < 0.01$) in their expression in infected siCtrl-treated cells relative to uninfected siCtrl-treated cells.

All computations of P values were subjected to multiple-testing correction using the Benjamini-Hochberg method. For purposes of presentation, genes represented by multiple probe sets in the microarray were plotted in the heat maps as the averaged values of those probe sets.

To determine the effect of Top1 depletion under basal conditions, we normalized raw signal values from uninfected siRNA-treated cells by quantile before baseline-transforming them to the median of all samples. A statistical ANOVA test followed by a post hoc test was then conducted. Genes regulated by the siRNA targeting the Top1 gene were defined as genes with a factor of ≥1.5 change ($P < 0.01$) in their expression relative to the siCtrl controls. Normalized signal intensity values of a list of canonical housekeeping genes were also used to determine the overall effect of the depletion of Top1 in cells. A full list of the affected genes is shown in table S1.

We used Ingenuity Pathways Analysis software (Ingenuity Systems) for the identification of canonical pathways that showed "enrichment" among groups of genes with significant changes in their expression by microarray analysis. The DAVID gene ontology analysis helped to identify genes associated with cytokine activity (*53*, *54*). A right-tailed Fisher's exact test was used for calculation of P values determining the probability that each pathway assigned to a specific data set was due to chance alone.

Mice and related experiments

C57BL/6J female mice were purchased from The Jackson Laboratories and housed under specific pathogen-free conditions in the animal care facility at the Icahn School of Medicine at Mount Sinai (ISMMS). Mice were studied at 7 to 12 weeks of age. All experiments were approved by the institutional animal care and use committee and carried out in accordance with the *Guide for the Care and Use of Laboratory Animals* (NIH publication 86-23, revised 1985).

For the septic shock model, mice were injected intraperitoneally (i.p.) with 10 mg/kg of ultrapure LPS (from *E. coli* 0111:B4 strain-TLR4 ligand, InvivoGen) resuspended in 200 μl of water. For the preventive protocol, one group of mice received, after isoflurane anesthesia, a first retro-orbital intravenous injection with a dose of 30 mg/kg of CPT 30 min before LPS treatment followed by an i.p. challenge with the same dose of CPT 1 hour after LPS injection.

For the acute liver failure model, mice were injected i.p. with a mixture of 5 mg of D-(+)-galactosamine (Sigma) and 500 ng of ultrapure LPS (Invivogen) (referred to as D-GalN/LPS), in 200 μl of water. One group of mice was also injected i.p. with CPT (110 mg/kg) 1 hour before (preventive protocol) or 2 hours and 30 min after (therapeutic protocol) GalN/LPS treatment.

For the sepsis model using *Staphylococcus aureus* infection (subsp. *aureus* Rosenbach, FDA 209P strain, ATCC) bacteria were grown in Bacto Tryptic Soy Broth (BDbioscience) until stationary phase, washed, and suspended in PBS at 25×10^8 bacteria/ml and mice intravenously injected with 200 μl of the bacterial suspension. We then started the treatment 3 hours after infection, when animals presented the first clinical signs of disease (ruffled fur, diminished activity, and hunched posture). One group of mice received a first dose of 30 mg/kg of CPT intravenously, followed by IP injections of 45 mg/kg of CPT 24 and 48 hours later.

For the co-infection model, the influenza virus PR8 (H1N1 PR8 A/Puerto Rico/8/1934) was administered intranasally in sterile PBS in a volume of 50 μl at a titer of $0.3 \times LD_{50}$. Three days after influenza infection, *S. aureus* stocks were grown until exponential phase and resuspended in sterile PBS in a volume of 50 μl containing 5×10^8 bacteria per mouse for intranasal administration. Mice were anesthetized with ketamine-xylazine before all intranasal injections. One group of mouse received 75 mg/kg of CPT i.p. at 12, 24, and 36 hours after viral infections.

Survival significance in the in vivo experiments was calculated using a log-rank Mantel-Cox test with the Graphpad software Prism.

During all treatments, mice were daily weighed and monitored two to six times per day until the end of the experiment. We considered a loss >20% of the initial weight as a humane end point, according to the policy of the institutional animal care and use committee at ISMMS. In case of survival, animals were under observation twice per day for the following month and every week for additional months. We did not detect any side effect of the CPT treatment in mice monitored for at least 3 months.

Quantitative PCR in tissue samples: Spleens and lungs were homogenized in 1 ml of TRIzol Reagent (Life Technologies) using a mechanical homogenizer. RNA separation and isolation were performed using chloroform and isopropanol (both from Sigma), respectively, according to manufacturer's instructions (Life Technologies). cDNA synthesis and qPCR were performed as described above.

Cytokine detection: Quantitative mRNA analysis for inflammatory gene expression was conducted after RNA isolation from the spleens of untreated and CPT-treated mice 90 min after LPS injection.

To determine the cytokine concentration during the treatment, 50 μl of blood was collected retro-orbitally 4 hours after LPS injection. Serum and plasma were separated after centrifugation at 10,000 rpm for 10 min. Quantitative determination of GM-CSF, IL-1β, IL-6, and TNF-α in mouse serum was performed using a Mouse Inflammatory Magnetic 4-Plex Panel (Novex Life Technology), according to the manufacturer's instructions. Data was acquired using a Luminex 100/200 plate reader.

Cell suspensions and ex vivo restimulation: Cell suspensions were obtained after cutting the organs into small pieces followed by 30 min incubation at 37°C in DMEM containing collagenase D (1 mg/ml; Roche) and DNase (20 μg/ml; Roche). Tissue suspensions were then filtered through a 70-μm cell strainer (BD Falcon), and red blood cells were lysed using 1 ml of RBC Lysis Buffer (Affymetrix eBioscience).

For surface staining, cells were suspended in PBS containing 2% FBS, anti-mouse CD16/32 (Biolegend) and 0.1% NaN_3. For intracellular staining, cells were fixed in Fixation/Permeabilization buffer (eBioscience) and stained in Perm/Wash buffer (eBioscience).

For antigen-specific restimulation, cells were resuspended in complete [i.e., supplemented with 10% FBS, penicillin (100 μg/ml), streptomycin (100 μg/ml), and 1 nM sodium pyruvate] DMEM (Sigma) and restimulated with 100 nM peptide ASNENMETM derived from viral A/PR8/34 nucleoprotein (NP, 366 to 374 amino acids) (MBL) in the presence of Brefeldin A (Biolegend), and incubated for 6 hours at 37°C.

All antibodies were purchased from Biolegend: anti-mouse CD45 (clone 30-F11), CD11c (N418), CD11b (M1/70), Ly6C (HK 4.1), CD69 (H1.2F3), MHC-II (M5/114.15.2), CD8β (Ly-3), CD44 (IM7), CD3ε (17A2), CD45 (30-F11), TNF-α (MΠ6-XT22), IFN-γ (XMG1.2). Dead cells were discriminated using the Zombie Aqua Fixable Viability Kit (Biolegend), referred to as Life/Death dye.

Acquisition of stained cells was made with a BD LSRII flow cytometer (BD Bioscience); data were analyzed with FlowJo software (Treestar).

Antibodies and immunoblotting

Antibodies used were as follows: anti–β-actin (3700; Cell Signaling); anti-TOP2A (ab52934; Abcam), anti-TOP2B (ab58442; Abcam), anti-TOP1 (A302-589A; Bethyl), anti-FLAG-HRP (A8592; Sigma). Gradient gels were used according to the molecular weight of the proteins to be evaluated, followed by wet transfer on polyvinylidene fluoride membranes.

ChIP

The following antibodies were used: anti-RNAPII (clone 8WG16; Covance/BioLegend), anti–topoisomerase I (TOP1) (rabbit polyclonal anti-human IgG; Bethyl Laboratories; rabbit polyclonal anti-human/mouse serum; Abcam), anti–histone H3 (rabbit polyclonal IgG; Abcam), anti–TATA binding protein (rabbit polyclonal antiserum; Abcam), and anti–histone H4ac (rabbit polyclonal anti-human/mouse serum; Active Motif).

Downloaded from http://science.sciencemag.org/ on May 26, 2016

ChIP experiments were conducted as described (55). For experiments with ChIP followed by qPCR, cross-linking was performed for 10 min. For sonication, we used a refrigerated Bioruptor (Diagenode), which we optimized to generate DNA fragments of approximately 200 to 1000 base pairs (bp). Lysates were precleared for 3 hours using the appropriate isotype-matched control antibody (rabbit IgG; Cell Signaling) or anti-mouse IgG (Cell Signaling). The specific antibodies were coupled with magnetic paramagnetic beads (Dynabeads M-280 sheep anti-mouse IgG; ThermoFisher Scientific) bound to anti-mouse IgG or anti-rabbit IgG for 6 hours. Antibody-bound beads and chromatin were then immune-precipitated overnight at 4°C with rotation. After washing, reverse crosslinking was carried out overnight at 65°C. After digestion with RNase and proteinase K (Roche), DNA was isolated with a MinElute kit (Qiagen) and used for downstream applications. The statistical significance of ChIP qPCR analysis was determined with a two-tailed Student's paired *t* test.

ChIP-seq sample preparation and sequencing

After sonication (Bioruptor Pico, Diagenode), input and IP samples were analyzed on an Agilent Bioanalyzer (DNA High Sensitivity kit) to confirm that the fragment distributions were within the expected size range. Sheared Input and ChIP DNA samples were then end-repaired using NEBNext End Repair Module (New England BioLabs) and cleaned up using 1.5× AMPure XP beads (Beckman Coulter) according to the manufacturer's instructions, except for the final elution step, which we omitted. Next, A-tailing was done on beads using the NEBNext dA-Tailing Module (New England BioLabs), followed by addition of 20% polyethylene glycol (PEG)/NaCl in a 1.5× ratio to AMPure XP bead cleanup, again omitting the final elution step. Adaptor ligation was performed using the NEBNext Quick Ligation Module (New England BioLabs) and 80 μM DNA Multiplex Adaptor. Then, 20% PEG/NaCl was added in a 1.5× ratio followed by the AMPure XP cleanup. Samples were then eluted from beads and split into two aliquots. Each aliquot was amplified for 28 cycles using KAPA HiFi HotStart ReadyMix PCR Kit (Kapa Biosystems), 25 μM PE forward primer, and 25 μM indexed reverse primer. PCR reactions were cleaned using 1.5× of the AMPure XP beads according to the manufacturer's protocol and selected on the basis of fragments with a size of 250 to 500 nucleotides on the BluePippin platform using 2% M1 Marker gels. Size selected libraries were cleaned using 1.8× of the AMPure XP beads and sequenced on the HiSEq 2500 platform in a 100-nucleotide single-end read format.

Adapters used for ligation: Adapter1, 5′ P-GATCGGAAGAGCACACGTCT; Adapter2, 5′ AC-ACTCTTTCCCTACACGACGCTCTTCCGATC*T (* = phosphorothioate).

Barcode PCR primers: 5′AATGATACGGCGA-CCACCGAGATCTACACTCTTTCCCTACACGAC-GCTCTTCCGATC*T, 5′CAAGCAGAAGACGGC-ATACGAGAT[NNNNNN]GTGACTGGAGTTCA-GACGTGTGCTCTTCCGATC*T (where N corresponds to the barcode sequences used).

ChIP-seq data processing

ChIP-seq reads were trimmed for adapter sequences using "cutadapt." Reads were then filtered using "sickle" with a minimum quality threshold of 20 and retaining only sequences containing at least 20 bases. QC-filtered reads were then aligned against the human reference genome (GRCh37) using STAR, selecting only nonambiguous alignments and allowing up to five mismatches for each alignment. The resulting BAM files were processed using the R package "Pasha" with default parameters in order to exclude artifactual enrichments, estimate fragments elongation, and prepare genome-wide read coverage tracks in variable-step WIG format. WIG scores were finally rescaled for each sample by dividing all values by the average genome wide enrichment value.

Average profile computation: The average read coverage for selected genes was calculated across the annotated gene regions, including 2-kb flanking regions. For each gene, coverage in flanking regions was sampled across 167 equally spaced bins, and the resulting values were averaged across the upstream and downstream regions of all selected genes. Coverage across the annotated region of each gene was calculated in 666 equally spaced bins within the annotated start and end coordinates, and the resulting vectors were averaged across all genes and combined with the gene-flanking regions to create a composite average profile of 1000 points, covering selected annotations and 2 kb of each flanking region. All average profiles were normalized based on the average ChIP signal across the third quartile (i.e., last 50 to 75%) of the gene body of active genes [previously identified by Gro-seq profiling (56)], to account for differences in ChIP efficiency between experiments.

Chemical synthesis of TPT-A

An alkyne group was introduced to the 10-hydroxyl group of TPT through a Mitsunobu reaction (57), as the 10-hydroxyl of TPT does not contribute to the binding between human topoisomerase I covalently joined to double-stranded DNA and TPT [according to the reported x-ray crystal structure (58)]. TPT hydrochloride was dissolved in distilled water and further neutralized by adding (dropwise) a saturated solution of sodium bicarbonate ($NaHCO_3$) until the pH reached 9 to 10. Hydrochloride-free TPT was extracted from this solution by washing the aqueous phase with dichloromethane (DCM) three times, combining the organic phase, drying it by incubation with sodium sulfate (Na_2SO_4) for 1 hour, and finally evaporating DCM under reduced pressure. The TPT was then fully dissolved together with 5 equiv of triphenylphospine (Ph_3P) and 5 equiv of propargyl alcohol in a small volume of anhydrous tetrahydrofuran (THF). Five equiv of diethyl azodicarboxylate (DEAD) was then added dropwise into the solution. The reaction was monitored using thin-layer chromatography (TLC). The reaction time was 2 hours at room temperature. The solvents were removed by using a rotary evaporator (Rotovap). The product was purified by applying preparative HPLC with a gradient elution consisting of methanol (MeOH) and H_2O. Purity was ≥ 95%, and the rude yield was 74%. ^{1}HNMR (MeOH-d_6, 600 MHz): δ 8.95 (1H, s), 8.43 (1H, d, J = 9.5 Hz), 8.02 (1H, d, J = 9.5 Hz), 7.68 (1H, s), 5.61 (1H, d, J = 16.2 Hz), 5.43 (1H, d, J = 16.2 Hz), 5.39 (2H, s), 5.20 (2H, d, J = 2.1 Hz), 4.18 (2H, s), 3.31 (1H, s), 3.03 (6H, s), 1.99 (2H, m), 1.04 (3H, t, J = 7.3 Hz). Calculated values for $C_{26}H_{26}N_3O_5$, $[M+H]^+$, and $C_{52}H_{51}N_6O_{10}$, $[2M+H]^+$, were 460.1871 and 919.3667, respectively; 460.2103 and 919.3643 were found in HRMS (59). All chemical reagents and solvents were commercially purchased from Sigma-Aldrich.

Chem-ChIP

A549 cells (10^8 cells per condition) were pretreated for 1 hour with 100 nM TPT-A or DMSO, infected with influenza PR8ΔNS1 virus, and, at 1 hour after infection, treated again with TPT-A or DMSO. Cells were collected 6 hours after infection and treated as described above for the ChIP procedure. Sonicated DNA fragments for each condition were separated into 500-μl aliquots. The following reagents were added sequentially with vortexing after each addition: 11.3 μl of 5 mM biotin-azide (final concentration: 100 μM), 11.3 μl of 50 mM tris(2-carboxyethyl) phosphine (TCEP, final concentration: 1 mM), 34 μl of 1.7 mM tris(benzyltriazolylmethyl) amine (TBTA, final concentration: 100 μM), and 11.3 μl of 50 mM copper(II) sulfate pentahydrate ($CuSO_4{\cdot}5H_2O$, final concentration: 1 mM). These mixtures were then incubated at room temperature for 1 hour, with vortexing after the first 30 min. Chromatin aliquots were combined and centrifuged for 5 min at 6500*g* at 4°C. The supernatant was then removed for downstream immunoprecipitation. ChIP qPCR was performed as described above. The statistical significance of ChIP qPCR analysis was determined with a two-tailed Student's paired *t* test.

Stranded RNA sequencing and data analysis

RNA (1 μg) was treated using the Ribo-Zero Gold rRNA Removal Kit (Human/Mouse/Rat, Illumina), and purified post-depletion with 1.6× ratio of AMPureXP beads. Directional RNA libraries were prepared using NEBNext Ultra Directional RNA library prep kit for Illumina (New England BioLabs), according to manufacturer's instructions. Fragment size distribution and concentration of the PCR-amplified libraries were assessed using the Qubit and the Agilent Bioanalyzer. Finally, samples were sequenced on the HiSEq 2500 platform in a 100-bp single-end read format.

After adapter removal with cutadapt and base quality trimming to remove 3′ ends if more than 20 bases with Q < 20 were present, reads were mapped to the human (hg19) and

Downloaded from http://science.sciencemag.org/ on May 26, 2016

Ebola virus (H.sapiens-tc/COD/1976/Yambuku-Mayinga, NC_002549) reference genomes using STAR (*60*), and gene and transcript count summaries were generated using Featurecounts (*61*). Read counts were then combined into a numeric matrix, with genes in rows and experiments in columns, and used as input for differential gene expression analysis with the Bioconductor edgeR package (*62*). Normalization factors were computed using the weighted trimmed mean of M-values (TMM), and dispersions (common, trended, and tagwise) were estimated before fitting a negative binomial general linearized model that accounted for experimental conditions with two biological replicates each. Finally, a likelihood ratio test was carried against selected contrasts. *P* values were corrected for multiple testing using the Benjamin-Hochberg (BH) method and used to select genes with significant expression differences ($q < 0.05$).

Proteomic analysis

A549 cells were treated with CPT or DMSO and infected with the influenza PR8ΔNS1 virus as described above, collected 6 hours after infection, washed three times with PBS [including protease inhibitors (Roche)], then frozen as cell pellets. These pellets were sent to Bioproximity LLC, where global proteomic profiling was acquired using ultraperformance liquid chromatography and tandem mass spectrometry.

For the analysis of mass spectrometry "hits," initial thresholds were calculated in duplicate experiments for protein abundances in both DMSO- and CPT-treated uninfected cells. Next, protein abundances were calculated in the respective infected conditions and normalized using noninfected abundances. We considered upregulated hits as having a normalized unique protein score above 5 in the DMSO-treated, infected cells. The statistical comparison between normalized infected identifications was determined with a two-tailed Student's *t* test under the assumption of equal variances between groups.

Transcription factor promoter enrichment analysis

Identification of transcription factors (TFs) regulating the genes affected by Top1 depletion was performed using a computational method that overlaps the genomic coordinates of a set of gene promoters with a large library of TF-genome interactions. We created the ChIP-seq library by compiling 1630 human ChIP-seq data sets from a variety of sources, including ENCODE (*63*), Cistrome (*64*), PAZAR (*65*), and Re-Map (*66*). As input, we took a set of genomic regions of interest (e.g., promoters of genes whose expression changes upon silencing of Top1) that we systematically overlapped with each ChIP-seq data set, and we counted the number of input regions overlapped by at least one base.

Next, a *P* value describing the significance of this overlap was estimated using a simulation-based procedure: A distribution of expected overlap values was created from 1000 iterations of randomly choosing RefSeq gene promoters with the same length as the input set (as an example, for 50 promoters of length 100 bp as input, 50 randomly chosen promoters of length 100 bp were used in each simulation). The distribution of the expected overlap values from the randomized data resembled a normal distribution and was used to generate a Z-score and *P* value estimating the significance of the observed number of input regions that overlapped each ChIP-seq data set. We obtained a ranked list of TFs, based on experimentally-determined binding sites located in the promoters of each gene set. We applied this procedure to each input gene list using three different promoter definitions, (−100, +1), (−1000, +1), and (−10,000, +1), relative to the transcription start site. Results were similar regardless of promoter length (table S3). We further annotated the results with TF binding site motif enrichment scores (using the same promoter definitions). For this, we used the HOMER motif enrichment algorithm (*67*) and a large library of human position weight matrices obtained from the CisBP database (*68*).

Mapping

ChIP-seq data from this study and publicly available data from ENCODE for DNase-seq (GSE26328) and histone H3 Lys^{27} acetylation (H3K27ac; GSE29611) in A549 cells were aligned to the human genome (hg19/GRCh37) using Bowtie2 with default parameters (*69*). Only reads that mapped to unique genomic positions were considered for downstream analysis. Normalized promoter ChIP-seq read densities were calculated using HOMER (http://homer.salk.edu) by counting the total number of reads per 10^7 aligned reads from each experiment found from −500 to +500 bp relative to the representative RefSeq defined transcription start site (TSS) for each gene (*67*). META gene plots were compiled by calculating ChIP-seq read densities along RefSeq gene bodies (>3 kb in length) using HOMER. CpG Island promoters were defined by RefSeq TSS found within 200 bp of an annotated CpG Island (*70*). IFN-stimulated response elements (ISREs) containing promoters were defined by searching for ISRE motifs from −500 to +100 relative to the TSS using HOMER.

REFERENCES AND NOTES

1. C. A. Janeway Jr., R. Medzhitov, Innate immune recognition. *Annu. Rev. Immunol.* **20**, 197–216 (2002). doi: 10.1146/annurev.immunol.20.083001.084359; pmid: 11861602
2. R. Medzhitov, Approaching the asymptote: 20 years later. *Immunity* **30**, 766–775 (2009). doi: 10.1016/j.immuni.2009.06.004; pmid: 19538928
3. B. Beutler *et al*., Genetic analysis of resistance to viral infection. *Nat. Rev. Immunol.* **7**, 753–766 (2007). doi: 10.1038/nri2174; pmid: 17893693
4. J. W. Schoggins *et al*., A diverse range of gene products are effectors of the type I interferon antiviral response. *Nature* **472**, 481–485 (2011). doi: 10.1038/nature09907; pmid: 21478870
5. Y. J. Crow, Type I interferonopathies: Mendelian type I interferon up-regulation. *Curr. Opin. Immunol.* **32**, 7–12 (2015). doi: 10.1016/j.coi.2014.10.005; pmid: 25463593
6. T. Hanada, A. Yoshimura, Regulation of cytokine signaling and inflammation. *Cytokine Growth Factor Rev.* **13**, 413–421 (2002). doi: 10.1016/S1359-6101(02)00026-6; pmid: 12220554
7. F. McNab, K. Mayer-Barber, A. Sher, A. Wack, A. O'Garra, Type I interferons in infectious disease. *Nat. Rev. Immunol.* **15**, 87–103 (2015). doi: 10.1038/nri3787; pmid: 25614319
8. M. Brandes, F. Klauschen, S. Kuchen, R. N. Germain, A systems analysis identifies a feedforward inflammatory circuit leading to lethal influenza infection. *Cell* **154**, 197–212 (2013). doi: 10.1016/j.cell.2013.06.013; pmid: 23827683
9. Y. M. Loo, M. Gale Jr., Influenza: Fatal immunity and the 1918 virus. *Nature* **445**, 267–268 (2007). doi: 10.1038/445267a; pmid: 17230179
10. P. A. Ward, New approaches to the study of sepsis. *EMBO Mol. Med.* **4**, 1234–1243 (2012). doi: 10.1002/emmm.201201375; pmid: 23208733
11. L. Strähle, D. Garcin, P. Le Mercier, J. F. Schlaak, D. Kolakofsky, Sendai virus targets inflammatory responses, as well as the interferon-induced antiviral state, in a multifaceted manner. *J. Virol.* **77**, 7903–7913 (2003). doi: 10.1128/JVI.77.14.7903-7913.2003; pmid: 12829830
12. G. L. Beretta, L. Gatti, P. Perego, N. Zaffaroni, Camptothecin resistance in cancer: Insights into the molecular mechanisms of a DNA-damaging drug. *Curr. Med. Chem.* **20**, 1541–1565 (2013). doi: 10.2174/0929867311320120006; pmid: 23432590
13. Y. Chen *et al*., Cordycepin induces apoptosis of C6 glioma cells through the adenosine 2A receptor-p53-caspase-7-PARP pathway. *Chem. Biol. Interact.* **216**, 17–25 (2014). doi: 10.1016/j.cbi.2014.03.010; pmid: 24704558
14. S. Kubicek *et al*., Reversal of H3K9me2 by a small-molecule inhibitor for the G9a histone methyltransferase. *Mol. Cell* **25**, 473–481 (2007). doi: 10.1016/j.molcel.2007.01.017; pmid: 17289593
15. I. Kubo, T. J. Ha, K. Shimizu, Lipoxygenase inhibitory activity of 6-pentadecanylsalicylic acid without prooxidant effect. *Nat. Prod. Commun.* **5**, 85–90 (2010). pmid: 20184028
16. S. Menazza *et al*., Oxidative stress by monoamine oxidases is causally involved in myofiber damage in muscular dystrophy. *Hum. Mol. Genet.* **19**, 4207–4215 (2010). doi: 10.1093/hmg/ddq339; pmid: 20716577
17. P. B. Rahl *et al*., c-Myc regulates transcriptional pause release. *Cell* **141**, 432–445 (2010). doi: 10.1016/j.cell.2010.03.030; pmid: 20434984
18. K. M. Regal, S. L. Mercer, J. E. Deweese, HU-331 is a catalytic inhibitor of topoisomerase IIα. *Chem. Res. Toxicol.* **27**, 2044–2051 (2014). doi: 10.1021/tx500245m; pmid: 25409338
19. N. A. Smith, J. A. Byl, S. L. Mercer, J. E. Deweese, N. Osheroff, Etoposide quinone is a covalent poison of human topoisomerase IIβ. *Biochemistry* **53**, 3229–3236 (2014). doi: 10.1021/bi500421q; pmid: 24766193
20. Q. Zhou, T. Li, D. H. Price, RNA polymerase II elongation control. *Annu. Rev. Biochem.* **81**, 119–143 (2012). doi: 10.1146/annurev-biochem-052610-095910; pmid: 22404626
21. P. Filippakopoulos, S. Knapp, Targeting bromodomains: Epigenetic readers of lysine acetylation. *Nat. Rev. Drug Discov.* **13**, 337–356 (2014). doi: 10.1038/nrd4286; pmid: 24751816
22. Y. Pommier, Topoisomerase I inhibitors: Camptothecins and beyond. *Nat. Rev. Cancer* **6**, 789–802 (2006). doi: 10.1038/nrc1977; pmid: 16990856
23. E. Nicodeme *et al*., Suppression of inflammation by a synthetic histone mimic. *Nature* **468**, 1119–1123 (2010). doi: 10.1038/nature09589; pmid: 21068722
24. P. Filippakopoulos *et al*., Selective inhibition of BET bromodomains. *Nature* **468**, 1067–1073 (2010). doi: 10.1038/nature09504; pmid: 20871596
25. G. Egger, G. Liang, A. Aparicio, P. A. Jones, Epigenetics in human disease and prospects for epigenetic therapy. *Nature* **429**, 457–463 (2004). doi: 10.1038/nature02625; pmid: 15164071
26. K. T. Atherton, D. C. Burke, Interferon induction by viruses and polynucleotides: A differential effect of comptothecin. *J. Gen. Virol.* **29**, 297–304 (1975). doi: 10.1099/0022-1317-29-3-297; pmid: 1239490
27. K. T. Atherton, D. C. Burke, The effects of some differential metabolic inhibitors on interferon superinduction. *J. Gen. Virol.* **41**, 2 (1975).
28. W. F. Chiou, C. J. Chou, C. F. Chen, Camptothecin suppresses nitric oxide biosynthesis in RAW 264.7 macrophages. *Life Sci.* **69**, 625–635 (2001). doi: 10.1016/S0024-3205(01)01154-7; pmid: 11476184
29. I. F. King *et al*., Topoisomerases facilitate transcription of long genes linked to autism. *Nature* **501**, 58–62 (2013). doi: 10.1038/nature12504; pmid: 23995680
30. S. Solier *et al*., Transcription poisoning by Topoisomerase I is controlled by gene length, splice sites, and miR-142-3p. *Cancer*

Downloaded from http://science.sciencemag.org/ on May 26, 2016

Res. **73**, 4830–4839 (2013). doi: 10.1158/0008-5472.CAN-12-3504; pmid: 23786772
31. F. Kouzine *et al*., Transcription-dependent dynamic supercoiling is a short-range genomic force. *Nat. Struct. Mol. Biol.* **20**, 396–403 (2013). doi: 10.1038/nsmb.2517; pmid: 23416947
32. M. Kretzschmar, M. Meisterernst, R. G. Roeder, Identification of human DNA topoisomerase I as a cofactor for activator-dependent transcription by RNA polymerase II. *Proc. Natl. Acad. Sci. U.S.A.* **90**, 11508–11512 (1993). doi: 10.1073/pnas.90.24.11508; pmid: 8265582
33. A. Merino, K. R. Madden, W. S. Lane, J. J. Champoux, D. Reinberg, DNA topoisomerase I is involved in both repression and activation of transcription. *Nature* **365**, 227–232 (1993). doi: 10.1038/365227a0; pmid: 8396729
34. K. W. Kohn, Y. Pommier, Molecular and biological determinants of the cytotoxic actions of camptothecins. Perspective for the development of new topoisomerase I inhibitors. *Ann. N.Y. Acad. Sci.* **922**, 11–26 (2000). doi: 10.1111/j.1749-6632.2000.tb07021.x; pmid: 11193886
35. S. Höing *et al*., Discovery of inhibitors of microglial neurotoxicity acthing thorugh multiple mechanisms using a stem-cell-based phenotypic assay. *Cell Stem Cell* **11**, 620–632 (2012). doi: 10.1016/j.stem.2012.07.005; pmid: 22770236
36. R. Madabhushi *et al*., Activity-induced DNA breaks govern the expression of neuronal early-reponse genes. *Cell* **161**, 1592–1605 (2015). doi: 10.1016/j.cell.2015.05.032; pmid: 26052046
37. L. Anders *et al*., Genome-wide localization of small molecules. *Nat. Biotechnol.* **32**, 92–96 (2014). doi: 10.1038/nbt.2776; pmid: 24336317
38. S. S. Teves, S. Henikoff, Transcription-generated torsional stress destabilizes nucleosomes. *Nat. Struct. Mol. Biol.* **21**, 88–94 (2014). doi: 10.1038/nsmb.2723; pmid: 24317489
39. V. R. Ramirez-Carrozzi *et al*., Selective and antagonistic functions of SWI/SNF and Mi-2β nucleosome remodeling complexes during an inflammatory response. *Genes Dev.* **20**, 282–296 (2006). doi: 10.1101/gad.1383206; pmid: 16452502
40. V. R. Ramirez-Carrozzi *et al*., A unifying model for the selective regulation of inducible transcription by CpG islands and nucleosome remodeling. *Cell* **138**, 114–128 (2009). doi: 10.1016/j.cell.2009.04.020; pmid: 19596239
41. D. C. Hargreaves, T. Horng, R. Medzhitov, Control of inducible gene expression by signal-dependent transcriptional elongation. *Cell* **138**, 129–145 (2009). doi: 10.1016/j.cell.2009.05.047; pmid: 19596240
42. S. T. Smale, G. Natoli, Transcriptional control of inflammatory responses. *Cold Spring Harb. Perspect. Biol.* **6**, a016261 (2014). doi: 10.1101/cshperspect.a016261; pmid: 25213094
43. S. Akira, S. Uematsu, O. Takeuchi, Pathogen recognition and innate immunity. *Cell* **124**, 783–801 (2006). doi: 10.1016/j.cell.2006.02.015; pmid: 16497588
44. H. K. Kim, D. Missiakas, O. Schneewind, Mouse models for infectious diseases caused by *Staphylococcus aureus*. *J. Immunol. Methods* **410**, 88–99 (2014). doi: 10.1016/j.jim.2014.04.007
45. J. A. McCullers *et al*., Influenza enhances susceptibility to natural acquisition of and disease due to *Streptococcus pneumoniae* in ferrets. *J. Infect. Dis.* **202**, 1287–1295 (2010). doi: 10.1086/656333; pmid: 20822454
46. G. Sass, K. Koerber, R. Bang, H. Guehring, G. Tiegs, Inducible nitric oxide synthase is critical for immune-mediated liver injury in mice. *J. Clin. Invest.* **107**, 439–447 (2001). doi: 10.1172/JCI10613; pmid: 11181643
47. M. Bray, S. Mahanty, Ebola hemorrhagic fever and septic shock. *J. Infect. Dis.* **188**, 1613–1617 (2003). doi: 10.1086/379727; pmid: 14639530
48. L. Martínez-Gil *et al*., Identification of small molecules with type I interferon inducing properties by high-throughput screening. *PLOS ONE* **7**, e49049 (2012). doi: 10.1371/journal.pone.0049049; pmid: 23145065
49. A. Baum, R. Sachidanandam, A. García-Sastre, Preference of RIG-I for short viral RNA molecules in infected cells revealed by next-generation sequencing. *Proc. Natl. Acad. Sci. U.S.A.* **107**, 16303–16308 (2010). doi: 10.1073/pnas.1005077107; pmid: 20805493
50. L. Martínez-Sobrido *et al*., Hemagglutinin-pseudotyped green fluorescent protein-expressing influenza viruses for the detection of influenza virus neutralizing antibodies. *J. Virol.* **84**, 2157–2163 (2010). doi: 10.1128/JVI.01433-09; pmid: 19939917
51. L. Martínez-Gil *et al*., A Sendai virus-derived RNA agonist of RIG-I as a virus vaccine adjuvant. *J. Virol.* **87**, 1290–1300 (2013). doi: 10.1128/JVI.02338-12; pmid: 23175362
52. C. F. Basler *et al*., The Ebola virus VP35 protein functions as a type I IFN antagonist. *Proc. Natl. Acad. Sci. U.S.A.* **97**, 12289–12294 (2000). doi: 10.1073/pnas.220398297; pmid: 11027311
53. W. Huang, B. T. Sherman, R. A. Lempicki, Systematic and integrative analysis of large gene lists using DAVID bioinformatics resources. *Nat. Protoc.* **4**, 44–57 (2009). doi: 10.1038/nprot.2008.211; pmid: 19131956
54. W. Huang, B. T. Sherman, R. A. Lempicki, Bioinformatics enrichment tools: Paths toward the comprehensive functional analysis of large gene lists. *Nucleic Acids Res.* **37**, 1–13 (2009). doi: 10.1093/nar/gkn923; pmid: 19033363
55. T. I. Lee, S. E. Johnstone, R. A. Young, Chromatin immunoprecipitation and microarray-based analysis of protein location. *Nat. Protoc.* **1**, 729–748 (2006). doi: 10.1038/nprot.2006.98; pmid: 17406303
56. M. S. Miller *et al*., Senataxin suppresses the antiviral transcriptional response and controls viral biogenesis. *Nat. Immunol.* **16**, 485–494 (2015). doi: 10.1038/ni.3132; pmid: 25822250
57. K. C. Swamy, N. N. Kumar, E. Balaraman, K. V. Kumar, Mitsunobu and related reactions: Advances and applications. *Chem. Rev.* **109**, 2551–2651 (2009). doi: 10.1021/cr800278z; pmid: 19382806
58. B. L. Staker *et al*., The mechanism of topoisomerase I poisoning by a camptothecin analog. *Proc. Natl. Acad. Sci. U.S.A.* **99**, 15387–15392 (2002). doi: 10.1073/pnas.242259599; pmid: 12426403
59. K. Hyz *et al*., Topotecan dynamics, tautomerism and reactivity—$^{1}H/^{13}C$ NMR and ESI MS study. *Magn. Reson. Chem.* **48**, 575–584 (2010). pmid: 20623719
60. A. Dobin *et al*., STAR: Ultrafast universal RNA-seq aligner. *Bioinformatics* **29**, 15–21 (2013). doi: 10.1093/bioinformatics/bts635; pmid: 23104886
61. Y. Liao, G. K. Smyth, W. Shi, featureCounts: An efficient general purpose program for assigning sequence reads to genomic features. *Bioinformatics* **30**, 923–930 (2014). doi: 10.1093/bioinformatics/btt656; pmid: 24227677
62. M. D. Robinson, D. J. McCarthy, G. K. Smyth, edgeR: A Bioconductor package for differential expression analysis of digital gene expression data. *Bioinformatics* **26**, 139–140 (2010). doi: 10.1093/bioinformatics/btp616; pmid: 19910308
63. ENCODE Project Consortium, An integrated encyclopedia of DNA elements in the human genome. *Nature* **489**, 57–74 (2012). pmid: 22955616
64. T. Liu *et al*., Cistrome: An integrative platform for transcriptional regulation studies. *Genome Biol.* **12**, R83 (2011). doi: 10.1186/gb-2011-12-8-r83; pmid: 21859476
65. E. Portales-Casamar *et al*., The PAZAR database of gene regulatory information coupled to the ORCA toolkit for the study of regulatory sequences. *Nucleic Acids Res.* **37**, D54–D60 (2009). doi: 10.1093/nar/gkn783; pmid: 18971253
66. A. Griffon *et al*., Integrative analysis of public ChIP-seq experiments reveals a complex multi-cell regulatory landscape. *Nucleic Acids Res.* **43**, e27 (2015). doi: 10.1093/nar/gku1280; pmid: 25477382
67. S. Heinz *et al*., Simple combinations of lineage-determining transcription factors prime cis-regulatory elements required for macrophage and B cell identities. *Mol. Cell* **38**, 576–589 (2010). doi: 10.1016/j.molcel.2010.05.004; pmid: 20513432
68. M. T. Weirauch *et al*., Determination and inference of eukaryotic transcription factor sequence specificity. *Cell* **158**, 1431–1443 (2014). doi: 10.1016/j.cell.2014.08.009; pmid: 25215497
69. B. Langmead, S. L. Salzberg, Fast gapped-read alignment with Bowtie 2. *Nat. Methods* **9**, 357–359 (2012). doi: 10.1038/nmeth.1923; pmid: 22388286
70. M. Gardiner-Garden, M. Frommer, CpG islands in vertebrate genomes. *J. Mol. Biol.* **196**, 261–282 (1987). doi: 10.1016/0022-2836(87)90689-9; pmid: 3656447

ACKNOWLEDGMENTS

We thank P. Palese for the FF-luciferase construct, chromatized cells, and Sendai virus; F. Kramer for the H3N2 virus; R. Cadagan for help with virus propagations; T. Kraus for use of the Luminex 100/200 plate reader; M. Schotsaert for help with co-infection experiments; S. Tripathi for providing IRF3 dependency data; the genomics facility at Icahn School of Medicine at Mount Sinai; Bioproximity LLC for proteomics work; J. K. Gregory for help with computer graphics; and H. Nakano for discussion about the history of Top1 inhibitors. I. Marazzi and M. Byun designed the graphical abstract illustration of the "the Vitruvian automaton"; the illustration is our homage to Marcus Vitruvius Pollio, Leonardo da Vinci, and the history of automata. The data presented in this manuscript are tabulated in the main paper and in the supplementary materials. Sequencing data are available in GEO, GSE80132, and linked superseries. Supported by HHSN272201400008C—Center for Research on Influenza Pathogenesis (CRIP), a Center of Excellence for Influenza Research and Surveillance (CEIRS) funded by the National Institute of Allergy and Infectious Diseases (A.G.-S., G.M., H.v.B., and I.M.); Public Health Service Institutional Research Training Award AI07647 (A.R.); Department of Defense grant W911NF-14-1-0353 (I.M.); NIH grants U19AI106754 (I.M. and A.G.-S.), 1R01AN3663134 (I.M. and H.v.B.), U19AI109945 (A.B. and C. Basler), U19AI109664 (A.B. and C. Basler), and 1R56AI114770-01A1 (I.M.); and the computational resources and staff of the Department of Scientific Computing at the Icahn School of Medicine at Mount Sinai. A patent application (62/267,608) was filed by Mount Sinai related to treatment of inflammatory diseases with Top1 inhibitors.

SUPPLEMENTARY MATERIALS

www.sciencemag.org/content/352/6289/aad7993/suppl/DC1
Figs. S1 to S15
Tables S1 to S4

3 November 2015; accepted 6 April 2016
Published online 28 April 2016
10.1126/science.aad7993

Downloaded from http://science.sciencemag.org/ on May 26, 2016

REPORTS

MARTIAN CLIMATE

An ice age recorded in the polar deposits of Mars

Isaac B. Smith,[1]*† Nathaniel E. Putzig,[1]† John W. Holt,[2] Roger J. Phillips[3,4]

Layered ice deposits at the poles of Mars record a detailed history of accumulation and erosion related to climate processes. Radar investigations measure these layers and provide evidence for climate changes such as ice advance and retreat. We present a detailed analysis of observational data showing that ~87,000 cubic kilometers of ice have accumulated at the poles since the end of the last ice age ~370,000 years ago; this volume is equivalent to a global layer of ~60 centimeters. The majority of the material accumulated at the north pole. These results provide both a means to understand the accumulation history of the polar deposits as related to orbital Milankovitch cycles and constraints for better determination of Mars' past and future climates.

Mars undergoes oscillations in obliquity, perihelion, and eccentricity that strongly affect the planet's climate (*1*). This variability determines the amount of sunlight that reaches the surface and in turn the stability of ice at all latitudes, creating pronounced climate cycles as on Earth (*2*, *3*). Because of this high degree of activity, the north polar layered deposits (NPLD; Fig. 1) exchange substantial amounts of water with the mid-latitudes over the course of an obliquity cycle (*2*–*5*), sometimes leading to periods when Mars has abundant ice coverage over a wide range of latitudes. Unlike their terrestrial counterparts, these martian ice ages occur when the poles are warmer than average and water ice is more stable at lower latitudes, creating a widespread ground-ice "mantle" (*3*, *6*) and mid-latitude glaciers (*7*, *8*) at the same time as the polar caps retreat. During interglacial periods, the NPLD are expected to experience rapid accumulation at the expense of the mid-latitude deposits (*2*, *3*). The transitions between erosion and accumulation can leave behind unconformities, or stratigraphic sequences of truncated layers draped by continuous layers. These unconformities are observed at the surface by optical instruments (*9*–*11*) and in the subsurface by the Shallow Radar (*12*) (SHARAD) sounder onboard the Mars Reconnaissance Orbiter (*13*, *14*).

According to models of ice stability, the bulk of the NPLD, which extend to 2000 m in thickness (*15*), likely accumulated during the past ~4 million years (*1*, *2*, *4*). Most of that ice was deposited during periods without erosion, leaving continuous layers across the entire deposit (*15*, *16*). However, major unconformities are also present, and observable temporal and geographic variability in net accumulation has occurred (*13*, *14*, *17*). Obtaining age estimates for individual layers of the NPLD is an active area of research with no consensus on the best technique for determination (*17*, *18*). However, detailed stratigraphic analyses of the layers within the NPLD and south polar layered deposits (SPLD) benefit our understanding of the entire depositional system. In particular, SHARAD studies near topographic features such as the spiral troughs (*11*, *19*, *20*), Chasma Boreale (*13*), Abalos Mensa (*21*), and the basal unit (*22*) have concluded that wind was a major player in accumulation patterns of ice and dust.

Using techniques developed in previous studies (*14*, *16*) (see supplementary materials), we analyzed hundreds of radargrams [two-dimensional (2D) radar sounding profiles] of the NPLD and SPLD (fig. S1). In the north, we found cap-wide evidence for simultaneous changes in layer properties suggestive of a global shift in the climate. The most easily recognized change is a widespread, recent accumulation package (WRAP) that overlies previously eroded materials, creating an unconformity (turquoise lines in Fig. 2 and fig. S3). Immediately above the unconformity, reflectors are generally continuous [except where interrupted by troughs (*14*, *19*)] and are conformable to the erosion surface.

Also recorded at this level are changes in the slope of migration paths of features such as the spiral troughs and undulations. A migration path is a bounding surface that traces the relative horizontal and vertical position of a feature through time as seen in cross-sectional views (*19*, *20*) (dashed yellow and orange lines in Fig. 2). In many instances the migration paths increase in slope, abruptly reverse direction, or are completely buried. Previous work demonstrated that varying rates of accumulation, wind transport, and sublimation from insolation alter the migration paths of the spiral troughs (*20*); that is, the steepening of a migration path indicates a relative increase in accumulation rate. We found an increase in the slopes of migration paths at many locations along the WRAP unconformity (e.g., Fig. 2E). A more complex example includes two trough migration paths, each with an accompanying set of undulations (*11*) (Fig. 2B). Below the unconformity, both sets of undulations had migrated poleward during several hundred meters of accumulation. Above the unconformity, the

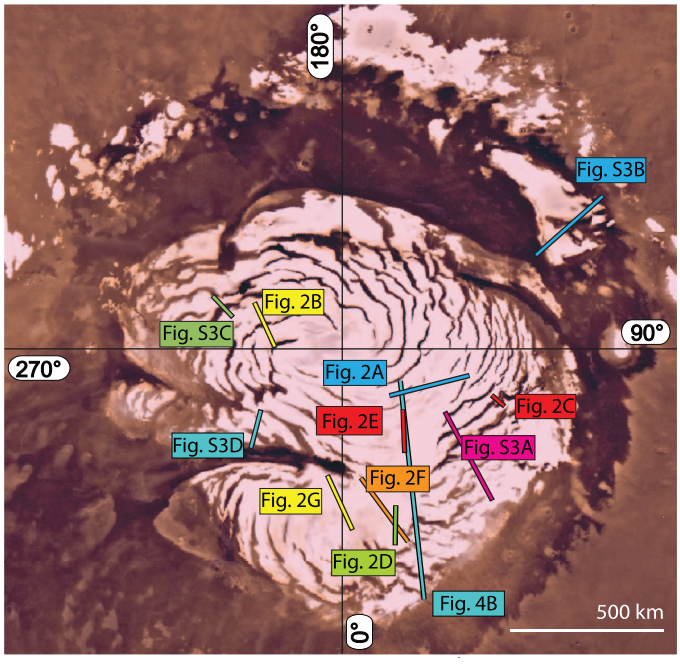


Fig. 1. Color mosaic of the north polar region from Viking Visual Imaging Subsystem data collected between 1976 and 1980 (*32*), including the north polar layered deposits (NPLD) and distal outliers. Ground-track footprints of radargrams in later figures are shown.

[1]Department of Space Studies, Southwest Research Institute, Boulder, CO 80302, USA. [2]University of Texas Institute for Geophysics, Jackson School of Geosciences, University of Texas, J. J. Pickle Research Campus, Austin, TX 78758, USA. [3]Planetary Science Division, Southwest Research Institute, Boulder, CO 80302, USA. [4]McDonnell Center for the Space Sciences and Department of Earth and Planetary Sciences, Washington University, St. Louis, MO 63130, USA.
*Corresponding author. Email: isaac@boulder.swri.edu
†Present address: Planetary Science Institute, Tucson, AZ 85719, USA.

Downloaded from http://science.sciencemag.org/ on May 26, 2016

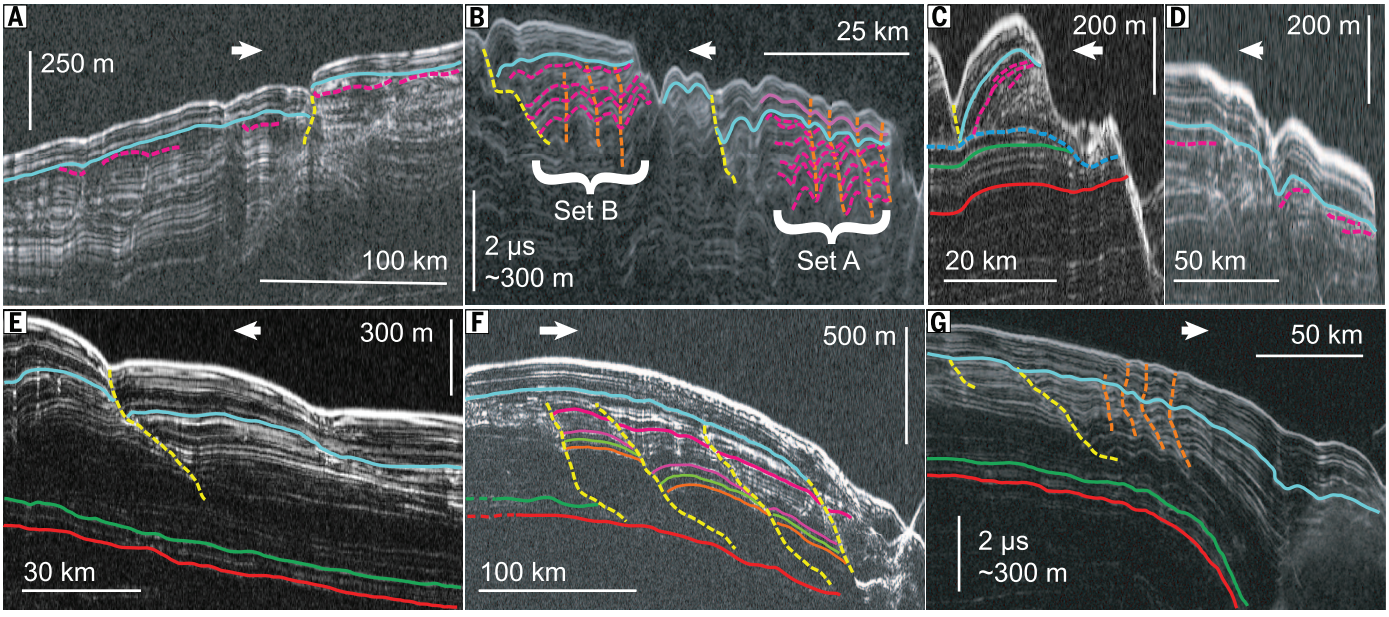


Fig. 2. SHARAD radargrams highlighting the widespread, recent accumulation package (WRAP). The WRAP unconformity (turquoise lines) is shown (**A**) within the uppermost 100 m of the NPLD, observation 1998901; (**B**) within the uppermost 90 m of the NPLD with changing properties of two sets of undulations, observation 2007101; (**C**) within the uppermost 80 m of the NPLD, observation 761602; (**D**) within the uppermost 150 m of the NPLD, observation 1247002; (**E**) with increased trough migration path slope in observation 598301; (**F**) above buried spiral troughs in Gemina Lingula, observation 725402; and (**G**) above buried spiral troughs and with reversing undulations, observation 2007101. Magenta lines, erosion and migration; yellow dashed lines, trough migration paths; orange dashed lines, undulation migration paths. Green and red reflectors are reflections 25 and 26 (R25 and R26) from (*14*), respectively. Arrows point north for each image. Ground track of each image is shown in Fig. 1. Uninterpreted radargrams are in fig. S2. Vertical exaggeration ranges between 50:1 and 150:1.

migration paths of the southernmost undulations (Fig. 2B, set A) reversed direction while maintaining approximately the same wavelength. The northern undulations (Fig. 2B, set B) were fully buried by subsequent deposition. Migration paths of undulations in Gemina Lingula also changed direction at this level (Fig. 2G), and troughs there are fully buried, leaving no detectable bounding surface with SHARAD and only minimal surface inflection (Fig. 2, F and G). Spiral troughs had previously been observed to persist continuously since their onset and often to grow in amplitude (*19*). Thus, the burial of several troughs across hundreds of kilometers represents a pronounced departure from previous climate conditions that sustained stable trough migration.

In locations where interpretations of 2D radar profiles are hindered by strong surface slopes that create interfering clutter, we analyzed data from a recently developed 3D data volume (*23*) that effectively removes such clutter to more completely map the WRAP. The 3D technique is especially powerful near 135°E at the NPLD, where clutter is abundant (*14*). With this new data set, we easily detected the WRAP as a capping unit in the uppermost hundreds of meters of the NPLD (fig. S5).

The spatial and stratigraphic distribution of the WRAP correlates with previous detections of an upper NPLD unit mapped using visible imagery of surface outcrops (*9*, *24*) in troughs (A_Bb_3 and "upper layered deposits" in those citations). Whereas those image-based mapping efforts were unable to determine the extent of and depth to the unconformity beyond the outcrops (estimating a maximum thickness of "tens of meters"), SHARAD provides the ability to trace layers through the areas between exposures at spiral troughs and accurately measure unit thicknesses.

The WRAP unconformity represents a single stratigraphic level, but subsequent regional net accumulation dictates the present depth to the unconformity. Near to the NPLD margin, where accumulation has been slower than in the interior, we find that the maximum depth to this unconformity ranges from 80 to 120 m. Closer to the center of the NPLD, where accumulation is greatest, the depth to the unconformity reaches 320 m, greater than estimates from surface observations by a factor of 10 (*9*). The average depth in areas where it exceeds 1 m is ~82 m (Fig. 3). The 1-m threshold was chosen to avoid extrapolations that extend beyond the NPLD margin as thin wedges. Additionally, we mapped basal SHARAD reflections in two thick, icy distal deposits (Fig. 3 and fig. S3B). Previous detailed geologic mapping from surface data determined that these outliers were likely deposited synchronously with the upper layers of the NPLD (*10*, *24*). Here, we measured the full extent and thickness of the deposits. Other distal deposits are widespread (topmost white regions in Fig. 3A), but they are too thin to measure with SHARAD.

We also measured recent accumulation above a shallow unconformity in the SPLD (Fig. 3B and fig. S4) and found it to be much less extensive than the WRAP in the north. The recent deposits on the SPLD are discontinuous (*25*), making it impossible to say with certainty that they accumulated simultaneously. However, the fresh appearance and lack of craters smaller than 200 m in these deposits led others to conclude that they are as young as 200,000 years (*26*). Therefore, we included them in our calculated volume of recent accumulation (Fig. 3B).

The volume of the recent north polar deposits (NPLD WRAP and outliers) is ~80,000 km^3, roughly equivalent to a global equivalent layer (GEL) of 55 cm (Fig. 3A). The SPLD recent deposits comprise 7000 km^3, contributing an additional 5 cm GEL, or 8% of the global ice flux during this period (Fig. 3B). The total contributed volume from both poles is ~87,000 km^3 or ~60 cm GEL, a sum that includes an interpolated region poleward of 87.4°N (where SHARAD cannot observe) but excludes the region poleward of 87.4°S.

Nominally, the burial of troughs and undulations by the WRAP could be attributed to a simple increase in accumulation rate, but the detection of reversing migration in some undulations tells a more complex story. Migrating undulations [niveo-aeolian antidunes (*14*, *27*)] arise in a very specific wind environment with Froude number between 0.9 and 1.2 (*20*), and a change in migration direction implies a change in Froude number. The Froude number is the ratio of the fluid speed to the speed of a gravity wave in the fluid and is determined to first order by the fluid thickness, density, and speed. From this relationship, we infer that the unconformity is the result of a shift in wind properties associated with climate change.

Downloaded from http://science.sciencemag.org/ on May 26, 2016

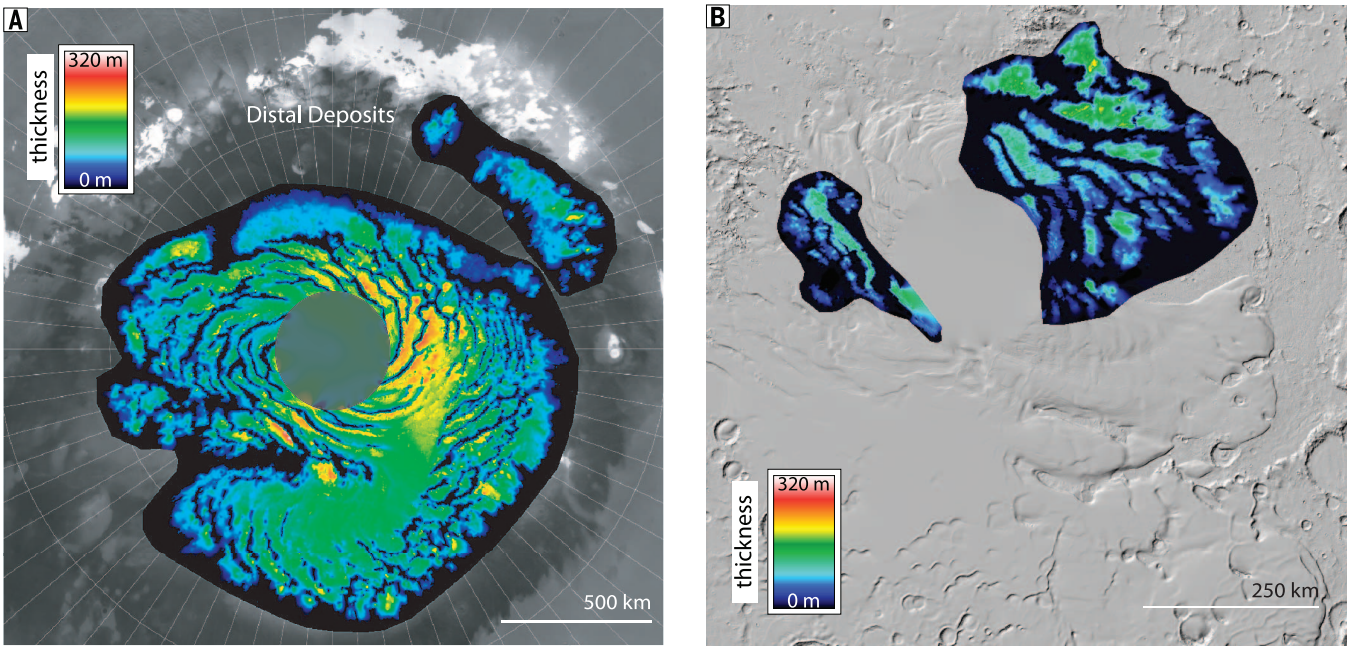


Fig. 3. Interpolated thickness maps of the NPLD WRAP, two outlier deposits, and the SPLD. (**A**) NPLD WRAP thickness ranges from 0 m at outcrops to 320 m at the NPLD interior. The integrated volume of the WRAP and outlier deposits is ~80,000 km^3. Fully interpolated region poleward of 87.4°N is shaded in gray. (**B**) Corresponding SPLD unit is discontinuous and less widespread, with a volume of ~7000 km^3. Thickness reaches 210 m locally. For maps showing uninterpolated thickness along radargram ground tracks, see fig. S1.

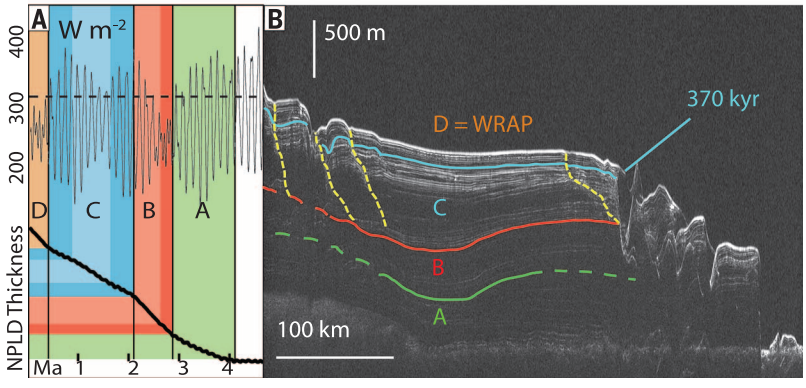


Fig. 4. Modeled ice accumulation and stratigraphic unconformities in the NPLD. (**A**) Solar insolation (W m^{-2}) correlated to ice thickness modeled for the north polar region from 4 million years ago (Ma) to the present [from (*2*)]. The accumulated thickness is shown normalized to the current NPLD value, so units are not displayed. Insolation varies by a factor of 2 through time, creating four climatologically distinct periods (vertical bars separated by colors). Applying the same logic that associates the WRAP (unit D) with the latest increase in accumulation modeled by (*2*), we assign units to periods of relatively low accumulation rates (units A and C) and relatively high accumulation rates (unit B). (**B**) SHARAD radargram 529701 annotated with stratigraphic unconformities mapped here and in (*13*, *14*). Yellow dashed line highlights spiral trough migration paths. The red reflector mapped between units B and C is reflector 29 (R29) from (*14*) and is associated with an unconformity in other locations. It represents the surface nearest which most of the spiral troughs formed. Packets of high radar reflectivity [in (B)] may correspond to darker shaded bands [in (A)] highlighting periods of greater insolation variability and potentially explaining the packet-interpacket reflectivity zones that SHARAD detects (*15*, *16*).

The discovery of a climate change recorded in the NPLD is not unexpected. Climate models predict recent and rapid north polar accumulation at the expense of mid-latitude ice loss due to obliquity changes (*2*). Those authors predicted that "the upper 300 m of the [northern] cap have accumulated during the last ~400 kyr" and that a major discontinuity "should be visible in the geological record." Although they did not provide a volume for comparison, a prior study estimated that 100 cm GEL should have been transferred from mid-latitude reservoirs to the poles over the same period (370,000 years) (*3*). The detection of mid-latitude ice reservoirs (*28*) and recent ice loss from those reservoirs (*6*, *29*) supports this hypothesis. Furthermore, detections of sublimation from fresh impacts suggest that mid-latitude ground ice is out of equilibrium with the current climate (*30*, *31*).

Our maximum accumulation finding of 320 m (and 55 cm GEL) in the north closely matches the predicted values of 300 m thickness (*2*) and 100 cm GEL (*3*). Using the modeled age of WRAP onset (370,000 years) and our maximum thickness of 320 m yields a maximum NPLD accumulation rate of ~0.86 mm/year. This value is about 3 times the published average estimates for the entire NPLD, which include periods of erosion and nonaccumulation (*17*), and it is well within the range of accelerated accumulation rates modeled for this shorter period (0.76 to 1.1 mm/year) (*2*). This implies an average transfer rate of ~0.24 km^3/year from lower latitudes to the poles, with 92% going to the north.

Our findings constitute evidence for a recent, widespread, and predominantly northern polar erosion event followed by accelerated accumulation to the present day, signaling the end of a martian glacial period. Our conclusion is supported by models that use orbital parameters to predict climate change and by observations of ongoing, mid-latitude ice loss. The total volumes transferred to the poles during this period are 55 cm GEL to the north and 5 cm GEL to the south, for a total of ~87,000 km^3 and 60 cm GEL. Besides the unconformity associated with the erosion event predating the current interglacial period, two other major unconformities and stratigraphic inflections have been mapped using SHARAD data (*13*, *14*). We infer that the processes active

Downloaded from http://science.sciencemag.org/ on May 26, 2016

today were also active in the past and suggest that these three inflection points correspond to the three predicted in models (*2*, *4*) (Fig. 4); if so, then the NPLD accumulated primarily in four climatologically distinct stages. More work is required to determine whether the lower unconformities match the predicted ages, as in the case of the WRAP, but we present them again here and revise the accumulation scenario posited by (*16*).

REFERENCES AND NOTES

1. J. Laskar, B. Levrard, J. F. Mustard, *Nature* **419**, 375–377 (2002).
2. B. Levrard, F. Forget, F. Montmessin, J. Laskar, *J. Geophys. Res.* **112**, E06012 (2007).
3. J. W. Head, J. F. Mustard, M. A. Kreslavsky, R. E. Milliken, D. R. Marchant, *Nature* **426**, 797–802 (2003).
4. R. Greve, B. Grieger, O. Stenzel, *Planet. Space Sci.* **58**, 931–940 (2010).
5. J.-B. Madeleine, F. Forget, E. Millour, T. Navarro, A. Spiga, *Geophys. Res. Lett.* **39**, L23202 (2012).
6. J. F. Mustard, C. D. Cooper, M. K. Rifkin, *Nature* **412**, 411–414 (2001).
7. J. W. Holt *et al.*, *Science* **322**, 1235–1238 (2008).
8. J. J. Plaut *et al.*, *Geophys. Res. Lett.* **36**, L02203 (2009).
9. K. L. Tanaka *et al.*, *Icarus* **196**, 318–358 (2008).
10. K. L. Tanaka, C. M. Fortezzo, Geologic map of the north polar region of Mars, U.S. Geological Survey Scientific Investigations Map 3177 (2012).
11. A. D. Howard, J. A. Cutts, K. R. Blasius, *Icarus* **50**, 161–215 (1982).
12. R. Seu *et al.*, *J. Geophys. Res.* **112**, E05S05 (2007).
13. J. W. Holt *et al.*, *Nature* **465**, 446–449 (2010).
14. I. B. Smith, J. W. Holt, *J. Geophys. Res.* **120**, 362–387 (2015).
15. R. J. Phillips *et al.*, *Science* **320**, 1182–1185 (2008).
16. N. E. Putzig *et al.*, *Icarus* **204**, 443–457 (2009).
17. K. E. Fishbaugh, C. S. Hvidberg, *J. Geophys. Res.* **111**, E06012 (2006).
18. S. Christian, J. W. Holt, S. Byrne, K. E. Fishbaugh, *Icarus* **226**, 1241–1251 (2013).
19. I. B. Smith, J. W. Holt, *Nature* **465**, 450–453 (2010).
20. I. B. Smith, J. W. Holt, A. Spiga, A. D. Howard, G. Parker, *J. Geophys. Res.* **118**, 1835–1857 (2013).
21. T. C. Brothers, J. W. Holt, A. Spiga, *Geophys. Res. Lett.* **40**, 1334–1339 (2013).
22. T. C. Brothers, J. W. Holt, A. Spiga, *J. Geophys. Res.* **120**, 1357–1375 (2015).
23. N. E. Putzig, F. J. Foss, B. A. Campbell, R. J. Phillips, *LPI Contrib.* **1791**, 1336 (2014).
24. K. L. Tanaka, *Nature* **437**, 991–994 (2005).
25. I. B. Smith, A. Spiga, J. W. Holt, *Geomorphology* **240**, 54–69 (2015).
26. M. Koutnik, S. Byrne, B. Murray, *J. Geophys. Res.* **107**, 10-1–10-10 (2002).
27. C. Herny *et al.*, *Earth Planet. Sci. Lett.* **403**, 56–66 (2014).
28. A. M. Bramson *et al.*, *Geophys. Res. Lett.* **42**, 6566–6574 (2015).
29. V.-P. Kostama, M. A. Kreslavsky, J. W. Head, *Geophys. Res. Lett.* **33**, L11201 (2006).
30. S. Byrne *et al.*, *Science* **325**, 1674–1676 (2009).
31. C. M. Dundas, S. Byrne, *Icarus* **206**, 716–728 (2010).
32. A. S. McEwen *et al.*, Global Color Views of Mars, *25th Lunar and Planetary Science Conference* (1994), pp. 871–872.

ACKNOWLEDGMENTS

Supported by the SHARAD instrument, NASA grants NNX10AQ32G (N.E.P.) and NNX11AL10G (J.W.H.), and the Institute for Geophysics, Jackson School of Geoscience, University of Texas at Austin (J.W.H.). Data used in this investigation are available at NASA's planetary data system (PDS), http://pds-geosciences.wustl.edu/mro/mro-m-sharad-5-radargram-v1/mrosh_2001/. We thank the SHARAD team and Mars polar group for supportive comments and suggestions, F. Foss and B. Campbell for their roles in generating the 3D radar volume, and Seisware International for use of its seismic mapping tools.

SUPPLEMENTARY MATERIALS

www.sciencemag.org/content/352/6289/1075/suppl/DC1
Methods
Figs. S1 to S5
References (*33*–*36*)

19 November 2015; accepted 19 April 2016
10.1126/science.aad6968

ORGANIC CHEMISTRY

Enantioselective synthesis of an ophiobolin sesterterpene via a programmed radical cascade

Zachary G. Brill, Huck K. Grover, Thomas J. Maimone*

Cyclase enzymes weave simple polyprenyl chains into the elaborate polycyclic ring systems of terpenes, a sequence that is often difficult to emulate under abiotic conditions. Here we report a disparate synthetic approach to complex terpenes whereby simple prenyl-derived chains are cyclized using radical, rather than cationic, reaction pathways. This strategy allowed us to efficiently forge the intricate 5-8-5 fused ring systems found in numerous complex natural product classes and also enabled a nine-step total synthesis of (−)-6-*epi*-ophiobolin N, a member of the large family of cytotoxic ophiobolin sesterterpenes. A small-molecule thiol catalyst was found to override the inherent diastereoselectivity observed during a reductive radical cascade cyclization process. This work lays the foundation for efficient synthesis of terpenoid ring systems of interest in medicinal research, particularly those that have been historically challenging to access.

Terpenes represent a highly diverse class of natural products whose derivatives have been developed into numerous medications approved by the U.S. Food and Drug Administration for the treatment of cancer, bacterial infection, malaria, and various other human diseases (*1*, *2*). Despite these successes, terpenes can pose distinct challenges for medicinal research because of their often-limited commercial availability, resistance to deep-seated structural modifications, and incompletely elucidated biosynthetic pathways. Owing to their nonmodular chemical structures, a unifying strategy for the chemical synthesis of terpenes does not exist, further exacerbating the difficulties of working with these compounds (*3*). Terpenes arise via the enzymatic conversion of simple polyprenyl chains into highly intricate polycyclic carbon networks of extraordinary diversity (*4*). Biomimetic synthesis, the act of emulating nature's bond construction process, would be an ideal synthetic tool in this context (*5*, *6*). Indeed, cationic polyene cyclizations are perhaps the best studied of all biomimetic cyclization reactions (*7*). To date, however, a very limited subset of terpenoid carbocyclic diversity can be accessed in this manner in a laboratory setting, and the synthesis of many medium and larger terpene ring frameworks has proven especially problematic. In contrast, shape-restricted enzyme cavities in terpene cyclases have evolved with appropriately placed amino acid residues to stabilize selective transition states and, in concert, dictate cyclization pathways. As a result of modulating this environment, the formation of myriad terpene skeletons, elaborate rearrangement processes, and various termination modes all become chemically possible (*4*). Here we describe a disparate approach, in which simple polyprenyl-derived chains are cyclized via radical-based (as opposed to cationic-based) methods. Through the use of different reagent combinations, we show that the termination modes of these cyclizations can be controlled and, with a chiral small-molecule thiol catalyst, their inherent stereochemical preferences altered.

Complex 5-8-*n* fused ring systems (*n* = 5 or 6) are found in numerous di- and sesterterpenes that possess notable antibiotic (*8*), cytotoxic (*9*), and immunosuppressant properties, among others (*10*) (Fig. 1). Central to this structural type is the continually expanding family of ophiobolin sesterterpenes featuring a stereochemically rich and synthetically formidable 5-8-5 fused ring system (Fig. 1A). Though compounds in this family were initially investigated for their phytotoxic effects, which negatively influence agricultural production, ophiobolin A (**1**) was later discovered to be a powerful inhibitor of calmodulin and remains an important tool for studying this calcium signaling protein (*11*). Most recently, these fungal metabolites have attracted much attention for their potent cytotoxic effects against multiple cancer cell lines, including the highly drug-resistant human brain tumor glioblastoma multiforme (*12*–*14*). Although more than 30 distinct members have been identified to date, often in minute and varying quantities, ophiobolin A (**1**), ophiobolin C (**2**), and 6-*epi*-ophiobolin N (**3**) highlight the major structural variations found in this terpenoid family, including (i) hydroxylation at carbon-3 or dehydration to an enone system; (ii) epimeric stereochemistry at carbon-6 for nearly all members; and (iii) myriad side-chain oxidation motifs, sometimes resulting in tetrahydrofuran (THF) ring formation (see **1**, for example) (*11*, *15*). Notwithstanding decades of research by numerous laboratories (*16*–*22*), only Rowley *et al.* (*23*) and, more recently, Tsuna *et al.* (*24*) have charted fully synthetic routes to various ophiobolin members. Despite these achievements, the long step

Department of Chemistry, University of California, Berkeley, 826 Latimer Hall, Berkeley, CA 94702, USA.
***Corresponding author. Email: maimone@berkeley.edu**

Downloaded from http://science.sciencemag.org/ on May 26, 2016

counts required (38 steps to **2**, 47 steps to **1**, respectively) are limitations for accessing numerous family members, conducting in-depth structure activity studies, and ultimately producing superior derivatives. Undoubtedly, these limitations are a direct consequence of the challenges posed by the carbogenic complexity of the ophiobolins.

In analyzing previous syntheses of ophiobolins, the lengthy, stepwise construction of the 5-8-5 fused ring system stands in marked contrast to the concise cyclase-mediated biosynthetic pathway (Fig. 2A). Chiba *et al.* proposed that the biosynthesis of the ophiobolins involves a cationic cyclization of geranylfarnesyl pyrophosphate to carbocation **4**, which—through a hydride shift, transannular cyclization, and hydration process—is then converted into the 5-8-5 fused skeleton of **5** (the process is shown in one step for simplicity) (*25*). In developing a retrosynthesis of ophiobolins, we were inspired by hypothetical carbon-centered radical **6** and considered its formation by the 8-endo/5-exo-cascade cyclization process shown (see **7**→**6**, Fig. 2B). Further disconnection, via the illustrated hypothetical four-component coupling sequence, led to the identification of linalool (C-10) and farnesol (C-15) as suitable materials wherein the carbons labeled in red are incorporated into the final target. Thus, the central tenet of our synthetic strategy was a desire to use the biochemical building blocks but to forge the bonds in an abiotic fashion—a strategy that we have previously found to facilitate the synthesis of simpler terpenoids (*26*).

Seeking to realize aspects of this synthetic blueprint, we prepared cyclopentenone **9** via a short sequence from the abundant monoterpene (–)-linalool (Fig. 3). A solvent-free ring closing metathesis reaction catalyzed by 0.1 mole percent (mol %) of the Hoveyda-Grubbs second-generation catalyst (HG-II) was first used to construct the cyclopentene ring (*27*), and upon complete consumption of linalool, the reaction mixture was diluted with THF and silylated in situ [NaH, *tert*-butyldimethylsilyl chloride (TBSCl)], affording chiral cyclopentene **8** in near-quantitative yield (>95%). After examining a variety of allylic oxidation conditions, we found that modifications to a ruthenium-catalyzed procedure developed by Miller *et al.* (*28*) smoothly furnished **9** in reasonable yield and on a multigram scale (57% isolated). In a separate vessel, we used Charette's asymmetric cyclopropanation methodology (*29*) in conjunction with a modified Appel procedure to prepare highly sensitive alkyl iodide **10** from geraniol. With two-step access to chiral fragments **9** and **10**, we developed and optimized a challenging three-component coupling reaction, bearing strong analogy to our retrosynthetic blueprint (Fig. 2B) but with the methylene (:CH_2) unit already incorporated. Treating **10** with *tert*-butyllithium induced lithium-halogen exchange and subsequent anionic cyclopropane fragmentation (*30*). After transmetallation with a copper iodide dimethylsulfide complex, an intermediate organocopper species (**12**) was formed, which cleanly added to cyclopentenone **9**. This 1,4-addition occurred in a diastereoselective fashion [diastereomeric ratio (dr) = 3:1], with the nucleophile approaching opposite the bulky OTBS group. After quenching with trichloroacetyl chloride, cyclopentenone **13** could be isolated via column chromatography. Even though this reaction proved sensitive to temperature and mixing efficiency, it was highly reproducible on half-gram scales.

Our efforts to effect the key radical cyclization of trichloroketone **13** were initially focused on copper-mediated atom-transfer radical cyclization processes to construct the 5-8-5 fused ring system. Though molecular models gave credence to the feasibility of this cascade process, both 8-endo and 7-exo cyclization pathways have been observed previously (*31*, *32*). Therefore, the outcome of this transformation, especially with

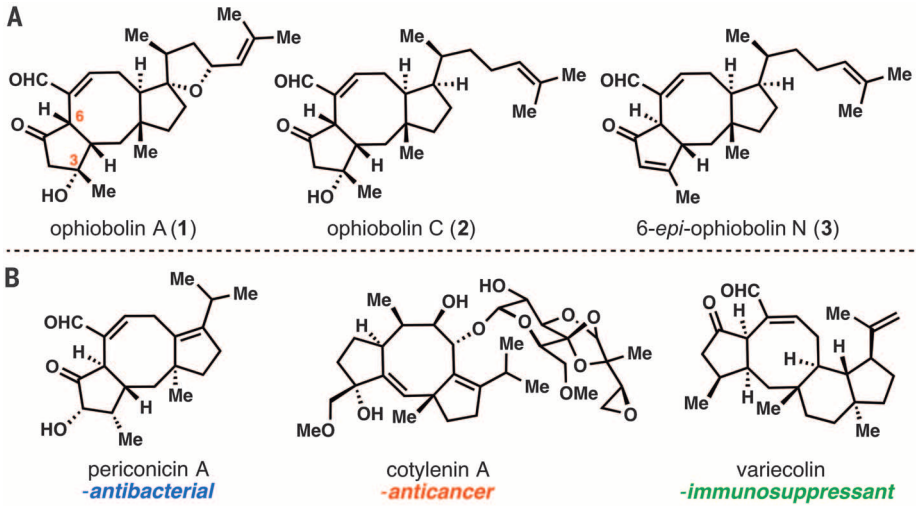


Fig. 1. Complex terpenoids containing 5-8-*n* fused carbocyclic skeletons. (**A**) Members of the ophiobolin sesterterpenes. Me, methyl. (**B**) Di- and sesterterpene classes of relevance to multiple therapeutic areas.

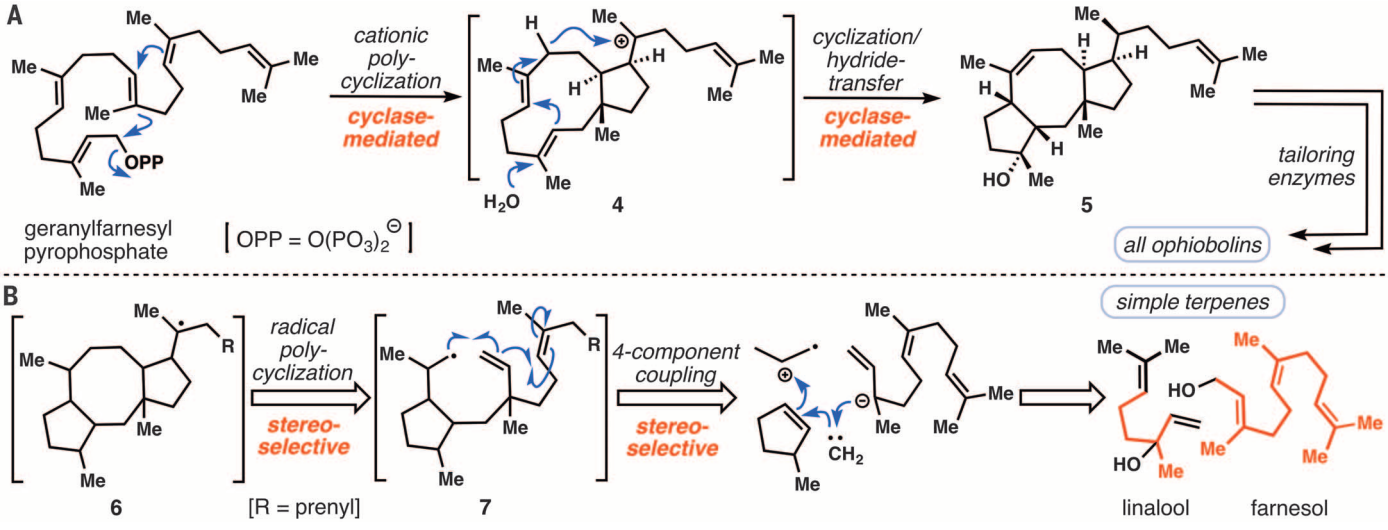


Fig. 2. Synthetic approaches to access complex ophiobolin ring systems. (**A**) Pathway for cyclase-mediated carbocationic cascades (*25*). (**B**) Retrosynthetic analysis with a strategic radical cascade involving simple polyprenyl building blocks.

Downloaded from http://science.sciencemag.org/ on May 26, 2016

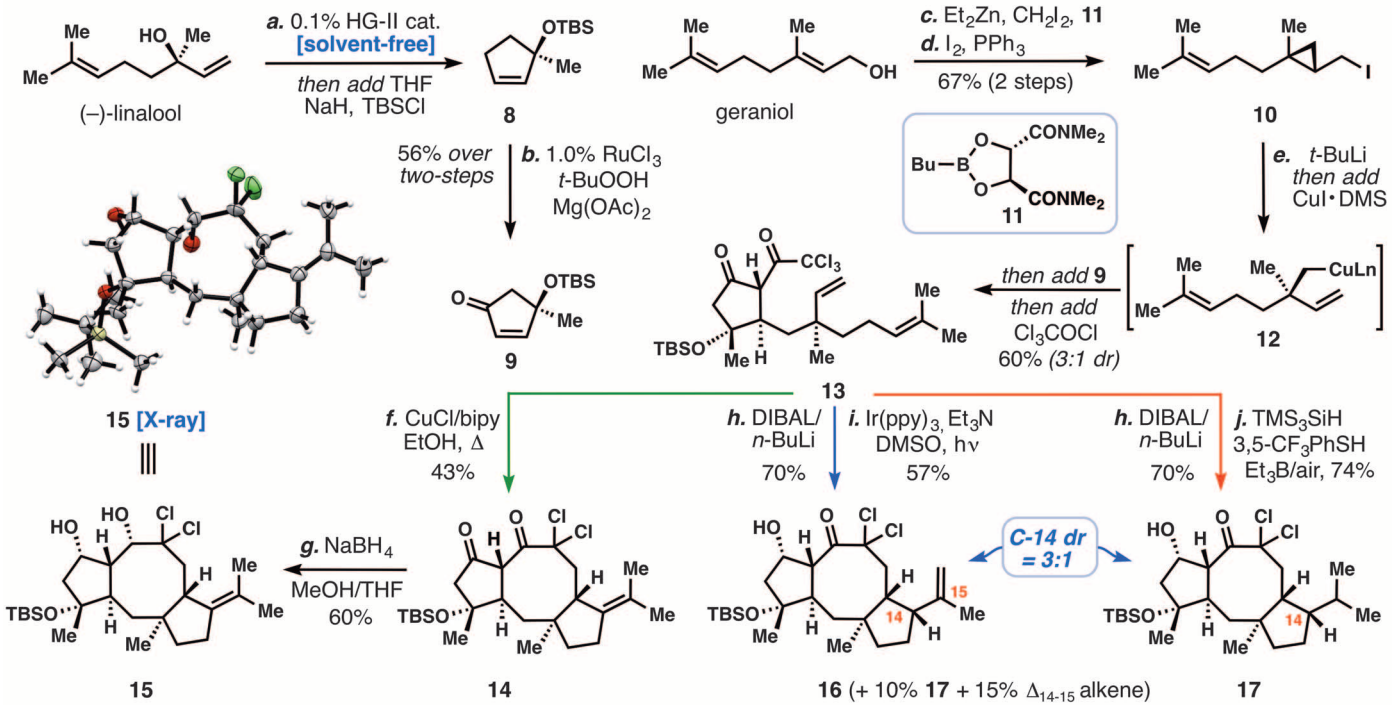


Fig. 3. Four-step entry into complex 5-8-5 fused ring systems. Reagents and conditions: (Step a) HG-II (0.1 mol %), 25°C, 1 hour; then add NaH [3.0 equivalents (equiv)], THF, 0°C, 5 min; then add TBSCl (1.5 equiv), 65°C, 2 hours, 98%. (Step b) $RuCl_3$ (1 mol %), $Mg(OAc)_2{\cdot}4H_2O$ (2.0 equiv), *t*-BuOOH (10.9 equiv), CH_2Cl_2/H_2O, 25°C, 57%. (Step c) Geraniol (1 equiv), boronic ester **11** (1.5 equiv), Et_2Zn (2 equiv), CH_2I_2 (4 equiv), CH_2Cl_2, 0°→25°C, 5 hours, 89%. (Step d) I_2 (1.1 equiv), PPh_3 (1.1 equiv), imidazole (1.8 equiv), CH_2Cl_2, 0°C, 1 hour, 75%. (Step e) **10** (1.3 equiv), *t*-BuLi (2.7 equiv), pentane/Et_2O, –78°C, 2.5 hours; then add CuI (0.53 equiv), Me_2S (2.1 equiv), –78°C, 15 min; then add **9** (1.0 equiv), –78°→–40°C, 4 hours; then add Cl_3CCOCl (3.3 equiv), –78°→–40°C, 2 hours, 60%, dr = 3:1. (Step f) CuCl (0.7 equiv), bipy (0.9 equiv), EtOH, 80°C, 1.5 hours, 43%. (Step g) $NaBH_4$ (2 equiv), MeOH/THF, 0°C, 1 hour, 60%. (Step h) DIBAL (1.0 equiv), *n*-BuLi (1.0 equiv), toluene/Et_2O, 2 hours; then add AcOH (6.0 equiv), 70%. (Step i) $Ir(ppy)_3$ (1 mol %), Et_3N (0.5 equiv), DMSO, blue light–emitting diodes, 25°C, 2 hours, 57%, dr = 3:1. (Step j) Et_3B (1.0 equiv), air, $(TMS)_3SiH$ (1.2 equiv), 3,5-*bis*(CF_3)-PhSH (2.0 equiv), PhH, 25°C, 74%, dr = 3:1. HG-II, (1,3-Bis-(2,4,6-trimethylphenyl)-2-imidazolidinylidene)dichloro(*o*-isopropoxyphenylmethylene) ruthenium; OAc, acetate; Bu, butyl; Et, ethyl; ppy, 2-phenylpyridinato; bipy, 2,2′-bipyridine; DMSO, dimethyl sulfoxide; TMS, trimethylsilyl.

regard to stereochemistry, was by no means certain (*33*). However, when **13** was heated with copper(I) chloride and bipyridine, polycycle **14**, which contains the desired trans 5-8 ring junction, was formed in 43% yield. The stereochemistry of this cascade, as well as of prior steps, was confirmed by x-ray crystallographic analysis of the sodium borohydride reduction product **15**. If a tertiary chloride intermediate is formed under these cyclization conditions, it eliminates selectively to the tetrasubstituted olefin isomer—a process we envision to be crucial in efforts to synthesize periconicin and cotylenin A, which possess internal alkenes in this sector (Fig. 1B). With respect to the ophiobolin synthetic problem, this termination mode is not ideal, as a key stereocenter on the newly forged cyclopentane ring is lost. After surveying a variety of options, we perceived two notable solutions. First, we found that through selective reduction of **13** [diisobutylaluminum hydride (DIBAL)/*n*-BuLi], the keto alcohol that subsequently formed could be converted into **16** via an Ir-catalyzed photoredox cyclization (*34*). Under these cyclization conditions, the exocyclic alkene product predominates (57%), and the tetrasubstituted alkene isomer is minimized (15%). This experiment also confirmed that the key cyclopentane stereocenter was correctly set during the cyclization cascade (dr = 3:1, see supplementary materials). A small amount of reductive cyclization product **17** (10%) was also formed under these conditions. Given that a reductive process could potentially construct the basic ophiobolin side chain in its correct oxidation state directly, we optimized this transformation. By employing polarity-reversal conditions (*35*) involving tris(trimethylsilyl)silane and a thiol additive [3,5-CF_3PhSH (Ph, phenyl) was found to be optimal], reductive cyclization product **17** could be formed in good yield (74%). Triethylborane/air-mediated initiation was found to be crucial, as the temperatures needed to cajole azobisisobutyronitrile-mediated processes resulted in lower diastereoselectivity at the isopropyl-containing stereocenter (dr ~ 1:1, temperature T = 90°C). Overall, these three cyclization modes offer rapid (four or five steps) synthetic entry into complex 5-8-5 fused tricycles with requisite handles to be converted into diverse terpenoid structures.

In an attempt to translate these results into the synthesis of full ophiobolin natural products, we subjected farnesol to an analogous four-step sequence previously described for geraniol (Fig. 4). After the final hydride reduction step, either free alcohol **18** or its acetylated variant **19** could be isolated in one pot. Subjecting **18** to the previously discovered conditions for reductive radical cyclization afforded tricycle **20** featuring the complete eastern sector of all minimally oxidized ophiobolins. Although we were pleased to find that the diastereoselectivity at the cyclopentane stereocenter (C-14) was slightly improved relative to the geraniol-based system (dr ~ 4:1, T = 5°C), our excitement was quickly diminished when we determined that the major product of the cascade possessed the incorrect stereochemistry at the neighboring C-15 methyl stereocenter. In particular, when using previously employed 3,5-CF_3PhSH as a catalyst (25 mol %), we obtained a 1.6:1 mixture favoring 15-*epi* **20** (Fig. 4B). Given that the thiol is believed to donate the final hydrogen atom under these conditions (*35*), we examined the effect of thiol structure on the diastereoselectivity of the process **18**→**20** (Fig. 4B). All achiral aromatic and aliphatic thiols tested favored the incorrect isomer with slightly varying preferences (1.4:1 to 1.6:1 dr in favor of 15-*epi* **20**). Taking inspiration from Cai *et al.*'s work on enantioselective radical hydrosilylation (*36*), we began to examine the potential of chiral thiol catalysts to override the inherent substrate bias of this terminating hydrogen atom abstraction event (*37*). Although known glucose-based thiol **24** and 1,1'-bi-2-naphthol dithiol **25** led

Downloaded from http://science.sciencemag.org/ on May 26, 2016

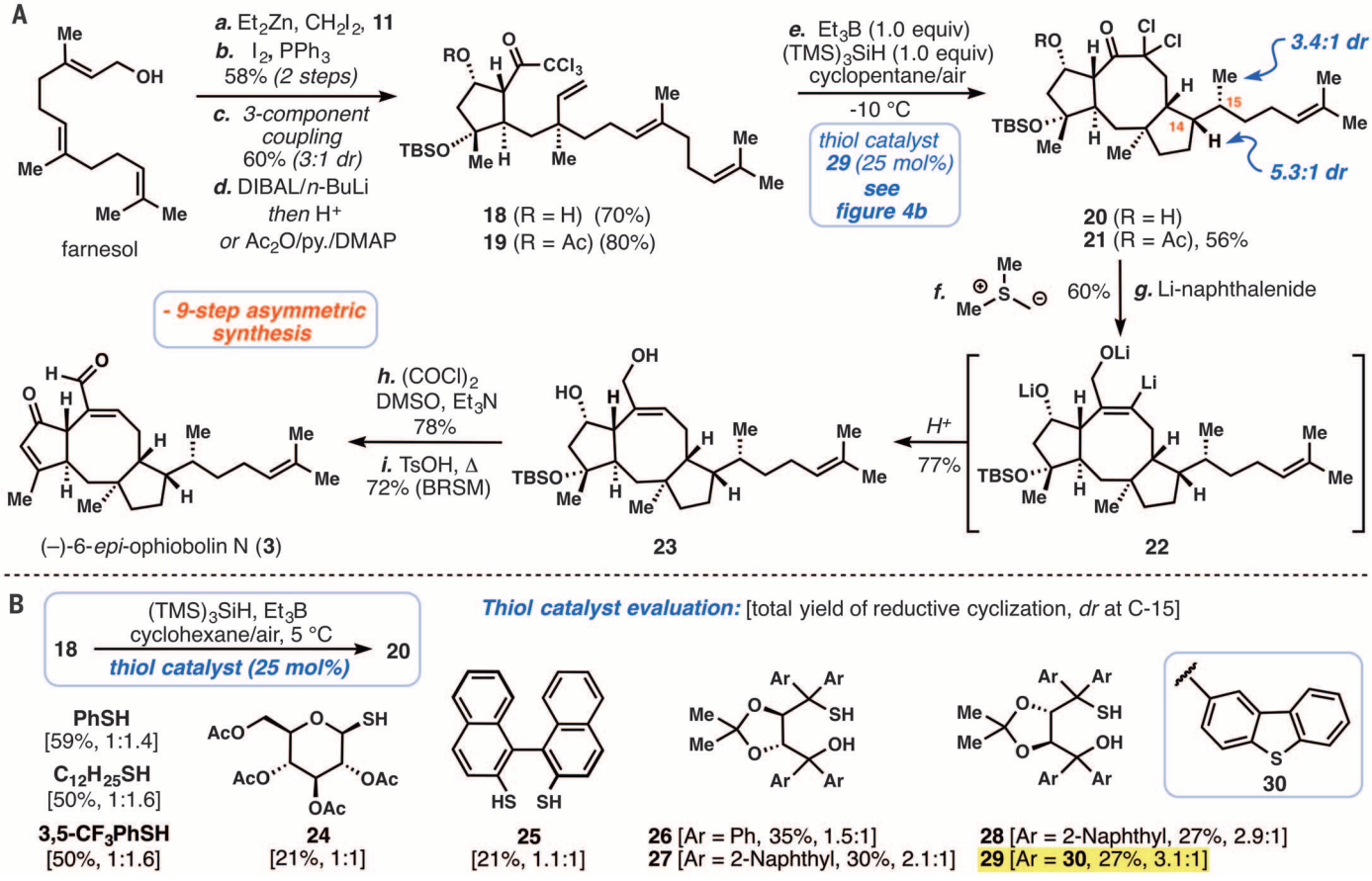


Fig. 4. Total synthesis of an ophiobolin sesterterpene. (**A**) Nine-step asymmetric synthesis of (–)-6-*epi*-ophiobolin N (**3**) (yields reported for synthetic steps e to h are for the diastereomeric mixture). (**B**) Evaluation of thiol catalysts for the transformation of **18**→**20** (yields and selectivity determined by ^{1}H nuclear magnetic resonance analysis; dr at C-14 was ~4:1). Reagents and conditions: (Steps a to d) See Fig. 3 for analogous conditions. (Step e) **19** (1.0 equiv), TMS_3SiH (1.0 equiv), **29** (25 mol %), Et_3B (1.0 M solution in THF, 1.25 equiv) added over 12 hours, air, cyclopentane (0.009 M), –10°C, 12 hours, 56% combined yield of reductively cyclized material [the reported dr values at C-14 (5.3:1) and C-15 (3.4:1) were determined after synthetic step h (see supplementary materials)]. (Step f) Me_3SI (24.0 equiv), *n*-BuLi (6.0 equiv), THF, 0°C, 15 min; then add **21** (1.0 equiv), 10 min, 60%. (Step g) Lithium naphthalenide (1.0 M solution in THF, 40 equiv), THF, –78°C, 20 min, 77%. (Step h) $(COCl)_2$ (10.0 equiv), DMSO (15.0 equiv), Et_3N (20.0 equiv), CH_2Cl_2, –78°→0°C, 3 hours, 78%. (Step i) *p*-TsOH (3.0 equiv), *t*-BuOH/CH_2Cl_2, 40°C, 24 hours, 59% plus 19% recovered starting material. *p*-TsOH, *para*-toluenesulfonic acid; py, pyridine; DMAP, 4-dimethylaminopyridine; BRSM, based on recovered starting material.

to slight improvements, we found that when employing α,α,α',α'-tetraaryl-2,2-disubstituted 1,3-dioxolane-4,5-dimethanol (TADDOL)–based monothiols **26** and **27** (derived from L-tartrate), the desired isomer was favored substantially (dr = 1.5:1 and 2.1:1, respectively). Surprisingly, the opposite enantiomer of thiol **27** (i.e., **28**) was even better in this regard, resulting in a 2.9:1 diastereomeric ratio at C-15, favoring **20**. The benzothiophene-based TADDOL monothiol **29** proved optimal, resulting in a 3.1:1 dr in favor of **20**. Optimization of the reaction conditions and use of acetate substrate **19** afforded a 56% combined yield of reductively cyclized material favoring **21** (Fig. 4A). The diastereoselectivity at the cyclopentane stereocenter (C-14) was further increased to >5:1 by conducting the transformation at –10°C in cyclopentane solvent. It was not possible to chromatographically separate the individual isomers of **21** at this stage, and the reported diastereomeric ratios were determined after synthetic step h in Fig. 4 (also see supplementary materials).

Tricycle **21**, accessible in only five steps from readily abundant farnesol, requires only one carbon to complete the full C-25 skeleton of the target. This task was readily accomplished via the Corey-Chaykovsky epoxidation reaction (*38*), which fortuitously also removed the acetate group in the process (Fig. 4A). A second reductive cascade process was then designed to convert this spiro-epoxide intermediate (not shown) into the requisite ophiobolin cyclooctene ring system. Thus, treatment with excess lithium naphthalenide induced reductive ring opening of the epoxide (*39*), with concomitant dehalogenation of the remaining chloride, presumably forming trianionic intermediate **22**. Following aqueous work-up, diol **23** could be isolated in excellent yield (77%). The extraneous chlorine atoms, which are required for efficient atom transfer cyclization, are seamlessly converted into the requisite olefinic functionality found in the final target, with minimal chemical expenditure—a task that may find use in other settings. Finally, double Swern oxidation of diol **23**, followed by treatment with *para*-toluenesulfonic acid under slightly elevated temperatures, forged (–)-6-*epi*-ophiobolin N (**3**), thus completing a nine-step enantioselective total synthesis in 2% overall yield. To date, we have used this sequence to prepare 15 mg of (–)-**3**.

The described synthesis of 6-*epi*-ophiobolin N (**3**) lays the foundation for the efficient synthesis of other complex 5-8-*n* fused terpenes for which no simple chemical or synthetic biological solutions exist. Moreover, this work also represents one of the shortest total syntheses of any known sesterterpene natural product (*40*). In addition, this strategy represents a departure from biomimetic, cationic cascade processes in that the chiral reagent exerts its influence during the termination of the cascade, rather than its initiation (*7*); combinations of both may prove even more powerful. Nevertheless, the synthesis described here is not without flaw: a lack of complete diastereocontrol is noted in several steps. Finally, myriad reductive radical cyclizations terminate

Downloaded from http://science.sciencemag.org/ on May 26, 2016

with a hydrogen atom abstraction step that creates a stereogenic carbon center (*41*). Using elements of the work demonstrated herein, it may be possible to create previously inaccessible stereochemical permutations—a process ideal from the vantage point of diverse analog preparation.

REFERENCES AND NOTES

1. T. P. Stockdale, C. M. Williams, *Chem. Soc. Rev.* **44**, 7737–7763 (2015).
2. E. Breitmaier, *Terpenes: Flavors, Fragrances, Pharmaca, Pheromones* (Wiley, 2006).
3. T. J. Maimone, P. S. Baran, *Nat. Chem. Biol.* **3**, 396–407 (2007).
4. D. W. Christianson, *Chem. Rev.* **106**, 3412–3442 (2006).
5. E. Poupon, B. Nay, vols. 1 and 2 of *Biomimetic Organic Synthesis* (Wiley, 2011).
6. M. Razzak, J. K. De Brabander, *Nat. Chem. Biol.* **7**, 865–875 (2011).
7. R. A. Yoder, J. N. Johnston, *Chem. Rev.* **105**, 4730–4756 (2005).
8. S. Kim, D. S. Shin, T. Lee, K. B. Oh, *J. Nat. Prod.* **67**, 448–450 (2004).
9. T. Kasukabe, J. Okabe-Kado, Y. Honma, *Cancer Sci.* **99**, 1693–1698 (2008).
10. H. Fujimoto, E. Nakamura, E. Okuyama, M. Ishibashi, *Chem. Pharm. Bull.* **48**, 1436–1441 (2000).
11. T. K. Au, W. S. Chick, P. C. Leung, *Life Sci.* **67**, 733–742 (2000).
12. T. Yang *et al.*, *Bioorg. Med. Chem. Lett.* **22**, 579–585 (2012).
13. W. Sun *et al.*, *Mar. Drugs* **11**, 4570–4584 (2013).
14. M. Bury *et al.*, *Cell Death Dis.* **4**, e561 (2013).
15. H. Wei *et al.*, *Tetrahedron* **60**, 6015–6019 (2004).
16. W. G. Dauben, D. J. Hart, *J. Org. Chem.* **42**, 922–923 (1977).
17. L. A. Paquette, J. A. Colapret, D. R. Andrews, *J. Org. Chem.* **50**, 201–205 (1985).
18. J. H. Rigby, C. Senanayake, *J. Org. Chem.* **52**, 4634–4635 (1987).
19. M. Michalak, K. Michalak, Z. Urbanczyk-Lipkowska, J. Wicha, *J. Org. Chem.* **76**, 7497–7509 (2011).
20. P. A. Wender *et al.*, *J. Org. Chem.* **62**, 4908–4909 (1997).
21. K. Li, C. Wang, G. Yin, S. Gao, *Org. Biomol. Chem.* **11**, 7550–7558 (2013).
22. G. Mehta, V. Singh, *Chem. Rev.* **99**, 881–930 (1999).
23. M. Rowley, M. Tsukamoto, Y. Kishi, *J. Am. Chem. Soc.* **111**, 2735–2737 (1989).
24. K. Tsuna, N. Noguchi, M. Nakada, *Angew. Chem. Int. Ed.* **50**, 9452–9455 (2011).
25. R. Chiba, A. Minami, K. Gomi, H. Oikawa, *Org. Lett.* **15**, 594–597 (2013).
26. Y.-M. Zhao, T. J. Maimone, *Angew. Chem. Int. Ed.* **54**, 1223–1226 (2015).
27. H. A. Meylemans, R. L. Quintana, B. R. Goldsmith, B. G. Harvey, *ChemSusChem* **4**, 465–469 (2011).
28. R. A. Miller, W. Li, G. R. Humphrey, *Tetrahedron Lett.* **37**, 3429–3432 (1996).
29. A. B. Charette, H. Juteau, H. Lebel, C. Molinaro, *J. Am. Chem. Soc.* **120**, 11943–11952 (1998).
30. A. B. Charette, J. Naud, *Tetrahedron Lett.* **39**, 7259–7262 (1998).
31. T. Sato, S. Ishida, H. Ishibashi, M. Ikeda, *J. Chem. Soc. Perkin Trans. 1* **1991**, 353–359 (1991).
32. L. Liu, Q. Chen, Y.-D. Wu, C. Li, *J. Org. Chem.* **70**, 1539–1544 (2005).
33. T. V. RajanBabu, *Acc. Chem. Res.* **24**, 139–145 (1991).
34. J. W. Tucker, J. D. Nguyen, J. M. R. Narayanam, S. W. Krabbe, C. R. J. Stephenson, *Chem. Commun.* **46**, 4985–4987 (2010).
35. B. P. Roberts, *Chem. Soc. Rev.* **28**, 25–35 (1999).
36. Y. Cai, B. P. Roberts, D. A. Tocher, *J. Chem. Soc. Perkin Trans. 1* **2002**, 1376–1386 (2002).
37. C. A. Lewis, S. J. Miller, *Angew. Chem. Int. Ed.* **45**, 5616–5619 (2006).
38. E. J. Corey, M. Chaykovsky, *J. Am. Chem. Soc.* **87**, 1353–1364 (1965).
39. J. M. Concellón, L. Llavona, P. L. Bernad Jr., *Tetrahedron* **51**, 5573–5584 (1995).
40. D. T. Hog, R. Webster, D. Trauner, *Nat. Prod. Rep.* **29**, 752–779 (2012).
41. A. J. McCarroll, J. C. Walton, *Angew. Chem. Int. Ed.* **40**, 2224–2248 (2001).

ACKNOWLEDGMENTS

Financial support for this work was provided by the University of California, Berkeley (UC Berkeley); the UC Berkeley Hellman Fellows Fund; the Alfred P. Sloan Foundation; and the NIH National Institute of General Medical Sciences (grant R01GM116952). Z.G.B. acknowledges UC Berkeley and the NSF for a Berkeley Fellowship and an NSF Graduate Research Fellowship (award DGE-1106400), respectively. We thank N. Shin for technical assistance, A. DiPasquale for x-ray crystallographic analysis and support from an NIH Shared Instrument grant (S10-RR027172), and N. Burns and F. Seidl (Stanford University) for various TADDOL diols used in early stages of this work. Metrical parameters for the structures of compounds **15** and **SI-6** are available free of charge from the Cambridge Crystallographic Data Centre under accession numbers CCDC-1474968 and CCDC-1474969, respectively.

SUPPLEMENTARY MATERIALS

www.sciencemag.org/content/352/6289/1078/suppl/DC1
Materials and Methods
Figs. S1 to S5
Tables S1 to S12
NMR Spectra
References (*42*–*49*)

11 March 2016; accepted 26 April 2016
10.1126/science.aaf6742

POLYMER CHEMISTRY

Organocatalyzed atom transfer radical polymerization driven by visible light

Jordan C. Theriot,[1] Chern-Hooi Lim,[1,2] Haishen Yang,[1] Matthew D. Ryan,[1] Charles B. Musgrave,[1,2,3] Garret M. Miyake[1,3]*

Atom transfer radical polymerization (ATRP) has become one of the most implemented methods for polymer synthesis, owing to impressive control over polymer composition and associated properties. However, contamination of the polymer by the metal catalyst remains a major limitation. Organic ATRP photoredox catalysts have been sought to address this difficult challenge but have not achieved the precision performance of metal catalysts. Here, we introduce diaryl dihydrophenazines, identified through computationally directed discovery, as a class of strongly reducing photoredox catalysts. These catalysts achieve high initiator efficiencies through activation by visible light to synthesize polymers with tunable molecular weights and low dispersities.

Over the past two decades, atom transfer radical polymerization (ATRP) (*1*–*4*) has matured into one of the most powerful methodologies for precision polymer synthesis (*5*). Strict control over the equilibrium between a dormant alkyl halide and an active propagating radical dictates a low concentration of radicals and minimizes bimolecular termination to achieve controlled polymer chain growth (*6*). ATRP has historically relied on transition-metal catalysts to mediate this equilibrium and polymerize monomers with diverse functionality into macromolecules with controlled molecular weight (MW), low MW dispersity (*Đ*), defined chemical composition, and complex architecture (*7*).

The caveat of traditional ATRP has been that the transition-metal catalysts present purification challenges for the polymer products and impede their use in biomedical and electronic applications (*8*). Despite substantial strides in lowering catalyst loading (*9*, *10*) and facilitating purification (*11*), organocatalyzed methods remain highly desirable for circumventing the need for metal removal, reducing toxicity concerns, and avoiding interference with electronic systems. Organocatalyzed variants of ATRP by use of alkyl iodide initiators have been established, although they are not a broadly applicable replacement for metal-catalyzed ATRP (*12*–*14*).

Our interest in this field originated in 2013 with the discovery that perylene could serve as an organic visible-light photoredox catalyst (PC) to mediate an ATRP mechanism with alkyl bromide initiators, albeit with less control over the polymerization than has become the benchmark for traditional metal-catalyzed ATRP (*15*–*17*). Our ongoing work has striven to establish organocatalyzed ATRP (O-ATRP) for the synthesis of polymers with the precision of traditional ATRP, using visible-light PCs to realize energy-efficient polymerization methods that eliminate a major limitation of ATRP. Although photoredox catalysis has been established for decades, visible-light photoredox catalysis has drawn increasing attention by presenting the opportunity to harness solar energy to mediate chemical transformations under mild conditions (*18*, *19*). Phenyl phenothiazine derivatives have since also proven effective as PCs for the ATRP of methacrylates (*20*) and acrylonitrile (*21*) but require irradiation by ultraviolet light and leave much room for improvement for generating polymers with higher molecular weights and lower dispersities coupled with increased initiator efficiency.

Our proposed mechanism of photoredox O-ATRP posits reversible electron transfer (ET) from

[1]Department of Chemistry and Biochemistry, University of Colorado Boulder, Boulder, CO 80309, USA. [2]Department of Chemical and Biological Engineering, University of Colorado, Boulder, CO 80309, USA. [3]Materials Science and Engineering Program, University of Colorado Boulder, Boulder, CO 80309, USA.
*Corresponding author. Email: garret.miyake@colorado.edu

Downloaded from http://science.sciencemag.org/ on May 26, 2016

the photoexcited PC in order to reversibly activate an alkyl bromide initiator (Fig. 1C). In addition to the requirement that the excited triplet state ^{3}PC* possess sufficiently strong reducing power to activate the initiator, a delicate interplay must be balanced between the stability of the radical cation ^{2}PC$^{\bullet+}$ and its capacity to oxidize the propagating radical so as to efficiently deactivate the propagating polymer and yield a controlled radical polymerization.

Computationally directed discovery (*22*, *23*) inspired us to focus on 5,10-diphenyl-5,10-dihydrophenazines as a potential class of PCs for O-ATRP (Fig. 1B). The phenazine core is shared by several biologically relevant molecules that serve as redox-active antibiotics (*24*, *25*), whereas synthetic derivatives have drawn interest in organic photovoltaics (*26*–*28*) and organic ferromagnets (*29*, *30*). We hypothesized that an appropriate union between the excited-state reduction potential (E^{0*}) and the stability of the radical cation PC$^{\bullet+}$ resulting from ET to the initiator would be required for the production of polymers with controlled MW and low $Đ$. As such, we investigated electron-donating (OMe, **1**), neutral (H, **2**), and electron-withdrawing (CF_3, **3**, and CN, **4**) moieties on the *N*-phenyl substituents.

Density functional theory (DFT) was used to calculate the reduction potentials of the triplet excited-state PCs, initiator, and propagating radicals (Fig. 1B) (*31*). We found that **2** possesses a triplet excited-state reduction potential of E^0(PC$^{\bullet+}$/^{3}PC*) = −2.34 V versus saturated calomel electrode (SCE). Functionalization of the phenyl substituents with an electron-donating group OMe (**1**) strengthened the E^{0*} to −2.36 V, whereas introduction of CF_3 or CN electron-withdrawing groups (EWGs) weakened the E^{0*} to −2.24 and −2.06 V for **3** and **4**, respectively, all of which is corroborated by the measured values within experimental error (table S1). The triplet excited states of these PCs are all strongly reducing with respect to 1e^- transfer to the ethyl α-bromophenylacetate (EBP) initiator; we calculated that E^0(EBP/EBP$^{\bullet-}$) = −0.74 V versus SCE for an adiabatic ET, which is consistent with our cyclic voltammetry results, which show that the onset of EBP reduction occurs at ~−0.8 V versus SCE (fig. S28). These phenazine derivatives are significantly more reducing than are commonly used metal PCs (*18*), including polypyridyl iridium complexes (E^{0*} as negative as −1.73 V versus SCE) that have been used in photomediated ATRP (*32*, *33*). Iridium PCs are expensive, challenging to remove from the product, and have only been demonstrated to produce polymers with $Đ$ as low as 1.19.

The remarkable reducing power of these dihydrophenazine-based PCs arises from a distinct combination of their high triplet-state energies (~2.2 to 2.4 eV) and the formation of relatively stable radical cations [E^0(PC$^{\bullet+}$/PC) = ~−0.1 to 0.2 V] upon their oxidation. These radical cations are also sufficiently oxidizing to deactivate the propagating chains. We computed E^0s for propagating radicals with n monomer repeat unit (or units) bound to ethyl phenylacetate (EPA) of E^0[(EPA − MMA$_n$)/(EPA − MMA$_n$)$^{\bullet-}$] =

Table 1. Results for the organocatalyzed ATRP of MMA catalyzed by 3 using white LEDs or sunlight.
Asterisk indicates use of sunlight. Experimental details are provided in the supplementary materials.

Run	[MMA]:[EBP]:[3]	Time (hours)	Conversion (%)	M_w (kDa)	$Đ$ (M_w/M_n)	I [$M_{n(theo)}/M_{n(exp)}$]
1	[1000]:[10]:[1]	8	98.4	17.9	1.17	65.9
2*	[1000]:[10]:[1]	7	33.8	7.54	1.10	52.9
3	[1000]:[20]:[1]	8	78.9	7.12	1.18	69.5
4	[1000]:[15]:[1]	8	67.8	8.74	1.18	64.3
5	[1000]:[5]:[1]	8	86.9	37.3	1.26	59.6
6	[1000]:[2]:[1]	8	95.2	85.5	1.54	86.3
7	[5000]:[10]:[1]	8	74.7	77.4	1.32	64.2
8	[2500]:[10]:[1]	8	96.3	61.3	1.31	52.0
9	[750]:[10]:[1]	6.5	53.2	7.75	1.30	71.1
10	[500]:[10]:[1]	6.5	64.0	4.83	1.12	79.9

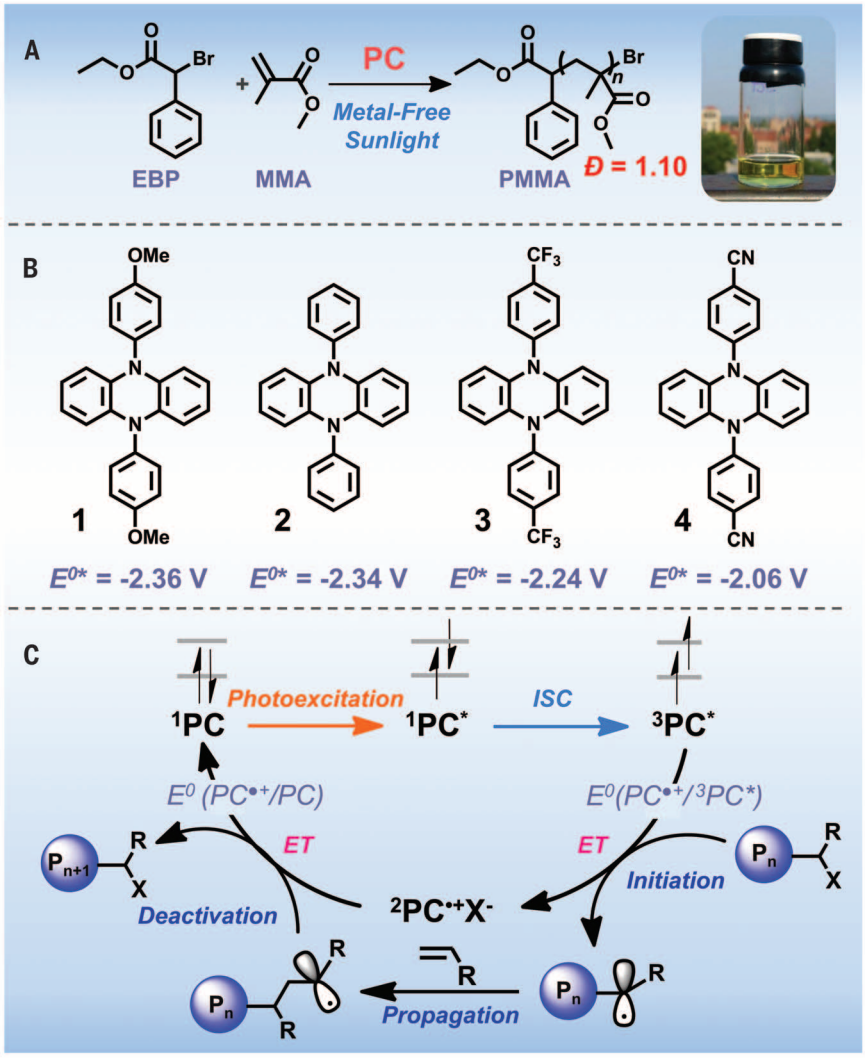


Fig. 1. PC development for O-ATRP. (**A**) Polymerization of MMA to well-defined polymers by using photoredox O-ATRP driven by sunlight. (**B**) Structures of the diphenyl dihydrophenazine PCs **1** to **4** used in this study. (**C**) A proposed mechanism for ATRP mediated by a PC via photoexcitation to ^{1}PC*, intersystem crossing (ISC) to the triplet state ^{3}PC*, ET to form the radical cation doublet ^{2}PC$^{\bullet+}$, and back ET to regenerate PC and reversibly terminate polymerization.

Downloaded from http://science.sciencemag.org/ on May 26, 2016

−0.74, −0.86, and −0.71 V for n = 0, 1, and 2, respectively. These E^0s are sufficiently negative with respect to oxidization by the radical cations to drive rapid radical deactivation and regeneration of the PC to complete the photocatalytic cycle.

An initial series of target PCs (**1** to **4**) were synthesized in two steps from commercial reagents in good yields. Under otherwise identical conditions, all of the PCs were tested in the polymerization of methyl methacrylate (MMA) by using EBP as the initiator and white light-emitting diodes (LEDs) for irradiation in dimethylacetamide (Table 1, run 1, and table S2, runs S1 to S3). All four PCs proved effective in polymerization after 8 hours of irradiation, with the PCs bearing EWGs exhibiting the best catalytic performance. PC **3** proved superior in producing polymers with a combination of not only the lowest dispersity ($Đ$ = 1.17) but also the highest initiator efficiency (I^* = 65.9%) (I^* is the ratio between the theoretical and experimentally measured number average molecular weight) (Table 1, run 1). Using methyl α-bromoisobutyrate as the initiator was also efficient but did not achieve the same level of control of the polymerization achieved with EBP (table S2, run S5). Additionally, polymerization could be driven by sunlight to produce poly(methyl methacrylate) (PMMA) with a low dispersity of $Đ$ = 1.10 (run 2).

Time-point aliquots were taken during polymerization to monitor the MW and $Đ$ progression as a function of monomer conversion (Fig. 2, A and B). The control provided by **3** was evidenced by the linear increase in polymer MW and low $Đ$ throughout the course of polymerization.

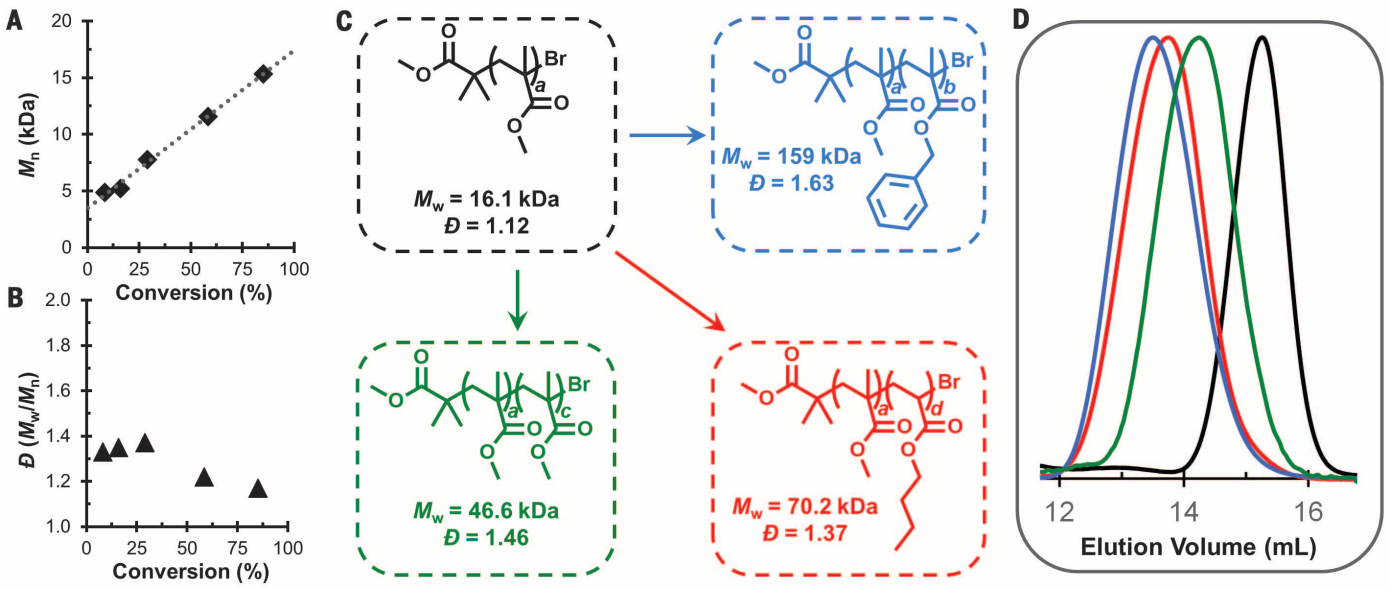


Fig. 2. Polymerization results using PC 3. (**A**) Plot of molecular weight as a function of monomer conversion and (**B**) plot of dispersity as a function of monomer conversion for the polymerization of MMA mediated by **3**. (**C**) Chain-extension from a PMMA macro-initiator (black) to produce block copolymers with MMA (green), BMA (blue), and BA (red). (**D**) GPC traces of each polymer depicted in (C) (color coded).

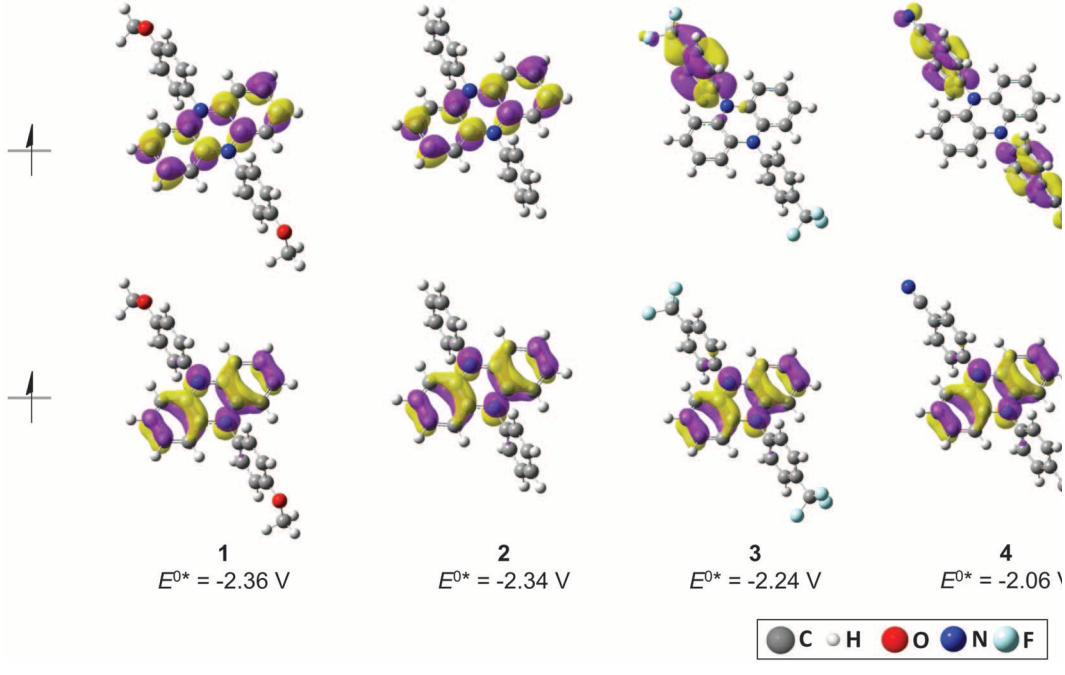


Fig. 3. Calculated triplet state (^{3}PC*) frontier orbitals and excited-state reduction potentials E^{0*} of diphenyl dihydrophenazine PCs 1 to 4. (Top) The higher-lying SOMO. (Bottom) The low-lying SOMO. Phenyl functionalization with electron-withdrawing groups (CF_3 and CN) localizes the high-lying SOMO on the phenyl.

Downloaded from http://science.sciencemag.org/ on May 26, 2016

However, the y intercept of the number-average molecular weight (M_n) versus conversion plot was 3.46 kDa, suggesting an uncontrolled chain-growth period with addition of ~32 MMA equivalents during the onset of polymerization before precise control was attained, whereas an ideal polymerization would have a y intercept equal to the mass of the initiator (MW of EBP = 243 Da).

We next examined the effect of adjusting the initiator ratio relative to monomer and PC (runs 3 to 6). The weight-average molecular weight (M_w) of the resulting PMMA could be modulated from 7.12 to 85.5 kDa. High EBP ratios resulted in controlled polymerizations and low dispersities ($Đ$ = 1.26 to 1.17), and despite the moderate loss of precise control over the polymerization at low EBP ratios ($Đ$ = 1.54), high-MW polymer was produced with high initiator efficiency (M_w = 85.5 kDa, I^* = 86.3%). Alternatively, adjusting the monomer ratio relative to EBP and PC regulated polymer MW while also maintaining low $Đ$ (runs 7 to 10).

One of the greatest strengths of traditional ATRP is its capacity to synthesize advanced polymeric architectures, including block copolymers. The reversible-deactivation mechanism enforced in ATRP repeatedly reinstalls the Br chain-end group onto the polymer, and thus, isolated polymers can be used to reinitiate polymerization. A combination of nuclear magnetic resonance spectroscopy and matrix-assisted laser desorption ionization mass spectroscopy were used to confirm the expected EBP-derived polymer chain-end groups for a polymer produced through the proposed photoredox O-ATRP mechanism (figs. S12 and S13). Additionally, to further support the posited O-ATRP mechanism, a series of block polymerizations were performed to probe the Br chain-end group fidelity.

First, after initial polymerization of MMA proceeded for 12 hours, additional MMA was added to the reaction mixture. Gel permeation chromatography (GPC) analysis revealed that the MW of the resulting polymer quantitatively increased (fig. S22). Second, after polymerization of MMA was allowed to proceed for 8 hours, the reaction mixture was placed in the dark for 8 hours, and subsequently, additional MMA, benzyl methacrylate (BMA), or butyl acrylate (BA) was added. No polymerization took place during the dark period, whereas the subsequent addition of monomer and further illumination resulted in continued and controlled polymer chain growth (figs. S23, S24, and S26). Third, an isolated polymer was reintroduced to a solution of monomer and catalyst and exposed to light in order to ascertain whether it would serve as a macroinitiator for the synthesis of block polymers. This chain-extension proved successful with MMA, BMA, and BA (Fig. 2, C and D). The chain-extension polymerization from an isolated polymer produced from this polymerization method firmly supports the conclusion that this methodology proceeds through the O-ATRP mechanism, whereas all of these experiments revealed baseline resolved peaks in the GPC traces, demonstrating high chain-end group fidelity.

DFT calculations were performed in order to gain insight into the differences in the performances of the PCs, all of which possess similar $E^0(PC^{\bullet+}/{}^3PC^*)$s and $E^0(PC^{\bullet+}/PC)$s that are sufficiently reducing and oxidizing, respectively, to drive the photocatalytic cycle of Fig. 1C. As such, we reasoned that the superior performances of **4** and, in particular, **3** must be qualitatively different from those of **1** and **2** and result from a more complex effect.

Inspection of the triplet state ($^3PC^*$) frontier orbitals reveals qualitative differences in these PCs (Fig. 3). The low-lying singly occupied molecular orbitals (SOMOs) of all the PCs are similar, with the electron localized over the phenazine π system. For PCs **1** (OMe) and **2** (H), the high-lying SOMO

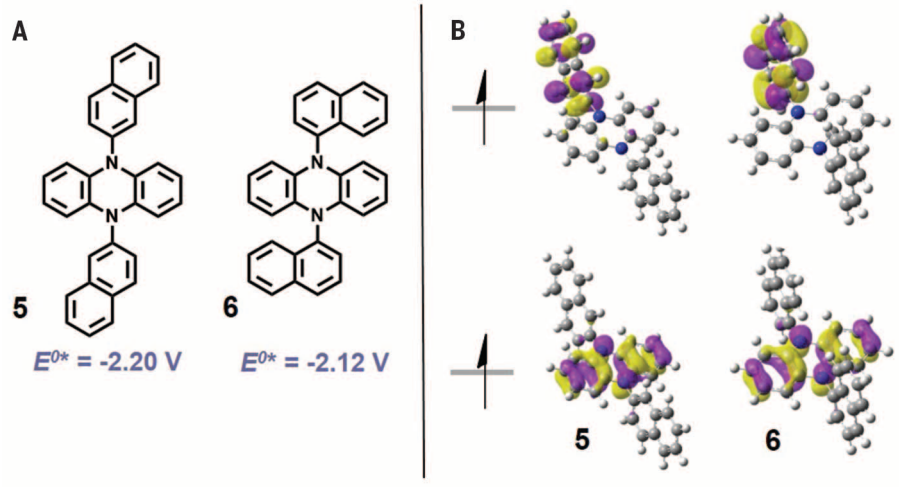


Fig. 4. Computationally directed discovery of PCs 5 and 6. (**A**) Structures of **5** and **6** and the calculated E^{0*}. (**B**) Triplet-state frontier orbitals of **5** and **6** showing the (top) higher-lying SOMO and (bottom) low-lying SOMO.

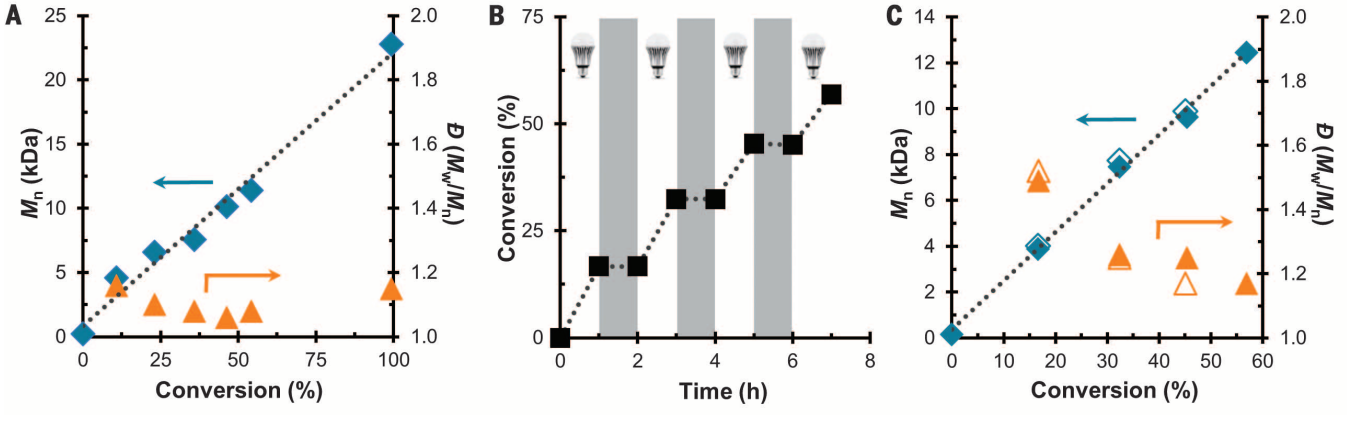


Fig. 5. Results for the polymerization of MMA using PC 6. (**A**) Plot of M_n and $Đ$ versus monomer conversion for the polymerization of MMA under continuous irradiation. (**B**) Plot of monomer conversion versus time and (**C**) plot of M_n and $Đ$ (solid symbols indicate after irradiation, and open symbols indicate after dark period) versus monomer conversion, using **6** as the PC during pulsed light irradiation with white LEDs. Experimental details are provided in the supplementary materials.

Downloaded from http://science.sciencemag.org/ on May 26, 2016

Table 2. Results for the organocatalyzed ATRP of MMA catalyzed by 6 using white LEDs. Experimental details are provided in the supplementary materials.

Run	[MMA]:[MBP]:[6]	Time (hours)	Conversion (%)	M_w (kDa)	$Đ$ (M_w/M_n)	I [$M_{n(theo)}/M_{n(exp)}$]
11	[1000]:[10]:[1]	8	71.7	10.6	1.28	88.1
12	[1000]:[20]:[1]	8	73.1	5.24	1.29	94.5
13	[1000]:[15]:[1]	8	70.8	7.52	1.36	88.5
14	[5000]:[10]:[1]	8	69.5	46.9	1.32	98.7
15	[2500]:[10]:[1]	8	64.5	21.9	1.34	99.3
16	[750]:[10]:[1]	8	69.0	6.93	1.23	94.7
17	[500]:[10]:[1]	8	76.4	5.74	1.39	95.7

is also localized on the phenazine rings; in contrast, for **3** (CF_3) and **4** (CN), the high-lying SOMO, occupied by the reducing e^-, resides on the phenyl ring (or rings). We contend that the CF_3 and CN EWGs of **3** and **4** stabilize their π* orbitals localized on the phenyl rings relative to the phenazine-localized π* orbital that is the high-lying SOMO of **1** and **2**. This reorders the energies of the π* orbitals so that a π* orbital localized on the phenyls becomes the high-lying SOMO of **3** and **4**, although the low-lying SOMO localized on the phenazine moiety remains singly occupied. Thus, **3** and **4** differ qualitatively from **1** and **2** in that their two triplet electrons reside on either the phenazine or the phenyl substituent and are thus spatially separated.

Furthermore, a comparison of **3** to **4** elucidates another important distinction. For **3**, the high-lying SOMO is localized on one of the phenyl rings, whereas in **4**, the reducing e^- is delocalized over both phenyl rings. Surprisingly, calculations revealed one of the C–F bonds of the CF_3 functionalized phenyl that bears the high-lying SOMO of **3** is lengthened from 1.35 to 1.40 Å, indicating partial localization of electron density on the C–F antibond. This symmetry-breaking effect in the triplet state of **3** creates a more localized, higher electron density of the reducing electron of **3** relative to **4** while also maintaining the spatial separation between the two SOMO electrons that preserves the reducing potential of the triplet.

With the above observations in mind, we attempted to discover even more efficient PCs to mediate O-ATRP using computational chemistry to design diaryl dihydrophenazines that possess sufficiently strong E^{0*}s and spatially separated excited-state SOMOs, with the higher-energy SOMO localized over only one of the aromatic substituents off the dihydrophenazine core. Using these principles, we designed and synthesized 2-napthyl (**5**) and 1-napthyl (**6**) derivatives—with strong E^{0*}s of −2.20 and −2.12 V, respectively—and SOMOs with the targeted desirable geometric features (Fig. 4). Using EBP as the initiator, both PCs proved successful in the polymerization of MMA (table S2, runs S8 and S9). Although **5** produced PMMA with an impressively low $Đ$ of 1.03 (M_w = 9.35 kDa, I^* = 46.1%)—rivaling metal ATRP catalysts—**6** produced PMMA with a slightly higher I^* (47.5%), faster polymerization rates, and a similarly low $Đ$ of 1.08 (M_w = 12.3 kDa). The plot of M_n versus monomer conversion exhibits a y intercept of 850 Da, demonstrating the attainment of control over polymerization after the addition of only ~6 MMA units, which is correspondingly much more efficient control in the O-ATRP mediated by **6** than is achieved with **3** (Fig. 5A). Thus, we investigated **6** in more detail as the PC in the polymerization of MMA.

A survey of initiators commonly used in traditional metal-catalyzed ATRP in conjunction with **6** (Table 2, run 11, and table S2, runs 9 to 12) revealed that methyl 2-bromopropionate (MBP) provided the best overall results for the polymerization of MMA (M_w = 10.6 kDa; $Đ$ = 1.28; I^* = 88.1%). Furthermore, temporal control was realized by using a pulsed-irradiation sequence (Fig. 5, B and C). Polymerization was only observed during irradiation and paused during dark periods, and the MW steadily increased with continued irradiation while producing a polymer with a low $Đ$ of 1.17. Efficient control over the polymerization by **6** is highlighted by the consistently high I^* achieved over broad reaction conditions to produce polymers with tunable MWs through varying initiator (runs 11 to 14) or monomer (runs 15 to 17) ratios.

We envision that this O-ATRP catalyst platform will expand the application scope for polymers beyond those synthesized by metal-catalyzed ATRP, and their impressively strong reducing power presents great promise for their application toward other challenging chemical transformations. We also anticipate that the governing principles that afford these organic photocatalysts with their desirable properties will be exploited through computational design to discover additional photochemical platforms with capacities for a variety of applications.

REFERENCES AND NOTES

1. T. E. Patten, J. Xia, T. Abernathy, K. Matyjaszewski, *Science* **272**, 866–868 (1996).
2. K. Matyjaszewski, J. Xia, *Chem. Rev.* **101**, 2921–2990 (2001).
3. M. Ouchi, T. Terashima, M. Sawamoto, *Chem. Rev.* **109**, 4963–5050 (2009).
4. K. Matyjaszewski, N. V. Tsarevsky, *Nat. Chem.* **1**, 276–288 (2009).
5. C. J. Hawker, K. L. Wooley, *Science* **309**, 1200–1205 (2005).
6. K. Matyjaszewski, *ACS Symposium Ser.* **1187**, 1–17 (2015).
7. K. Matyjaszewski, N. V. Tsarevsky, *J. Am. Chem. Soc.* **136**, 6513–6533 (2014).
8. N. V. Tsarevsky, K. Matyjaszewski, *Chem. Rev.* **107**, 2270–2299 (2007).
9. A. J. D. Magenau, N. C. Strandwitz, A. Gennaro, K. Matyjaszewski, *Science* **332**, 81–84 (2011).
10. K. Matyjaszewski *et al.*, *Proc. Natl. Acad. Sci. U.S.A.* **103**, 15309–15314 (2006).
11. T. Pintauer, K. Matyjaszewski, *Chem. Soc. Rev.* **37**, 1087–1097 (2008).
12. A. Ohtsuki, L. Lei, M. Tanishima, A. Goto, H. Kaji, *J. Am. Chem. Soc.* **137**, 5610–5617 (2015).
13. A. Goto, A. Ohtsuki, H. Ohfuji, M. Tanishima, H. Kaji, *J. Am. Chem. Soc.* **135**, 11131–11139 (2013).
14. A. Goto *et al.*, *J. Am. Chem. Soc.* **129**, 13347–13354 (2007).
15. G. M. Miyake, U.S. Patent application no. 61,212 (2013).
16. G. M. Miyake, U.S. Patent no. US 9,156,921 B2 (2015).
17. G. M. Miyake, J. C. Theriot, *Macromolecules* **47**, 8255–8261 (2014).
18. C. K. Prier, D. A. Rankic, D. W. C. MacMillan, *Chem. Rev.* **113**, 5322–5363 (2013).
19. D. M. Schultz, T. P. Yoon, *Science* **343**, 1239176 (2014).
20. N. J. Treat *et al.*, *J. Am. Chem. Soc.* **136**, 16096–16101 (2014).
21. X. Pan, M. Lamson, J. Yan, K. Matyjaszewski, *ACS Macro Lett.* **4**, 192–196 (2015).
22. A. Aguirre-Soto, C.-H. Lim, A. T. Hwang, C. B. Musgrave, J. W. Stansbury, *J. Am. Chem. Soc.* **136**, 7418–7427 (2014).
23. C.-H. Lim, A. M. Holder, J. T. Hynes, C. B. Musgrave, *J. Am. Chem. Soc.* **136**, 16081–16095 (2014).
24. L. E. P. Dietrich, T. K. Teal, A. Price-Whelan, D. K. Newman, *Science* **321**, 1203–1206 (2008).
25. J. B. Laursen, J. Nielsen, *Chem. Rev.* **104**, 1663–1686 (2004).
26. Z. Zhang *et al.*, *J. Am. Chem. Soc.* **137**, 8509–8520 (2015).
27. Z. Zheng, Q. Dong, L. Gou, J.-H. Su, J. Huang, *J. Mater. Chem. C* **2**, 9858–9865 (2014).
28. T. Okamoto *et al.*, *Org. Lett.* **5**, 373–376 (2003).
29. E. Terada *et al.*, *J. Org. Chem.* **70**, 10073–10081 (2005).
30. S. Hiraoka *et al.*, *J. Am. Chem. Soc.* **126**, 58–59 (2004).
31. Recently, it was suggested that the singlet excited state of phenyl phenothiazines may be responsible for dehalogenations. Because of the oxygen intolerance of this polymerization system and the well-known phenomenon that the triplet state possesses a substantially longer lifetime sufficient for photocatalysis, we have based our computational interpretations on this polymer mechanism proceeding via the triplet state of the diphenyl dihydrophenazines (*34*).
32. B. P. Fors, C. J. Hawker, *Angew. Chem. Int. Ed. Engl.* **51**, 8850–8853 (2012).
33. N. J. Treat *et al.*, *ACS Macro Lett.* **3**, 580–584 (2014).
34. E. H. Discekici *et al.*, *Chem. Commun.* **51**, 11705–11708 (2015).

ACKNOWLEDGMENTS

G.M.M. is grateful for financial support from the University of Colorado Boulder and Advanced Research Projects Agency–Energy. This work was supported in part by NSF grant CHE-1214131 (C.B.M. and C.-H.L.). J.C.T. is thankful for a NSF Graduate Research Fellowship Program fellowship. M.D.R. acknowledges support from a Graduate Assistance in Areas of National Need fellowship. We also gratefully acknowledge use of Extreme Science and Engineering Development Environment supercomputing resources (NSF ACI-1053575) and the Janus supercomputer, which is supported by NSF (CNS-0821794) and the University of Colorado Boulder. We thank L. Hansman, A. Lockwood, S. Fatur, and N. Damrauer for technical assistance and enlightening discussions. We have filed a provisional patent application on the work described here.

SUPPLEMENTARY MATERIALS

www.sciencemag.org/content/352/6289/1082/suppl/DC1
Materials and Methods
Figs. S1 to S28
Tables S1 to S3
Coordinates of Calculated Molecular Structures
References (*35*–*39*)

3 February 2016; accepted 22 March 2016
Published online 31 March 2016
10.1126/science.aaf3935

Downloaded from http://science.sciencemag.org/ on May 26, 2016

QUANTUM PHYSICS

A Schrödinger cat living in two boxes

Chen Wang,[1]* Yvonne Y. Gao,[1] Philip Reinhold,[1] R. W. Heeres,[1] Nissim Ofek,[1] Kevin Chou,[1] Christopher Axline,[1] Matthew Reagor,[1] Jacob Blumoff,[1] K. M. Sliwa,[1] L. Frunzio,[1] S. M. Girvin,[1] Liang Jiang,[1] M. Mirrahimi,[1,2] M. H. Devoret,[1] R. J. Schoelkopf[1]*

Quantum superpositions of distinct coherent states in a single-mode harmonic oscillator, known as "cat states," have been an elegant demonstration of Schrödinger's famous cat paradox. Here, we realize a two-mode cat state of electromagnetic fields in two microwave cavities bridged by a superconducting artificial atom, which can also be viewed as an entangled pair of single-cavity cat states. We present full quantum state tomography of this complex cat state over a Hilbert space exceeding 100 dimensions via quantum nondemolition measurements of the joint photon number parity. The ability to manipulate such multicavity quantum states paves the way for logical operations between redundantly encoded qubits for fault-tolerant quantum computation and communication.

Rapid progress in controlling individual quantum systems over the past 20 years (*1*, *2*) has opened a wide range of possibilities of quantum information processing. Potential applications, from universal quantum computation to long-distance quantum communication, share the central theme of exploiting quantum superpositions within a large Hilbert space. Further stimulated by curiosity about the quantum-classical boundary, there has been growing interest in generating superpositions of "macroscopically distinguishable" states that are far apart in phase space. The canonical example is superpositions of coherent states of a harmonic oscillator, i.e. $N(|\alpha\rangle + |-\alpha\rangle)$ with $N \approx 1/\sqrt{2}$ at large $|\alpha|$, known as "cat states." The two components correspond to distinct quasi-classical wave packets, in analogy to Schrödinger's *gedankenexperiment* of an unfortunate cat inside a closed box being simultaneously dead and alive. Cat states have so far been realized with single-mode optical (*3*) or microwave fields (*1*, *4*, *5*) with up to about 100 photons (*6*) but are increasingly susceptible to decoherence at large size.

Manipulating a large number of excitations in such harmonic oscillator states is one of two possible approaches to expand the information capacity of fully controlled quantum systems. Cat states, which span a Hilbert space whose dimension grows linearly with the number of photons, are an attractive approach for redundantly encoding quantum information for error correction (*7*–*9*). The other, more traditional, way to scale up a quantum system is to build many modes of excitations, each operated as a two-level qubit, so that the Hilbert space dimension increases exponentially with the number of modes (*10*, *11*). Is it possible to combine the benefits of both approaches by creating a cat state that lives in more than a single mode or box? The idea of nonlocal or multimode cat dates back to the early days of cavity quantum electrodynamics (QED) (*12*), but experimental demonstration has remained a formidable challenge.

Here, we deterministically create a two-mode cat state of microwave fields in two superconducting cavities, using the strong dispersive interaction with a Josephson junction–based artificial atom. This state can be expressed as

$$|\psi_\pm\rangle = N(|\alpha\rangle_A|\alpha\rangle_B \pm |-\alpha\rangle_A|-\alpha\rangle_B) \qquad (1)$$

where $|\pm\alpha\rangle_A$ and $|\pm\alpha\rangle_B$ are coherent states of two microwave eigenmodes (Alice and Bob) at different frequencies. Each of the two modes is predominantly localized in one of the two cavities that are weakly connected. For convenience, we will refer to the state of each mode as the state of each cavity. Previous realization of the state $|\psi_\pm\rangle$ has been limited to using small and nonorthogonal coherent states (*13*). For larger $|\alpha|$ (i.e., $|\alpha|^2 \gtrsim 2$), $|\psi_\pm\rangle$ can be considered a single cat state living in two boxes, whose superposed components are coherent states in a linearly hybridized mode of Alice and Bob (*14*). Alternatively, in the more natural eigenmode basis, $|\psi_\pm\rangle$ has been known as the entangled coherent states in theoretical studies (*15*) and may also be understood as two single-cavity cat states that are entangled with each other.

The two-mode cat state is an eigenstate of the joint photon number parity operator $\hat{P}_J$.

$$\hat{P}_J = \hat{P}_A\hat{P}_B = e^{i\pi\hat{a}^\dagger\hat{a}}e^{i\pi\hat{b}^\dagger\hat{b}} \qquad (2)$$

where $\hat{a}^\dagger(\hat{a})$ and $\hat{b}^\dagger(\hat{b})$ are the creation (annihilation) operators of photons in Alice and Bob, and $\hat{P}_A$ and $\hat{P}_B$ are the photon number parity operators in individual cavities. Remarkably, $|\psi_+\rangle$ (or $|\psi_-\rangle$) has definitively an even (or odd) number of photons in the two cavities combined, whereas the photon number parity in each cavity separately is maximally uncertain. Quantum nondemolition (QND) measurements of such parity operators not only illustrate the highly nonclassical properties of the state but also are instrumental for quantum error correction in general.

We realize measurements of the joint photon number parity and single-mode parities using the dispersive interaction with three energy levels of an artificial atom. Based on joint parity measurements, we further demonstrate full quantum state tomography of the two-cavity system (*16*). This is obtained in the form of the joint Wigner function $W_J(\beta_A, \beta_B)$, which is a continuous-variable representation of the quantum state with β_A and β_B being complex variables in Alice and Bob, respectively. Without correcting for the infidelity of the $\hat{P}_J$ measurement operator, we observe quantum state fidelity of 81% for a two-mode cat state with $\alpha = 1.92$. The high-quality and high-dimensional quantum control is further manifested by the presence of entanglement exceeding classical bounds in a Clauser-Horne-Shimony-Holt (CHSH)–style inequality for two continuous-variable systems (*16*). Finally, our two-cavity space effectively encodes two coupled logical qubits in the coherent state basis, and we present efficient two-qubit tomography in this encoded space.

Our experiment uses a three-dimensional (3D) circuit QED architecture (*17*), where two high-quality 3D cavities and a quasiplanar readout resonator simultaneously couple to a fixed-frequency transmon-type superconducting artificial atom (Fig. 1, A and B) (*14*). The two cavities that host the cat state of microwave photons are implementations of the longest-lived quantum memory in circuit QED to date (*18*). We use the transmon as an ancilla to manipulate the multiphoton states in the two cavities, and its lowest three levels, $|g\rangle$, $|e\rangle$, and $|f\rangle$, are accessed in this

Table 1. Hamiltonian parameters and coherence times of the two storage cavities and the transmon ancilla. These include transition frequencies ($\omega/2\pi$), energy relaxation times (T_1), Ramsey coherence times (T_2^*), and the dispersive frequency shifts ($\chi/2\pi$) between each cavity and each ancilla transition. The cavity frequencies are given with a precision of ±100 Hz and are stable over the course of several months.

	$\omega/2\pi$	T_1	T_2^*	$\chi^{ge}/2\pi$	$\chi^{ef}/2\pi$
Cavity Alice	4.2196612 GHz	2.2–3.3 ms	0.8–1.1 ms	0.71 MHz	1.54 MHz
Cavity Bob	5.4467679 GHz	1.2–1.7 ms	0.6–0.8 ms	1.41 MHz	0.93 MHz
Ancilla $\|e\rangle\rightarrow\|g\rangle$	4.87805 GHz	65–75 μs	30–45 μs	—	—
Ancilla $\|f\rangle\rightarrow\|e\rangle$	4.76288 GHz	28–32 μs	12–24 μs	—	—

[1]Department of Applied Physics and Physics, Yale University, New Haven, CT 06511, USA. [2]INRIA Paris-Rocquencourt, Domaine de Voluceau, B.P. 105, 78153 Le Chesnay Cedex, France.
*Corresponding author. Email: chen.wang@yale.edu (C.W.); robert.schoelkopf@yale.edu (R.J.S.)

Downloaded from http://science.sciencemag.org/ on May 26, 2016

experiment. The device is cooled down to 20 mK in a dilution refrigerator, and microwave transmission through the readout resonator is used to projectively measure the ancilla state with a heterodyne detection at room temperature after multiple stages of amplification.

We consider the Hamiltonian of the system (with parameters listed in Table 1), including two harmonic cavity modes with angular frequencies ω_A and ω_B, a three-level atom with transition frequencies ω_{ge} and ω_{ef}, and their dispersive interaction

$$H/\hbar \approx \omega_A \hat{a}^\dagger\hat{a} + \omega_B \hat{b}^\dagger\hat{b} + \omega_{ge}|e\rangle\langle e| + (\omega_{ge}+\omega_{ef})|f\rangle\langle f|$$
$$-\chi_A^{ge}\hat{a}^\dagger\hat{a}|e\rangle\langle e| - (\chi_A^{ge}+\chi_A^{ef})\hat{a}^\dagger\hat{a}|f\rangle\langle f|$$
$$-\chi_B^{ge}\hat{b}^\dagger\hat{b}|e\rangle\langle e| - (\chi_B^{ge}+\chi_B^{ef})\hat{b}^\dagger\hat{b}|f\rangle\langle f| \quad (3)$$

where χ_i^{ge} and χ_i^{ef} represent the dispersive frequency shifts of cavity i associated with the two ancilla transitions. The readout resonator and small high-order nonlinearities are omitted for simplicity (*14*). Using time-dependent classical drives in the form of microwave pulses, we can perform arbitrary ancilla rotations in both $|g\rangle$–$|e\rangle$ and $|e\rangle$–$|f\rangle$ manifolds and arbitrary cavity state displacements in Alice ($\hat{D}_{\beta_A} = e^{\beta_A\hat{a}^\dagger - \beta_A^*\hat{a}}$) and Bob ($\hat{D}_{\beta_B} = e^{\beta_B\hat{b}^\dagger - \beta_B^*\hat{b}}$) independently. More important, the state-dependent frequency shifts (χ's) allow cavity state manipulations conditioned on the ancilla level or vice versa using spectrally selective control pulses, thus realizing atom-photon quantum logic gates (*6*). It can be further shown that with separate drives on the two cavities and a drive on the ancilla, this Hamiltonian permits universal quantum control of the entire system (*19*).

We generate the two-mode cat state $|\psi_\pm\rangle$ deterministically using a series of logic gates as shown in Fig. 1C (*20*). In particular, we implement effective displacements ($\hat{D}_{2\alpha}^g$) of both cavities conditional on ancilla being in $|g\rangle$ (*14*), which realizes a three-way entangling gate, $\frac{1}{\sqrt{2}}(|g\rangle+|e\rangle)|0\rangle_A|0\rangle_B \rightarrow N(|g\rangle|0\rangle_A|0\rangle_B + |e\rangle|2\alpha\rangle_A|2\alpha\rangle_B)$. Then an ancilla rotation (R_π^{00}) conditional on the cavity state $|0\rangle_A|0\rangle_B$ disentangles the ancilla, and subsequent cavity displacements bring the cavities to a two-mode cat state. The rotation axis determines the sign (or more generally, the phase angle) of the cat state superposition.

We probe the cavity state by QND measurements of the photon number parity. Parity measurement of a single cavity has been previously demonstrated (*9*, *21*), where a conditional cavity phase shift (*4*), $C_\phi = \mathbf{I}\otimes|g\rangle\langle g| + e^{i\phi\hat{a}^\dagger\hat{a}}\otimes|e\rangle\langle e|$, with $\phi = \pi$, maps cavity states with even or odd photon numbers to $|g\rangle$ or $|e\rangle$ of a two-level ancilla, respectively, for subsequent readout. To achieve joint parity mapping in our two-cavity system, we exploit three levels of the ancilla to realize simultaneous C_π in both Alice and Bob. With the ancilla frequency designed to be in between those of the two cavities, the $|e\rangle\rightarrow|g\rangle$ transition shows stronger interaction with Bob ($\chi_B^{ge} > \chi_A^{ge}$), whereas the $|f\rangle\rightarrow|e\rangle$ transition shows stronger interaction with Alice ($\chi_A^{ef} > \chi_B^{ef}$). Manipulating the ancilla in different superposition states among the three levels allows us to concatenate conditional phase gates associated with χ_i^{ge} and χ_i^{ef} with arbitrary weights (*14*). This additional degree of freedom not only allows for measurement of $\hat{P}_J$ but also enables parity measurement of each cavity individually without affecting the other.

Based on single-cavity parity measurements, we can measure the Wigner function of individual cavities, $W_i(\beta_i) = \frac{2}{\pi}\mathrm{Tr}[\rho\hat{D}_{\beta_i}\hat{P}_i\hat{D}_{\beta_i}^\dagger]$ ($i = A$ or B) (*5*, *21*). The Wigner function is a standard method to fully determine the quantum state of a single-continuous-variable system, which represents the quasiprobability distribution of photons in the quadrature space [Re(β)-Im(β)]. Our measured W_A and W_B for a two-mode cat state $|\psi_-\rangle$ with $\alpha = 1.92$ (Fig. 2) illustrates that the quantum state of either Alice or Bob on its own is a statistical mixture of two clearly separated coherent states. However, single-cavity Wigner functions do not contain full information on the global quantum state. We find strong correlation between cavities by measuring joint photon number party $\langle\hat{P}_J\rangle = -0.81\pm0.01$, even though each cavity alone shows mean photon number parity of $\langle\hat{P}_A\rangle \approx \langle\hat{P}_B\rangle \approx 0$. Additional evidence of the joint parity can be seen in a spectroscopy measurement (*14*).

A full quantum state tomography of the two-cavity system can be realized by measuring the joint Wigner function (*22*):

$$W_J(\beta_A,\beta_B) = \frac{4}{\pi^2}\mathrm{Tr}[\rho\hat{D}_{\beta_A}\hat{D}_{\beta_B}\hat{P}_J\hat{D}_{\beta_B}\hat{D}_{\beta_A}^\dagger]$$
$$\equiv \frac{4}{\pi^2}P_J(\beta_A,\beta_B) \quad (4)$$

W_J is a function in the 4D phase space, whose value at each point [Re(β_A), Im(β_A), Re(β_B), and Im(β_B)], after rescaling by $\pi^2/4$, can be directly measured from the expectation value of the joint parity after independent displacements in Alice and Bob (*16*). We will therefore use the scaled joint Wigner function, or "displaced joint parity function," $P_J(\beta_A,\beta_B)$ to represent the cavity state. To illustrate the core features in this 4D Wigner function of the state $|\psi_-\rangle$, we show its 2D cuts along the Re(β_A)-Re(β_B) plane and Im(β_A)-Im(β_B) plane for both the calculated ideal state (Fig. 3, A

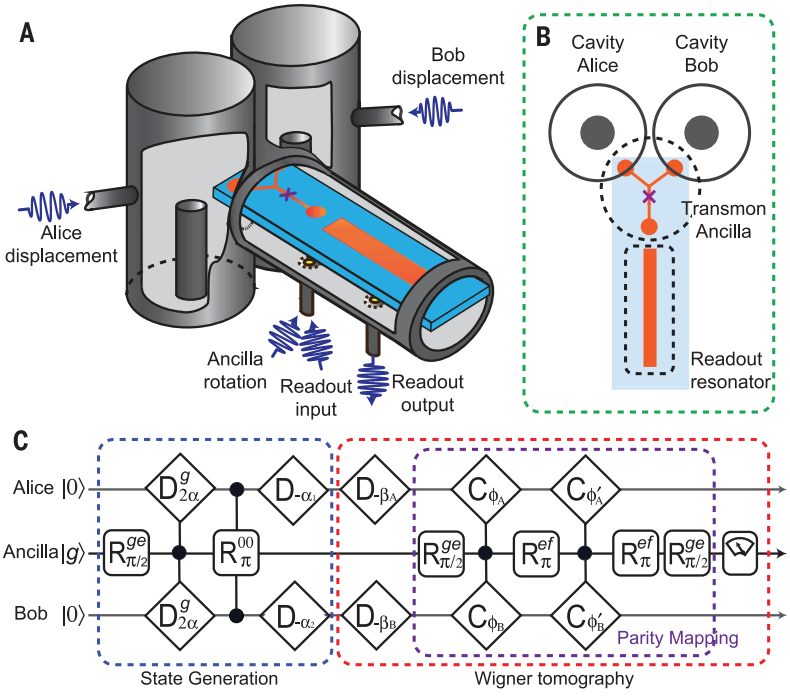


Fig. 1. Cartoon schematic of device architecture and experimental protocol. (**A**) A 3D view of the device consisting of two coaxial cavities (Alice and Bob), a Y-shaped transmon with a single Josephson junction (marked by ×), and a stripline readout resonator. All components are housed inside a single piece of bulk high-purity aluminum, with artificial windows drawn for illustration purposes. (**B**) A top view of the same device, showing the relative position of the sapphire chip, center posts of the coaxial cavities, transmon antenna, and the readout resonator. (**C**) The microwave control sequences for generating the two-mode cat state and performing Wigner tomography. $\hat{D}_\beta$ represents cavity displacement by β, and a superscript *g* is added if the displacement is conditional on the ancilla being in $|g\rangle$. R_θ^{ge} or R_θ^{ef} represents ancilla rotation by θ (around an axis in the *x*-*y* plane) in the $|g\rangle$–$|e\rangle$ or $|e\rangle$–$|f\rangle$ manifold. R_π^{00} is an ancilla $|g\rangle$–$|e\rangle$ rotation conditional on the cavities being in $|0\rangle_A|0\rangle_B$. $C_\phi$represents a cavity phase shift of ϕ, conditional on the ancilla being in an excited state. By choosing $\phi_i + \phi_i' = \pi$ or 2π, we can measure photon number parity of Alice ($\hat{P}_A$), Bob ($\hat{P}_B$), or the two combined ($\hat{P}_J$), to perform Wigner tomography of individual cavities or the joint Wigner tomography.

Downloaded from http://science.sciencemag.org/ on May 26, 2016

and B) (*16*) and the measured data (Fig. 3, C and D). The Wigner function contains two positively valued Gaussian hyperspheres representing the probability distribution of the two coherent-state components and an interference structure around the origin with strong negativity. Excellent agreement is achieved between measurement and theory, with the raw data showing an overall 81% contrast of the ideal Wigner function. Comprehensive 4D measurements of P_J further allow us to reconstruct the density matrix of the quantum state, which shows a total fidelity of also about 81% against the ideal $|\psi_-\rangle$ state. The actual state fidelity may be substantially higher if various errors associated with tomography are removed (*14*). Additional visualization of the Wigner function data is presented in a supplementary movie (*14*).

Analyzed within the eigenmode basis, the two-mode cat state is a manifestation of quantum entanglement between two quasiclassical systems. The entanglement can be tested against a CHSH-style Bell's inequality constructed from P_J at four points in the phase space (*16*). We observe a Bell signal (*14*) of 2.17 ± 0.01 for the state in Fig. 3, exceeding the classical bound of 2. Without complete spatial separation and fully independent readout of the two modes, this violation should be considered a demonstration of the fidelity of the entanglement and the measurement rather than a true test of nonlocality. Nevertheless, various schemes exist to further separate the two modes, such as converting the cavity fields into itinerant microwave signals and/or optical photons (*23*).

Compared with other experimentally realized quantum states of two harmonic oscillators, a striking property of the two-mode cat state is that its underlying compositions are highly distinguishable. Two-mode squeezed states in various physical implementations—e.g. (*24*)—show strong entanglement but are Gaussian states without the Wigner negativity and the phase space separation, as in a cat state. Generation of the "*N*00*N*" state, an entangled state in the discrete Fock state basis, typically requires quantum

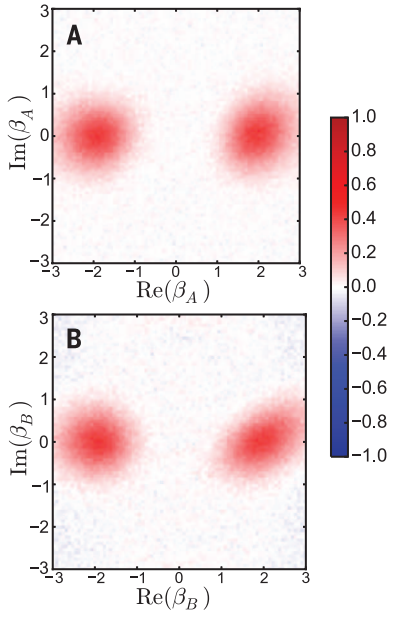


Fig. 2. Wigner tomography of individual cavities. Measured scaled Wigner function of (**A**) Alice $[\frac{\pi}{2}W_A(\beta_A)]$ and (**B**) Bob $[\frac{\pi}{2}W_B(\beta_B)]$, respectively, for the two-mode cats state $|\psi_-\rangle$, each plotted in the complex plane of $\mathrm{Re}(\beta_i)$ and $\mathrm{Im}(\beta_i)$ (i = *A* or *B*). For either cavity, the lack of interference fringes indicates a statistical mixture of two coherent states, in striking contrast to the regular (single-mode) cat state that can also be straightforwardly generated in our experiment (*14*). The distortion of the coherent states is due to higher-order Hamiltonian terms (*14*). The photon number parity within each cavity is close to 0, reflected by the value of respective Wigner functions near the origin.

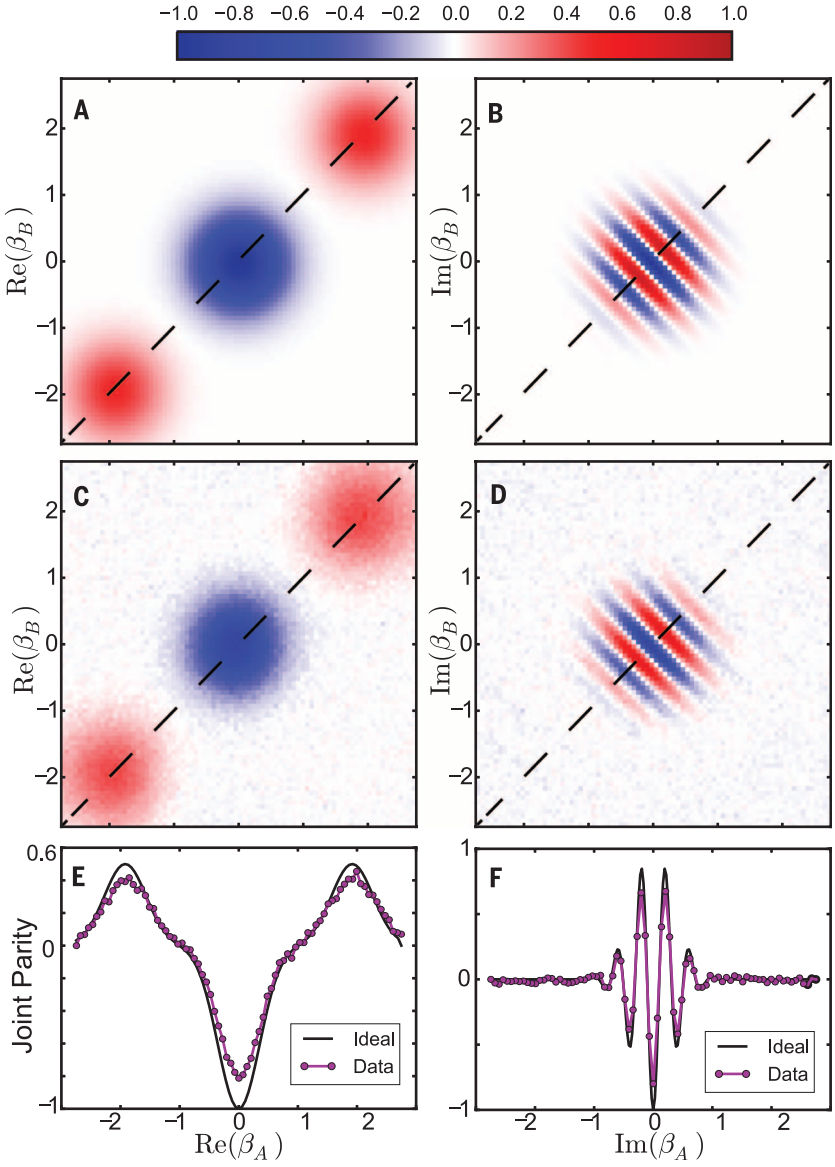


Fig. 3. Joint Wigner tomography. (**A** and **B**) A 2D plane-cut along (A) axes $\mathrm{Re}(\beta_A)$-$\mathrm{Re}(\beta_B)$ and (B) axes $\mathrm{Im}(\beta_A)$-$\mathrm{Im}(\beta_B)$ of the calculated 4D scaled joint Wigner function $P_J(\beta_A, \beta_B)$ of the ideal odd-parity two-mode cat state $|\psi_-\rangle$ with $\alpha = 1.92$. The red features in (A) represent the probability distribution of the two coherent states components. The central blue feature in (A) and fringes in (B) demonstrate quantum interference between the two components. (**C** and **D**) The corresponding $\mathrm{Re}(\beta_A)$-$\mathrm{Re}(\beta_B)$ and $\mathrm{Im}(\beta_A)$-$\mathrm{Im}(\beta_B)$ plane-cuts of the measured $P_J(\beta_A, \beta_B)$ of $|\psi_-\rangle$, to be compared with the ideal results in (A) and (B), respectively. Data are taken in an 81 by 81 grid, where every point represents an average of about 2000 binary outcomes of joint parity measurements. (**E**) Diagonal line-cuts of the data shown in (A) and (C), corresponding to 1D plots of the calculated (black) and measured (purple) scaled joint Wigner function along $\mathrm{Re}(\beta_A) = \mathrm{Re}(\beta_B)$ with $\mathrm{Im}(\beta_A) = \mathrm{Im}(\beta_B) = 0$. (**F**) Diagonal line-cuts of the data shown in (B) and (D), corresponding to 1D plots of the calculated (black) and measured (purple) scaled joint Wigner function along $\mathrm{Im}(\beta_A) = \mathrm{Im}(\beta_B)$, with $\mathrm{Re}(\beta_A) = \mathrm{Re}(\beta_B) = 0$.

Downloaded from http://science.sciencemag.org/ on May 26, 2016

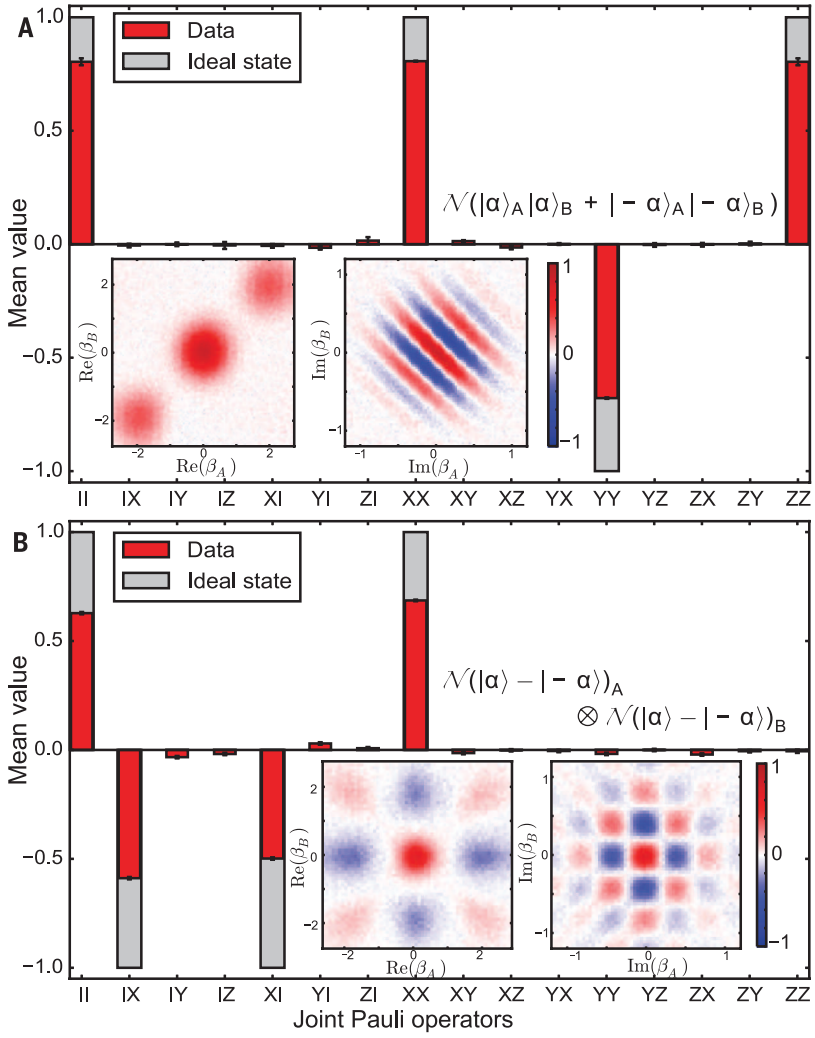


Fig. 4. Encoded two-qubit tomography. (**A**) Red bars show tomography of two logical qubits encoded in the coherent state basis of two cavities, with the prepared state being an even-parity two-mode cat state, $|\psi_+\rangle$ with $\alpha = 1.92$. Gray bars represent the ideal state. Insets show the $\mathrm{Re}(\beta_A)$-$\mathrm{Re}(\beta_B)$ and $\mathrm{Im}(\beta_A)$-$\mathrm{Im}(\beta_B)$ plane-cuts of the measured scaled joint Wigner function of the same state. (**B**) Encoded two-qubit tomography of an approximate product state of single-cavity cat states, $N(|\alpha\rangle_A - |-\alpha\rangle_A) \otimes N(|\alpha\rangle_B - |-\alpha\rangle_B)$, also with $\alpha = 1.92$. Insets show plane-cuts of the measured P_J of the same state. These Wigner function patterns can be understood by considering $W_J(\beta_A, \beta_B) = W_A(\beta_A)W_B(\beta_B)$ for separable states. For example, the checkerboard patterns in the $\mathrm{Im}(\beta_A)$-$\mathrm{Im}(\beta_B)$ plane-cuts arise from multiplying orthogonal fringes from the two independent cat states.

operations of photons one by one and so far has been limited to five photons (*25*, *26*). The two components of the cat state shown here are separated by a distance of $\sqrt{30}$ in the 4D phase space, giving a cat size (*5*) of 30 photons. Our technique in principle allows generation of two-mode cat states with arbitrary size. So far, we have measured cat sizes of up to 80 photons (*14*), and more macroscopic states can be achieved by implementing numerically optimized control pulses.

Compared with single-cavity quantum states, the addition of the second cavity mode increases the quantum information capacity significantly. Despite the modest mean photon numbers, a full tomography of the two-mode cat state (partly shown in Fig. 3) requires a Hilbert space of at least 100 dimensions to be described (capturing 99% of the population), comparable to a six- or seven-qubit Greenberger-Horne-Zeilinger (GHZ) state. Our conservatively estimated quantum state fidelity is comparable to that reported for an eight-qubit GHZ state in trapped ions (*10*) and the largest GHZ state in superconducting circuits (five qubits) (*11*).

An important motivation for creating multicavity cat states is to implement a promising paradigm toward fault-tolerant quantum computation (*7*, *8*), where information is redundantly encoded in the quasi-orthogonal coherent state basis (*6*). This approach has recently led to the first realization of quantum error correction of a logical qubit achieving the break-even point (*9*). In this context, our experiment realizes an architecture of two coupled logical qubits, where the coherent states $|\pm\alpha\rangle$ in each of the two cavities represent $|0\rangle$ and $|1\rangle$ of a logical qubit. For any two-qubit logical state encoded in this subspace, we can perform efficient tomography without extensive measurement of the joint Wigner function. This is carried out by measuring $P_J(\beta_A, \beta_B)$ at 16 selected points (*14*). The encoded two-qubit tomography of a state $|\psi_+\rangle$ with $\alpha = 1.92$ is shown in Fig. 4A, providing a direct fidelity estimation (*27*) of $\frac{1}{4}(\langle\hat{I}\hat{I}\rangle + \langle\hat{X}\hat{X}\rangle - \langle\hat{Y}\hat{Y}\rangle + \langle\hat{Z}\hat{Z}\rangle) = 78\%$ against the ideal Bell state, surpassing the 50% bound for classical correlation. As a comparison, Fig. 4B illustrates a product state of single-mode cat states in Alice and Bob, equivalent to $|-X\rangle_A|-X\rangle_B$ in the logical space. For both states illustrated here, the two-qubit tomography suggests that errors within the encoded space are quite small. The reduced overall contrast, as indicated by the measured identity operator smaller than 1, can be attributed to the infidelity of the joint parity measurement and leakage from the code space (due to higher-order Hamiltonian terms).

We have demonstrated a Schrödinger's cat that lives in two cavities. This two-mode cat state is not only a manifestation of mesoscopic superposition and entanglement constructed from quasiclassical states (*15*) but also a resource for quantum metrology (*28*), quantum networks, and teleportation (*29*). Moreover, the demonstration of high-fidelity quantum control over the large two-cavity Hilbert space has important implications for continuous-variable-based quantum computation. The measurement of the joint photon number parity realized here is QND by design and will play a central role in quantum error correction (*7*, *9*, *19*) and facilitating concurrent remote entanglement (*30*) in a modular architecture of quantum computation.

REFERENCES AND NOTES

1. S. Haroche, *Rev. Mod. Phys.* **85**, 1083–1102 (2013).
2. D. J. Wineland, *Rev. Mod. Phys.* **85**, 1103–1114 (2013).
3. A. Ourjoumtsev, H. Jeong, R. Tualle-Brouri, P. Grangier, *Nature* **448**, 784–786 (2007).
4. M. Brune *et al.*, *Phys. Rev. Lett.* **77**, 4887–4890 (1996).
5. S. Deléglise *et al.*, *Nature* **455**, 510–514 (2008).
6. B. Vlastakis *et al.*, *Science* **342**, 607–610 (2013).
7. I. L. Chuang, D. W. Leung, Y. Yamamoto, *Phys. Rev. A* **56**, 1114–1125 (1997).
8. M. Mirrahimi *et al.*, *New J. Phys.* **16**, 045014 (2014).
9. N. Ofek, *et al.*, Quantum error correction that extends the lifetime of quantum information. http://arxiv.org/abs/1602.04768 (2016).
10. T. Monz *et al.*, *Phys. Rev. Lett.* **106**, 130506 (2011).
11. J. Kelly *et al.*, *Nature* **519**, 66–69 (2015).
12. L. Davidovich, A. Maali, M. Brune, J. M. Raimond, S. Haroche, *Phys. Rev. Lett.* **71**, 2360–2363 (1993).
13. A. Ourjoumtsev, F. Ferreyrol, R. Tualle-Brouri, P. Grangier, *Nat. Phys.* **5**, 189–192 (2009).
14. For additional information, see the supplementary materials on *Science* Online.
15. B. C. Sanders, *J. Phys. A: Math. Theor.* **45**, 244002 (2012).
16. P. Milman *et al.*, *Eur. Phys. J. D* **32**, 233–239 (2005).
17. H. Paik *et al.*, *Phys. Rev. Lett.* **107**, 240501 (2011).

Downloaded from http://science.sciencemag.org/ on May 26, 2016

18. M. Reagor *et al.*, A quantum memory with near-millisecond coherence in circuit QED. http://arxiv.org/abs/1508.05882 (2015).
19. M. H. Michael *et al.*, New class of quantum error-correcting codes for a bosonic mode. http://arxiv.org/abs/1602.00008 (2016).
20. Z. Leghtas *et al.*, *Phys. Rev. A* **87**, 042315 (2013).
21. P. Bertet *et al.*, *Phys. Rev. Lett.* **89**, 200402 (2002).
22. K. E. Cahill, R. J. Glauber, *Phys. Rev.* **177**, 1882–1902 (1969).
23. R. W. Andrews *et al.*, *Nat. Phys.* **10**, 321–326 (2014).
24. Z. Y. Ou, S. F. Pereira, H. J. Kimble, K. C. Peng, *Phys. Rev. Lett.* **68**, 3663–3666 (1992).
25. I. Afek, O. Ambar, Y. Silberberg, *Science* **328**, 879–881 (2010).
26. H. Wang *et al.*, *Phys. Rev. Lett.* **106**, 060401 (2011).
27. S. T. Flammia, Y.-K. Liu, *Phys. Rev. Lett.* **106**, 230501 (2011).
28. J. Joo, W. J. Munro, T. P. Spiller, *Phys. Rev. Lett.* **107**, 083601 (2011).
29. S. J. van Enk, O. Hirota, *Phys. Rev. A* **64**, 022313 (2001).
30. A. Roy, L. Jiang, A. D. Stone, M. Devoret, *Phys. Rev. Lett.* **115**, 150503 (2015).

ACKNOWLEDGMENTS

We thank A. Petrenko, Z. Leghtas, B. Vlastakis, W. Pfaff, M. Silveri, R. T. Brierley, and A. Roy for helpful discussions, and M. J. Hatridge and A. Narla for assistance on the parametric amplifier. This research was supported by the U.S. Army Research Office (W911NF-14-1-0011), NSF DMR-1301798, and the Multidisciplinary University Research Initiatives program (MURI) through the Air Force Office of Scientific Research (FA9550-14-1-0052). Facilities use was supported by the Yale Institute for Nanoscience and Quantum Engineering (YINQE), the Yale SEAS cleanroom, and the NSF (MRSECDMR 1119826). Y.Y.G. acknowledges support from a National Science Scholarship from Agency for Science, Technology, and Research (A*STAR) of Singapore.

SUPPLEMENTARY MATERIALS

www.sciencemag.org/content/352/6289/1087/suppl/DC1
Materials and Methods
Supplementary Text
Figs. S1 to S16
Tables S1 to S3
Movie S1
References (*31*–*49*)

20 January 2016; accepted 14 April 2016
10.1126/science.aaf2941

QUANTUM SIMULATION

Experimental reconstruction of the Berry curvature in a Floquet Bloch band

N. Fläschner,[1,2]* B. S. Rem,[1,2]* M. Tarnowski,[1] D. Vogel,[1] D.-S. Lühmann,[1] K. Sengstock,[1,2,3]† C. Weitenberg[1,2]

Topological properties lie at the heart of many fascinating phenomena in solid-state systems such as quantum Hall systems or Chern insulators. The topology of the bands can be captured by the distribution of Berry curvature, which describes the geometry of the eigenstates across the Brillouin zone. Using fermionic ultracold atoms in a hexagonal optical lattice, we engineered the Berry curvature of the Bloch bands using resonant driving and show a full momentum-resolved measurement of the ensuing Berry curvature. Our results pave the way to explore intriguing phases of matter with interactions in topological band structures.

Topology is a fundamental concept for our understanding of many fascinating systems, such as topological superconductors or topological insulators, which conduct only at their edges (*1*). The topology of the bulk band is quantified by the Berry curvature (*2*), the integral of which over the full Brillouin zone is a topological invariant called the Chern number. According to the bulk boundary correspondence principle, the Chern number determines the number of chiral conducting edge states (*1*). Although edge states have been directly observed in a variety of lattice systems—ranging from solid-state systems to photonic waveguides, and even coupled mechanical pendula (*3*–*7*)—the underlying Berry curvature as the central measure of topology is not easily accessible. In recent years, ultracold atoms in optical lattices have emerged as a platform with which to study topological band structures (*8*, *9*), and these systems have seen considerable experimental and theoretical progress. Whereas in condensed-matter systems, topological properties arise thanks to external magnetic fields or intrinsic spin-orbit coupling of the material, in cold atom systems they can be engineered by periodic driving analogous to illuminated graphene (*10*, *11*). The resulting Floquet system can have topological properties very different from those of the original system (*12*). The driving can, for example, be realized through lattice shaking (*13*–*17*) or Raman coupling (*18*–*20*) with high-precision control in a large parameter space. In particular, the driving can break time-reversal symmetry (*14*, *15*, *17*) and thus allows for engineering nontrivial topology (*17*, *19*). In quantum gas experiments, topological properties have been probed via the Hall drift of accelerated wave packets (*17*, *19*), via an interferometer in momentum space (*21*, *22*), and via edge states (*23*, *24*), but so far, the full underlying Berry curvature was not measured quantitatively.

We measured the Berry curvature with full momentum resolution based on a method proposed in (*25*, *26*). We performed a full tomography of the Bloch states across the entire Brillouin zone by observing the dynamics at each momentum point after a projection onto flat bands. The topological bands were engineered through resonant dressing of the two lowest bands of an artificial boron nitride lattice and feature a rich distribution of Berry curvature. Other relevant quantities such as the Berry phase or the Chern number can easily be obtained from the Berry curvature, which is thus the central concept for the description of topology.

Our system consists of ultracold fermionic atoms in a hexagonal optical lattice (*27*) formed by three interfering laser beams. With an appropriate polarization (*28*), a variable energy offset $h\Delta_{AB}$ between the A and B sites (Fig. 1A), which breaks inversion symmetry, can be engineered. With the emerging band gap hw_{AB}, the Dirac points at K and K′ become massive, and for a large offset, the bands are flat (Fig. 1B) (*28*). This is a key ingredient for our tomography, because the flat band acts as the reference frame in which we reconstruct the eigen states. Then as a central experimental method, we could accelerate the lattice on circular trajectories in real space by modulating the phases of the three lattice beams, thus realizing circular shaking (*13*–*17*). When the shaking frequency is near resonant with respect to a band transition, the two bands couple and form two new dressed Floquet bands. In Fig. 1C, we show the dressed Floquet bands for different accessible driving amplitudes. Apart from the dramatic change in the dispersion relation, the topological properties of the bands are changed. This manifests itself in the creation of a new Dirac point at the Γ-point and the annihilation of a Dirac point at the K point (Fig. 1D). A threefold symmetry also becomes visible in the dispersion relation (Fig. 1E).

The topological properties are not captured by the mere dispersion relation but by the Berry curvature, which describes the winding of the eigenstates across the Brillouin zone. Therefore, a complete tomography of the eigenstates of a Bloch band is mandatory for a measurement of the Berry curvature. The key idea behind our tomography is to reconstruct the eigenvectors from dynamics after a projection onto flat bands (*26*). Consider the Bloch sphere (Fig. 2A), whose poles are given by $|\mathbf{k},A\rangle$ and $|\mathbf{k},B\rangle$, which are the Bloch states restricted to the A and B sublattice, respectively. The lower band can be written as $|\mathbf{k}\rangle = \sin(\theta_k/2)|\mathbf{k},A\rangle - \cos(\theta_k/2)\exp(i\phi_k)|\mathbf{k},B\rangle$, and after a projection onto flat bands, the state oscillates around $|\mathbf{k},B\rangle$, with the frequency v_k

[1]Institut für Laserphysik (ILP), Universität Hamburg, Luruper Chaussee 149, 22761 Hamburg, Germany. [2]Hamburg Centre for Ultrafast Imaging, Luruper Chaussee 149, 22761 Hamburg, Germany. [3]Zentrum für Optische Quantentechnologien (ZOQ), Universität Hamburg, Luruper Chaussee 149, 22761 Hamburg, Germany.
*These authors contributed equally to this work. †Corresponding author. Email: klaus.sengstock@physnet.uni-hamburg.de

Downloaded from http://science.sciencemag.org/ on May 26, 2016

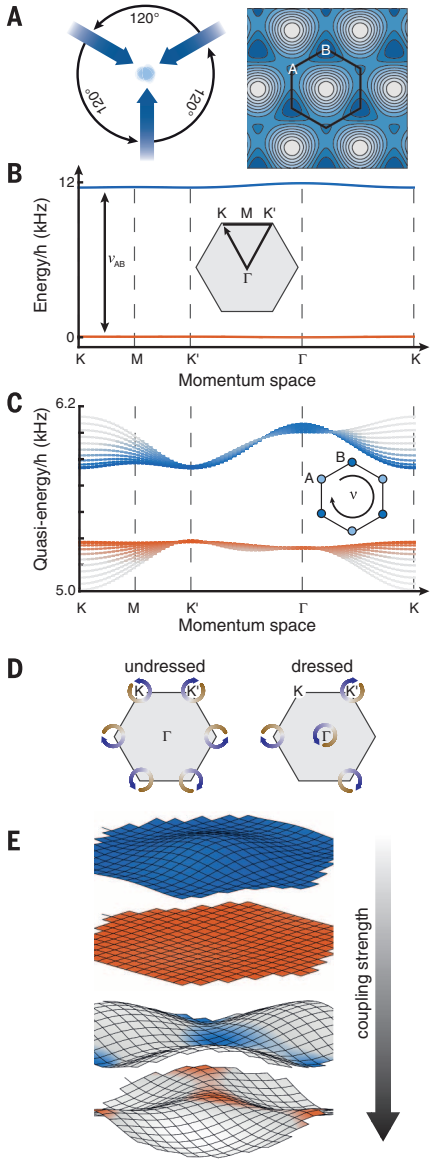


Fig. 1. Engineering of the topology by band dressing. (**A**) Three laser beams intersecting at 120° angles interfere to form a tunable honeycomb lattice (*28*) with a variable offset energy $h\Delta_{AB}$ between A and B sites. (**B**) Red and blue lines indicate the two lowest bands of the honeycomb lattice plotted along a high-symmetry path (K, M, K′, Γ, and K). (**C**) Circular shaking of the lattice (inset) with frequency ν resonantly ($\nu \approx \nu_{AB}$) couples the two bands from (B). The lattice is accelerated along a circular trajectory, thus breaking time-reversal symmetry. Shown are dressed Floquet bands for different shaking amplitudes between 0 and 223 nm at a shaking frequency of ν = 11 kHz. The dressed bands are calculated by use of Floquet theory (*28*). (**D**) Sketch of the position of the topological defects in the undressed and dressed cases, illustrating the dramatic change of the topology. The arrow indicates the direction of the phase winding around the Dirac point. (**E**) Two-dimensional dispersion relations of the bare and dressed bands showing, respectively, a six- and threefold symmetry. In (C) and (E), the fading of the color represents the dressing (less color corresponds to stronger dressing).

given by the energy difference of the flat bands. Then, the momentum distribution after time-of-flight is given by

$$n(\mathbf{k},t) = f(\mathbf{k})[1 - \sin(\theta_k)\cos(\phi_k + 2\pi v_k t)] \quad (1)$$

from which both θ_k and ϕ_k can be easily obtained, yielding the desired tomography of the eigenstates for each quasimomentum. The method we use hence allows for a direct reconstruction of the Berry curvature according to

$$\Omega(\mathbf{k}) = \frac{1}{2}(\partial_{k,x}\hat{\mathbf{h}} \times \partial_{k,y}\hat{\mathbf{h}}) \cdot \hat{\mathbf{h}} \quad (2)$$

with $\hat{\mathbf{h}} = [\sin(\theta_k)\cos(\phi_k), \sin(\theta_k)\sin(\phi_k), \cos(\theta_k)]$ (*26*). Our experimental sequence for this state tomography is sketched in Fig. 2. We start with a

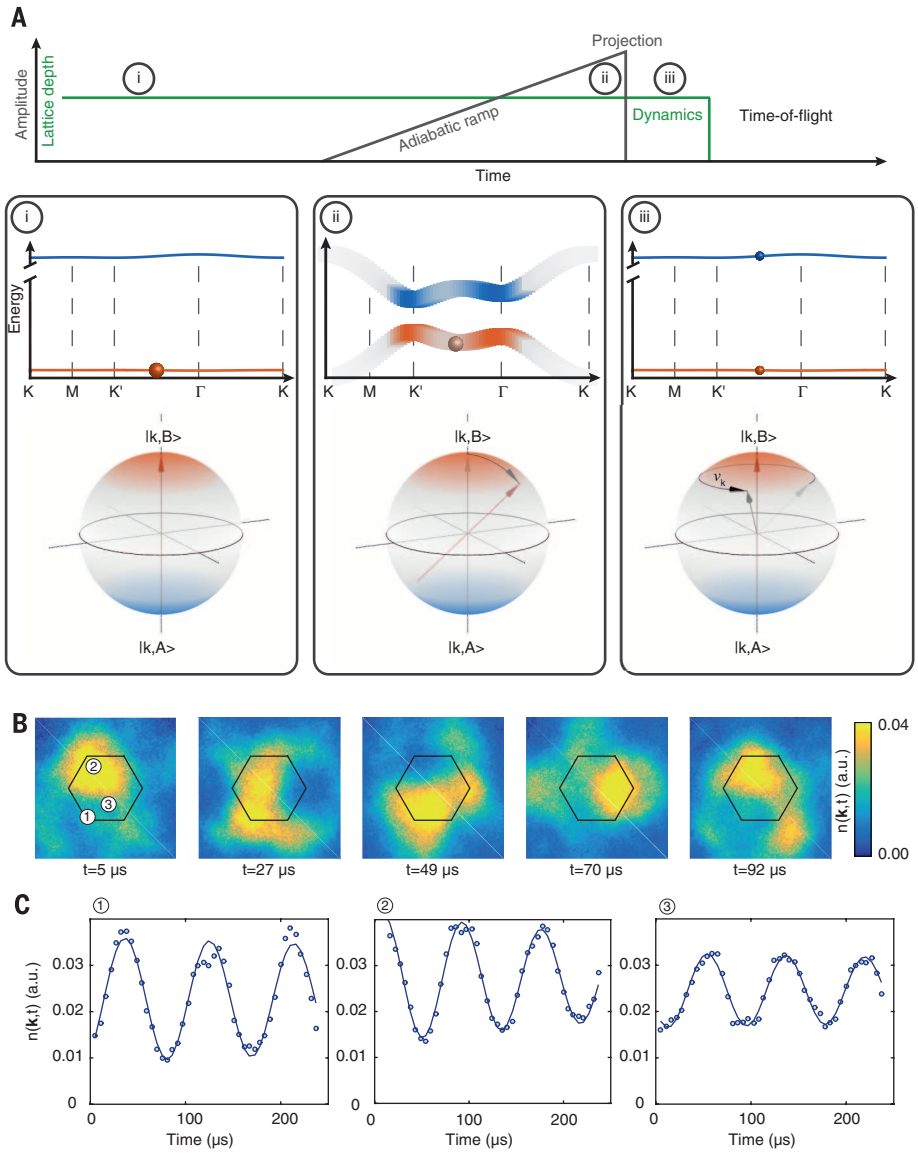


Fig. 2. Dynamical measurement of the topology of the dressed bands. (**A**) Illustration of the experimental protocol. (i) We start in a band insulator in the lowest undressed band and (ii) adiabatically ramp up the coupling strength (shaking amplitude). Now the Bloch state at each quasimomentum is a superposition of $|\mathbf{k},A\rangle$ and $|\mathbf{k},B\rangle$, pointing in different directions on the Bloch sphere. (iii) When the dressing is switched off, the state is projected onto the flat bands and rotates on the Bloch sphere with the band difference ν_k. After time-of-flight, this yields an oscillation of the density at each momentum. (**B**) Experimental momentum distributions for different hold times after the projection onto flat bands. The color is the atomic density in momentum space (after time-of-flight), and the hexagon marks the first Brillouin zone. The oscillations of the density at different momenta stem from interference of the two bands (Eq. 1). (**C**) Oscillations at different quasimomenta. The solid lines are sinusoidal fits. From the amplitude and phase of the oscillation, we reconstruct the dressed state according to Eq. 1. The experimental parameters are V_l = 15.15(15)E_r, ν_{AB} = 11.65(11) kHz, ν = 11 kHz, and a shaking amplitude of 223 nm (*28*). $E_r = h^2/2m\lambda^2$ = 4.41 kHz is the recoil energy, where λ = 1064 nm is the lattice wavelength and m is the atomic mass of ^{40}K. The lattice depth V_l is defined in (*28*).

Downloaded from http://science.sciencemag.org/ on May 26, 2016

cloud of 5×10^4 single-component fermionic ^{40}K atoms forming a noninteracting band insulator in the undressed lattice. Thanks to a large offset between the A and B sites, leading to a band gap of ν_{AB} = 11.65(11) kHz, the undressed bands are flat, so that for all quasimomenta $|\mathbf{k}\rangle \approx |\mathbf{k}, B\rangle$. We adiabatically ramped up the shaking amplitude to 223 nm within 5 ms at a shaking frequency of v = 9 kHz and then ramped the frequency to v = 11 kHz within 2 ms. By suddenly switching off the dressing, we projected onto the bare flat bands, so that Eq. 1 can be applied. In Fig. 2B, we show typical time-of-flight images for different hold times in the flat bands. The images feature dynamics with very large contrast. Time evolutions for different quasimomenta are shown in Fig. 2C, revealing the pure sinusoidal oscillations with clearly distinct amplitudes $\sin(\theta_k)$ and phases ϕ_k, which are obtained by a simple fit to Eq. 1. We observed very large and long-lived oscillations after the projection, yielding relative amplitudes of up to 0.8. Additionally, with more than 2800 pixels in the first Brillouin zone, the resolution in momentum space is very high.

As the central result, we reconstructed the Berry curvature of the dressed band structure from these fits, which fully visualize the Bloch states (Fig. 3A). The amplitude map features a pronounced threefold symmetry, illustrating the breaking of equivalence between the K and K′ points. The amplitude has a maximum at the K point and is zero at the K′ and Γ points. Even more striking is the very distinct threefold symmetry of the phase map with nearly discrete values of 0, $2\pi/3$, and $4\pi/3$. Where the amplitudes are zero at the K′ and Γ points, the phase map correspondingly displays vortices. The phase vortices are clear signatures of Dirac points, which constitute topological defects. Furthermore, the data clearly show that we annihilated the Dirac point of the undressed hexagonal lattice at K and created a Dirac point in the dressed system at the Γ point, changing the topology of the band. The resulting Berry curvature is localized at the new Dirac points and also shows this clear threefold symmetry. It has opposite signs at the two Dirac points, which results from the opposite chirality of the phase vortices. By inverting the chirality of the shaking, we instead annihilated the Dirac point at the K′ point and inverted the chirality of the phase windings, which also resulted in an inverted symmetry in the Berry curvature. All quantities agree well with a Floquet theory calculation (Fig. 3B), based on a tight-binding model as described in (*28*). In Fig. 3C, we plot the Berry curvature pixelwise evaluated along a high-symmetry path, illustrating the very good agreement with the theory.

As mentioned above, with the fully momentum-resolved Berry curvature, we can easily obtain the further relevant quantities such as the Berry phase or Chern number. A discussion of the respective Berry phases is available in (*28*). The integral over the closed area of the full first Brillouin zone must be quantized to 2π times the integer Chern number C. From our data, we obtain C = 0.005(6) and C = −0.016(8) for the two different shaking

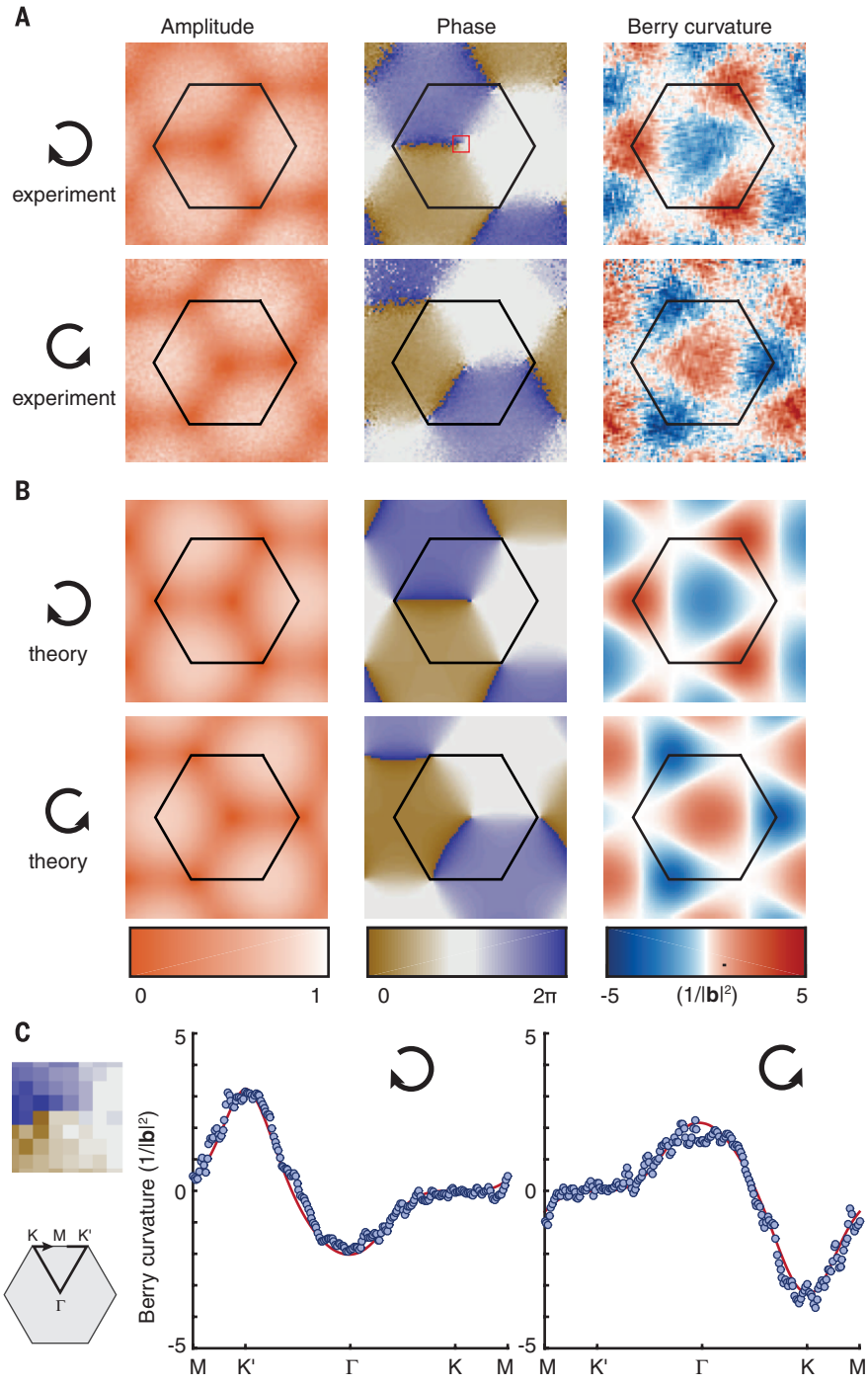


Fig. 3. Momentum-resolved measurement of the Berry curvature. (**A**) Amplitude (left column) and phase (middle column) obtained from the fits to the oscillations from Fig. 2, performed for each pixel in and around the first Brillouin zone (hexagon). From those fit results, we obtain, as our central result, the momentum-resolved Berry curvature (right column). The experiment was performed for different chiralities of the lattice shaking, destroying the Dirac point at either K (top) or K′ (bottom). (**B**) Theoretical results from a tight-binding Floquet calculation (*28*) by using the experimental parameters, yielding a very good agreement. (**C**) (Top left) A detailed view of a phase vortex [(A), red square], illustrating the high momentum resolution of our method. The plots show the experimental Berry curvature (blue points) along the high-symmetry path in comparison with the theoretical calculation (red solid lines). In (B) and (C), the Berry curvature is given in units of the inverse reciprocal lattice vector length $|\mathbf{b}|$ squared (*28*).

Downloaded from http://science.sciencemag.org/ on May 26, 2016

chiralities (*28*), which clearly confirms this quantization within the experimental errors. Our measurements demonstrate that even when the global topology has Chern number zero, the distribution of Berry curvature can be very rich.

Our measurement scheme can be readily extended to characterize bands with Chern numbers different from zero (*17*, *19*). In principle, one could start in a shallow lattice, where reaching nonzero Chern numbers is feasible, and for the tomography project onto flat bands, which can be reached, such as by dynamical control over the offset. Our method for generating the topological bands is spin-independent and does not couple different spin states. It therefore can be extended to high-spin systems (*29*) or to strongly interacting spin mixtures, which are expected to lead to interesting many-body phases (*30*–*32*).

REFERENCES AND NOTES

1. M. Z. Hasan, C. L. Kane, *Rev. Mod. Phys.* **82**, 3045–3067 (2010).
2. D. Xiao, M.-C. Chang, Q. Niu, *Rev. Mod. Phys.* **82**, 1959–2007 (2010).
3. M. Hafezi, S. Mittal, J. Fan, A. Migdall, J. M. Taylor, *Nat. Photonics* **7**, 1001–1005 (2013).
4. M. C. Rechtsman *et al.*, *Nature* **496**, 196–200 (2013).
5. Z. Wang, Y. Chong, J. D. Joannopoulos, M. Soljačić, *Nature* **461**, 772–775 (2009).
6. J. Ningyuan, C. Owens, A. Sommer, D. Schuster, J. Simon, *Phys. Rev. X* **5**, 021031 (2015).
7. R. Süsstrunk, S. D. Huber, *Science* **349**, 47–50 (2015).
8. N. Goldman, J. Dalibard, *Phys. Rev. X* **4**, 031027 (2014).
9. T. Kitagawa, E. Berg, M. Rudner, E. Demler, *Phys. Rev. B* **82**, 235114 (2010).
10. T. Oka, H. Aoki, *Phys. Rev. B* **79**, 081406 (2009).
11. E. J. Sie *et al.*, *Nat. Mater.* **14**, 290–294 (2015).
12. M. Bukov, L. D'Alessio, A. Polkovnikov, *Adv. Phys.* **64**, 139–226 (2015).
13. H. Lignier *et al.*, *Phys. Rev. Lett.* **99**, 220403 (2007).
14. J. Struck *et al.*, *Phys. Rev. Lett.* **108**, 225304 (2012).
15. J. Struck *et al.*, *Nat. Phys.* **9**, 738–743 (2013).
16. C. V. Parker, L.-C. Ha, C. Chin, *Nat. Phys.* **9**, 769–774 (2013).
17. G. Jotzu *et al.*, *Nature* **515**, 237–240 (2014).
18. Y.-J. Lin, K. Jiménez-García, I. B. Spielman, *Nature* **471**, 83–86 (2011).
19. M. Aidelsburger *et al.*, *Nat. Phys.* **11**, 162–166 (2015).
20. C. J. Kennedy, W. C. Burton, W. C. Chung, W. Ketterle, *Nat. Phys.* **11**, 859–864 (2015).
21. L. Duca *et al.*, *Science* **347**, 288–292 (2015).
22. T. Li *et al.*, arXiv:1509.02185 (2015).
23. M. Mancini *et al.*, *Science* **349**, 1510–1513 (2015).
24. B. K. Stuhl, H.-I. Lu, L. M. Aycock, D. Genkina, I. B. Spielman, *Science* **349**, 1514–1518 (2015).
25. E. Alba, X. Fernandez-Gonzalvo, J. Mur-Petit, J. K. Pachos, J. J. Garcia-Ripoll, *Phys. Rev. Lett.* **107**, 235301 (2011).
26. P. Hauke, M. Lewenstein, A. Eckardt, *Phys. Rev. Lett.* **113**, 045303 (2014).
27. P. Soltan-Panahi *et al.*, *Nat. Phys.* **7**, 434–440 (2011).
28. Materials and methods are available as supplementary materials on *Science* Online
29. J. S. Krauser *et al.*, *Science* **343**, 157–160 (2014).
30. T. Neupert, L. Santos, C. Chamon, C. Mudry, *Phys. Rev. Lett.* **106**, 236804 (2011).
31. A. G. Grushin, Á. Gómez-León, T. Neupert, *Phys. Rev. Lett.* **112**, 156801 (2014).
32. N. R. Cooper, J. Dalibard, *Phys. Rev. Lett.* **110**, 185301 (2013).

ACKNOWLEDGMENTS

We acknowledge stimulating discussions with A. Eckardt, M. Lewenstein, L. Mathey, and C. Sträter. This work has been supported by the excellence cluster "The Hamburg Centre for Ultrafast Imaging—Structure, Dynamics and Control of Matter at the Atomic Scale" and the GrK 1355 of the Deutsche Forschungsgemeinschaft.

SUPPLEMENTARY MATERIALS

www.sciencemag.org/content/352/6289/1091/suppl/DC1
Supplementary Text
Figs. S1 and S2
References (*33*–*36*)

18 September 2015; accepted 23 March 2016
10.1126/science.aad4568

QUANTUM SIMULATION

Bloch state tomography using Wilson lines

Tracy Li,[1,2] Lucia Duca,[1,2] Martin Reitter,[1,2] Fabian Grusdt,[3,4,5] Eugene Demler,[5] Manuel Endres,[5,6] Monika Schleier-Smith,[7] Immanuel Bloch,[1,2] Ulrich Schneider[1,2,8]*

Topology and geometry are essential to our understanding of modern physics, underlying many foundational concepts from high-energy theories, quantum information, and condensed-matter physics. In condensed-matter systems, a wide range of phenomena stem from the geometry of the band eigenstates, which is encoded in the matrix-valued Wilson line for general multiband systems. Using an ultracold gas of rubidium atoms loaded in a honeycomb optical lattice, we realize strong-force dynamics in Bloch bands that are described by Wilson lines and observe an evolution in the band populations that directly reveals the band geometry. Our technique enables a full determination of band eigenstates, Berry curvature, and topological invariants, including single- and multiband Chern and Z_2 numbers.

Geometric concepts play an increasingly important role in elucidating the behavior of condensed-matter systems. In band structures without degeneracies, the geometric phase acquired by a quantum state during adiabatic evolution elegantly describes a spectrum of phenomena (*1*). This geometric phase— known as the Berry phase— is used to formulate the Chern number (*2*), which is the topological invariant characterizing the integer quantum Hall effect (*3*). However, condensed-matter properties that are determined by multiple bands with degeneracies, such as in topological insulators (*4*, *5*) and graphene (*6*), can seldom be understood with standard Berry phases. Recent work has shown that such systems can instead be described using Wilson lines (*7*–*10*).

Wilson lines encode the geometry of degenerate states (*11*), providing indispensable information for the ongoing effort to identify the topological structure of bands. For example, the eigenvalues of Wilson-Zak loops (i.e., Wilson lines closed by a reciprocal lattice vector) can be used to formulate the Z_2 invariant of topological insulators (*7*) and identify topological orders protected by lattice symmetries (*8*, *9*). Although experiments have accessed the geometry of isolated bands through various methods, including transport measurements (*3*, *12*, *13*), interferometry (*14*, *15*), and angle-resolved photoemission spectroscopy (*5*, *16*), Wilson lines have thus far remained a theoretical construct (*7*–*10*).

[1]Fakultät für Physik, Ludwig-Maximilians-Universität München, Schellingstrasse 4, 80799 Munich, Germany. [2]Max-Planck-Institut für Quantenoptik, Hans-Kopfermann-Str. 1, 85748 Garching, Germany. [3]Department of Physics and Research Center OPTIMAS, University of Kaiserslautern, Germany. [4]Graduate School Materials Science in Mainz, Gottlieb-Daimler-Strasse 47, 67663 Kaiserslautern, Germany. [5]Department of Physics, Harvard University, Cambridge, MA 02138, USA. [6]Institute for Quantum Information and Matter, Department of Physics, California Institute of Technology, Pasadena, CA 91125, USA. [7]Department of Physics, Stanford University, Stanford, CA 94305, USA. [8]Cavendish Laboratory, University of Cambridge, J. J. Thomson Avenue, Cambridge CB3 0HE, UK.
***Corresponding author. Email: uws20@cam.ac.uk**

Using ultracold atoms in a graphene-like honeycomb lattice, we demonstrate that Wilson lines can be accessed and used as versatile probes of band structure geometry. Whereas the Berry phase merely multiplies a state by a phase factor, the Wilson line is a matrix-valued operator that can mix state populations (*11*) (Fig. 1A). We measure the Wilson line by detecting changes in the band populations (*17*) under the influence of an external force, which transports atoms through reciprocal space (*18*). In the presence of a force $\mathbf{F}$, atoms with initial quasimomentum $\mathbf{q}(0)$ evolve to quasimomentum $\mathbf{q}(t) = \mathbf{q}(0) + \mathbf{F}t/h$ after a time t. If the force is sufficiently weak and the bands are nondegenerate, the system will undergo adiabatic Bloch oscillations and remain in the lowest band (*18*). In this case, the quantum state merely acquires a phase factor composed of the geometric Berry phase and a dynamical phase. At stronger forces, however, transitions to other bands occur, and the state evolves into a superposition over several bands.

When the force is infinite with respect to a chosen set of bands, the effect of the dispersion vanishes, and the bands appear as effectively degenerate (Fig. 1B). The system then evolves according to the formalism of Wilczek and Zee for adiabatic motion in a degenerate system (*11*). The unitary time-evolution operator describing the dynamics is the Wilson line matrix (*19*)

$$\hat{\mathbf{W}}_{\mathbf{q}(0)\to\mathbf{q}(t)} = \mathcal{P}\exp[i\int_{\mathcal{C}} d\mathbf{q}\hat{\mathbf{A}}_{\mathbf{q}}] \qquad (1)$$

where the path-ordered ($\mathcal{P}$) integral runs over the path $\mathcal{C}$ in reciprocal space from $\mathbf{q}(0)$ to $\mathbf{q}(t)$ and $\hat{\mathbf{A}}_{\mathbf{q}}$ is the Wilczek-Zee connection, which encodes the local geometric properties of the state space.

In a lattice system with Bloch states $|\Phi_{\mathbf{q}}^n\rangle = e^{i\mathbf{q}\cdot\hat{\mathbf{r}}}|u_{\mathbf{q}}^n\rangle$ in the nth band at quasimomentum $\mathbf{q}$, where $\hat{\mathbf{r}}$ is the position operator, the elements of the Wilczek-Zee connection are determined by the cell-periodic part $|u_{\mathbf{q}}^n\rangle$ as $\mathbf{A}_{\mathbf{q}}^{n,n'} = i\langle u_{\mathbf{q}}^n|\nabla_{\mathbf{q}}|u_{\mathbf{q}}^{n'}\rangle$. The diagonal elements ($n = n'$) are the Berry connections of the individual Bloch bands, which yield the Berry phase when integrated along a

Downloaded from http://science.sciencemag.org/ on May 26, 2016

closed path. The off-diagonal elements ($n \neq n'$) are the interband Berry connections, which couple the bands and induce interband transitions.

Although the evolution described by Eq. 1 must be path-ordered when the Wilczek-Zee connections at different quasimomenta do not commute, it can also be path-independent under certain circumstances (*9*, *20*). For example, when the relevant bands span the same Hilbert space for all quasimomenta, as is the case in our system, the Wilson line operator describing transport of a Bloch state from $\mathbf{Q}$ to $\mathbf{q}$ reduces to $\hat{\mathbf{W}}_{\mathbf{Q}\to\mathbf{q}} = e^{i(\mathbf{q}-\mathbf{Q})\cdot\hat{\mathbf{r}}}$ (*9*, *19*, *21*)). Consequently, the elements of the Wilson line operator simply measure the overlap between the cell-periodic Bloch functions at the initial and final quasimomenta (*9*, *21*)

$$W^{mn}_{\mathbf{Q}\to\mathbf{q}} = \langle \Phi^m_{\mathbf{q}} | e^{i(\mathbf{q}-\mathbf{Q})\cdot\hat{\mathbf{r}}} | \Phi^n_{\mathbf{Q}} \rangle = \langle u^m_{\mathbf{q}} | u^n_{\mathbf{Q}} \rangle \quad (2)$$

Hence, access to the Wilson line elements facilitates the characterization of band structure topology in both path-dependent and path-independent evolution. In both cases, the topological information is encoded in the eigenvalues of the Wilson-Zak loops. In the latter case, the simplified form of the Wilson line in Eq. 2 additionally enables a map of the cell-periodic Bloch functions over the entire Brillouin zone (BZ) in the basis of the states $|u^n_{\mathbf{Q}}\rangle$ at the initial quasimomentum $\mathbf{Q}$.

We create the honeycomb lattice by interfering three blue-detuned laser beams at 120(1)° angles (Fig. 2A). At a lattice depth $V_0 = 5.2(1)E_r$, where $E_r = h^2/(2m\lambda_L^2)$ is the recoil energy, λ_L is the laser wavelength, and m is the mass of ^{87}Rb, the combined width $\varepsilon \approx h \times 3$ kHz of the lowest two bands is much smaller than the $h \times 15$ kHz gap to higher bands. Consequently, there exists a regime of forces where transitions to higher bands are suppressed, and the system is well approximated by a two-band model (*19*).

We probe the lattice geometry with a nearly pure Bose-Einstein condensate of ^{87}Rb, which is initially loaded into the lowest band at quasimomentum $\mathbf{q} = \Gamma$, the center of the BZ (Fig. 2B). To move the atoms in reciprocal space, we linearly sweep the frequency of the beams to uniformly accelerate the lattice, thereby generating a constant inertial force in the lattice frame. By independently controlling the frequency sweep rate of two beams (Fig. 2A), we can tune the magnitude and direction of the force and move the atoms along arbitrary paths in reciprocal space.

To verify that we can access the Wilson line regime, where the dynamics are governed entirely by geometric effects, we transport the atoms from Γ to different final quasimomenta using a variable force $|\mathbf{F}|$ and perform band-mapping (*17*) to measure the population remaining in the lowest band (Fig. 2C). For vanishing forces, we recover the adiabatic limit, where the population remains in the lowest band. For increasing forces (i and ii in Fig. 1B), where the gradient $|\mathbf{F}|d$ over the distance between A and B sites d is less than the combined width ε, the population continuously decreases. However, at strong forces (iii in Fig. 1B), where $|\mathbf{F}|d > \varepsilon$, the population saturates at a finite value. For example, after transport by one reciprocal lattice vector (blue data in Fig. 2C), about one-quarter of the atoms remain in the first band, in stark contrast to typical Landau-Zener dynamics, where the population vanishes for strong forces (*22*).

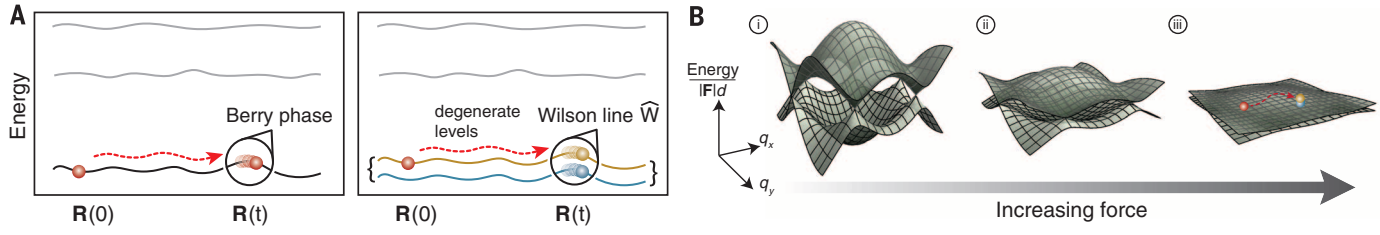
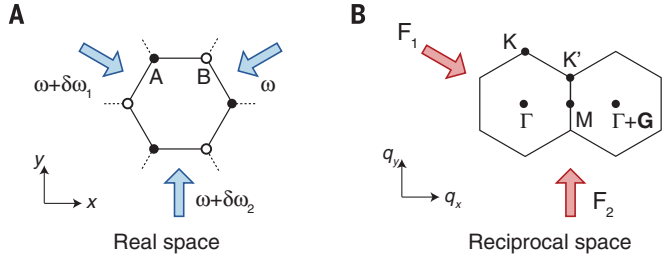


Fig. 1. Wilson lines and effectively degenerate Bloch bands. (**A**) In a nondegenerate system (left), adiabatic evolution of a state through parameter space $\mathbf{R}$ results in the acquisition of a geometric phase factor, known as the Berry phase. In a degenerate system (right), the evolution is instead governed by a matrix-valued quantity called the Wilson line. If the degenerate levels can be experimentally distinguished (blue and yellow coloring), then population changes between the levels are detectable. (**B**) The band structure of the lowest two bands of the honeycomb lattice is given in effective energy units of $|\mathbf{F}|d$, where $\mathbf{F}$ is the applied force used to transport the atoms and d is the distance between nearest-neighbor lattice sites. As $|\mathbf{F}|$ is increased, the largest energy scale of the bands becomes small compared to $|\mathbf{F}|d$. At large forces (iii), the effect of the band energies is negligible, and the system is effectively degenerate. In this regime, the evolution is governed by the Wilson line operator. We distinguish between the bands using a band-mapping technique that detects changes in the band population along the Wilson line path.



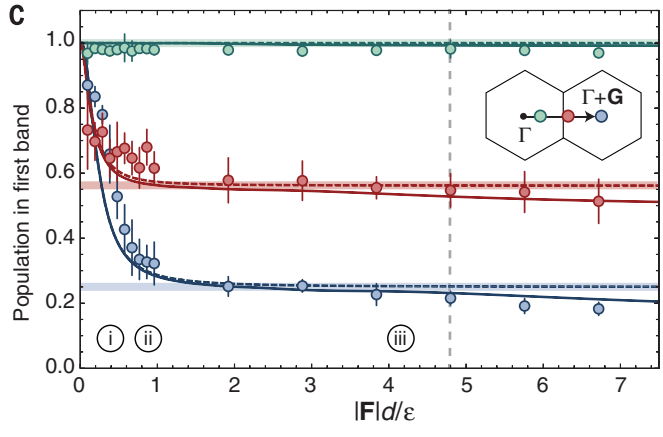


Fig. 2. Reaching the Wilson line regime in the honeycomb lattice. (**A**) Schematic of the honeycomb lattice in real space with A (B) sublattice sites denoted by solid (open) circles. The lattice is formed by interfering three in-plane laser beams (blue arrows) with frequency ω. Sweeping the frequency of beam i by $\delta\omega_i$ creates a force $\mathbf{F}_i$ in the lattice frame in the propagation direction of beam i (*19*). (**B**) Two copies of the first BZ of the honeycomb lattice, separated by a reciprocal lattice vector $\mathbf{G}$. By changing the relative strengths of $\mathbf{F}_i$ (red arrows), the atoms can be moved along arbitrary paths in reciprocal space. Each BZ features nonequivalent Dirac points K and K′ at the corners of the hexagonal cell. High-symmetry points Γ, at the center of the BZ, and M, at the edge of the BZ, are also shown. (**C**) The population remaining in the first band for different forces after transport to $\Gamma + 0.2\mathbf{G}$ (green), $\Gamma + 0.55\mathbf{G}$ (red), and $\Gamma + \mathbf{G}$ (blue). Inset numbers i to iii refer to band schematics in Fig. 1B, representing the diminishing effect of the dispersion for increasing force. The data agree well with a two-level, tight-binding model (dashed line) that approaches the Wilson line regime (thick shaded line) at large forces. Discrepancies at larger forces result from transfer to higher bands and match well with ab initio theory using a full band structure calculation including the first six bands (thin solid line) (*19*). For all subsequent data, we use $|\mathbf{F}|d/\varepsilon = 4.8$, indicated by the dashed gray line. Error bars indicate the standard error of the mean (SEM) from 10 shots per data point.

Downloaded from http://science.sciencemag.org/ on May 26, 2016

Theoretically, the population in the first band after the strong-force transport directly measures the Wilson line element $|W^{11}_{\Gamma\to\mathbf{q}}|^2 = |\langle\Phi^1_{\mathbf{q}}|\hat{\mathbf{W}}_{\Gamma\to\mathbf{q}}|\Phi^1_{\Gamma}\rangle|^2$ in the basis of the band eigenstates. Based on Eq. 2, the saturation value $|W^{11}_{\Gamma\to\mathbf{q}}|^2 = |\langle u^1_{\mathbf{q}}|u^1_{\Gamma}\rangle|^2$ of the population after transport to $\mathbf{q}$ is a measure of the overlap between the cell-periodic Bloch functions of the first band $|u^1_{\mathbf{q}}\rangle$ at Γ and $\mathbf{q}$. Notably, for the case of transport by one reciprocal lattice vector $\mathbf{G}$, the cell-periodic parts $|u^n_{\mathbf{q}}\rangle$ are not identical, despite the unity overlap of the Bloch states $|\Phi^n_{\mathbf{q}}\rangle$ at Γ and $\Gamma+\mathbf{G}$. In contrast to the typical Landau-Zener case, they are also not orthogonal—hence the finite saturation value.

To corroborate that our experiment measures the Wilson line, we transport atoms initially in the ground state at Γ by up to three reciprocal lattice vectors (Fig. 3). The threefold rotational symmetry of the lattice, combined with the symmetry of its s-orbitals, makes the path from Γ to $\Gamma+3\mathbf{G}$ equivalent to the triangular path shown in Fig. 3A, such that the overlap between cell-periodic components of the Bloch wave functions at the two endpoints is unity (see Eq. 2). Correspondingly, we expect to recover all the population in the lowest band after transport from Γ to $\Gamma+3\mathbf{G}$. This prediction is confirmed in Fig. 3B, where we plot the population remaining in the first band after transport to final quasimomentum $\mathbf{q}$. The data are well described by a tight-binding model that takes into account the relative phase between orbitals on A and B sites of the lattice due to the Wilson line $\hat{\mathbf{W}}_{\Gamma\to\mathbf{q}} = e^{i\mathbf{q}\cdot\hat{\mathbf{r}}}$. Physically, this can be understood by assuming that the real-space wave function simply accumulates a position-dependent phase when the strong force $\mathbf{F} = \hbar(\mathbf{q}-\mathbf{Q})/t$ is applied for a short time t (Fig. 3C). Notably, the result depends crucially on the real-space embedding of the lattice and would be different in, e.g., a brick-wall incarnation (*23*) of the same tight-binding model. Discrepancies from the tight-binding model result from population transfer to higher bands (*19*).

As the Wilson line enables a comparison of the cell-periodic Bloch functions at any two quasimomenta (Eq. 2), it can in principle be applied to fully reconstruct these states throughout reciprocal space. To this end, it is convenient to represent the state $|u^1_{\mathbf{q}}\rangle$ at quasimomentum $\mathbf{q}$ in the basis of cell-periodic Bloch functions

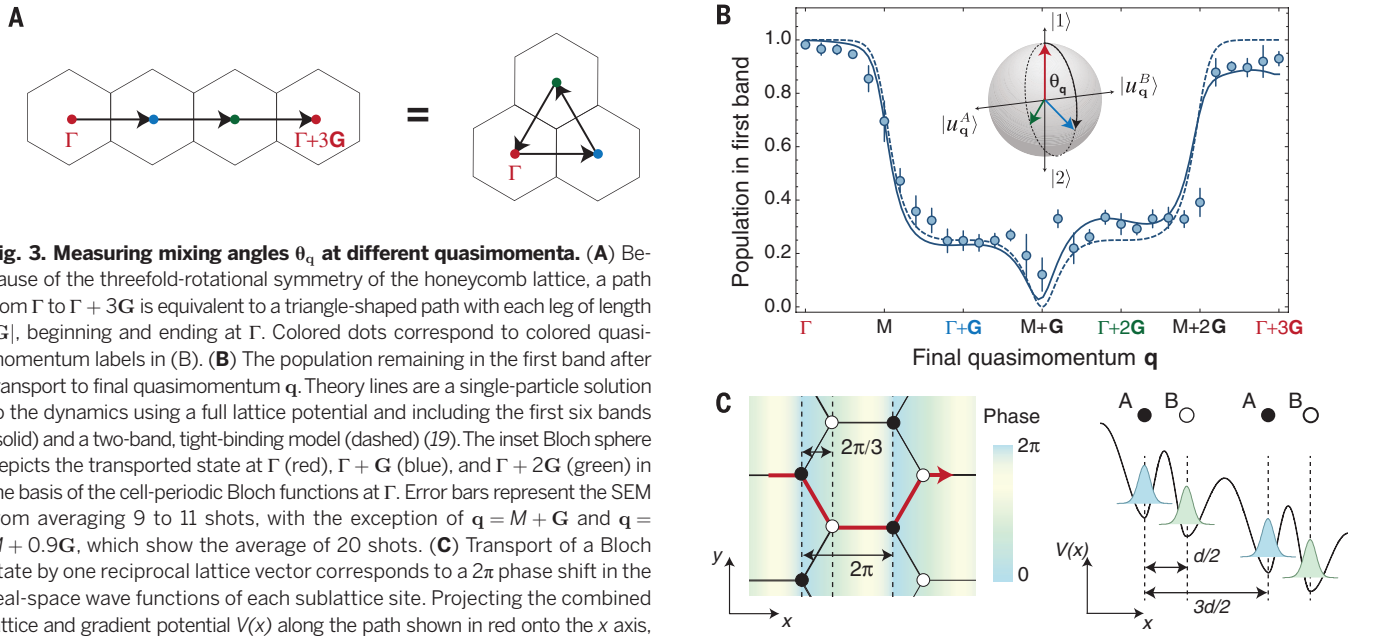


Fig. 3. Measuring mixing angles $\theta_{\mathbf{q}}$ at different quasimomenta. (**A**) Because of the threefold-rotational symmetry of the honeycomb lattice, a path from Γ to $\Gamma+3\mathbf{G}$ is equivalent to a triangle-shaped path with each leg of length $|\mathbf{G}|$, beginning and ending at Γ. Colored dots correspond to colored quasimomentum labels in (B). (**B**) The population remaining in the first band after transport to final quasimomentum $\mathbf{q}$. Theory lines are a single-particle solution to the dynamics using a full lattice potential and including the first six bands (solid) and a two-band, tight-binding model (dashed) (*19*). The inset Bloch sphere depicts the transported state at Γ (red), $\Gamma+\mathbf{G}$ (blue), and $\Gamma+2\mathbf{G}$ (green) in the basis of the cell-periodic Bloch functions at Γ. Error bars represent the SEM from averaging 9 to 11 shots, with the exception of $\mathbf{q}=M+\mathbf{G}$ and $\mathbf{q}=M+0.9\mathbf{G}$, which show the average of 20 shots. (**C**) Transport of a Bloch state by one reciprocal lattice vector corresponds to a 2π phase shift in the real-space wave functions of each sublattice site. Projecting the combined lattice and gradient potential $V(x)$ along the path shown in red onto the x axis, which is the direction of the applied force in the measurements of Figs. 2B and 3B, highlights the effect of the real-space embedding of the honeycomb lattice. Since the distance between A (solid circles) and B sites (open circles) is 1/3 the distance between sites of the same type, there is a phase difference of $2\pi/3$ between the real-space wave functions of A and B sites, which gives rise to the band mixing.

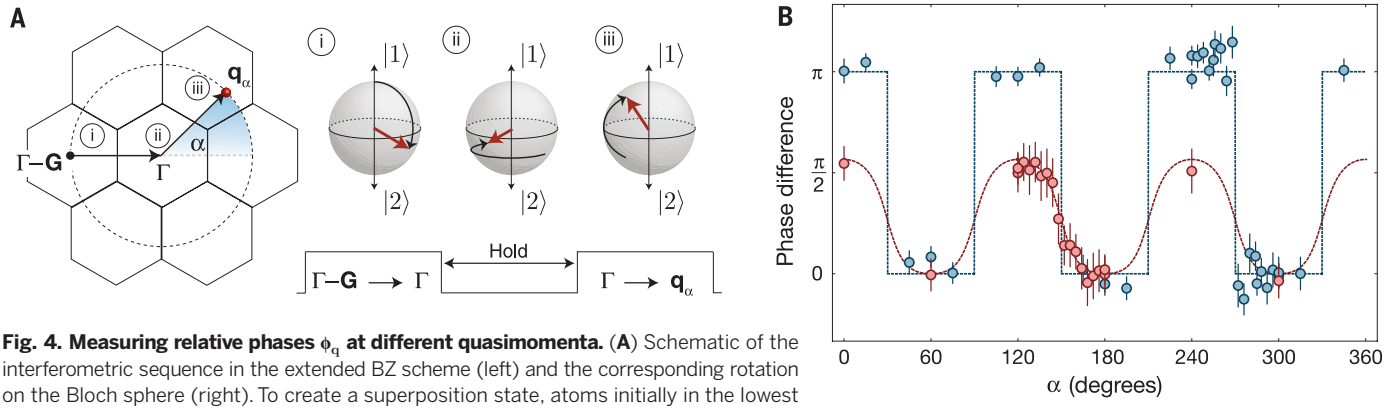


Fig. 4. Measuring relative phases $\phi_{\mathbf{q}}$ at different quasimomenta. (**A**) Schematic of the interferometric sequence in the extended BZ scheme (left) and the corresponding rotation on the Bloch sphere (right). To create a superposition state, atoms initially in the lowest eigenstate at $\Gamma-\mathbf{G}$ are rapidly transported to Γ (i). The phase of the superposition state is controlled by varying the hold time at Γ (ii). After the state preparation, the atoms are transported to a final quasimomentum $\mathbf{q}_\alpha$, which is parametrized by the angle α and lies on a circle of radius $|\mathbf{G}|$ centered at Γ (iii). (**B**) Phases ϕ_α referenced to $\alpha = 180°$ for the lattice with AB-site degeneracy (blue) and AB-site offset (red). Data in blue have been offset by +120° for visual clarity. Dashed lines are a two-band, tight-binding calculation with $\Delta/J = 0$ (blue) and $\Delta/J = 3.1$ (red), where $J = h \times 500(10)$ Hz. Error bars indicate fit errors.

Downloaded from http://science.sciencemag.org/ on May 26, 2016

$|1\rangle = |u^1_{\mathbf{Q}}\rangle$ and $|2\rangle = |u^2_{\mathbf{Q}}\rangle$ at a fixed reference quasimomentum $\mathbf{Q}$ as

$$|u^1_{\mathbf{q}}\rangle = \cos\frac{\theta_{\mathbf{q}}}{2}|1\rangle + \sin\frac{\theta_{\mathbf{q}}}{2}e^{i\phi_{\mathbf{q}}}|2\rangle \qquad (3)$$

Mapping out the geometric structure of the lowest band therefore amounts to obtaining $\theta_{\mathbf{q}}$ and $\phi_{\mathbf{q}}$, which parametrize the amplitude and phase of the superposition between the reference Bloch states, for each quasimomentum $\mathbf{q}$ (*24*, *25*). Whereas the total phase of $|u^1_{\mathbf{q}}\rangle$ is gauge dependent—i.e., it can be chosen for each $\mathbf{q}$—the relative phase $\phi_{\mathbf{q}}$ is fixed for all $\mathbf{q}$ once the basis states $|1\rangle$ and $|2\rangle$ are fixed. Throughout this work, we choose the basis states at reference point $\mathbf{Q} = \Gamma$.

In this framework, the population measurements in Fig. 3B constitute a reconstruction of the mixing angle $\theta_{\mathbf{q}} = 2\arccos|W^{11}_{\Gamma\to\mathbf{q}}|$. This can be visualized as the rotation of a pseudospin on a Bloch sphere, where the north (south) pole represents $|1\rangle$ ($|2\rangle$). As a function of quasimomentum $\mathbf{q}$, the angle $\theta_{\mathbf{q}}$ winds by $2\pi/3$ per reciprocal lattice vector (see inset of Fig. 3B).

To obtain the relative phase $\phi_{\mathbf{q}}$, which is directly connected to the Wilson line via $\phi_{\mathbf{q}} = \mathrm{Arg}[W^{11}_{\mathbf{Q}\to\mathbf{q}}] - \mathrm{Arg}[W^{12}_{\mathbf{Q}\to\mathbf{q}}]$ (*19*), we perform a procedure analogous to Ramsey or Stückelberg interferometry (*26*, *27*). We initialize atoms in the lowest band at $\Gamma - \mathbf{G}$ and rapidly transport them by one reciprocal lattice vector to prepare a superposition of band eigenstates at the reference point Γ (i in Fig. 4A). We then hold the atoms at Γ for a variable time (ii), during which the phase of the superposition state precesses at a frequency set by the energy difference between the bands at Γ. Following this preparation sequence, we rapidly transport the superposition state to a final quasimomentum $\mathbf{q}_\alpha$, lying at angular coordinate α on a circle of radius $|\mathbf{G}|$ centered at Γ. Measuring the population of the first band as a function of hold time yields an interference fringe that reveals the relative phase ϕ_α (*19*).

We observe quantized jumps of π in the phase of the interference fringe each time α is swept through a Dirac point, i.e., every 60° (blue circles in Fig. 4B) (*28*, *29*). The binary nature of the phases is a consequence of the degeneracy between A and B sites, which dictates that the band eigenstates at each quasimomentum be an equal superposition of states $|\Phi^A_{\mathbf{q}}\rangle$ and $|\Phi^B_{\mathbf{q}}\rangle$ on the A and B sublattices (*19*). Therefore, on the Bloch sphere, the pseudospin is constrained to rotate on a meridian about an axis whose poles represent the corresponding cell-periodic functions $|u^A_{\mathbf{q}}\rangle$ and $|u^B_{\mathbf{q}}\rangle$ (inset of Fig. 3B). When we remove this constraint by introducing an energy offset between A and B sites (*19*, *30*)), we observe smoothly varying phases that are always less than π (red circles in Fig. 4B). The dependence of the phase on angle α indicates both the breaking of inversion symmetry and the preservation of the threefold rotational symmetry of the lattice.

Apart from reconstructing the cell-periodic Bloch functions, our method also provides access to eigenvalues of Wilson-Zak loops, $\hat{\mathbf{W}}_{\mathbf{q}\to\mathbf{q}+\mathbf{G}}$, which is essential for determining various topological invariants (*7*–*9*). To this end, we split the Wilson-Zak-loop matrix into a global phase factor, which can be measured by extending previous methods (*13*–*15*, *31*), and an $SU(2)$ matrix with eigenvalues $e^{\pm i\xi}$. Using the data from Figs. 3B and 4B, we reconstruct the eigenvalues for a loop transporting from Γ to $\Gamma + \mathbf{G}$, up to multiples of π (*19*). We find the eigenvalue phases to be $\xi = 1.03(2)\pi/3$, in good agreement with the value of $\pi/3$ predicted from the two-band model. Notably, we measure the same eigenvalues even when the band eigenstates are modified by an energy offset between A and B sites (*19*). This invariance is a direct consequence of the real-space representation of the Wilson-Zak loop, $\hat{\mathbf{W}}_{\Gamma\to\Gamma+\mathbf{G}} = e^{i\mathbf{G}\cdot\hat{\mathbf{r}}}$ [see Eq. 2 and (*19*)]. Because the Wilson-Zak loop depends only on the position operator $\hat{\mathbf{r}}$, the eigenvalues are determined solely by the physical locations of the lattice sites, which are unchanged by the energy offset.

Our versatile approach only employs standard techniques that are broadly applicable in ultracold-atom experiments and can be extended to higher numbers of bands by adopting ideas from quantum process tomography (*32*). Provided that the relevant local Hilbert space is identical for all quasimomenta, our method provides a complete map of the eigenstates over the BZ, giving access to the Berry curvature and Chern number. When this is not the case, the same techniques enable the reconstruction of Wilson-Zak loop eigenvalues, which directly probe the geometry of the Wannier functions (*9*) and, therefore, the polarization of the system (*21*, *33*). Consequently, these eigenvalues can reveal the topology of bands with path-dependent and non-Abelian Wilson lines (*9*, *11*). Such systems can be realized in cold-atom experiments by periodically modulating the lattice (*12*, *30*, *34*–*36*) to create a quasimomentum-dependent admixture of additional bands (*37*) or coupling between internal states (*38*–*41*). Moreover, the addition of spin-orbit coupling (*42*) would enable the investigation of the Z_2 invariant characterizing time-reversal invariant topological insulators (*33*, *41*, *43*–*46*).

REFERENCES AND NOTES

1. D. Xiao, M.-C. Chang, Q. Niu, *Rev. Mod. Phys.* **82**, 1959–2007 (2010).
2. D. J. Thouless, M. Kohmoto, M. P. Nightingale, M. den Nijs, *Phys. Rev. Lett.* **49**, 405–408 (1982).
3. K. Klitzing, G. Dorda, M. Pepper, *Phys. Rev. Lett.* **45**, 494–497 (1980).
4. M. Z. Hasan, C. L. Kane, *Rev. Mod. Phys.* **82**, 3045–3067 (2010).
5. X.-L. Qi, S.-C. Zhang, *Rev. Mod. Phys.* **83**, 1057–1110 (2011).
6. A. H. Castro Neto, F. Guinea, N. M. R. Peres, K. S. Novoselov, A. K. Geim, *Rev. Mod. Phys.* **81**, 109–162 (2009).
7. R. Yu, X. L. Qi, A. Bernevig, Z. Fang, X. Dai, *Phys. Rev. B* **84**, 075119 (2011).
8. A. Alexandradinata, B. A. Bernevig, http://arxiv.org/abs/1409.3236 (2014).
9. A. Alexandradinata, X. Dai, B. Bernevig, *Phys. Rev. B* **89**, 155114 (2014).
10. F. Grusdt, D. Abanin, E. Demler, *Phys. Rev. A* **89**, 043621 (2014).
11. F. Wilczek, A. Zee, *Phys. Rev. Lett.* **52**, 2111–2114 (1984).
12. G. Jotzu *et al.*, *Nature* **515**, 237–240 (2014).
13. M. Aidelsburger *et al.*, *Nat. Phys.* **11**, 162–166 (2014).
14. L. Duca *et al.*, *Science* **347**, 288–292 (2015).
15. M. Atala *et al.*, *Nat. Phys.* **9**, 795–800 (2013).
16. M. Zahid Hasan, S.-Y. Xu, M. Neupane, in *Topological Insulators: Fundamentals and Perspectives* (Wiley-VCH, Weinheim, Germany, 2015), pp. 55–100.
17. M. Greiner, I. Bloch, O. Mandel, T. W. Hänsch, T. Esslinger, *Phys. Rev. Lett.* **87**, 160405 (2001).
18. M. Ben Dahan, E. Peik, J. Reichel, Y. Castin, C. Salomon, *Phys. Rev. Lett.* **76**, 4508–4511 (1996).
19. See supplementary materials on *Science* Online
20. J. W. Zwanziger, M. Koenig, A. Pines, *Annu. Rev. Phys. Chem.* **41**, 601–646 (1990).
21. R. D. King-Smith, D. Vanderbilt, *Phys. Rev. B Condens. Matter* **47**, 1651–1654 (1993).
22. S. Shevchenko, S. Ashhab, F. Nori, *Phys. Rep.* **492**, 1–30 (2010).
23. L. Tarruell, D. Greif, T. Uehlinger, G. Jotzu, T. Esslinger, *Nature* **483**, 302–305 (2012).
24. P. Hauke, M. Lewenstein, A. Eckardt, *Phys. Rev. Lett.* **113**, 045303 (2014).
25. E. Alba, X. Fernandez-Gonzalvo, J. Mur-Petit, J. K. Pachos, J. J. Garcia-Ripoll, *Phys. Rev. Lett.* **107**, 235301 (2011).
26. A. Zenesini, D. Ciampini, O. Morsch, E. Arimondo, *Phys. Rev. A* **82**, 065601 (2010).
27. S. Kling, T. Salger, C. Grossert, M. Weitz, *Phys. Rev. Lett.* **105**, 215301 (2010).
28. L.-K. Lim, J.-N. Fuchs, G. Montambaux, *Phys. Rev. Lett.* **112**, 155302 (2014).
29. L.-K. Lim, J.-N. Fuchs, G. Montambaux, *Phys. Rev. A* **91**, 042119 (2015).
30. S. K. Baur, M. H. Schleier-Smith, N. R. Cooper, *Phys. Rev. A* **89**, 051605 (2014).
31. D. A. Abanin, T. Kitagawa, I. Bloch, E. Demler, *Phys. Rev. Lett.* **110**, 165304 (2013).
32. J. F. Poyatos, J. I. Cirac, P. Zoller, *Phys. Rev. Lett.* **78**, 390–393 (1997).
33. A. A. Soluyanov, D. Vanderbilt, *Phys. Rev. B* **83**, 035108 (2011).
34. M. Aidelsburger *et al.*, *Phys. Rev. Lett.* **111**, 185301 (2013).
35. H. Miyake, G. A. Siviloglou, C. J. Kennedy, W. C. Burton, W. Ketterle, *Phys. Rev. Lett.* **111**, 185302 (2013).
36. N. H. Lindner, G. Refael, V. Galitski, *Nat. Phys.* **7**, 490–495 (2011).
37. C. V. Parker, L.-C. Ha, C. Chin, *Nat. Phys.* **9**, 769–774 (2013) Letter.
38. Y. J. Lin, R. L. Compton, K. Jiménez-García, J. V. Porto, I. B. Spielman, *Nature* **462**, 628–632 (2009).
39. N. R. Cooper, *Phys. Rev. Lett.* **106**, 175301 (2011).
40. J. Dalibard, F. Gerbier, G. Juzeliūnas, P. Öhberg, *Rev. Mod. Phys.* **83**, 1523–1543 (2011).
41. B. Béri, N. R. Cooper, *Phys. Rev. Lett.* **107**, 145301 (2011).
42. Y.-J. Lin, K. Jiménez-García, I. B. Spielman, *Nature* **471**, 83–86 (2011).
43. N. Goldman *et al.*, *Phys. Rev. Lett.* **105**, 255302 (2010).
44. G. Liu, S.-L. Zhu, S. Jiang, F. Sun, W. M. Liu, *Phys. Rev. A* **82**, 053605 (2010).
45. C. J. Kennedy, G. A. Siviloglou, H. Miyake, W. C. Burton, W. Ketterle, *Phys. Rev. Lett.* **111**, 225301 (2013).
46. F. Mei, S.-L. Zhu, Z.-M. Zhang, C. H. Oh, N. Goldman, *Phys. Rev. A* **85**, 013638 (2012).

ACKNOWLEDGMENTS

We acknowledge illuminating discussions with A. Alexandradinata, J.-N. Fuchs, N. Goldman, D. Greif, L.-K. Lim, G. Montambaux, A. Polkovnikov, and G. Refael. This work was supported by the Alfred P. Sloan Foundation, the European Commision (UQUAM, AQuS), Nanosystems Initiative Munich, the Harvard Quantum Optics Center, the Harvard–Massachusetts Institute of Technology Center for Ultracold Atoms, NSF grant DMR–1308435, the Defense Advanced Research Projects Agency Optical Lattice Emulator program, the Air Force Office of Scientific Research, Quantum Simulation Multidisciplinary University Research Initiative (MURI), the Army Research Office (ARO)–MURI on Atomtronics, and the ARO-MURI Qubit Enabled Imaging, Sensing, and Metrology program.

SUPPLEMENTARY MATERIALS

www.sciencemag.org/content/352/6289/1094/suppl/DC1
Supplementary Text
Figs. S1 to S7
References (*47*–*52*)

5 October 2015; accepted 15 April 2016
10.1126/science.aad5812

Downloaded from http://science.sciencemag.org/ on May 26, 2016

BIOCHEMISTRY

Extracellular electron transfer systems fuel cellulose oxidative degradation

Daniel Kracher,[1]* Stefan Scheiblbrandner,[1]* Alfons K. G. Felice,[1] Erik Breslmayr,[1] Marita Preims,[1] Karolina Ludwicka,[1,2] Dietmar Haltrich,[1] Vincent G. H. Eijsink,[3] Roland Ludwig[1]†

Ninety percent of lignocellulose-degrading fungi contain genes encoding lytic polysaccharide monooxygenases (LPMOs). These enzymes catalyze the initial oxidative cleavage of recalcitrant polysaccharides after activation by an electron donor. Understanding the source of electrons is fundamental to fungal physiology and will also help with the exploitation of LPMOs for biomass processing. Using genome data and biochemical methods, we characterized and compared different extracellular electron sources for LPMOs: cellobiose dehydrogenase, phenols procured from plant biomass or produced by fungi, and glucose-methanol-choline oxidoreductases that regenerate LPMO-reducing diphenols. Our data demonstrate that all three of these electron transfer systems are functional and that their relative importance during cellulose degradation depends on fungal lifestyle. The availability of extracellular electron donors is required to activate fungal oxidative attack on polysaccharides.

Fungi play a central role in the terrestrial carbon cycle; their elaborate enzymatic machineries deconstruct plant biomass into its molecular building blocks (*1*). Cellulose, the most abundant and economically valuable polymer in plant cell walls, is broken down to glucose by endo- and exo-acting hydrolases through acid-base catalysis (*2*). Lytic polysaccharide monooxygenase [LPMO; family AA9 in the Carbohydrate-Active Enzymes (CAZy) database] has been shown to enhance such degradation by attacking crystalline cellulose and providing new chain ends as starting points for the hydrolases (*3*). Originally discovered in chitin-degrading bacteria (*4*), LPMO activity has since been found to degrade all major polysaccharides, including cellulose (*5*, *6*), hemicellulose (*7*), and starch (*8*). High LPMO expression by fungi growing on lignocellulose substrates (*9*, *10*) underscores the importance of these auxiliary redox activities. LPMOs use a single active-site copper ion to activate molecular oxygen and hydroxylate the polysaccharide backbone, eventually leading to chain breaks (*11*). Oxygen activation in the active site depends on exogenous electron donors (*4*, *12*), several of which have been reported, including cellobiose dehydrogenase [CDH; CAZy subfamily AA3.1 (*11*, *13*)], small-molecule reductants (*4*, *6*), and photosynthetic pigments (*14*). Existing data are inconclusive, however, regarding the nature, availability, efficiency, and physiological relevance of extracellular electron donors.

To understand the nature and relevance of extracellular LPMO-reducing systems, we studied the LPMO-activating potential of phenols (mostly benzenediols) derived from plants and fungi together with redox enzymes, such as CDH, or other members of the glucose-methanol-choline (GMC) family of oxidoreductases (CAZy subfamily AA3.2). We compared these redox enzyme–based electron systems with small-molecule reductants such as ascorbate (*4*), sulfur-containing species (*5*), gallic acid (*6*), and pyrogallol (*15*) by biochemical and electrochemical methods (supplementary materials). We also analyzed 97 fungal genomes to elucidate the relative importance of the various LPMO-activating mechanisms and their correlation with fungal lifestyle.

At least three electron transfer systems reduce LPMOs during fungal lignocellulose attack (Fig. 1). The extracellular flavocytochrome CDH (system 1) can reduce LPMO directly, whereas members of the GMC oxidoreductases (system 3) use plant-derived or fungal diphenols as redox mediators. The diphenols (system 2) efficiently reduce LPMO in the absence of regenerating enzymes but are irreversibly depleted by LPMO activity. The co-occurrence of *lpmo* genes with the genes of these LPMO-regenerating enzymes indicates the incidence of the three electron transfer systems in fungi.

Genes encoding LPMO were found in 92% of the fungal genomes, whereas 58% contained *cdh* genes. Although white rots, soft rots, and plant pathogens had an overlap between these two gene families of 63 to 85%, brown rots, plant symbionts, and animal pathogens had a much lower co-occurrence of both genes (22 to 30%; Fig. 2A, figs. S1 to S4, and table S1). Ascomycota and Basidiomycota had a similar co-occurrence of *cdh* and *lpmo* genes, suggesting that the observed difference is independent of the species' phylogenetic origin. On average, the number of *lpmo* genes was slightly higher when *gmc* genes (*cdh* excluded) were present in the genome

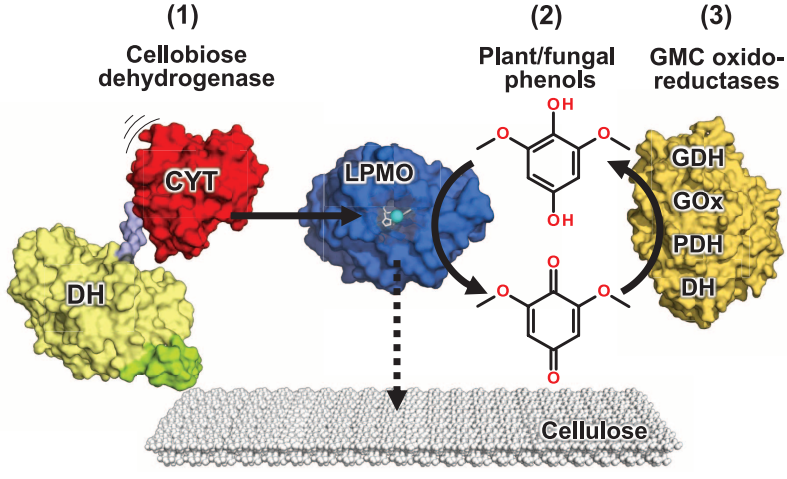


Fig. 1. Three electron transfer systems reduce the LPMO (blue) active-site copper (cyan) to initiate cellulose attack. System 1: CDH transfers electrons from its catalytic dehydrogenase domain (DH, yellow; CAZy subfamily AA3.1) via its mobile cytochrome domain (CYT, red) to the LPMO (*32*). System 2: Various plant-derived and fungal phenols can act as direct sources of electrons. The figure shows a LPMO electron donor identified in this study, 2,6-dimethoxy-1,4-benzenediol, and the oxidized quinoid reaction product. System 3: GMC oxidoreductases, such as GDH, GOx, or PDH (CAZy subfamily AA3.2), and the dehydrogenase domain of CDH regenerate the quinoid form of the redox couple (redox mediator) to reduce the LPMO active-site copper.

[1]Department of Food Science and Technology, BOKU—University of Natural Resources and Life Sciences, Muthgasse 18, 1190 Vienna, Austria. [2]Institute of Technical Biochemistry, Lodz University of Technology, Stefanowskiego 4/10, 90-924 Lodz, Poland. [3]Department of Chemistry, Biotechnology and Food Science, Norwegian University of Life Sciences, 1432 Ås, Norway.
*These authors contributed equally to this work. †**Corresponding author. Email: roland.ludwig@boku.ac.at**

Downloaded from http://science.sciencemag.org/ on May 26, 2016

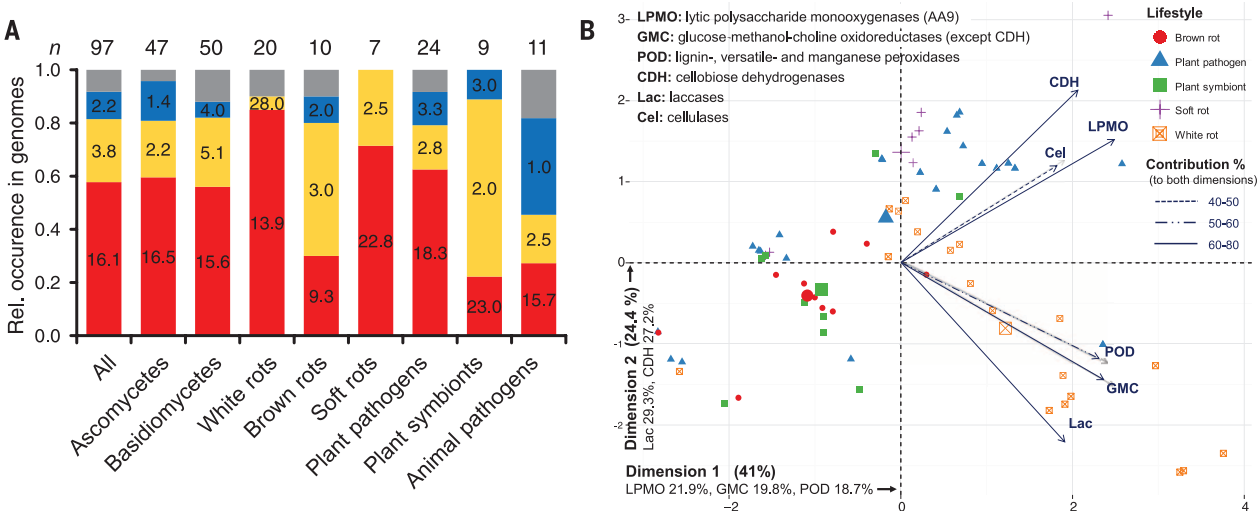


Fig. 2. Occurrence and analysis of oxidoreductases linked to lignocellulose degradation. (**A**) Relative occurrence of *cdh*, *lpmo*, and *gmc* (*cdh* excluded) genes in 97 genomes grouped by fungal lifestyles. The relative occurrence is indicated by color-coded bars, normalized to the number (*n*) of analyzed genomes given above [*cdh* and *lpmo* genes, red; *gmc* (*cdh* excluded) and *lpmo* genes, yellow; only *lpmo* genes, blue; none of these, gray]. None of the genomes contained *cdh* without *lpmo*. Numbers in the bars indicate the average number of *lpmo* genes for fungi in each category. The lifestyle of a fungus is often uncertain, and published data allowed the assignment of only 81 genomes (table S1). (**B**) Principal component analysis. The numbers of genes encoding CDH, GMC (CDH excluded), LPMO (CAZy family AA9), cellulase (Cel), laccase (Lac), and ligninolytic activities (POD) per genome were used as variables (small symbols; large symbols indicate group-specific centers of gravity). A high correlation among the analyzed genes is indicated by a similar orientation of the dark blue vectors. The contribution of the variables to the overall data variance is indicated by the line style of the vectors. The individual contribution (percent) to each dimension is further specified in the axis legend. Outliers in the lifestyle-dependent clustering of individual data sets could originate from an incorrect assignment.

(fig. S5) but much higher in genomes that also contained *cdh*. The latter genomes contained between 9 and 23 *lpmo* genes on average, which indicates the presence of a diversified set of LPMOs that are likely to carry out a range of catalytic tasks. The factor map generated by principal component analysis shows a high correlation between the LPMO and CDH variables (Fig. 2B and fig. S6). The clustering of individual data sets corresponds to the reported lifestyles for most of the investigated fungal species. The clusters of brown rots and plant symbionts correlate negatively with all extracellular oxidoreductase variables. The loss of oxidoreductases in brown rots has been explained by an evolutionary contraction (*16*).

CDH is a reported activator of LPMO (*11*, *13*). To investigate the catalytic efficiency of CDH and thus the biological relevance of LPMO-CDH co-occurrence, the interactions of both enzymes were tested by rapid spectroscopy. The *Neurospora crassa* genome has two *cdh* and 14 *lpmo* genes, and both CDHs [CDH IIA, carrying a family 1 carbohydrate binding module (CBM1), and CDH IIB, lacking

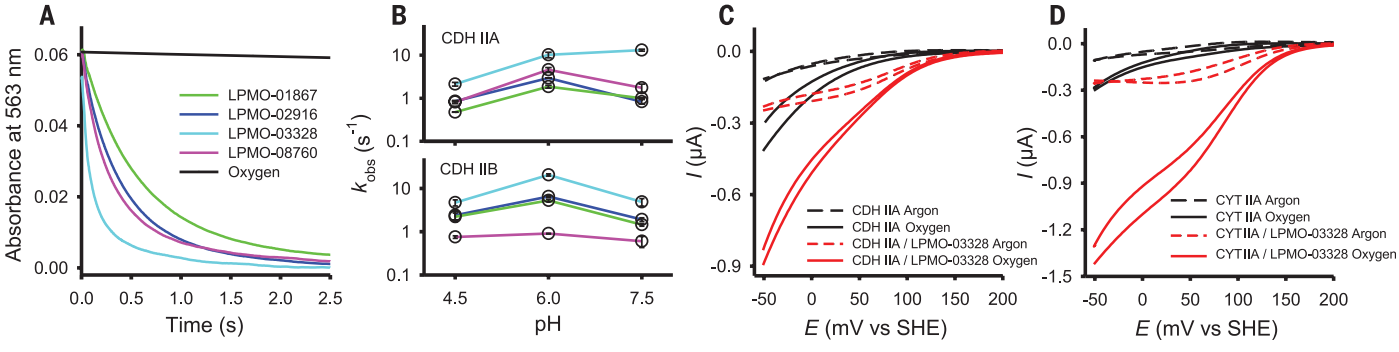


Fig. 3. CDH-catalyzed LPMO reduction. (**A**) Electron transfer rates from *N. crassa* CDH IIA to LPMOs were measured by stopped-flow spectroscopy. LPMOs with different oxidative regioselectivity and cellulose-binding properties were tested (LPMO-02916, which has a CBM1, oxidizes cellulose at position C4; LPMO-01867 and LPMO-08760 oxidize at C1 and have a CBM1; LPMO-03328 oxidizes at C1 and lacks a CBM1). The observed heme *b* oxidation rates (0.9 to 20.6 s^{-1}) at pH 6.0 were much higher than the reoxidation rate with oxygen (100 to 2100 times as high; table S6) or ferric iron (30 to 660 times as high; table S7). (**B**) The pH dependency of the observed electron transfer rates from CDH IIA or CDH IIB to each of the four LPMOs [same color code as in (A)] indicates a slightly acidic optimum pH. LPMO-08760 shows a preference for CDH IIA as an electron donor, whereas LPMO-02916 and LPMO-01867 were reduced faster by CDH IIB. Circles represent mean values of at least three replicates, and error bars represent standard deviations. (**C** and **D**) Electron transfer from a glassy carbon electrode to LPMO, mediated by (C) CDH IIA or (D) its isolated cytochrome domain (*I*, current; *E*, redox potential). Cyclic voltammetry showed a charging current for LPMO in the absence of oxygen; the onset potential is limited by the reduction potential of the heme *b* cofactor. In the presence of oxygen, a catalytic current was observed. The higher current observed for the cytochrome domain–mediated process may be due to its higher mobility compared with that of CDH. Data for LPMO-02916 are presented in fig. S9.

Downloaded from http://science.sciencemag.org/ on May 26, 2016

such a module] and four LPMOs from this soft rot were recombinantly produced and characterized (figs. S7 and S8 and tables S2 to S4). Fast electron transfer from the CDH was observed for all investigated enzyme combinations, albeit with different rates (k_{obs} at pH 6.0 was between 0.9 s^{-1} and 20.6 s^{-1}) and pH dependencies (Fig. 3, A and B, and tables S5 and S6). The observed interprotein electron transfer rates between CDH and LPMO at pH 6.0 exceeded the side activities of CDH with oxygen or ferric iron by two to three orders of magnitude. This shows that a previously suggested function of CDH, namely, the generation of hydroxyl radicals in a Fenton reaction through concomitant production of ferrous iron and H_2O_2 (*17*), is kinetically unfavorable. However, at pH 4.0, the production of H_2O_2 and ferrous iron became more competitive with LPMO reduction (table S7). Preferences of LPMOs for particular CDHs were demonstrated by higher electron transfer rates; such preferences could be due to variation in surface complementarity at the protein/protein interface. An inspection of isoelectric points showed no correlation to interprotein electron transfer rates (tables S3 and S6).

We also investigated electron transfer to LPMOs by cyclic voltammetry, which allows the direct monitoring of the flow of electrons between an electrode and a biomolecule (Fig. 3, C and D, and fig. S9). The LPMOs did not directly interact with a glassy carbon cathode but rather required either CDH or its isolated cytochrome domain as mediators to obtain electrons. LPMO catalytic currents were observed only in the presence of oxygen, thus demonstrating catalytic reduction of oxygen at the LPMO copper site. These results prove that the cytochrome domain alone is the structural element responsible for electron transfer. Several fungal genomes encode extracellular cytochrome domains carrying a cellulose-binding CBM1 (*18*), which could play a role in electron transfer to cellulose-bound LPMOs. Our data show that CDH is part of a specific extracellular redox chain, which is scarcely affected by oxygen and which comprises the FAD (flavin adenine dinucleotide) cofactor in CDH's catalytic dehydrogenase domain [~0 mV versus the standard hydrogen electrode (SHE)], heme *b* in the cytochrome domain [~93 to 163 mV (*19*)], and the active-site copper in the LPMO [~224 mV in (*20*); ~250 mV in this work].

A variety of small-molecule reductants, including plant-derived compounds such as gallic acid and low-molecular-weight lignin products, can initiate LPMO activity under laboratory conditions (*21*–*23*). The action of such reductants is essential in cases in which CDH is not expressed or is absent from the genome. Although several reductants have been found, it is not clear whether these compounds are biologically relevant, in terms of either their occurrence in biological systems or their reducing efficiency on LPMOs compared with that of CDH. Another uncertainty concerns the limited stability of some of these reductants (fig. S10) and their availability in decaying plant material. Screening of a large number of phenolic compounds revealed substantial differences in their LPMO-reducing efficiency (fig. S11 and tables S8 and S9). The highest product release occurred in experiments that used ascorbic acid and the diphenols 2,5-dimethoxy-1,4-benzenediol and 2,6-dimethoxy-1,4-benzenediol. Cellulose conversion by LPMO-02916 and various phenols resulted in typical degradation products (fig. S12).

The screening showed that plant-derived phenols are capable of efficiently reducing LPMOs. Spectroscopy and cyclic voltammetry were used to further investigate LPMO-catalyzed oxidation of monophenols to their corresponding phenoxy radicals and of diphenols to their corresponding quinones (figs. S13 and S14 and tables S10 to S13). We found no evidence for the oxidation of

Downloaded from http://science.sciencemag.org/ on May 26, 2016

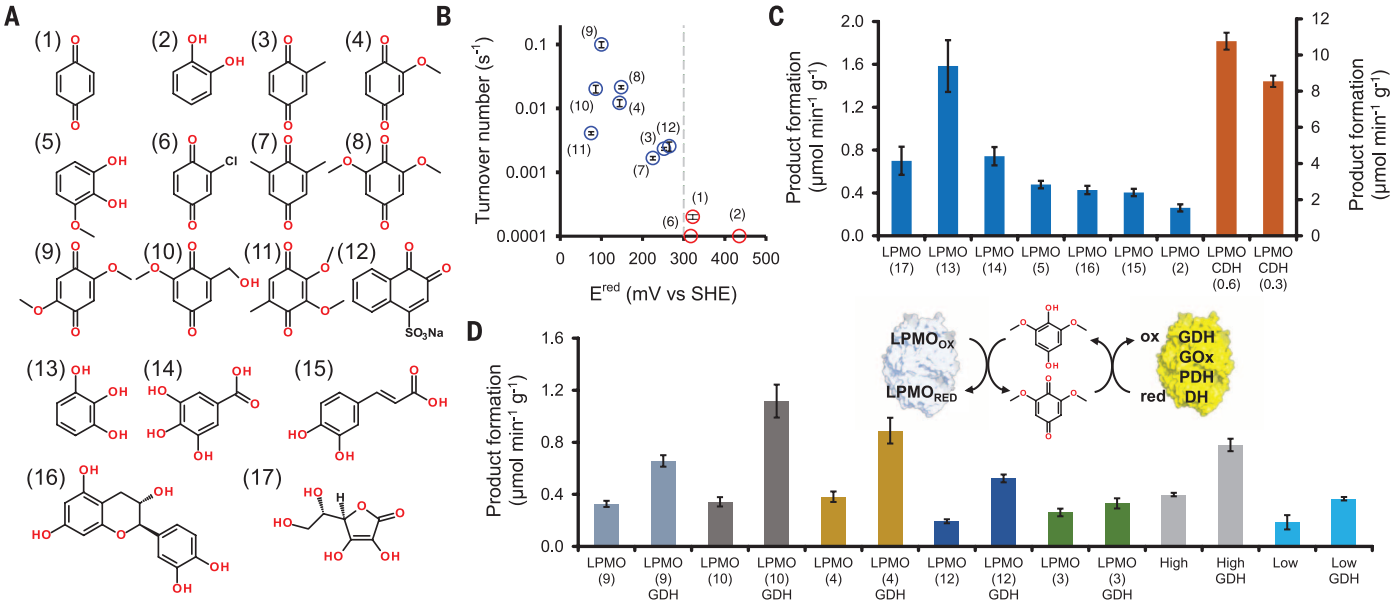


Fig. 4. Activation of LPMO by different reducing systems. (**A**) LPMO-reducing substances from plants or fungi identified in this study are either di- or triphenols. Often, only the quinoid form of a diphenol was available. Ascorbic acid (17) is a commonly used LPMO reductant. (**B**) Plot of diphenol and quinone midpoint redox potentials (E^{red}) at pH 6.0 versus their reactivity with LPMO, as assessed by the turnover number for hydroquinone oxidation, which was obtained by means of spectrophotometric assays (table S13). The dashed line indicates the limiting oxidation potential, suggesting an LPMO midpoint potential close to 250 mV versus SHE (circles, mean values of at least three replicates; error bars, standard deviations; circle colors are a guide to the eye). (**C**) Oligosaccharides with a degree of polymerization from 2 to 5 that were released from cellulose during 24-hour conversion experiments in the presence of 1 mM reductant [ascorbic acid (17), pyrogallol (13), gallic acid (14), 3-methoxycatechol (5), catechin (16), caffeic acid (15), and catechol (2)]. In the presence of CDH (0.6 or 0.3 μM; orange bars), the quantification of oxidized cellodextrin reaction products is difficult. Substrate turnover was therefore estimated by the turnover of the cosubstrate lactose (right axis). Bars indicate means (error bars, standard deviations of at least three replicates). (**D**) LPMO reduction by diphenol and/or quinone redox mediators at final concentrations of 100 μM. The tested substances include 2,5-dimethoxy-1,4-benzoquinone (9), 2-hydroxymethyl-6-methoxy-1,4-benzoquinone (10), methoxy-1,4-benzoquinone (4), 1,2-naphthquinone-4-sulfonic acid (12), methyl-1,4-benzoquinone (3), and wood (hot water) extract in a concentration of 0.42 (high) and 0.084 (low) mg ml^{-1}. LPMO activity was analyzed as in (C). GDH, its substrate glucose, and the redox mediators establish an electron transfer system that performs as well as the LPMO reducing substances in (C).

monophenols by LPMO, probably because of their high oxidation potential (>400 mV versus SHE; fig. S15), which is higher than the LPMO midpoint potential. In contrast, most diphenols have an oxidation potential close to or below that of the LPMO copper site. Among the investigated naturally occurring diphenols (Fig. 4A), methoxylated and methylated diphenols have oxidation potentials below 250 mV versus SHE and result in the fastest LPMO reduction rates (Fig. 4B). In 24-hour experiments, cellulose degradation by LPMO in combination with the reductants ascorbic acid, pyrogallol, and gallic acid, as well as diphenols or CDH, showed that all of these substances can reduce LPMO efficiently. The product release was highest for the CDH-catalyzed LPMO reduction in this experimental setup (Fig. 4C).

We then hypothesized that plant-derived diphenols and quinones (*24*, *25*) and diphenols secreted by fungi (*26*, *27*) can act as redox mediators by accepting electrons from GMC oxidoreductases of CAZy family AA3, which are abundantly present in the genomes and secretomes of biomass-degrading fungi. In the investigated fungal genomes, genes encoding non-CDH GMC oxidoreductases (CAZy subfamily AA3.2) showed a strong positive correlation with the presence of *lpmo* genes (fig. S5). Extending this observation, we demonstrated the ability of glucose oxidase (GOx), glucose dehydrogenase (GDH), pyranose dehydrogenase (PDH), and the isolated flavodehydrogenase domain of CDH to reduce these quinones (fig. S16 and tables S10 and S11). GDH was used together with LPMO to investigate the electron mediating process in more detail (Fig. 4D). The results demonstrate that diphenolic-quinoid redox couples perform as redox mediators, provided that there is efficient regeneration by a GMC oxidoreductase (fig. S17). In the presence of the redox mediators 2,5-dimethoxy-1,4-benzenediol, methoxy-1, 4-benzenediol, or 2-hydroxymethyl-6-methoxy-1, 4-benzenediol, 6 nM GDH regenerated a LPMO concentration that was 1670 times as high, and it did so as efficiently as 1-mM concentrations of the typically used reductants ascorbic acid and gallic acid. This finding suggests a role for secreted fungal oxidoreductases and could explain why "-omics" studies tend to lead to the conclusion that these enzymes are associated with biomass conversion. To compare the efficiency of wood-derived phenols with that of the isolated redox mediators described above, we investigated a beech wood (hot water) extract. The LPMO activity on microcrystalline cellulose (Fig. 4D and table S14) showed that beech wood extract reduced LPMO directly and in combination with GDH with the same efficiency as the isolated diphenols did. The addition of small amounts of GDH resulted in about a twofold increase in product formation, nearly reaching the product concentration obtained with 1 mM gallic acid.

Our data show that LPMO action—and thus cellulose degradation—can be fueled by different electron transfer systems. When LPMO and CDH are both present, interprotein interactions ensure specificity and efficiency of the extracellular electron transfer chain. Alternatively, plant-derived phenols and lignin fractions can serve as electron donors in fresh plant material through an unspecific reduction mechanism. Lastly, plant-derived or fungal diphenols and/or quinones serve as redox mediators between LPMO and GMC oxidoreductases, thus establishing an efficient electron transfer system. The lattermost observation may in part explain the abundance of GMC oxidoreductases, which supply H_2O_2 to peroxidases and hydroxyl radical–producing systems but whose roles remain enigmatic. The redox-mediating systems described in detail here bear resemblance to similar mediator-based systems that were hypothesized as early as 1977 to play a role in lignin conversion (*28*). Although we cannot yet pinpoint the biological relevance, our data reveal connections between enzymes involved in lignin degradation, Fenton reactions, and LPMO-catalyzed cellulose degradation. The quinone reductases of CAZy family AA6, which have been implicated in the recycling of quinones during the production of extracellular oxidizers by wood-rotting fungi (*29*), were present in 93 out of 96 screened genomes and may play a role in fueling LPMO action. Also, the recently discovered PQQ (pyrroloquinoline quinone)–containing dehydrogenase belonging to CAZy family AA12 (*30*) contains a cytochrome domain that could transfer electrons generated in its AA12 dehydrogenase domain to a LPMO.

The ability of LPMOs to versatilely accept electrons from different donors may allow a fungus to better adapt to different substrates, thus supporting LPMO activity during different stages of biomass degradation. This capacity to interact with different electron donors could include the ability to interact with electron transfer systems from different fungi, as a possible adaptation to co-occurrences of fungal species (*31*). The interaction of CDHs and LPMOs from different fungi was shown in previous work (*8*, *11*, *13*). Arguably, fungi secreting CDH or other GMC oxidoreductases as alternative electron transfer systems to plant-derived phenolic reductants can better regulate LPMO activity independently of changes in biomass composition, which may be caused by variation in available plant material or by depletion of reductants during the degradation process. We propose plant-derived phenols as the first electron donors that were available during the evolution of LPMOs. The advance of extracellular GMC oxidoreductases connected to enzymes involved in lignin degradation then introduced an additional electron transfer system based on plant-derived diphenols and/or quinones or diphenols secreted by fungi as redox mediators. Last, the fusion of one of these GMC oxidoreductases with a cytochrome domain evolved CDH as a specific and efficient electron transfer system.

REFERENCES AND NOTES

1. S. M. Cragg *et al.*, *Curr. Opin. Chem. Biol.* **29**, 108–119 (2015).
2. C. M. Payne *et al.*, *Chem. Rev.* **115**, 1308–1448 (2015).
3. M. Eibinger *et al.*, *J. Biol. Chem.* **289**, 35929–35938 (2014).
4. G. Vaaje-Kolstad *et al.*, *Science* **330**, 219–222 (2010).
5. Z. Forsberg *et al.*, *Protein Sci.* **20**, 1479–1483 (2011).
6. R. J. Quinlan *et al.*, *Proc. Natl. Acad. Sci. U.S.A.* **108**, 15079–15084 (2011).
7. J. W. Agger *et al.*, *Proc. Natl. Acad. Sci. U.S.A.* **111**, 6287–6292 (2014).
8. V. V. Vu, W. T. Beeson, E. A. Span, E. R. Farquhar, M. A. Marletta, *Proc. Natl. Acad. Sci. U.S.A.* **111**, 13822–13827 (2014).
9. C. Tian *et al.*, *Proc. Natl. Acad. Sci. U.S.A.* **106**, 22157–22162 (2009).
10. C. M. Phillips, A. T. Iavarone, M. A. Marletta, *J. Proteome Res.* **10**, 4177–4185 (2011).
11. C. M. Phillips, W. T. Beeson IV, J. H. Cate, M. A. Marletta, *ACS Chem. Biol.* **6**, 1399–1406 (2011).
12. W. T. Beeson, C. M. Phillips, J. H. D. Cate, M. A. Marletta, *J. Am. Chem. Soc.* **134**, 890–892 (2012).
13. J. A. Langston *et al.*, *Appl. Environ. Microbiol.* **77**, 7007–7015 (2011).
14. D. Cannella *et al.*, *Nat. Commun.* **7**, 11134 (2016).
15. L. Lo Leggio *et al.*, *Nat. Commun.* **6**, 5961 (2015).
16. D. Floudas *et al.*, *Science* **336**, 1715–1719 (2012).
17. P. M. Wood, *FEMS Microbiol. Rev.* **13**, 313–320 (1994).
18. M. Yoshida *et al.*, *Appl. Environ. Microbiol.* **71**, 4548–4555 (2005).
19. C. Sygmund *et al.*, *Appl. Environ. Microbiol.* **78**, 6161–6171 (2012).
20. A. S. Borisova *et al.*, *J. Biol. Chem.* **290**, 22955–22969 (2015).
21. B. Westereng *et al.*, *Sci. Rep.* **5**, 18561 (2015).
22. M. Dimarogona, E. Topakas, L. Olsson, P. Christakopoulos, *Bioresour. Technol.* **110**, 480–487 (2012).
23. J. Hu, V. Arantes, A. Pribowo, K. Gourlay, J. N. Saddler, *Energy Environ. Sci.* **7**, 2308–2315 (2014).
24. M. R. Mäkelä *et al.*, *Adv. Appl. Microbiol.* **91**, 63–137 (2015).
25. R. H. Thomson, in *Naturally Occurring Quinones* (Academic Press, ed. 2, 1971), pp. 1–38.
26. M. R. Suzuki, C. G. Hunt, C. J. Houtman, Z. D. Dalebroux, K. E. Hammel, *Environ. Microbiol.* **8**, 2214–2223 (2006).
27. V. Arantes, B. Goodell, in *Deterioration and Protection of Sustainable Biomaterials* (ACS Symposium Series vol. 1158, American Chemical Society, 2014), pp. 3–21.
28. T. R. Green, *Nature* **268**, 78–80 (1977).
29. Z. Kerem, K. A. Jensen, K. E. Hammel, *FEBS Lett.* **446**, 49–54 (1999).
30. K. Takeda *et al.*, *PLOS ONE* **10**, e0115722 (2015).
31. A. van der Wal, T. D. Geydan, T. W. Kuyper, W. de Boer, *FEMS Microbiol. Rev.* **37**, 477–494 (2013).
32. T.-C. Tan *et al.*, *Nat. Commun.* **6**, 7542 (2015).

ACKNOWLEDGMENTS

This work was supported by the European Commission (project INDOX FP7-KBBE-2013-7-613549). D.K., M.P., and E.B. acknowledge support from the Austrian Science Fund (project BioToP; grant FWF W1224); S.S. acknowledges support from the BMWFW (Austrian Federal Ministry of Science, Research and Economy) IGS BioNanoTech; and A.K.G.F. acknowledges support from the Austrian Academy of Sciences (doctoral grant recipient). We thank C. Lorenz for technical assistance, M. Ravber for his generous gift of beech wood (hot water) extracts, and C. Keuschnig for discussing statistical topics. Data are available in the Knowledge Network for Biocomplexity data repository at http://doi.org/10.5063/F1086389.

SUPPLEMENTARY MATERIALS

www.sciencemag.org/content/352/6289/1098/suppl/DC1
Materials and Methods
Supplementary Text
Figs. S1 to S17
Tables S1 to S14
References (*33*–*110*)

25 January 2016; accepted 15 April 2016
Published online 28 April 2016
10.1126/science.aaf3165

Downloaded from http://science.sciencemag.org/ on May 26, 2016

PLANT SCIENCE

Nuclear-localized cyclic nucleotide–gated channels mediate symbiotic calcium oscillations

Myriam Charpentier,[1]* Jongho Sun,[1] Teresa Vaz Martins,[2] Guru V. Radhakrishnan,[1] Kim Findlay,[1] Eleni Soumpourou,[1] Julien Thouin,[3] Anne-Aliénor Véry,[3] Dale Sanders,[4] Richard J. Morris,[2] Giles E. D. Oldroyd[1]*

Nuclear-associated Ca^{2+} oscillations mediate plant responses to beneficial microbial partners—namely, nitrogen-fixing rhizobial bacteria that colonize roots of legumes and arbuscular mycorrhizal fungi that colonize roots of the majority of plant species. A potassium-permeable channel is known to be required for symbiotic Ca^{2+} oscillations, but the calcium channels themselves have been unknown until now. We show that three cyclic nucleotide–gated channels in *Medicago truncatula* are required for nuclear Ca^{2+} oscillations and subsequent symbiotic responses. These cyclic nucleotide–gated channels are located at the nuclear envelope and are permeable to Ca^{2+}. We demonstrate that the cyclic nucleotide–gated channels form a complex with the postassium-permeable channel, which modulates nuclear Ca^{2+} release. These channels, like their counterparts in animal cells, might regulate multiple nuclear Ca^{2+} responses to developmental and environmental conditions.

Nuclear calcium (Ca^{2+}) signals transduce a variety of stimuli in animal (*1*) and plant cells (*2*). Plant genomes lack genes similar to those that encode mammalian nuclear-localized Ca^{2+} channels (*3*), implying that plants have alternative mechanisms for nuclear Ca^{2+} release. Legume root cells show nuclear Ca^{2+} oscillations in response to signaling molecules from nitrogen-fixing rhizobial bacteria and arbuscular mycorrhizal (AM) fungi (*4*). In *Medicago truncatula*, the potassium (K^+)–permeable channel DMI1 (does not make infections 1) and the Ca^{2+}-dependent adenosine triphosphatase (Ca^{2+}-ATPase) MCA8 are necessary for symbiotic Ca^{2+} oscillations; both are located on nuclear membranes, suggesting that the nuclear envelope [contiguous with the endoplasmic reticulum (ER)] acts as the Ca^{2+} store (*5*). Here we identify the Ca^{2+}-permeable channels responsible for Ca^{2+} release from the nuclear envelope–ER stores.

We screened the *M. truncatula* protein database (*6*) to identify transmembrane proteins containing motifs present in Ca^{2+} channels (PF00622, PF02815, PF08763, PF00036, and PF06459), motifs related to ion channels (PF00520, PF07885, PF02386, PF02026, and PF08709), and nuclear localization signal (NLS) motifs (fig. S1A). We assessed their impact on symbioses by silencing the genes that encode these candidates in *M. truncatula* roots. We found that members of the cyclic nucleotide–gated channel (CNGC) family are required for symbiotic associations (fig. S1, B to E). Among the 21 CNGCs of *M. truncatula*, 14 are predicted to contain NLS motifs such as those in DMI1 (*5*) and CASTOR (*7*) (fig. S2), and these fall into CNGC groups II, III, IVA, and IVB (*8*) (fig. S2A).

To differentiate which NLS-containing CNGCs contribute to symbiotic signaling, we used RNA interference to reduce expression of one or several genes from each CNGC group (figs. S3 and S4). Silencing of *CNGC15a, CNGC15b*, and/or *CNGC15c*—all members of group III—correlated with defects in symbiotic associations (Fig. 1A; fig. S3; and fig. S5, A, C, and D). Of the other group III members, *CNGC16* is not expressed in roots (fig. S5B), and silencing *CNGC17* and *CNGC18* did not reduce nodulation (fig. S5, E to J).

We identified mutants in *CNGC14*, *CNGC15a*, *CNGC15b*, and *CNGC15c*, as well as in a CNGC gene that falls outside group III, *CNGC4a*, as a control. One or two insertion alleles were identified for each gene (fig. S6), and these were confirmed to reduce mRNA levels (fig. S6). Nodulation and fungal colonization were assessed in all mutant lines 25 days after inoculation with *Sinorhizobium meliloti* or 5 weeks after inoculation with *Rhizophagus irregularis*. The mutants *cngc15a*, *cngc15b*, and *cngc15c* all showed reduced nodulation and reduced *R. irregularis* colonization (Fig. 1, B and C, and fig. S7, A and B), whereas *cngc4a* and *cngc14* did not. The symbiotic defects of *cngc15* mutants were complemented with their respective genes (Fig. 1, D and E). The mutant lines showed defects in rhizobial infection (Fig. 1F) and induction of early gene expression in response to lipochitooligosaccharide (LCO) signals produced by *S. meliloti* (Nod factor) or *R. irregularis* [non-sulfated (NS)–LCO] (Fig. 1, G and H). We conclude that *CNGC15a, CNGC15b*, and *CNGC15c* function early in the establishment of both rhizobial and mycorrhizal associations.

Oscillations in nuclear Ca^{2+} levels are a feature of the common symbiotic signaling pathway (*9*). The mutants *cngc15a*, *-b*, and *-c*, but not *cngc4a* or *cngc14*, reduced nuclear-associated Ca^{2+} oscillations in response to Nod factor treatment (Fig. 2A and fig. S7C). Fewer cells responded and many cells showed defective Ca^{2+} oscillations in *cngc15* mutants (Fig. 2B), as measured by interspike intervals and probability density functions. Defects included poor maintenance of Ca^{2+} oscillations and irregular oscillation frequencies (Fig. 2, A and B, and fig. S7C). Similar effects were observed after treatments with a mycorrhizal-produced signaling molecule (fig. S8). Nod factor also activates an influx of Ca^{2+} across the plasma membrane, but considering the location of the CNGC15 proteins (discussed below), we do not believe that these proteins will be involved in this Ca^{2+} response. Our data demonstrate that the CNCG15 proteins are required for full activation of nuclear-localized Ca^{2+} oscillations.

We generated double mutants to further assess the function of these channels, but we found equivalent defects to those observed in the single mutants (fig. S7, C to E). Our attempts to generate a triple mutant by crossing *cngc15b-1 cngc15c* with *cngc15a-1 cngc15b-2* or *cngc15a* with *cngc15b-1 cngc15c* were unsuccessful. The efficiency of the crosses, as demonstrated by pod formation, dropped from ~90% (for instance, 9 in 10 crosses of *cngc15a-1* with *cngc15b-2* were successful) to 0% for the generation of the triple mutant (no successful crosses in 103 attempts) (fig. S7F). Fertilization requires coordinated Ca^{2+} signals from the female gametophyte in response to the Ca^{2+} dynamics of the pollen tube (*10*, *11*). *CNGC15a*, *CNGC15b*, and *CNGC15c* are all expressed in flowers and pods (fig. S5B), and *cngc15a* and *cngc15b* had decreased fertilization rates, similar to the double mutants *cngc15b-1 cngc15c* and *cngc15a-1 cngc15b-1* (fig. S9). This suggests a possible function for these channels during fertilization in both female and male gametophytic Ca^{2+} signaling.

Our results demonstrate that CNGC15 proteins support Nod factor– and Myc factor–induced nuclear-localized Ca^{2+} oscillations. We assessed the location of these channels by using functional green fluorescent protein (GFP) fusions (Fig. 1, D and E), analyzed by confocal microscopy and transmission electron microscopy of GFP immunogold–labeled sections (Fig. 3 and figs. S10 and S11A). We found that CNGC15a, CNGC15b, and CNGC15c all localized to the nuclear envelope. We also generated antibodies specific to CNGC15a (fig. S11B), with which we were able to confirm the presence of CNCG15a specifically on nuclear membrane fractions (Fig. 3K). These CNGC proteins and DMI1 have predicted NLS motifs in the N terminus or between the first few transmembrane domains. This is similar to many nuclear membrane–targeted proteins in yeast and animals (*12*); however, additional work is necessary to test the relevance of this positioning of the NLS in plant proteins.

[1]Cell and Developmental Biology, John Innes Centre, Norwich Research Park, Norwich NR4 7UH, UK. [2]Computational and Systems Biology, John Innes Centre, Norwich Research Park, Norwich NR4 7UH, UK. [3]Laboratoire de Biochimie et Physiologie Moléculaire des Plantes, UMR 5004 CNRS–386 INRA (French National Institute for Agricultural Research)–SupAgro-M–Université Montpellier, Campus SupAgro–INRA, 34060 Montpellier, France. [4]Metabolic Biology, John Innes Centre, Norwich Research Park, Norwich NR4 7UH, UK.
*Corresponding authors. Email: myriam.charpentier@jic.ac.uk (M.C.); giles.oldroyd@jic.ac.uk (G.E.D.O.)

Downloaded from http://science.sciencemag.org/ on May 26, 2016

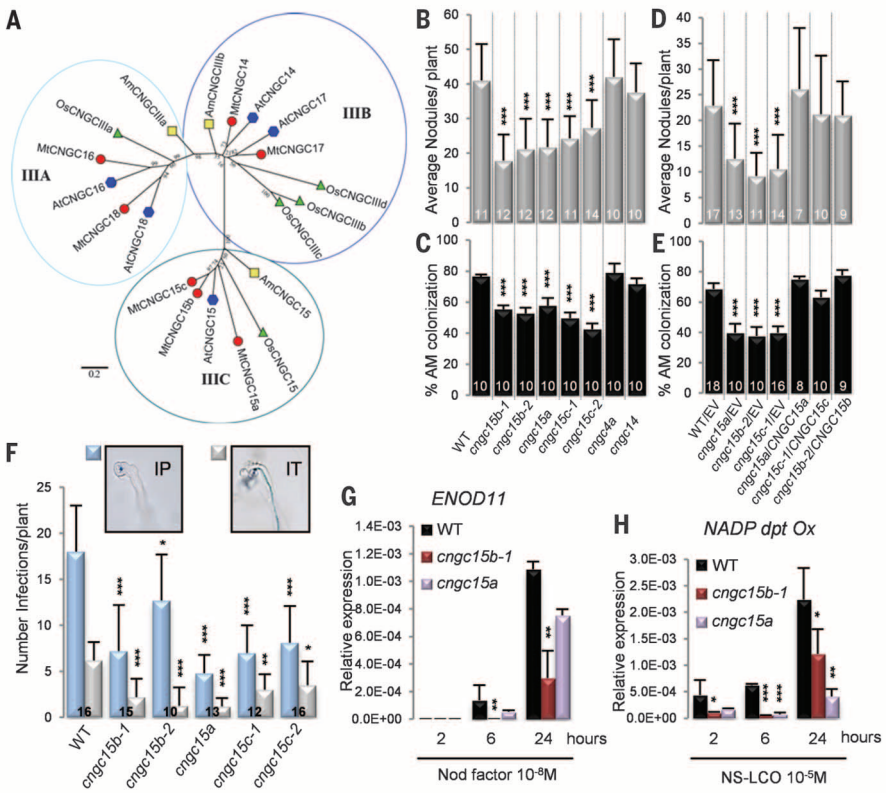


Fig. 1. *CNGC15* gene mutants show symbiotic defects. (**A**) CNGC15a, CNGC15b, and CNGC15c belong to subclass C of the group III CNGCs. The phylogenetic tree includes CNGC group III members from *Amborella trichopoda* (Am, yellow squares), *Oryza sativa* (Os, green triangles), *Arabidopsis thaliana* (At, blue polygons), and *M. truncatula* (Mt, red dots). Numbers at the branch points indicate the percentage bootstrap values (for 1000 iterations) of the consensus tree. (**B**) The *cngc15a*, *-b*, and *-c* mutants were assessed at 25 days after inoculation with *S. meliloti* strain 2011 and (**C**) 5 weeks after inoculation with *R. irregularis* (WT, wild-type *M. truncatula*). (**D**) Complementation of the nodulation and (**E**) mycorrhization phenotypes of *cngc15a*, *-b*, and *-c* by expressing *CNGC15a*, *-b*, and *-c* fused to GFP, driven by the *Lotus japonicus Ubiquitin* promoter (EV, empty vector). (**F**) Infection pockets (IP) and infection threads (IT) were quantified from two biological replicates, 7 days after inoculation with *S. meliloti*. (**G**) Nod factor–induced *ENOD11* expression and (**H**) NS-LCO–induced *NADP dpt Ox* (nicotinamide adenine dinucleotide phosphate–dependent oxidoreductase) expression in WT and *cngc15* mutants after 2, 6, and 24 hours of treatment. Values in (G) and (H) are from three biological replicates each of ten roots, and expression is normalized to that of *EF-1α* (elongation factor 1α). In (B), (D), (F), (G), and (H), error bars show standard deviation. In (C) and (E), error bars show standard error. The number of plants analyzed is given at the bottom of each column. *$P < 0.05$; **$P < 0.01$; ***$P < 0.001$ (*t* test).

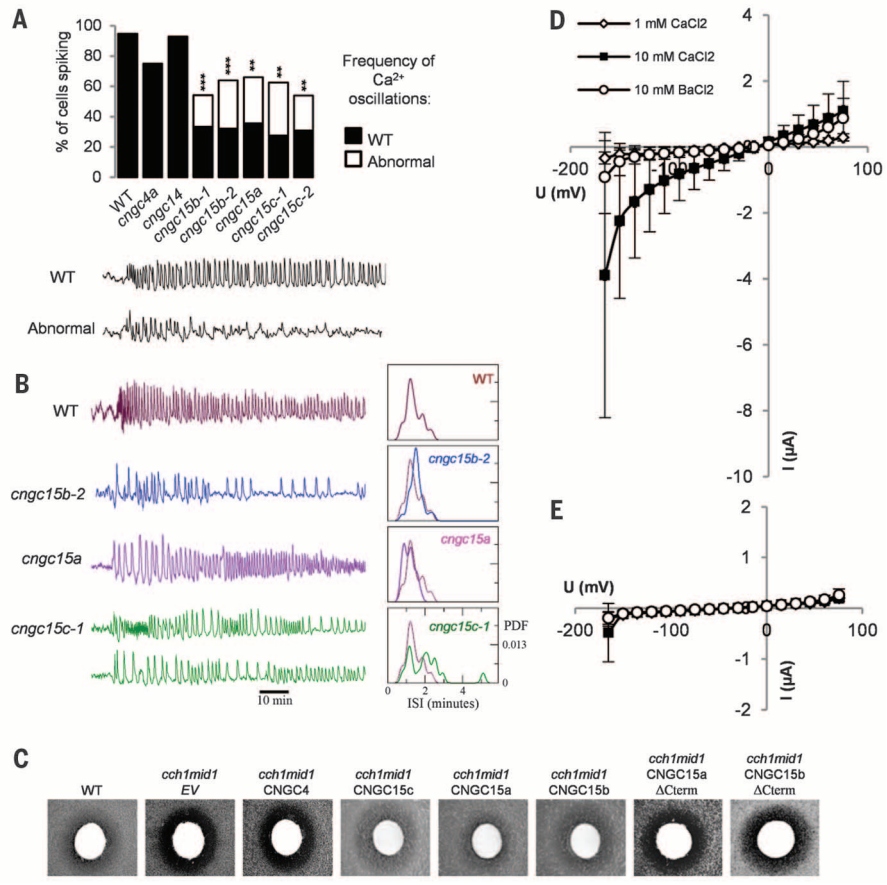


Fig. 2. CNGC15 proteins are required for nuclear Ca^{2+} oscillations and transport Ca^{2+}. (**A**) Nod factor (10^{-9} M)–induced Ca^{2+} spiking, assayed in WT and *cngc* mutants. The number of cells analyzed is shown in fig. S7C. **$P < 0.01$; ***$P < 0.001$ (χ^2 test). Below, black traces show examples of calcium traces that were scored as WT or abnormal. (**B**) Representative Ca^{2+} traces of WT roots and mutants, showing detrended Oregon green/Texas red ratios in arbitrary units. The panels on the right show density plots of average interspike intervals (ISI) during 60 min, starting 7 min after the first spike (n = 26 WT, 26 *cngc15b-2*, 24 *cngc15a*, and 17 *cngc15c-1*; PDF, probability density function). (**C**) CNGC15 proteins complement *cch1/mid1*. Discs containing α factor inhibit growth in the mutant but not the WT or *CNGC15*-complemented strains. CNGC15a and CNGC15b with their C termini truncated (ΔCterm) and CNGC4 do not complement *cch1/mid1*. (**D** and **E**) Average current-voltage (*I-U*) relationship in oocytes expressing *CNGC15a* (D) or injected with water (E) in presence of $CaCl_2$ or $BaCl_2$. Error bars represent standard deviation (n = 4).

Downloaded from http://science.sciencemag.org/ on May 26, 2016

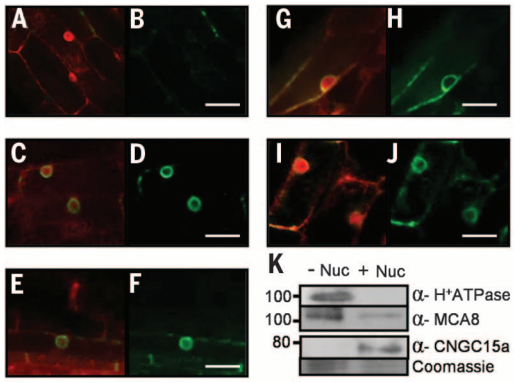


Fig. 3. CNGC15 proteins localize to nuclear membranes. Confocal microscopy of roots expressing the plant marker DsRed alone (**A** and **B**) and with CNGC15b:GFP (**C** and **D**), CNGC15a:GFP (**E** and **F**), CNGC15c:GFP (**G** and **H**), and DMI1:GFP (**I** and **J**) (where the colon denotes fusion). In (A), (C), (E), (G), and (I), the overlay of the green and red channels is shown. In (B), (D), (F), (H), and (J), the green channel is shown. Scale bars, 20 μm. (**K**) The microsomal fraction depleted of nuclei (−Nuc) and the membrane fraction of purified nuclei (+Nuc) from *M. truncatula* roots, assessed with indicated antibodies. Antibodies to H^+ATPase and MCA8 were used as plasma membrane and ER–nuclear membrane markers, respectively. The presence of CNGC15a was detected with its native antibody.

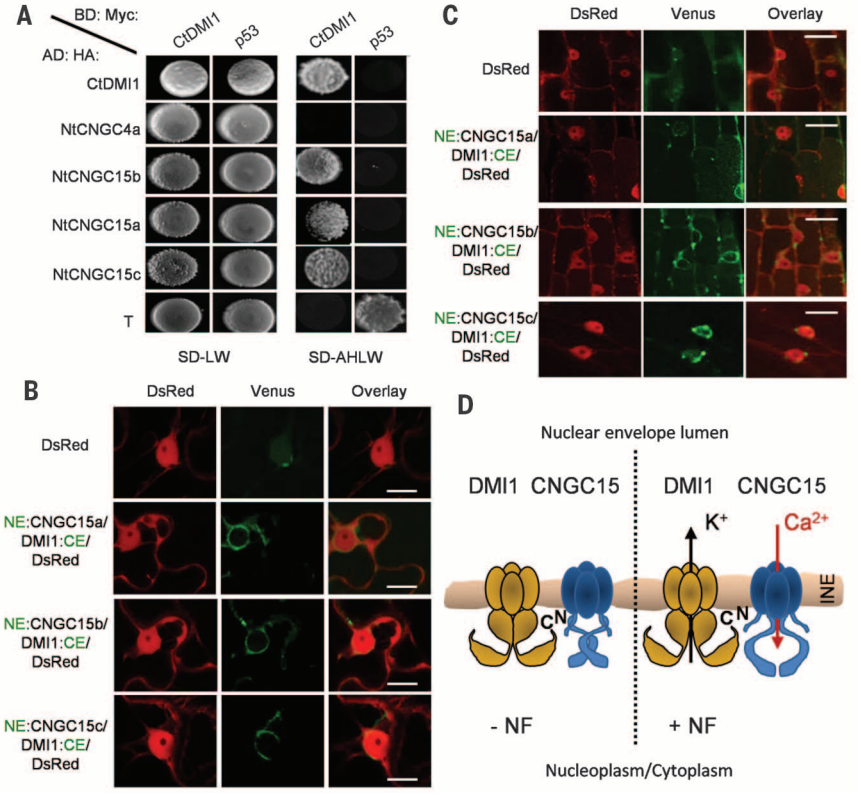


Fig. 4. CNGC15 and DMI1 interact at the nuclear envelope. (**A**) Yeast two-hybrid assays between the C-terminal domain of DMI1 as bait (BD) and the N-terminal domains of CNGC4a, the N-terminal domains of CNGC15 proteins, and the C-terminal domain of DMI1 as prey (AD) (details are given in the supplementary materials). Murine p53 and its interacting partner SV40 large T antigen (simian virus large tumor antigen) were used as a control. SD-LW, synthetic dropout medium lacking Leu and Trp; SD-AHLW, synthetic dropout medium lacking adenine, His, Leu, and Trp. (**B**) *N. benthamiana* leaves transiently expressing N-terminal Venus (NE) fused to the N termini of each CNGC15 and C-terminal Venus (CE) fused to the C terminus of DMI1. DsRed was present in all vectors. Scale bars, 16 μm. (**C**) *M. truncatula* root cells expressing the same fusions. Scale bars, 10 μm. (**D**) A model of CNGC15 and DMI1 dynamics at the inner nuclear envelope (INE). DMI1 interacts physically with CNGC15 to control the simultaneous opening of both channels through direct binding of a secondary messenger to DMI1 or CNGC15 after stimulation with Nod factor (+NF).

To determine whether CNGC15 subgroup members are permeable to Ca^{2+}, we expressed them in the *cch1/mid1* yeast mutant. In response to mating pheromone (α factor), *cch1/mid1* fails to generate cytosolic Ca^{2+} signals, resulting in growth arrest (*13*). This phenotype can be complemented by the release of Ca^{2+} into the cytosol from any Ca^{2+} store. Each of the three CNGC15 proteins was individually able to complement the *cch1/mid1* growth-arrest phenotype (Fig. 2C), suggesting that they are Ca^{2+}-permeable. Additionally, expression of *CNGC15a* in *Xenopus laevis* oocytes triggered an inward Ca^{2+} current (Fig. 2D) that was not observed in control oocytes (Fig. 2E), further demonstrating the Ca^{2+} permeability of this group of channels.

Mathematical modeling has demonstrated that the interplay between the K^+-permeable channel DMI1, a Ca^{2+} channel, and a Ca^{2+}-ATPase can give rise to sustained Ca^{2+} oscillations (*14*). Based on our findings regarding the involvement of CNGC, we adapted this model to introduce a cyclic nucleotide–gating mechanism for the Ca^{2+} channel (*15*) and demonstrated that this system can recapitulate the observed Ca^{2+} oscillations (fig. S12). This model suggests that the activation of DMI1 and CNGC15 must occur simultaneously; introducing lag times in their activation stopped the Ca^{2+} oscillations (fig. S13). One possible mechanism for such simultaneous activation would be the presence of both channels in a single complex. We found that the soluble C terminus of DMI1 and the N termini of CNGC15a, CNGC15b, and CNGC15c interact in yeast (Fig. 4A and fig. S11C). Using bimolecular fluorescence complementation (*16*) of the full-length proteins, we observed interactions at the nuclear envelope between DMI1 and the CNGC15 proteins in both *Nicotiana benthamiana* leaves and *M. truncatula* roots (Fig. 4, B and C); we did not observe interactions in control iterations (fig. S14). Nod factor had no effect on these interactions (fig. S15), implying that the complex is maintained after activation.

We have shown that CNGC15 proteins are responsible for nuclear Ca^{2+} oscillations in the symbiotic signaling pathway of *M. truncatula*. CNGCs have been demonstrated to locate at vacuoles (*17*) or the plasma membrane (*18*). In contrast, CNGC15 proteins are located at the nuclear envelope and are permeable to Ca^{2+}. We propose that the location of these Ca^{2+} channels allows a targeted nuclear release of the ER Ca^{2+} store. Physical interactions between the CNGC15 proteins and DMI1 may support synchronous activation and modulate the Ca^{2+} signal (Fig. 4D). Further work on this nuclear channel complex should clarify how it is regulated and its implication in developmental processes such as fertility.

REFERENCES AND NOTES

1. A. G. Oliveira, E. S. Guimarães, L. M. Andrade, G. B. Menezes, M. Fatima Leite, *Physiology* **29**, 361–368 (2014).
2. N. Pauly *et al.*, *Nature* **405**, 754–755 (2000).
3. G. L. Wheeler, C. Brownlee, *Trends Plant Sci.* **13**, 506–514 (2008).
4. G. E. Oldroyd, *Nat. Rev. Microbiol.* **11**, 252–263 (2013).
5. W. Capoen *et al.*, *Proc. Natl. Acad. Sci. U.S.A.* **108**, 14348–14353 (2011).
6. N. D. Young *et al.*, *Nature* **480**, 520–524 (2011).
7. M. Charpentier *et al.*, *Plant Cell* **20**, 3467–3479 (2008).
8. P. Mäser *et al.*, *Plant Physiol.* **126**, 1646–1667 (2001).
9. R. J. Wais *et al.*, *Proc. Natl. Acad. Sci. U.S.A.* **97**, 13407–13412 (2000).
10. M. Iwano *et al.*, *Development* **139**, 4202–4209 (2012).
11. Y. Hamamura *et al.*, *Nat. Commun.* **5**, 4722 (2014).

Downloaded from http://science.sciencemag.org/ on May 26, 2016

12. J. K. Laba, A. Steen, L. M. Veenhoff, *Curr. Opin. Cell Biol.* **28**, 36–45 (2014).
13. M. Fischer *et al.*, *FEBS Lett.* **419**, 259–262 (1997).
14. M. Charpentier, T. Vaz Martins, E. Granqvist, G. E. Oldroyd, R. J. Morris, *Plant Signal. Behav.* **8**, e22894 (2013).
15. D. P. Dougherty, G. A. Wright, A. C. Yew, *Proc. Natl. Acad. Sci. U.S.A.* **102**, 10415–10420 (2005).
16. R. Waadt *et al.*, *Plant J.* **56**, 505–516 (2008).
17. C. C. Yuen, D. A. Christopher, *AoB Plants* **5**, plt012 (2013).
18. T. Borsics, D. Webb, C. Andeme-Ondzighi, L. A. Staehelin, D. A. Christopher, *Planta* **225**, 563–573 (2007).

ACKNOWLEDGMENTS

We thank J.-M. Ané for the construct *35S:DMI1:GFP*, E. Peiter for the *cch1/mid1* mutant, G. Calder for confocal help, E. Barclay for immunogold labeling, P. Bailey for bioinformatics, K. Mysore and J. Wen for *Tnt1* mutant screening, and M. Hopkins for models of CNGC action. The work was supported by the Biotechnology and Biological Sciences Research Council (grants BB/J004553/1 and BB/J018627/1) and by the European Research Council (SYMBIOSIS project). M.C. and G.E.D.O. directed the research. M.C. performed the experiments with contributions by J.S. (calcium spiking), T.V.M. and R.J.M. (mathematical modeling), G.V.R. (phylogeny), K.F. (immunogold labeling and electron microscopy), E.S. (RNA extraction and quantitative reverse transcriptase polymerase chain reaction), and J.T. and A.-A.V. (electrophysiology). M.C., G.E.D.O., and D.S. wrote the manuscript. The supplementary materials contain additional data.

SUPPLEMENTARY MATERIALS

www.sciencemag.org/content/352/6289/1102/suppl/DC1
Materials and Methods
Figs. S1 to S15
Tables S1 to S2
References (*19*–*35*)

7 December 2015; accepted 20 April 2016
10.1126/science.aae0109

METAL ACQUISITION

Biosynthesis of a broad-spectrum nicotianamine-like metallophore in *Staphylococcus aureus*

Ghassan Ghssein,[1,2,3]* Catherine Brutesco,[1,2,3]* Laurent Ouerdane,[4]* Clémentine Fojcik,[5] Amélie Izaute,[1,2,3] Shuanglong Wang,[4] Christine Hajjar,[1,2,3] Ryszard Lobinski,[4] David Lemaire,[2,3,6] Pierre Richaud,[2,3,7] Romé Voulhoux,[8] Akbar Espaillat,[9] Felipe Cava,[9] David Pignol,[1,2,3] Elise Borezée-Durant,[5] Pascal Arnoux[1,2,3]†

Metal acquisition is a vital microbial process in metal-scarce environments, such as inside a host. Using metabolomic exploration, targeted mutagenesis, and biochemical analysis, we discovered an operon in *Staphylococcus aureus* that encodes the different functions required for the biosynthesis and trafficking of a broad-spectrum metallophore related to plant nicotianamine (here called staphylopine). The biosynthesis of staphylopine reveals the association of three enzyme activities: a histidine racemase, an enzyme distantly related to nicotianamine synthase, and a staphylopine dehydrogenase belonging to the DUF2338 family. Staphylopine is involved in nickel, cobalt, zinc, copper, and iron acquisition, depending on the growth conditions. This biosynthetic pathway is conserved across other pathogens, thus underscoring the importance of this metal acquisition strategy in infection.

Metals are required in many life processes, and consequently all organisms have developed mechanisms for their uptake and homeostasis. Pathogenic bacteria must face an additional barrier of metal limitation that is usually set by the host, precisely in order to prevent bacterial growth (*1*). This strategy of "nutritional immunity" by the hosts also extends to many micronutrients with dedicated mechanisms of sequestration for iron, manganese, or zinc (*2*, *3*). The paradigm of metal acquisition in metal-deprived environments is associated with iron: Whereas one strategy consists in transporting the reduced form, the most common scheme involves the synthesis of high-affinity ferric siderophores, their extracellular release before capture, and import of the siderophore-Fe^{3+} complex (*4*). These siderophores are frequently associated with virulence and may also be used for the transport of metals other than iron (*5*, *6*), with only a few examples of other types of microbial metallophores. Methanobactin, for example, is a peptide-based chalkophore used for copper scavenging by methane-oxidizing bacteria (*7*). Free L-histidine (L-His) is used as a nickelophore by some bacteria, and more complex molecules are possibly used by *Staphylococcus aureus* or *Helicobacter pylori*, although their identity or functional relevance are unknown (*8*, *9*). Recently, a nickel/cobalt uptake system (called CntA-F) was uncovered in *S. aureus* and was found to play a role in the virulence of this strain (*10*).

Plants have also evolved their own metal chelators, and among them, nicotianamine is an important metabolite that is essential in the homeostasis of iron, copper, nickel, and zinc (*11*, *12*). Nicotianamine is also the first precursor of phytosiderophores, a family of molecules chemically different from but functionally equivalent to siderophores (*13*). Nicotianamine is enzymatically synthesized by nicotianamine synthase (NAS), which catalyzes the condensation of three α-aminobutyric acid moieties from *S*-adenosylmethionine (SAM) with the cyclization of one of them to form an azetidine ring (*14*–*16*). Nicotianamine and its phytosiderophore derivatives seem to be restricted to plants and some fungi, although some archaea apparently produce a nicotianamine-related molecule called thermonicotianamine, the functional role of which remains unknown (*17*).

Trying to better understand this family of plant NAS and archaeal NAS-like enzymes, we found a gene putatively coding for a NAS-like enzyme in bacterial genomes, including that of *S. aureus*. The NAS-like gene from *S. aureus* (*sav2469*), here called *cntL*, shares 12% sequence identity with one of the four NASs from *Arabidopsis thaliana*, which corresponds to a very distant homology. However, threading-based structure prediction programs detected a structural homology of CntL with eukaryotic NAS and archaeal NAS-like enzymes (fig. S1). The gene coding for CntL is systematically located upstream of a gene whose product belongs to the DUF2338 family (*cntM* in *S. aureus*, *sav2468*; Fig. 1 and fig. S2). Threading-based prediction indicates with high confidence that this family of protein is related to octopine dehydrogenase, a NAD(P)H-dependent enzyme that reductively condensates a free amino acid, such as arginine, with an α-ketoacid, such as pyruvate (*18*). This family of enzymes is known to be involved in the escape of scallops from their starfish predators (*19*) or in the growth of parasitic bacteria, such as *Agrobacterium tumefaciens*, at the expense of plants in which they induce opine-producing tumors, offering bacteria a selective growth advantage (*20*). In *S. aureus*, the gene upstream of *cntL* (*cntK*, *sav2470*) appears restricted to the phylum of Firmicutes and encodes a protein that is distantly related to a diaminopymelate epimerase (DapF).

On the basis of these predictions, the putative activity of each of these three enzymes could be joined together to form a biosynthetic machinery: The CntK epimerase would produce an amine substrate of proper stereochemistry that would be

[1]Laboratoire de Bioénergétique Cellulaire, Institut de Biosciences et Biotechnology Aix-Marseille (BIAM), Commissariat à l'Energie Atomique et aux Energies Alternatives (CEA), 13108 Saint-Paul-lès-Durance, France. [2]UMR 7265, Centre National de Recherche Scientifique, Saint-Paul-lès-Durance, France. [3]Aix Marseille Université, Marseille, France. [4]Université de Pau et des Pays de l'Adour/CNRS, Laboratoire de Chimie Analytique Bio-inorganique et Environnement, IPREM-UMR5254, Hélioparc, 2, Avenue Angot, 64053 Pau, France. [5]Micalis Institute, INRA, AgroParisTech, Université Paris-Saclay, 78350 Jouy-en-Josas, France. [6]Lab Interact Protein Metal, BIAM, CEA, 13108 Saint-Paul-lès-Durance, France. [7]Lab Bioenerget Biotechnol Bacteries et Microalgues, BIAM, CEA, 13108 Saint-Paul-lès-Durance, France. [8]CNRS et Aix-Marseille Université, Laboratoire d'Ingénierie des Systèmes Macromoléculaires (UMR7255), Institut de Microbiologie de la Méditerranée, Marseille, France. [9]Laboratory for Molecular Infection Medicine Sweden, Department of Molecular Biology, Umeå Centre for Microbial Research, Umeå University, Umeå, Sweden.
*These authors contributed equally to this work. **†Corresponding author. Email: pascal.arnoux@cea.fr**

Downloaded from http://science.sciencemag.org/ on May 26, 2016

modified by the CntL NAS-like enzyme through the addition of one or two α-aminobutyric acid moieties, and CntM would reductively condensate an α-ketoacid to the previously formed product, leading to the formation of a candidate molecule. Although their putative activity was not recognized at the time, the three corresponding genes (*cntKLM*) were shown to belong to an operonic structure involved in the import of nickel and cobalt ions through an ABC transporter named *cntA-F* (*8*) (Fig. 1A). Two independent genetic studies targeting either the solute binding protein (SBP; *cntA)* or the MFS transporter (major facilitator superfamily, here called *cntE*) indicated that this operon is important for the virulence and fitness of *S. aureus* (*10*, *21*). The phenotype of these mutations could be reconciled by the hypothesis of a siderophore-like system with a biosynthetic machinery (CntKLM), a putative exporter (CntE), and a putative importer of a metal-metallophore complex (CntABCDF).

We attempted to identify the candidate metallophore through an ab initio approach using *Escherichia coli* or *S. aureus* strains and through a knowledge-based approach using purified proteins (*22*). For the first approach, we cloned the entire 10-kb *cnt* operon (*cntKLMABCDFE*) in *E. coli* and induced gene expression and protein production. After adding nickel, we tracked small molecules co-eluting with nickel by metabolomic studies using hydrophilic interaction liquid chromatography (HILIC; fig. S3). We also constructed a mutant strain of *S. aureus* devoid of the *cntL* gene and cultivated both the wild-type (WT) and this mutant strains in chemically defined medium (CDM), a medium with low metal concentration, in which expression of the operon is known (*10*). We then detected metal complexes in the extracellular fractions by coupling HILIC separation with inductively coupled plasma mass spectrometry (ICP-MS) and electrospray ionization mass spectrometry (ESI-MS) (Fig. 1). A main peak was found to elute between 30 and 33 min in the HILIC/ICP-MS experiment, with the retention time depending on the detected metal (Fig. 1B). In all the cases, these peaks were absent in the *cntL* mutant strain, therefore corroborating our central hypothesis of the existence of a direct link between these metal complexes and the central NAS-like enzyme. Investigation of these metal complexes by coupling HILIC and ESI-MS led us to find a candidate molecule showing the characteristic metal isotopic patterns (Fig. 1C and fig. S3). The retention times of these compounds in HILIC/ESI-MS match those of the metals elution found by HILIC/ICP-MS, indicating that the same metal complexes were observed by the two techniques. The knowledge-based approach consisted of trapping the nickel-metallophore complex: We expressed and purified the SBP (CntA) from *E. coli* and incubated it in a supernatant of a *cntA* mutant of *S. aureus* grown in CDM medium. We then supplemented this mix with nickel to force nickel-metallophore complex formation and binding to CntA. After repurification of the SBP and further analysis by MS, we looked for the characteristic nickel isotopic pattern and found a candidate molecule with the same mass as found by the metabolomic approaches (fig. S4). Using our set of accurate masses with molecular formula finder software programs, we proposed an empiric formula of $C_{13}H_{19}N_4O_6$-metal.

We attempted to fit this formula by using simple rules derived from our proposed enzymes activities and putative substrates (*22*), and we finally propose the structure of a candidate molecule that would be the result of three biosynthetic enzyme activities: (i) racemization of L-His in D-His by CntK, (ii) nucleophylic attack of one α-aminobutyric acid moiety from SAM onto D-His to produce an intermediate (denoted xNA) by CntL, and (iii) reductive condensation of the xNA intermediate with a molecule of pyruvate by CntM (Fig. 2A). Gas-phase fragmentation of zinc and nickel metal complexes confirmed the proposed structure of the discovered molecule (fig. S5), which we name staphylopine to recall its origin in *S. aureus* and its inclusion in the opine family (*23*).

We then tested and refined this hypothetical biosynthetic pathway by cloning, expressing, and purifying the three enzymes and testing their respective activities (Fig. 2, B to D, and fig. S6). First, we incubated CntK with L- or D-His and found that it indeed produces D-His from the L-stereoisomer and vice versa, thus establishing CntK as a histidine racemase (Fig. 2B). Because co-incubation with L-His and a competing concentration of either L-alanine or L-methionine did not inhibit the histidine racemase activity, CntK appears to be specific for histidine (fig. S7). CntK is therefore not a diaminopimelate epimerase as its sequence similarity could suggest, but rather represents a novel enzyme family of histidine racemase. With regard to CntL, we determined a dissociation constant (K_d) of 68 μM for SAM, which corroborates our central hypothesis that CntL binds to SAM (fig. S8). We then tested our prediction suggesting the binding of NAD(P)H to CntM by incubating either NADH or NADPH with the purified enzyme. This indicated a preference of the enzyme for NADPH, and fluorescence resonance energy transfer (FRET) between the tryptophan residue of the protein (excitation 280 nm, emission 340 nm) and NAD(P)H (340 nm and 460 nm, respectively) further revealed that CntM is specific for NADPH, with a K_d of about 50 μM (Fig. 2C), a value that was confirmed with microcalorimetric titrations (fig. S8). Therefore, CntM has the biochemical characteristics of members of the opine synthase enzyme family, as suggested by the results of threading programs.

We then investigated the combined enzymatic activities of CntK, CntL, and CntM through the

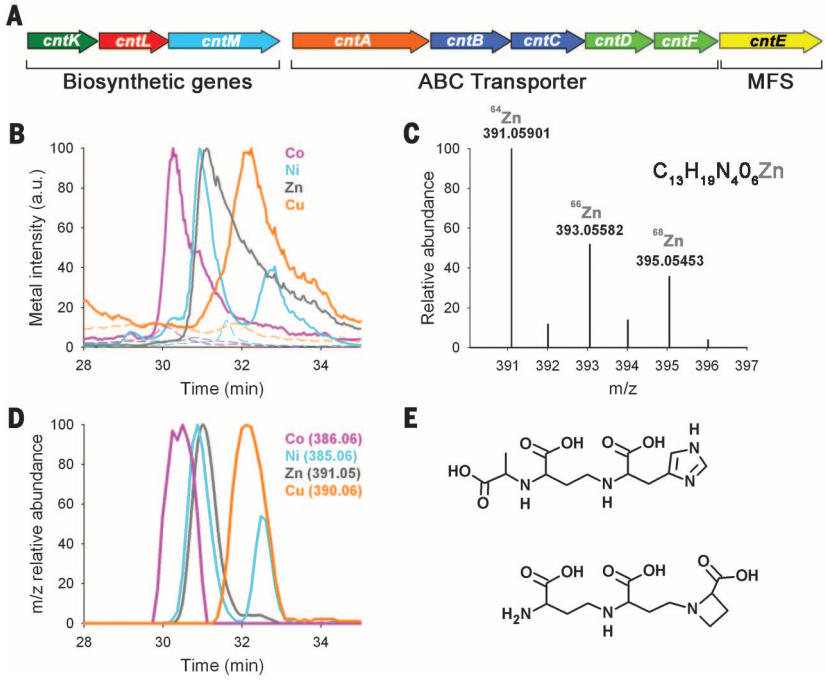


Fig. 1. The *cnt* operon and detection of a broad-spectrum metallophore. (**A**) The *cnt* operon encodes three putative biosynthetic genes, together with the genes coding for a full ABC transporter and a transporter belonging to the MFS family. (**B**) HILIC/ICP-MS chromatograms of extracellular fractions of *S. aureus* and comparison of the WT strain (solid line) with the *cntL* mutant (dotted lines). (**C**) Mass spectra of a chelating compound present in its free and complexed forms (here shown in complex with Zn) in the extracellular fraction of the WT strain but absent in the *cntL* mutant, as observed in chromatogram around 31 min during HILIC/ESI-MS analyses. The empirical molecular formula was deduced from exact masses. (**D**) HILIC/ESI-MS extracted ion chromatograms (XIC) of some metal ions observed to form a complex with the above-mentioned chelator. Chromatograms were traced using the exact masses (±3 parts per million) of the expected complex, and these masses were absent in the extracellular fraction of the *cntL* mutant. (**E**) Proposed chemical structure of staphylopine (top) and comparison with nicotianamine (bottom).

Downloaded from http://science.sciencemag.org/ on May 26, 2016

use of a carboxyl-[^{14}C]–labeled SAM substrate. The use of this radiolabeled substrate allowed us to follow the α-aminobutyric acid moiety of SAM after product separation by thin-layer chromatography (TLC) and autoradiography. We found that [^{14}C]-labeled SAM alone gave one strong band, with three bands of lower intensity, probably corresponding to SAM and some degradation products, such as *S*-adenosyl-L-homocysteine (Fig. 2D). Although the incubation of [^{14}C]-SAM with CntL and L-His did not change this SAM pattern, the incubation with D-His led to a novel prominent band, which migrated below the lowest SAM band (Fig. 2D). According to our model, this band corresponds to the intermediate called xNA. We then tested the effect of co-incubating both CntL and CntM enzymes together with their putative substrates: L- and D-His, pyruvate, and NADPH (Fig. 2D, lanes 4 and 5). Here again the SAM pattern stayed unchanged when L-His was used. However, using D-His, we could detect two novel bands: one corresponding to the previous intermediate xNA and one that migrated between the two upper bands of SAM and would correspond to staphylopine. This identification is further supported by the fact that the staphylopine band appears at the expense of the xNA intermediate, as expected in such a case. We also confirmed the histidine racemase activity of CntK by co-incubating all three enzymes together with their substrates. In this case, the incubation with L- or D-His both led to the appearance of the xNA and staphylopine bands, in accordance with the CntK activity, which produces both L- and D-His when supplied with either stereoisomer (Fig. 2D, lanes 6 and 7). Incubation of the three enzymes

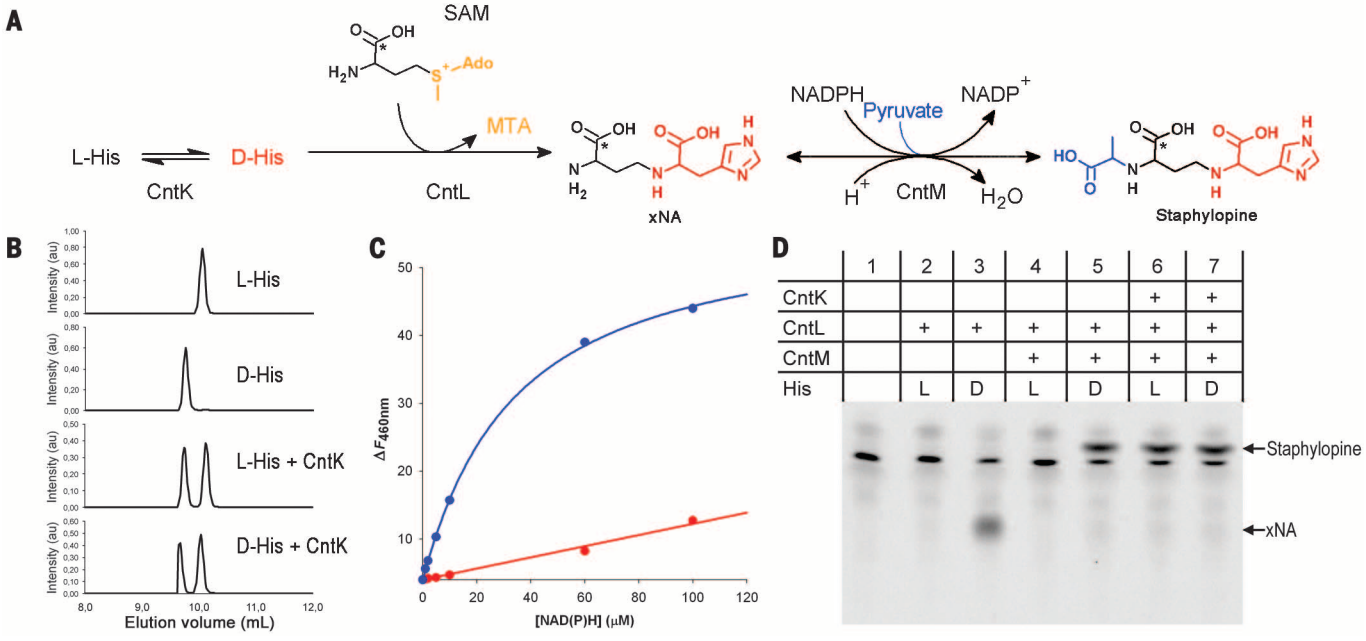


Fig. 2. Biosynthesis of staphylopine and biochemical characterization of the biosynthetic enzymes. (**A**) Biosynthesis pathway for the assembly of staphylopine from L-His, SAM, and pyruvate. (**B**) Epimerase assay of CntK and comparison with L- and D-His standards. (**C**) Titration of NADH (red) and NADPH (blue) binding to CntM (5 μM) followed by fluorescence energy transfer between tryptophan excitation (280 nm) and NAD(P)H emission (460 nm). Fitting of the data obtained for NADPH binding led to a K_d of 50 μM. (**D**) TLC separation of reaction products incubating [^{14}C]-SAM [labeled on its α-aminobutyric acid moiety; marked with an asterisk in (A)] with various purified enzymes, pyruvate, NADPH, and either L- or D-His.

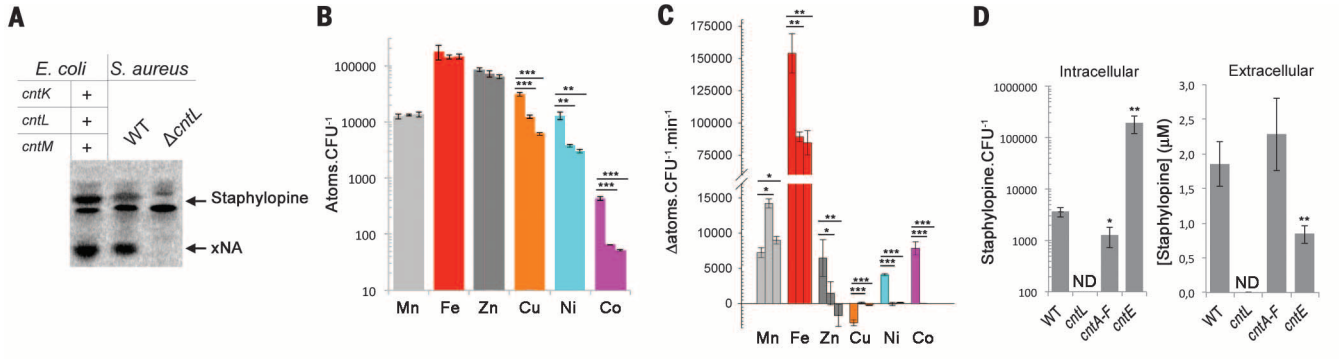


Fig. 3. Effect of *cnt* mutations in metal content and staphylopine localization. (**A**) TLC separation of co-incubation of *E. coli* cell extracts separately expressing CntK, CntL, and CntM with [^{14}C]-SAM and comparison with the cell extracts from WT *S. aureus* and *cntL* mutant strains. (**B**) Intracellular metal content of the *S. aureus* WT (left), *cntL* (middle), and *cntA-F* (right) strains grown in CDM and determined by ICP-MS. Error bars, mean ± SD $^{**}P < 0.01$ and $^{***}P < 0.001$. (**C**) Intracellular metal content change of the *S. aureus* WT (left), *cntL* (middle), and *cntA-F* (right) strains grown in dCDM until late exponential phase (T0) and then incubated for 10 min with 0.3 μM Fe(II) and Zn and 0.1 μM Mn, Ni, Co, and Cu. Metal content variation was determined by ICP-MS and expressed as the differential of atoms after 10 min as compared to T0. Error bars, mean ± SD. $^{*}P < 0.05$, $^{**}P < 0.01$, and $^{***}P < 0.001$. (**D**) Staphylopine level in the intracellular (left; note the logarithm scale) and supernatant (right) fractions of the WT, *cntABCDF*, *cntL*, and *cntE* mutant strains. Error bars, mean ± SD. $^{*}P < 0.05$ and $^{**}P < 0.01$; ND, not detected.

Downloaded from http://science.sciencemag.org/ on May 26, 2016

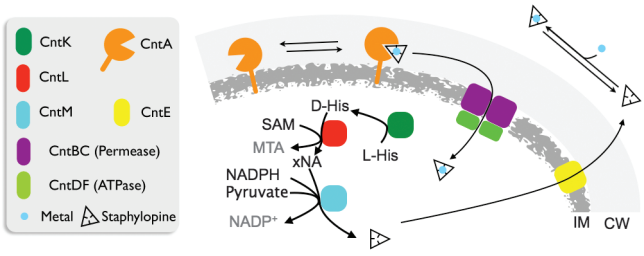


Fig. 4. Model of staphylopine biosynthesis, export, and recovery of staphylopine-metal complexes through the ABC transporter. IM, inner membrane; CW, cell wall.

with different aminoacids, α-keto acids, and reducing agents confirmed that the histidine racemase CntK is indeed specific for histidine and that CntM could use neither NADH nor α-keto glutarate in place of NADPH and pyruvate, respectively (fig. S9). Overall, these in vitro studies of the three biosynthetic enzymes show that they sequentially synthesize staphylopine according to our proposed scheme, using common and defined substrates.

We confirmed that staphylopine biosynthesis is impaired in the *cntL* mutant of *S. aureus* and explored the effect of mutations of several genes in the *cnt* operon on metal homeostasis and staphylopine production and trafficking (Fig. 3). When compared to the WT strain of *S. aureus*, both the xNA and the staphylopine bands disappeared in the *cntL* mutant, confirming that both bands are dependent on CntL activity (Fig. 3A). Furthermore, the bands corresponding to xNA and staphylopine migrated at the same distance in *E. coli* or *S. aureus* cell extracts, confirming that both molecules are produced heterologously in *E. coli*.

We next sought to determine the effect of the *cntL* mutation with regard to intracellular metal accumulation in various culture conditions: CDM, where metal concentration is rather low; Chelex-demetalated CDM (dCDM), where the metal level is even lower; nitrilotriacetic acid (NTA)–demetalated CDM supplemented with metalated NTA resin to supposedly mimic a chelating environment (rCDM); and lysogeny broth (LB), where metal concentration is high. The growth of the *cntL* mutant was nearly identical to that of the WT strain in these media (fig. S10), indicating that metal content would be attributable to the absence of staphylopine and not to a growth defect. In all these culture conditions, we established that the *cnt* genes, transcribed from two promoters upstream, *cntKLM* and *cntA-E*, are highly expressed in metal-poor media, whereas their activities are lower but still significant in LB (fig. S11). In CDM and dCDM, the *cntL* mutation caused a decrease in the intracellular accumulation of nickel, copper, and cobalt as determined by ICP-MS (Fig. 3B and fig. S12A). This metal accumulation defect is comparable to the one observed in the *cntA-F* mutant, indicating that metal or metal-staphylopine complexes are transported via CntA (Fig. 3B). This defect in metal accumulation is complemented when the *cntL* gene is reintroduced in the mutant, although using slightly different conditions adapted for ICP-AES metal content determination (fig. S13). In this case, there is no decrease in intracellular copper, but a decrease in intracellular zinc, nickel, and cobalt. In rCDM, the tendency observed in CDM is confirmed, although in this condition iron, zinc, copper, nickel, and cobalt content are all affected in the mutant strain as compared to the wild type (fig. S12B). Finally, in a metal-rich medium such as LB, the *cntL* deletion mutant accumulated less iron, copper, and cobalt (fig. S12C).

Taken together, these sets of experiments suggest that depending on the nature of the metal, its concentration, and the bacterial growth status, staphylopine is involved in the import of a large array of divalent metals in *S. aureus*. Testing metal transport over 10 min supports the involvement of both staphylopine and CntA-F in the import of all these metals. Indeed, the import of iron, zinc, nickel, and cobalt are all decreased in both *cntL* and *cntA-F* mutants (Fig. 3C). The short-term transport of iron and zinc is consistent with their known regulatory effect exerted on the *cnt* operon (*10*, *21*). The transport of copper is somehow different, because WT cells efficiently export this metal during this short time, probably in response to its toxicity. In this case, the absence of CntL or CntA-F appears to decrease this toxicity and its consecutive efflux.

In order to investigate the transport of metal-staphylopine complexes through CntA, we exploited the sensitivity of *S. aureus* to high cobalt concentration. We found that *cntL* and *cntA-F* mutant strains are resistant to a concentration of cobalt that is toxic to the WT strain, whereas supplementation of synthetic staphylopine in the media restores its toxicity in the *cntL* but not in *cntA-F* strain (fig. S14). This suggests a cotransport of cobalt-staphylopine complexes via CntA-F, because the ABC transporter is still present in the *cntL* mutant (hence the cobalt toxicity), whereas it is absent in the *cntA-F* mutant (where cobalt-staphylopine cannot enter the cell). Finally, we measured the staphylopine level in the intracellular and supernatant fractions of the WT, *cntABCDF*, *cntL*, and *cntE* mutants (Fig. 3D). This experiment confirmed the absolute need for CntL in the biosynthesis of staphylopine, further supported the function of CntA-F in the import of staphylopine-metal complexes, and clearly indicated that CntE is involved in the export of staphylopine. Overall, despite being distantly related, staphylopine apparently mirrors the effect that nicotianamine has on the same range of metals but in the context of metal homeostasis and transport in plants (*17*). Chemically synthesized staphylopine has the same range of metal affinity as nicotianamine (similar K_d and affinity order: $Cu^{2+} > Ni^{2+} > Co^{2+} > Zn^{2+} > Fe^{2+}$; fig. S15), further supporting their functional comparison as broad-spectrum metallophores.

The biosynthesis of staphylopine aggregates three unprecedented enzyme activities with the use of D-His, the fusion of a single α-aminobutyric acid moiety from SAM, and the fabrication of an opine derivative (Fig. 4). This latter activity was so far restricted to plants' bacterial transfection or anaerobic glycolysis in marine invertebrates (*19*, *23*). The use of histidine as a building block is interesting, because the free amino acid has a relatively high affinity for nickel on its own and is directly used for nickel uptake by bacteria (*8*, *24*–*26*). However, the use of the D- stereoisomer of histidine is surprising because D- amino acids are mainly used in cell wall biosynthesis and have been mostly restricted to alanine and glutamate (*27*), although other "non-canonical" D- amino acids are reported to be involved in the composition of the cell wall (*28*, *29*), biofilm stability (*30*), virulence (*31*), or sporulation (*32*). Another peculiarity of the staphylopine biosynthetic machinery resides in the NAS-like CntL enzyme that only uses one α-aminobutyric acid moiety from SAM, whereas the NAS-like enzyme from *M. thermotautrophicum* uses two, and plant enzymes use three such moieties. The evolution from bacterial staphylopine to plants' nicotianamine preserves a large part of the molecule's backbone, therefore suggesting a conservative chemical evolution occurring together with enzymatic simplifications, in which plant nicotianamine is synthesized by a single enzyme. Finally, homologous genes involved in staphylopine biosynthesis are conserved in other pathogenic bacteria such as *Yersinia pestis* or *Pseudomonas aeruginosa*, underscoring the likely influence of this metallophore in bacterial pathogenicity. Indeed, the export pathway of this metallophore was recently identified as a critical function for the growth of *P. aeruginosa* in airway mucus secretions, where metal access is severely limited (*33*).

REFERENCES AND NOTES

1. M. L. Reniere, G. Pishchany, E. P. Skaar, in *Iron Uptake and Homeostasis in Microorganisms*, P. Cornelis, S. C. Andrews, Eds. (Caister Academic Press, 2010), pp. 264–274.
2. B. D. Corbin *et al.*, *Science* **319**, 962–965 (2008).
3. M. I. Hood, E. P. Skaar, *Nat. Rev. Microbiol.* **10**, 525–537 (2012).
4. Z. Ma, F. E. Jacobsen, D. P. Giedroc, *Chem. Rev.* **109**, 4644–4681 (2009).
5. A. G. Bobrov *et al.*, *Mol. Microbiol.* **93**, 759–775 (2014).
6. I. J. Schalk, M. Hannauer, A. Braud, *Environ. Microbiol.* **13**, 2844–2854 (2011).
7. H. J. Kim *et al.*, *Science* **305**, 1612–1615 (2004).
8. H. Lebrette *et al.*, *Metallomics* **7**, 613–621 (2015).
9. K. Schauer, B. Gouget, M. Carrière, A. Labigne, H. de Reuse, *Mol. Microbiol.* **63**, 1054–1068 (2007).
10. L. Remy *et al.*, *Mol. Microbiol.* **87**, 730–743 (2013).
11. C. Curie *et al.*, *Ann. Bot. (London)* **103**, 1–11 (2009).
12. E. L. Walker, B. M. Waters, *Curr. Opin. Plant Biol.* **14**, 318–324 (2011).
13. R. Hell, U. W. Stephan, *Planta* **216**, 541–551 (2003).
14. A. Herbik *et al.*, *Eur. J. Biochem.* **265**, 231–239 (1999).
15. K. Higuchi *et al.*, *Plant Physiol.* **119**, 471–480 (1999).
16. H. Q. Ling, G. Koch, H. Bäumlein, M. W. Ganal, *Proc. Natl. Acad. Sci. U.S.A.* **96**, 7098–7103 (1999).
17. C. Dreyfus, D. Lemaire, S. Mari, D. Pignol, P. Arnoux, *Proc. Natl. Acad. Sci. U.S.A.* **106**, 16180–16184 (2009).
18. S. H. Smits, A. Mueller, L. Schmitt, M. K. Grieshaber, *J. Mol. Biol.* **381**, 200–211 (2008).
19. M. Harcet, D. Perina, B. Pleše, *Biochem. Genet.* **51**, 666–676 (2013).

Downloaded from http://science.sciencemag.org/ on May 26, 2016

20. M. W. Bevan, M. D. Chilton, *Annu. Rev. Genet.* **16**, 357–384 (1982).
21. Y. Ding, Y. Fu, J. C. Lee, D. C. Hooper, *J. Bacteriol.* **194**, 6586–6593 (2012).
22. Materials and methods are available as supplementary materials on *Science* Online.
23. J. Thompson, J. A. Donkersloot, *Annu. Rev. Biochem.* **61**, 517–554 (1992).
24. P. T. Chivers, E. L. Benanti, V. Heil-Chapdelaine, J. S. Iwig, J. L. Rowe, *Metallomics* **4**, 1043–1050 (2012).
25. H. Lebrette, M. Iannello, J. C. Fontecilla-Camps, C. Cavazza, *J. Inorg. Biochem.* **121**, 16–18 (2013).
26. M. M. Shaik, L. Cendron, M. Salamina, M. Ruzzene, G. Zanotti, *Mol. Microbiol.* **91**, 724–735 (2014).
27. W. Vollmer, D. Blanot, M. A. de Pedro, *FEMS Microbiol. Rev.* **32**, 149–167 (2008).
28. F. Cava, M. A. de Pedro, H. Lam, B. M. Davis, M. K. Waldor, *EMBO J.* **30**, 3442–3453 (2011).
29. H. Lam *et al.*, *Science* **325**, 1552–1555 (2009).
30. I. Kolodkin-Gal *et al.*, *Science* **328**, 627–629 (2010).
31. A. T. Anfora, B. J. Haugen, P. Roesch, P. Redford, R. A. Welch, *Infect. Immun.* **75**, 5298–5304 (2007).
32. K. A. O'Connor, D. R. Zusman, *Mol. Microbiol.* **24**, 839–850 (1997).
33. M. Gi *et al.*, *Sci. Rep.* **5**, 14644 (2015).

ACKNOWLEDGMENTS

We thank the Commissariat à l'Energie Atomique et aux Energies Alternatives (CEA), the Agence Nationale de la Recherche (ANR, program ANR-14-CE09-0007), and the CEA program ToxNuc-E for financial support. Support was also provided by the HélioBiotec platform (funded by the European Regional Development Fund, the Région Provence Alpes Côte d'Azur, the French Ministry of Research, and the "Commissariat à l'Energie Atomique et aux Energies Alternatives"). G.G. was supported by the Région PACA. Work at the F.C. lab was supported by the Laboratory for Molecular Infection Medicine Sweden, the Knut and Alice Wallenberg Foundation, the Swedish Research Council, and a Kempe foundation scholarship to A.E. S.W. was supported by a fellowship from the Chinese Scholarship Council. We thank J. Lavergne for careful reading of the manuscript and A. Verméglio, C. Cavazza, and H. Lebrette for fruitful discussions. All data are presented in the supplementary materials.

SUPPLEMENTARY MATERIALS

www.sciencemag.org/content/352/6289/1105/suppl/DC1
Materials and Methods
Figs. S1 to S16
Tables S1 to S3
References (*34*–*49*)

17 December 2015; accepted 12 April 2016
10.1126/science.aaf1018

ATMOSPHERIC PARTICLES

New particle formation in the free troposphere: A question of chemistry and timing

F. Bianchi,[1,2,3]* J. Tröstl,[1] H. Junninen,[3] C. Frege,[1] S. Henne,[4] C. R. Hoyle,[1,5] U. Molteni,[1] E. Herrmann,[1] A. Adamov,[3] N. Bukowiecki,[1] X. Chen,[3] J. Duplissy,[3,6] M. Gysel,[1] M. Hutterli,[7] J. Kangasluoma,[3] J. Kontkanen,[3] A. Kürten,[8] H. E. Manninen,[3] S. Münch,[8] O. Peräkylä,[3] T. Petäjä,[3] L. Rondo,[8] C. Williamson,[8]† E. Weingartner,[1]‡ J. Curtius,[8] D. R. Worsnop,[3,9] M. Kulmala,[3] J. Dommen,[1] U. Baltensperger[1]*

New particle formation (NPF) is the source of over half of the atmosphere's cloud condensation nuclei, thus influencing cloud properties and Earth's energy balance. Unlike in the planetary boundary layer, few observations of NPF in the free troposphere exist. We provide observational evidence that at high altitudes, NPF occurs mainly through condensation of highly oxygenated molecules (HOMs), in addition to taking place through sulfuric acid–ammonia nucleation. Neutral nucleation is more than 10 times faster than ion-induced nucleation, and growth rates are size-dependent. NPF is restricted to a time window of 1 to 2 days after contact of the air masses with the planetary boundary layer; this is related to the time needed for oxidation of organic compounds to form HOMs. These findings require improved NPF parameterization in atmospheric models.

Atmospheric aerosols influence climate through direct interaction with radiation and by acting as cloud condensation nuclei (*1*, *2*). There is considerable uncertainty about what fraction of cloud condensation nuclei is attributable to new particle formation (NPF) (*3*–*5*). Studies of NPF in the free troposphere have used ground-based (*6*–*9*) and airborne (*10*) platforms but with limited instrumentation and/or over short time scales. Because of the lack of data at high altitudes, the vast majority of models use free-troposphere NPF schemes in which particle formation rates depend only on the concentration of sulfuric acid, relative humidity, and temperature (*11*). Recently, comprehensive NPF measurements performed as part of the CLOUD (Cosmics Leaving Outdoor Droplets) project detected ternary nucleation of sulfuric acid with water and oxidized organics (*12*). Implementation of this NPF scheme in GLOMAP (Global Model of Aerosol Processes) (*13*) yielded a photochemically and biologically driven seasonal cycle of particle concentrations in the continental boundary layer, comparable to observations (*12*). Further CLOUD experiments observed NPF without involvement of sulfuric acid, which is expected to be important especially in pristine regions and the preindustrial atmosphere (*14*). These laboratory and modeling studies call for field verification.

To chemically and physically characterize the early stage of NPF in the free troposphere, we used a suite of state-of-the-art mass spectrometers and particle counters at the high-altitude research station Jungfraujoch (JFJ), Switzerland [3580 m above sea level (*15*)]. At this site, NPF occurs on 15 to 20% of days, without apparent seasonal dependence (fig. S9), as shown by long-term observations (*16*) and dedicated campaigns (*17*). We report measurements collected over the period of a year, including two intensive 1-month campaigns (table S1).

We identified three typical situations, represented by consecutive example days (days 1 to 3) (Fig. 1); in addition, we show a special case (day 4) where the sulfuric acid concentration was unusually high (~6×10^6 cm^{-3}). Day 1 (25 February 2014) is an example of one of the many non-event days during sunny conditions. During the afternoon, there is a slight enhancement in the concentration of 5- to 10-nm particles, but the simultaneous increase in larger particles (up to 90 nm) suggests that this enhancement is related to vertical transport of particles formed elsewhere (*15*). Day 2 (26 February 2014) is typical of days when the JFJ is within clouds, when NPF is suppressed by reduced global radiation and the high condensation sink of the cloud droplets. Days 3 and 4 (27 February and 2 March 2014) are two examples of NPF days, classified as 1A events (*15*), where the number concentration of particles larger than 3.2 nm increases strongly from a few hundred to 40,000 cm^{-3}.

On most sunny days, the sulfuric acid concentration followed a consistent diurnal cycle, with concentrations <10^4 cm^{-3} during the night and ≤5×10^5 cm^{-3} during the day (except day 4, which had much higher concentrations). However, no link was found between sulfuric acid and NPF, suggesting that sulfuric acid at these concentrations does not explain NPF at the JFJ (Fig. 1D). Highly oxygenated molecules (HOMs), which we detected with a chemical ionization–atmospheric pressure interface–time of flight mass spectrometer (CI-APi-TOF), were formed on some sunny days (e.g., day 3) but not on others (e.g., day 1) (Fig. 1D). This variability is probably dependent on the presence of organic precursors in the free troposphere. Figure 1E shows the time evolution

[1]Laboratory of Atmospheric Chemistry, Paul Scherrer Institute, 5232 Villigen, Switzerland. [2]Institute for Atmospheric and Climate Science, ETH Zurich, 8092 Zurich, Switzerland. [3]Department of Physics, University of Helsinki, 00014 Helsinki, Finland. [4]Empa, Swiss Federal Laboratories for Materials Science and Technology, 8600 Dübendorf, Switzerland. [5]WSL (Swiss Federal Institute for Forest, Snow and Landscape Research) Institute for Snow and Avalanche Research SLF, 7260 Davos, Switzerland. [6]Helsinki Institute of Physics, University of Helsinki, 00014 Helsinki, Finland. [7]Tofwerk, 3600 Thun, Switzerland. [8]Institute for Atmospheric and Environmental Sciences, Goethe University Frankfurt, 60438 Frankfurt am Main, Germany. [9]Aerodyne Research, Billerica, MA 01821, USA.
***Corresponding author. Email: federico.bianchi@psi.ch (F.B.); urs.baltensperger@psi.ch (U.B.)** †Present address: Cooperative Institute for Research in Environmental Sciences, University of Colorado, Boulder, CO 80309, USA. ‡Present address: Institute for Aerosol and Sensor Technology, University of Applied Sciences (FHNW), 5210 Windisch, Switzerland.

Downloaded from http://science.sciencemag.org/ on May 26, 2016

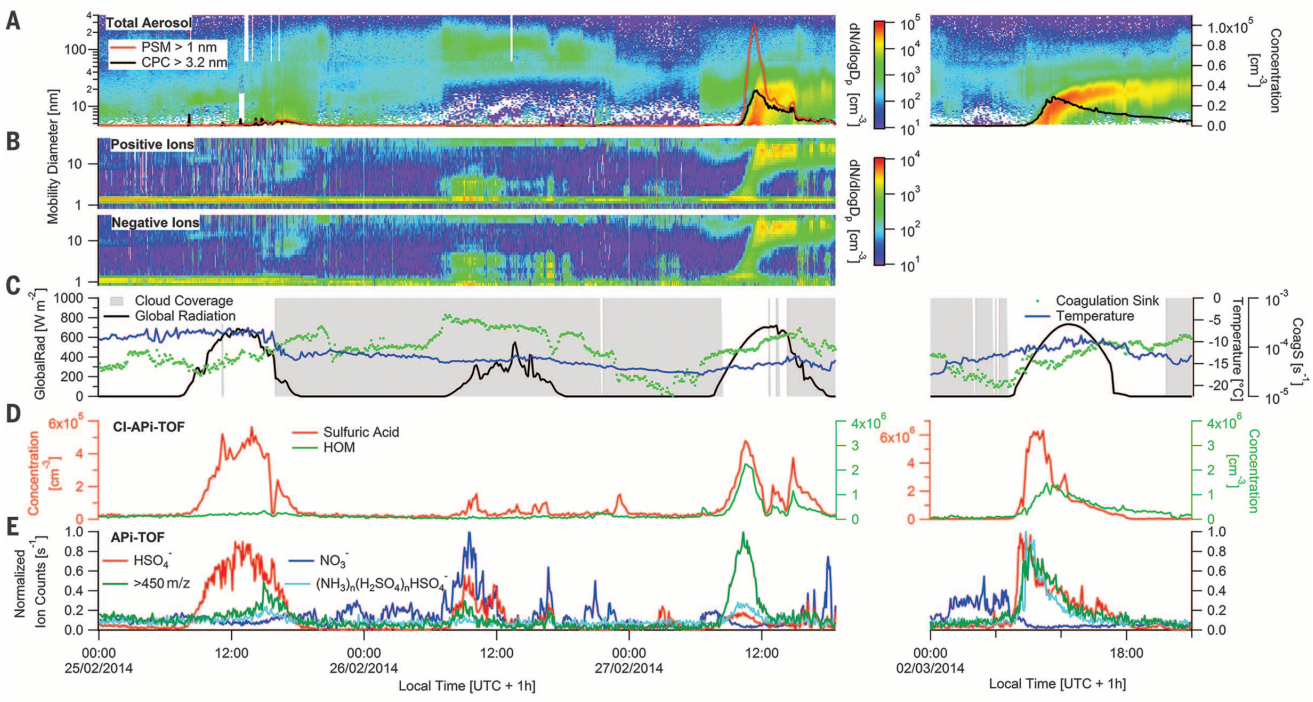


Fig. 1. Four representative situations observed at the JFJ. Shown are data from a sunny day with no nucleation (25 February, day 1), a cloudy day (26 February, day 2), a nucleation day with HOMs (27 February, day 3); and a nucleation day with H_2SO_4, NH_3, and HOMs (2 March, day 4) (h, hours). (**A**) Particle size distribution ($dN/d\log D_p$), measured with a nano-SMPS (scanning mobility particle sizer), and particle number concentration above 1 and 3.2 nm, measured with a particle size magnifier (PSM) and a condensation particle counter (CPC), respectively. (**B**) Size distributions of the positive and negative ions measured by the NAIS. (**C**) Global radiation, temperature, coagulation sink, and cloud coverage. (**D**) Concentrations of sulfuric acid (red) and HOMs (green) measured with the CI-APi-TOF. A different axis is used for sulfuric acid in the right panel. (**E**) Measurements of specific ions with the APi-TOF (HSO_4^- in red, NO_3^- in blue, and the sum of ions with m/z >400 Th in green). The clusters containing sulfuric acid and ammonia are shown by the light blue line.

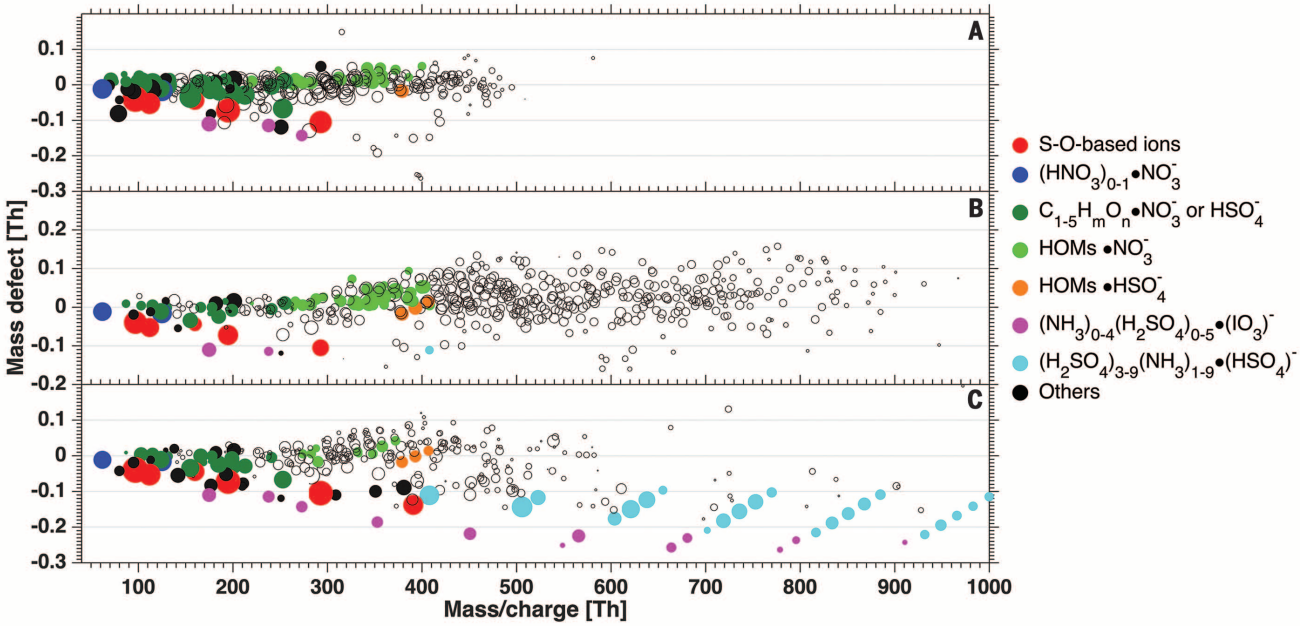


Fig. 2. Mass defect plots (negative ions). (**A**) Measurements from day 1, (**B**) day 3, and (**C**) day 4. The abscissa shows the mass/charge ratio and the ordinate shows the mass defect, which is the difference between the nominal (integer) mass and the exact mass. Colors relate to pure sulfuric acid clusters (red), nitrate (blue), small organic compounds alone or clustered with NO_3^- or HSO_4^- (dark green), HOMs clustered with NO_3^- (light green), HOMs clustered with HSO_4^- (orange), H_2SO_4-NH_3-HIO_3 (violet), and H_2SO_4-NH_3 clusters (light blue). Open circles represent unidentified peaks. The marker size is proportional to the logarithm of the count rate. The mass spectra for the same events are shown in fig. S3.

Downloaded from http://science.sciencemag.org/ on May 26, 2016

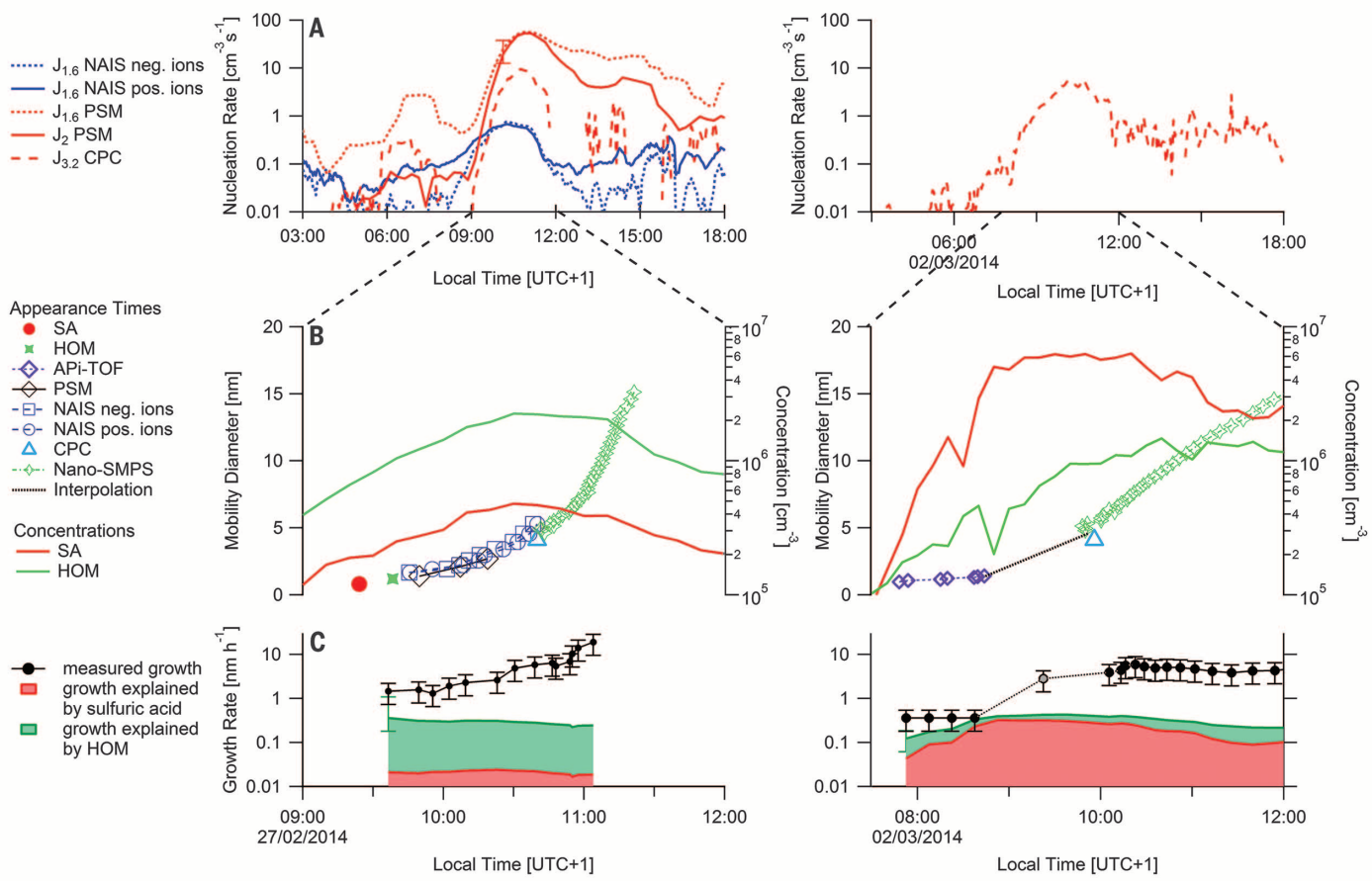


Fig. 3. Particle evolution during the nucleation events observed on days 3 and 4. Throughout, data for day 3 are shown on the left, and data from day 4 are shown on the right. (**A**) Formation rates (J) of the particles and ions at different sizes. (**B**) Evolution of particle diameter during the nucleation events. The two solid lines (red and green) show the concentrations of sulfuric acid (SA) and HOMs. (**C**) Comparison of the measured growth rates (black; error bars indicate systematic scale uncertainty) with growth rates calculated by assuming that solely sulfuric acid contributes to the growth (red) (*30*) or by also assuming a contribution from HOMs (green) (*29*). In addition to a much higher sulfuric acid concentration, the data for day 4 show a $J_{3.2}$ and growth rate that are slightly lower than those of day 3. On day 4, not all of the instruments required to measure particles across the full range from 1 to 15 nm were functioning. Therefore, the growth rate was interpolated between about 08:40 and 10:00.

of several negative ions measured with an APi-TOF: HSO_4^-, NO_3^-, the family of clusters containing NH_3 and H_2SO_4, and ions with mass/charge ratios m/z > 400 thomsons (Th; 1 Th = 1 Da e^{-1}, where e is the elementary charge), which are likely to be mainly organic compounds (*15*). Nucleation nearly exclusively occurred on days when the concentration of organic compounds was high. The nucleation event on day 4 had a somewhat different ion cluster composition; the organic ions were present, but HSO_4^- and the H_2SO_4-NH_3 cluster family were of equal magnitude, probably because the H_2SO_4 concentration was very high (Fig. 1). However, throughout the year of APi-TOF measurements, we never observed pure H_2SO_4 clusters with more than four molecules (table S3), confirming the findings of previous studies, which showed that binary H_2SO_4-H_2O nucleation does not explain atmospheric NPF (*18*, *19*).

The role of HOMs is further illustrated in Fig. 2, which shows mass defect plots (*20*, *21*) for negative ions for three of the days depicted in Fig. 1 (fig. S4 shows plots for corresponding neutral clusters). During the sunny day without NPF (day 1), most of the ions observed had m/z values <300 Th and were small acid clusters. These ions appear to be spectators (ions that are always present but unlikely to participate in cluster growth, such as nitrate, oxalate, and other organic acids that are too volatile to condense on such small particles). The smaller ions observed on day 3 (Fig. 2B) did not greatly differ from those observed on day 1; however, many ions with m/z values >300 Th were also present. The organic contribution is confirmed by the chemical composition of neutral clusters, shown in figs. S4 and S5 and table S2. The most intense organic peaks measured by the APi-TOF overlap with those measured by the CI-APi-TOF. In both cases, we attribute these peaks to HOMs clustered with nitrate (table S2). The difference is that in one case (in which ions were detected by the APi-TOF), the HOMs were clustered with NO_3^- in the ambient atmosphere, whereas neutral HOMs were clustered with NO_3^- inside the CI-APi-TOF ion source. Even though the chemical formulae of these HOMs differ from those of HOMs generated by monoterpene oxidation (*22*–*25*), they are similar in mass range and O:C ratio. They are therefore expected to have similarly low volatility and nucleating properties. Chemical identification of the negative ions detected on day 3 (Fig. 2 and fig. S5) indicates that the HOMs cluster exclusively with NO_3^-, except the three most abundant peaks, which also cluster to a minor extent with HSO_4^- (peaks 2a, 3a, and 4a in fig. S5). This confirms recent CLOUD findings that sulfuric acid is not important for NPF (*14*) at this concentration.

On day 4, we detected a distinctive sequence of ions, $(H_2SO_4)_m(NH_3)_nHSO_4^-$ (where m and n are integers varying from 3 to 9 and from 1 to 9, respectively), which closely resembles the sequence identified in CLOUD experiments involving purely H_2SO_4-NH_3 nucleation (*18*, *20*, *21*). In addition to this sequence, we observed other similar clusters in which the charging ion was IO_3^- instead of HSO_4^- (pink dots, Fig. 2). However, because these ions were only a minor fraction of all the clusters, and only a single iodate was found, we do not consider iodate to be important for this nucleation event.

Downloaded from http://science.sciencemag.org/ on May 26, 2016

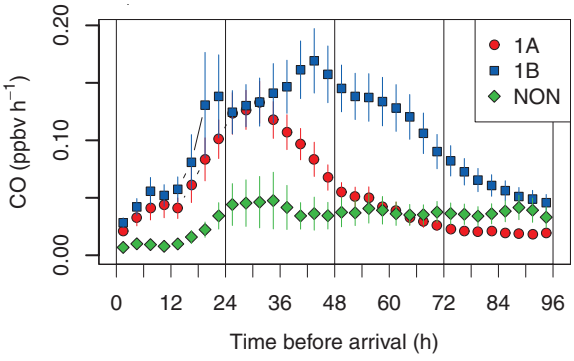


Fig. 4. Uptake of anthropogenic carbon monoxide versus time before arrival at the JFJ, for air masses sampled under different nucleation conditions. Shown are simulated means (symbols) and standard uncertainties of the means (error bars). Type 1A events (red) include pronounced and clearly identifiable events, type 1B events (blue) include less well-defined nucleation events, and NON (green) indicates no nucleation events.

On day 3, the total particle formation rate J decreased as a result of the coagulation processes that occur with increasing size, with $J_{1.6}$ = 51 cm^{-3} s^{-1} and J_2 = 46 cm^{-3} s^{-1} (where subscripts denote mobility diameter in nanometers) (Fig. 3A). The formation rates of positive and negative ions with a diameter of 1.6 nm, determined from neutral cluster air ion spectrometer (NAIS) ion-mode measurements, were much lower (<1 cm^{-3} s^{-1}) than those of the neutral particles of the same size, suggesting that the neutral process dominated (*26*) in this nucleation event. CLOUD results for pure sulfuric acid nucleation indicate a $J_{1.7}$ below 10^{-5} cm^{-3} s^{-1} (*27*) at a similar concentration and temperature. There is strong indication of the presence of HOMs in the nucleating clusters but not of ammonia or amines. Because the saturation concentration is expected to decrease substantially with decreasing temperature, we consider this to be in good agreement with the findings of Kirkby *et al.* (*14*), who reported $J_{1.7}$ = 40 cm^{-3} s^{-1} at [HOM] = 4 × 10^8 cm^{-3} and temperature T = 5°C.

On day 4, the observed $J_{3.2}$ of ~4.5 cm^{-3} s^{-1} at temperatures between −12°C and −15°C was similar to that measured by CLOUD: $J_{1.7}$ ~ 4 cm^{-3} s^{-1} for [H_2SO_4] = 6 × 10^6 cm^{-3} and [NH_3] = 1 part per billion by volume (ppbv) at T = −15°C (*18*). Because the ammonia concentration during this event at the JFJ is expected to have been lower than 1 ppbv, we hypothesize a synergistic effect of H_2SO_4, NH_3, and nonnegligible concentrations of HOMs. This event was a special case where the sulfuric acid concentration was extremely high. However, APi-TOF measurements show that HOMs were present in the initial clusters in 13 out of 19 nucleation events (type 1A or 1B; table S3). Nucleation thus appears to be influenced by the presence of organic compounds in the majority of cases. The importance of HOMs is further illustrated by the size-dependent growth rates observed during particle formation (Fig. 3), confirming that nano-Köhler growth (*3*) also applies in free troposphere conditions. On day 3, the growth rate was initially driven by HOMs and continued to increase after the HOM concentration began to decline, probably due to a reduced Kelvin effect at larger particle sizes, enabling the condensation of more volatile (unmeasured) molecules (fig. S8) (*28*) [as recently found in laboratory experiments (*29*)]. On day 4, a greater part of the initial growth rate can be explained by sulfuric acid and water under the assumption of condensation at the kinetic limit (fig. S7) (*30*). After that, the higher growth rate cannot be explained by sulfuric acid alone, which is again probably indicative of condensation of more volatile (unmeasured) molecules (*29*) on the newly formed particles, showing that this process is also not entirely inorganic.

An important question is where the condensable vapors or their precursors originate. We used the Lagrangian particle dispersion model FLEXPART in time-inverse mode and compared air mass origins of all the major events (type 1A and 1B) with those of typical non-event days during the same period (*15*). Increases in simulated carbon monoxide concentration and the strength of the source-receptor relationship, indicative of influence by the planetary boundary layer, were evident in individual backward simulations (Fig. 4 and fig. S10). This suggests an anthropogenic source of the HOM precursors but does not preclude a biogenic source. For all simulated cases, the small increase in CO within 6 hours before air mass arrival suggests no substantive influence from local emissions during this period. Air masses experienced enhanced uptake of CO and also an increase in the strength of the source-receptor relationship (fig. S11) 12 to 40 hours before type 1A events were detected at the JFJ, caused by contact with polluted boundary layer air. Similarly, air masses connected to type 1B events experienced increased CO uptake, though somewhat farther upwind, between 12 and 72 hours before arrival at the JFJ, with a maximum uptake at 48 hours. In contrast, for non-event days, CO uptake was considerably below that during nucleation events. This indicates that one requirement for observing NPF at the JFJ is nonlocal contact (fig. S12) with the planetary boundary layer and, hence, the uptake of emissions hours before arrival at the JFJ, allowing a sufficiently long processing time in the free troposphere. An optimal transport time from the planetary boundary layer to foster nucleation appears to be around 1 day, whereas longer transport times result in less clear nucleation events, due to ongoing oxidation and dilution of the precursor gases.

Combining in situ observations and modeling results, we thus find that NPF in the free troposphere depends on the availability of highly oxidized organic species, providing confirmation for NPF pathways observed in recent laboratory experiments. The availability of these highly oxidized organic species in turn depends on previous surface contact of the air mass and appropriate time to process the precursors from the boundary layer on their way up. In short, chemistry and timing play the main roles. To properly represent nucleation in the free troposphere, future atmospheric models should take these factors into account.

REFERENCES AND NOTES

1. T. L. Anderson *et al.*, *Bull. Am. Meteorol. Soc.* **86**, 1795–1809 (2005).
2. R. J. Charlson *et al.*, *Science* **255**, 423–430 (1992).
3. M. Kulmala *et al.*, *J. Aerosol Sci.* **35**, 143–176 (2004).
4. J. Merikanto, D. V. Spracklen, G. W. Mann, S. J. Pickering, K. S. Carslaw, *Atmos. Chem. Phys.* **9**, 8601–8616 (2009).
5. R. Zhang, A. Khalizov, L. Wang, M. Hu, W. Xu, *Chem. Rev.* **112**, 1957–2011 (2012).
6. S. Rodríguez *et al.*, *Atmos. Chem. Phys.* **9**, 6319–6335 (2009).
7. C. Rose *et al.*, *Atmos. Environ.* **102**, 18–29 (2015).
8. H. Venzac *et al.*, *Proc. Natl. Acad. Sci. U.S.A.* **105**, 15666–15671 (2008).
9. F. Q. Yu, A. G. Hallar, *J. Geophys. Res. Atmos.* **119**, 12246–12255 (2014).
10. S. Mirme *et al.*, *Atmos. Chem. Phys.* **10**, 437–451 (2010).
11. M. Kulmala, A. Laaksonen, L. Pirjola, *J. Geophys. Res. Atmos.* **103**, 8301–8307 (1998).
12. F. Riccobono *et al.*, *Science* **344**, 717–721 (2014).
13. G. W. Mann *et al.*, *Geosci. Model Dev.* **3**, 519–551 (2010).
14. J. Kirkby *et al.*, *Nature* 10.1038/nature17953 (2016).
15. Materials and methods are available as supplementary materials on *Science* Online.
16. E. Herrmann *et al.*, *J. Geophys. Res. Atmos.* **120**, 9459–9480 (2015).
17. J. Boulon *et al.*, *Atmos. Chem. Phys.* **10**, 9333–9349 (2010).
18. J. Kirkby *et al.*, *Nature* **476**, 429–433 (2011).
19. F. L. Eisele *et al.*, *J. Geophys. Res. Atmos.* **111**, D04305 (2006).
20. F. Bianchi *et al.*, *Environ. Sci. Technol.* **48**, 13675–13684 (2014).
21. S. Schobesberger *et al.*, *Proc. Natl. Acad. Sci. U.S.A.* **110**, 17223–17228 (2013).
22. M. Ehn *et al.*, *Nature* **506**, 476–479 (2014).
23. T. Jokinen *et al.*, *Proc. Natl. Acad. Sci. U.S.A.* **112**, 7123–7128 (2015).
24. T. F. Mentel *et al.*, *Atmos. Chem. Phys.* **15**, 6745–6765 (2015).
25. M. P. Rissanen *et al.*, *J. Am. Chem. Soc.* **136**, 15596–15606 (2014).
26. C. Rose *et al.*, *Atmos. Chem. Phys.* **15**, 3413–3428 (2015).
27. J. Duplissy *et al.*, *J. Geophys. Res. Atmos.* **121**, 1752–1775 (2016).
28. M. Kulmala *et al.*, *Science* **339**, 943–946 (2013).
29. J. Tröstl *et al.*, *Nature* 10.1038/nature18271 (2016).
30. T. Nieminen, K. E. J. Lehtinen, M. Kulmala, *Atmos. Chem. Phys.* **10**, 9773–9779 (2010).

ACKNOWLEDGMENTS

We thank the International Foundation High Altitude Research Stations Jungfraujoch and Gornergrat for the opportunity to perform experiments at the Jungfraujoch and especially the research station's custodians J. and M. Fischer and M. and U. Otz for their support and hospitality. This work was supported by the Swiss National Science Foundation (grant nos. 200020_135307, 20020_152907, 206021_144947, and 200021_140663), MeteoSwiss in the framework of the Global Atmosphere Watch program, and the EC FP7 (European Commission Seventh Framework Programme for Research and Technological Development) project ACTRIS (Aerosols, Clouds, and Trace Gases Research Infrastructure Network) (grant agreement no. 262254). Funding was also received from the Academy of Finland Centre of Excellence (grant nos. 272041 and 1118615), the EC FP7 Marie Curie Initial Training Network (CLOUD-TRAIN, grant no. 316662), the German Federal Ministry of Education and Research (project no. 01LK1222A), the EC FP7 project BACCHUS (Impact of Biogenic Versus Anthropogenic Emissions on Clouds and Climate: Towards a Holistic Understanding; grant agreement no. 603445), and the European Research Council (grant no. 615922-BLACARAT). We thank the tofTools team for providing tools for mass spectrometry analysis. The authors declare no competing financial interests.

SUPPLEMENTARY MATERIALS

www.sciencemag.org/content/352/6289/1109/suppl/DC1
Materials and Methods
Figs. S1 to S12
Tables S1 to S4
References (*31*–*58*)

4 October 2015; accepted 29 March 2016
Published online 25 May 2016
10.1126/science.aad5456

Downloaded from http://science.sciencemag.org/ on May 26, 2016

GENETIC MAPPING

CRISPR-directed mitotic recombination enables genetic mapping without crosses

Meru J. Sadhu,* Joshua S. Bloom,* Laura Day, Leonid Kruglyak*

Linkage and association studies have mapped thousands of genomic regions that contribute to phenotypic variation, but narrowing these regions to the underlying causal genes and variants has proven much more challenging. Resolution of genetic mapping is limited by the recombination rate. We developed a method that uses CRISPR (clustered, regularly interspaced, short palindromic repeats) to build mapping panels with targeted recombination events. We tested the method by generating a panel with recombination events spaced along a yeast chromosome arm, mapping trait variation, and then targeting a high density of recombination events to the region of interest. Using this approach, we fine-mapped manganese sensitivity to a single polymorphism in the transporter Pmr1. Targeting recombination events to regions of interest allows us to rapidly and systematically identify causal variants underlying trait differences.

Identification of DNA sequence differences that underlie trait variation is a central goal of modern genetic research. The primary tools for connecting genotype and phenotype are linkage and association studies. In these studies, coinheritance of genetic markers with the trait of interest in large panels of individuals is used to localize variants that influence the trait to specific regions of the genome. The localization relies on meiotic recombination events that break up linkage between markers on a chromosome. Therefore, the spatial resolution of genetic mapping is limited by the recombination rate. In practice, the recombination rate in most settings is too low to resolve mapped regions to individual genes, much less to specific variants within genes. Increasing mapping resolution requires construction of ever-larger panels of individuals and/or additional generations of recombination, and these approaches are laborious to the point of often being impractical. As a consequence, the genes and variants underlying trait variation remain unidentified for the vast majority of regions implicated by linkage or association mapping.

To address this problem, we have devised a new method for genetic mapping that precisely targets recombination events to regions of interest. The method uses recombination events that occur during mitosis rather than meiosis. Rare mitotic recombination events occur naturally when a chromosomal double-strand break (DSB) is repaired by homologous recombination (HR) that leads to the formation of a recombined chromosome (*1*). In a heterozygous individual, cell division can then generate daughter cells with a new genotype that is completely homozygous from the recombination site to the telomere and unchanged heterozygous everywhere else (Fig. 1A); such an event is termed "loss of heterozygosity" (LOH). Individuals with LOH events at various locations in the genome have been used to construct a genetic map (*2*), and this and related approaches (*3*) can, in principle, be used to map the genetic basis of trait variation (Fig. 1B). However, this approach has been limited in practice by the very low frequency of natural mitotic recombination events.

We have leveraged the CRISPR-Cas9 system to produce targeted mitotic recombination events at high frequency and at any desired location, allowing facile construction of LOH-based mapping panels. In the CRISPR (clustered, regularly interspaced, short palindromic repeats) system, the endonuclease Cas9 creates a DSB at a site specified by the targeting sequence of a bound guide RNA (gRNA) (*4*). Successful cutting requires the targeted sequence to be followed by an invariant protospacer-adjacent motif (PAM). In a heterozygous diploid individual, an LOH event can be generated by cutting only one chromosome, leaving its homolog intact to serve as a template for repair by HR. This is accomplished by using polymorphic heterozygous PAM sites.

To demonstrate that LOH events can be targeted to precise loci using CRISPR, we designed 95 gRNAs targeting the bacterial *Streptococcus pyogenes* Cas9 to sites distributed across the left arm of the yeast *Saccharomyces cerevisiae* chromosome 7 (Chr 7L). The gRNAs targeted heterozygous sites in a diploid yeast strain generated by crossing a laboratory strain (BY) and a vineyard strain (RM), using PAMs polymorphic between the two strains. After cutting, repair, and mitosis, cells in which the DSB repair led to an LOH event were isolated by fluorescence-activated cell sorting (FACS) through their loss of a telomere-proximal green fluorescent protein (GFP) gene. We picked approximately four GFP$^-$ lines per targeted site, for a total of 384 lines. Whole-genome sequencing demonstrated that CRISPR-induced recombination was highly effective, with LOH events in more than 95% of lines and few off-target effects (*5*). About 75% of LOH recombination events occurred within 20 kb of the targeted site (Fig. 2A), consistent with previous measurements of LOH gene conversion tract length (*6*). LOH events were generated at sites across the entire targeted chromosome arm (Fig. 2A), demonstrating that our method is not limited to certain genomic contexts.

We next used the LOH panel to map quantitative traits to loci on Chr 7L. We measured growth of the 384 LOH lines in 12 different conditions, chosen because we previously mapped quantitative trait loci (QTLs) for growth in these conditions to Chr 7L (*7*). In parallel, we measured growth of 768 segregants from a cross between BY and RM. One of the traits, growth on 10 mM manganese sulfate, mapped to a large-effect QTL with a maximum logarithm-of-odds (LOD) score of 109.4 in the LOH panel (Fig. 2B). The confidence interval obtained with the 384 LOH lines overlapped with and was narrower (2.9 kb) than that obtained with 768 segregants (3.9 kb). The LOH-based interval contained two genes and 12 polymorphisms between BY and RM. We identified concordant QTLs of smaller effect in the two panels for eight other traits (fig. S1). Two traits mapped to a QTL of small effect in just one panel, likely due to low statistical power (fig. S2). One trait lacked a Chr 7L QTL in both panels.

To rapidly fine-map the causal variant for manganese sensitivity, we generated a second panel of LOH lines whose recombination events were all targeted to the mapped manganese sensitivity interval. We took advantage of the fact that LOH gene conversion tracts vary in length, which means that in different individuals, DSBs generated by the same gRNA can lead to slightly different LOH crossover sites, typically within 10 kb of the DSB (*6*). We isolated 358 GFP$^-$ lines generated with three gRNAs that target sites near the mapped interval. Sequencing revealed that 46 lines (13.1%) had a recombination event within the 2.9-kb QTL interval; together, the recombination events separated almost all the variants in the interval (Fig. 3A). In contrast, only 0.7% of segregants had recombination events in the interval (*7*). To obtain a comparable number of recombination events at this locus by random meiotic segregation, a segregant panel would require more than 7500 lines. Thus, with targeted LOH events, we can generate very strong mitotic recombination hot spots at any region of interest (fig. S3).

We measured manganese sensitivity in this fine-mapping panel (Fig. 3B). Comparison of the panel phenotypes with the breakpoint locations pinpointed a single polymorphism as responsible for increased sensitivity in BY. The variant encodes a phenylalanine in BY and a leucine in RM at position 548 of Pmr1, a manganese transporter. Six lines had recombination events between Pmr1-F548L (F, Phe; L, Leu) and the closest polymorphism to the right, 402 base pairs (bp) away, and were either fully sensitive or resistant to manganese, depending on which Pmr1-F548L allele was homozygous in the line. One line had a recombination between Pmr1-F548L and the closest polymorphism to the left, 125 bp away, and showed the intermediate manganese sensitivity

Department of Human Genetics, Department of Biological Chemistry, and Howard Hughes Medical Institute, University of California, Los Angeles, Los Angeles, CA 90095, USA.
*Corresponding author. Email: msadhu@mednet.ucla.edu (M.J.S.); jbloom@mednet.ucla.edu (J.S.B.); lkruglyak@mednet.ucla.edu (L.K.)

Downloaded from http://science.sciencemag.org/ on May 26, 2016

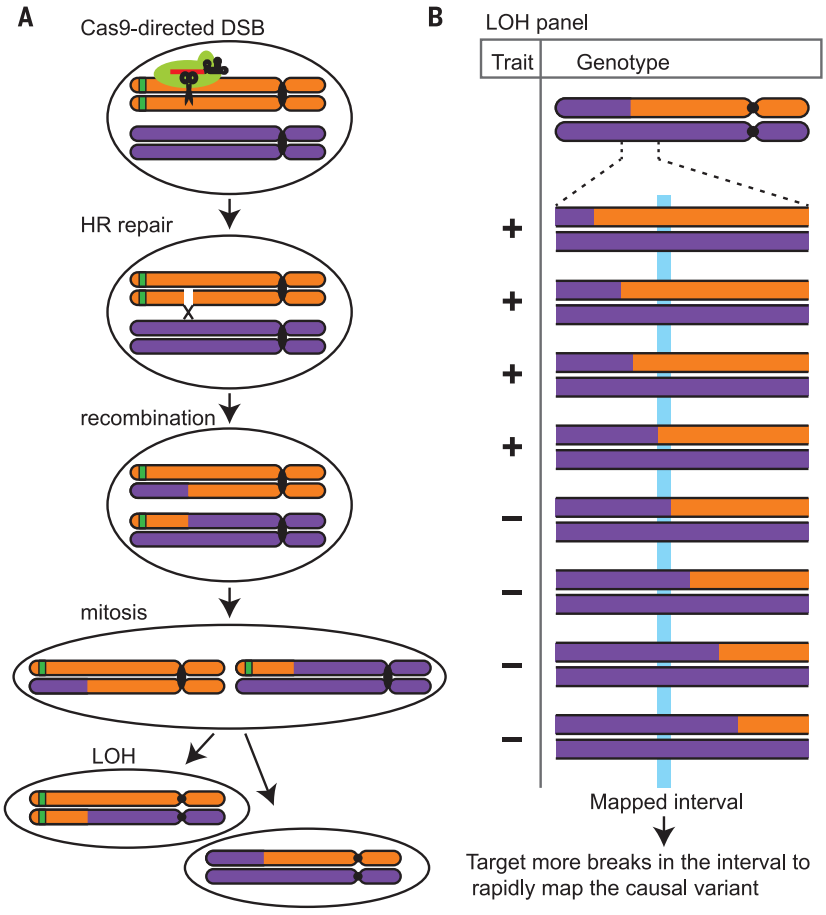


Fig. 1. DSBs generated by Cas9 in diploid mitotic cells can lead to mitotic recombination and loss of heterozygosity (LOH). (**A**) LOH can result from repair after a DSB in mitotically dividing cells, which is generated by CRISPR. (The *Streptococcus pyogenes* Cas9 protein is depicted as a green cartoon.) The orange and purple chromosomes are homologs. Individuals with LOH events are isolated via the loss of a heterozygous dominant marker, denoted with a green bar. (**B**) By measuring trait values in a panel of individuals with LOH events distributed across a region of interest, we can map genetic variants that contribute to trait variation. The process can be iterated to increase mapping resolution.

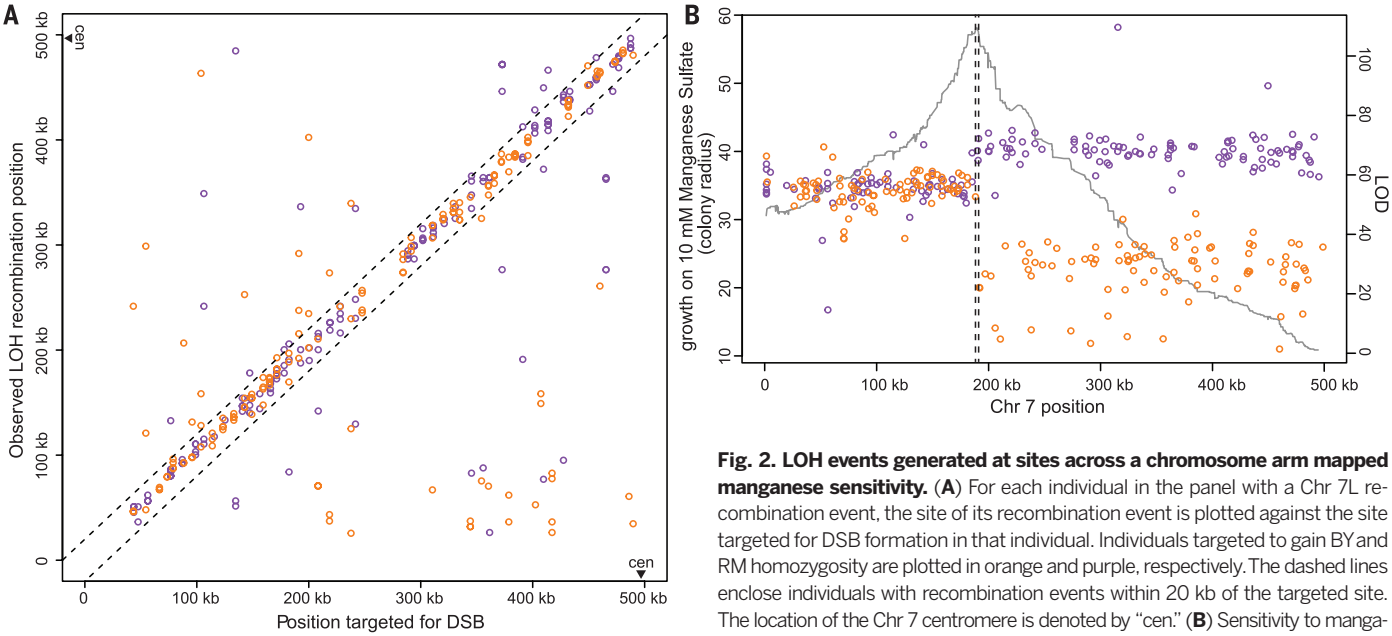


Fig. 2. LOH events generated at sites across a chromosome arm mapped manganese sensitivity. (**A**) For each individual in the panel with a Chr 7L recombination event, the site of its recombination event is plotted against the site targeted for DSB formation in that individual. Individuals targeted to gain BY and RM homozygosity are plotted in orange and purple, respectively. The dashed lines enclose individuals with recombination events within 20 kb of the targeted site. The location of the Chr 7 centromere is denoted by "cen." (**B**) Sensitivity to manganese versus observed LOH recombination location. For each individual in the Chr 7L panel, the site of the LOH recombination event is plotted against manganese sensitivity, measured as colony radius after growth on 10 mM manganese sulfate plates. Orange and purple points denote individuals that are homozygous BY and RM to the left of their recombination events, respectively. (All individuals are heterozygous BY/RM to the right of their recombination events.) The gray line plots the LOD score by position along Chr 7L for manganese sensitivity. Dashed vertical lines denote the QTL support interval.

Downloaded from http://science.sciencemag.org/ on May 26, 2016

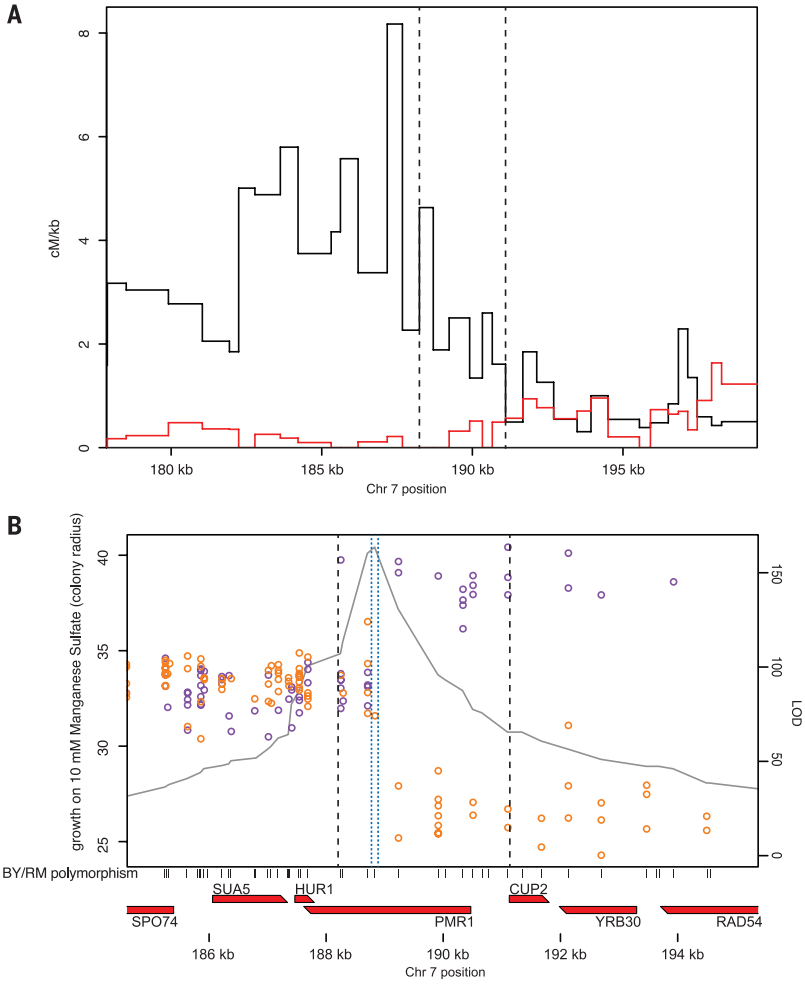


Fig. 3. Targeted high-resolution mapping of manganese sensitivity. (**A**) Ratio of recombination rate (in cM) to physical distance (in kb) near the manganese sensitivity QTL, for the manganese fine-mapping LOH panel (black line) and a segregant panel (red line) (*7*). The ratio is plotted for every interval between adjacent BY/RM polymorphisms that are at least 300 bp apart. The fine-mapping panel contains recombination events between all such pairs of polymorphisms in the interval, as indicated by the observation that the ratio does not drop to zero. The 2.9-kb QTL interval is denoted with dashed lines. (**B**) Recombination sites of individuals in the fine-mapping panel plotted against their manganese sensitivity, as in Fig. 2B, near the manganese sensitivity QTL. Dashed blue lines denote the QTL support interval for the fine-mapping panel, and dashed black lines denote the QTL support interval for the whole–Chr 7L panel. Shown below the plot are all BY/RM polymorphisms in the region (black bars), as well as all open reading frames (red lines).

phenotype expected for a heterozygote at the causal variant. LOD score analysis of the fine-mapping panel also identified a support interval containing only Pmr1-F548L (Fig. 3B).

To directly test the effect of Pmr1 variants on manganese sensitivity, we individually engineered into BY the RM alleles of Pmr1-F548L, the two neighboring polymorphisms, and the two remaining nonsynonymous Pmr1 polymorphisms, using a CRISPR-based variant replacement approach. As expected from the LOH fine-mapping, changing phenylalanine-548 to leucine conferred significant manganese resistance, whereas none of the other four polymorphisms had a significant effect (Fig. 4).

PMR1 encodes an ion pump that transports manganese and calcium into the Golgi (*8*). Pmr1 is a member of the P-type adenosine triphosphatase (ATPase) family of ion and lipid pumps found in all branches of life, and many other P-type ATPases have a conserved leucine at the position homologous to phenylalanine-548 of Pmr1. Solved structures of P-type ATPases with this leucine (*9*, *10*) show it directly contacting adenosine triphosphate (ATP) (fig. S4). Furthermore, mutating the homologous leucine of the rabbit calcium pump to phenylalanine decreases

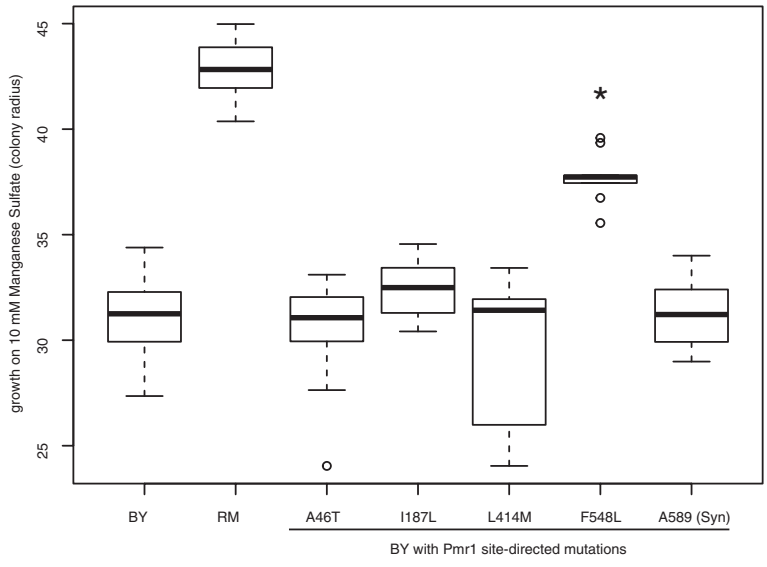


Fig. 4. Direct introduction of Pmr1-F548L into BY enhances manganese resistance. Box plots of manganese sensitivity for strains with single *PMR1* variants introduced from RM into BY, along with the BY and RM parental strains (first and second leftmost boxes). $n \geq 10$ for all genotypes. *$P < 0.001$ in comparison to BY; Welch's two-sided t test.

Downloaded from http://science.sciencemag.org/ on May 26, 2016

its function by affecting ATP binding (*11*). Thus, the F548L polymorphism is expected to reduce the ability of $Pmr1^{BY}$ to transport manganese into the Golgi, relative to $Pmr1^{RM}$, consistent with BY's manganese sensitivity.

Pmr1 leucine-548 is conserved across fungi, with some species having an isoleucine or valine at the homologous position and none with phenylalanine (fig. S5). In the *S. cerevisiae* population, almost all sequenced *PMR1* alleles have leucine-548, with phenylalanine-548 found only in BY and other laboratory strains (*12*, *13*) whose PMR1 alleles are likely directly related to BY (*14*). BY is derived from EM93, a diploid strain isolated from a fig (*15*). Sequencing of *PMR1* in EM93 revealed that EM93 is heterozygous for Pmr1-F548L (fig. S6), suggesting that either the mutation is not laboratory-derived or that it occurred between EM93's isolation and its entry into a stock collection.

Decades of mapping studies have uncovered loci for myriad traits, but identification of the underlying genes and variants has lagged. Our CRISPR-assisted mapping approach promises to close this gap. In contrast to previous strategies, our method generates a higher density of recombination events, is easily targetable to any region of the genome, and does not require time-consuming extra generations of crossing to increase recombination frequency. Conversely, the strength of a traditional meiotic mapping panel is the ability to scan the entire genome. Complex traits, with multiple small-effect QTLs, pose a greater challenge for any mapping method. Importantly, in LOH mapping the rest of the genome outside the region targeted for LOH is held constant when a given QTL is being queried, thus effectively reducing the complexity of a trait by eliminating variance due to other segregating QTLs.

We anticipate that trait mapping with targeted LOH panels will aid efforts to understand the genetic basis of trait variation. In addition to applications in single-celled organisms, LOH panels could be generated from cultured cells, enabling in vitro genetic dissection of human traits with cellular phenotypes. In multicellular organisms, mapping resolution could be enhanced with CRISPR-directed meiotic recombination events. Indeed, the mutagenic chain reaction system developed in vivo in fruit flies (*16*) and mosquitos (*17*, *18*) uses CRISPR to generate gene conversion events in meiosis with high efficiency. Additionally, LOH in early development could generate chimeric individuals. The targeted LOH method also has the potential to be applied to viable interspecies hybrids that cannot produce offspring, allowing trait variation between species to be studied genetically beyond the few systems where it is currently possible (*19*, *20*).

In addition to their research applications, targetable endonucleases hold promise for gene therapy (*21*, *22*). Certain disease alleles may be difficult to directly target by CRISPR because of their sequence complexity, such as the expanded trinucleotide repeats that underlie Huntington's disease. In these cases, directing a DSB to occur in the vicinity of a pathogenic allele so that it is replaced with its nonpathogenic counterpart by LOH may represent a more feasible alternative.

REFERENCES AND NOTES

1. Y. Yin, T. D. Petes, *PLOS Genet.* **9**, e1003894 (2013).
2. V. Henson, L. Palmer, S. Banks, J. H. Nadeau, G. A. Carlson, *Proc. Natl. Acad. Sci. U.S.A.* **88**, 6486–6490 (1991).
3. R. Laureau *et al.*, *PLOS Genet.* **12**, e1005781 (2016).
4. J. A. Doudna, E. Charpentier, *Science* **346**, 1258096 (2014).
5. Materials and methods are available as supplementary materials on *Science* Online.
6. J. St. Charles, T. D. Petes, *PLOS Genet.* **9**, e1003434 (2013).
7. J. S. Bloom, I. M. Ehrenreich, W. T. Loo, T.-L. V. Lite, L. Kruglyak, *Nature* **494**, 234–237 (2013).
8. V. C. Culotta, M. Yang, M. D. Hall, *Eukaryot. Cell* **4**, 1159–1165 (2005).
9. M. Hilge *et al.*, *Nat. Struct. Biol.* **10**, 468–474 (2003).
10. C. Toyoshima, T. Mizutani, *Nature* **430**, 529–535 (2004).
11. J. D. Clausen, D. B. McIntosh, B. Vilsen, D. G. Woolley, J. P. Andersen, *J. Biol. Chem.* **278**, 20245–20258 (2003).
12. G. Liti *et al.*, *Nature* **458**, 337–341 (2009).
13. G. Song *et al.*, *PLOS ONE* **10**, e0120671 (2015).
14. J. Schacherer, J. A. Shapiro, D. M. Ruderfer, L. Kruglyak, *Nature* **458**, 342–345 (2009).
15. R. K. Mortimer, J. R. Johnston, *Genetics* **113**, 35–43 (1986).
16. V. M. Gantz, E. Bier, *Science* **348**, 442–444 (2015).
17. V. M. Gantz *et al.*, *Proc. Natl. Acad. Sci. U.S.A.* **112**, E6736–E6743 (2015).
18. A. Hammond *et al.*, *Nat. Biotechnol.* **34**, 78–83 (2016).
19. H. A. Orr, D. C. Presgraves, *BioEssays* **22**, 1085–1094 (2000).
20. G. C. Woodruff, O. Eke, S. E. Baird, M.-A. A. Félix, E. S. Haag, *Genetics* **186**, 997–1012 (2010).
21. P. Tebas *et al.*, *N. Engl. J. Med.* **370**, 901–910 (2014).
22. P. D. Hsu, E. S. Lander, F. Zhang, *Cell* **157**, 1262–1278 (2014).

ACKNOWLEDGMENTS

We thank Kruglyak laboratory members for helpful discussion, S. Clarke for strain BY4742, G. Church for plasmids, and S. Kosuri for his flow cytometer. Funding was provided by the Howard Hughes Medical Institute and NIH grants R01 GM102308 (L.K.) and F32 GM116318 (M.J.S). Sequencing data was deposited at the Sequence Read Archive under accession no. SRP072527, and other data and code was deposited at https://github.com/joshsbloom/crispr_loh.

SUPPLEMENTARY MATERIALS

www.sciencemag.org/content/352/6289/1113/suppl/DC1
Materials and Methods
Figs. S1 to S7
Tables S1 and S2
References (*23*–*36*)

19 February 2016; accepted 25 April 2016
Published online 5 May 2016
10.1126/science.aaf5124

MUCOSAL IMMUNOLOGY

Gene-microbiota interactions contribute to the pathogenesis of inflammatory bowel disease

Hiutung Chu,[1]* Arya Khosravi,[1] Indah P. Kusumawardhani,[1] Alice H. K. Kwon,[1] Anilton C. Vasconcelos,[2] Larissa D. Cunha,[3] Anne E. Mayer,[4] Yue Shen,[1] Wei-Li Wu,[1] Amal Kambal,[4] Stephan R. Targan,[5] Ramnik J. Xavier,[6] Peter B. Ernst,[2] Douglas R. Green,[3] Dermot P. B. McGovern,[5] Herbert W. Virgin,[4] Sarkis K. Mazmanian[1]*

Inflammatory bowel disease (IBD) is associated with risk variants in the human genome and dysbiosis of the gut microbiome, though unifying principles for these findings remain largely undescribed. The human commensal *Bacteroides fragilis* delivers immunomodulatory molecules to immune cells via secretion of outer membrane vesicles (OMVs). We reveal that OMVs require IBD-associated genes, *ATG16L1* and *NOD2*, to activate a noncanonical autophagy pathway during protection from colitis. ATG16L1-deficient dendritic cells do not induce regulatory T cells (T_{regs}) to suppress mucosal inflammation. Immune cells from human subjects with a major risk variant in *ATG16L1* are defective in T_{reg} responses to OMVs. We propose that polymorphisms in susceptibility genes promote disease through defects in "sensing" protective signals from the microbiome, defining a potentially critical gene-environment etiology for IBD.

Intestinal microbiota modulate development and function of the immune system and play a critical role in inflammatory bowel disease (IBD), a family of idiopathic intestinal disorders including Crohn's disease (CD) and ulcerative colitis (UC) (*1*–*6*). Concordance rates of 40 to 50% between monozygotic twins implicate gene-environment interactions in the pathogenesis of CD (*7*–*10*), albeit in ways that are poorly understood. Advances in DNA-sequencing technologies have empowered unprecedented insights into the human genome and the gut microbiome in IBD, enabling detailed genomic characterization of patients (*11*) and chronicling alterations in the composition and gene content of the gut microbiome (dysbiosis) (*12*).

[1]Division of Biology and Biological Engineering, California Institute of Technology, Pasadena, CA 91125, USA. [2]Center for Veterinary Sciences and Comparative Medicine, University of California, San Diego, San Diego, CA 92093, USA. [3]Department of Immunology, St. Jude Children's Research Hospital, Memphis, TN 38105, USA. [4]Department of Pathology and Immunology, Washington University School of Medicine, St. Louis, MO 63110, USA. [5]F. Widjaja Foundation Inflammatory Bowel and Immunobiology Research Institute, Cedars-Sinai Medical Center, Los Angeles, CA 90048, USA. [6]Gastrointestinal Unit and Center for the Study of Inflammatory Bowel Disease, Massachusetts General Hospital and Harvard Medical School, Boston, MA 02114, USA.
***Corresponding author. Email: hiuchu@caltech.edu (H.C.); sarkis@caltech.edu (S.K.M.)**

Downloaded from http://science.sciencemag.org/ on May 26, 2016

Close to 200 risk loci have been proposed for CD, with several susceptibility genes linked to the regulation of autophagy (e.g., autophagy-related 16–like 1, *ATG16L1*) (*13*–*15*) or to microbial sensors that activate autophagy [e.g., nucleotide-binding oligomerization domain–containing protein 2 (*NOD2*)] (*16*–*18*). Although previous studies have shown that disruption of ATG16L1 and NOD2 affects CD susceptibility through defects in microbial clearance (*19*–*23*), recent reports reveal that immune cells impaired in autophagy are hyperinflammatory (*24*–*29*). This suggests that deficiencies in ATG16L1 or NOD2 may contribute to CD risk through impaired anti-inflammatory responses, a hypothesis not mutually exclusive with microbial clearance functions.

The microbiome of CD patients is altered, with emerging evidence for cause-and-effect relationships to disease. Among other recent examples of host-microbe interactions (*3*, *5*, *6*), the human commensal *Bacteroides fragilis* has evolved beneficial immunomodulatory properties. During colonization of mice, *B. fragilis* capsular polysaccharide A (PSA) is packaged in outer membrane vesicles (OMVs) and delivered to intestinal dendritic cells (DCs) to induce interleukin-10 (IL-10) production from $CD4^+Foxp3^+$ regulatory T cells (T_{regs}), which protects from experimental colitis (*30*–*32*). To explore gene-environment interactions during host-microbiota symbiosis, we tested if genetic pathways linked to CD are involved in the immune response to *B. fragilis* OMVs.

Bone marrow–derived DCs (BMDCs) differentiated from wild-type (WT) and ATG16L1-deficient (*Atg16l1*$^{f/f1}$ *Cd11c-Cre*; *Atg16l1*$^{\Delta Cd11c}$) mice were pulsed with OMVs harvested from wild-type *B. fragilis* (WT-OMV), or an isogenic mutant lacking PSA (ΔPSA-OMV), and cocultured with $CD4^+$ T cells. As previously reported (*33*), WT-OMVs, but not vehicle or ΔPSA-OMVs, promote IL-10 production (Fig. 1, A to C, and fig. S1). Conversely, ATG16L1-deficient DCs do not support IL-10 production in response to WT-OMVs (Fig. 1, A to C). We observe similar results using *Atg16l1*$^{f/f1}$ *LysM-Cre* mice (fig. S3). Purified PSA does not require ATG16L1 for its activity (Fig. 1, A and C, and fig. S2). Next, we tested functional outcomes using in vitro T cell suppression assays. T_{regs} isolated from cocultures with *Atg16l1*$^{\Delta Cd11c}$ BMDCs treated with *B. fragilis* OMVs exhibit impaired suppressive activity (Fig. 1D and fig. S2A). Neither WT-OMVs nor pure PSA have any effect on IL-10 production among $CD4^+Foxp3^-$ type 1 regulatory T cells (fig. S4). ATG16L1, ATG5, and ATG7 are components of the autophagy elongation complex; BMDCs deleted in these genes likewise do not induce IL-10 production from T_{regs} (fig. S5). Further, recent reports reveal a role for autophagy components in T_{reg} homeostasis (*34*, *35*). Our findings indicate that ATG16L1-deficient DCs fail to respond to *B. fragilis* OMVs, demonstrating that autophagy components in DCs are required for commensal-driven T_{reg} induction and function.

ATG16L1, ATG5, and ATG7 participate in both canonical and noncanonical autophagy pathways (*36*). Interestingly, the classical autophagy-specific genes *Ulk1*, *Fip200*, or *Atg14* are not required for $CD4^+Foxp3^+IL\text{-}10^+$ T_{reg} induction upon WT-OMV treatment (fig. S6). We hypothesized that OMVs use the noncanonical autophagy pathway, LC3-associated phagocytosis (LAP), which is specifically activated by microbial ligands delivered as particles rather than as soluble molecules. LAP

Downloaded from http://science.sciencemag.org/ on May 26, 2016

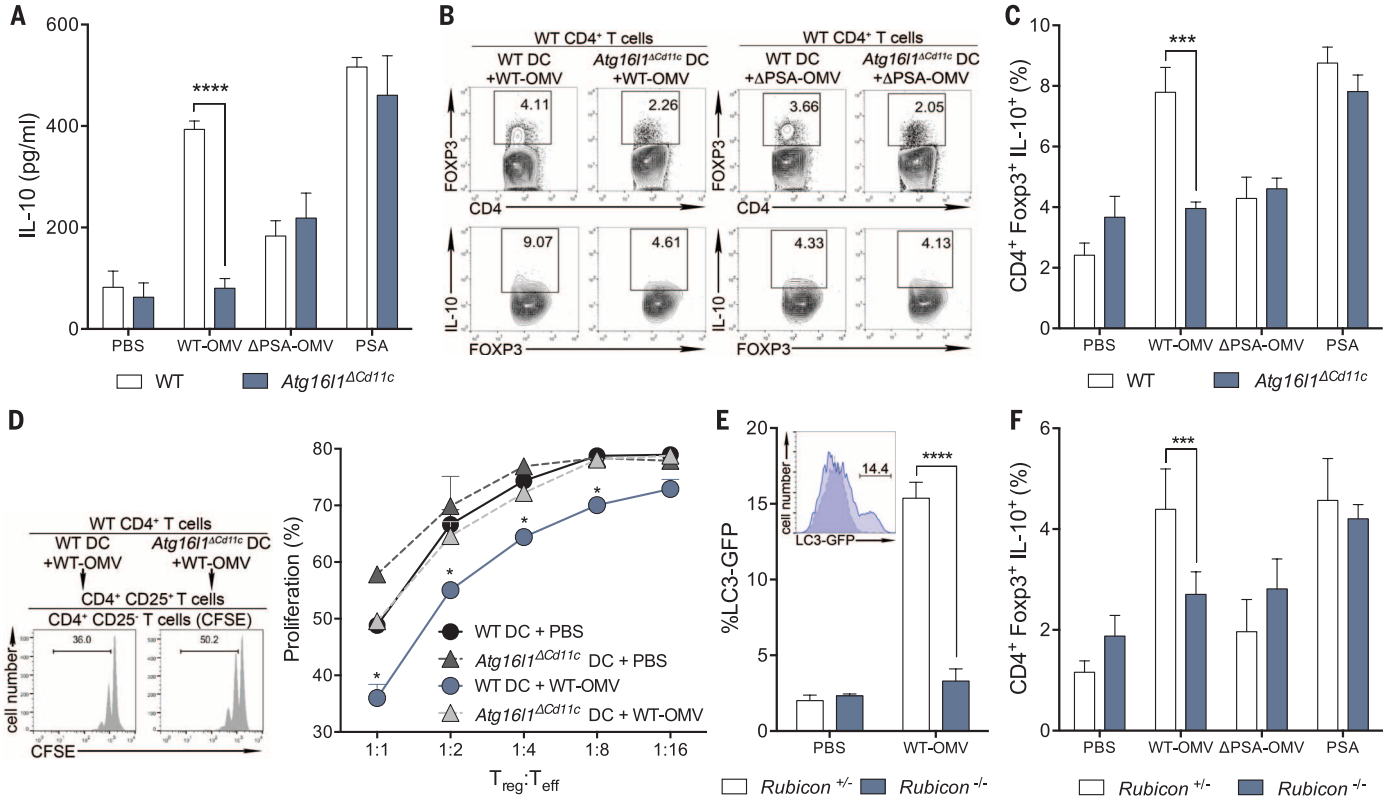


Fig. 1. ATG16L1 signals via a noncanonical autophagy pathway during OMV-mediated T_{reg} induction. (**A**) Enzyme-linked immunosorbent assay for IL-10 production during DC–T cell cocultures with WT or *Atg16l1*$^{\Delta Cd11c}$ BMDCs treated with phosphate-buffered saline (PBS), *B. fragilis* WT-OMV, ΔPSA-OMV, or purified PSA. (**B** and **C**) Representative flow cytometry plots (B) and frequency (C) of $CD4^+Foxp3^+IL\text{-}10^+$ T_{regs} from DC–T cell cocultures with WT or *Atg16l1*$^{\Delta Cd11c}$ DCs treated with PBS, *B. fragilis* WT-OMV, ΔPSA-OMV, or purified PSA. (**D**) T cell suppression assay analyzing in vitro–generated T_{regs} from WT or *Atg16l1*$^{\Delta Cd11c}$ DCs treated with WT-OMVs. (**E**) Quantification of LC3-GFP accumulation by *B. fragilis* WT-OMV treatment of *Rubicon*$^{+/-}$ or *Rubicon*$^{-/-}$ DCs. Representative flow cytometry histogram plot (inset). PBS, gray; WT-OMV, blue. (**F**) Frequency of $CD4^+Foxp3^+IL\text{-}10^+$ T_{regs} from *Rubicon*$^{+/-}$ or *Rubicon*$^{-/-}$ DC–T cell cocultures treated with PBS, *B. fragilis* WT-OMV, ΔPSA-OMV, or purified PSA. Error bars represent SEM. *$P < 0.05$, ***$P < 0.001$, ****$P < 0.0001$. Two-way analysis of variance (ANOVA), followed by Tukey's post-hoc analysis. Data are representative of at least two independent experiments.

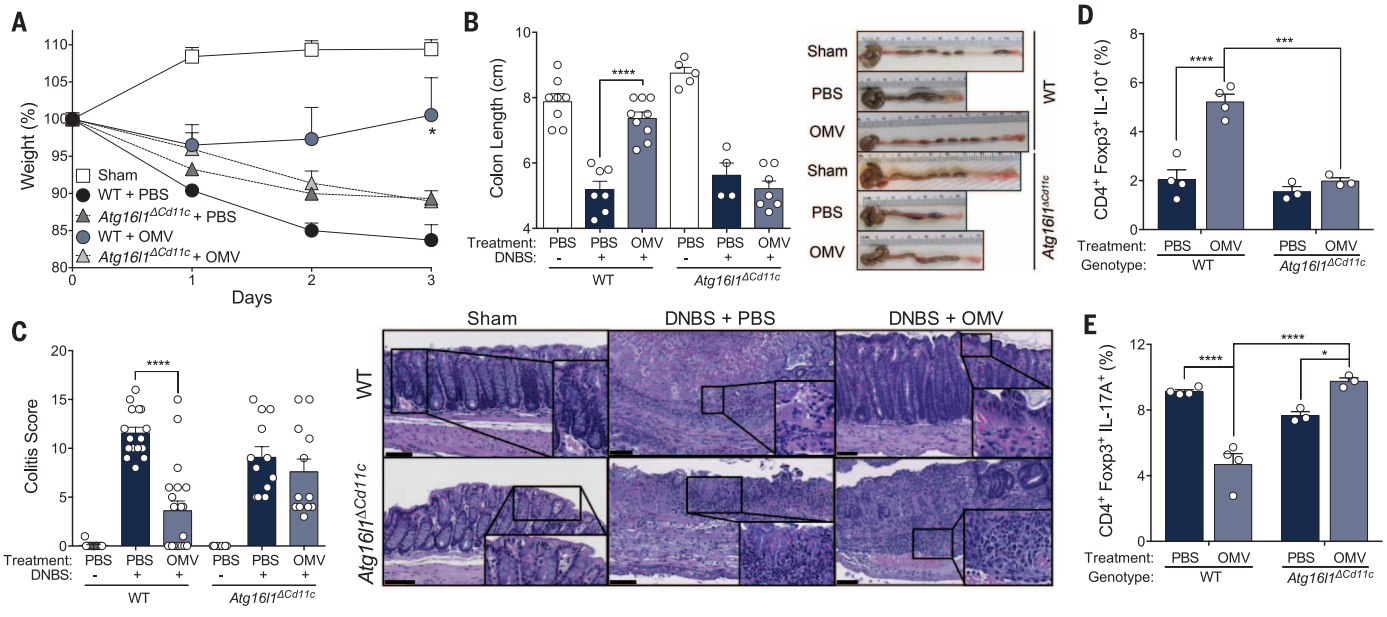


Fig. 2. *B. fragilis* OMVs require ATG16L1 in CD11c$^+$ DCs for protection from colitis. (**A** and **B**) Weight loss (A), colon length, and gross pathology (B) of WT and *Atg16l1*$^{\Delta Cd11c}$ mice orally treated with PBS or *B. fragilis* WT-OMV during DNBS colitis. Sham groups were treated with ethanol. (**C**) Colitis scores by a blinded pathologist using a standard scoring system, and representative hematoxylin and eosin (H&E) images. Scale bar, 100 μm. (**D** and **E**) MLN lymphocytes isolated post-DNBS analyzed for IL-10 (D) and IL-17A (E) production among CD4$^+$Foxp3$^+$ T_{regs}, as assessed by flow cytometry. Error bars represent SEM. *P < 0.05, ***P < 0.001, ****P < 0.0001. Two-way ANOVA, followed by Tukey's post-hoc analysis. Data are representative of at least three independent experiments, with three to nine mice per group.

activation requires RUBICON, which represses canonical autophagy (*36*). *Rubicon*$^{+/-}$ but not *Rubicon*$^{-/-}$ BMDCs display increased accumulation of lipidated, membrane-bound LC3-GFP (green fluorescent protein) (LC3-II) upon *B. fragilis* WT-OMV treatment (Fig. 1E). As expected, neither ΔPSA-OMVs nor purified PSA are able to activate LAP (fig. S7). Moreover, treatment of *Rubicon*$^{-/-}$ DCs fails to induce T_{reg} responses (Fig. 1F). As RUBICON is upstream of ATG16L1 signaling, OMVs preferentially use the noncanonical autophagy pathway LAP to mediate tolerogenic responses to *B. fragilis*. Further, these data suggest a reconsideration of previous literature assigning the role of ATG16L1 in IBD to defects exclusively in autophagy.

As a CD-risk gene, we investigated the in vivo requirement for ATG16L1 in CD11c$^+$ DCs during OMV-mediated protection from experimental colitis. Indeed, WT mice treated by oral gavage with WT-OMVs are protected from 2,4-dinitrobenzenesulfonic acid (DNBS) colitis (*33*), whereas *Atg16l1*$^{\Delta Cd11c}$ mice exhibit acute weight loss and increased mortality similar to that of untreated mice (Fig. 2A and fig. S8A). WT, but not *Atg16l1*$^{\Delta Cd11c}$, mice orally administered OMVs are protected from shortening of the colon, a hallmark of colitis models (Fig. 2B), with colitis scoring and cytokine profiles verifying protection from disease (Fig. 2C and fig. S8B). Prevention of colitis is not due to an overall defect in T_{reg} development in *Atg16l1*$^{\Delta Cd11c}$ mice (fig. S9). Further, although proportions of CD4$^+$Foxp3$^+$ cells are comparable in all groups of mice during colitis (fig. S10), *Atg16l1*$^{\Delta Cd11c}$ mice produce significantly less IL-10 from gut Foxp3$^+$ T_{regs} compared to WT mice after WT-OMV treatment (Fig. 2D and fig. S8C). Thus, WT-OMVs require ATG16L1 within DCs to induce IL-10 expression from Foxp3$^+$ T_{regs} and to suppress intestinal inflammation in a colitis model.

In addition to impaired IL-10 production in response to OMV treatment, *Atg16l1*$^{\Delta Cd11c}$ mice display an increase in IL-17A expression (Fig. 2E), but not IFN-γ (fig. S11), among mucosal CD4$^+$Foxp3$^+$ T cells during colitis. Further, in vitro cocultures of OMV-pulsed *Atg16l1*$^{\Delta Cd11c}$ BMDCs result in impaired IL-10 expression among T_{regs} (Fig. 1C) and increased IL-17A production in CD4$^+$Foxp3$^+$ T cells (fig. S12). Interestingly, whereas OMVs from other enteric bacteria each elicited a unique ATG16L1-dependent immune profile, only *B. fragilis* OMVs exclusively induce an anti-inflammatory response (fig. S13). Together, these data suggest that ATG16L1 deficiency in DCs alters the quality of the T cell response to OMVs.

As DCs coordinate adaptive immunity, we sought to determine how *Atg16l1*$^{\Delta Cd11c}$ DCs are impaired in promoting tolerogenic responses. After OMV stimulation, we observe no differences by WT or *Atg16l1*$^{\Delta Cd11c}$ DCs in internalizing OMVs or in surface expression of major histocompatibility complex class II (MHC II), CD80, and CD86 (fig. S14) (*27*). However, stimulation with OMVs results in an increase transcription of multiple proinflammatory cytokines in *Atg16l1*$^{\Delta Cd11c}$ DCs compared to WT cells (fig. S15). These data are consistent with previous reports of a hyperinflammatory response in ATG16L1-deficient macrophages and DCs stimulated with other microbial ligands (*24*, *26*). Abrogation of T_{reg} responses by ATG16L1-deficient DCs is likely due to increased proinflammatory cytokine production, which may impair DC–T cell interactions. *Atg16l1*$^{\Delta Cd11c}$ mice do not display more severe colitis than WT mice in the absence of OMV treatment (Fig. 2), suggesting that lack of protection is not due to more fulminant inflammation, but rather to an inability to induce T_{regs} in mice deficient in ATG16L1 among CD11c$^+$ DCs.

NOD2 encodes an intracellular sensor of bacterial peptidoglycan, and polymorphisms in this gene contribute to the largest fraction of genetic risk for CD (*13*). NOD2 has been shown to physically recruit ATG16L1 (*20*, *21*), a process that is impaired in human cells homozygous for a *NOD2* frameshift mutation (*20*). Accordingly, *Nod2*$^{-/-}$ BMDCs pulsed with WT-OMVs are unable to support IL-10 production from Foxp3$^+$ T_{regs} during in vitro cocultures (Fig. 3, A and B), revealing a crucial role for NOD2 signaling in microbiome-mediated immune tolerance. This notion is supported by in vivo studies showing that *Nod2*$^{-/-}$ mice are not protected from colitis by WT-OMV treatment (Fig. 3, C and D). Similar to *Atg16l1*$^{\Delta Cd11c}$ animals, *Nod2*$^{-/-}$ mice produce significantly less IL-10 from Foxp3$^+$ T_{regs} of the mesenteric lymph node (MLN) after WT-OMV treatment (fig. S16A), and proportions of T_{regs} remain unchanged during DNBS colitis (fig. S16B). Previous studies have shown that Toll-like receptor 2 (TLR2) is required for the PSA response (*33*, *37*). Although the role of NOD2 in inducing LAP is currently unknown, signaling through TLR2 potently activates LAP (*36*, *38*). *B. fragilis* OMVs induce reactive oxygen species from WT DCs,

Downloaded from http://science.sciencemag.org/ on May 26, 2016

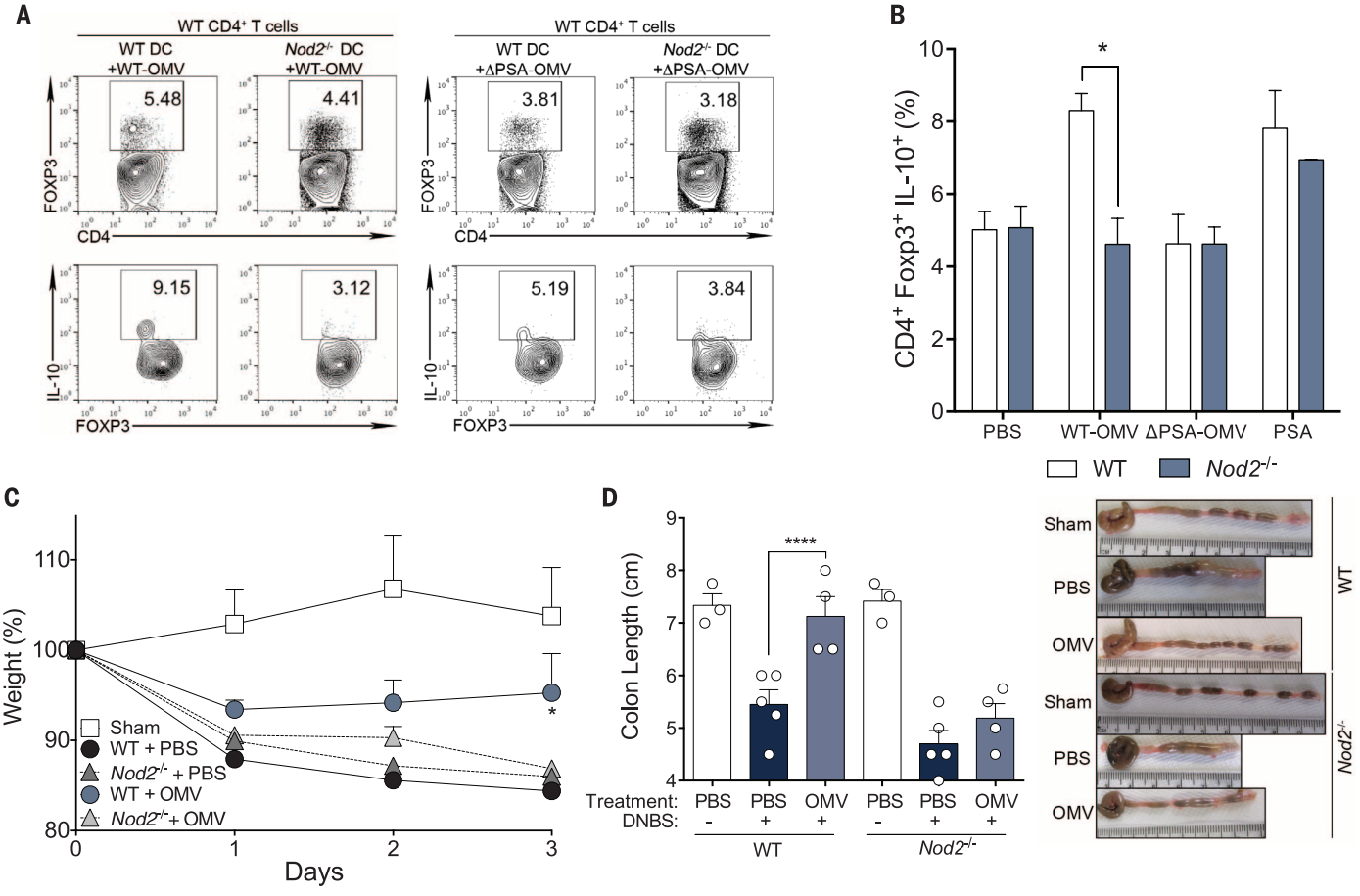


Fig. 3. NOD2 is required for OMV-mediated T_{regs} induction and protection from colitis. (**A** and **B**) Representative flow cytometry plots (A) from WT-OMV (left)– and ΔPSA-OMV (right)–treated BMDCs cocultured with $CD4^+$ T cells, and frequency (B) of $CD4^+Foxp3^+IL\text{-}10^+$ T_{regs} from DC–T cell cocultures. (**C** and **D**) Weight loss (C), colon length, and gross pathology (D) of WT or *Nod2*$^{-/-}$ mice treated with PBS or *B. fragilis* WT-OMV during DNBS colitis. Error bars represent SEM. *P < 0.05, ****P < 0.0001. Two-way ANOVA, followed by Tukey's post-hoc analysis. Data are representative of at least three independent experiments, with three to five mice per group.

a known product of LAP activation (*36*), but at significantly reduced levels in *Nod2*$^{-/-}$ or *Tlr2*$^{-/-}$ DCs (fig. S17). Though further studies are needed to define the mechanism of LAP activation by OMVs, these data reveal that *NOD2* and *ATG16L1* may cooperate as part of a common pathway to promote anti-inflammatory immune responses to the microbiome.

To extend and validate gene deletion approaches, we tested responses to OMVs by immune cells carrying the CD-associated variant of *ATG16L1* (*13*, *14*, *39*). The *ATG16L1* T300A variant leads to protein instability and altered cellular responses (*23*). BMDCs from transgenic mice expressing the T300A allele are also unable to promote IL-10 expression from $Foxp3^+$ T_{regs} in response to WT-OMVs (fig. S18A). Further, *ATG16L1* T300A transgenic mice are not protected from DNBS colitis and do not mount a potent T_{reg} response when administered WT-OMV compared to WT mice (fig. S18, B to G). These findings prompted us to investigate if human immune cells from CD patients with the *ATG16L1* T300A risk variant (table S1) are also defective in promoting $Foxp3^+$ T_{reg} development by *B. fragilis* OMVs. Monocyte-derived dendritic cells (MoDCs) from CD patients and healthy controls harboring either the protective allele (T300) or the risk allele (A300) were pulsed with OMVs or PSA and cocultured with syngeneic $CD4^+$ T cells. Consistent with our mouse data, human cells homozygous for the risk allele are unable to support induction of IL-10 from $Foxp3^+$ T_{regs} by WT-OMVs compared to MoDCs carrying the protective allele (Fig. 4). Notably, all samples tested display the predicted outcome based on genotype and not disease status. However, cells from most subjects, regardless of genotype, respond to purified PSA (Fig. 4). Collectively, we conclude that mouse and human DCs require functional ATG16L1 for induction of $CD4^+Foxp3^+IL\text{-}10^+$ T_{regs} in response to *B. fragilis* OMVs.

IBD affects more than 1.5 million people in the United States, with rates of diagnosis increasing and treatment options remaining limited (*40*, *41*). The etiology of IBD is complex and incompletely resolved (*1*). Here, we describe how interactions between genetic (*ATG16L1*/*NOD2*) and environmental (microbiome) factors cooperate to promote beneficial immune responses. *B. fragilis* OMVs use LAP, an ATG16L1-dependent cellular trafficking and signaling pathway, to induce mucosal tolerance. The hyperinflammatory responses that occur with mutations in *ATG16L1* likely alter antigen-processing pathways and impair signaling by DCs to T cells and may explain why CD-associated polymorphisms abrogate T_{reg} induction by OMVs. Collectively, discovery of genetic circuits co-opted by the microbiome to engender health provides unprecedented functional insights into gene-environment interactions relevant to the pathogenesis of IBD. We propose an additional role for genes previously implicated in killing bacteria—namely, mutations in genetic pathways linked to IBD result in an inability to sense and/or respond to beneficial microbes. This hypothesis may represent a new perspective for the etiology of microbiome-related diseases.

Downloaded from http://science.sciencemag.org/ on May 26, 2016

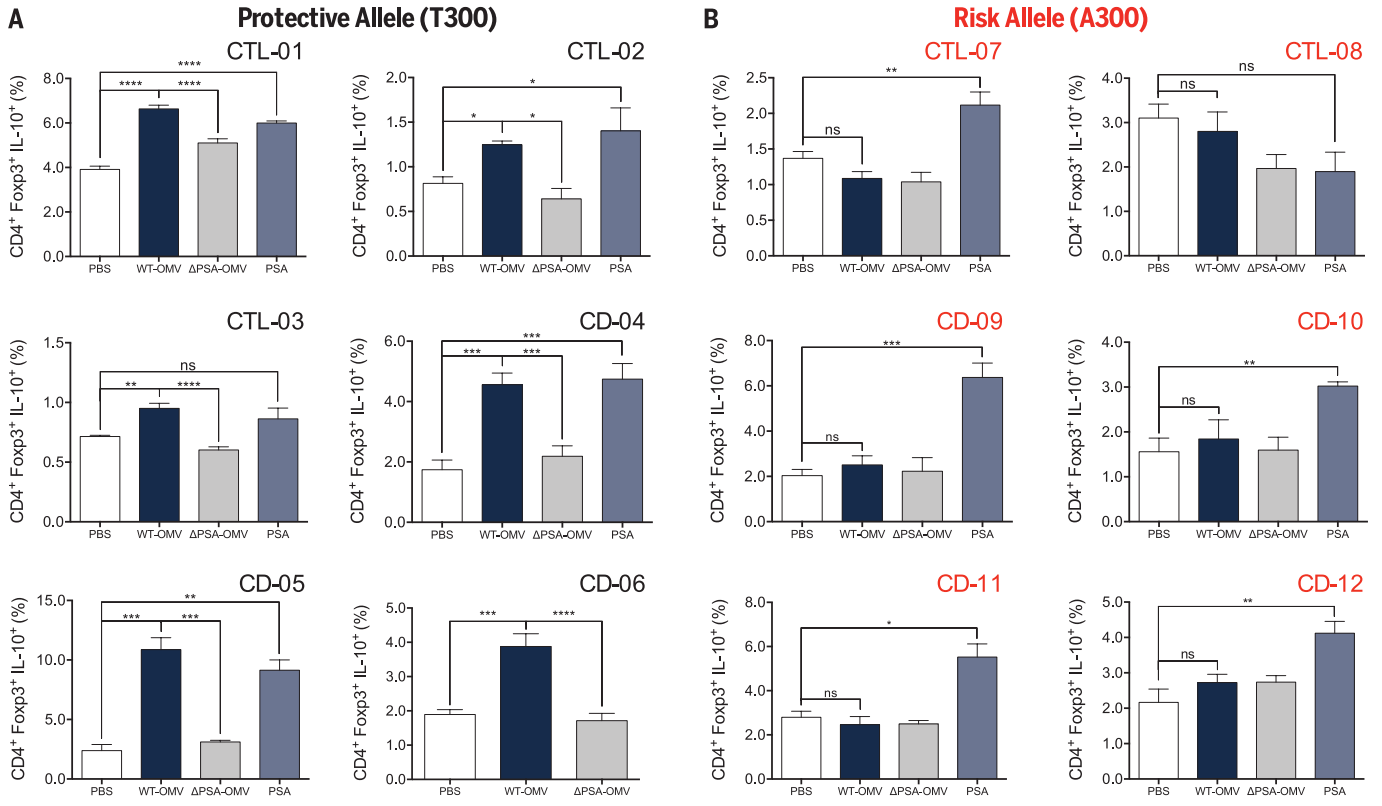


Fig. 4. The T300A risk variant of *ATG16L1* in human cells is unable to support OMV responses. (**A** and **B**) MoDCs with either the protective (A) or risk (B) allele were treated with PBS, *B. fragilis* WT-OMV, ΔPSA-OMV, or purified PSA; washed; and cocultured with syngeneic $CD4^+$ T cells. IL-10 expression was analyzed by flow cytometry among $CD4^+Foxp3^+$ T_{regs}. Human samples were processed and analyzed in a blinded fashion. CTL, control subjects; CD, Crohn's disease subjects. Error bars represent SEM. $^*P < 0.05$, $^{**}P < 0.01$, $^{***}P < 0.001$, $^{****}P < 0.0001$; ns, not significant. One-way ANOVA, followed by Tukey's post-hoc analysis.

REFERENCES AND NOTES

1. D. A. Peterson, D. N. Frank, N. R. Pace, J. I. Gordon, *Cell Host Microbe* **3**, 417–427 (2008).
2. D. A. Hill, D. Artis, *Annu. Rev. Immunol.* **28**, 623–667 (2010).
3. K. Honda, D. R. Littman, *Annu. Rev. Immunol.* **30**, 759–795 (2012).
4. E. M. Brown, M. Sadarangani, B. B. Finlay, *Nat. Immunol.* **14**, 660–667 (2013).
5. Y. Belkaid, T. W. Hand, *Cell* **157**, 121–141 (2014).
6. L. V. Hooper, D. R. Littman, A. J. Macpherson, *Science* **336**, 1268–1273 (2012).
7. S. R. Brant, *Inflamm. Bowel Dis.* **17**, 1–5 (2011).
8. M. Orholm *et al.*, *Scand. J. Gastroenterol.* **35**, 1075–1081 (2000).
9. J. Halfvarson, L. Bodin, C. Tysk, E. Lindberg, G. Järnerot, *Gastroenterology* **124**, 1767–1773 (2003).
10. C. Tysk, E. Lindberg, G. Järnerot, B. Flodérus-Myrhed, *Gut* **29**, 990–996 (1988).
11. L. Jostins *et al.*, *Nature* **491**, 119–124 (2012).
12. M. Wlodarska, A. D. Kostic, R. J. Xavier, *Cell Host Microbe* **17**, 577–591 (2015).
13. J. Hampe *et al.*, *Nat. Genet.* **39**, 207–211 (2007).
14. J. D. Rioux *et al.*, *Nat. Genet.* **39**, 596–604 (2007).
15. M. Parkes *et al.*, *Nat. Genet.* **39**, 830–832 (2007).
16. A. Gardet, R. J. Xavier, *Curr. Opin. Immunol.* **24**, 522–529 (2012).
17. J. P. Hugot *et al.*, *Nature* **411**, 599–603 (2001).
18. Y. Ogura *et al.*, *Nature* **411**, 603–606 (2001).
19. K. S. Kobayashi *et al.*, *Science* **307**, 731–734 (2005).
20. L. H. Travassos *et al.*, *Nat. Immunol.* **11**, 55–62 (2010).
21. R. Cooney *et al.*, *Nat. Med.* **16**, 90–97 (2010).
22. A. Murthy *et al.*, *Nature* **506**, 456–462 (2014).
23. K. G. Lassen *et al.*, *Proc. Natl. Acad. Sci. U.S.A.* **111**, 7741–7746 (2014).
24. T. Saitoh *et al.*, *Nature* **456**, 264–268 (2008).
25. K. Cadwell *et al.*, *Cell* **141**, 1135–1145 (2010).
26. V. M. Hubbard-Lucey *et al.*, *Immunity* **41**, 579–591 (2014).
27. S. Park *et al.*, *Cell Host Microbe* **19**, 91–101 (2016).
28. Q. Lu *et al.*, *Cell Host Microbe* **19**, 102–113 (2016).
29. J. M. Kimmey *et al.*, *Nature* **528**, 565–569 (2015).
30. S. K. Mazmanian, J. L. Round, D. L. Kasper, *Nature* **453**, 620–625 (2008).
31. J. L. Round, S. K. Mazmanian, *Proc. Natl. Acad. Sci. U.S.A.* **107**, 12204–12209 (2010).
32. S. E. Allan *et al.*, *Immunol. Rev.* **223**, 391–421 (2008).
33. Y. Shen *et al.*, *Cell Host Microbe* **12**, 509–520 (2012).
34. J. Wei *et al.*, *Nat. Immunol.* **17**, 277–285 (2016).
35. A. M. Kabat *et al.*, *eLife* **5**, e12444 (2016).
36. J. Martinez *et al.*, *Nat. Cell Biol.* **17**, 893–906 (2015).
37. J. L. Round *et al.*, *Science* **332**, 974–977 (2011).
38. M. A. Sanjuan *et al.*, *Nature* **450**, 1253–1257 (2007).
39. Wellcome Trust Case Control Consortium, *Nature* **447**, 661–678 (2007).
40. C. D. Packey, R. B. Sartor, *Curr. Opin. Infect. Dis.* **22**, 292–301 (2009).
41. N. A. Molodecky *et al.*, *Gastroenterology* **142**, 46–54.e42, quiz e30 (2012).

ACKNOWLEDGMENTS

We thank L. Hwang, E. Park, and M. Salas for clinical research coordination (Cedars-Sinai); A. Maskell, L. Sandoval, and C. Rumaldo for animal husbandry (Caltech); and members of the Mazmanian laboratory for discussions and critical reading of the manuscript. The data presented in this manuscript are tabulated in the main paper and in the supplementary materials. This work was supported by the National Institutes of Health (NIH) under a Ruth L. Kirschtein National Research Service Award (DK100109) to H.C.; NIH DK097485 to R.J.X.; NIH PO1DK046763, the Cedars-Sinai F. Widjaja Foundation Inflammatory Bowel and Immunobiology Research Institute Research Funds, and The Feintech Family Chair in IBD to S.R.T.; Wayne and Gladys Valley Foundation and NIH AI079145 to P.B.E.; The Lupus Research Institute and NIH AI40646 to D.R.G; NIH U19 AI109725 to H.W.V.; The Lisa Z. Greer Endowed Chair in IBD Genetics, NIH DK062413, NIH DE023789-01, grant 305479 from the European Union, The Crohn's and Colitis Foundation of America, and The Leona M. and Harry B. Helmsley Charitable Trust to D.P.B.M.; NIH AI109725 to H.W.V.; and NIH DK078938, NIH GM099535, The Crohn's and Colitis Foundation of America, and the Heritage Medical Research Institute to S.K.M. Rubicon and ULK1 knockout mice were obtained from D. R. Green and M. Kundu, respectively, under a materials transfer agreement with St. Jude Children's Research Hospital. A provisional patent application entitled "Beneficial Activation of Autophagy Components by the Microbiome" has been filed by H.C., H.W.V., and S.K.M.

SUPPLEMENTARY MATERIALS

www.sciencemag.org/content/352/6289/1116/suppl/DC1
Materials and Methods
Figs. S1 to S18
Table S1
References (*42*–*47*)

3 December 2015; accepted 21 April 2016
Published online 5 May 2016
10.1126/science.aad9948

Downloaded from http://science.sciencemag.org/ on May 26, 2016

CELL CYCLE

Cyclin-dependent kinase 1–dependent activation of APC/C ubiquitin ligase

Kazuyuki Fujimitsu, Margaret Grimaldi, Hiroyuki Yamano*

Error-free genome duplication and segregation are ensured through the timely activation of ubiquitylation enzymes. The anaphase-promoting complex or cyclosome (APC/C), a multisubunit E3 ubiquitin ligase, is regulated by phosphorylation. However, the mechanism remains elusive. Using systematic reconstitution and analysis of vertebrate APC/Cs under physiological conditions, we show how cyclin-dependent kinase 1 (CDK1) activates the APC/C through coordinated phosphorylation between Apc3 and Apc1. Phosphorylation of the loop domains by CDK1 in complex with p9/Cks2 (a CDK regulatory subunit) controlled loading of coactivator Cdc20 onto APC/C. A phosphomimetic mutation introduced into Apc1 allowed Cdc20 to increase APC/C activity in interphase. These results define a previously unrecognized subunit-subunit communication over a distance and the functional consequences of CDK phosphorylation. Cdc20 is a potential therapeutic target, and our findings may facilitate the development of specific inhibitors.

Many biological processes are regulated by posttranslational modifications, such as phosphorylation and ubiquitylation. The anaphase-promoting complex or cyclosome (APC/C) (*1*–*3*) is an unusually large multisubunit (>13) enzyme and a key component of the cellular machinery that regulates cell cycle progression and genome stability by catalyzing ubiquitylation of regulatory proteins, such as securin and cyclin B, which leads to their proteolysis (*4*–*6*). The activity of the APC/C controls mitotic exit. Antimicrotubule agents that disrupt spindle function are effective in the clinic, because they cause mitotic delay, which triggers apoptosis of cancer cells. However, microtubules have key roles in neuronal functions, so the development of agents that block cells in mitosis without altering microtubules is important. One way to do this would be to target the APC/C (*7*–*11*). Mitotic kinases, including cyclin-dependent kinase 1 (CDK1), phosphorylate vertebrate APC/C at more than 50 sites during mitosis (*12*, *13*), and the coactivator subunit Cdc20 preferentially binds to and activates phosphorylated APC/C (*14*–*16*). However, all the evidence in vertebrates that CDK1 activates the APC/C comes from in vitro phosphorylation and ubiquitylation studies, and no mutagenesis of these sites has been done. To elucidate how CDK phosphorylates and activates the APC/C, we reconstituted recombinant *Xenopus* APC/C by simultaneous coexpression of all the subunits using an advanced baculovirus–insect cell expression system (*17*, *18*) (fig. S1, A and B). The activities of purified APC/C were assessed under physiological conditions in a cyclin B–destruction assay reconstituted in *Xenopus* egg extracts. Incubation of reconstituted recombinant APC/C in extract from which endogenous APC/C was depleted (ΔAPC/C+APC/C) revealed that the reconstituted APC/C was active and degraded a substrate, cyclin B (fig. S1, C and D). The purified APC/C also ubiquitylated and degraded substrates in a manner dependent on the Cdc20 homolog 1 (Cdh1) (fig. S1, E and F). Cdh1, an alternative coactivator of the APC/C in the G_1 phase, activates the APC/C independently of subunit phosphorylation. These results indicated that our reconstituted *Xenopus* APC/C was functional. We mutated all conserved (between *Xenopus* and humans) CDK consensus phosphorylation sites of each individual subunit to alanine (A) and made mutant APC/Cs, one subunit at a time (table S1). The cyclin-destruction assay in anaphase revealed that only APC/$C^{Apc1\text{-}15A}$ (the reconstituted APC/C containing 15 mutated CDK sites on Apc1) and APC/$C^{Apc3\text{-}12A}$ mutants showed decreased activity (Fig. 1A and fig. S2A). The integrity of the APC/C was confirmed in a Cdh1-dependent assay. The activities of APC/$C^{Apc3\text{-}12A}$ and APC/$C^{Apc1\text{-}15A}$ were similar to that of wild type (WT), although APC/$C^{Apc1\text{-}15A}$ showed reduced activity (fig. S2, B and C). These results prompted us to further investigate Apc3 and Apc1.

In the absence of a coactivator, the APC/C is always inactive. We examined the binding of Cdc20 to APC/$C^{Apc3\text{-}12A}$ and APC/$C^{Apc1\text{-}15A}$. We confirmed that APC/C^{WT} bound Cdc20 in a cell cycle–dependent manner; binding was low in interphase and high in anaphase (Fig. 1B). Consistent with the destruction assay in anaphase, APC/$C^{Apc3\text{-}12A}$ showed a lower affinity for Cdc20 than APC/C^{WT} (Fig. 1B). Cdc20 also failed to bind APC/$C^{Apc1\text{-}15A}$ in anaphase (Fig. 1C). No shift in the electrophoretic band containing Apc3 or Apc1 was detected in anaphase extract for APC/$C^{Apc3\text{-}12A}$ or APC/$C^{Apc1\text{-}15A}$, respectively (Fig. 1, B and C), consistent with the mutated CDK sites no longer being phosphorylated. This was confirmed by in vitro phosphorylation using purified CDK1-cyclin B (Fig. 1D).

Why is the phosphorylation of two subunits, Apc3 and Apc1, of particular importance? Cdc20 directly binds the Apc3 subunit through the C-terminal IR (Ile-Arg) motif of Cdc20 (*19*).

Cell Cycle Control Group, UCL Cancer Institute, University College London, London WC1E 6DD, UK.
*Corresponding author. Email: h.yamano@ucl.ac.uk

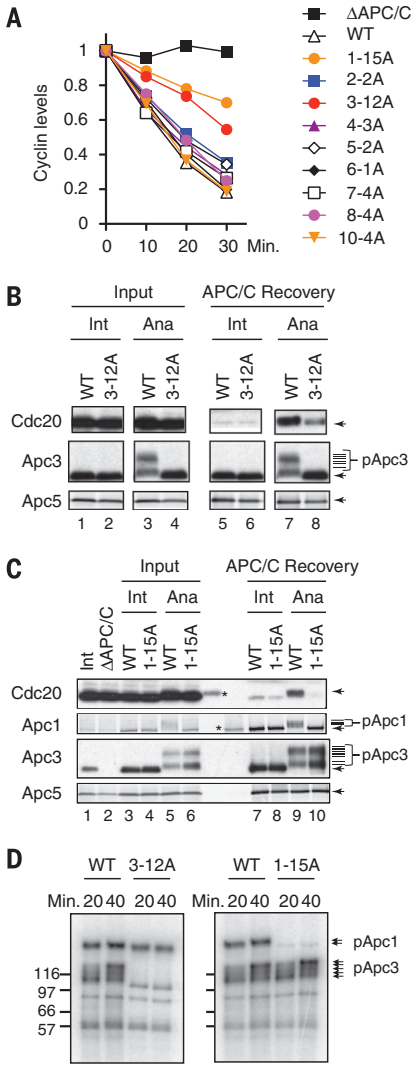


Fig. 1. Effect of phosphorylation of Apc3 and Apc1 on APC/C-Cdc20 activation. (**A**) Cyclin destruction assay in *Xenopus* egg extracts. APC/C-depleted extracts (ΔAPC/C) were supplemented with a range of reconstituted APC/Cs with CDK site mutations. Samples taken at indicated time points after addition of cyclin were analyzed by SDS–polyacrylamide gel electrophoresis (SDS-PAGE) and autoradiography. Quantification of gels in fig. S2A. The relative cyclin levels are shown, normalized with reference to the intensities found at time 0 for each time point. (**B**) WT APC/C or APC/$C^{Apc3\text{-}12A}$ was incubated with ΔAPC/C interphase (Int) or anaphase (Ana) extract. The APC/C was recovered with Apc3-specific antibody (anti-Apc3) beads, and bound Cdc20 was analyzed by SDS–PAGE and immunoblotting. (**C**) Same as (B), but APC/$C^{Apc1\text{-}15A}$ was used. (**D**) Phosphorylation of APC/$C^{Apc3\text{-}12A}$ and APC/$C^{Apc1\text{-}15A}$ by CDK1–cyclin B. (Left) WT APC/C or APC/$C^{Apc3\text{-}12A}$ was incubated with CDK1-cyclin B and p9 in the presence of [γ-^{32}P]ATP at 23°C for the indicated minutes. The APC/C was recovered using anti-Apc3 affinity beads and analyzed by SDS-PAGE and autoradiography. (Right) Same as left panel but APC/$C^{Apc1\text{-}15A}$ was used.

Downloaded from http://science.sciencemag.org/ on May 26, 2016

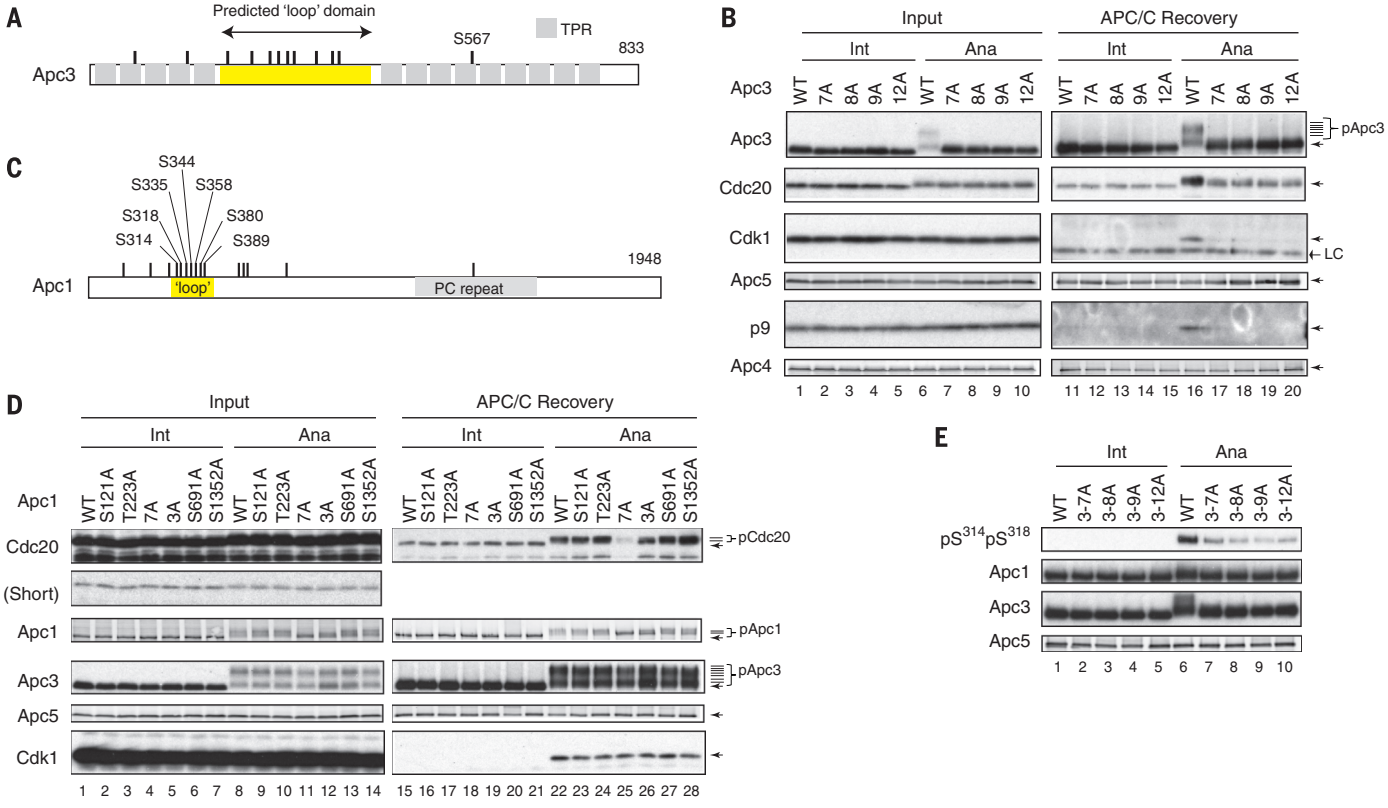


Fig. 2. Interaction of phosphorylation on Apc3 and Apc1 subunits. (**A**) Schematic diagram of Apc3. CDK sites shared between *Xenopus* and human Apc3 are shown in black. (**B**) WT APC/C or Apc3 mutant APC/Cs were incubated with ΔAPC/C interphase or anaphase extracts. The APC/C was recovered with anti-Apc3 beads, and bound proteins were analyzed by immunoblotting. LC, immunoglobulin G light chain. (**C**) Schematic diagram of Apc1. CDK sites shared between *Xenopus* and human Apc1 are shown in black. (**D**) Binding of Cdc20 to APC/C in anaphase. WT APC/C or Apc1 mutant APC/Cs were incubated with ΔAPC/C interphase or anaphase extracts. APC/C was recovered with anti-Apc3 beads, and bound proteins were analyzed by immunoblotting. (**E**) Phosphorylation of WT or Apc3 mutant APC/Cs incubated in ΔAPC/C extracts and then recovered with anti-Apc3 beads, as detected by immunoblotting with $pS^{314}pS^{318}$ antibody and the indicated APC/C antibodies.

However, because the sites phosphorylated by CDK [except serine 567 (S567)] are distant from tetratricopeptide repeat (TPR) motifs implicated in engaging coactivator IR motifs, the role of CDK might not simply be to increase the affinity of Apc3 to Cdc20 by phosphorylation. The 12 CDK sites on Apc3 are widely spread throughout the protein (Fig. 2A). To understand the CDK-driven APC/C activation mechanism, we constructed several mutant APC/Cs carrying CDK mutations in Apc3 and tested their activities (fig. S3). Mutations within the dimerization domain in which alanine replaces threonine 68 and S150 (T68A/S150A) or adjacent to the IR-binding domain (S567A) had no impact on APC/C activity. In contrast, CDK mutations in the predicted loop domain (Apc3-7A, -8A, and -9A) reduced APC/C activity in anaphase as seen with Apc3-12A, which highlights the importance of loop domain phosphorylation (fig. S3, A to C). APC/$C^{Apc3\text{-}7A}$, APC/$C^{Apc3\text{-}8A}$, and APC/$C^{Apc3\text{-}9A}$ mutants also showed reduced Cdc20 binding in anaphase extract (Fig. 2B, lanes 16 to 20). Although the predicted loop domain consists of ~280 residues, all of which are conserved among vertebrates (fig. S4), their function remains uncharacterized. Complexes of the *Xenopus* p9 protein (Suc1 or Cks1/2 in other organisms) (*20*) with CDK1 only bound to WT APC/C when phosphorylated in anaphase but not in interphase (Fig. 2B and fig. S5A). The Apc3 loop mutants failed to bind p9-CDK1 (Fig. 2B, lanes 17 to 19), consistent with findings that p9 is required for phosphorylation of Apc3 in anaphase (*15*, *21*, *22*). The Suc1/Cks family of proteins may recognize CDK sites and stimulate phosphorylation-dependent CDK signaling (*23*, *24*). Thus, CDK phosphorylation of the loop domain in Apc3 might recruit p9-CDK1 and lead to phosphorylation of Apc1, another key CDK target in the APC/C. Furthermore, we examined the physical interaction between Apc3 fragments and p9. A bacterially purified fragment from the loop domain (residues 202 to 342) bound to p9 in mitotic egg extracts, whereas the same fragment with CDK site mutations did not bind p9 (fig. S5B). These results indicate that Apc3 functions as a scaffold for p9-CDK1 through the loop domain.

To investigate the mechanism of Apc1 phosphorylation–dependent APC/C activation, we sought to identify key phosphorylation sites on Apc1 (Fig. 2C). We made a series of mutant Apc1-APC/Cs (fig. S6A). The construct with CDK mutations in a predicted flexible loop domain (Apc1-7A) reduced cyclin destruction in anaphase, whereas all the others showed similar, more rapid cyclin B destruction kinetics (fig. S6, B and C, and fig. S7). In a Cdh1-supplemented destruction assay, all the constructs showed activity similar to that of APC/C^{WT} (fig. S6, D and E). Cdc20 loading was also assessed. Cdc20 loading to the APC/C in anaphase was abolished by the 7A mutation (Fig. 2D, lane 25), whereas in interphase extract, APC/$C^{Apc1\text{-}7A}$ retained basal Cdc20 binding as seen with APC/C^{WT} (Fig. 2D, lanes 15 and 18). These results indicate that phosphorylation of the loop domain mutated in APC/$C^{Apc1\text{-}7A}$ is necessary for Cdc20 binding and subsequent APC/C activation. To verify the relation between Apc1 and Apc3 phosphorylation, we raised a phosphospecific antibody that bound to the Apc1 loop domain only when S314 and S318 were phosphorylated (fig. S8). The specificity of this antibody was verified with bacterially produced peptide containing Apc1 residues 294 to 399 (hereafter $Apc1^{loop}$) incubated either in anaphase or interphase extract (fig. S8, A and C). The CDK sites on $Apc1^{loop}$ were barely phosphorylated in Apc3 CDK–site mutant APC/Cs, whereas they were highly phosphorylated in APC/C^{WT} in anaphase (Fig. 2E). Thus, CDK phosphorylation in the $Apc1^{loop}$ appears to

Downloaded from http://science.sciencemag.org/ on May 26, 2016

depend on Apc3 phosphorylation, which highlights the influence of Apc3 on Apc1 by recruitment of p9-CDK1.

Because both APC/$C^{Apc1\text{-}7A}$ and APC/$C^{Apc3\text{-}9A}$ retain some APC/C-dependent cyclin-destruction activity, we tested the phenotype of the double mutant. APC/$C^{Apc3\text{-}9A/Apc1\text{-}7A}$ appeared more deficient in cyclin destruction than APC/$C^{Apc1\text{-}7A}$ or APC/$C^{Apc3\text{-}9A}$ alone (Fig. 3A and fig. S9). APC/$C^{Apc3\text{-}9A/Apc1\text{-}7A}$ failed to destroy cyclin A as well as securin (Fig. 3B). We also investigated the activity of APC/$C^{Apc3\text{-}9A/Apc1\text{-}7A}$ using a "cycling" frog egg extract where the endogenous APC/C is replaced by APC/$C^{Apc3\text{-}9A/Apc1\text{-}7A}$ (fig. S10). Unlike WT, APC/$C^{Apc3\text{-}9A/Apc1\text{-}7A}$ could not support cyclin or securin destruction. Consistently, an in vitro phosphorylated APC/$C^{Apc3\text{-}9A/Apc1\text{-}7A}$ showed less activity than APC/C^{WT} in an in vitro ubiquitylation assay (Fig. 3C and fig. S11). Thus, phosphorylation of Apc1 and Apc3 subunits is crucial for APC/C activation. However, it is conceivable that phosphorylation of other subunits or an alternative pathway (e.g., by means of phosphatases) might be involved to some extent in vivo (Fig. 3A and fig. S12). Nevertheless, if phosphorylation of Apc3 and Apc1 is important, an Apc1 phosphomimetic mutation [Asp (D)] might bypass both Apc3 and Apc1 phosphorylation and make CDK phosphorylation dispensable. We tested this in interphase extracts, in which neither CDK nor APC/C-Cdc20 is active. If Apc1 had the phosphomimetic mutation (7D), the APC/C was activated by Cdc20 even in interphase, which triggered cyclin B destruction, albeit with slower kinetics than those observed with APC/C in anaphase (Fig. 3D and fig. S13A). The Apc1-7D gain-of-function phenotype was further confirmed by a "cycling" extract and an in vitro ubiquitylation assay (fig. S13, B and C). These results indicate that the phosphorylation status of

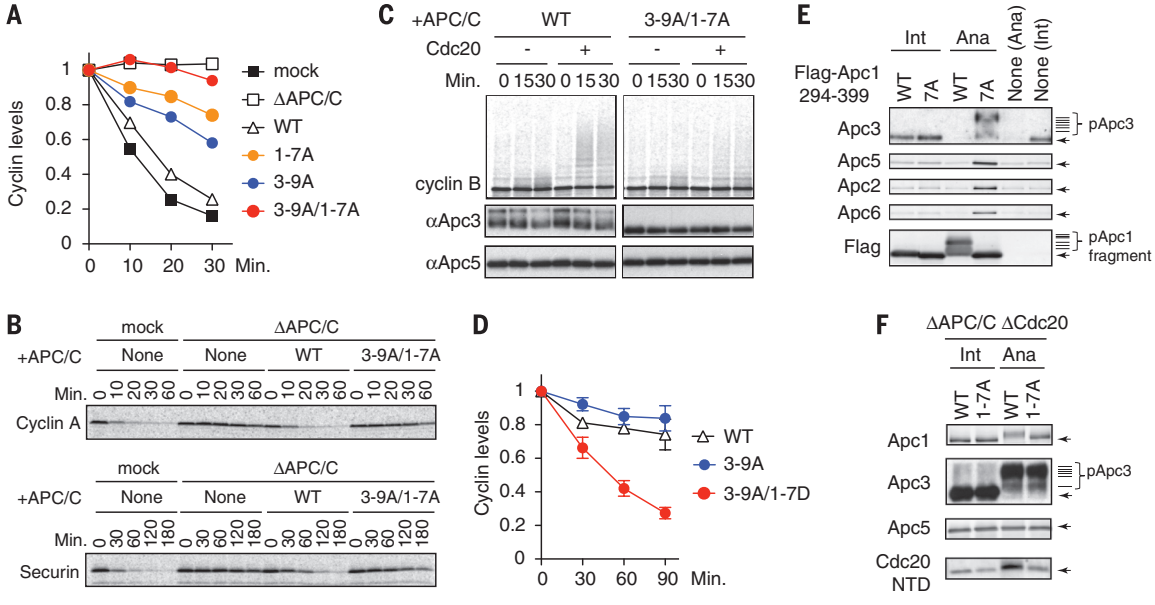


Fig. 3. Role of CDK phosphorylation in the activation of the APC/C ubiquitin ligase. (**A**) Cyclin-destruction assay in mock or fjAPC/C anaphase extracts supplemented with APC/C^{WT}, APC/$C^{Apc1\text{-}7A}$, APC/$C^{Apc3\text{-}9A}$, or APC/$C^{Apc3\text{-}9A/Apc1\text{-}7A}$ (fig. S9). Same as Fig. 1A, relative cyclin levels are shown. (**B**) Same as (A), but human cyclin A2 or *Xenopus* securin destruction was examined in ΔAPC/C anaphase extract supplemented with WT or Apc3-9A/Apc1-7A double-mutant APC/C. (**C**) WT APC/C or APC/$C^{Apc3\text{-}9A/Apc1\text{-}7A}$ was phosphorylated by p9-CDK1-cyclin B. APC/Cs recovered using anti-Apc3 affinity beads were subjected to cyclin B ubiquitylation assay in the presence or absence of Cdc20. ^{35}S-labeled cyclin B was used as substrate. Samples taken at indicated time points were analyzed by SDS-PAGE and autoradiography. The APC/Cs used were monitored by anti-Apc3 and anti-Apc5 immunoblotting. (**D**) Cyclin-destruction assay in interphase extracts supplemented with APC/C^{WT}, APC/$C^{Apc3\text{-}9A}$, or APC/$C^{Apc3\text{-}9A/Apc1\text{-}7D}$ (fig. S13A). Error bars, SEM from three independent experiments. (**E**) Bacterially purified Flag-tagged Apc1 fragment (294 to 399 WT) or its 7A mutant was incubated with interphase or anaphase extract and immunopurified by anti-Flag beads, and bound proteins were analyzed by immunoblotting. (**F**) Interaction of Cdc20 NTD with APC/C^{WT} or APC/$C^{Apc1\text{-}7A}$. APC/C complexes were incubated with Cdc20 NTD (N159-5A) in interphase or anaphase extract depleted of endogenous APC/C and Cdc20 (ΔAPC/C ΔCdc20). APC/C was recovered with anti-Apc3 beads, and bound proteins were analyzed by immunoblotting.

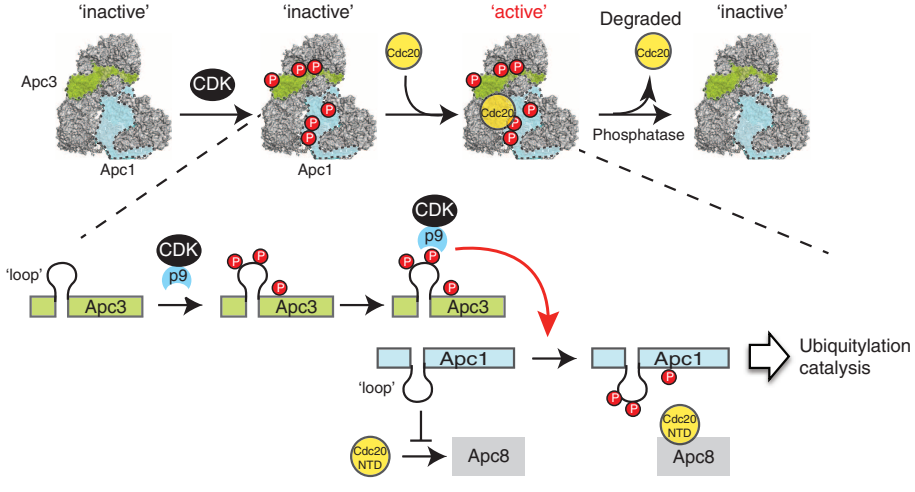


Fig. 4. Proposed model for CDK1 activation of the APC/C. (**Top**) CDK1 phosphorylates the APC/C and stimulates Cdc20 loading and subsequent ubiquitylation catalysis ("active"). Conversely, at the end of mitosis, the APC/C is dephosphorylated by an as-yet-unidentified phosphatase, which contributes to the inactivation of APC/C-Cdc20. (**Bottom**) CDK1-dependent phosphorylation-relay for activation of the APC/C. p9-CDK1-cyclinB initially phosphorylates the internal loop domain of Apc3, which allows p9 (Cks2) bound CDK1-cyclin B loading to Apc3. p9-CDK1-cyclin B then stimulates phosphorylation of the internal loop domain of Apc1. The loop domain seems to block Cdc20-NTD access to the APC/C (e.g., Apc8) when it is not phosphorylated, but upon phosphorylation, the loop loses its inhibitory function, which allows Cdc20 NTD loading and subsequent ubiquitylation catalysis.

Downloaded from http://science.sciencemag.org/ on May 26, 2016

the Apc1^{loop} is a crucial determinant of Cdc20 loading and activation of the APC/C.

We found that, in coimmunoprecipitation assays, Apc1$^{loop\text{-}7A}$ (the Apc1^{loop} carrying 7A mutation) bound to the APC/C in anaphase extract, whereas the WT Apc1^{loop} fragment did not (Fig. 3E). Conversely, these phosphomimetic mutations abolished the interaction with the APC/C (fig. S14), which highlighted how the interaction of the Apc1^{loop} with the APC/C depends on its phosphorylation status. In the atomic structure of human APC/C$^{Cdh1.Emi1}$ determined using cryo–electron microscopy (*25*), residues corresponding to the Apc1^{loop} are disordered and not observed in the electron microscopy density map. However, given the putative location of Apc1^{loop} proximal to the regulatory N-terminal domain of Cdh1 (Cdh1^{NTD}) (*25*) (fig. S15), phosphorylation-dependent structural changes of Apc1^{loop} could influence the APC/C binding sites for the NTD of coactivator located on Apc8 (*25*, *26*), the PC domain of Apc1 (*25*), and Apc6 (*26*). Consistent with this idea, Cdc20-NTD binding was reduced in APC/C$^{Apc1\text{-}7A}$ compared with APC/C^{WT} (Fig. 3F).

Our results reveal the presence and importance of the coordinated phosphorylation of Apc3 and Apc1 within the APC/C complex for the control of the APC/C in mitosis (Fig. 4). Extended flexible loops in both subunits have a key role; one acts as a scaffold of p9-CDK1 and the other for phosphorylation-dependent interaction with Cdc20-NTD. Previous studies in yeast and *Drosophila* provide in vivo evidence that CDK1 phosphorylation of the APC/C is required for its mitotic activity (*22*, *27*, *28*). Our present study extends past findings of (*13*–*16*, *22*) and uncovers the mechanistic insight and the functional consequences of APC/C phosphorylation in vertebrates. Cdc20 [not Cdh1, which is a tumor suppressor (*29*)] is a promising anticancer therapeutic target (*7*, *8*, *10*, *30*). The Apc1^{loop} may provide a target for strategies to specifically inhibit APC/C-Cdc20.

REFERENCES AND NOTES

1. V. Sudakin *et al.*, *Mol. Biol. Cell* **6**, 185–197 (1995).
2. S. Irniger, S. Piatti, C. Michaelis, K. Nasmyth, *Cell* **81**, 269–277 (1995).
3. R. W. King *et al.*, *Cell* **81**, 279–288 (1995).
4. I. Primorac, A. Musacchio, *J. Cell Biol.* **201**, 177–189 (2013).
5. L. Chang, D. Barford, *Curr. Opin. Struct. Biol.* **29**, 1–9 (2014).
6. J. Pines, *Nat. Rev. Mol. Cell Biol.* **12**, 427–438 (2011).
7. H. C. Huang, J. Shi, J. D. Orth, T. J. Mitchison, *Cancer Cell* **16**, 347–358 (2009).
8. E. Manchado *et al.*, *Cancer Cell* **18**, 641–654 (2010).
9. X. Zeng *et al.*, *Cancer Cell* **18**, 382–395 (2010).
10. K. L. Sackton *et al.*, *Nature* **514**, 646–649 (2014).
11. K. E. Gascoigne, S. S. Taylor, *Cancer Cell* **14**, 111–122 (2008).
12. J. A. Steen *et al.*, *Proc. Natl. Acad. Sci. U.S.A.* **105**, 6069–6074 (2008).
13. C. Kraft *et al.*, *EMBO J.* **22**, 6598–6609 (2003).
14. E. R. Kramer, N. Scheuringer, A. V. Podtelejnikov, M. Mann, J. M. Peters, *Mol. Biol. Cell* **11**, 1555–1569 (2000).
15. M. Shteinberg, A. Hershko, *Biochem. Biophys. Res. Commun.* **257**, 12–18 (1999).
16. G. Fang, H. Yu, M. W. Kirschner, *Mol. Cell* **2**, 163–171 (1998).
17. Z. Zhang *et al.*, *Biochem. J.* **449**, 365–371 (2013).
18. I. Berger, D. J. Fitzgerald, T. J. Richmond, *Nat. Biotechnol.* **22**, 1583–1587 (2004).
19. M. E. Matyskiela, D. O. Morgan, *Mol. Cell* **34**, 68–80 (2009).
20. D. Patra, W. G. Dunphy, *Genes Dev.* **10**, 1503–1515 (1996).
21. D. Patra, W. G. Dunphy, *Genes Dev.* **12**, 2549–2559 (1998).
22. A. D. Rudner, A. W. Murray, *J. Cell Biol.* **149**, 1377–1390 (2000).
23. M. Kõivomägi *et al.*, *Nat. Struct. Mol. Biol.* **20**, 1415–1424 (2013).
24. D. A. McGrath *et al.*, *Nat. Struct. Mol. Biol.* **20**, 1407–1414 (2013).
25. L. Chang, Z. Zhang, J. Yang, S. H. McLaughlin, D. Barford, *Nature* **522**, 450–454 (2015).
26. H. Labit *et al.*, *EMBO J.* **31**, 3351–3362 (2012).
27. N. Lianga *et al.*, *J. Cell Biol.* **201**, 843–862 (2013).
28. J. Y. Huang, G. Morley, D. Li, M. Whitaker, *J. Cell Sci.* **120**, 1990–1997 (2007).
29. I. García-Higuera *et al.*, *Nat. Cell Biol.* **10**, 802–811 (2008).
30. K. E. Gascoigne, S. S. Taylor, *J. Cell Sci.* **122**, 2579–2585 (2009).

ACKNOWLEDGMENTS

We thank J. Gannon for monoclonal Apc3-, Cdc20-, and pPlx1-specific antibodies; C. Ellenrieder for p9-specific antibodies; K. Ohsumi for securin-specific antibodies; J. Endicott for purified CDK1–cyclin B; F. Esashi for helpful advice on affinity purification of antibodies; Z. Zhang and D. Barford for providing the methodology and MultiBac-USER expression vectors; members of the Yamano laboratory for helpful discussion; and I. Hagan and F. Uhlmann for critical reading of the manuscript. This work was supported by Marie Curie Cancer Care, Cancer Research UK (C8320/A13586), and Medical Research Council (MR/M010899/1).

SUPPLEMENTARY MATERIALS

www.sciencemag.org/content/352/6289/1121/suppl/DC
Materials and Methods
Figs. S1 to S15
Table S1
References (*31*–*36*)

9 September 2015; accepted 11 April 2016
Published online 21 April 2016
10.1126/science.aad3925

CELL DIVISION

A force-generating machinery maintains the spindle at the cell center during mitosis

Carlos Garzon-Coral,[1] Horatiu A. Fantana,[1] Jonathon Howard[2]*

The position and orientation of the mitotic spindle is precisely regulated to ensure the accurate partition of the cytoplasm between daughter cells and the correct localization of the daughters within growing tissue. Using magnetic tweezers to perturb the position of the spindle in intact cells, we discovered a force-generating machinery that maintains the spindle at the cell center during metaphase and anaphase in one- and two-cell *Caenorhabditis elegans* embryos. The forces increase with the number of microtubules and are larger in smaller cells. The machinery is rigid enough to suppress thermal fluctuations to ensure precise localization of the mitotic spindle, yet compliant enough to allow molecular force generators to fine-tune the position of the mitotic spindle to facilitate asymmetric division.

The position and orientation of the mitotic spindle determines the plane of cell division, which, in turn, determines how the cytoplasmic contents are partitioned to the daughter cells (*1*) and how the daughter cells are localized within the tissue (*2*). After the spindle reaches the cell center before metaphase, its position and orientation must be precisely maintained (*3*) until the cell enters anaphase. The molecular forces underlying the maintenance of spindle position and orientation are not known.

Although much is known about how force is generated by purified proteins (*4*) and in cell extracts (*5*), little is understood about how molecular forces are integrated in vivo to serve complex cellular processes, such as spindle positioning. This is due to the difficulties of exerting and measuring forces in intact cells. Indeed, with the exception of the landmark paper by Nicklas in 1983 (*6*) that measured forces associated with spindle elongation during anaphase, there has been no direct quantitative measurement of forces on mitotic spindles in cells [see (*7*, *8*)].

[1]Max Planck Institute of Molecular Cell Biology and Genetics, Dresden, Germany. [2]Department of Molecular Biophysics and Biochemistry, Yale University, New Haven, CT, USA.
*Corresponding author. Email: jonathon.howard@yale.edu

To measure mitotic forces in vivo, we injected 1.0-μm–diameter superparamagnetic beads (*9*) and used magnetic tweezers (*10*) to exert calibrated forces of up to 200 pN to mitotic spindles in one- and two-cell *Caenorhabditis elegans* embryos, a model system for studying mitosis (*1*) (Fig. 1A and figs. S1 to S4) (see supplementary methods). We applied forces of 20 to 60 pN to the centrosome at one of the spindle's poles for up to 20 s during metaphase, when the spindle is in a relatively quiescent phase at the cell center (Fig. 1A). In response to force, the spindle rotated as the centrosome was displaced up to 3 μm from the anterior-posterior (A-P) axis (Fig. 1, B and C, and movie S1). Thus, it was possible to perturb the position and orientation of the spindle by using magnetic forces.

The kinetics of spindle displacement indicated that the mitotic spindle is held at the cell center by viscoelastic forces. First, after the onset of the force, the centrosome moved with an approximately constant velocity during the first few seconds (Fig. 2A, average displacement), which suggested that the spindle is subject to viscous forces. Second, the displacement speed decreased after several

Downloaded from http://science.sciencemag.org/ on May 26, 2016

seconds (Figs. 1C and 2A), which indicated that there is an elastic force (i.e., a spring) that opposes the external force. Third, after cessation of the force, the centrosome partially relaxed back toward its initial position (Figs. 1C and 2B), which suggested that the elastic element returns part of its stored mechanical energy. Finally, higher external forces were required to displace the centrosome through larger distances, as expected for an elastic element (fig. S5).

To estimate the stiffness of the elastic element, we fit the spindle's rising phase (Fig. 2A) with a Voigt model (Fig. 2A, left inset), in which a spring and a viscous damper are in parallel. A curve fit of the data to the Voigt model gave a stiffness (κ) of 16.4 ± 2.1 pN/μm (Table 1, uncertainties are SEs): 16 pN force, on average, was needed to displace the centrosome 1 μm from the A-P axis. We call the force the centering force and the stiffness the centering stiffness. The drag coefficient (γ) of the damper was 134 ± 27 pN·s/μm (Table 1). The associated time constant (κ/γ) was 8.1 ± 1.5 s. The time constant of the relaxation phase was 14.5 ± 2.8 s (Fig. 2B, solid red line), longer than the rising phase (see discussion in supplementary text). The dynamics of the spindle are very different from the dynamics of beads in the cytoplasm, which relax incompletely and much more quickly (0.65 ± 0.08 s) (Fig. 2B, fig. S6, and movie S2). Thus, a centering machinery opposes motion of the spindle away from the cell center and has viscoelastic properties distinct from those of the cytoplasm.

We propose that the centering machinery acts like a set of four damped springs that oppose movements transverse to the A-P axis (Fig. 2B, right inset, black). These springs orient the spindle so that when one centrosome is perturbed, the spindle pivots around the other centrosome (Fig. 1B). Correct orientation along the A-P axis ensures that the cleavage plane is perpendicular to the A-P axis during cytokinesis.

As the cell cycle progresses from metaphase through anaphase, several morphological and mechanical changes take place (*11*–*14*). Concomitant with these changes, we found that the centering stiffness increased fivefold (Fig. 3A, Table 1, fig. S7, and movie S3): During anaphase, forces on the order of 100 pN were required to displace the spindle 1 μm. These forces are similar in magnitude to the forces measured during chromosome segregation by Nicklas in grasshopper cells (*6*). An increase in the centering force may help to stabilize spindle position against high centrifugal forces that occur during the anaphase, such as those driving transverse oscillations (*12*–*14*).

Mitotic spindles remain centered throughout *C. elegans* development, during which cell and spindle size decrease (*15*). To study the influence of the cell size on the centering force, we performed the force experiments in the smaller cells of the two-cell embryo, P1 and AB (Fig. 3A, figs. S7 and S8, and movie S4), which have different cytoplasmic and cortical compositions (*1*). We found that the centering stiffness increased about twofold in both cells (Table 1), which indicated that the relative precision of centering may be independent of cell size and cell type.

Dynein-based cortical force generators, which drive posterior spindle displacement during anaphase (*12*, *14*), are not necessary for the initial centration of the spindle (*13*) but have been proposed to contribute to the maintenance phase (*4*, *16*). To the contrary, we found that the cortical force generators antagonize, rather than augment, the maintenance of centration: The centering stiffness in *gpr-1/2 (RNAi)* embryos, in which the force generators are inactivated by RNA interference, was about twice that in control embryos (Fig. 3B and Table 1). Consistent with the destabilizing effect, spindles arrested in metaphase using *fzy-1 (RNAi)* (*3*) were quiescent only when the cortical pulling forces were absent [*gpr-1/2+fzy-1 (RNAi)*] (fig. S9). The *gpr-1/2+fzy-1 (RNAi)* embryos had similar high centering stiffness to *gpr-1/2 (RNAi)* embryos, and they underwent almost complete recovery of the spindle position after 45 s (Fig. 3B inset, Table 1, fig. S6B, and movie S5), as expected for the Voigt model. Finally, the centering stiffness did not change in *gpr-1/2 (RNAi)* embryos even during anaphase (Fig. 3A), when the cortical forces are strongest (*12*, *14*). Together, these experiments show that the cortical force generators are not required for the maintenance of centration, and suggest instead that the cortical force generators play an anticentering role, namely, the posterior displacement of the spindle that leads to asymmetric division.

We used RNAi to explore the roles of microtubules in the centering machinery. When we increased the number of astral microtubules by RNAi against *klp-7* (fig. S10), which encodes a depolymerizing kinesin, we found that the centering stiffness increased about twofold (Fig. 3A and Table 1). Thus, the centering stiffness scales with the number of microtubules. We also found that the number of microtubules reaching the cortex in P1 cells, which have higher centering stiffness, was twice that in one-cell embryos (fig. S11). Furthermore, the high centering stiffness of em-

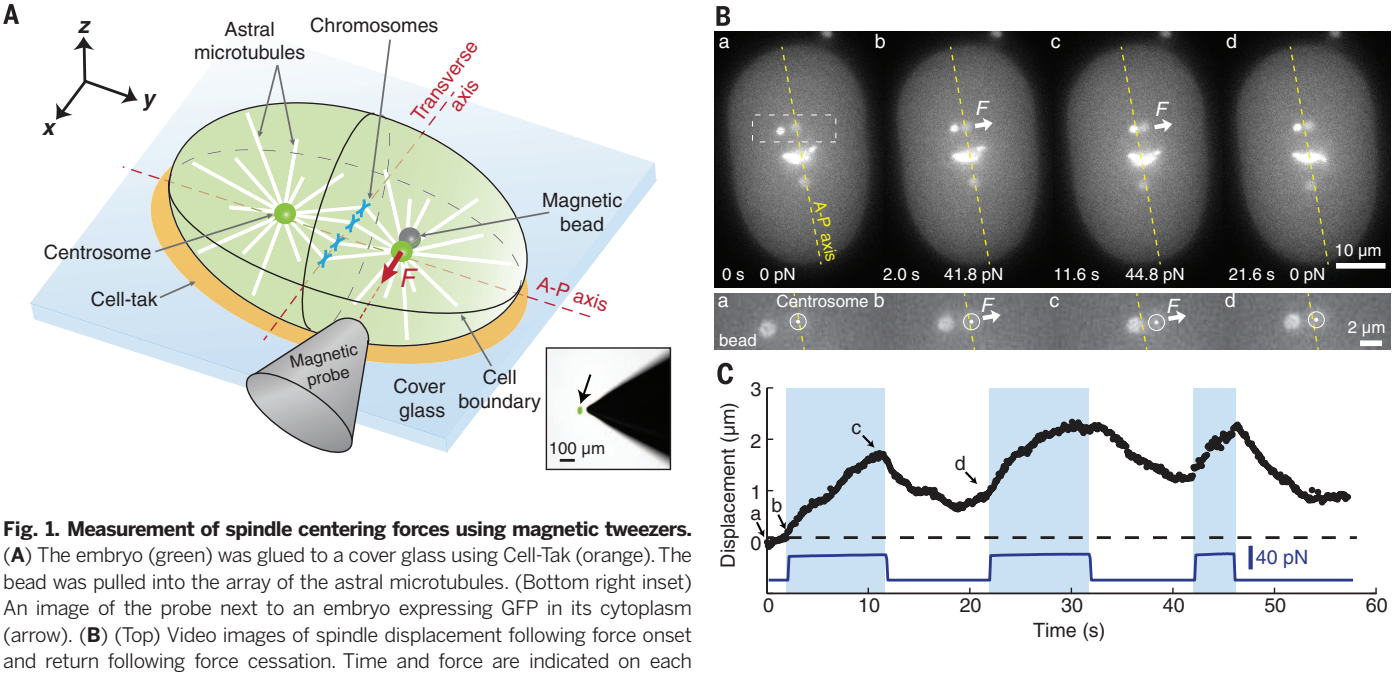


Fig. 1. Measurement of spindle centering forces using magnetic tweezers. (**A**) The embryo (green) was glued to a cover glass using Cell-Tak (orange). The bead was pulled into the array of the astral microtubules. (Bottom right inset) An image of the probe next to an embryo expressing GFP in its cytoplasm (arrow). (**B**) (Top) Video images of spindle displacement following force onset and return following force cessation. Time and force are indicated on each frame. (Bottom) Close-up of the displacement. The centrosome is circled. (**C**) Force (blue line) and centrosome displacement (black circles) are plotted against time. The dashed line corresponds to the A-P axis. The letters indicate when the images in (B) were taken. Blue shaded area indicates when the bead pushed on the centrosome.

Downloaded from http://science.sciencemag.org/ on May 26, 2016

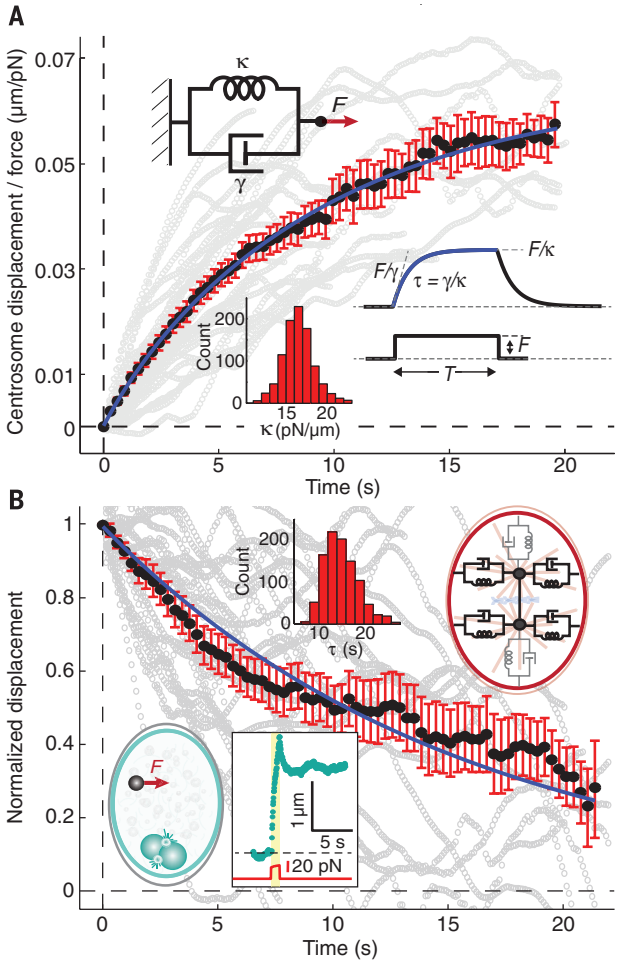


Fig. 2. Viscoelasticity of the centering apparatus during metaphase. (**A**) The average movement of the spindle away from the A-P axis in response to external forces (black circles). Displacement traces (n = 34) from 27 cells were averaged and scaled by the force over time, $F(t)$. The gray traces in the background are the individual traces, smoothed using an 11-point window. The blue curve is $x(t)/F(t) = (1/\kappa)[1 - \exp(-t\kappa/\gamma)]$, where κ is the stiffness and γ is the drag coefficient of a Voigt element (top inset). (**B**) The average relaxation of the spindle back toward the A-P axis after cessation of the force (black circles) superimposed on individual traces (gray). The blue curve is $x(t)/x(0) = \exp(-t/\tau)$, where τ is the time constant. The left inset shows the rising and relaxation phases of a 1.0-μm bead in the cytoplasm (see fig. S6). The right inset shows a model comprising six Voigt elements; the four that were probed in the experiments shown in (A) and (B) are indicated in black. Histograms show parameter values obtained by bootstrapping. Errors are SEs.

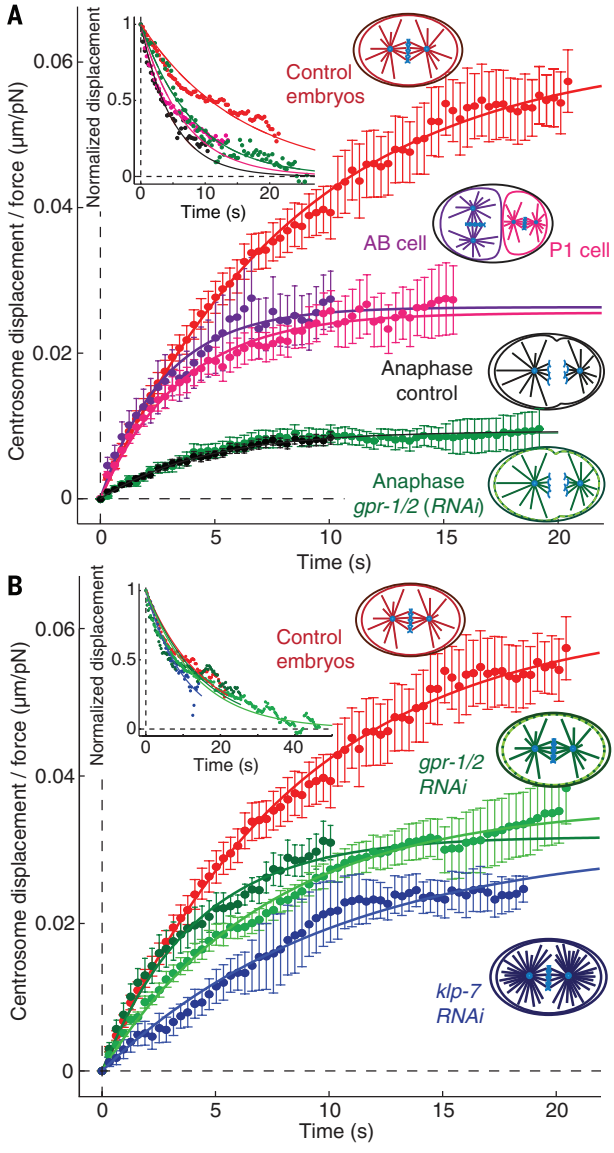


Fig. 3. Spindle responses during anaphase in two-cell embryos and after *klp-7 RNAi* and *gpr-1/2 RNAi*. (**A**) Averaged rising phases during metaphase in one-cell (red) and two-cell (P1, fuschia; AB, purple) embryos and during anaphase of control (black) and *gpr-1/2 (RNAi)* (green) embryos. (**B**) Averaged rising phases in *klp-7 (RNAi)* (blue), *gpr-1/2 (RNAi)* (dark green), *gpr-1/2+fzy-1* (green), and control embryos (red). The solid lines show fits of the Voigt model. (Top left inset) The corresponding falling phases. Errors are SEs.

bryos during anaphase is associated with a combination of more microtubule nucleation (*11*) and longer times that microtubule ends remain at the cortex (*17*) (fig. S12). Thus, the mechanical properties of the force-generating machinery appears to depend on microtubules.

The centering machinery is remarkably compliant. Microtubules are among the most rigid cellular polymers [Young's modulus $E \approx 2$ GPa, (*18*)], so that even a single microtubule (cross-sectional area $A \approx 200$ nm^2) spanning the distance R = 15 μm between the centrosome and the cortex will have a static compressive stiffness of $EA/R \approx 25{,}000$ pN/μm. This is more than 1000 times the measured centering stiffness, which is associated with an entire microtubule array. This suggests that the the distance R = 15 μm between the centering stiffness is due to dynamical properties, such as buckling of microtubules under compression or conversion of growing microtubules to shrinking ones (*17*, *19*).

A dynamic array of astral microtubules that grow out from the centrosome and transiently push against the cortex can account for the centering machinery (*17*, *19*). Such an array has springlike properties: When the spindle moves away from the center, more microtubules push against the closer cortex, as it takes less time for the microtubules to reach the closer cortex. This imbalance generates a net force—the centering force—that directs the spindle back to the cell center. The force imbalance increases with larger displacements away from the cell center, which gives rise to springlike behavior: the centering stiffness (*17*, *19*). The predicted centering stiffness of an ensemble of M pushing microtubules is $\kappa \approx Mf/R$ (*17*, *19*), where $f \approx 1$ pN is the polymerization force (*20*) or the buckling force of a 15-μm microtubule (*18*). A stiffness of 16 pN/μm is therefore consistent with an average of ~200 microtubules in contact with and pushing against the cortex at any time, as observed in (*21*) (see supplementary

Downloaded from http://science.sciencemag.org/ on May 26, 2016

Table 1. Stiffness, drag coefficients, and time constants under several different conditions. Errors are SEs obtained from bootstrapping. Values in parentheses are 95% confidence intervals for asymmetric bootstrap distributions.

Group	Rising phase				Falling phase	
	n	Stiffness (κ, pN/μm)	Drag (γ, pN·s/μm)	τ (s)	*n*	τ (s)
Metaphase						
Control	34	16.4 ± 2.1	134 ± 17	8.1 ± 1.5	27	14.5 ± 2.8
gpr-1/2 (all)	33	29.1 ± 3.9	174 ± 19	6 ± 1	25	14.3 ± 1.9
gpr-1/2	10	30.6 ± 5.1	129 ± 35	4.2 ± 1.4	9	13.7 ± 3.9
gpr-1/2+fzy-1	23	27.7 ± 4.7	195 ± 28	7.1 ± 1.6	21	16.3 ± 3
klp-7	6	31.4 (24.1–44.1)	271 (75–491)	8.6 (3.1–11.1)	6	10.2 ± 1.3
P1 cell	18	39.6 ± 7	137 ± 35	3.4 ± 1.1	17	5.8 ± 2.2
AB cell	12	35.6 ± 10.5	116 ± 43	3.3 ± 1.6	–	–*
Anaphase						
Control	33	91.1 ± 17.9	522 ± 100	5.7 ± 1.6	30	4.4 ± 0.9
gpr-1/2	27	119.4 ± 21.3	389 ± 81	3.3 ± 0.9	14	9.5 ± 3.6
P1 cell	11	104.8 (43.6–178.3)	1134 (174–1713)	10.8 (3.99–19.6)	–	–†

*Not measured because the spindle rotated during late metaphase and anaphase. †Not measured because cytokinesis occurred shortly after anaphase onset.

methods). This number corresponds to about 10% of the total number of astral microtubules (*22*). The pushing model accounts for the high centering stiffness of *klp-7* (*RNAi*) embryos (they have more microtubules) (fig. S10A), as well as the higher stiffness of smaller cells (Fig. 3) (they have a higher density of microtubule ends at the cortex) (fig. S10B). The model also predicts drag forces: Movement of the aster increases the rate of arrival of ends at one cortex and, therefore, leads to an effective drag force (*17*). The measured drag coefficient is in quantitative agreement with this prediction (see supplementary text). Thus, our results support a model in which microtubule polymerization against the cortex generates the centering force.

In a remarkable adaptation of mechanical properties to cellular function, the magnitudes of the stiffness and damping of the centering machinery are ideally suited for cellular function. A centering spring with stiffness 16 pN/μm is rigid enough to stabilize the spindle against thermal forces: The displacement fluctuations of a spring due to Brownian motion have a standard deviation of $\sqrt{(k_B T/\kappa)}$ where k_B is the Boltzmann constant and T is absolute temperature), which is about 16 nm for the single-cell embryo. Thus, the precision of centration is not limited by thermal fluctuations. Indeed, fluctuations from other sources, such as stochastic variation in the number of force generators (i.e., microtubules) with a predicted standard deviation of $R/\sqrt{M} \approx 1000$ nm (*17*), are expected to exceed the thermal fluctuations.

On the other hand, the centering spring is compliant enough to allow adjustments of spindle position by a small number of motor proteins. During metaphase, the spindle moves through displacement $d \approx 3$ μm along the A-P axis into the posterior half of the embryo to set up asymmetric cell division (*3*). If the centering stiffness is similar along the A-P axis as transverse to it (Fig. 2B, gray springs), which is reasonable given the symmetry of the microtubule asters, then such a posterior displacement requires a force imbalance of $\kappa d \approx 50$ pN. This could be exerted by as few as 10 to 20 cortical force generators (*14*). The drag coefficient is also well adapted. If it were much lower, then transient force imbalances due to motor stochasticity would not be smoothed out; if it were much higher, then it would prevent posterior displacement from being completed on the minute time scale.

In conclusion, a force-generating centration apparatus with spring-like properties maintains the spindle at the cell center. The centering stiffness is high enough to ensure the precise maintenance of spindle position against thermal and other fluctuations while spindle assembly is completed and the cell prepares for chromosome segregation. Yet it is low enough to allow force generators to fine-tune the position of the spindle to facilitate asymmetric cell division.

REFERENCES AND NOTES

1. M. Galli, S. van den Heuvel, *Annu. Rev. Genet.* **42**, 389–411 (2008).
2. T. E. Gillies, C. Cabernard, *Curr. Biol.* **21**, R599–R609 (2011).
3. E. K. McCarthy Campbell, A. D. Werts, B. Goldstein, *PLOS Biol.* **7**, e1000088 (2009).
4. L. Laan *et al.*, *Cell* **148**, 502–514 (2012).
5. Y. Shimamoto, Y. T. Maeda, S. Ishiwata, A. J. Libchaber, T. M. Kapoor, *Cell* **145**, 1062–1074 (2011).
6. R. B. Nicklas, *J. Cell Biol.* **97**, 542–548 (1983).
7. S. Dumont, T. J. Mitchison, *Curr. Biol.* **19**, R749–R761 (2009).
8. J. R. McIntosh, M. I. Molodtsov, F. I. Ataullakhanov, *Q. Rev. Biophys.* **45**, 147–207 (2012).
9. B. R. Daniels, B. C. Masi, D. Wirtz, *Biophys. J.* **90**, 4712–4719 (2006).
10. P. Kollmannsberger, B. Fabry, *Rev. Sci. Instrum.* **78**, 114301 (2007).
11. M. Srayko, A. Kaya, J. Stamford, A. A. Hyman, *Dev. Cell* **9**, 223–236 (2005).
12. J.-C. Labbé, E. K. McCarthy, B. Goldstein, *J. Cell Biol.* **167**, 245–256 (2004).
13. J. Pecreaux *et al.*, *Curr. Biol.* **16**, 2111–2122 (2006).
14. S. W. Grill, J. Howard, E. Schäffer, E. H. K. Stelzer, A. A. Hyman, *Science* **301**, 518–521 (2003).
15. Y. Hara, A. Kimura, *Mol. Biol. Cell* **24**, 1411–1419 (2013).
16. S. W. Grill, A. A. Hyman, *Dev. Cell* **8**, 461–465 (2005).
17. J. Howard, *Phys. Biol.* **3**, 54–66 (2006).
18. F. Gittes, B. Mickey, J. Nettleton, J. Howard, *J. Cell Biol.* **120**, 923–934 (1993).
19. R. Ma, L. Laan, M. Dogterom, N. Pavin, F. Jülicher, *New J. Phys.* **16**, 013018 (2014).
20. M. Dogterom, B. Yurke, *Science* **278**, 856–860 (1997).
21. C. Kozlowski, M. Srayko, F. Nedelec, *Cell* **129**, 499–510 (2007).
22. T. Müller-Reichert, J. Mäntler, M. Srayko, E. O'Toole, *J. Microsc.* **230**, 297–307 (2008).

ACKNOWLEDGMENTS

We thank J. Alper, A. Hyman, S. Grill, H. Bowne-Anderson, and F. Carrillo-Oesterreich for comments on the manuscript and R. Ma, C. Bruchatz, V. Thacker, J. Mücksch, and V. Duran for discussion and assistance. C.G.-C. was funded by the European network MitoSys project. H.A.F., C.G.-C., and J.H. designed the experiments. H.A.F. and C.G.-C. performed experiments and analyzed data. C.G.-C. and J.H. wrote the paper. All the authors discussed the results and commented on the manuscript. H.A.F., C.G.-C., and J.H. declare no competing financial interest. We thank the Max Planck Society and Yale University for support.

SUPPLEMENTARY MATERIALS

www.sciencemag.org/content/352/6289/1124/suppl/DC1
Materials and Methods
Supplementary Text
Figs. S1 to S14
Tables S1 and S2
References (*23*–*33*)
Movies S1 to S5

1 December 2015; accepted 13 April 2016
10.1126/science.aad9745

Downloaded from http://science.sciencemag.org/ on May 26, 2016



A force-generating machinery maintains the spindle at the cell center during mitosis
Carlos Garzon-Coral, Horatiu A. Fantana and Jonathon Howard
(May 26, 2016)
Science **352** (6289), 1124-1127. [doi: 10.1126/science.aad9745]

Editor's Summary

Forcing the spindle to the cell center

As a cell divides, the mitotic spindle segregates chromosomes to daughter cells. It does so while maintaining a centralized position; however, the mechanism for spindle placement is unclear. Garzon-Coral *et al.* used magnetic tweezers to show that the dynamical properties of the astral microtubules act as a force-generating machinery to keep the spindle at the cell center. The stiffness of the spring-like force increases during anaphase and also with decreasing cell size. This machinery is strong enough to quench thermal fluctuations to ensure precise localization of the spindle, but soft enough to allow molecular force generators to fine-tune the position of the mitotic spindle.

Science, this issue p. 1124

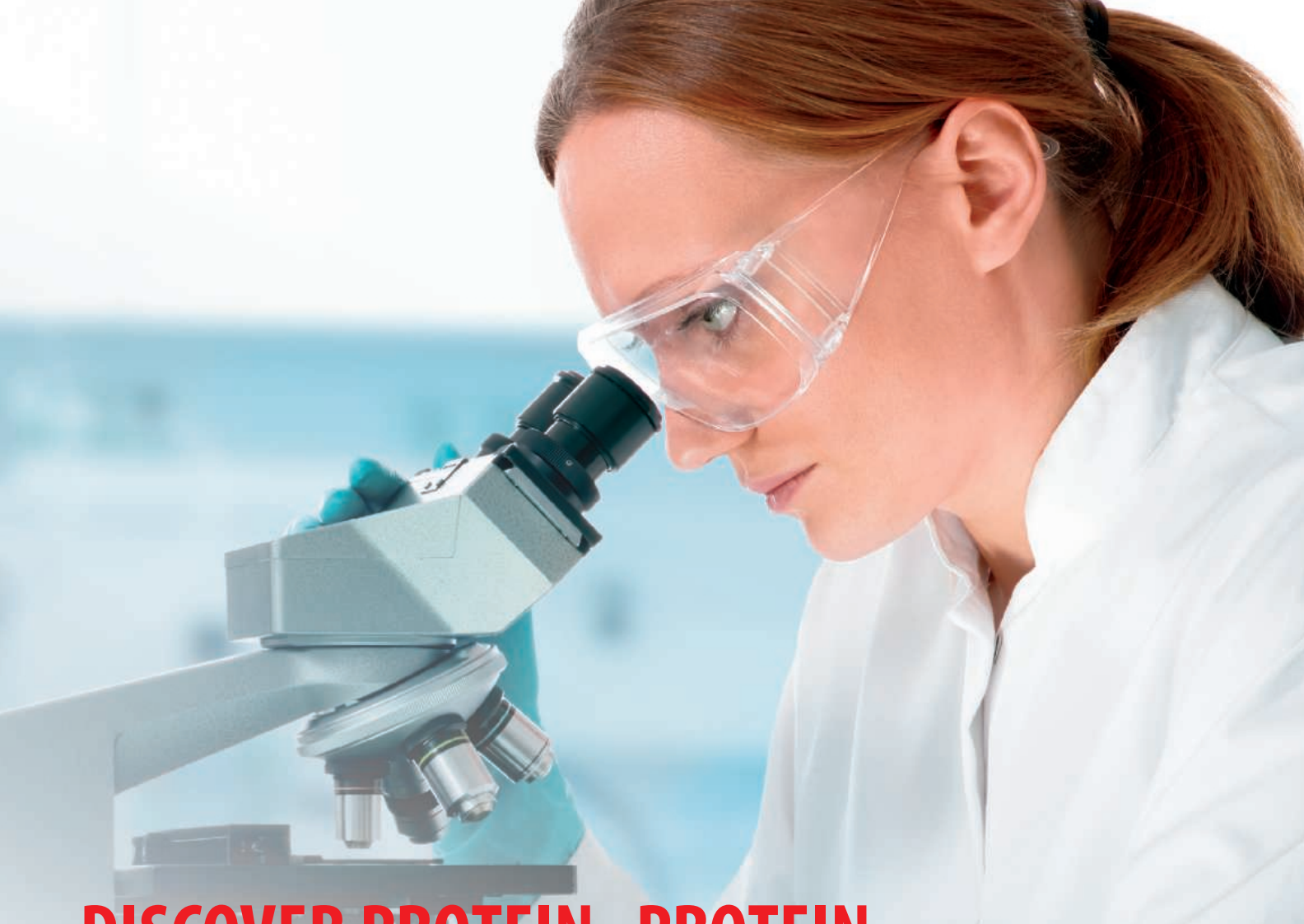
This copy is for your personal, non-commercial use only.

Article Tools Visit the online version of this article to access the personalization and article tools:
http://science.sciencemag.org/content/352/6289/1124

Permissions Obtain information about reproducing this article:
http://www.sciencemag.org/about/permissions.dtl

Science (print ISSN 0036-8075; online ISSN 1095-9203) is published weekly, except the last week in December, by the American Association for the Advancement of Science, 1200 New York Avenue NW, Washington, DC 20005. Copyright 2016 by the American Association for the Advancement of Science; all rights reserved. The title *Science* is a registered trademark of AAAS.

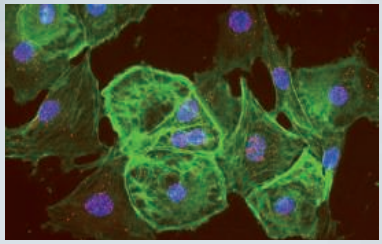
Downloaded from http://science.sciencemag.org/ on May 26, 2016



DISCOVER PROTEIN–PROTEIN INTERACTIONS WITH DUOLINK® USING PLA® TECHNOLOGY

Proximity Ligation Assay (PLA) Technology provides sensitive *in situ* detection of endogenous proteins

- Visualize individual interactions without overexpressing proteins
- Gain high specificity with dual binding of primary antibodies
- Increased sensitivity of single molecule due to signal amplification
- Analyze using standard immunofluorescence instruments



For more information, visit
sigma-aldrich.com/duolink

©2016 Sigma-Aldrich Co. LLC. All rights reserved. SIGMA and SIGMA-ALDRICH are trademarks of Sigma-Aldrich Co. LLC, registered in the US and other countries. Duolink and PLA are registered trademarks of Olink AB.
Sigma-Aldrich Corp. is a subsidiary of Merck KGaA, Darmstadt, Germany.

SIGMA-ALDRICH®





Even at 60k RPM, there was room for **one more revolution.**

Introducing the Optima AUC

Our newly upgraded Optima AUC returns analytical ultracentrifugation to the forefront of analysis, by offering powerful optics that help you get accurate, reproducible data, furthering your research's validity and success. The Optima AUC is a fast, sophisticated and easy-to use analytical research tool. The Optima AUC lets molecules float free and unbound—letting you characterize them in their native state. A large touch-screen display (visible from across labs) eases operation and boosts efficiency. Modern, intuitive software allows for simple run-monitoring and data exports performed either locally or remotely.

Discover the Optima AUC at **info.beckmancoulter.com/OptimaAUC**

© 2016 Beckman Coulter, Inc. All rights reserved. Beckman Coulter, the stylized logo, and the Beckman Coulter product and service marks used herein are trademarks or registered trademarks of Beckman Coulter, Inc. in the United States and other countries.

For Beckman Coulter's worldwide office locations and phone numbers, please visit "Contact Us" at **beckman.com**

CENT-1576ADV03.16-A

BECKMAN COULTER
Life Sciences

WHO WILL WIN THE PRIZE

The result will be unveiled in June.
The winners will receive:

★A Grand Prize of $25,000 and a Runner-Up Prize of $5,000 will be awarded.
★The Grand Prize Winning Essay will be published in *Science*;
a brief abstract of the Runner-Up Essay will be published in *Science*.

The 2016 award ceremony will be held in San Francisco, on 23rd June, 2016.

Stem cells and regenerative medicine is the new frontier in life sciences. Boyalife, *Science*, and *Science Translational Medicine* jointly establish a global award to recognize and reward scientists in the fields of stem cells and regenerative medicine with a focus on developing cell-based treatments for cancer, degenerative disorders, immunotherapy and stem cells transplantation.



BOYALIFE Science & Science Translational Medicine Award | in Stem Cells and Regenerative Medicine

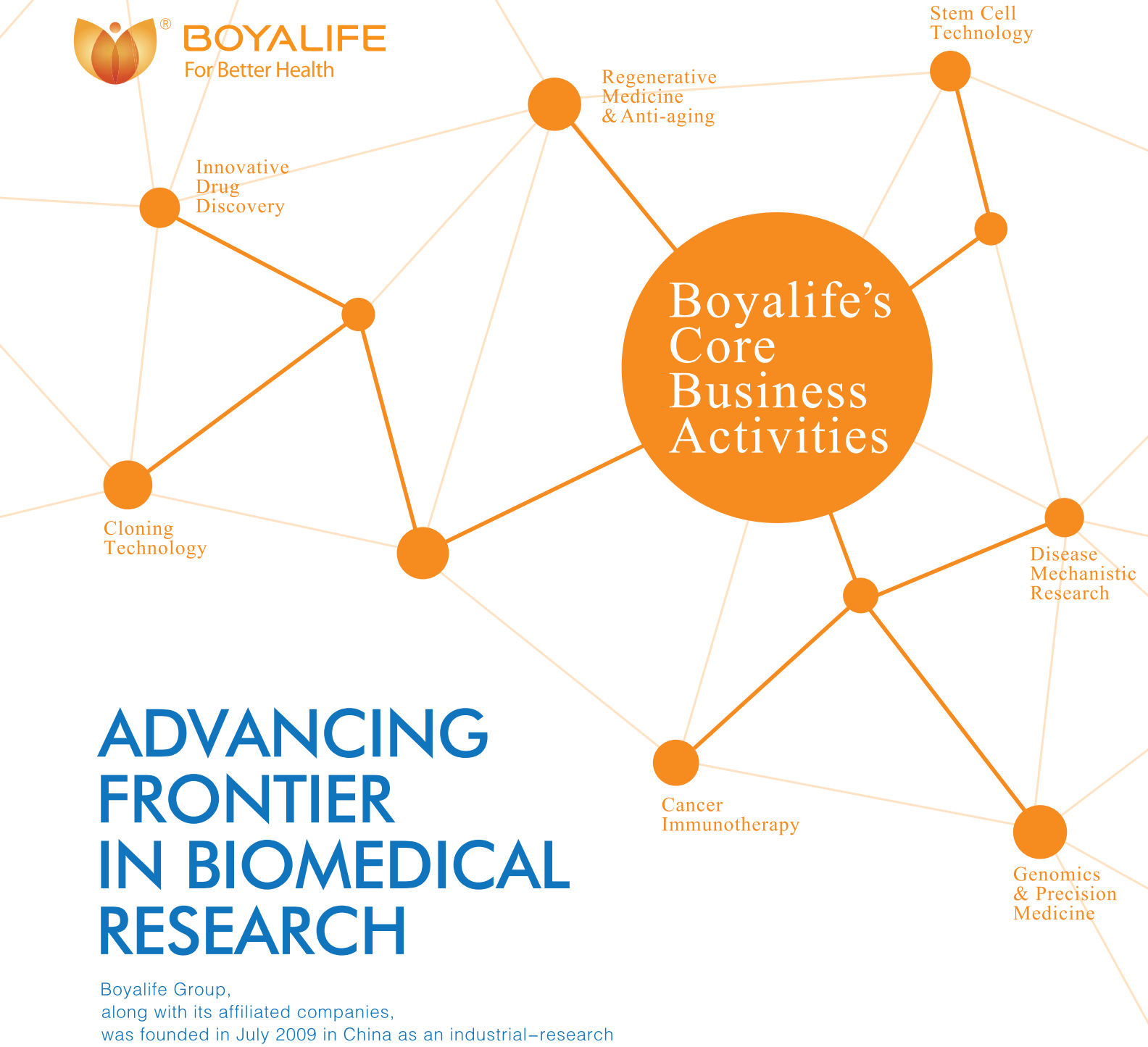
Learn more about the Prize, visit :
http://www.sciencemag.org/prizes/boyalife

BOYALIFE® For Better Health

Science AAAS

Science Translational Medicine AAAS

BOYALIFE®
For Better Health



ADVANCING FRONTIER IN BIOMEDICAL RESEARCH

Boyalife Group,
along with its affiliated companies,
was founded in July 2009 in China as an industrial–research alliance among top research institutes for stem cell and regenerative medicine.
In 2012, Boyalife Group won the prestigious "2012 CCTV China Brand Award",
emerging as a leading brand in healthcare in China.

Start your career at Boyalife!
Contact:career@boyalife.com
www.boyalifegroup.com



WORLD-RENOWNED SCIENCE

starts with an **abstract**

my science **SUBMIT**

The American Heart Association is bringing the premier cardiovascular conference for basic, translational, clinical, and population science to New Orleans, Louisiana this November. Attracting nearly 18,000 professional attendees from more than 100 countries, AHA's Scientific Sessions provides an elite forum for presentation of innovative research findings.

Opportunity for Publication:

Accepted abstracts are published in *Circulation*, an American Heart Association journal.

About *Circulation*:

Top-ranked for total cites, Impact Factor, 5-Year Impact Factor, *Article Influence® Score*, and *Eigenfactor®* Score (Thomson Reuters, 2015)

Global Reach:

2015 abstracts were featured in:

Associated Press
TIME Magazine
The New York Times
USA Today
NBC News
FOX News
BBC
MSNBC.com
Reuters Wire Service
U.S. News
World Report

Member Benefits:

More than $160,000 in council awards and travel grants available to professional members, early career investigators, trainees and students submitting abstracts to Scientific Sessions.

American Heart Association®
life is why™

SCIENTIFIC SESSIONS 2016

Abstract & Council Award Submissions:

Open | Wednesday, April 20, 2016
Close | Wednesday, June 8, 2016

Registration:

Open | Wednesday, June 15, 2016

Submit Your Science Now!

scientificsessions.org

Expect **big** In **2016** Things

©2016, American Heart Association



TRANSLATIONAL RESEARCH WITH LC-MS

Dedicated life science research experience. Proven clinical application know-how. Industry-leading LC-MS solutions. Give your discoveries a bridge to becoming practical, clinical applications. Learn how Waters can help deliver specificity, consistency and simultaneous multi-analyte measurement capabilities to advance your research on the path to enhancing human health. Visit waters.com/translation

Waters

THE SCIENCE OF WHAT'S POSSIBLE.®

PHARMACEUTICAL ▪ HEALTH SCIENCES ▪ FOOD ▪ ENVIRONMENTAL ▪ CHEMICAL MATERIALS

©2016 Waters Corporation. Waters and The Science of What's Possible are registered trademarks of Waters Corporation.

eppendorf & Science

PRIZE FOR NEURO BIOLOGY



2015 Winner
Shigeki Watanabe, Ph.D.
Johns Hopkins University
For research on synaptic vesicle endocytosis

Application Deadline
June 15, 2016

Call for Entries

Eppendorf & Science Prize for Neurobiology
The annual Eppendorf & Science Prize for Neurobiology is an international award which honors young scientists for their outstanding contributions to neurobiological research based on methods of molecular and cell biology. The winner and finalists are selected by a committee of independent scientists, chaired by Science's Senior Editor, Dr. Peter Stern. Researchers who are not older than 35 years are invited to apply.

You could be next to win this prize and to receive
> Prize money of US$25,000
> Publication of your work in Science
> Full support to attend the Prize Ceremony held in conjunction with the Annual Meeting of the Society for Neuroscience in the USA
> An invitation to visit Eppendorf in Hamburg, Germany

It's easy to apply!
Learn more about the Prize and its past winners at:

www.eppendorf.com/prize

eppendorf Science AAAS

AAAS® and Science® are registered trademarks of the American Association for the Advancement of Science, USA. Eppendorf® and the Eppendorf logo are registered trademarks of Eppendorf AG, Germany. U.S. Design Patents are listed on www.eppendorf.com/ip. All rights reserved, including graphics and images. Copyright © 2016 by Eppendorf AG. Kurstin Roe Photography.

Setting the stage for the great minds of diagnostics to advance medicine together

Next Generation Dx SUMMIT

EIGHTH ANNUAL

MOVING ASSAYS TO THE CLINIC

AUGUST 23-26, 2016 | GRAND HYATT, WASHINGTON, DC



CONFERENCE PROGRAMS

August 23-24

Enabling Point-of-Care Diagnostics
Circulating Tumor Cells
Companion Diagnostics: Strategy & Partnerships
Coverage and Reimbursement of Advanced Diagnostics
DNA Forensics
Clinical NGS Assays
Hospital Laboratory Design and Renovation

August 24-25

Molecular Diagnostics for Infectious Disease
Clinical Application of Cell-Free DNA
Diagnostics to Guide Cancer Immunotherapy
Commercialization of Molecular Diagnostics
Leveraging Pharmacies for Rapid Diagnostics
NGS Diagnostics: Data Considerations, Annotation and Interpretation

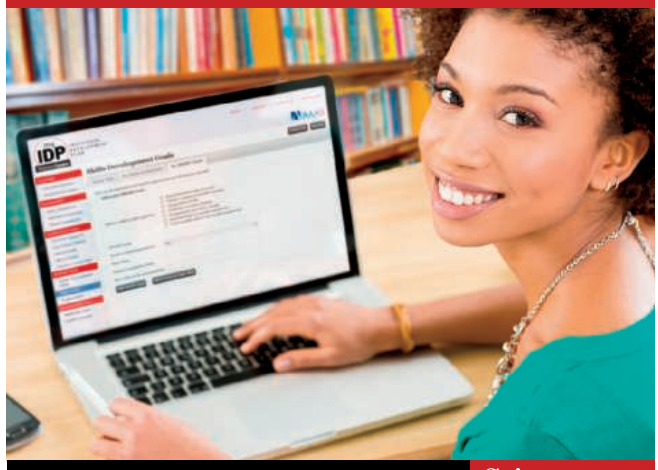
Register Early and Save up to $350!

Mention keycode L35

Organized by Cambridge HEALTHTECH Institute

NextGenerationDx.com

myIDP: A career plan customized for you, by you.



For your career in science, there's only one Science

my IDP ScienceCareers

Recommended by leading professional societies and the NIH

Features in myIDP include:

- Exercises to help you examine your skills, interests, and values.
- A list of 20 scientific career paths with a prediction of which ones best fit your skills and interests.
- A tool for setting strategic goals for the coming year, with optional reminders to keep you on track.
- Articles and resources to guide you through the process.
- Options to save materials online and print them for further review and discussion.
- Ability to select which portion of your IDP you wish to share with advisors, mentors, or others.
- A certificate of completion for users that finish myIDP.

Visit the website and start planning today!
myIDP.sciencecareers.org

ScienceCareers In partnership with:

advancing the life sciences 1912-2012 FASEB Federation of American Societies for Experimental Biology

Medical College of Wisconsin

UCSF University of California San Francisco

Burroughs Wellcome Fund

Be Among the First to Publish in *Science Robotics*



Image: jim/AdobeStock

NOW ACCEPTING MANUSCRIPTS

ScienceRobotics.org

Science Robotics is a unique journal created to help advance the research and development of robotics for all environments. *Science Robotics* will provide a much-needed central forum to share the latest technological discoveries and to discuss the field's critical issues.

Join in the excitement for the Fall 2016 debut!

Science Robotics

AAAS

Field-Flow Fractionation

The Postnova AF2000 MultiFlow is a high-performance, flow field-flow fractionation (FFF) platform for separation of proteins, macromolecules, and nanoparticles. Incorporating a range of FFF modules in a single integrated system to provide universal separation, the AF2000 MultiFlow offers more flexibility, better performance, and more robust results than any system previous to it. It uses a unique crossflow field design in which samples are separated by their dynamic diffusion on the basis of molar mass or particle size. Because of this design and the absence of any stationary phase, FFF on the AF2000 MultiFlow can be performed without exerting shear forces and stress on the molecules or particles being separated. The AF2000 can be run with different eluents and wide-ranging temperature conditions, and the same system can be used for running planar Asymmetric Flow FFF or circular Hollow Fiber Flow FFF separations. Consequently it is an ideal platform for the characterization of proteins, antibodies, aggregates, vaccines, virus-like particles (VLPs), liposomes, nanoparticles, and natural or synthetic polymers.

Postnova Analytics
For info: +44-(0)-1885-475007
www.postnova.com



Chemiluminescence Detection

The Omega Lum C is optimized for the superior detection of chemiluminescent Western blots, fluorescence imaging such as DNA gels, blue light, and visible light applications. It is compact, affordable, and comes with all you need for the complete imaging package, including a camera with over 8 megapixels of resolution, cooled to –50°C, and a high-quality f0.95 lens. Add to this a wide dynamic range and fast imaging speeds, and you will spend less time while capturing high-quality images. The system provides the high levels of sensitivity, broad dynamic range, and accuracy required to perform quantitative Western blotting. Preloaded protocols enable the user to quickly access the rapid automatic functions of the system through its SmartCapture technology. The system contains a dual-wavelength transilluminator and an integrated tablet PC. The Omega Lum C has one of the smallest footprints for this type of product on the market.

Gel Company/Aplegen
For info: +44-(0)-1223-515440
www.gelcompany.com

3D Structure-Based Design

Optibrium has launched version 6.3 of its StarDrop software platform, which includes a new module providing seamless access to best-in-class, structure-based design technologies, based on BioSolveIT's SeeSAR package. The addition of intuitive visualization of 3-dimensional (3D) protein-ligand interactions to StarDrop results in a fully integrated environment for analysis and visualization of compound data, coupled with a comprehensive range of ligand- and structure-based design capabilities that guide the optimization of high-quality compounds. The new SeeSAR module for StarDrop provides a state-of-the-art, scientifically rigorous approach to understanding the binding of compounds in their protein targets in 3D. Users can import ligand and protein structures derived from crystal structures or predicted with any docking software, and visualize the key interactions driving potency. This is seamlessly linked to StarDrop's chemoinformatics methods based on 2D-compound structure and its unique Card View approach to interpreting the resulting structure-activity relationships.

Optibrium
For info: +44-(0)-1223-815900
www.optibrium.com

Mass Spectrometer

Advion recently announced the introduction of a proteins and peptides analysis system, 'TIDES EXPRESS. The system combines a new, easy-to-use, high-performance liquid chromatography (HPLC) system with the extended mass range expression L compact mass spectrometer (CMS). The new platform improves the workflow for chemists performing peptide synthesis and needing fast mass analysis of each reaction step as well as final products. It is the perfect technique for monitoring reactions in solid-phase peptide synthesizers. Additional fragmentation analysis and charge deconvolution tools enhance its use for protein characterization. Solid-phase peptide synthesis (SPPS) allows for rapid, parallel synthesis of peptides of various lengths. Mass spectrometry provides both molecular mass and amino acid sequence information through specific and selective molecule fragmentation along the amino acid backbone. The 'TIDES EXPRESS includes an easy-to-use HPLC gradient system with a manual sample injector and expression L CMS, as well as fragmentation analysis and charge deconvolution software tools for easy and excellent data interpretation.

Advion
For info: 607-379-4565
www.advion.com

Streptavidin Microcolumns

The new MSIA Streptavidin EVO microcolumns have been designed to bring the novel mass spectrometric immunoassay (MSIA) affinity purification technology to Tecan's Freedom EVO series of robotic platforms that are equipped with a 96-multichannel arm (MCA96). When combined with the Tecan Freedom EVO robotic platform, MSIA Streptavidin EVO microcolumns enable fast, accurate isolation of target analytes from complex biological matrices. Housed within a pipette tip, the proprietary monolithic columns are densely coated with streptavidin for analytical affinity purification of any biotinylated affinity ligand, even at low concentration. Because this technology is incorporated into a pipette tip, users can analyze sample volumes as low as 10 µL, saving precious samples. Furthermore, when compared to traditional resin- and bead-based methods, MSIA technology provides lower background noise and improved analytical sensitivity, while the simple workflow enables easier method standardization and transfer between labs.

Thermo Fisher Scientific
For info: 800-556-2323
www.thermofisher.com

Electronically submit your new product description or product literature information! Go to www.sciencemag.org/about/new-products-section for more information.

Newly offered instrumentation, apparatus, and laboratory materials of interest to researchers in all disciplines in academic, industrial, and governmental organizations are featured in this space. Emphasis is given to purpose, chief characteristics, and availability of products and materials. Endorsement by *Science* or AAAS of any products or materials mentioned is not implied. Additional information may be obtained from the manufacturer or supplier.

Don't miss the debut of *Science Immunology*.

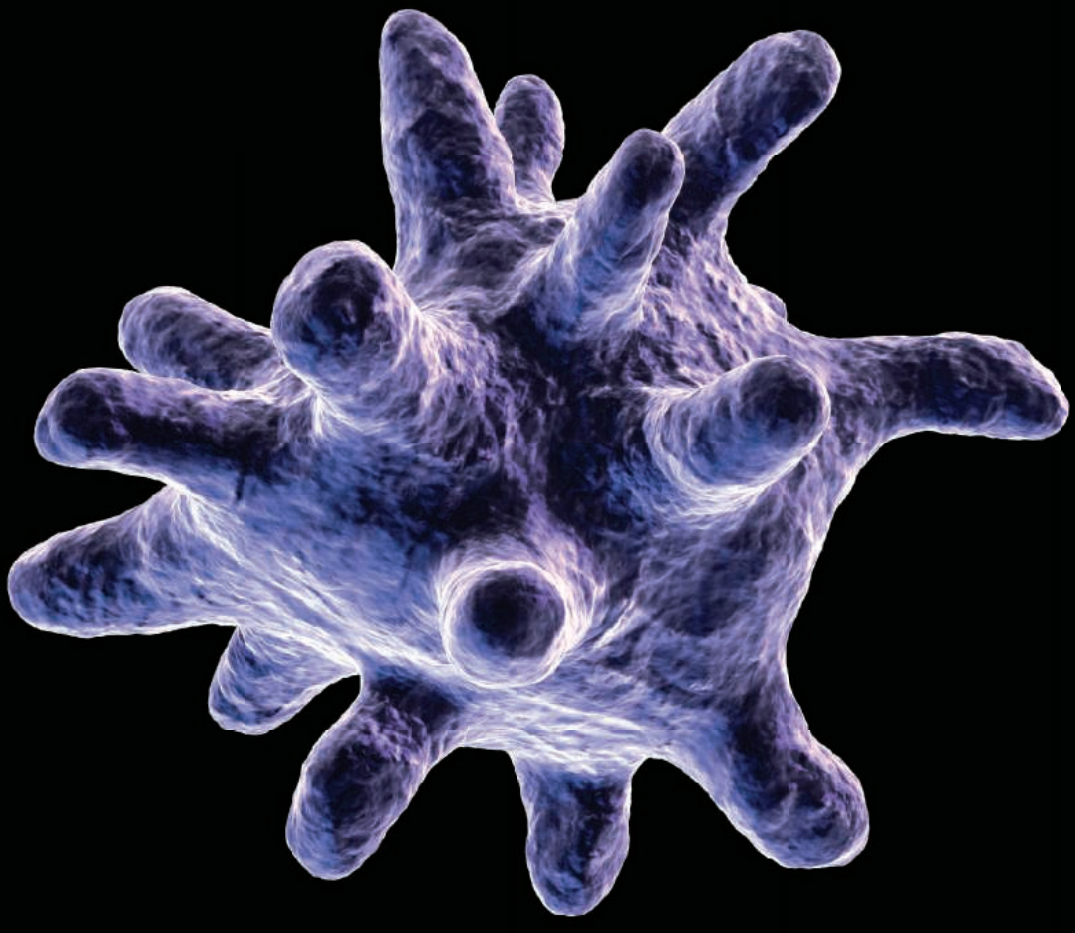


Image: Eraxion / iStockPhoto

NOW ACCEPTING PAPERS

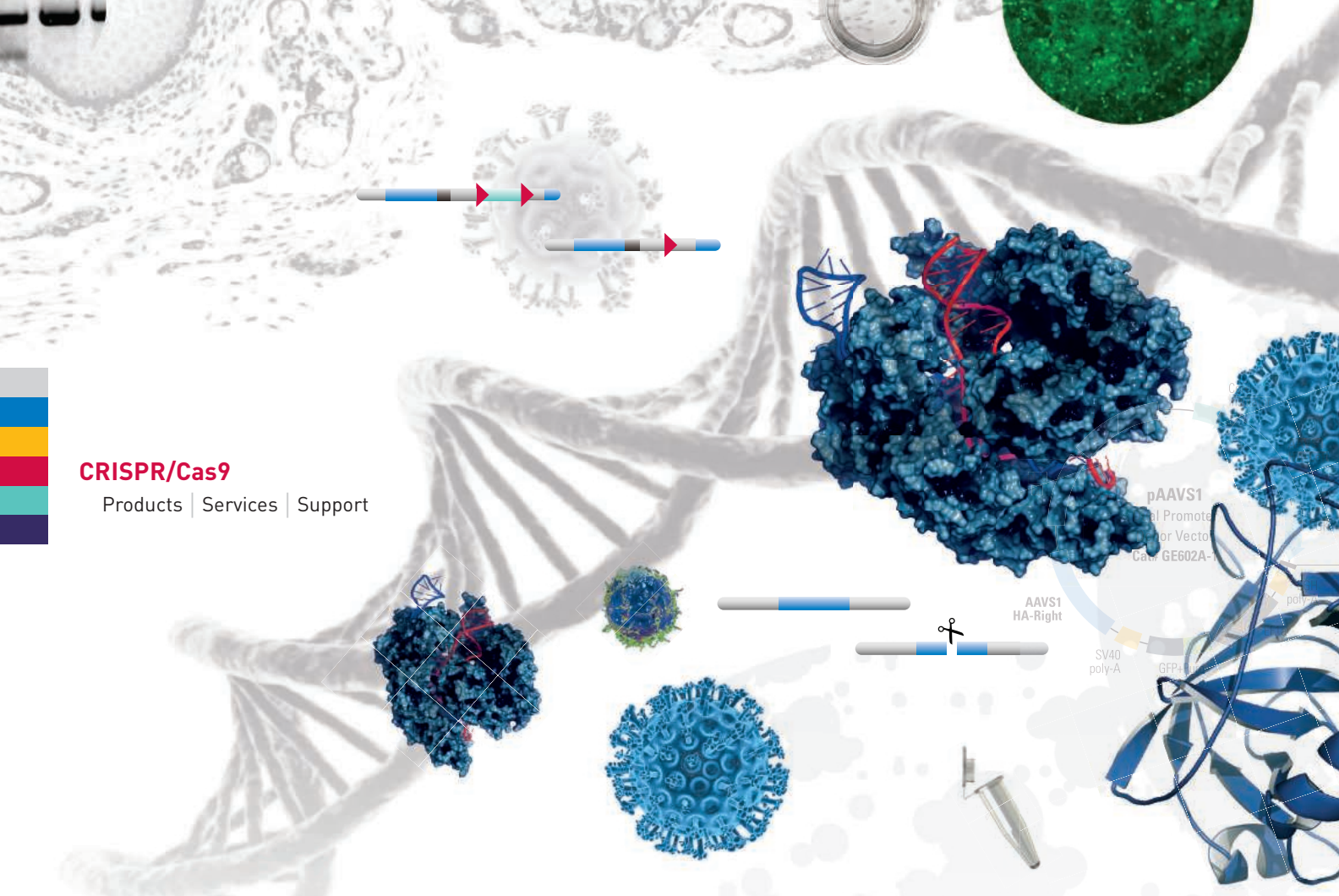
Science is expanding its reach into immunology—now offering the newest online-only, weekly journal in the *Science* family of publications. *Science Immunology* will provide original, peer-reviewed research articles that report critical advances in all areas of immunological research, including studies that provide insight into the human immune response in health and disease.

Be a part of the *Science Immunology* debut issue publishing Summer 2016!

Submit your manuscript today at **ScienceImmunology.org.**

Science Immunology

AAAS



CRISPR/Cas9

Products | Services | Support

GETTING STARTED WITH CRISPR/Cas9

CRISPR/Cas9 is revolutionizing biology, giving scientists unparalleled power and precision for genome engineering. But like many other life science tools, there's a learning curve. To help you bring this innovative technology into your lab, SBI has put together a series of tutorials on how to use CRISPR/Cas9.

Start using CRISPR/Cas9 today, watch the tutorials at: *systembio.com/crispr-cas9-tutorials*

Or, to speed up your research, take advantage of SBI's expertise and have our team of scientists design and build custom constructs and/or engineered cell lines. Contact us to learn more at *services@systembio.com*

SBI System Biosciences
Harnessing innovation to drive discoveries



Science Careers Advertising

For full advertising details, go to ScienceCareers.org and click For Employers, or call one of our representatives.

Tracy Holmes
Worldwide Associate Director
Science Careers
Phone: +44 (0) 1223 326525

THE AMERICAS

E-mail: advertise@sciencecareers.org
Fax: +1 (202) 289 6742

Tina Burks
Phone: +1 (202) 326 6577

Nancy Toema
Phone: +1 (202) 326 6578

Online Job Posting Questions
Phone: +1 (202) 312 6375

EUROPE / INDIA / AUSTRALIA / NEW ZEALAND / REST OF WORLD

E-mail: ads@science-int.co.uk
Fax: +44 (0) 1223 326532

Sarah Lelarge
Phone: +44 (0) 1223 326527

Kelly Grace
Phone: +44 (0) 1223 326528

Online Job Posting Questions
Phone: +44 (0) 1223 326528

JAPAN

Katsuyoshi Fukamizu (Tokyo)
E-mail: kfukamizu@aaas.org
Phone: +81 3 3219 5777

Hiroyuki Mashiki (Kyoto)
E-mail: hmashiki@aaas.org
Phone: +81 75 823 1109

CHINA / KOREA / SINGAPORE / TAIWAN / THAILAND

Ruolei Wu
E-mail: rwu@aaas.org
Phone: +86 186 0082 9345

Danny Zhao
E-mail: dzhao@aaas.org
Phone: +86 131 4114 0012

All ads submitted for publication must comply with applicable U.S. and non-U.S. laws. *Science* reserves the right to refuse any advertisement at its sole discretion for any reason, including without limitation for offensive language or inappropriate content, and all advertising is subject to publisher approval. *Science* encourages our readers to alert us to any ads that they feel may be discriminatory or offensive.

ScienceCareers
FROM THE JOURNAL SCIENCE AAAS

ScienceCareers.org

University of Zurich[UZH]

Faculty of Science

The Faculty of Science (www.mnf.uzh.ch) of the University of Zurich and the Department of Information Technology and Electrical Engineering (www.ee.ethz.ch) at ETH Zurich invite applications for a

Full Professor of Neurocomputation

to join the multidisciplinary Institute of Neuroinformatics (INI) and complement and extend its vigorous research activities.

We seek innovative candidates with a strong record in research and teaching who will strengthen our interests in experimental and theoretical approaches to neural computation, brain architectures and behavior.

Neurosciences are driven by modern experimental tools such as high-throughput electron microscopy, optogenetics, in-vivo imaging, electrode arrays, CRISPR, etc. However, to advance our understanding of brain functions, neuroscience also needs theory that is either validated or rejected by experiments. The INI is looking for outstanding candidates who can bridge the gap between theories of neural circuits and modern experimental approaches. By strengthening the role of technology and theory in neuroscience, INI wants to contribute to the discovery of important principles about brain function and subject these principles to stringent tests. The successful candidate will present a scientific vision on neural information processing and computation that closes the loop with experimental research of neuronal circuits and behavior.

The University of Zurich and the ETH Zurich provide generous research support, including dedicated funds for personnel and running expenses, and competitive start-up packages. The University of Zurich, the ETH Zurich, and the city of Zurich also offer a stimulating cultural environment and are family-friendly.

Application packages should include a motivation letter, a full curriculum vitae, a vision statement of research and teaching interests outlining major unsolved problems and how they could be tackled and the names and addresses of three potential referees. Documents should be addressed to Prof. Dr. Bernhard Schmid, Dean of the Faculty of Science, University of Zurich, and uploaded as a single PDF file to http://www.mnf.uzh.ch/PBD by 15 June 2016. A brief questionnaire will have to be filled out at the beginning of the upload process. For further information, please contact Prof. Dr. Michael Schaepman at Michael.Schaepman@geo.uzh.ch or Prof. Dr. Richard Hahnloser at rich@ini.ethz.ch.

The University of Zurich and the ETH Zurich are equal opportunities employers.

ScienceCareers online @sciencecareers.org

St. Jude Children's Research Hospital
ALSAC • Danny Thomas, Founder

FACULTY POSITIONS
Department of Computational Biology

Recognized as a world leader of genomic research in pediatric cancer, the Computational Biology department at St. Jude Children's Research Hospital is currently seeking exceptional and creative scientists for multiple FACULTY positions. We are seeking investigators to lead multidisciplinary research programs of systems biology, cellular image analysis and genetics/epigenetics by integrating dry-lab computational methods development with wet-lab experiments. Early career investigators interested in contributing to a culture of excellence at St. Jude are particularly encouraged to apply. This search is also open for mid-career or senior investigators with a strong record of independent research.

As part of a significant expansion from a research program to an academic department, the newly established Computational Biology department occupies 28,700-square-feet of laboratory and office space. Computational Biology investigators have access to dedicated departmental shared resources established for BIG data analysis and functional validation. They include priority access to a high-performance computing facility, a core wet lab available to support dry lab faculty, an engineering team for high throughput data analysis and a genomics laboratory for developing new sequencing technologies and assays. The research environment at St. Jude is highly interactive with collaborative opportunities across all basic research and clinical departments, as well as access to institutional shared resources managed by PhD-level scientists.

We offer very competitive packages, including generous startup funds, computing resources, equipment, laboratory space, personnel support and potential institutional support beyond the start-up phase. A faculty position at the Assistant, Associate or Full Member level may be considered. Successful applicants must hold a PhD degree, have at least three years of relevant postgraduate experience or a demonstrated track record of developing novel, high-impact computational methods. Interested applicants should send via email a curriculum vitae, a 2-3 page summary of research interests, and the names of three references to: **ComputationalBiologyRecruitment@stjude.org**.

EOE/Minorities/Females/Vet/Disability/Sexual Orientation/Gender Identity

St. Jude Children's Research Hospital
ALSAC • Danny Thomas, Founder

POSTDOCTORAL RESEARCH ASSOCIATE POSITIONS
Department of Computational Biology

Recognized as a world leader of genomic research in pediatric cancer, the Computational Biology department at St. Jude Children's Research Hospital is currently seeking exceptional and creative scientists for multiple **POSTDOCTORAL RESEARCH ASSOCIATE** positions in the lab of Dr. Jinghui Zhang to develop and apply innovative analytical and visualization approaches for studying the genome and epigenome of pediatric cancer. The fellows will have access to a wealth of resources including high-quality data, a state-of-art high-performance computing facility, robust analytical pipelines, the latest laboratory technology and research expertise in genomics, cancer biology, mathematics and computer science. The fellows will lead or participate in all aspects of cancer omics studies via multi-disciplinary teamwork and have opportunities to interact with leaders of pediatric cancer and translational research within and outside the institution. For those with ambitious career goals including those with no prior computing experience, inter-disciplinary training will be provided to broaden or strengthen computational or biological expertise.

Job # 34109 is immediately available to join our scientific visualization team to design and implement novel features and to expand the data content for our pediatric cancer genomic data portal initiative (https://pecan.stjude.org/proteinpaint/). Review the full description and apply at http://tinyurl.com/Postdoc34109

Job # 35345 is immediately available to further ongoing research in developing clonal evolution models of pediatric cancer based on the analysis of next-generation sequencing data. Review the full description and apply at http://tinyurl.com/Postdoc35345

Job # 35262 is immediately available to work as part of the NIH-funded Precision Medicine Center established in collaboration with the departments of Pharmaceutical Sciences and Pathology. The fellow will interact with the genomic discovery and visualization team to receive training and contribute new insight in these two areas. Review the full description and apply at http://tinyurl.com/Postdoc35262

Contact Information
Jinghui Zhang, PhD
Chair, Department of Computational Biology
St. Jude Children's Research Hospital
E-mail: ComputationalBiologyRecruitment@stjude.org
https://www.stjude.org/zhang

EOE/Minorities/Females/Vet/Disability/Sexual Orientation/Gender Identity

UNIVERSITY OF SOUTH CAROLINA

Director, Viral Vector Core

Individual sought to oversee the day-to-day operations of the Viral Vector Core (VVC) (http://ppn.med.sc.edu/vector.core.asp) at the University of South Carolina (USC) School of Medicine. The appointment will be made at the level of a Research Assistant or Research Associate Professor in the Department of Pharmacology, Physiology and Neuroscience, depending on experience. Responsibilities include interaction with investigators, overseeing and participating in the various services provided by the Viral Vector Core, and assisting in the design, production, and characterization of genetically modified viral vectors and vector libraries designed to alter gene expression *in vitro* and *in vivo*. The candidate will join a collegial and collaborative environment with a major USC-wide focus in neurobiology, as well as cancer and cardiovascular research, and this viral core provides a resource for investigators across the University. A PhD and at least three years of experience in using viral vectors and genetic modification of mammalian cells, particularly in vivo, is required. Experience in conducting gene expression profiling and measurements also desirable, and individual will interact closely with a COBRE-funded Functional Genomics Core in Targeted Therapeutics (www.sccp.sc.edu/functional_genomics_core).

To apply please submit a single electronic file (PDF or Word) that includes a cover letter summarizing qualifications, curriculum vitae and publication list, a statement of experience and professional goals, and contact information for four references. The file should be attached to an e-mail message sent to **Dr. Marlene Wilson** at **director.search@uscmed.sc.edu** with Core Director Search as the subject. Review of applications will begin **June 1, 2016** and continue until the position is filled.

The University of South Carolina is an AA/EOE.

Research Assistant Professor of Systems Pharmacology and Translational Therapeutics

Perelman School of Medicine
University of Pennsylvania

The Department of Pharmacology at the **Perelman School of Medicine** at the **University of Pennsylvania** seeks candidates for an Assistant Professor position in the non-tenure research track. The successful applicant will have experience in the field of mass spectrometry and bioanalytical chemistry. Responsibilities include playing a key role in running the Translational Biomarker Core of the Center of Excellence in Environmental Toxicology. This will involve the maintenance of instrumentation, the conduct of research, and the participation in both routine and collaborative studies with other Center Investigators. Applicants must have a Ph.D. degree and have demonstrated excellent qualifications in research.

A demonstrated record of excellence in studies that leverage interdisciplinary approaches to the study of environmental science is required. Candidates with a record of innovative and collaborative research in mass spectrometry and bioanalytical chemistry are encouraged to apply. Applicants must have a Ph.D. together with postdoctoral experience and a strong publication record.

We seek candidates who embrace and reflect diversity in the broadest sense.

The University of Pennsylvania is an EOE. Minorities/Women/Individuals with disabilities/ Protected Veterans are encouraged to apply.

Apply online at:
http://www.med.upenn.edu/apps/faculty_ad/index.php/g/d4292



MEDICAL BREAKTHROUGHS MAY COME OUT OF THE LAB.

BUT THEY BEGIN IN THE HEART.

For more than a century, a very special passion has driven the people of Merck*. Our goal is to discover and develop medicines, vaccines and animal health innovations that will improve the lives of millions. Still, we know there is much more to be done. And we're doing it, with a long-standing commitment to research and development.

We're cultivating a culture of scientific inquiry, invention and collaboration. Our integrated R&D sites contribute to major biopharmaceutical ecosystems, including the San Francisco Bay area, Calif.; Boston/Cambridge, Mass.; New Jersey and Pennsylvania. Colleagues at our multi-disciplinary sites are working to advance many of Merck's key therapeutic areas of focus, including immunology, oncology, infectious disease, diabetes, neurosciences and vaccines.

We're just as committed to expanding access to healthcare and working with others who share our passion to create a healthier world. Together, we'll meet that challenge. With all our heart.

We're building a healthier world.
JOIN US.

Learn more about our mission and our opportunities at:
www.merck.com/careers
Merck is an equal opportunity employer.
Minority/Female/Disability/Veteran –
proudly embracing diversity in all of its manifestations.

MERCK
Be well

125 YEARS SINCE 1891

*Merck & Co., Inc., Kenilworth, NJ, USA, is known as MSD outside the United States and Canada.

Copyright © 2016 Merck Sharp & Dohme Corp., a subsidiary of **Merck & Co., Inc.** All rights reserved. CORP-1064987-0038 05/16

Jefferson Science Fellowship

USAID
FROM THE AMERICAN PEOPLE

The National Academies of Science, Engineering, and Medicine is pleased to announce a call for nominations and applications for the 2017 Jefferson Science Fellowship (JSF) program. Initiated by the Secretary of State in 2003, this fellowship program engages the American academic science, technology, engineering and medical communities in the design and implementation of U.S. foreign policy and international development objectives.

Fellows spend one year at the U.S. Department of State or the U.S. Agency for International Development (USAID) for an on-site assignment in Washington, D.C. As part of their assignments, Fellows may also have the opportunity to travel to U.S. embassies and missions overseas.

The fellowship is open to tenured, or similarly ranked, academic scientists, engineers, and physicians from U.S. institutions of higher learning. Nominees/applicants must hold U.S. citizenship and will be required to obtain a security clearance.

The deadline for 2017-2018 program year applications/nominations is **October 31, 2016.** To learn more about the Jefferson Science Fellowship and to apply, visit the website at:

www.national-academies.org/jsf

The National Academies of
SCIENCES • ENGINEERING • MEDICINE



Conduct your job search the easy way.

- Search thousands of job postings
- Create job alerts based on your criteria
- Get career advice from our Career Forum experts
- Download career advice articles and webinars
- Complete an individual development plan at "myIDP"

Target your job search using relevant resources on **ScienceCareers.org**.

ScienceCareers
FROM THE JOURNAL SCIENCE AAAS



Career Feature:
China

Issue date: June 24
Reserve space by June 7
Ads accepted until June 17 if space allows

There's only one *Science*.

Deliver your message to a global audience of targeted, qualified scientists.

129,574 subscribers in print every week

352,966 monthly unique browsers on ScienceCareers.org

Why choose this feature for your advertisement?

- Relevant ads lead off the career section with a special China banner
- Bonus distributions:

  10th FENS Forum of Neuroscience, July 2–6, Copenhagen, Denmark

  Single Molecule Approaches to Biology, July 3–8, Hong Kong, China.

Produced by the *Science*/AAAS Custom Publishing Office.



ScienceCareers
FROM THE JOURNAL SCIENCE AAAS

SCIENCECAREERS.ORG

To book your ad: **advertise@sciencecareers.org**

The Americas
202 326 6582

Europe/RoW
+44 (0) 1223 326500

Japan
+81 3 3219 5777

China/Korea/Singapore/Taiwan
+86 186 0082 9345

AAAS

American Association for the Advancement of Science

Science & Technology Policy Fellowships

Enhancing Policy, Transforming Careers



Where science and policy change the world. And you.

Apply your scientific knowledge and technical skills to important societal challenges. Fellows serve in the executive, legislative, and judicial branches of the federal government.



"An experience of a lifetime, for a lifetime, regardless of where your path may take you."

Horacio Murillo, M.D., Ph.D.,
Molecular Pharmacology

AAAS Congressional Fellow, Senate Committee on Health, Education, Labor and Pensions
Current: Radiologist, Sutter Health, and Adjunct Clinical Associate Professor, Stanford Medical School

Application deadline: November 1.

To learn more and apply visit **go.stpf-aaas.org/science1.html**

10 ways that *Science* Careers can help advance your career

1. Register for a free online account on **ScienceCareers.org**.
2. Search thousands of job postings and find your perfect job.
3. Sign up to receive e-mail alerts about job postings that match your criteria.
4. Upload your resume into our database and connect with employers.
5. Watch one of our many webinars on different career topics such as job searching, networking, and more.
6. Download our career booklets, including Career Basics, Careers Beyond the Bench, and Developing Your Skills.
7. Complete an interactive, personalized career plan at "my IDP."
8. Visit our Career Forum and get advice from career experts and your peers.
9. Research graduate program information and find a program right for you.
10. Read relevant career advice articles from our library of thousands.



Visit **ScienceCareers.org** today — all resources are free

ScienceCareers

FROM THE JOURNAL SCIENCE AAAS

SCIENCECAREERS.ORG

AMES LABORATORY
Creating Materials & Energy Solutions
U.S. DEPARTMENT OF ENERGY

Ames Laboratory, a multi-disciplinary National Laboratory for scientific research operated for the Department of Energy through a contractual agreement by Iowa State University, is seeking nominations and applications for the position of Chief Research Officer.

The **Chief Research Officer (CRO)** is responsible for initiating, developing, and supervising the scientific divisions, institutes, and programs for Ames Laboratory. In this capacity, the CRO will formulate and evaluate new initiatives that fall within our mission – to create materials, inspire minds to solve problems, and address global challenges – often emphasizing the cross-disciplinary collaborations with other DOE national laboratories, academia, and industry that have become the hallmark of the Laboratory. In conjunction with the director, deputy director, and scientific and operational leadership, the CRO will ensure that scientific programs are appropriately prioritized, budgeted, and scheduled within the overall Laboratory Strategic Plan. As member of the Executive Council, the CRO will oversee all research at Ames Laboratory and provide leadership for physics, chemistry, biology, and materials research.

For requirements and a more inclusive description, see www.iastatejobs.com, Vacancy **#60179P.** Applications must be submitted through this website. Nominations and inquiries should be sent to CROSearch@ameslab.gov. Position description available at: **https://www.ameslab.gov/sites/default/files/CRO-Position-Description.pdf**. To guarantee consideration, applications must be submitted by **July 1, 2016**.

The Ames Laboratory respects, appreciates, and encourages diversity. We especially seek candidates who are interested in contributing to the diversity of our research environment. Ames Laboratory/Iowa State University is an Affirmative Action/Equal Opportunity Employer. Iowa State University does not discriminate on the basis of race, color, age, ethnicity, religion, national origin, pregnancy, sexual orientation, gender identity, genetic information, sex, marital status, disability, or status as a U.S. veteran. Inquiries regarding non-discrimination policies may be directed to Office of Equal Opportunity, 3350 Beardshear Hall, 515 Morrill Road, Ames, Iowa 50011, Tel. 515 294-7612, email eooffice@iastate.edu.

IOWA STATE UNIVERSITY OF SCIENCE AND TECHNOLOGY *Ames Laboratory is operated by Iowa State University for the U.S. Department of Energy. Ames, Iowa 50011-3020*

Smithsonian Tropical Research Institute

Three Post-Doctoral Fellowships for Tropical Microbial Ecologists

The Smithsonian Tropical Research Institute (STRI), with generous support from the Simons Foundation, is pleased to announce a new research initiative to understand the roles played by microbiomes in tropical forests. This initiative is intended to expand dramatically our understanding of the identity, distribution, and function of tropical terrestrial microbiomes. As part of this initiative, we are accepting applications for three postdoctoral fellowships. The fellowships are for three years, and each includes a stipend, travel and research funds, and relocation expenses to Panamá.

Candidates should propose their own research projects related to this initiative. The proposed research should incorporate genomic and meta-genomic approaches and complement one or more existing strengths at STRI, including forest ecology, evolutionary biology of mutualisms, soil biology and biochemistry, behavioral ecology and evolution, and plant physiology [see www.stri.si.edu]. The positions will be based at STRI, and proposed research should be based primarily at facilities in Panamá, although comparative studies involving other sites may be included if strongly justified.

Applications should consist of a single PDF containing a cover letter, a research proposal, a complete curriculum vitae, and the names and contact information of three referees. The research proposal should not exceed five single-spaced pages plus references and include a research budget. Please also include up to three significant reprints as separate files. Applications should be addressed to **Adriana Bilgray**, Office of Academic Programs (**BilgrayA@si.edu**). For inquiries contact **Dr. William Wcislo**, Deputy Director for Research (**WcisloW@si.edu**). Review of applications will begin **15 August 2016** and continue until positions are filled.

STRI is an Equal Opportunity Employer and is committed to diversity in its workforce. Appointments are made regardless of nationality.

EMBL Australia | MONASH University | ARMI AUSTRALIAN REGENERATIVE MEDICINE INSTITUTE | CSIRO

EMBL Australia Group Leaders

Accelerate your research career – fully funded research positions for 5 years

- Form and lead your own independent research group
- Modelled on the European Molecular Biology Laboratory (EMBL) to support independent, interdisciplinary, quality research
- Designed for high potential, early-career scientists who are dedicated to research excellence
- Excellent salary package, including (where required) arrangements for relocation, travel, work permits and visas for the successful candidate and their family
- Position includes funding for a research team and generous annual research budget
- Based at new world-class life and medical research facilities at the Australian Regenerative Medicine Institute at Monash University
- Unique opportunity to join an innovative, growing organisation.

EMBL Australia enables research groups to have access to the complementary facilities and expertise at EMBL and a growing network of groups at other national participating institutions in a dynamic, collaborative, internationally focused network. We encourage scientists interested in rapidly accelerating their research career in a highly supportive environment to apply. During the course of their tenure, applicants will be encouraged to apply for prestigious fellowships and grants to expand their research program.

Group Leaders in Tissue Engineering and Organoid Biology with joint appointments to the Australian Regenerative Medicine Institute (ARMI) at Monash University and CSIRO (up to 2 positions)

ARMI is the national headquarters of EMBL Australia, hosts the Systems Biology Institute - Australia and and is the Monash University headquarters of Stem Cells Australia.

The Commonwealth Scientific and Industrial Research Organisation (CSIRO) is Australia's paramount publicly funded industrial research organization.

We seek applicants with research interests in broad aspects of tissue engineering which could include but are not limited to organoid and organ on a chip technology, decellularized tissue scaffolds, bioactive biomaterials and biointerfaces that simulate the cellular microenvironment at the micro and nanoscale, functional biomaterials and advance manufacturing (3D scaffolds), and synthetic and biological matrices for tissue engineering and transplant development.

ARMI currently has 16 research groups, and a total of 230 researchers, students and support staff from 21 different countries. Its location on the Monash University campus offers a highly stimulating biomedical research environment allowing Institute researchers to work closely with other university research organisations including the Monash Institute for Medical Engineering (MIME) and Biomedical Discovery Institute (BDI) and CSIRO, one of Australia's leading multi disciplinary research organisations. The vision promoted at ARMI is to exploit and connect the multi disciplinarity of its groups, aligning their complementary capacities around key research pipelines; Heart and muscle development and regeneration, Immunity and Regeneration, Stem cells and Regeneration and Neural regeneration.

CSIRO currently delivers impact through 9 Business Units including Manufacturing which is co-located with Monash University. The Manufacturing Business Unit which has approximately 750 researchers, students and affiliates includes our Biomedical Manufacturing Programme which houses over 150 multi-disciplinary researchers and students at sites in Melbourne and Sydney. Using our leading science and technical expertise, we are working on next generation therapies to treat diseases, new ways to deliver drugs, advanced medical materials and devices and drug discovery. CSIRO collaborates with all of Australia's leading universities, including Monash and a range of companies, both national and international and has a track record of translating research to the marketplace.

Both CSIRO and ARMI aim for a representative gender balance at all levels of staff. Therefore we strongly encourage women to apply.

More details are available at **www.armi.org.au**

EMBL Australia

The EMBL Australia Partner Laboratory is based on the EMBL model, with distributed, highly integrated research nodes focusing on complementary aspects of biological research. Currently there are three nodes: at Monash University with a total of four research groups, at the University of New South Wales, with two groups and in South Australia, at SAHMRI, with three groups. EMBL Australia also oversees the EMBL Australia Bioinformatics Resource, based at Melbourne University and SBI Australia, based at Monash University. More details at www.emblaustralia.org

To apply for a position

Please email (in English) a cover letter clearly outlining a summary of current and future research interests, a CV and 3 written references, to: **sandra.fernandes@emblaustralia.org** Incomplete applications cannot be considered.

Applications close: 29th July 2016

Interviews will be held in Australia and are likely to be in November 2016

The anticipated commencement date is mid/late 2017.

Science Careers online @sciencecareers.org

Science Careers online @sciencecareers.org

Advance your career with expert advice from *Science* Careers.



Download Free Career Advice Booklets!
ScienceCareers.org/booklets

Featured Topics:

- Networking
- Industry or Academia
- Job Searching
- Non-Bench Careers
- And More



Science Careers
FROM THE JOURNAL SCIENCE AAAS

Expression of Interest

Professor of Cardiovascular Research
Australian Regenerative Medicine Institute
Monash University

Expressions of interest are invited from established researchers to build a research program focused on Cardiovascular Science at the Australian Regenerative Medicine Institute at Monash University (**http://www.armi.org.au/**). Applications in all areas of Cardiac and Vascular Biology and disease are welcome, but we are particularly interested in those researchers focused on regeneration and stem cell biology or tissue engineering as applied to cardiovascular diseases.

Candidates for this Associate Professorial or Professorial level position must have a PhD and/or MD, evidence of sustained competitive funding, and an outstanding publication record of quality peer reviewed science. Successful candidates will be expected to maintain a vigorous research program that addresses fundamental questions in the broad field of cardiovascular biology. Candidates with a focus on clinical research and with research expertise that complements those of current investigators at the Institute are of special interest. Clinician scientists are particularly encouraged to apply and an option for a clinical appointment may be available within Monash Heart to appropriate candidates.

The Australian Regenerative Medicine Institute currently has 14 research groups, and a total of 230 researchers, students and support staff from 21 different countries. Its location on the Monash University campus offers a highly stimulating biomedical research environment allowing Institute researchers to work closely with other university research organisations including the Monash Institute for Medical Engineering (MIME) and Biomedical Discovery Institute (BDI) and CSIRO, one of Australia's leading multi-disciplinary research institutions. The vision promoted at ARMI is to exploit and connect the multi disciplinarity of its groups, aligning their complementary capacities around key research pipelines; Heart and muscle development and regeneration, Immunity and Regeneration, Stem cells and Regeneration and Neural regeneration.

Of particular importance for this position is the establishment of the Victorian Heart Hospital (VHH) on the Monash University Campus. The VHH will enable world class research and education in addition to specialised clinical care with key features including an expanded medical and cardiovascular health research program that builds upon the current activities of both Monash University and the Monash Cardiovascular Research Centre.

The successful applicant will have access to the state-of-the-art clinical and basic science research facilities planned for this hospital and have significant opportunity to shape the research environment of the hospital precinct as it emerges.

An increasing focus on translational research is an integral part of the Institute's research mission, and individuals that have a demonstrable ability to integrate clinical and basic science elements into a successful translational research program will be highly sought after. The successful candidate will be expected to strengthen the Institute and Monash's profile and research networks both from an internal and external perspective, engaging with the wider cardiovascular research community, locally, nationally and internationally.

The successful applicant will have access to state-of-the-art technological core facilities within the university, which include but are not restricted to flow cytometry, advanced molecular preclinical and clinical imaging facilities, light-based micro-imaging and state-of-the-art animal facilities.

Further details are available from:
Prof. Peter Currie, Director, peter.currie@monash.edu

To Apply: Applicants should submit an expression of interest including a cover letter, curriculum vitae, a list of publications (indicating ten most significant publications), a statement of previous research achievements, a research plan (maximum 8 pages/font 12) and a list of at least three reference persons, all in a .pdf binder. Your complete submission, referenced "ARMI Research Group Leader in Cardiovascular Research" should be sent to **sandra.fernandes@monash.edu** by **29th July 2016**.

We look forward to receiving your application!

POSITIONS OPEN

POSTDOCTORAL FELLOW POSITION

Rush University Medical Center, Chicago IL USA. Leading kidney investigative group moving to Rush in July 2016 seeks Ph.D. postdoctoral fellows to study molecular mechanisms of kidney/glomerular disease (Clement LC *Nature Medicine* **2011 17:**117-122; Chugh SS *Nature Medicine* **2012 18:**26-27; Clement LC *Nature Medicine* **2014 20:**37-46). No postdoctoral training after Ph.D. or experience in kidney disease research required. Commitment to science and academia are necessary. Email curriculum vitae to **sumant_s_chugh@rush.edu**

Post your jobs
Fast and Easy



ScienceCareers
employers.sciencecareers.org

DIRECTOR FOR THE THOMAS JEFFERSON NATIONAL ACCELERATOR FACILITY (JEFFERSON LAB)

Jefferson Science Associates, LLC (JSA) invites nominations and applications for the position of Lab Director for the Department of Energy's Thomas Jefferson National Accelerator Facility (Jefferson Lab) in Newport News, Virginia. The JSA Board seeks a strong and visionary scientific leader with effective management skills and who enjoys stature among peers in the scientific and lab communities.

The successful candidate will be responsible for leading and managing all Lab initiatives and activities in support of a world-class research facility, including its strategic and long-range planning and its building of a comprehensive external relations program to serve and promote the interests of the lab and its users. Reporting to the JSA Board, the Director is the Chief Executive Officer of Jefferson Lab and is responsible for the Lab's 700-plus staff and total annual budget of approximately $100 million.

Jefferson Lab (www.jlab.org) is a national laboratory for nuclear physics research. As a user facility for scientists worldwide, its primary mission is to conduct basic research to advance the understanding of the fundamental constituents of the atomic nucleus and their interactions. The tools for probing the structure of the nucleus are the Lab's Continuous Electron Beam Accelerator Facility (CEBAF) and the advanced particle-detection and ultra-high-speed data-acquisition equipment in four experimental halls. The lab is now completing a major, $338 million upgrade of the electron accelerator from 6 GeV to 12 GeV with addition of the fourth experimental hall to specifically investigate exotic structures. The international user community includes over 1,500 scientists over half of whom are actively involved in the Lab's experimental program.

JSA (www.jsallc.org) is a joint venture comprised of the Southeastern Universities Research Association (SURA) and Pacific Architects and Engineers (PAE). JSA was created specifically to manage and operate Jefferson Lab for the Nuclear Physics User Community, so its members can continue to conduct innovative research. SURA is the university consortium that propelled Jefferson Lab into the forefront of nuclear and hadronic physics as well as in superconducting radiofrequency technologies. PAE is a global leader in providing enduring support for the essential missions of the U.S. government, its allied partners and international organizations.

Nominations, applications, and inquiries should be directed to: **Donald Geesaman, Chair; Director Search Committee; c/o SURA; 1201 New York Avenue, NW; Suite 430; Washington, DC 20005** or to **directorsearch@sura.org**. For timely consideration, submit an outline of qualifications and accomplishments and a curriculum vitae by **15 August 2016**. Candidate must be willing and able to obtain a federal security clearance. Hugh Montgomery will continue to lead the lab until a suitable candidate is identified.

JSA is an Equal Opportunity, Affirmative Action Employer.

By **Michael J. Orsini**

Three strikes and research is out

After 14 years in pharmaceutical discovery research, the first day of my new career in project management was disorienting. I was still at the company where I had been working as a researcher, but now my office was on the opposite side of the building. It had taken me a long time, and a lot of fits and starts, to get here. Between graduate school and two postdocs, I had spent nearly 12 years preparing for a career in pharmaceutical research, and I was reluctant to leave it. But after giving research three chances, I decided that it was time to explore a different path. Now, two-and-a-half years later, I don't regret my decision to leave the lab, and I am enjoying this second act of my career.

Early in my career, I thought my first position at a large pharmaceutical company, where I was surrounded by colleagues who had been there for 20 or 30 years, might be my one and only stop. It was a good entry-level job that allowed me to learn the basics of discovery research in big pharma, but after about 7 years, the company closed my site. Strike one.

I reasoned that these things happen, and it didn't take me too long to find a new job at a nearby biotech company. I was quickly promoted to a position that gave me a seat at the leadership table. I helped shape key decisions, and I was happy—until 18 months after starting, when I was laid off following a U.S. Food and Drug Administration decision that severely compromised the company's value and ability to raise capital. Strike two.



"After giving research three chances, I decided ... to explore a different path."

I felt defeated and taken aback by the capriciousness of corporate science. I saw that a corporate bench research position was no recipe for security. I reasoned that a career transcending specialization in one therapeutic area would be more stable and potentially allow me to cast a wider net. So, for my next job search, I considered nonbench careers for the first time.

I had colleagues who had left research careers for related fields, such as clinical trials management or patent law, that required either extensive further education or a drastic pay cut to land an entry-level position. I didn't want to take that route. Instead, I began looking for jobs that leveraged my research experience and leadership abilities and required skills I could learn on the job. My first nonbench job offer, for a medical writing position, felt a little *too* far from the bench, and I declined it. I interviewed for a sales and support position with a startup company but quickly realized that it was not for me. I even applied for an intriguing position with an investment firm hiring Ph.D.s to research financial opportunities—a job that I never imagined was possible for a Ph.D. scientist.

But I ended up declining an interview for that job (though I now wish I had learned more) because I had just accepted a principal scientist position at another big pharmaceutical company. I couldn't resist the familiarity and comfort. I had spent so much time and effort preparing for this career that I decided to give research one last chance.

I enjoyed this job tremendously. Unfortunately, there were still more reasons to lose a job than those I'd already experienced. This time, the company decided to cease work in my therapeutic area. Strike three.

So, finally, I chose to actively seek a change, and I ultimately moved into project management. The desire for a more stable, or at least more fungible, career was the practical appeal. The professional appeal was the opportunity to interact with and learn from professionals working across the full spectrum of pharmaceutical development, from discovery to brand launch and life cycle management. I enjoy the broad perspective and jack-of-all trades nature of the job, and I hope it will be my last career change.

Some former colleagues ask, "So, you're not doing science anymore?" Nothing could be further from the truth. My job cannot be done well without understanding both the science and strategy behind the programs I manage. I use my training every day, and I will always be a scientist at heart. ■

Michael J. Orsini is a project manager in R&D strategy and planning at Bristol-Myers Squibb in Lawrenceville, New Jersey. Send your story to SciCareerEditor@aaas.org.

ILLUSTRATION: ROBERT NEUBECKER

Downloaded from http://science.sciencemag.org/ on May 26, 2016

Published by AAAS